NASA/DOD CONTROLS-STRUCTURES INTERACTION TECHNOLOGY 1989... 1 OF 6

NAS 1.55:3041 NASA CONFERENCE PUBLICATION 3041... NASA... JANUARY 29-FEBRUARY 2,1989

24X

SUPTDOCS/GPO

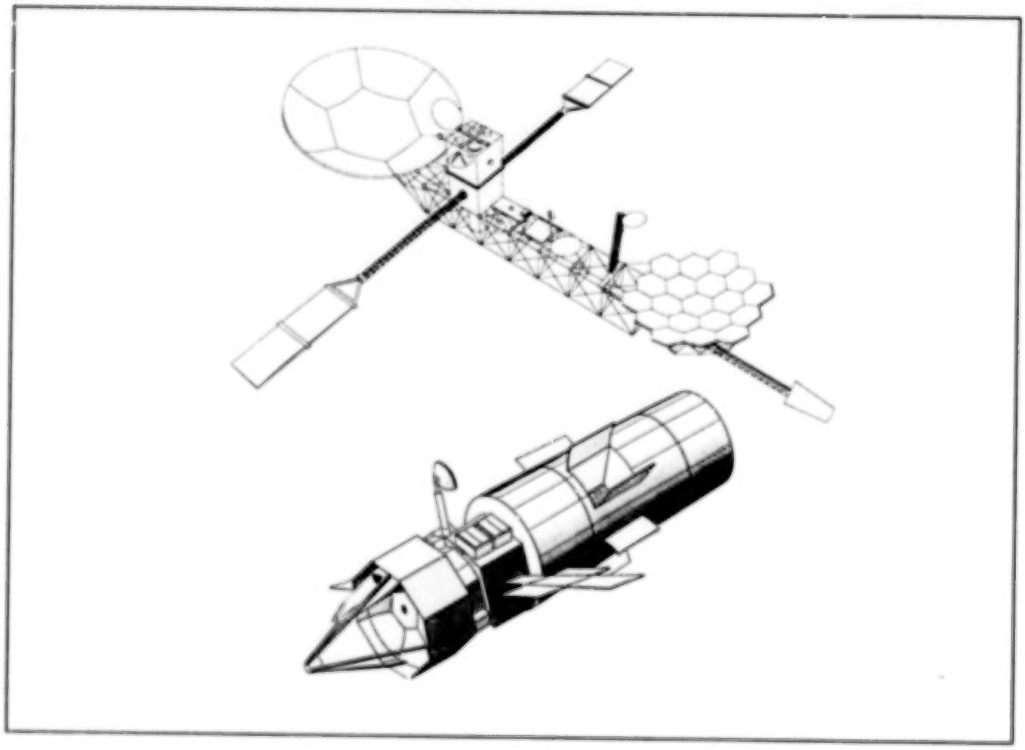
P. 0001-0078

SEP 2 3 1989

NAS1.55:3041

NASA Conference Publication 3041

NASA/DOD Controls-Structures Interaction Technology 1989



Proceedings of a conference held in
San Diego, California
January 29-February 2, 1989

NASA

COMPLETED

NASA Conference Publication 3041

NASA/DOD Controls-Structures Interaction Technology 1989

Compiled by
Jerry R. Newsom
NASA Langley Research Center
Hampton, Virginia

Proceedings of a conference cosponsored by NASA Langley Research Center, Hampton, Virginia, and Wright Research Development Center, Wright-Patterson Air Force Base, Ohio, and held in San Diego, California January 29–February 2, 1989

NASA
National Aeronautics and Space Administration
Office of Management
Scientific and Technical Information Division
1989

PREFACE

The National Aeronautics and Space Administration (NASA) and the Department of Defense (DOD) are actively involved in the development of a validated technology data base in the area of controls-structures interaction (CSI) for large flexible spacecraft. The generation of this technology is essential to the efficient and confident development of future spacecraft to meet stringent goals in performance and cost. Both NASA and DOD have programs in CSI, structural dynamics, and controls. The activities of these programs provide a systematic approach to address technology voids through development and validation of analytical tools, extensive ground testing of representative structures, and future in-space experiments for verification of analysis and ground test methods.

In order to promote timely dissemination of technical information acquired in these programs, the NASA Langley Research Center and the Wright Research Development Center alternately sponsor an annual conference to report to industry, academia, and government agencies on the current status of controls-structures interaction technology. This publication is a compilation of the papers presented at the third NASA/DOD CSI Technology Conference.

The use of trade names or manufacturers in this publication does not constitute an official endorsement of such products or manufacturers, either expressed or implied, by the National Aeronautics and Space Administration.

Jerry R. Newsom
Technical Program Chairman

CONTENTS

PREFACE iii

ATTENDEES ix

SYSTEMS AND CONCEPTS
William E. Layman, Chairman
Jet Propulsion Laboratory, Pasadena, CA

A SPACEBORNE OPTICAL INTERFEROMETER: THE JPL CSI MISSION FOCUS 1
R. A. Laskin

ZENITH STAR: A STRUCTURAL CONTROL CHALLENGE 17
L. A. Morine

PACOSS PROGRAM STATUS AND RESULTS 31
K. E. Richards, Jr.

VIBRATION ISOLATION VERSUS VIBRATION COMPENSATION ON MULTIPLE PAYLOAD PLATFORMS 67
S. W. Sirlin

GOES I-M AND BEYOND: SCIENCE REQUIREMENTS AND TECHNOLOGY CHALLENGES 83
William E. Shenk

ANALYSIS
Henry B. Waites, Chairman
NASA Marshall Space Flight Center, Huntsville, AL

CONTROLLED MULTIBODY DYNAMICS SIMULATION FOR LARGE SPACE STRUCTURES 91
J. M. Housner, S. C. Wu, and C. W. Chang

ELEMENT-SPECIFIC MODAL FORMULATIONS FOR LARGE-DISPLACEMENT MULTIBODY DYNAMICS 111
R. R. Ryan and H. H. Yoo

NONLINEAR AND DISTRIBUTED PARAMETER MODELS OF THE MINI-MAST TRUSS 131
Lawrence W. Taylor, Jr.

A DISTRIBUTED FINITE-ELEMENT MODELING AND CONTROL APPROACH FOR LARGE FLEXIBLE STRUCTURES 151
K. D. Young

EFFECTIVE TECHNIQUES FOR THE IDENTIFICATION AND ACCOMMODATION OF DISTURBANCES 163
C. D. Johnson

INTEGRATED DESIGN
Ernest S. Armstrong, Chairman
NASA Langley Research Center, Hampton, VA

MODELING AND CONTROL OF FLEXIBLE SPACE PLATFORMS WITH ARTICULATED PAYLOADS 181
Philip C. Graves and Suresh M. Joshi

DETECTION OF POTENTIAL SPACE STATION CONTROL/STRUCTURE INTERACTION WITH CO-ST-IN 211
Kelly Carney, Ron Graham, Doug Kyr, and Paul Blelloch

OPTIMIZATION OF THE STRUCTURAL AND CONTROL SYSTEM FOR LSS WITH REDUCED-ORDER MODEL 229
N. S. Khot

COMPUTATIONAL ARCHITECTURE FOR INTEGRATED CONTROLS AND STRUCTURES DESIGN 241
W. Keith Belvin and K. C. Park

CONTROLLER REDUCTION FOR EFFECTIVE INTERDISCIPLINARY DESIGN OF ACTIVE STRUCTURES 261
Mark J. Balas and Ralph Quan

RECENT EXPERIENCE IN SIMULTANEOUS CONTROL-STRUCTURE OPTIMIZATION 271
M. Salama, R. Ramaker, and M. Milman

GROUND TESTING
Jer-Nan Juang, Chairman
NASA Langley Research Center, Hampton, VA

A SURVEY OF EXPERIMENTS AND EXPERIMENTAL FACILITIES FOR ACTIVE CONTROL OF FLEXIBLE STRUCTURES 285
Dean W. Sparks, Jr., Garnett C. Horner, Jer-Nan Juang, and Gerhard Klose

NASA CSI SUSPENSION METHODS OVERVIEW 317
Stanley E. Woodard and Victor M. Cooley

AN AIR-BEARING WEIGHT OFFLOAD SYSTEM FOR GROUND TEST OF HEAVY LSS STRUCTURES 335
R. B. Rice

ASCIE: AN INTEGRATED EXPERIMENT TO STUDY CSI IN LARGE SEGMENTED OPTICAL SYSTEMS 349
Jean-Noel Aubrun and Kenneth R. Lorell

CSI SENSING AND CONTROL: ANALYTICAL AND EXPERIMENTAL RESULTS 363
J. L. Junkins, T. C. Pollock, and Z. H. Rahman

EXPERIMENTAL EVALUATION OF ACTIVE-MEMBER CONTROL OF PRECISION STRUCTURES 387
James Fanson, Gary Blackwood, and Cheng-Chih Chu

FLIGHT EXPERIMENTS
Major Al Janiszewski, Chairman
Wright Research Development Center/FIBGC, WPAFB, OH

CONTROLS, ASTROPHYSICS, AND STRUCTURES EXPERIMENT IN SPACE (CASES) 411
Henry B. Waites and John P. Sharkey

LACE FLIGHT DYNAMICS EXPERIMENT 427
Shalom Fisher

SPACE TRUSS ZERO GRAVITY DYNAMICS 445
Captain Andy Swanson

UNITED STATES AIR FORCE ACADEMY GET-AWAY-SPECIAL FLEXIBLE BEAM EXPERIMENT 459
Captain Keith W. Bubb, Major Steven E. Lamberson, and Captain Thomas A. Lash

SPECIAL TOPICS
L. Kevin S. Slimak, Chairman
AFAL/DYSS, Edwards AFB, CA

CSI TECHNOLOGY VALIDATION OF AN LSS GROUND EXPERIMENT FACILITY 475
S. J. Wang and D. B. Eldred

STRAIN AND DYNAMIC MEASUREMENTS USING FIBER OPTIC SENSORS EMBEDDED INTO GRAPHITE/EPOXY TUBES 497
D. W. DeHart, T. Doederlein, J. Koury, R. S. Rogowski, J. S. Heyman, and M. S. Holben, Jr.

INITIAL OPERATIONAL CAPABILITY OF THE ASTREX LARGE SPACE STRUCTURES TEST BED 507
1Lt. G. A. Norris

IN-HOUSE EXPERIMENTS IN LARGE SPACE STRUCTURES AT THE AIR FORCE WRIGHT AERONAUTICAL LABORATORIES' FLIGHT DYNAMICS LABORATORY 523
Robert W. Gordon, Umit Ozguner, and Steven Yurkovich

ATTENDEES

A. Louis Abrahamson
Bus. Phone: 804-898-3753
COMTEK
702 E. Woodland Road
Grafton, VA 23692

Joseph K. Alexander
Bus. Phone: 202-453-1430
NASA Headquarters
Code E
Washington, DC 20546

Gerry B. Andeen
Bus. Phone: 415-859-3165
SRI International
EL 160, SRI International
Menlo Park, CA 94025

Willard W. Anderson
Bus. Phone: 804-864-1718
NASA Langley Research Center
Mail Stop 479
Hampton, VA 23665-5225

Panos J. Antsaklis
Bus. Phone: 219-239-5792
University of Notre Dame
Dept. of Electrical & Computer Eng
Notre Dame, IN 46556

Ernest S. Armstrong
Bus. Phone: 804-864-4084
NASA Langley Research Center
Mail Stop 499
Hampton, VA 23665-5225

Jean-Noel Aubrun
Bus. Phone: 415-424-2748
Lockheed Palo Alto Research Lab.
O/92-30, B/250
3251 Hanover Street
Palo Alto, CA 94304

Fred Austin
Bus. Phone:
Grumman Aerospace Corporation
A08-35
Bethpage, NY 11714

Bharat Bagetalli
Bus. Phone: 518-387-7036
GE Corporate R&D
Room K1-3A32
Schenectady, NY 12301

Mark Balas
Bus. Phone: 303-492-3177
University of Colorado
Aerospace Engineering Sciences Dept.
Campus Box 429
Boulder, CO 80309-0429

Arun K. Banerjee
Bus. Phone:
Lockheed Missiles & Space Co.
62-18/104
Sunnyvale, CA 94089

Michael Barrett
Bus. Phone: 612-782-7286
Honeywell Systems & Research Ctr.
3660 Technology Drive
Minneapolis, MN 55418

Robin J. Bruno
Bus. Phone: 818-354-7586
Jet Propulsion Laboratory
Mail Stop 157-316
4800 Oak Grove Drive
Pasadena, CA 91109

Kelly Carney
Bus. Phone: 216-433-2386
NASA Lewis Research Center
Mail Stop 86-10
Cleveland, OH 44135

Che-Wei Chang
Bus. Phone: 804-864-4356
NASA Langley Research Center
Mail Stop 230
Hampton, VA 23665-5225

J. Michael Chapman
Bus. Phone: 206-773-9554
Boeing Aerospace Company
Mail Stop 82-97
P.O. Box 3999
Seattle, WA 98124

C. P. Chen
Bus. Phone: 202-453-1691
NASA Headquarters
Code EM
Washington, DC 20546

Jay C. Chen
Bus. Phone: 818-354-2717
Jet Propulsion Laboratory
Mail Stop 157-316
Pasadena, CA 91109

Cheng-Chih Chu
Bus. Phone: 818-354-7457
Jet Propulsion Laboratory
Mail Stop 198-326
4800 Oak Grove Drive
Pasadena, CA 91109

Kwang L. Chuang
Bus. Phone: 818-354-9360
Planning Research Corporation - JPL
Mail Stop 158-224
4800 Oak Grove Drive
Pasadena, CA 91109

Victor M. Cooley
Bus. Phone: 804-864-4345
NASA Langley Research Center
Mail Stop 230
Hampton, VA 23665-5225

Paul R. Corder
Bus. Phone: 409-880-8772
Lamar University
Dept. of Mechanical Engineering
P.O. Box 10028
Beaumont, TX 77710

Judy H. Cottle
Bus. Phone: 804-864-1604
NASA Langley Research Center
Mail Stop 469
Hampton, VA 23665-5225

Dennis C. Coyne
Bus. Phone: 617-272-1990
Kaman Sciences Corporation
83 Second Avenue
Burlington, MA 01803

James L. Fanson
Bus. Phone: 818-354-7014
Jet Propulsion Laboratory
Mail Stop 157-316
Pasadena, CA 91109

Charbel Farhat
Bus. Phone: 303-492-6838
University of Colorado
Ctr. for Space Structures & Controls
Campus Box 429
Boulder, CO 80309-0429

Shalom Fisher
Bus. Phone: 202-767-3914
Naval Research Laboratory
Code 8241
Washington, DC 20375-5000

Anthony Fontana
Bus. Phone: 804-864-6491
NASA Langley Research Center
Mail Stop 161
Hampton, VA 23665-5225

William Frank
Bus. Phone: 303-939-4468
Ball Aerospace Systems
P. O. Box 1062
Boulder, CO 80306

Joseph R. Freelin
Bus. Phone: 301-595-5500
Swales and Associates, Inc.
5050 Powder Mill Road
Beltsville, MD 20705

Jon-Shen Fuh
Bus. Phone: 203-243-7216
Kaman Aerospace Corporation
Old Windsor Road
Bloomfield, CT 06002

John A. Garba
Bus. Phone: 818-354-2085
Jet Propulsion Laboratory
Mail Stop 157-316
4800 Oak Grove Drive
Pasadena, CA 91109

Donald S. Gardiner
Bus. Phone: 801-251-3510
Hercules Inc.
P.O. Box 98
Magna, UT 84044

Joseph F. Garibotti
Bus. Phone: 714-545-8825
Ketema, Composite Materials Division
3611 South Harbor Boulevard
Suite 225
Santa Ana, CA 92704

Richard M. Gates
Bus. Phone: 206-773-9568
Boeing Aerospace Company
P. O. Box 3999
Mail Stop 82-97
Seattle, WA 98124

Robert L. Gates
Bus. Phone: 303-977-1038
Martin Marietta
P.O. Box 179
Denver, CO 80201

Robert Hayduk
Bus. Phone: 804-864-4323
NASA Langley Research Center
Mail Stop 230
Hampton, VA 23665-5225

John M. Hedgepeth
Bus. Phone: 805-684-6641
Astro Aerospace Corporation
6384 Via Real
Carpinteria, CA 93013

Maj. Terry D. Hinnerichs
Bus. Phone: 505-844-2986
AFWL/ARCD
Kirtland AFB, NM 87117

Robert E. Holman
Bus. Phone: 213-616-0902
Hughes Aircraft
Electro-Optical & Data Systems Group
P.O. Box 902, Mail Code EO/E1/D102
El Segundo, CA 90245

Garnett Horner
Bus. Phone: 804-864-6489
NASA Langley Research Center
Mail Stop 161
Hampton, VA 23665-5225

Jerrold M. Housner
Bus. Phone: 804-864-4322
NASA Langley Research Center
Mail Stop 230
Hampton, VA 23665-4322

Whittak H. Huang
Bus. Phone: 303-971-5825
Martin Marietta Astronautics
P.O. Box 179, MS L8005
Denver, CO 80201

B. Lee Huffman
Bus. Phone: 205-544-6481
Teledyne Brown Engineering
Cummings Research Park
MS 172
Huntsville, AL 35807

Capt. Robert Hunt
Bus. Phone: 505-844-1705
AFWL/ARCD
Kirtland AFB, NM 87117

K. Scott Hunziker
Bus. Phone: 206-773-9554
Boeing Aerospace Company
P. O. Box 3999
Mail Stop 82-97
Seattle, WA 98124

David C. Hyland
Bus. Phone: 407-729-2138
Harris Corporation
Mail Stop 22/4842
P. O. Box 94000
Melbourne, FL 32902

A. Dean Jacot
Bus. Phone: 206-773-4055
Boeing Aerospace Company
P.O. Box 3999, MS 82-24
Seattle, WA 98124

Andrew J. Kalish
Bus. Phone: 716-726-2484
Eastman Kodak Company
901 Elmgrove Rd., Bldg. 101
Rochester, NY 14653-9527

Karen E. Kane
Bus. Phone: 213-813-5909
TRW, Inc.
One Space Park, R4/1082
Redondo Beach, CA 90278

Claude R. Keckler
Bus. Phone: 804-864-1716
NASA Langley Research Center
Mail Stop 479
Hampton, VA 23665-5225

Leehyun Keel
Bus. Phone: 615-320-3268
Tennessee State University
Department of Electrical Engrg
3500 John A. Merritt Boulevard
Nashville, TN 37209-1561

Gary L. Ketner
Bus. Phone: 509-375-2399
Battelle PNL
P.O. Box 999, MS K5-22
Richland, WA 99352

Richard W. Key
Bus. Phone: 818-354-3060
Jet Propulsion Laboratory
Mail Stop 180-701
4800 Oak Grove Drive
Pasadena, CA 91109

Narendra S. Khot
Bus. Phone: 513-255-6992
AFWAL/FDSRA
WPAFB, OH 45433-6553

Taras Kiceniuk
Bus. Phone: 818-354-1940
Jet Propulsion Laboratory
Mail Stop 158-225
4800 Oak Grove Drive
Pasadena, CA 91109

David A. Kienholz
Bus. Phone: 415-494-7351
CSA Engineering, Inc.
560 San Antonio Road
Suite 101
Palo Alto, CA 94306-4682

Glen J. Kissel
Bus. Phone: 818-354-4379
Jet Propulsion Laboratory
Mail Stop 198-326
4800 Oak Grove Drive
Pasadena, CA 91109

Gerhard J. Klose
Bus. Phone: 818-354-8123
Jet Propulsion Laboratory
Mail Stop 158-224
4800 Oak Grove Drive
Pasadena, CA 91109

Chin-Po Kuo
Bus. Phone: 818-354-4246
Jet Propulsion Laboratory
Mail Stop 157-316
4800 Oak Grove Drive
Pasadena, CA 91109

Carolyn Major
Bus. Phone: 213-536-1891
TRW, Inc.
One Space Park, R9/2139
Redondo Beach, CA 90278

James W. Mar
Bus. Phone: 617-253-2426
Massachusetts Inst. of Technology
Dept. of Aero & Astro, R 33-303
Cambridge, MA 02139

Edward L. Marek
Bus. Phone: 505-844-3966
Sandia National Laboratories
P.O. Box 5800
Albuquerque, NM 87185

Virginia B. Marks
Bus. Phone: 804-864-1714
NASA Langley Research Center
Mail Stop 479
Hampton, VA 23665-5225

S. F. Masri
Bus. Phone: 213-743-2941
University of Southern California
Civil Engineering Department
B-VHE406
Los Angeles, CA 90089-0242

Bruce W. Maxfield
Bus. Phone: 415-568-7720
Innovative Sciences Inc.
400 Hester Street
San Leandro, CA 94577

James D. McAleese
Bus. Phone: 216-433-5417
NASA Lewis Research Center
Mail Stop 86-2
Cleveland, OH 44135

Dennis J. McGovern
Bus. Phone: 714-896-1002
McDonnell Douglas Space Systems Co.
5301 Bolsa Avenue
Huntington Beach, CA 92647-2048

Todd L. Mendenhall
Bus. Phone: 213-813-5852
TRW Dynamics
One Space Park, R4/1050 TRW
Redondo Beach, CA 90278

David W. Miller
Bus. Phone: 617-253-3288
Massachusetts Inst. of Technology
Room 37-355
Cambridge, MA 02139

Mark H. Milman
Bus. Phone: 818-354-7548
Jet Propulsion Laboratory
Mail Stop 198-326
4800 Oak Grove Drive
Pasadena, CA 91109

D. Lewis Mingori
Bus. Phone:
University of California-Los Angeles
Dept. of Mech., Aero., & Nuclear Eng.
5731 Boelter Hall
Los Angeles, CA 90024

Michael C. O'Neal
Bus. Phone: 818-354-2875
Jet Propulsion Laboratory
Mail Stop 158-224
4800 Oak Grove Drive
Pasadena, CA 91109

David J. Olkowski
Bus. Phone: 805-275-5420
Air Force Astronautics Laboratory
AFAL/VS
Edwards AFB, CA 93523

Randall Olsen
Bus. Phone:
Chronos Research Laboratories, Inc.
4186 Sorrento Valley Road
Suite H
San Diego, CA 92024

Umit Ozguner
Bus. Phone: 614-292-5940
The Ohio State University
Dept. of Electrical Engineering
2015 Neil Avenue
Columbus, OH 43210

Young H. Pak
Bus. Phone: 714-896-4682
McDonnell Douglas Astronautics Co.
5301 Bolsa Avenue, A3-218, 13-3
Huntington Beach, CA 92649

Richard S. Pappa
Bus. Phone: 804-864-4321
NASA Langley Research Center
Mail Stop 230
Hampton, VA 23665-5225

K. C. Park
Bus. Phone: 303-492-6330
University of Colorado
Ctr. for Space Structures & Controls
Campus Box 429
Boulder, CO 80309-0429

Jerome Pearson
Bus. Phone: 513-255-6622
AFWAL/FDSG
WPAFB, OH 45433-6553

Lee D. Peterson
Bus. Phone: 505-846-6115
Sandia National Laboratories
P.O. Box 5800
Albuquerque, NM 87185

Christopher M. Piaszczyk
Bus. Phone: 516-575-3653
Grumman Aerospace Corporation
MS A07-25
Bethpage, NY 11714

Edward A. Pinsley
Bus. Phone: 203-243-7228
Kaman Aerospace
P.O. Box 2, MS Dept. 431/B21
Old Windsor Road
Bloomfield, CT 06002

Larry D. Pinson
Bus. Phone: 804-864-2934
NASA Langley Research Center
Mail Stop 242
Hampton, VA 23665-5225

Heidi M. Rosner
Bus. Phone: 213-813-8906
TRW
One Space Park, R4/2190
Redondo Beach, CA 90278

Linda B. Rowell
Bus. Phone: 804-864-1718
NASA Langley Research Center
Mail Stop 479
Hampton, VA 23665-5225

Robert R. Ryan
Bus. Phone: 313-994-3800
Mechanical Dynamics, Inc.
3055 Plymouth Road
Ann Arbor, MI 48105

Moktar Salama
Bus. Phone: 818-354-2874
Jet Propulsion Laboratory
Mail Stop 157-316
4800 Oak Grove Drive
Pasadena, CA 91109

Paul A. Sanneman
Bus. Phone: 818-354-9723
Jet Propulsion Laboratory
Mail Station T1201
4800 Oak Grove Drive
Pasadena, CA 91109

Celeste M. Satter
Bus. Phone: 818-354-9246
Jet Propulsion Laboratory
Mail Stop 157-410
4800 Oak Grove Drive
Pasadena, CA 91109

Robert Scheid
Bus. Phone: 818-354-7548
Jet Propulsion Laboratory
Mail Code 198-326
4800 Oak Grove Drive
Pasadena, CA 91109

Eric Schmitz
Bus. Phone: 303-971-7144
Martin Marietta Astronautics Group
MS 4443
P. O. Box 179
Denver, CO 80201

Jeffrey F. Schoenwald
Bus. Phone: 805-373-4236
Rockwell International Science Ctr.
P.O. Box 1085
Thousand Oaks, CA 21360

S. R. Schubert
Bus. Phone:
TRW, Inc.
Mail Code R4-2198
One Space Park
Redondo Beach, CA 90278

Kenneth P. Schultz
Bus. Phone: 713-333-6690
Lockheed Engineering and Sciences
Mail Code B-14
P. O. Box 58561
Houston, TX 77258

Joe Sciabica
Bus. Phone: 805-275-5334
Air Force Astronautics Laboratory
AFAL/VSSC
Edwards AFB, CA 93523-5000

Keto Soosaar
Bus. Phone: 617-354-1522
Photon Research Associates
Cambridge Research Division
1033 Massachusetts Avenue
Cambridge, MA 02138

Jimmy E. Sorrells
Bus. Phone: 205-837-9230
Dynetics, Inc.
1000 Explorer Boulevard
Huntsville, AL 35806

James J. Spaeth
Bus. Phone: 714-896-2979
McDonnell Douglas Space Systems Co.
Mail Station 11-2
5301 Bolsa Avenue
Huntington Beach, CA 92647-2048

John T. Spanos
Bus. Phone: 818-354-6572
Jet Propulsion Laboratory
Mail Stop 198-326
4800 Oak Grove Drive
Pasadena, CA 91109

Dean W. Sparks, Jr.
Bus. Phone: 804-864-4349
NASA Langley Research Center
Mail Stop 230
Hampton, VA 23665-5225

Victor A. Spector
Bus. Phone: 213-536-2090
TRW Inc.
MS R9/2163
One Space Park
Redondo Beach, CA 90278

James L. Starr
Bus. Phone: 213-336-1219
Aerospace Corporation
2350 E. El Segundo Boulevard
El Segundo, CA 90245-4691

Robert R. Strunce
Bus. Phone: 703-284-1823
United Technologies Optical Systems
2111 Wilson Boulevard, Suite 800
Arlington, VA 22201

John M. Stubstad
Bus. Phone: 213-336-6473
Aerospace Corporation
P.O. Box 92957, MS M4-920
Los Angeles, CA 90009-2957

John Sudey, Jr.
Bus. Phone: 301-286-8908
NASA Goddard Space Flight Center
Mail Code 716
Greenbelt, MD 20771

Capt. Andrew D. Swanson
Bus. Phone: 513-255-5236
AFWAL/FDSGC
WPAFB, OH 45433-6553

Lawrence W. Taylor, Jr.
Bus. Phone: 804-864-4040
NASA Langley Research Center
Mail Stop 489
Hampton, VA 23665-5225

Lt. Col. David A. Wagie
Bus. Phone: 719-472-3471
USAFA/DFAS
USAF Academy, CO 80840-5701

Henry B. Waites
Bus. Phone: 205-544-1441
NASA Marshall Space Flight Center
Mail Stop ED-12
Marshall Sp. Flt. Cntr, AL 35812

Joseph E. Walz
Bus. Phone: 804-864-4053
NASA Langley Research Center
Mail Stop 499
Hampton, VA 23665-5225

Shyh J. Wang
Bus. Phone: 818-354-7288
Jet Propulsion Laboratory
Mail Stop 198-326
Pasadena, CA 91109

Lt. John Ward
Bus. Phone: 805-275-5205
AFAL/VSSS
Edwards AFB, CA 93523-5000

Capt. Steven G. Webb
Bus. Phone: 719-472-3859
USAF Academy
USAFA/DFEM
USAF Academy, CO 80840

Raymond V. Welch
Bus. Phone: 301-428-6449
Fairchild Space Company
Mail Stop D-4
Germantown, MD 20874

Bong Wie
Bus. Phone: 512-471-5322
University of Texas at Austin
Department of ASE/EM
Austin, TX 78712

James L. Williams
Bus. Phone: 804-864-4022
NASA Langley Research Center
Mail Stop 499
Hampton, VA 23665-5225

Jim Wilson
Bus. Phone: 602-561-3253
Honeywell, Inc.
Box 52199
Pheonix, AZ 85072

William P. Witt
Bus. Phone: 202-693-1568
SDIO T/DE
SDIO TIDE The Pentagon
Washington, DC 20301

Stanley E. Woodard
Bus. Phone: 804-864-4358
NASA Langley Research Center
Mail Stop 230
Hampton, VA 23665-5225

A SPACEBORNE OPTICAL INTERFEROMETER: THE JPL CSI MISSION FOCUS

R. A. Laskin
Jet Propulsion Laboratory
California Institute of Technology
Pasadena, California

3rd Annual NASA/DoD CSI Conference
San Diego, California
January 29 - February 2, 1989

The research described in this paper was performed by the Jet Propulsion Laboratory, California Institute of Technology, under contract with the National Aeronautics and Space Administration.

INTRODUCTION

The JPL Control Structure Interaction (CSI) program is part of the larger NASA-wide CSI Program and as such is a focused technology effort in intellectual partnership with the Langley Research Center and the Marshall Space Flight Center. NASA's CSI Program is managed from the Office of Aeronautics and Space Technology (OAST) by the Materials and Structures Division. OAST is specifically focusing CSI technology to enable or enhance classes of missions which are supported by NASA's Office of Space Science and Applications (OSSA). OAST and OSSA are coordinating to assure direct applicability of the CSI effort to future missions.

Within this larger context, the JPL CSI program will emphasize technology for systems that demand micron or sub-micron level control, so-called Micro-Precision Controlled Structures (u-PCS). The development of such technology will make it practical to fly missions with large optical or large precision antenna systems. In keeping with the focused nature of the desired technology, the JPL approach is to identify a focus mission, develop the focus mission CSI system design to a preliminary level, and then use this design to drive out requirements for CSI technology development in the design and analysis, ground test bed, and flight experiment areas.

- **JPL CSI PROGRAM**
  - **PART OF THE NASA-WIDE CSI PROGRAM**
  - **PARTNERSHIP WITH NASA LANGLEY RESEARCH CENTER AND NASA MARSHALL SPACE FLIGHT CENTER**
  - **EMPHASIS ON MICRO-PRECISION CONTROLLED STRUCTURES (μ-PCS)**
    - **ENABLING FOR CLASS OF LARGE OPTICAL SYSTEMS**
    - **ENHANCING FOR LARGE PRECISION ANTENNA SYSTEMS**
- **STRATEGY**
  - **IDENTIFY A JPL CSI FOCUS MISSION**
  - **USE THE FOCUS MISSION TO ESTABLISH TECHNOLOGY DEVELOPMENT REQUIREMENTS**
    - **REQUIREMENTS FOR GROUND TEST BED**
    - **REQUIREMENTS FOR DESIGN/ANALYSIS TOOLS**
    - **REQUIREMENTS FOR THE CSI DESIGN ENVIRONMENT**
    - **REQUIREMENTS FOR FLIGHT EXPERIMENTS**

CSI FOCUS MISSION IDENTIFICATION

In the intial phase of choosing a focus mission a number of potential future missions were under consideration. These included:

1. Precision Optical Interferometers such as
   COSMIC - Coherent Optical System of Modular Imaging Collectors
   OSI - Optical Space Interferometer
   POINTS - Precision Optical Interferometry in Space
2. Large Segmented Reflectors such as
   LDR - Large Deployable Reflector
   AST - Advanced Space Telescope
3. Multiple Payload Platforms such as evolutionary versions of
   EOS - Earth Observing System
   SSF - Space Station Freedom
4. Large Telescopes with Monolithic Primaries such as
   ATF - Astrometric Telescope Facility
   CIT - Circumstellar Imaging Telescope
5. Large Space Antennas such as MSS (Mobile Satellite System)
6. Flexible Space Manipulators for use on space platforms

Some of these and others are discussed in the References.

The criteria for selection of the focus mission are listed on the chart below. Particular care had to be exercised to ensure that the last two criteria could be satisfied simultaneously.

- **MISSIONS CONSIDERED**
  - **PRECISION OPTICAL INTERFEROMETERS (COSMIC, OSI, POINTS)**
  - **SEGMENTED REFLECTORS (LDR, ADVANCED SPACE TELESCOPE)**
  - **MULTIPAYLOAD PLATFORMS (EOS, SSF, EVOLUTIONARY EOS & SS)**
  - **LARGE TELESCOPES WITH MONOLITHIC PRIMARIES (ATF, CIT)**
  - **LARGE SPACE ANTENNAS (MSS)**
  - **FLEXIBLE SPACE MANIPULATORS**
- **CRITERIA FOR SELECTION**
  - **IMPORTANCE OF MISSION TO NASA**
  - **MISSION'S NEED FOR CSI TECHNOLOGY**
  - **ABILITY TO DRIVE DEVELOPMENT OF GENERAL PURPOSE CSI TECHNOLOGY**
  - **CONSISTENT WITH JPL EMPHASIS ON μ-PCS**
- **SELECTION**
  - **FOCUS MISSION INTERFEROMETER (FMI)**

MISSION CHARACTERISTICS MATRIX

The rationale for choosing a spaceborne optical interferometer as the focus mission can be gleaned from the table below. All of the missions listed were judged to be of significant importance to NASA's future plans for space science and exploration. Likewise all the missions were seen as benefiting from CSI technology development, although the benefits are least compelling for multiple payload platform payloads such as large telescopes with monolithic primaries.

The key to choosing the focus mission interferometer (FMI) lies in the column of the table labeled "Positional Accuracy". Optical interferometers, with positional control tolerances on the order of one nanometer over baselines of 10 to 30 meters and up, are most clearly consistent with JPL's emphasis on u-PCS. In addition the FMI configuration that has been evolved has numerous articulating and translating controlled elements. In this respect it is similar to a multiple payload platform (MPP) which was judged to be the second most fertile JPL CSI focus mission. Hence the FMI would seem to be a good means of promoting generic CSI technology development.

FLIGHT EXPERIMENT	SIZE	OPERATING WAVELENGTH	POSITIONAL ACCURACY	ANGULAR ACCURACY	DISTURBANCE ENVIRONMENT
INTERFERO-METERS	10 to 30 m baseline	0.1 to 1.5 microns (UV to IR)	10^{-9} meter	Optics: 10 milliarcsec Siderostats: 0.1 arcsec	LEO: Drag, Thermal Stresses, Gravity Gradient, Internal
SEGMENTED REFLECTORS	20 m across	30 microns (LDR) 0.5 micron (AST)	5×10^{-7} meter 10^{-8} meter	<.05 arcsec (LDR) <.001 arcsec (AST)	LEO
MULTI-PAYLOAD PLATFORMS	9 to 150 m	Not Applicable	$\sim 10^{-3}$ meter	3 to 5 arcsec	LEO
MPP PAYLOADS	8 to 21.3 m length 1.5 to 2.5 m dia	0.4 to 0.9 micron (Visible)	2×10^{-6} meter to 3×10^{-4} meter	.01 to .50 arcsec for several hours	LEO
LARGE ANTENNAS	5 to 200 m dia	8.3 to 200 mm (K,X,C, and S Bands)	$\sim 10^{-4}$ meter	14 to 430 arcsec	GEO
LARGE MANIPULATOR ARMS	10 to 50 m	Not Applicable	10^{-3} meter	Not Applicable	LEO

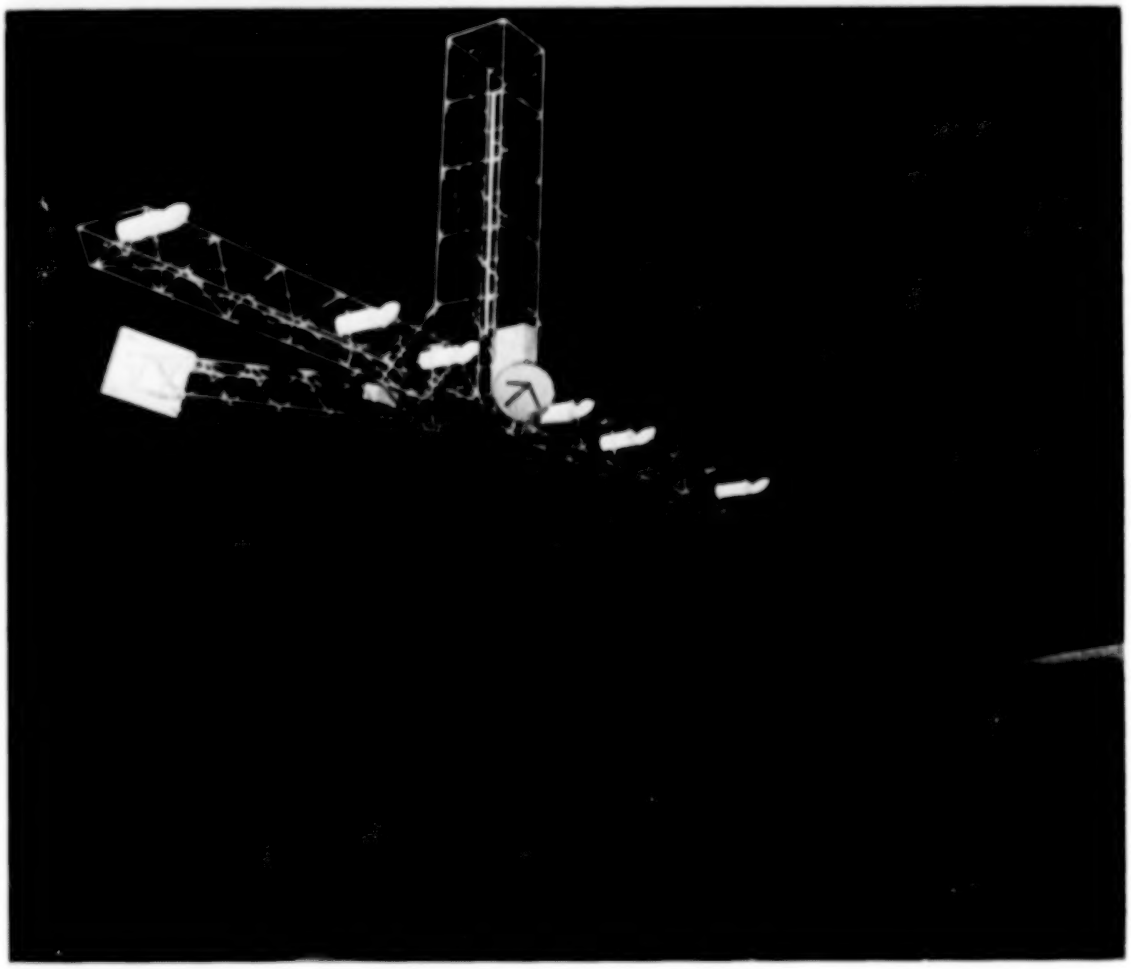
BEST COPY AVAILABLE

THE FOCUS MISSION INTERFEROMETER (FMI)

Shown below is an artist's conception of the FMI in its 750 km orbit around the earth. An optical interferometer is an instrument that utilizes a number of distinct telescopes, each of modest aperture, whose outputs are combined in such a way as to produce an effective aperture equivalent to the largest baseline distance between telescopes. In the case of the FMI, six telescopes are used in an extremely sparse linear array. The telescope outputs are combined in pair-like fashion such that the FMI operates as three distinct two telescope interferometers.

An optical interferometer can be used for high resolution imaging as well as extremely precise astrometry (astrometry is the mapping of stellar positions in the sky). When used for imaging, the FMI's effective baseline of 24 meters would give it roughly 10 times the resolving power of the Hubble Space Telescope. This translates into a resolution of 5 milliarcseconds.

The basic layout of the FMI was inspired by the work of Mike Shao of the Harvard Smithsonian Astrophysical Observatory. Dr. Shao currently has in operation, on Mount Wilson in Southern California, a ground based version of the FMI.

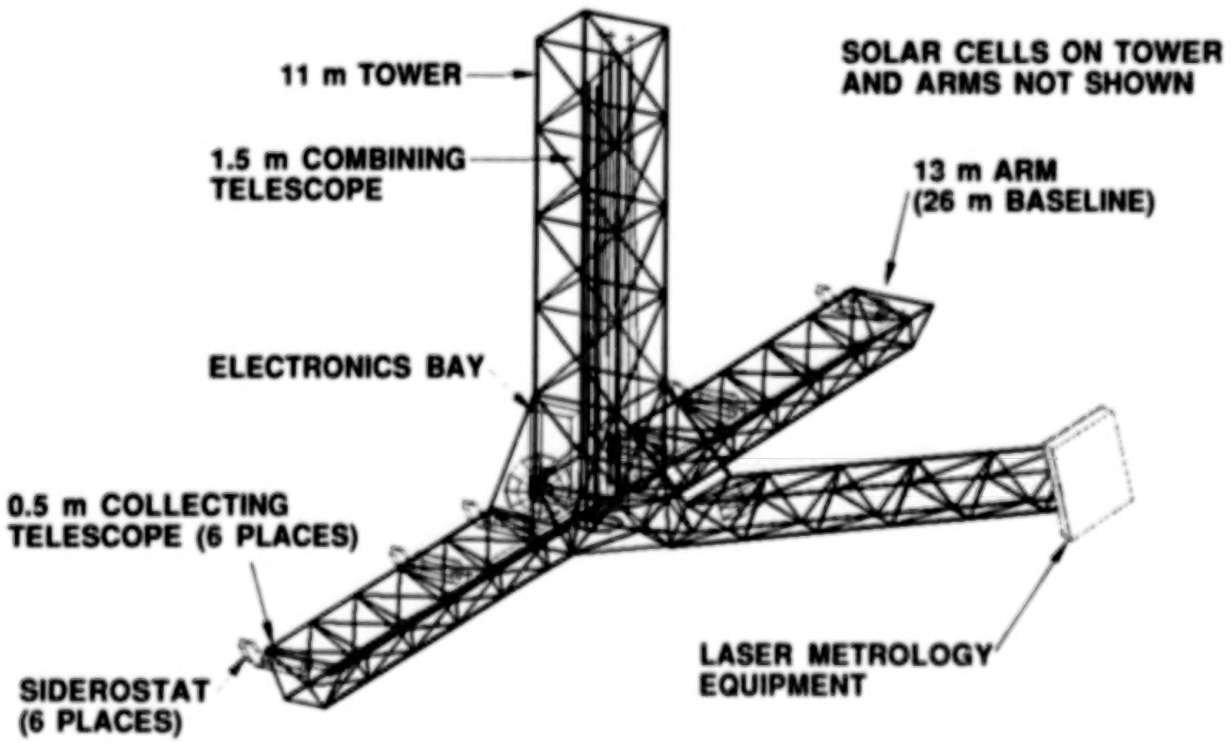


BEST COPY AVAILABLE

FMI CONFIGURATION

The line rendering below shows the essential features of the FMI. The six 0.5 meter aperture collecting telescopes are arrayed along the FMI's two 13 meter "arms". In front of each telescope is an appropriately sized flat mirror called a siderostat whose function it is to steer stellar photons into the telescope. Each siderostat is articulated in two axes, $\pm$ 20 degrees about the axis of the telescope and $\pm$ 5 degrees about an axis parallel to the arms. Hence the siderostats can expose the FMI to a 40 by 20 degree field of view without any attitude motion of the overall system. When a pair of siderostats on one of the three interferometers rotates about the axes of its respective collecting telescopes and "looks off to the side", it is effectively reducing the baseline of that interferometer. In this way all baselines intermediate in length between those of the inner and outer interferometers can be synthesized. Combining this effect with rotation of the system around the target line-of-sight allows a filled aperture of diameter equal to the largest baseline to be synthesized. This is in fact the mode in which the FMI would be operated for stellar imaging.

Other FMI features of note are the 11 meter "tower" that houses the combining telescope and the similarly sized laser metrology boom. A very precise laser metrology system is necessary to measure the individual interferometer baselines as well as the internal optical pathlengths through the system.



OPERATIONAL SCENARIO - ASTROMETRY MODE

The mode in which the FMI would be operated for stellar imaging was very briefly described on the preceding page. The operational mode for stellar astrometry is at once more straightforward than for imaging and at the same time places tighter CSI requirements on the FMI. Hence it is described in greater detail here.

The general procedure discussed below is one of acquiring guide stars with the two inner interferometers and then mapping target stars relative to the guide stars within the 20 by 40 degree target field using the outer, highest resolution, interferometer. By proceeding from target field to target field, with the appropriate angular overlap, the entire sky can be mapped. In fact the entire procedure must be accomplished twice: once as described and then again with the baselines rotated by 90 degrees around the tower axis. This is due to the fact that, as is explained in the ensuing pages, the FMI, with its linear interferometric array, is fundamentally a one axis machine capable of measuring angles about only a single axis when in a given orientation.

One of the things, besides the extreme precision, that makes the astrometry mode so challenging for CSI is the timeline on which it is to be accomplished. Target star acquisitions are expected to occur at roughly 40 second intervals and over siderostat slew angles of up to 40 degrees, thus driving structural settling time requirements.

1. **SLEW SYSTEM TO 10° x 40° TARGET FIELD**
2. **ACQUIRE FIRST GUIDE STAR WITH INTERFEROMETERS A, B, & C**
3. **TRUE UP METROLOGY SYSTEM**
4. **ACQUIRE SECOND GUIDE STAR WITH INTERFEROMETER B**
5. **ACQUIRE FIRST TARGET STAR WITH INTERFEROMETER A**
6. **ACQUIRE SECOND TARGET STAR WITH INTERFEROMETER A**
7. **REPEAT FOR N TARGETS WITHIN 20° x 40° TARGET FIELD**
8. **SLEW SYSTEM TO NEXT TARGET FIELD**
9. **REPEAT FOR M TARGET FIELDS**

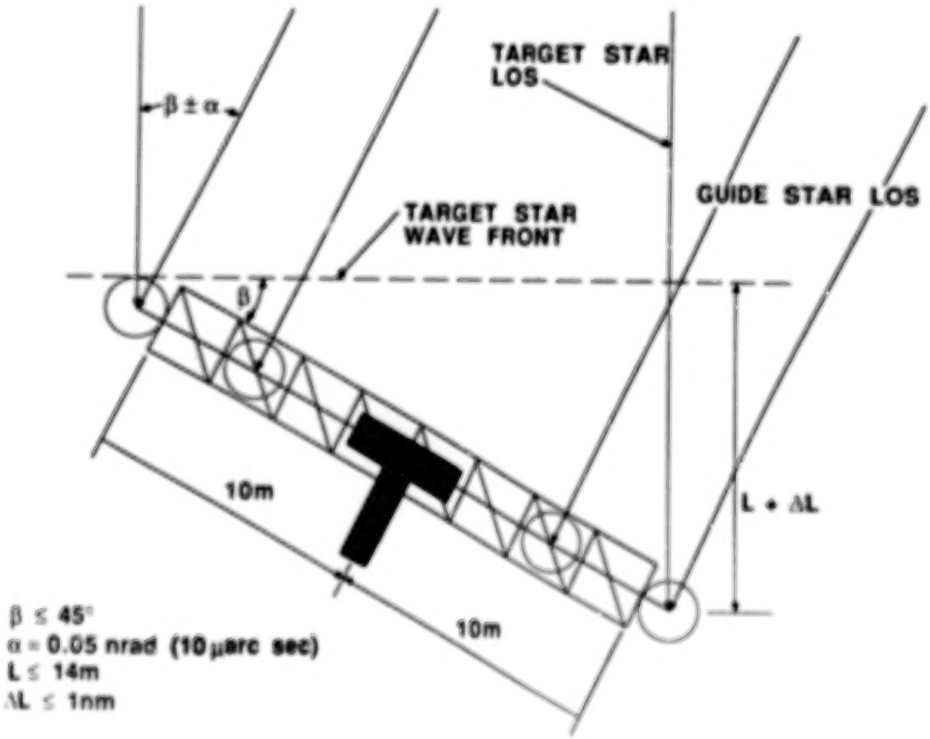
FMI - FUNDAMENTAL ACCURACY REQUIREMENT FOR ASTROMETRY

The figure below, along with the one on the next page, illustrates the way in which an optical interferometer can measure angles between stars for astrometry. For the sake of simplicity, only two interferometers are shown. Each of them is first commanded to lock on to a guide star. For an interferometer, "locking on" means more than angular acquisition of a star by both siderostats. In addition the two wavefronts, one from each collecting telescope, must be combined on the interferometric focal plane where fringes are produced. The object is to track the "zero fringe" which results when the optical pathlengths from the star to the focal plane coming through each side of the interferometer are equal.

Once guide star acquisition has been accomplished, the siderostats of the "science" interferometer (in this case the outer interferometer) are slewed to acquire a target star. If the target star is an angle beta from the guide star, and if the baselines are precisely perpendicular to the guide star line-of-sight, then a differential path length of

$$L = \text{Baseline} * \sin(\text{beta})$$

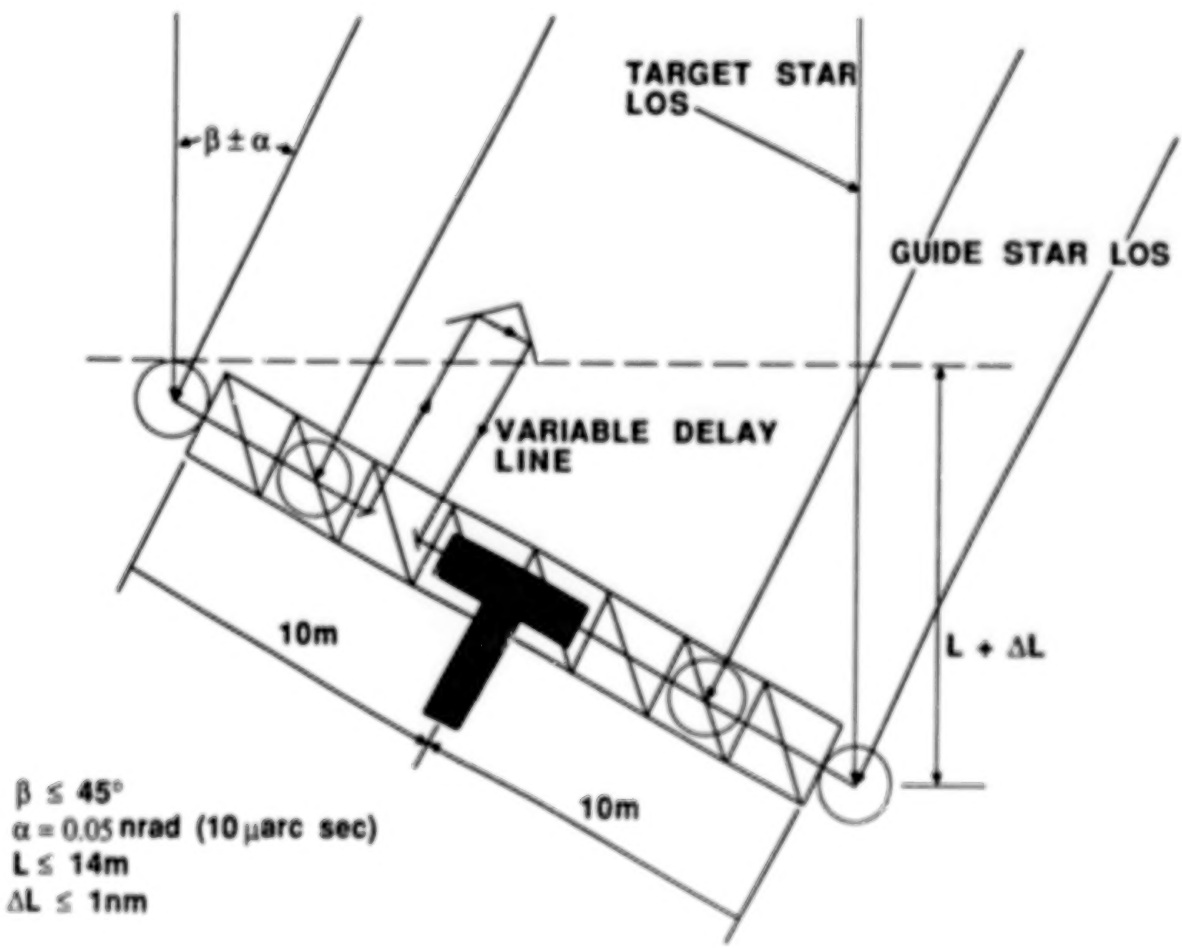
will exist across the science interferometer. The instrument is able to measure the length, L, and in this way the angle, beta, can be derived. The manner in which L is measured is described on the next page. Note that if L is measured to an accuracy of, dL = 1 nm, then the angle beta can be solved to an accuracy of, alpha = dL/Baseline = 10 microarcsecs.



INTERFEROMETRIC PATHLENGTH COMPENSATION

What remains is to describe the manner in which the differential pathlength, L, is measured. This is fairly straightforward. Internal to each interferometer is an optical element, variously known as a "trolley" or a "trombone" or a "delay line", which translates along a track and is capable of changing the optical pathlength along one leg of the interferometer. The position of this delay line is monitored, to nanometer accuracy, by the internal metrology system. Thus when the science interferometer is slewed to the target star and locked onto the target star's zero fringe, the internal metrology system is all the while measuring the distance that the trolley had to move in order to effect zero fringe acquisition. This distance is precisely the differential pathlength, L.

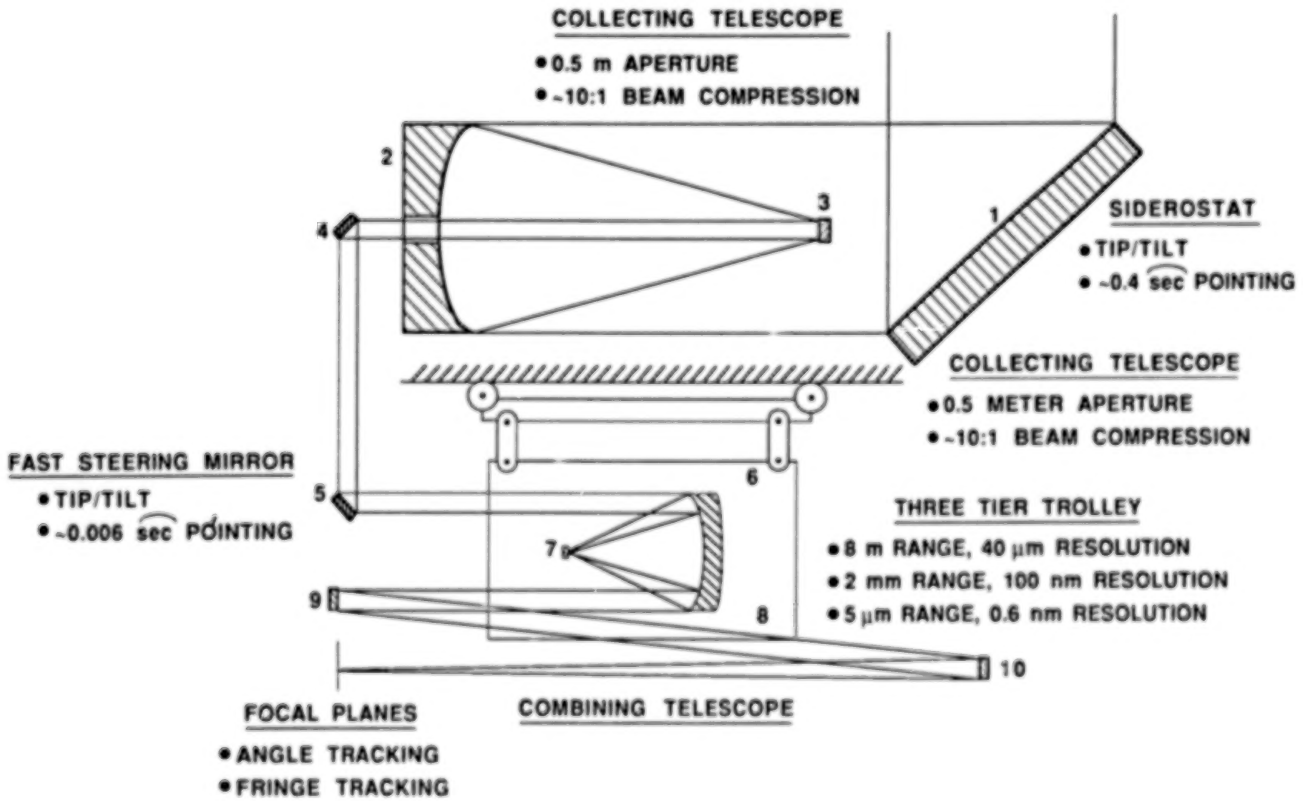
Note that in order to solve the equation (previous page) for beta, it is necessary to know not only L but also the baseline. This is what necessitates the external metrology system mounted on the metrology boom.



SIMPLIFIED FMI OPTICAL SCHEMATIC

A schematic representation of one leg of one of the FMI's interferometers is pictured below. Photons will encounter at least ten optical surfaces before reaching the focal planes, which will put a premium on optical coating technology, particularly if ultraviolet science is a requirement.

Preliminary control requirements on the positioning and articulation of the optical elements are listed. The 6 milliarcsec fast steering mirror spec looks relatively innocuous next to the sub-nanometer requirement on trolley position. Note that the trolley consists of three levels of control: a "boxcar" on a track driven by a timing belt for gross positioning, a voice coil actuated flexure stage for intermediate accuracy, and a piezoelectrically driven vernier mirror for fine control. Although one nanometer positional measurement capability would be necessary to support 10 uarcsec astrometry, it is likely that tolerances on positioning control could be relaxed to the sub 10 nm level.



ON-ORBIT DISTURBANCE SOURCES

Although the FMI will be exposed to the LEO orbital environment, it is expected that the most stressing disturbances to the control system will be generated on board the vehicle itself. In fact nonlinearities and parasitic forces/torques in control system prime movers will likely dominate. Thus far preliminary investigation has shown that reaction wheel imbalance forces, from Hubble Space Telescope class wheels, result in 1 to 2 micron open loop pathlength error response. This response is rather broadband, out to the 50 - 100 Hz region, and hence the higher harmonics can be expected to be beyond the trolley control loops ability to compensate. Some means of structural disturbance suppression would seem to be indicated.

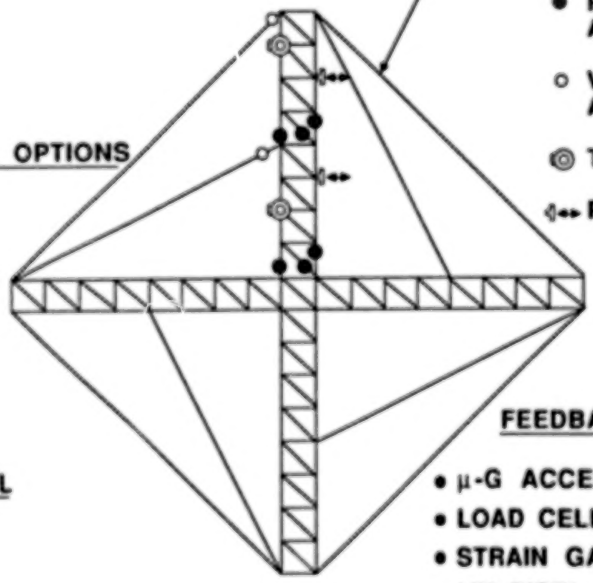
The environmental disturbances all occur at low frequency and so the expectation would normally be that they are easily compensated by the optical positioning/articulation control loops. However, very little is known about the sub-micron regime with which we are dealing. It is quite possible that phenomena such as thermal "snapping" in a joint dominated structure such as the FMI could present the CSI system with a low, but significant, level of background structural vibrations.

- **ORBITAL ENVIRONMENT**
  - **GRAVITY GRADIENT**
  - **THERMAL GRADIENTS**
  - **AERO - DRAG**
- **ON-BOARD ENVIRONMENT**
  - **REACTION WHEELS/CMG's**
  - **SIDEROSTATS**
    - **MOTOR COGGING, RIPPLE, AND IMBALANCE**
    - **BEARING NOISE**
    - **SLEW REACTION TORQUES**
  - **TROMBONES**
    - **NONLINEARITIES**
    - **SLEW REACTION FORCES**
    - **MOTOR AND BEARING NOISE**
  - **TAPE RECORDERS**
    - **START/STOP TRANSIENTS**
    - **MECHANISM NOISE**

CSI STRUCTURAL CONTROL HARDWARE SYSTEM BUILDING BLOCKS

To achieve the levels of optical surface control required by the FMI will require great resourcefulness in the CSI system. We expect to reach deep into the CSI bag of tricks for design solutions. Some of the hardware "tricks" that we are considering are delineated below.

At this point we have yet to make the system and component trades necessary to arrive at a strawman CSI system design. We are confident, however, that the design that emerges will be comprised of a combination of high bandwidth controlled optical elements and active/passive structural control and isolation. Such a design exhibits the essential features of the CSI problem. Hence, at this early stage at least, we are satisfied that we have a focus mission capable of driving generic CSI technology development.



PASSIVE DAMPING OPTIONS

- VISCOELASTIC
- VISCOUS

VIBRATION ISOLATION OPTIONS

- MAGNETIC
- PIEZOELECTRIC
- ELECTRODYNAMIC
- VISCOUS
- ELASTOMERIC

CONTROL ACTUATOR OPTIONS

- PIEZO/INCH WORM ACTUATORS
- VOICE COIL/SCREW JACK ACTUATORS
- TORQUE WHEEL ACTUATORS
- PROOF MASS ACTUATORS

STRUCTURAL CONTROL REQUIREMENTS

300 μm, DC
3μm, 1 Hz
30 nm, 10 Hz
0.3 nm, 100 Hz AND ABOVE
(REPRESENTS ~12 μ-G LEVEL)

FEEDBACK SENSOR OPTIONS

- μ-G ACCELEROMETERS
- LOAD CELL FORCE SENSORS
- STRAIN GAUGE FORCE/DISPL SENSORS
- LIN DISPL VOLT TRANSDCRS
- CAPACITIVE DISPL SENSORS
- LASER METROLOGY DISPL SENSORS
- EDDY CURRENT RATE SENSORS
- ANGLE RATE/ACCELERATION SENSORS

FMI - MAJOR ISSUES

There are several major issues that face the development of the FMI design in the months ahead. The high level CSI system trades first need to be accomplished. These trades will involve determination of the proper mix of vibration compensation, vibration suppression, and vibration isolation for the problem at hand. Sirlin discusses the considerations involved in making these high level trades for multiple payload platform systems in another paper presented at this conference (see Reference).

The metrology system certainly represents a critical area with bearing on the feasibility of the FMI. Since there is virtually no hope of implementing an absolute metrology system with sub-nanometer capability, the realizability of a relative system will be addressed. Such a system will demand an initial calibration of the interferometer baselines, based on stellar observations, before operation can commence. It is important to point out that our interest in metrology lies mainly in establishing the feasibility of using this technology on the FMI. Once this has been established we will focus our attention on CSI related issues like the use of a metrology system in a closed loop setting.

Component level trades and the issue of actuator/sensor placement will be addressed following completion of the system level trades. Plans call for the FMI to be at a preliminary design stage in the May/June 1989 timeframe.

- **SYSTEM TRADES**
  - **VIBRATION COMPENSATION**
    - **HIGH BANDWIDTH OPTICAL ELEMENT CONTROL**
    - **ACTUATOR/SENSOR NONCOLLOCATION**
  - **VIBRATION SUPPRESSION & DISTORTION CORRECTION**
    - **ACTIVE STRUCTURAL CONTROL**
    - **PASSIVE DAMPING**
  - **VIBRATION ISOLATION**
    - **ACTIVE ISOLATORS**
    - **PASSIVE ISOLATORS**
- **METROLOGY SYSTEM**
  - **SUBNANOMETER RELATIVE POSITION MEASUREMENT**
  - **SYSTEM ARCHITECTURE IN A CLOSED-LOOP SETTING**
- **COMPONENT LEVEL TRADES**
  - **ACTUATOR & SENSOR TYPES**
  - **DAMPER TYPES**
  - **ISOLATOR TYPES**
- **ACTUATOR/SENSOR PLACEMENT**

SUMMARY AND CONCLUSIONS

The JPL CSI team is concentrating its efforts on designing the control/structure system for a large spaceborne interferometer. The Focus Mission Interferometer will be carried to a preliminary design level in order to drive CSI technology development requirements in the principal analysis, software, and hardware disciplines and to shape the process of developing the new CSI design methodology within which the disciplines fit.

In addition it is intended that the FMI will serve an on-going purpose as a benchmark u-PCS problem so that the benefits accruing from the new CSI methods and tools can be demonstrated and quantified.

- **JPL's CSI TEAM IS DESIGNING THE CONTROL/STRUCTURE SYSTEM FOR A LARGE OPTICAL INTERFEROMETER (THE FMI)**
- **INITIAL FMI REQUIREMENTS CHALLENGE CSI TECHNOLOGY TO PROVIDE 3 TO 4 ORDERS OF MAGNITUDE RESPONSE REDUCTION**
- **THE FMI DESIGN WILL BE CARRIED TO A PRELIMINARY DESIGN LEVEL IN ORDER TO**
  - **DRIVE REQUIREMENTS ON THE GROUND TEST BED**
  - **DRIVE REQUIREMENTS ON DESIGN/ANALYSIS TOOLS**
  - **DRIVE REQUIREMENTS ON FLIGHT EXPERIMENTS**
  - **SHAPE THE PROCESS OF DEVELOPING THE NEW CSI DESIGN METHODOLOGY**
- **THE FMI DESIGN WILL SERVE AS A BENCHMARK μ-PCS PROBLEM TO DEMONSTRATE CSI METHODS AND TOOLS**

BIBLIOGRAPHY

1. Space Science in the Twenty-First Century: Imperatives for the Decades 1995 to 2015 (Astronomy and Astrophysics), National Academy Press, Washington, DC, 1988.

2. NASA Office of Space Science and Applications 1988 Strategic Plan.

3. Tolivar, A. F. and Wang, S. J., "Control of Large Space Antennas," Large Space Antenna Systems Technology, December, 1982.

4. Soosar, K. and Larkin, L., "Opportunities for Ground Test of Large Space Structures," Proceedings of the 2nd NASA/DoD CSI Conference, Colorado Springs, CO, December, 1987.

5. Sirlin, S. W., "Vibration Isolation Versus Vibration Compensation on Multiple Payload Platforms," Proceedings of the 3rd NASA/DoD CSI Conference, San Diego, CA, January/February, 1989, **NASA CP-3041, pp. 67-83.**

Zenith Star:
A Structural Control Challenge

L. A. Morine
Martin Marietta Aerospace Group
Denver, Colorado

3rd Annual NASA/DOD CSI Conference
San Diego, California
January 29 - February 2, 1989

INTRODUCTION

The Zenith Star experiment (Figure 1) is designed to demonstrate and evaluate the performance of a laser in space to answer critical issues relevant to SDI. This experiment is fully compliant with the restrictive interpretation of the 1972 Anti-ballistic Missile (ABM) Treaty. As such it does not directly perform all of the functions of a defensive system nor to the level required by an operational system. Its results however, do provide a measure of the potential of the operational systems by applying the appropriate scaling from the benchmarks achieved by it in space.

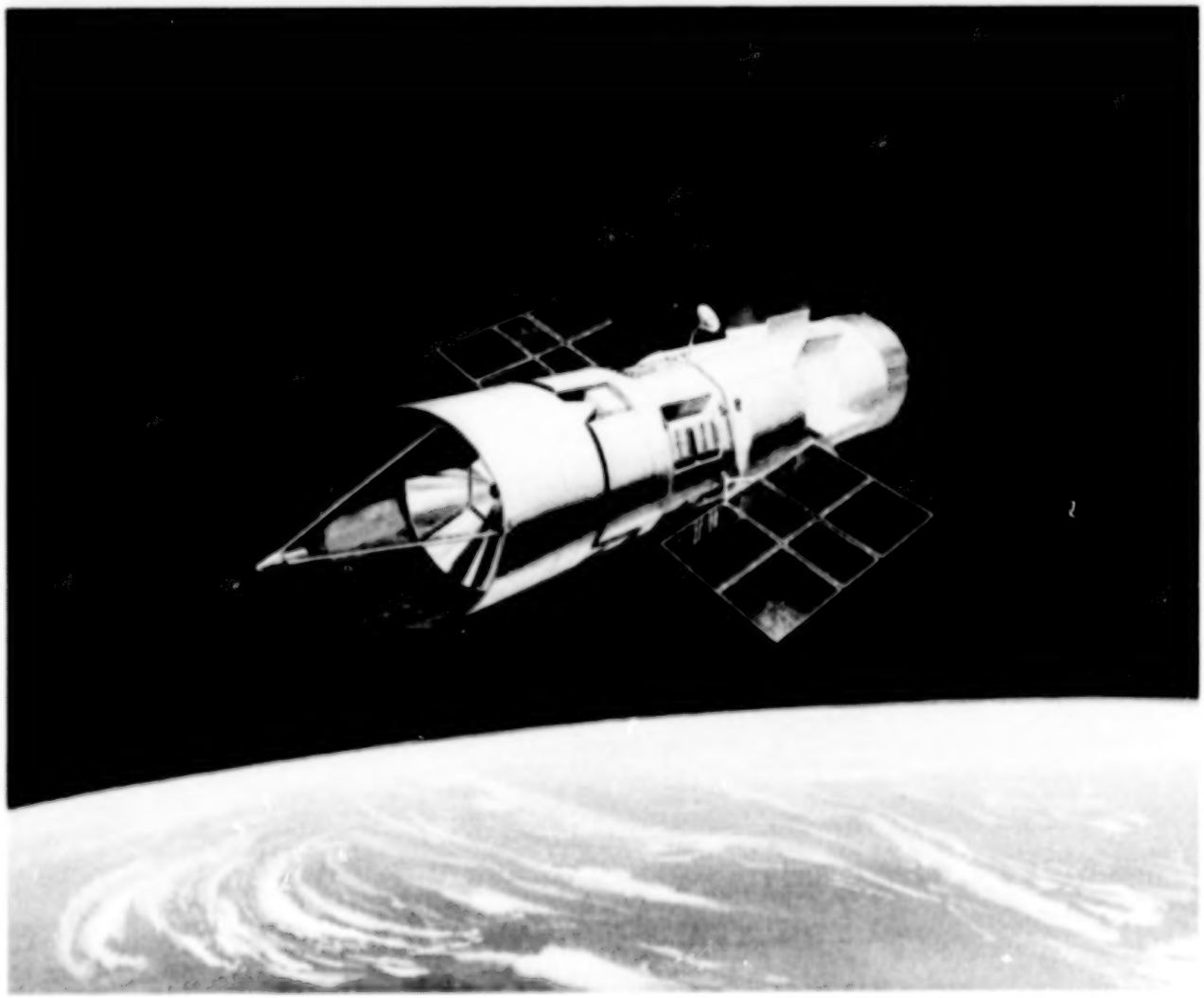


Figure 1: Zenith Star Experiment

The experiment (Figure 2) consists of a series of high power evaluations of beam control and a series of low power evaluations of the tracking and pointing functions of the system.

The high power experiments evaluate the beam control by direct measurement of the far field beam performance with a high power target board. Both space propagation and upper atmospheric effects are measured.

The low power experiments evaluate the tracking and pointing function performance while tracking a booster throughout its boost phase flight. The Agile Control Performance is evaluatd by performing structured characterization and large and small angle repointing of the system against a star field, small test objects (carried on board), and multiple boosters to exercise the system under multiple conditions.

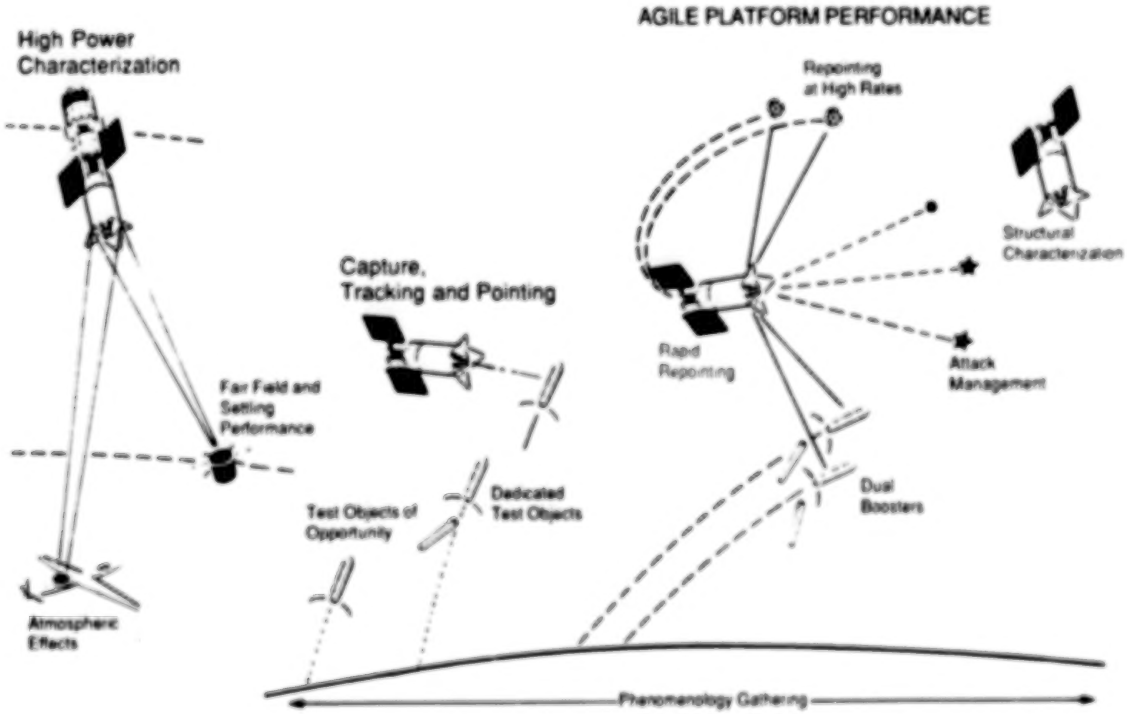


Figure 2: Zenith Star Objectives

ZENITH STAR SPACECRAFT

The basic hardward for the Zenith Star experiment is shown in Figure 3. It consists of a chemical laser of the class of the alpha program, a beam expander that utilizes the segmented LAMP mirror for the primary optical element, an actuator for pointing the beam expander, and an isolator for attenuating the laser noise from the beam expander. The latter two are combined into one subsystem called the actuator/isolator. The laser energy is directed through the aft body to the beam expander by a series of transfer optics and steering mirrors (beam control transfer assembly) on the aft body. A capture track system (consisting of a suite of sensors) is utilized to point the beam expander and optical train for tracking a series of test objects. The remainder of the equipment is a set of standard spacecraft subsystems that allow it to be in orbit as a free flyer that is commanded by ground operations personnel.

The system is delivered into orbit by two Titan IV launch vehicles. The forward spacecraft is launched first and checked out completely. Then the aft spacecraft consisting of the Alpha laser and spacecraft support subsystems is launched into the same orbit as the first, orbit phased, and remotely operated from the ground for rendezvous and docking.

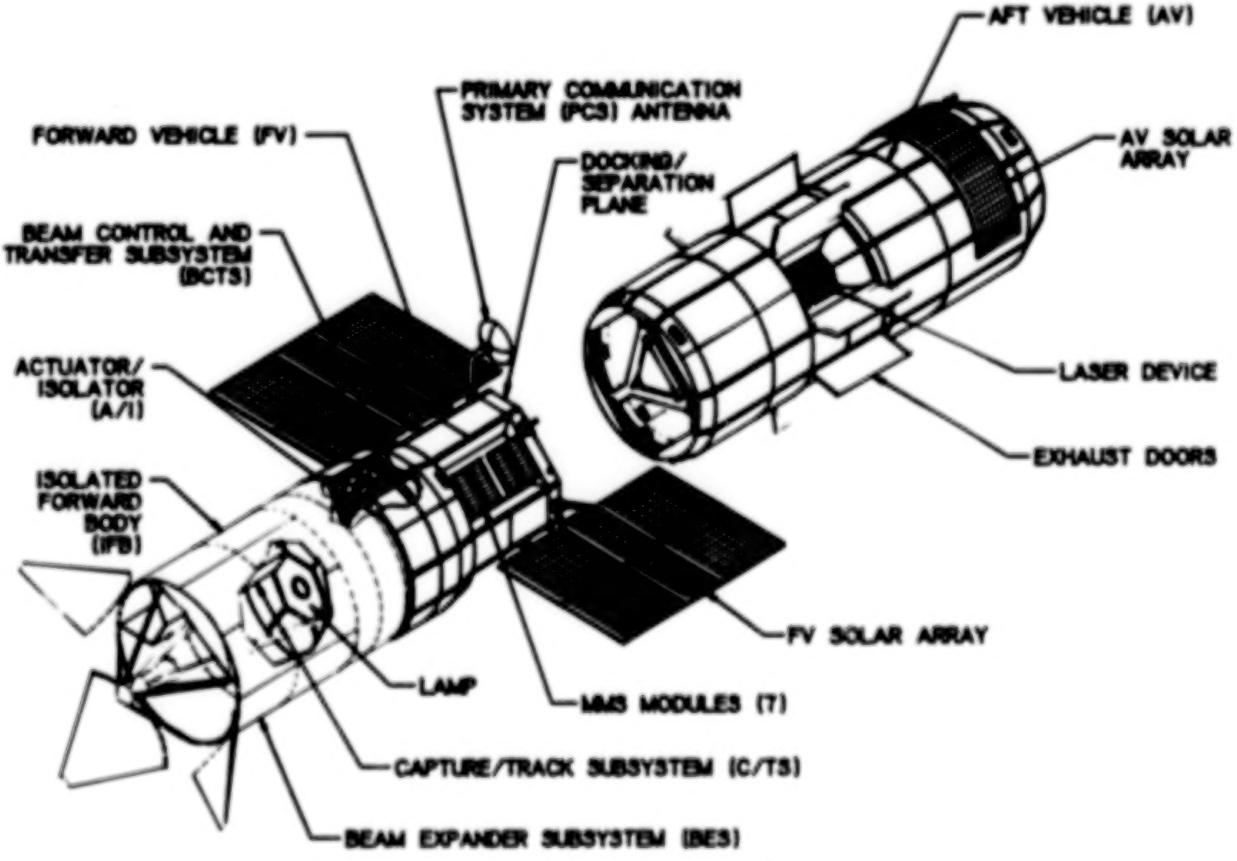


Figure 3: Zenith Star Space Vehicles

BEST COPY AVAILABLE

CONTROL SYSTEM ARCHITECTURE

The control architecture for the space based laser is derived from a series of stringent tracking and pointing requirements depicted in Figure 4 and the resulting interactive implications lead to a complex hierarchical control architecture. Tight accuracy and jitter requirements combined with the need for rapid repointing of the line-of-sight from one object to another necessitates isolation and suppression of disturbances to the large beam expander. The Zenith Star control system is designed to duplicate this architecture so that the experiment results can be directly related to the SBL performance.

The precision and jitter are analogous to hitting a basketball on the Empire State Building in New York from Pike's Peak in Colorado. It must accomplish this while tracking objects at angular rates more than an order of magnitude higher than the capability of the Hubble Space Telescope. To accomplish this, the line-of-sight must be isolated from disturbances by as much as 100 million to one and yet be able to repoint from one object to another in less than one second so that the system effectiveness can be high.

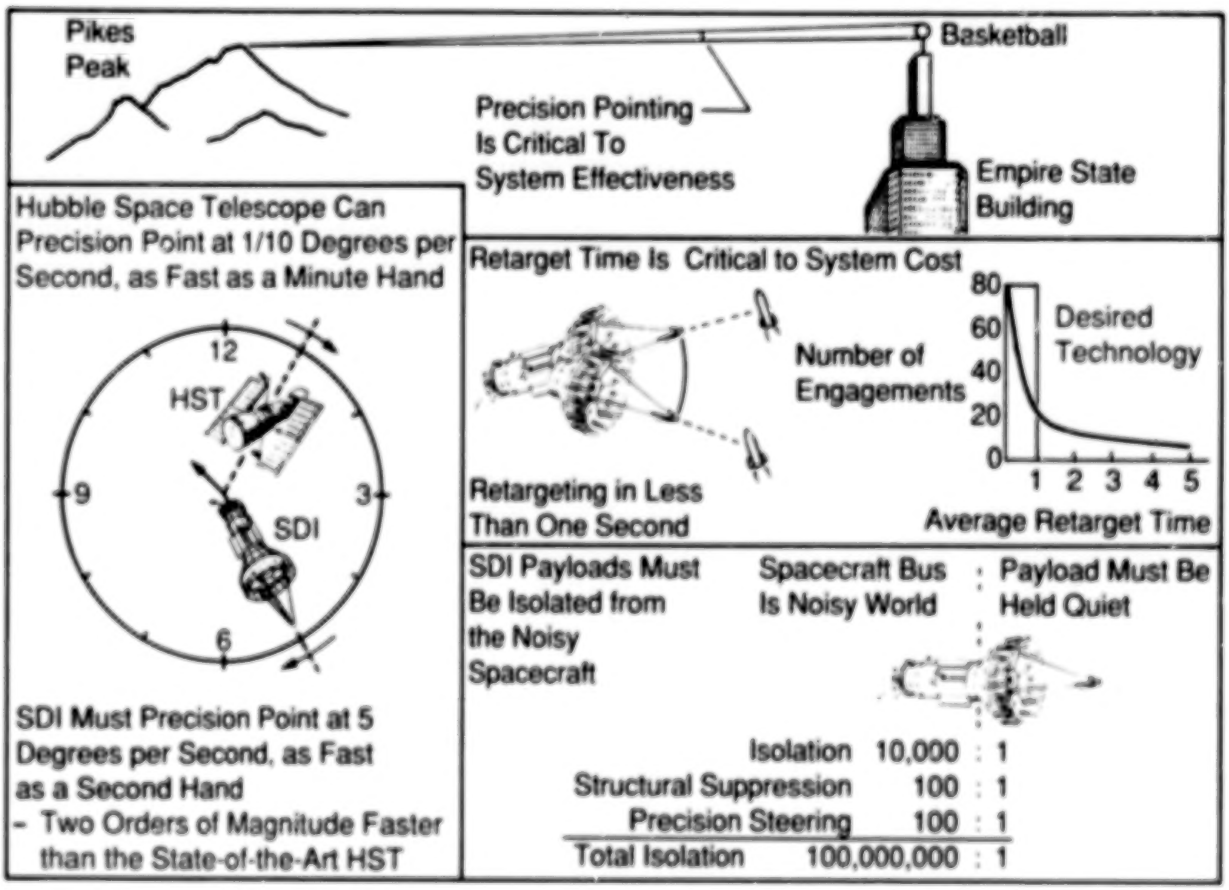


Figure 4: Space Based Laser Control Requirements

While the structure is made as stiff as possible, there is sufficient deformation (Figure 5) of the beam expander structure and optical geometry resulting in line-of-sight disturbances to require isolation of aft body noise from the beam expander. There are other self-induced beam expander disturbances such as fluid flow and rapid repointing that require structural disturbance suppression on the beam expander itself.

Either technique can be readily handled without two body interaction, but when combined an actuator/isolator is required between the bodies. This actuator/isolator must provide six degrees of freedom operation which introduces other control issues, such as translation and beam walk control, that further complicate the controls problem.

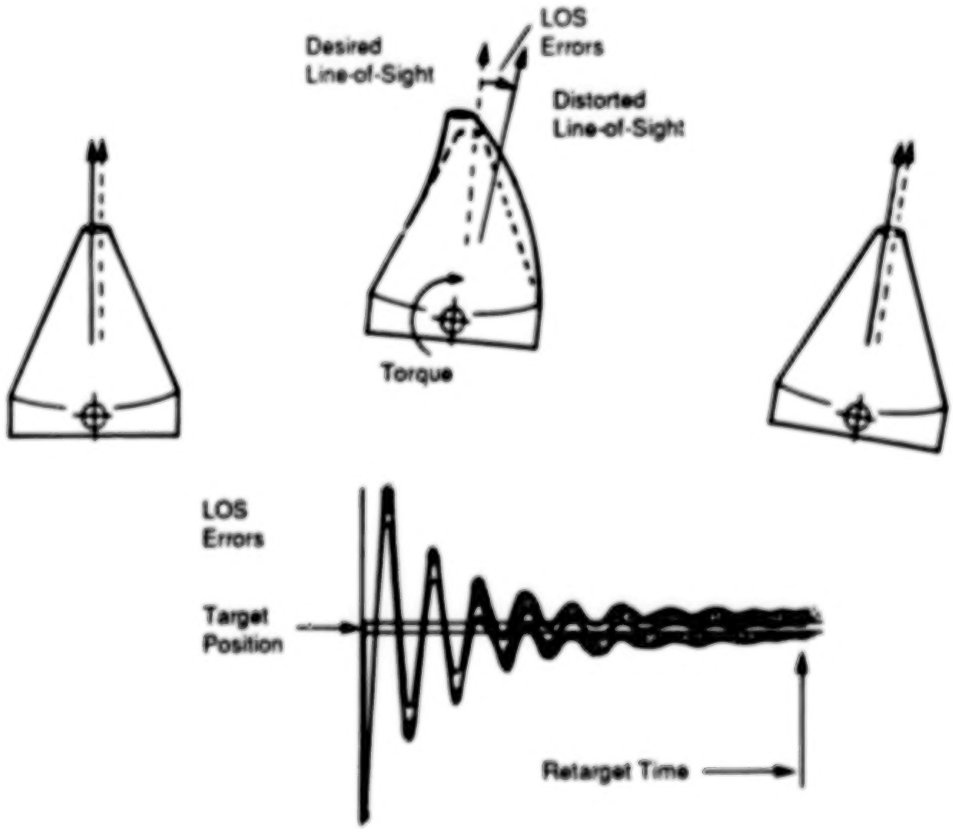


Figure 5 Beam Expander/Optical Distortions

In order to ease the burden of pointing the line-of-sight of the system, a precision pointing set of controllers is introduced to provide beam expander off-axis pointing and stabilization so that the structure control can be relaxed within a small field of view and as shown in Figure 6. So long as the line-of-sight disturbance is within the range of the precision pointing controller authority the beam expander controller requirements are eased. In other words, the settling time is satisfied when the beam expander line-of-sight is within this band.

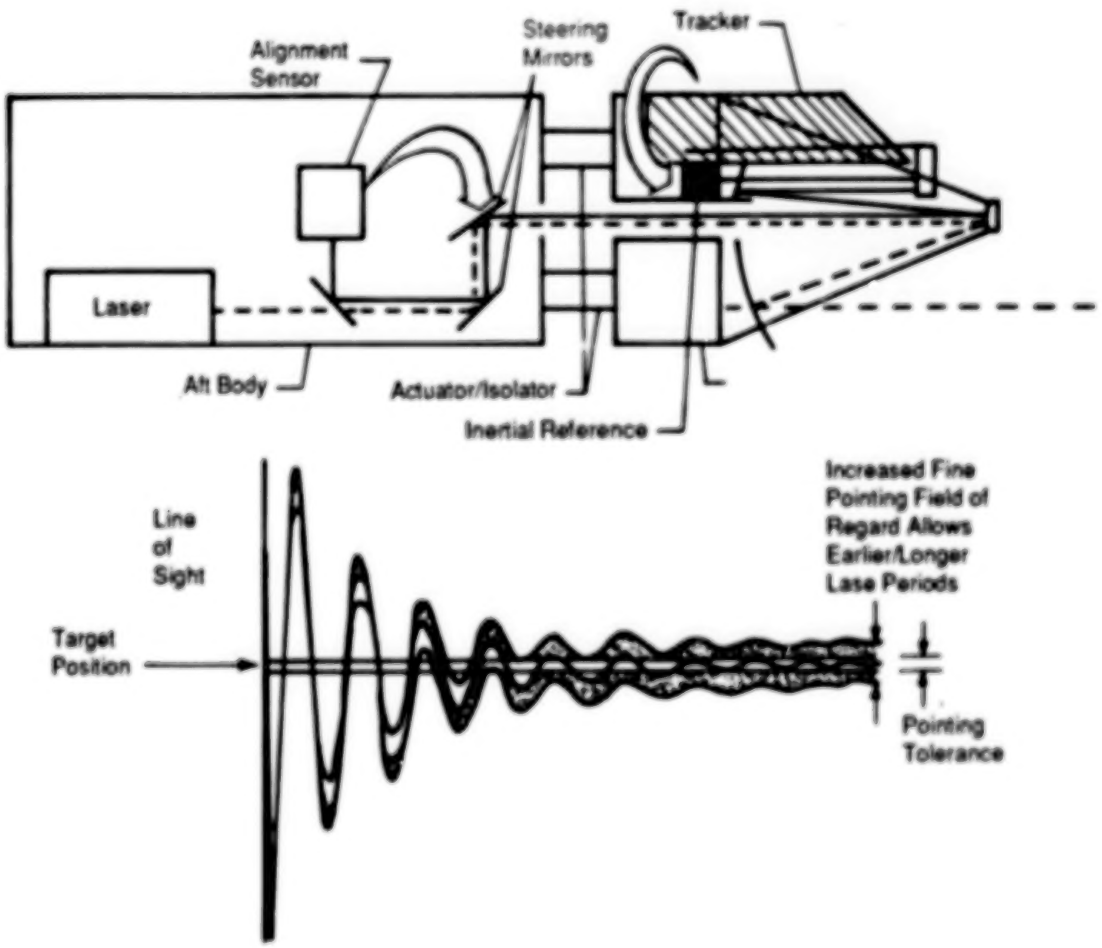


Figure 6 Precision Pointing Control System

VEHICLE CONTROL

The formulation of the control architecture for the beam expander can be described as follows in the next series of figures in Figure 7.

An easy method of isolation (Figure 7a) of the aft body disturbances from the beam expander is to provide a gap between the forward and aft bodies, control the beam expander to point to the test object from on-board sensor data by external torques (such as control moment gyros), and control the aft body to follow this motion by external forces and torques to maintain the desired gap within some tolerance. This is ideal isolation since there is no actuation between the bodies to force alignment of the two bodies, hence there is no transfer of disturbances from one body to the other.

Since each body tends to rotate about its own center of mass there will be large translational displacements (Figure 7b) at the optical interface between the beam expander and aft body. Also since the beam expander disturbances are to be minimized the aft body must be translated as well as rotated by external forces and torques to maintain the proper separation. This is not practical for a highly agile control system because of the large heavy aft body and the fact that the gap must be small, on the order of centimeters. Consequently an actuator between these bodies is required.

This actuator introduces a coupling path from the aft body to the beam expander which then requires an isolator between the bodies (Figure 7c). This actuation and isolation must be combined into one subsystem because of this interaction. This subsystem is called the actuator/isolator and it must minimize this coupling while producing the desired pointing forces and torques. This function is nontrivial even for the baseline magnetic isolator because of nonlinear magnetic forces and eddy currents which must be cancelled.

Self-induced disturbances on the beam expander arising from fluid flow and rapid pointing must be dissipated through damping in the structure, transferred to noncritical structural motion (non-critical modes), or transferred off the beam expander to the aft body (Figure 7d). The incorporation of the actuator/isolator allows this energy to be transferred to the aft body which can then remain isolated. Hence the beam expander line of sight can be stabilized while still tracking objects.

The pointing of the beam expander causes severe disturbances. In order to move the line-of-sight from one object to another (rapid repointing)it is desirable to make maximum use of the available torque from the actuator/isolator. In fact, the optimal repointing for a rigid body is a bang-bang command. This, however, causes severe disturbances to the line-of-sight.

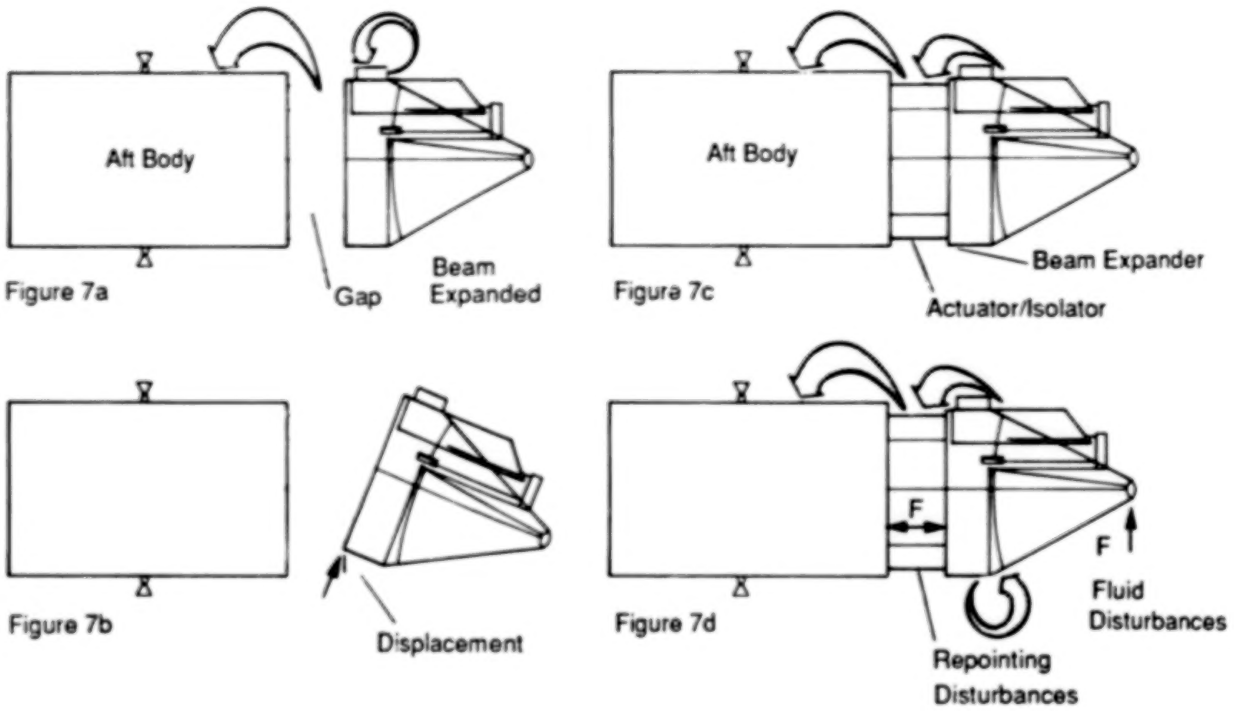


Figure 7 Vehicle Control Architecture Evolution

The severity is dependent on the relationship of the angle to be repointed (frequency of the bang-bang torques) and the structural frequencies. Figure 8 shows the effects of a single structural frequency of 4 Hz and 8 Hz separately as a function of repointing angle. The time to hand over is the time that the line-of-sight error takes to settle to within the field of reguard of the beam expander where the fine off-axis steering takes over. The rigid body response is included since it represents the lower bound of maneuver time for the system.

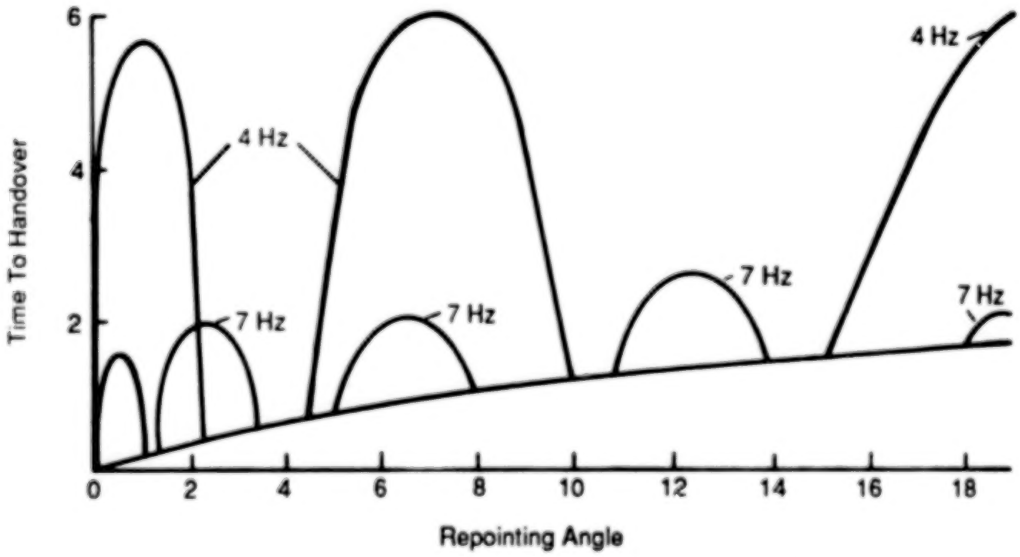


Figure 8 Effects of Structural Frequencies on Repointing Time To Precision Track Handover

When all structural modes are considered the picture is not quite so easily displayed because the relative effects on the line-of-sight are intermixed. An envelope of these effects is indicated in Figure 9 where the lower bound is limited by the rigid body response and the upper bound depends on advanced structural controllability.

The regions of interest for structural control are the torque-limited and rate-limited regions. The algorithm-limited region is the area of responsiveness of the precision off-axis control system for scene interpretation and control.

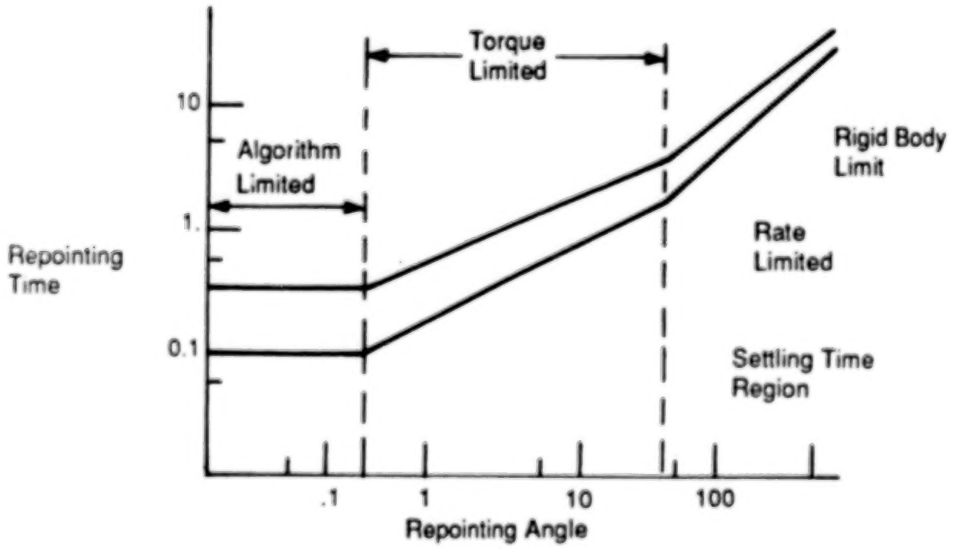


Figure 9 Repointing Characteristics

Figure 10 shows the improvement in repointing time that can be made by a simple modulation. The technique is based on the relationship of the repointing angle and the knowledge of the structural frequencies of the beam expander. By properly commanding or modulating the torque commands, disturbances can be minimized as shown in the figure for one technique called modulated bang-bang control.

This technique concentrates on modal avoidance and cancellation and its effectiveness. There are other techniques that have been investigated by several members of the community that should also be evaluated in space. These include both other modal avoidance, modal suppression, and modal displacement.

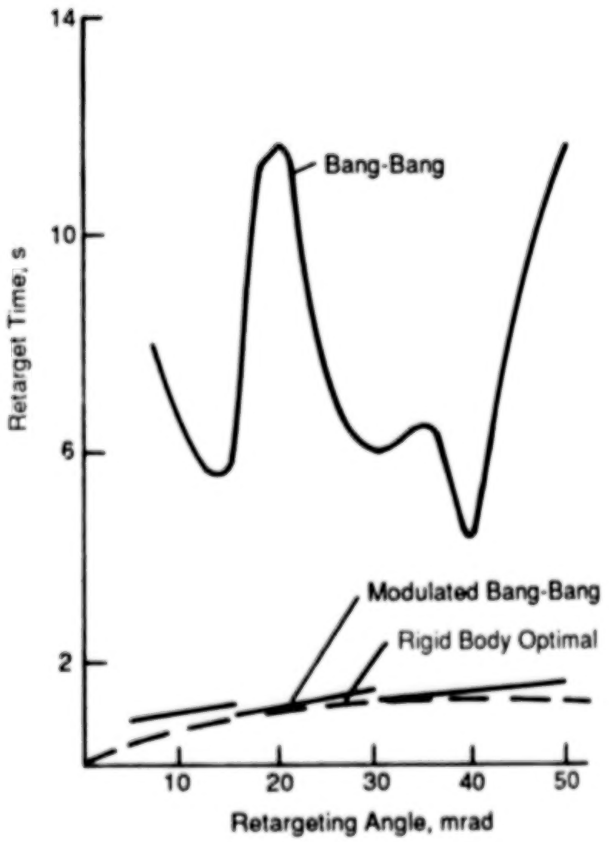


Figure 10 Multiple Mode Controller Characteristics

SUMMARY

The space based laser control tasks are indeed challenging because of the variety of requirements that demand different types of controllers, all competing simultaneously. The architecture derived for the SBL resulted in a hierachical control formulation that demands advanced control techniques. Each portion of the architecture has interaction with the others which demands careful orchestration of the control commands to fulfill the control requirements.

The Zenith Star duplicates the SBL functions and provides performance levels close enough to the SBL performance to provide valid scaling for evaluation of the SBL expectations.

One dominant crucial control function is the beam expander controller. It must place and stabilize the beam expander line-of-sight within a few hundred microradians of the object tracked in a very short time. The accuracies involved require careful control of the structural deformations even with structural resonances on the order of 20 Hz.

There is no precedence for this type of structure control since this is the first opportunity to control a structure of this nature in space. Experiments such as structural identification and modal surveys are also planned for in the experiment objectives. Utilization of other techniques for controlling the structure, such as distributed actuator structural control, are not currently available on Zenith Star but may be available in the future depending in the interest within the community and the risk to the other Zenith Star objectives.

In either case there is ample opportunity for industry participation during the Zenith Star mission operations. This can be accomplished by submitting ideas for structural control techniques to SDIO for consideration. If approved, these experiment ideas will be integrated into the experiment objectives and the implementation incorporated into the mission planning.

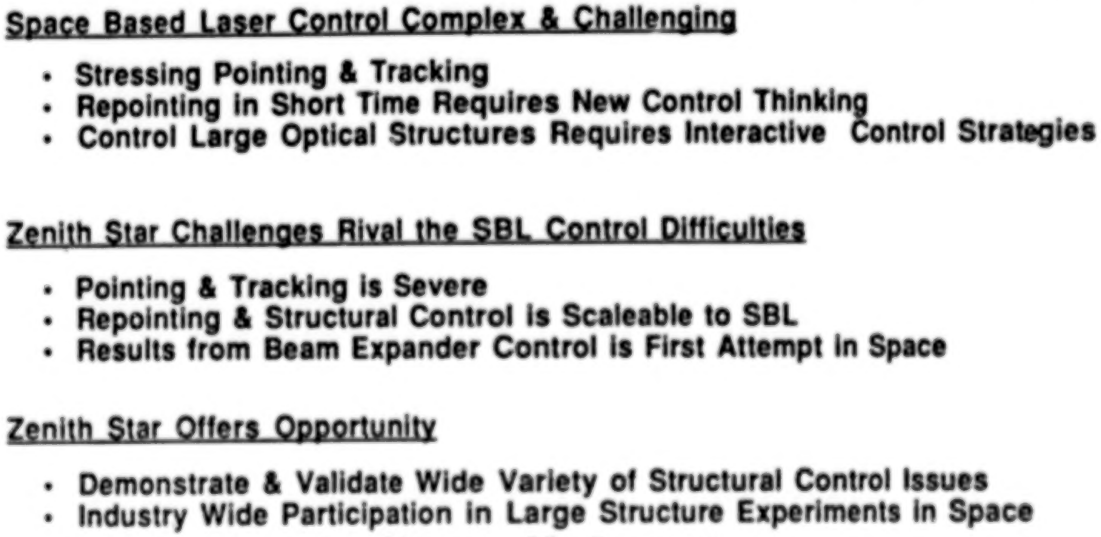


Figure 11 Summary

PACOSS PROGRAM
STATUS AND RESULTS

K. E. Richards, Jr.
Martin Marietta Astronautics Group
Denver, Colorado

Third NASA/DoD Controls-Structures
Interaction (CSI) Technology Conference
January 2-February 2, 1989

Future large space systems (LSS), both civilian and military, will have performance objectives which require stringent pointing accuracies, relatively fast retargeting times, short settling times, accurate dynamic shape requirements, or combinations thereof. Many of these structures will be large but lightweight and will exhibit a dense, low-frequency modal spectrum with significant content within the control bandwidth.

Although it is possible in principle to achieve structural vibration control with purely active means, experience with complex structures has shown that the realities of plant model inaccuracies and real sensor and actuator dynamics frequently combine to produce disappointing results.

It has been shown (References 1-2) that a combination of passive and active control will result in a simpler system which can be expected to be more reliable and less expensive than a corresponding system utilizing active control exclusively.

The goals of the PACOSS (Passive and Active COntrol of Space Structures) program consist of a thorough investigation of the relative roles of passive and active vibration control, and the development of validated means of vibration control. (Fig. 1.)

Introduction

- Future Large Space Structures (LSS) Will Require Structural Vibration Control To Achieve Performance Goals
- Vibration Damping May Be Achieved by Passive or Active Means, or Both
- Major Goals of PACOSS Program
  - Demonstrate Roles of Passive and Active Control for Future LSS
  - Develop Means of Passive Vibration Control
  - Experimentally Verify Damping Predictions and Control Algorithms

Figure 1

The outline of this presentation is shown in Figure 2.

Outline

- Program Approach
- Representative System Article
- Dynamic Test Article
- Test Status and Results
- Conclusions

Figure 2

PACOSS, being a generic program, has as one objective to provide passive damping technology to as broad a spectrum of military and civilian large space systems as possible. Fundamental to this objective is the selection of analytic and test articles of broad applicability. These articles are then designed by analysis, and hardware components are fabricated and tested to validate design and analysis practices.

Once the hardware components are validated, substructures are designed and analyzed. These substructures are then tested to validate the higher level design and analysis practices.

Finally, the entire system is synthesized, and analytical predictions of dynamic characteristics are again validated by test. System synthesis includes active control measures as well as passive damping treatments.

The resulting technology will have broad applicability to real future space systems. Programs will be able to apply the technology with a high degree of confidence due to the careful, systematic approach applied to test hardware of a complexity similar to actual flight items. (Fig. 3.)

Program Approach

- Broad Applications
- Analysis Validated by Test
- Component-Substructure-System
- Open- and Closed-Loop Testing

Figure 3

Figure 4 is an artist's concept of the PACOSS Representative System Article (RSA). PACOSS is a generic program, and the RSA was designed to provide an analytic test bed for system design studies that would be relevant to as many future large space systems as possible. Altogether, the RSA is traceable to 19 future systems (Reference 3).

This broad applicability was accomplished by designing a system comprised of components or substructures found on one or more future LSS. As can be seen in Figure 4, the RSA consists of seven substructures. The ring truss, 20 meters in diameter, serves as a structural "hardback" for the system. The tripod structure is part of a Cassegrain optical system and supports a secondary mirror. The box truss represents the backup structure for an optical surface. The dish antenna is for communication with the ground. The linear truss supports sensitive equipment. The two solar arrays are sized for 25 kilowatts of power.

Passive damping treatments are designed for each selected substructure. It is possible to provide passive damping treatments to all components, but it was decided not to damp the ring truss to simulate systems where some components would be unavailable for damping treatments.

The level of passive damping to be applied was based on a performance simulation of the system with various levels of passive damping (References 2,4), a technique to be followed in the design of real systems.

PACOSS RSA

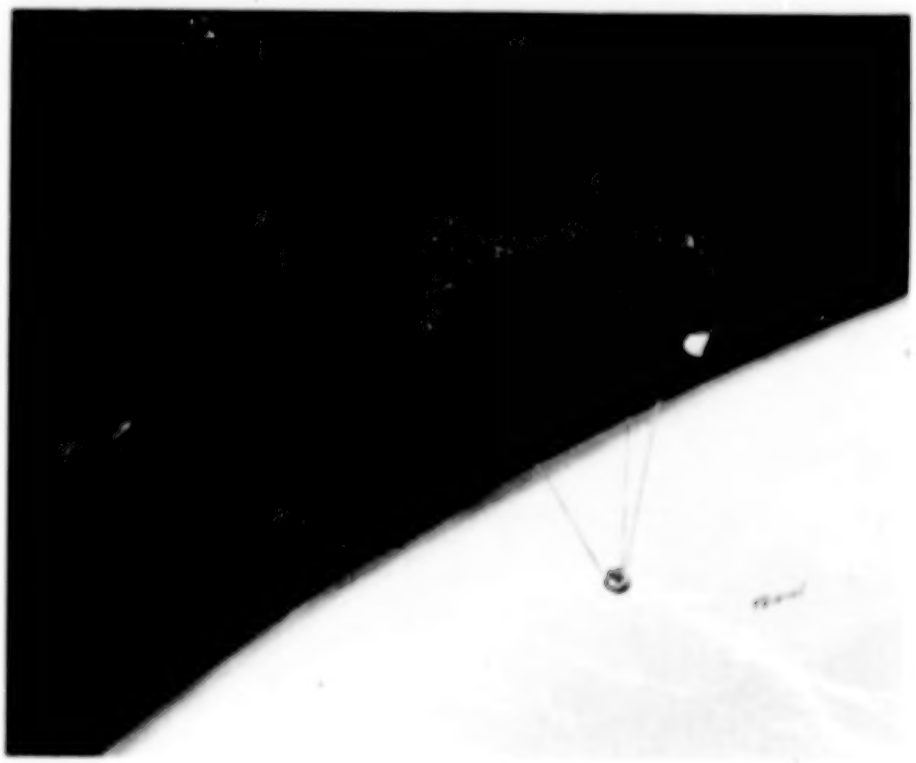


Figure 4

The DTA was designed to be dynamically similar to the RSA and is serving as a hardware validation tool for the analytic methods and design practices used to provide passive damping to realistic structures. The requirements shown in Figure 5 have been selected to assure traceability to the RSA within the realities of the test environment and budgetary constraints. It is noted that the DTA is space-qualifiable, although there are currently no plans to fly it.

Because the DTA is a validation device, it is important that no inadvertent sources of damping are present. This function was the major reason the PACOSS program chose to avoid exotic or complicated suspension techniques for the DTA. A consequence of this decision was that it was necessary to stiffen the DTA to permit it to survive the one-g test environment without extensive distributed support. This stiffening resulted in a frequency increase of approximately two Hz. The frequency shift does not compromise program objectives, however.

Dynamic Test Article (DTA) Requirements

- Validation of Damping Treatment Design and Analysis Techniques
- Dynamically Similar to RSA
- Deliverable to Orbit As Single Shuttle Payload
- Negligible Unpredicted Damping
- Suitable for 1-g Test
- Easily and Inexpensively Fabricated

Figure 5

All components of the DTA have been fabricated and tested. Figure 6 shows the sizes of the DTA structural components.

Summary of Final DTA Dimensions

Component	*Dimension, m*	*Mass, kg*
* 1) Box Truss	2.89x2.59x0.324	180.5
* 2) Ring Truss	Diameter: 2.9	59.7
* 3) Tripod	Diameter at Base: 2.59 Height: 2.59	29.9
* 4) Equipment Platform	Length: 1.295	7.04
* 5) Antenna	Diameter: 0.648	4.52
*6,7) Solar Arrays	Length: 2.59	12.0
* *Fabricated and Tested*		

Figure 6

The first component modal survey was of the ring truss (References 2,5). This substructure is the central element of the system, and it is critical that this portion of the system be modelled accurately.

Figure 7 shows the ring truss suspended in its test configuration. The truss is suspended by three lightweight cables approximately 25 feet long. Each cable was suspended from a zero spring-rate mechanism (ZSRM). This arrangement results in three virtually zero rigid-body modes and three pendulum modes of approximately 0.25 Hz for the suspension, thereby providing good separation from the flexible modes of the system.

The modelling of the interfaces between the ring truss and the remaining substructures is critical. To exercise these interfaces, thereby permitting evaluation of the accuracy of the model, the ring truss was mass-loaded at all interface points during this test.

DTA Ring Truss in Test Configuration

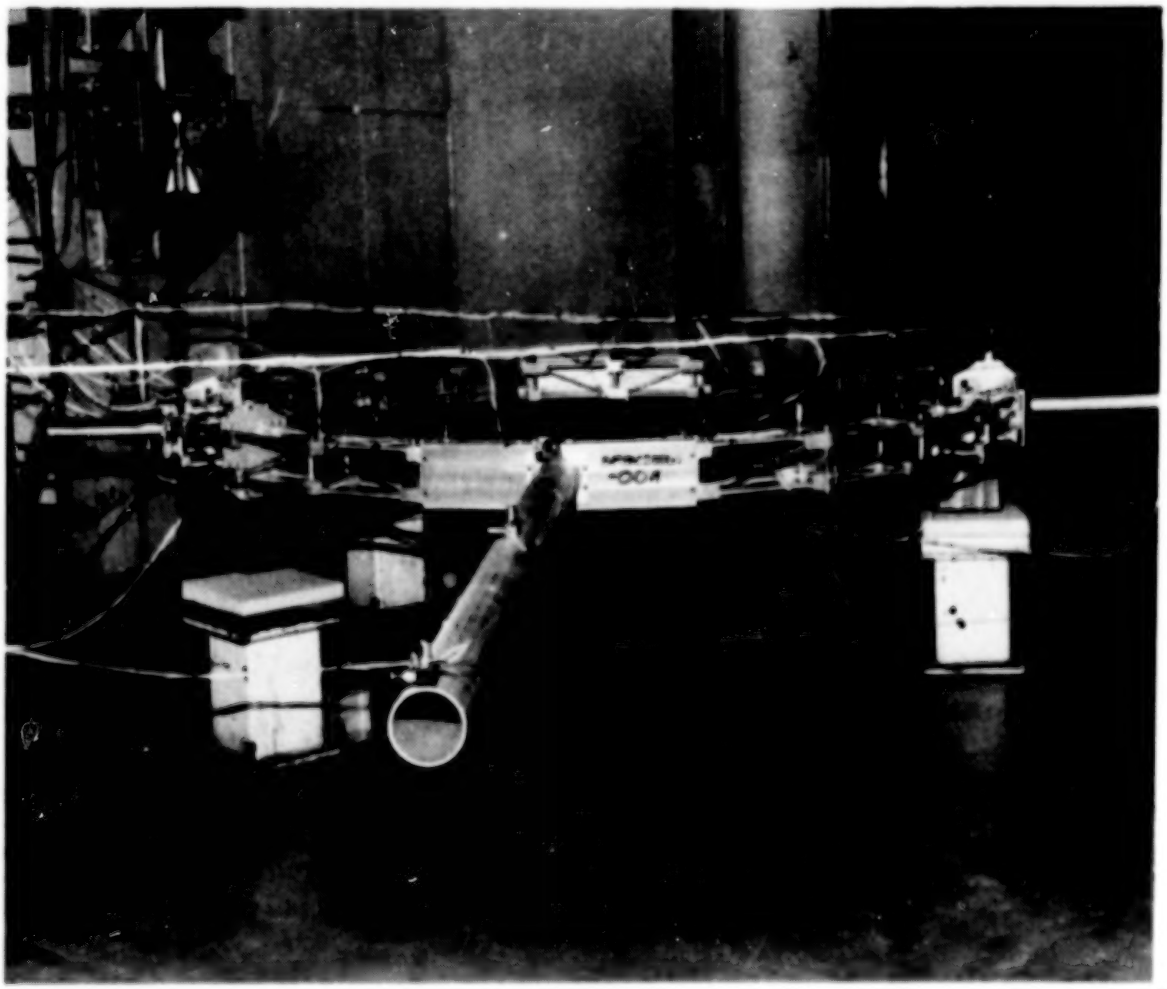


Figure 7

Figure 8 shows one of the three identical ZSRMs. The large vertical spring supports the static load due to the weight of the DTA. The position of this spring is adjusted so that the two side members, which pivot about their ends, are horizontal. The large nuts on the side members are turned to place the springs on the side members into states of equal compression.

The vertical spring and side members are connected to a common pivot point. A pair of guide rods connect this point to the DTA suspension cable. Downward displacement of the pivot results in an incremental spring force in the vertical spring, accompanied by rotations of the side members. The incremental downward forces due to the rotations of the compressed side members tend to cancel the incremental upward force in the large spring. Proper selection of the ZSRM parameters produces perfect cancellation for small displacements, resulting in a suspension with zero stiffness for the displacements normally encountered during a modal survey.

Zero Spring-Rate Mechanism

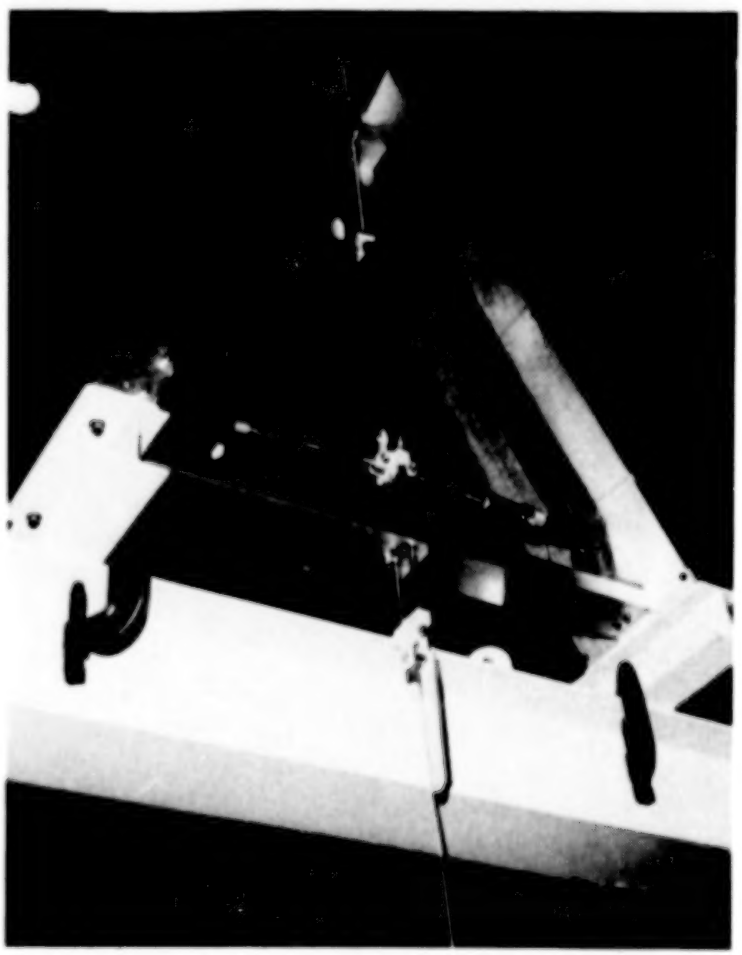


Figure 8

The results of the test and comparison with the analytic model are shown in Figure 9. Note the extremely low damping in the higher modes.

The damping values shown in this figure were obtained from tuned-decay tests, a very accurate method for those cases where damping is low and the modes can be separated. Note that the 12.5 and 12.7 Hz modes were too close in frequency to be separated well, and the 13.2 Hz mode could not be tuned. Damping values for these modes are available from the single-point random tests and have been presented elsewhere (Reference 2).

The comparatively high damping values (relative to the other modes but low in the absolute sense) for modes one and two were due to excessive wear in the mild steel ZSRM guide rods which occurred during testing. This situation was corrected by the use of case hardened rods during final testing.

Ring Truss Modal Survey—Results

f_n, Hz		ζ, %
Measured	Post Test Analytic	Measured
3.25	3.29	0.3
6.33	6.47	0.7
8.78	9.40	0.14
9.28	9.91	0.17
12.5	14.9	0.2 - 0.3
12.7	12.2	0.2 - 0.3
13.1	12.5	0.16
13.2	14.1	Not Measured
15.1	15.6	0.15

Figure 9

The tripod is shown in the test configuration in Figure 10 (References 2,5). The dark color of the legs is due to the graphite-epoxy constraining layer. Rotational shear dampers are located at each of the three interfaces between the tripod legs and the sixty pound secondary mirror. The bottoms of the tripod legs are fixed to the floor. The model assumed an effectively rigid floor, and experimental data confirmed the assumption.

DTA Tripod in Test Configuration

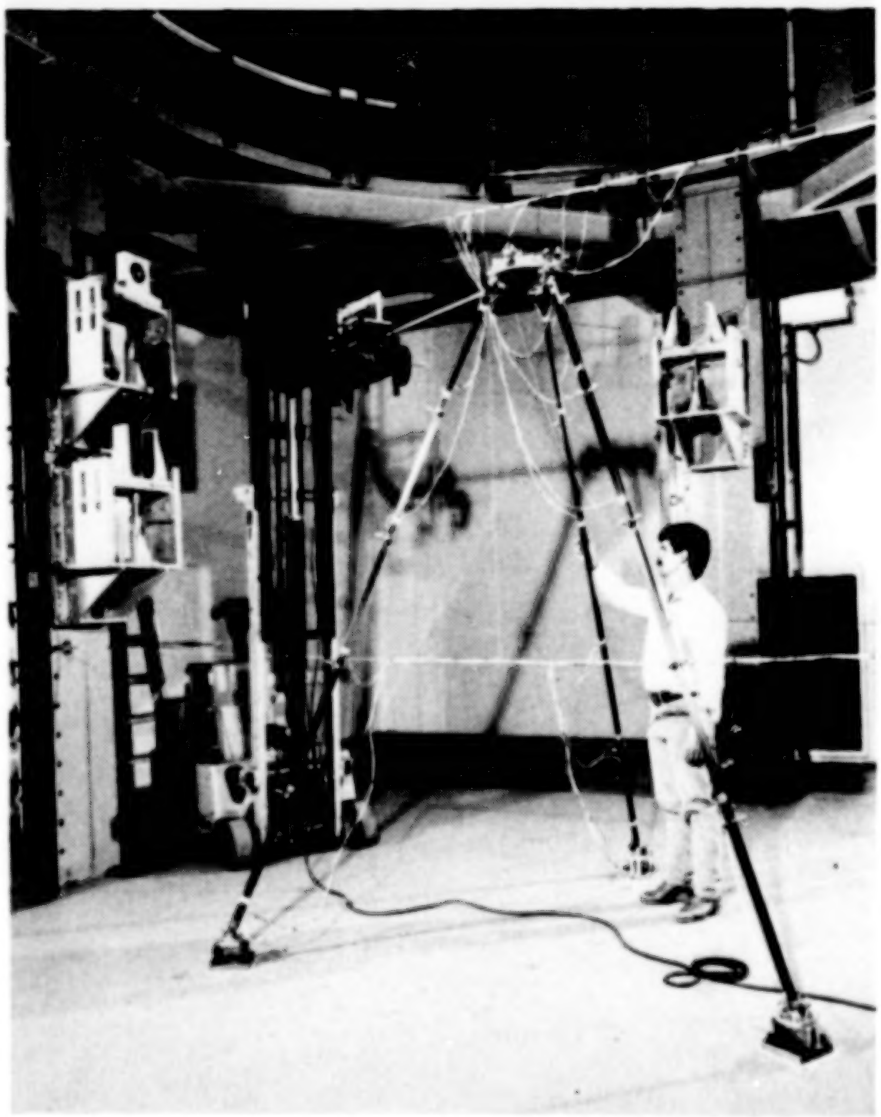


Figure 10

The details of the constrained-layer damping treatment on the tripod legs are shown in Figure 11 (Reference 4). The tubing used was aluminum. A layer of viscoelastic material is bonded to the tube and to the graphite/epoxy constraining layer. Care is used to avoid bonding adjacent constraining layers together, as this would drastically reduce the damping level.

Detail Design of Damping Treatment for DTA Tripod

- Tripod Model Predicted 5% Modal Damping Using Constrained Layer Treatment

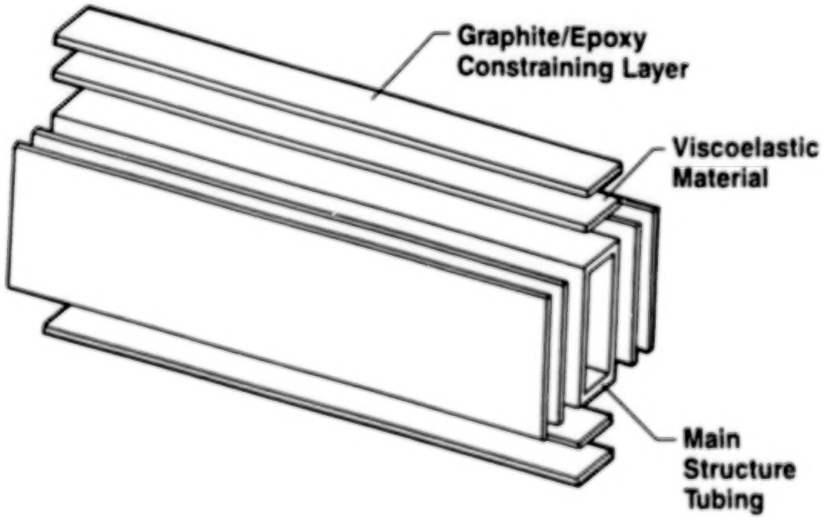
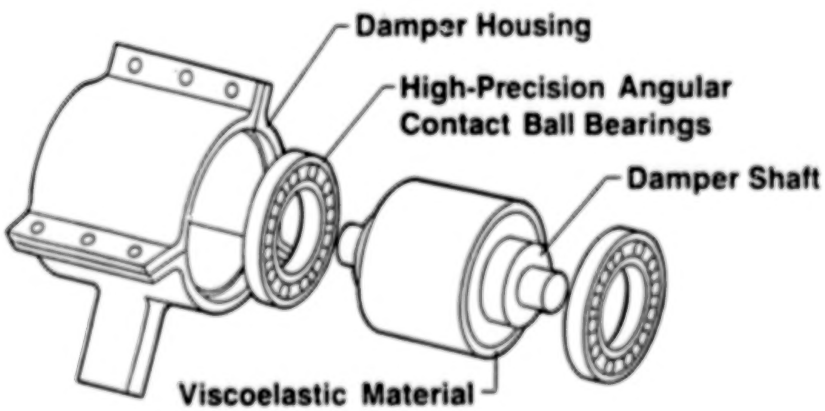


Figure 11

The details of the rotational shear damper are shown in Figure 12 (Reference 4). The damper housing is connected to the tripod legs and the damper shaft is connected to the secondary mirror. The viscoelastic material is bonded to both the shaft and housing so that relative rotation between the housing and shaft induces shear strain into the VEM (viscoelastic material).

Detail Design of Damping Treatment for DTA Tripod (cont)

- Determine Dimensions of Viscoelastic Cylinder for Chosen Material (Acrylic Core Foam)
- Design Method of Supporting Weight and Dynamic Loads in Other DOFs*



*Degree of freedom (DOF)

Figure 12

The comparison between predicted and measured frequency and damping is shown in Figure 13 (Reference 5). The predicted values were derived considering the frequency dependence of the VEM properties as well as the geometric stiffness effects induced by the weight of the heavy secondary mirror acting on the tripod legs. Note that these two effects tend to offset each other, and both must be considered if predictions are to be accurate.

VEM properties under current manufacturing standards frequently vary by 50 percent from batch to batch, so these results are exceptionally good.

Tripod Modal Survey—Results

f_n, Hz		ζ, %	
Measured	*Predicted*	*Measured*	*Predicted*
3.91	3.84	15.9	17.9
3.97	3.84	15.7	17.9
4.78	4.63	6.7	7.1
9.55	9.89	9.2	8.7
9.66	9.89	8.6	8.7
11.7	11.7	9.2	8.4
12.7	13.8	11.4	12.3
13.3	13.8	11.1	12.0

Figure 13

The box truss is shown in the test configuration in Figure 14. The large yellow structure is known as the "T-beam", and is part of the test facility. The box truss is clamped to the T-beam, and both the box truss and T-beam were instrumented for the test (Reference 5).

DTA Box Truss in Test Configuration

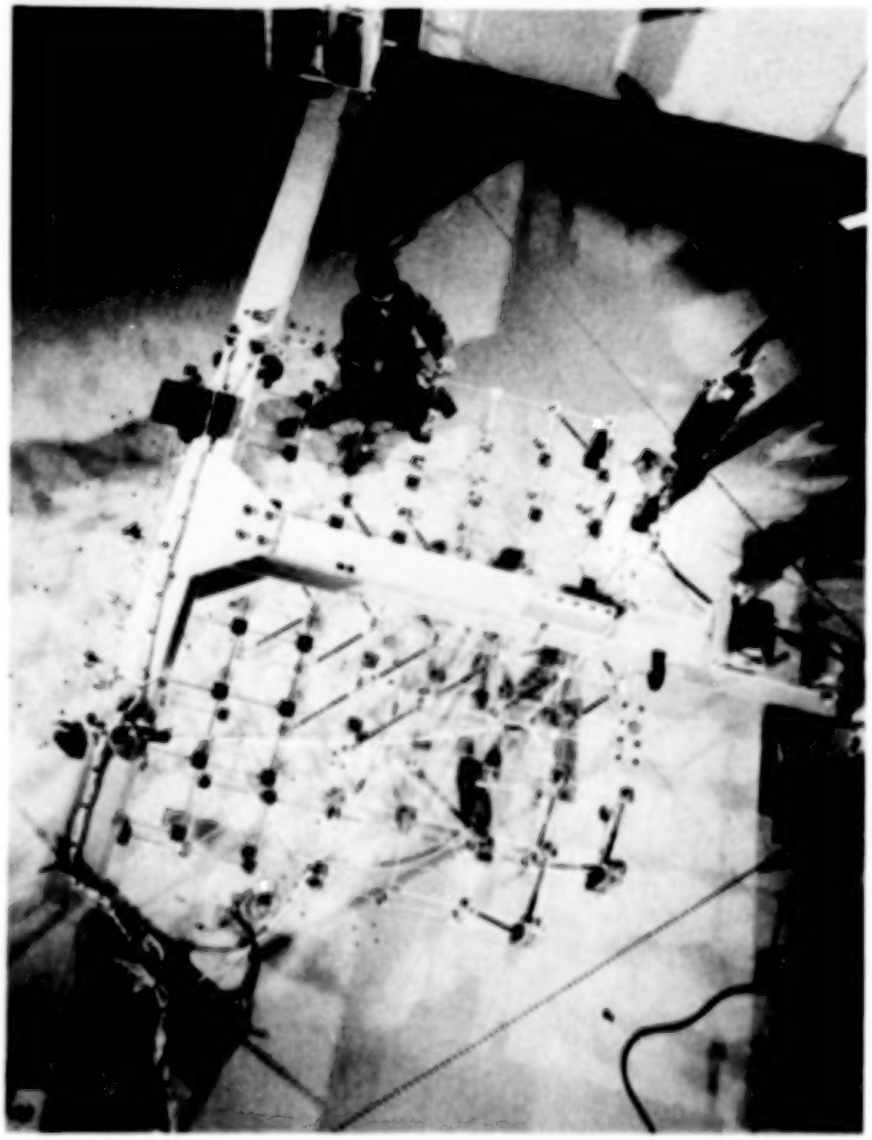


Figure 14

Figure 15 is a close-up of one corner of the box truss. The two large gray assemblies are steel thruster mass simulators weighing approximately 25 pounds each. The small grey blocks are segmented mirror mass simulators. The brass cylinders are extensional shear dampers.

The design goal was to achieve at least five percent modal damping in the first two fixed interface modes. This required damping treatment of 31 members out of more than 500. It should be noted that the truss members are highly stressed due to the large amount of non-structural mass in the one-g environment, and optimum placement of the viscoelastic dampers is not possible. To achieve the same level of damping in a zero-g environment would require only 23 damping members of much smaller size placed in more optimum positions.

Box Truss Mass Simulators

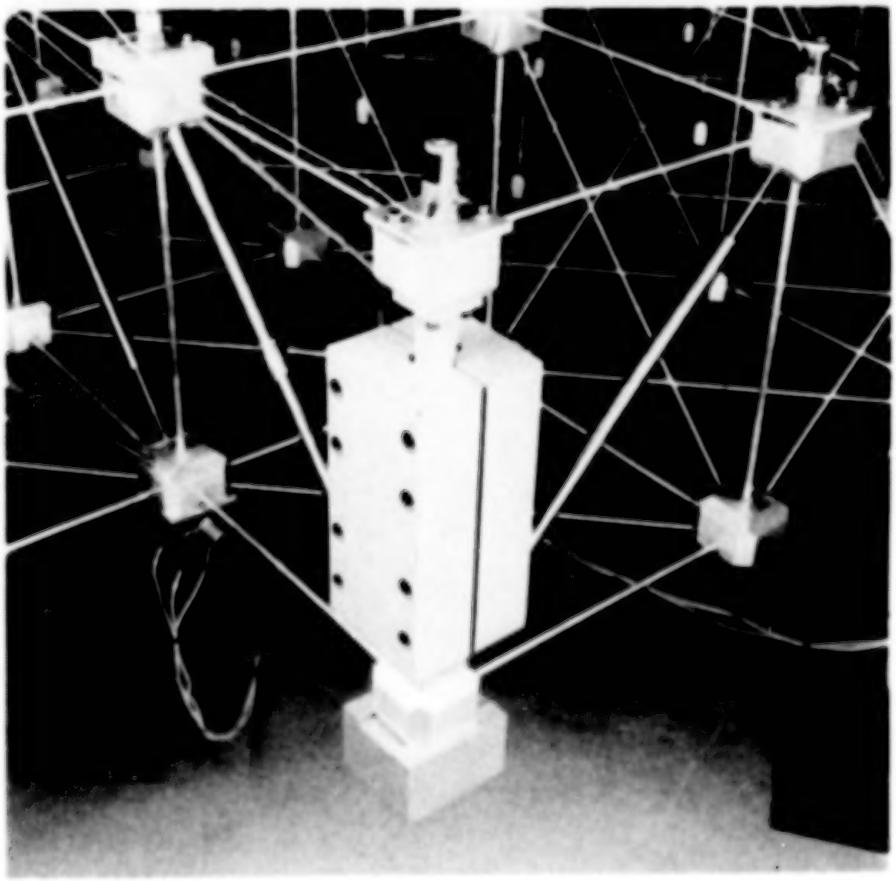


Figure 15

Details of the extensional shear dampers are shown in Figure 16 (Reference 4). The damper rods enter the box truss joint blocks. The rods are wrapped with self-adhesive VEM as shown, and the clamshells bonded to the VEM. The solid sleeve is then bonded to the clamshells. Relative extensional motion of the damper rods induces shear strain into the VEM. A parallel elastic path to control creep is provided by the helix spring. Approximately 85 percent of the strain energy in the damper in the first box truss mode is in the VEM. Thus, the efficiency of this design is 85 percent.

Extensional Shear Damper Design

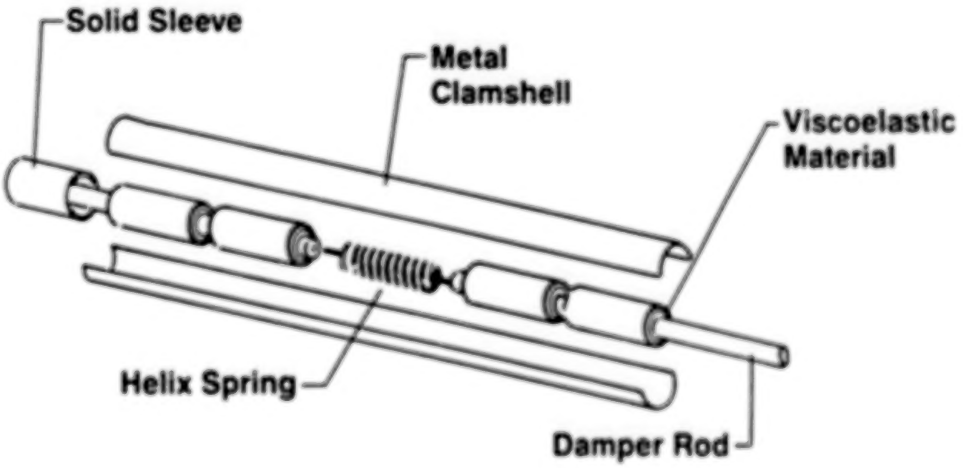


Figure 16

Figure 17 shows the analytical values for the fixed interface modal frequencies and damping ratios. The damping design goal of at least five percent modal damping in the first two fixed interface modes was met with an additional benefit in the other modes due to "damping spillover," wherein the dampers, being active in the higher modes, provide some damping to those modes.

DTA Box Truss Fixed Interface Frequencies and Damping (Analytic)

Mode No.	f_n (Hz)	ζ %
1	4.02	8.6
2	8.75	5.7
3	16.3	3.6
4	17.1	1.7
5	17.7	1.1
6	18.9	5.3

Figure 17

To construct a test fixture which would behave rigidly for the large box truss was beyond program resources. A T-beam, part of the test facility, was used for the test fixture.

The modal test results for the box truss/T-beam setup are shown in Figure 18 (Reference 5). The T-beam participated in all the modes more than anticipated, with the third system mode being principally a T-beam torsion mode. Model tuning involved only a refinement of the T-beam portion of the model. Thus, the clamped modal damping ratios shown in the Figure 17 were achieved for the box truss with fixed interfaces.

Box Truss Modal Survey - Post Test Analysis

- Third Test Mode Was I-Beam Torsion Mode
- Only Analytic Modification Was Adjustment of I-Beam Torsional Stiffness

f_n, Hz		ζ, %	
Measured	*Predicted*	*Measured*	*Predicted*
4.38	4.09	6.6	6.9
10.3	9.39	3.6	3.8
13.6	13.0	0.6	0.5
15.9	15.6	< 0.5	0.3
18.0	18.3	< 0.5	1.6
19.2	18.4	< 0.5	0.3

Figure 18

The equipment platform in the cantilevered test configuration is shown in Figure 19. The brass cylinders are extensional shear dampers similar to those in the box truss, with the exception that those in the upper and lower planes are shorter in length and, being under only light static loads, do not require springs. The large steel tip mass simulates on-board equipment.

There are two aspects of this design that require further discussion, the first being the placement of the dampers. It is obvious that a more efficient application of the dampers would be to damp those bays at and near the root of the truss. Unfortunately, in the one-g environment, the members in those bays are highly loaded. The resulting shear stresses in the VEM would exceed design limits if dampers were placed in those bays.

The next aspect is the relatively large size of the dampers. A large shear area is necessary to reduce the VEM shear stresses to an acceptable level in the one-g environment. This results in long dampers. However, merely increasing the length would result in overly stiff dampers. Increasing the diameter reduces the stiffness to the proper level.

From this discussion, it is obvious that a zero-g design would have fewer, smaller dampers more optimally placed near the root of the truss to achieve the same level of damping.

DTA Equipment Platform in Test Configuration



Figure 19

Results of the equipment platform are shown in Figure 20. The analytic values are derived from a model which accounts for the relatively large static deflection of the structure under the one-g loading. Failure to account for this deflection results in very poor cross-orthogonality checks between the analytic and experimental mode shapes.

As can be seen, predictions of the modal frequencies are quite good, but damping predictions are not as accurate as have been obtained for the tripod and box truss.

Mode 1 is principally a lateral bending mode, but with some torsional coupling due to the gravity-induced droop. Mode two is a bending mode in the vertical plane. Mode three is principally torsion.

In the first mode, the majority of the damping is provided by the top and bottom plane dampers. In the second mode, the side plane dampers provide virtually all the damping. The torsion mode derives its damping from all dampers. The side plane dampers are thus suspect, and it is possible that their shorter length results in significant "end-effects" of the VEM.

DTA Equipment Platform Results

Mode No.	f, Hz			ζ %		
	Test	Analytic	% Error	Test	Analytic	% Error
1	3.78	3.64	3.70	8.3	10.0	20.5
2	3.79	3.81	0.53	5.2	4.6	11.5
3	13.3	12.9	3.01	27.1	25.2	7.01

Figure 20

The DTA antenna is shown in the test configuration in Figure 21. This test setup is somewhat unique in that non-contacting proximity probes were used in place of accelerometers due to the extremely fragile nature of the dish.

The DTA antenna dish actually buckles due to gravity loads. The dish was modelled in its buckled shape, and analytic modes shapes and damping ratios were calculated. As would be expected, results were not as good as for the other structures.

A similar dish without damping treatment was fabricated and tested. That test verified that air damping was not significant.

DTA Antenna in Test Configuration

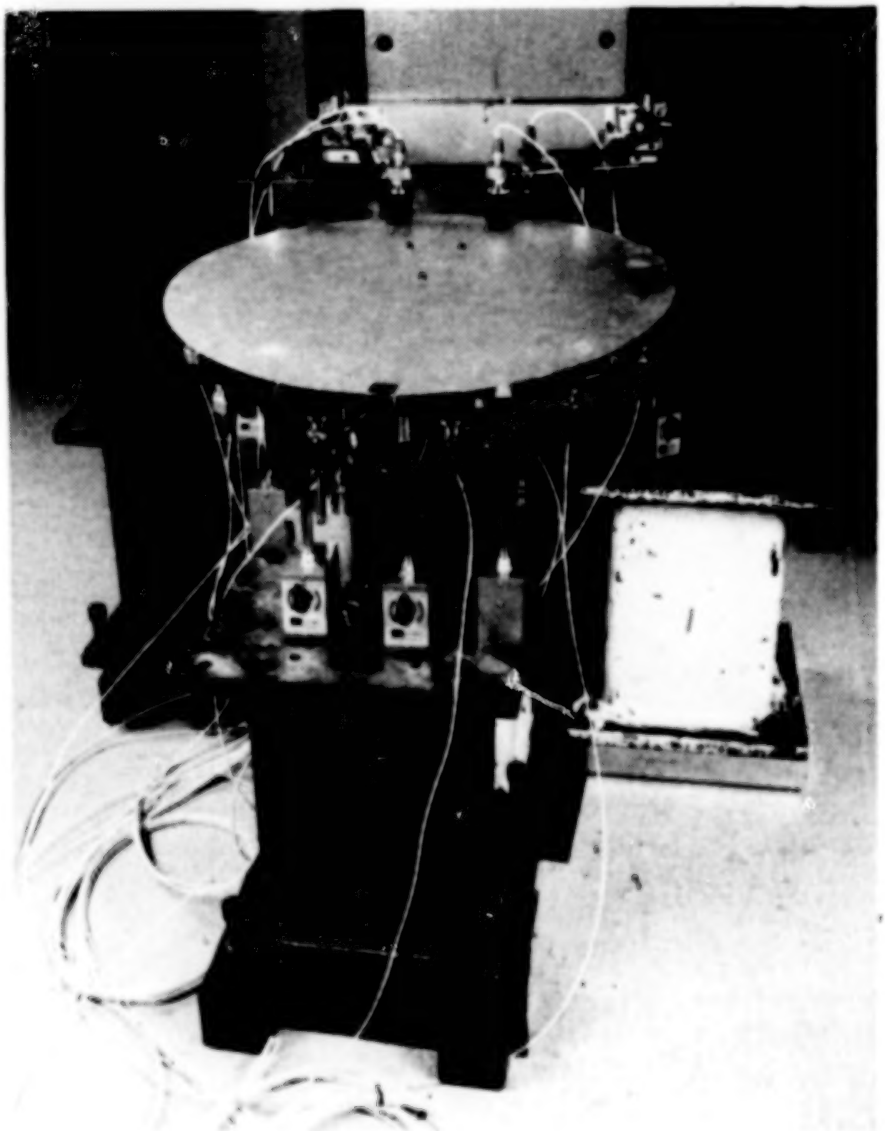


Figure 21

One of the two DTA solar arrays is shown in Figure 22. The array blanket is simulated by an aluminum gridwork to reduce air damping. The solar array mast has damping treatments similar to the tripod legs. Viscoelastic tuned mass dampers (TMDs) are placed on the fourth and seventh blanket ribs to damp the out-of-plane blanket modes. Viscoelastic shear straps were also placed at the spreader bar/blanket interfaces.

The curve in the mast illustrates the effect of the gravity field. When the deformation is accounted for, results were generally good, although the TMDs were extremely flexible and behaved nonlinearly, making prediction of blanket mode damping difficult. We note that the TMDs did provide effective blanket damping, however.

DTA Solar Array

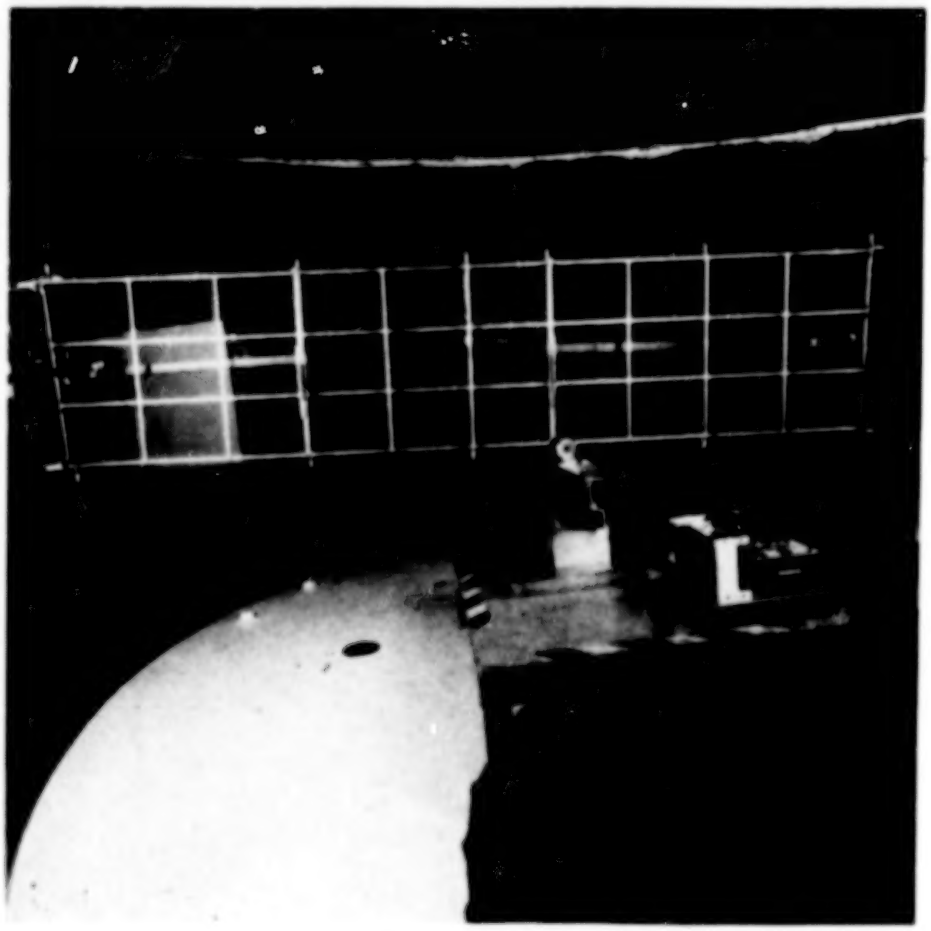


Figure 22

BEST COPY AVAILABLE

The PACOSS program also investigated active control of structural modes. Figure 23 shows the prototype proof-mass actuator in a bench test configuration. The power supply and the control circuits are in the background.

The actuator base is mounted, through three force gauges, to a shaker. This setup was used to validate the analytic actuator model.

Prototype Proof-Mass Actuator in Bench Test Configuration

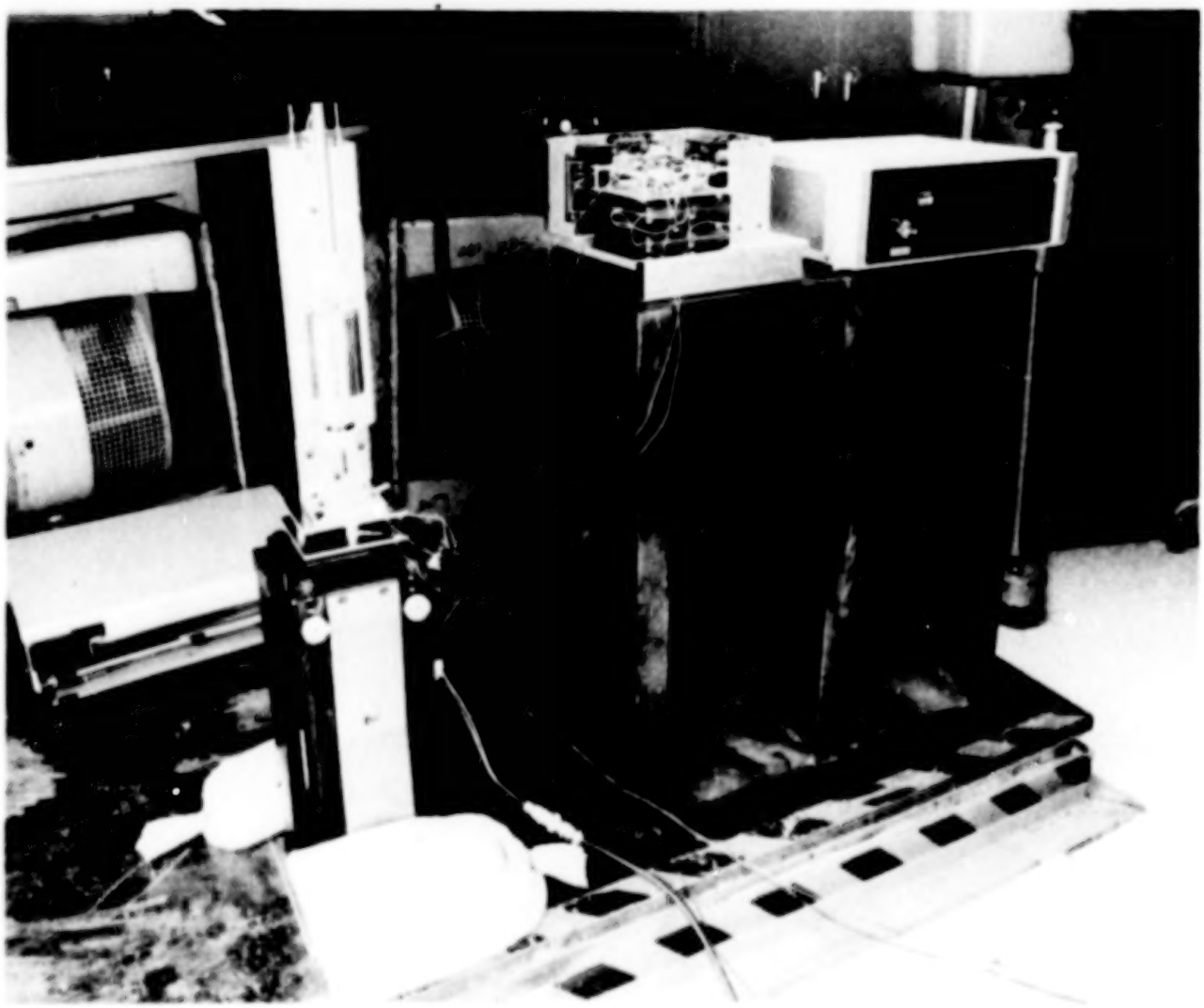


Figure 23

Figure 24 shows details of the actuator construction. A linear motor is fastened rigidly to the thin shaft, which passes through linear bearings at the top and middle of the thirteen inch frame. The bearings were matched to the shaft by the manufacturer, resulting in a very low sliding friction. This design is somewhat unique compared to similar actuators in that there is no relative motion between the motor and the shaft, thereby eliminating eddy-current damping.

The 4.3-lb. motor is suspended on springs as a gravity offload. The springs are sized so the open-loop frequency is approximately 1.5 Hz. The larger cylinder, parallel to the motor and shaft, is an LVT which measures relative velocity between the actuator frame and the motor. The thin LVT core shaft passes through a Teflon sleeve. The LVT is used to provide damping to the actuator, and the gain on this portion of the circuit is adjustable to permit selection of the desired damping level.

An accelerometer is mounted on the top of the frame. The output from this accelerometer is integrated by a bi-quad filter (which has zero gain at DC) to provide inertial velocity to the modal controller. The actuator will act effectively as a dashpot connected between the DTA and ground.

Six of these actuators were manufactured. The weight of each actuator is approximately six pounds. These actuators, when combined with the passive damping augmentation, were designed to provide at least five percent modal damping to the targeted DTA modes.

Actuator

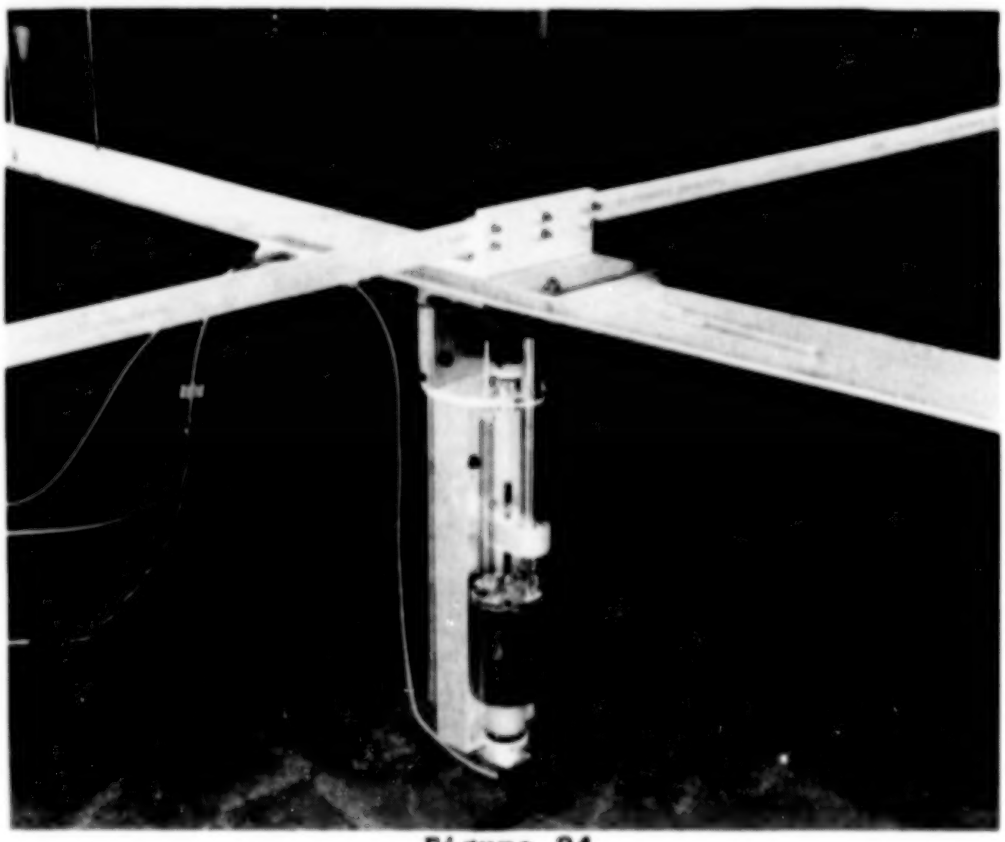


Figure 24

Figure 25 shows the relative to inertial velocity FRF (frequency response function), where the relative velocity is the output of the LVT and the inertial velocity is the integrated output of the accelerometer. The lower pair of curves is for the open-loop case and the upper pair is for the control loop closed case. The smoother curves are the predicted FRFs, and the more jagged curves are the experimental FRFs. The agreement is obviously excellent.

Figure 25 also presents the base force to inertial velocity FRFs. Again, the upper curves are closed loop and the lower open loop. It should be noted that the accelerometer and LVT are accurate down to DC, whereas the force gauges are not. Thus, the predicted and measured values differ at low frequency. Any problems with either the LVT or accelerometer would have been apparent in the relative to inertial velocity FRF.

The resonance at approximately 8.5 Hz, most obvious in the closed-loop measured response in the second plot, is in the experimental setup.

Actuator Transfer Functions

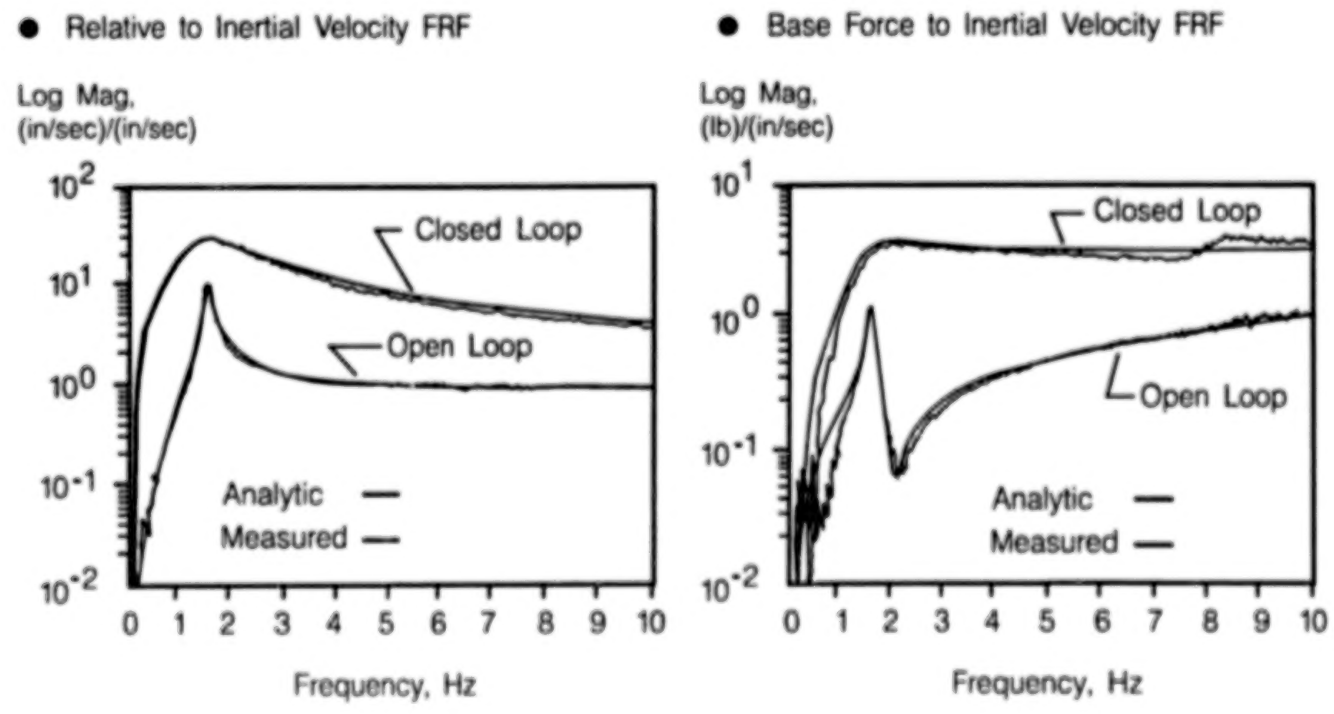


Figure 25

The DTA solar array blanket modes are below one Hz. Thus, they could be destabilized by the 1.5 Hz actuators. However, analysis showed that the blanket mode motion is almost totally in a horizontal plane and thus should not be observable to the actuator accelerometers, which have their sensitive axes vertical in the installed configuration. To provide additional confidence in the analysis, a simple undamped cruciform structure was fabricated and damped actively.

The cruciform beam experiment is shown in Figure 26. The larger beam vibrates vertically in its first mode at a frequency approximating the DTA mode targeted for active augmentation. The smaller beam vibrates horizontally in its first mode at approximately the DTA solar array blanket mode frequency.

This simple test was performed successfully. Approximately 30 percent active modal viscous damping was given to the 32 lb. beam by the actuator, and predicted performance matched measured results nearly perfectly.

Cruciform Beam Experiment

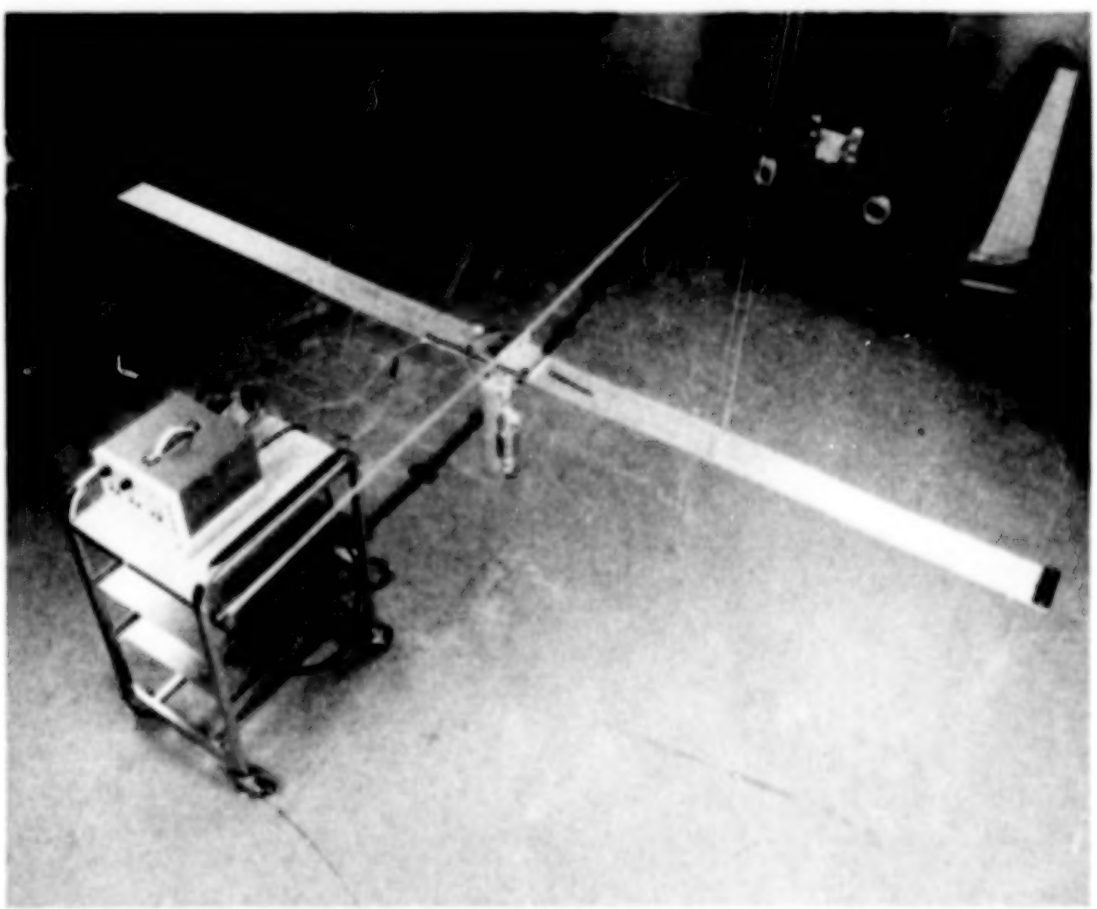


Figure 26

The DTA was assembled for a program review following the Second NASA/DoD CSI Conference. This activity provided a final fit check of all components. The assembled DTA is shown in Figure 27.

Assembled DTA

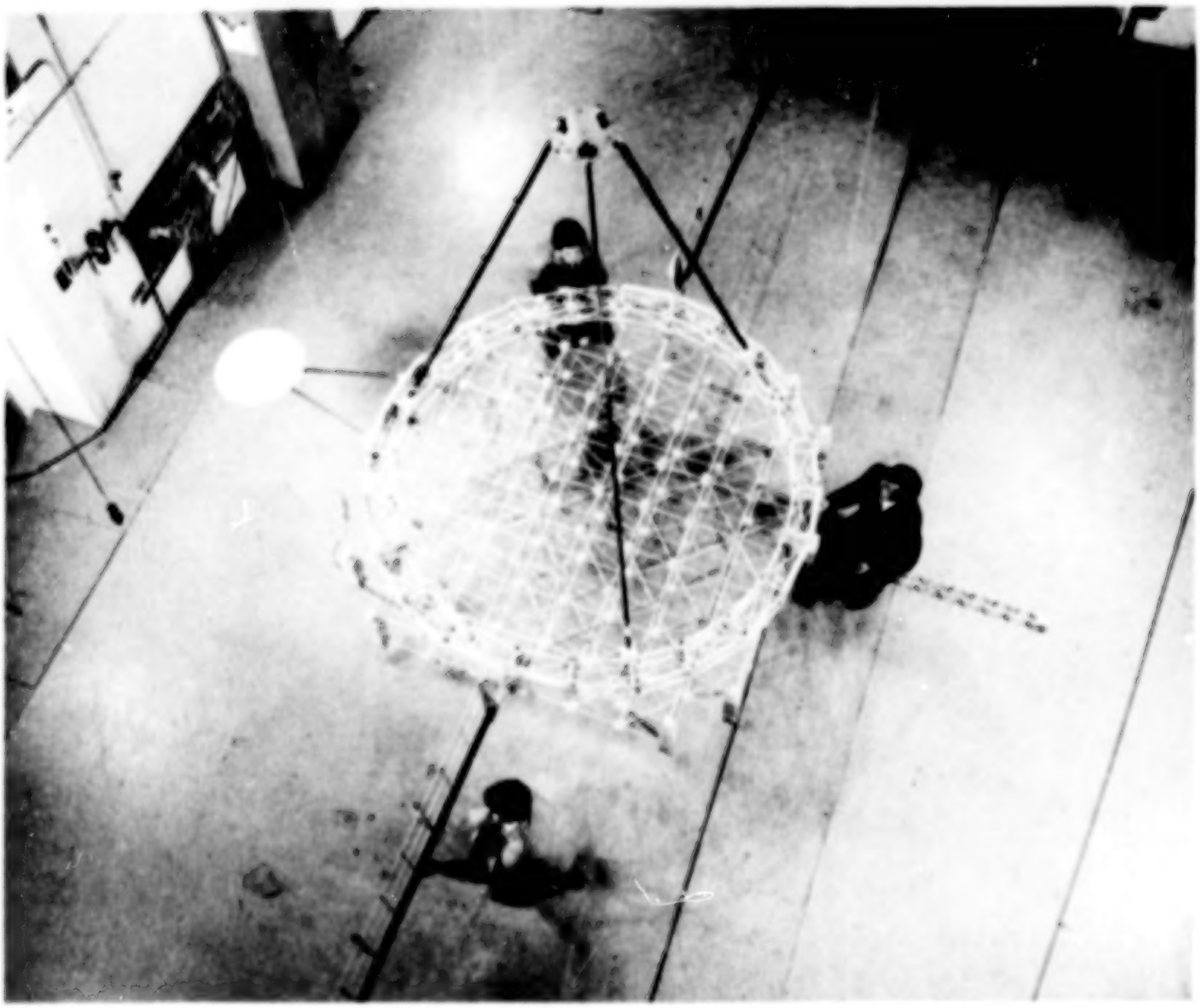


Figure 27

The DTA was assembled, the modal control system was installed, and open- and closed-loop testing were performed. Figure 28 shows the test article in a specially constructed test chamber, which provided a quiet, temperature-controlled environment. The suspension techniques were identical to those used for the ring truss modal survey, although the suspension cables were somewhat shorter.

Several test methods were investigated. Multi-point burst random modal test techniques were chosen as most appropriate for this structure. As many as four simultaneous drive points were used, with a total of five different setups. In addition, sine sweep tests were run to provide data for comparison with those obtained during burst random testing.

DTA in Test Chamber

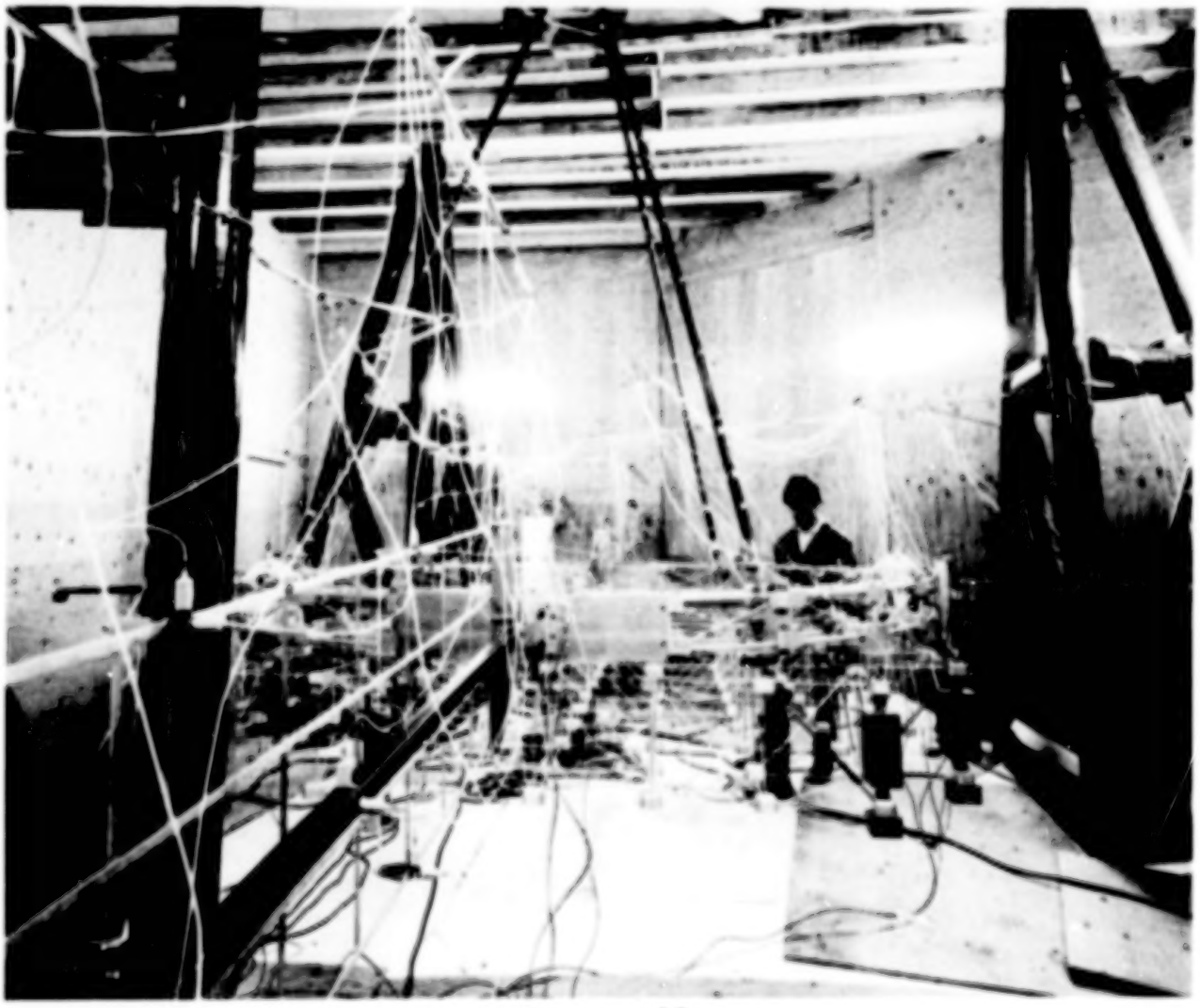


Figure 28

BEST COPY AVAILABLE

Approximately 200 channels of data were obtained for each drive point. Figure 29 shows a comparison between one measured and two analytic FRFs from the open-loop tests. The sharp curve shows the response of the tip of a solar array to a vertical excitation at the solar array mast tip, assuming the 0.2 percent modal damping found during the ring truss modal survey to be characteristic of an untreated structure of this type. The second curve shows the corresponding FRF with the predicted levels of passive modal damping from the coupled model. The third curve shows the measured FRF. There are some obvious differences, but the agreement is generally very good. We note that the general trend is to underpredict the passive damping level.

Solar Array Drive Point FRF

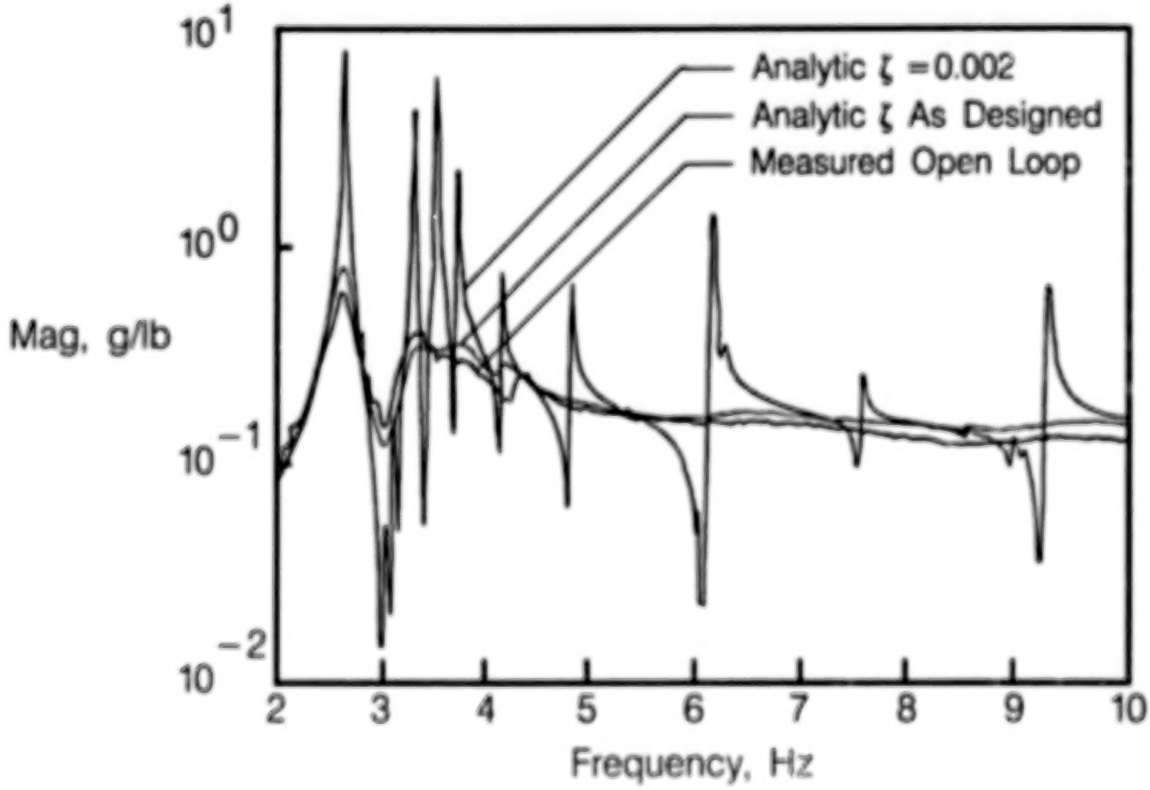


Figure 29

Figure 30 displays the results of open loop tests compared with analytic results. Corrections have been made for VEM frequency effects and the effects of geometric stiffness and the deformed shape of the structure due to the one-g loading.

The high modal density of heavily damped modes (40 modes below 10 Hz) and experimental noise due to the low frequencies and low excitation levels resulted in a challenging parameter identification problem. Modal analysis requires curve fits of the experimental data, and the damping levels identified by apparently equally good attempts would frequently vary by 20 percent, i.e., if the mean value of damping for a given mode was found to be 10 percent, apparently equally good curve fits would produce results between 8 percent and 12 percent.

Most of these results fall within the 20 percent band of parameter identification uncertainty.

DTA Open-Loop Global Modes

System Mode	Global Mode	f, Hz		ζ, %	
		Test	Analytic	Test *	Analytic
15	1	2.61	2.61	3.6	2.8
20	2	3.25	3.29	5.0	4.4
21	3	3.53	3.50	8.8	8.2
22	4	3.72	3.70	5.2	4.7
26	5	4.83	4.60	4.5	7.8
27	6	5.04	4.81	11.4	10.4
35	7	6.48	6.12	12.7	10.0
37	8	9.40	7.52	10.3	6.0
42	9	8.92	9.04	7.0	6.8
45	10	9.26	9.28	8.6	7.0

* Accuracy Approximately ± 20%

Figure 30

Figure 31 shows the open-loop FRF previously shown in Figure 29 and the corresponding measured FRF for the closed-loop system. The global mode at approximately 2.5 Hz was targeted for active damping augmentation. The effect of the active damping is noticeable at the targeted resonance, but has relatively small effect at other frequencies.

Solar Array Drive Point FRF

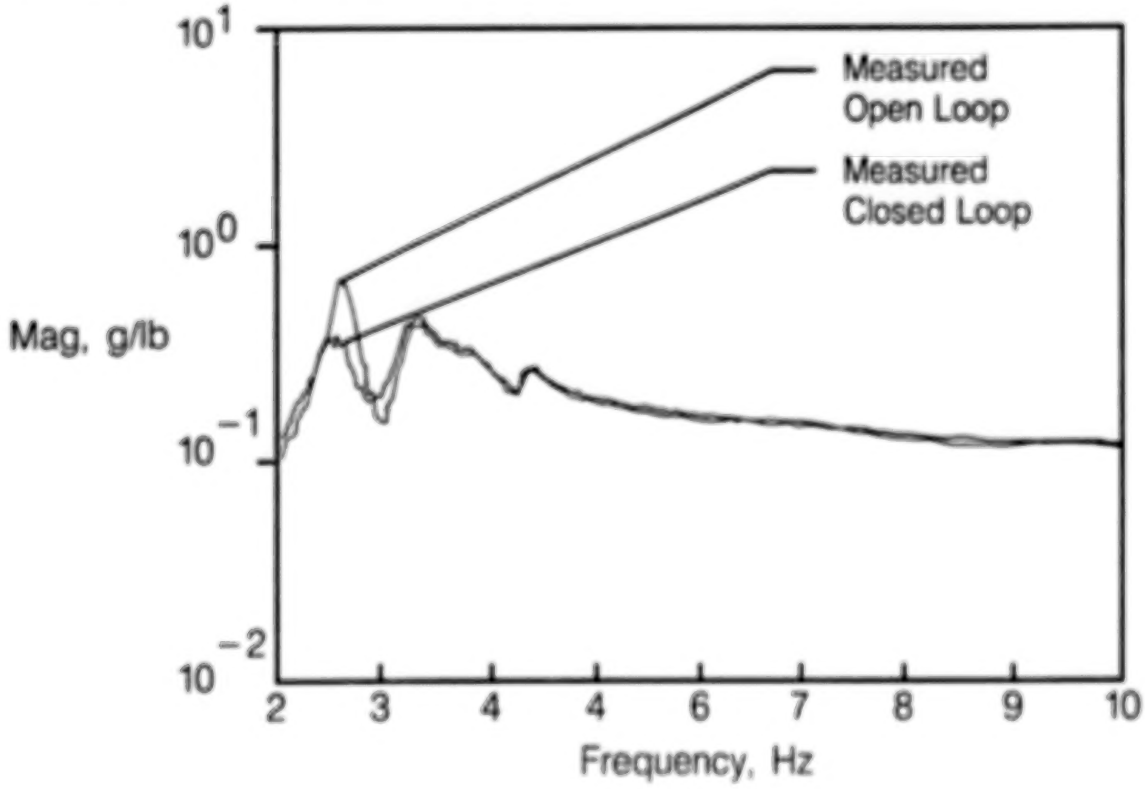


Figure 31

Figure 32 shows the analytic and measured results for the modes which received significant damping from the active augmentation. The agreement between predicted and measured values is excellent. We note, however, that the same 20 percent band as in the open-loop case must be applied to the experimental damping levels.

DTA Closed-Loop Global Modes

	Global Mode +	f, Hz		ζ, %	
		Test	Analytic	Test *	Analytic
Open Loop	1	2.61	2.61	3.6	2.8
	6	5.04	4.81	11.4	10.4
	7	6.48	6.12	12.7	10.0
	10	9.26	9.28	8.6	7.0
Closed Loop	1	2.55	2.54	7.5	8.4
	6	5.00	4.68	15.0	15.8
	7	6.40	5.98	17.0	18.2
	10	9.30	9.30	13.0	12.0

+ Other Modes Not Appreciably Affected by Active Damping

* Accuracy Approximately ± 20%

Figure 32

Several important conclusions can be drawn from work performed on the PACOSS program. Most importantly, the best technique for control of large, flexible space structures is a combination of passive and active control. Passive augmentation is critical because the inherent damping in untreated precision structures is very small and unpredictable. It is possible, however, to design significant, predictable levels of passive damping into large space structures. Finally, the effects of active augmentation of a passively damped structure are predictable, due in large part to the benign nature of the passively damped structure. (Fig. 33.)

Conclusions

- **Best LSS Control Strategy a Combination of Passive and Active**
- **It Is Possible To Design a Predictable Amount of Passive Damping Into a Structure**
- **DTA Open and Closed-Loop Properties Predictable**

Figure 33

REFERENCES

1. Gehling, R. N.: Active Augmentation of a Passively Damped Representative Large Space System. Damping 1986 Proceedings, May 1986, (AFWAL-TR-86-3059)

2. Richards, K. E., and Rogers, L. C.: PACOSS Program Overview and Status. NASA/DOD Control/Structures Interaction Technology 1986 (NASA Conference Publication 2447)

3. Morgenthaler, D. R., and Gehling, R. N.: Design and Analysis of the PACOSS Representative System. Damping 1986 Proceedings, May 1986, (AFWAL-TR-86-3059)

4. Morgenthaler, D. R.: Design and Analysis of Passively Damped Large Space Structures. ASME Publication DE-Vol. 5, The Roll of Damping in Vibration and Noise Control, September, 1987.

5. Gehling, R. N.: Large Space Structure Damping Treatment Performance: Analytic and Test Results. ASME Publication DE-Vol. 5, The Roll of Damping in Vibration and Noise Control, September, 1987.

VIBRATION ISOLATION VERSUS VIBRATION COMPENSATION ON MULTIPLE PAYLOAD PLATFORMS*

S. W. Sirlin
Jet Propulsion Laboratory
California Institute of Technology
Pasadena, California

3rd Annual NASA/DOD CSI Conference
January 30 - February 2, 1989

*The Research described in this paper was performed by the Jet Propulsion Laboratory, California Institute of Technology, under contract with the National Aeronautics and Space Administration.

Overview

There are many future science instruments with high performance pointing (sub microradian) requirements. To build a separate spacecraft for each payload is prohibitively expensive, especially as not all instruments need to be in space for a long duration. Putting multiple payloads on a single basebody that supplies power, communications, and orbit maintenance is cheaper, easier to service, and allows for the spacecraft bus to be reused as new instruments become available to replace old instruments.

Once several payloads are mounted together, the articulation of one may disturb another. The situation is even more extreme when the basebody serves multiple purposes, such as Space Station which has construction, satellite servicing, and man motion adding to the disturbance environment. The challenge then is to maintain high performance at low cost in a multiple payload environment.

The Goal:

- Supply many future science instruments with high performance pointing (sub microradian).

Options:

- Independent spacecraft for each payload - expensive.
- Multiple payloads on a single basebody - cheaper, easier to service, basebody reusable for several short duration payloads.

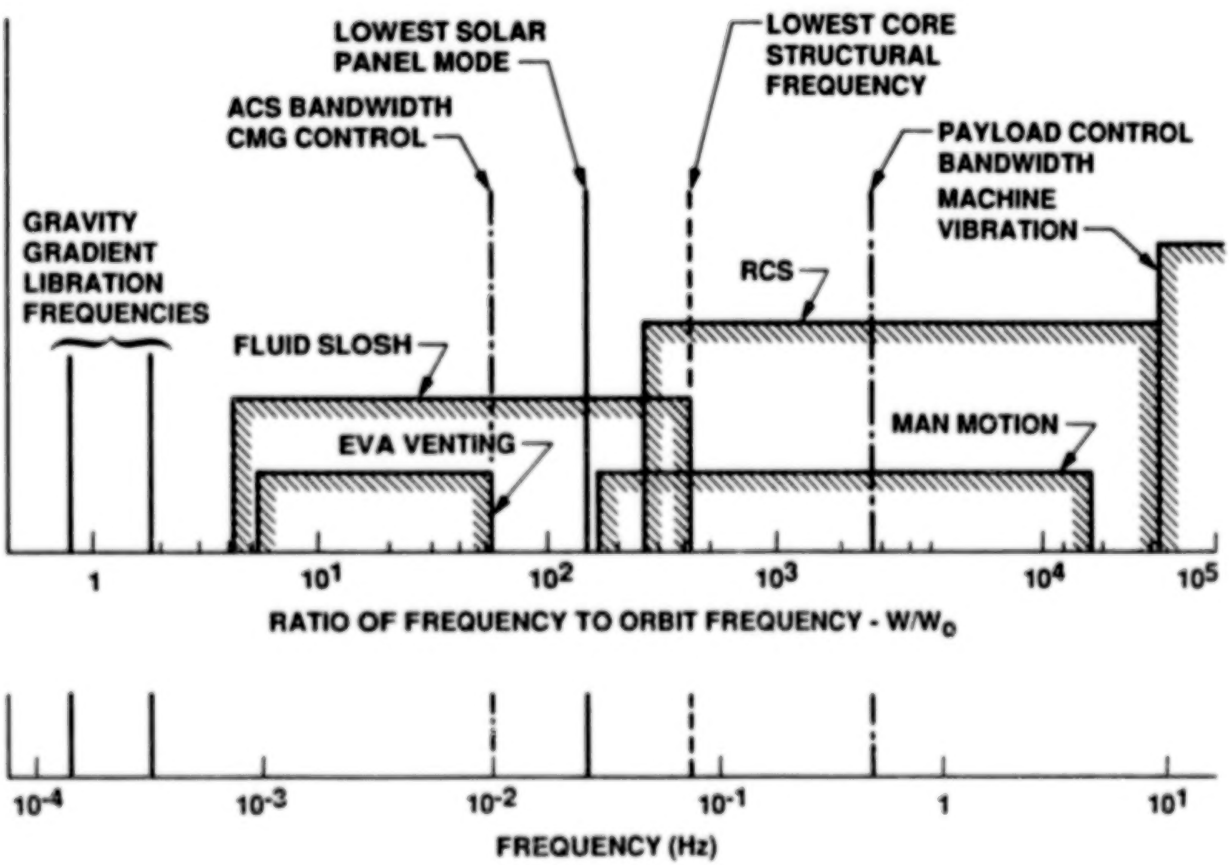
The Problem:

- One payload can disturb another.
- Other activities create large disturbances - construction, satellite servicing, and man motion.

Typical Disturbance Environment

Large, multi-function space platforms, especially manned systems, will have a variety of noise sources that can disturb pointing systems. The platform attitude control system (ACS) of such systems will be of low frequency, able to control only a few of the disturbances such as gravity gradient libration and the low frequency liquid slosh and gas venting. The reaction control system (RCS) can itself excite many of the platform structural modes. The RCS and various activities of the crew (such as push offs, landing, and treadmill walking) are likely to be the dominant noise sources, but vibrations from a variety of machines (pumps, the CMG's, and the washing machine) will also contribute heavily.

SPACE STATION GENERIC INTERACTIONS



Design Approaches

There are three main approaches to the multi-payload pointing problem: vibration suppression, vibration compensation, and vibration isolation. Vibration suppression consists of global reduction of spacecraft disturbances over the whole spacecraft. Examples of global suppression include the use of the spacecraft attitude control system to eliminate vibrations caused by predictable machine vibrations, or the addition of passive damper elements at strategic locations to reduce vibrations at structure resonances.

Vibration compensation consists of active compensation for local vibrations. An example of this is control of a payload gimbal system based on knowledge of the expected spacecraft dynamics, the disturbance sources, and global vibration knowledge. In this case the payload may point accurately even though the basebody vibrates at large amplitudes.

The idea of vibration isolation is not to control all spacecraft vibrations, but allow vibration only in certain places by isolating the noisy parts from the payloads that require precise pointing. The isolation can be done for each disturbance source individually, or for each payload, or "noisy" or "quiet" bus structures for compatible payloads can be built with isolation interfaces.

Three Main Approaches: Vibration Suppression, Vibration Compensation or Vibration Isolation:

- Vibration Suppression:
  - Global Suppression of Spacecraft Disturbances
- Vibration Compensation:
  - Active Compensation for Local Vibrations
- Vibration Isolation:
  - Allow vibration only in certain places
- These approaches are not mutually exclusive.

Vibration Suppression

The possible sources of disturbances can of course be constrained in both amplitude and frequency so as not to disturb the basebody or other payloads.

The vibrations of a structure can be reduced by adding passive damping elements at strategic locations with large participation in the motion. Passive techniques include constrained layer damping, elastomeric or viscous damping at the joints. Active structural elements such as piezoelectric actuators may be used to improve damping performance.

Active disturbance suppression must utilize a wide variety of actuators to reduce vibrations induced by both internal and external torques and forces. A wide variety of centralized active control methods are available to handle this multi-input multi-output problem, ranging from LQG/LTR, and L_∞, H_∞ synthesis to methods specifically addressing disturbances such as disturbance accommodating control. A flight system will require substantial computational capability to implement a design of this type. All of these centralized techniques depend on detailed knowledge of the system dynamics. Since this is likely to change for large structures as they evolve, some kind of on board adaptation system such as system identification or adaptive control is necessary.

- Global Reduction of Spacecraft Disturbances
- Control by Requirements:
  - Constrain possible disturbance sources
  - Allocate allowable payload motion to certain spectral bands
- Passive:
  - Constrained layer damping
  - Elastomeric damping at joints
  - Viscous Damping
- Active:
  - Reaction wheels, thrusters, or CMG's
  - Proof mass actuators
  - Active structural elements
  - Centralized control design
  - Multi-input multi-output

Vibration Compensation

Vibration compensation may be applied to existing hardware, such as hard mounted gimbal systems. Accurate knowledge of the basebody as well as the payload dynamics is required however, since the actuator torques between the two. Due to the rich disturbance spectrum, high performance compensation systems will use a more hardware based approach, consisting of a hierarchy of actuation and control bandwidths. An example is a gimbal system with a bandwidth in the neighborhood of 1 Hz, with a high bandwidth (100 Hz) fast steering mirror for line of sight stabilization. This kind of system is of course unique to a particular payload, though some design elements may be reusable.

A wide variety of centralized active control methods are available, as for vibration suppression. Substantial computational capability may be required, especially if a more modular, non-hierarchical approach is used.

- Active Compensation for Local Spacecraft Disturbances
  - Hard mounted gimbal system
  - Fast steering mirrors
  - Many control options:
    - Centralized control design
    - LQG/LTR
    - L_∞, H_∞
    - Disturbance accommodating control
    - Need detailed system model
    - System Identification
    - Adaptive control

Vibration Isolation

Vibration isolation is essentially a hardware based approach. An active or passive interface is built that is soft in the frequency range of the expected disturbances. This can be used either to keep a disturbance source isolated by itself, or to isolate a payload (or a group of commonly mounted payloads) from the general basebody motion caused by a variety of disturbances.

The isolation can be along single or multiple degrees of freedom, rotational or translational. For gimbaled pointing, translational isolation is key, since if there are even small offsets of the mass center from the gimbal axis, then basebody translations may couple into substantial torques on the payload.

Passive isolators have a long history. One of the more promising common active isolators is active suspension for cars. Some examples of isolators for space based pointing are discussed below.

- Allow vibration only in certain places

Options:

- Active or passive isolator
- Local (isolate each payload separately) or bus systems (isolate a group together)
- Isolation along single or multiple degrees of freedom, rotational or translational

Examples:

Automobile suspension, Honeywell Space Telescope reaction wheel mount, Honeywell magnetic suspension (VIPS), MMC Gimbalflex, Ames KITE tether, JPL Reactuator on a soft mount, JPL SIRPNT concepts, various gravity gradiometer designs.

Design Approaches - Tradeoffs

Vibration suppression must be considered in three parts. Disturbance requirements of some kind must be levied on all payloads. When the variety of payloads is large however, imposing constraints so that all payloads are undisturbed may impose severe constraints on science performance, and hence be unworkable. The passive techniques are simple to apply, but do require extensive hardware and have limited performance. The active techniques are very complex for both hardware and software. Substantial improvements in both design and implementation technology are required to make such an approach feasible.

Vibration compensation can consist of either complex hardware or software. The hierarchical hardware approach has been demonstrated in practice. Obtaining high performance in a modular, non-hierarchical way may require advanced hardware designs and new control technologies beyond the state of the art.

The vibration isolation approach, using hardware to decouple the payload from the noise source, requires much less knowledge of the basebody dynamics. While new hardware is required, it is easily adapted for a variety of payloads. Active methods promise high performance.

- Vibration Suppression:

  Control by Requirements: - Limits payload performance

  Passive: - New hardware, simple implementation
  - Performance may be limited

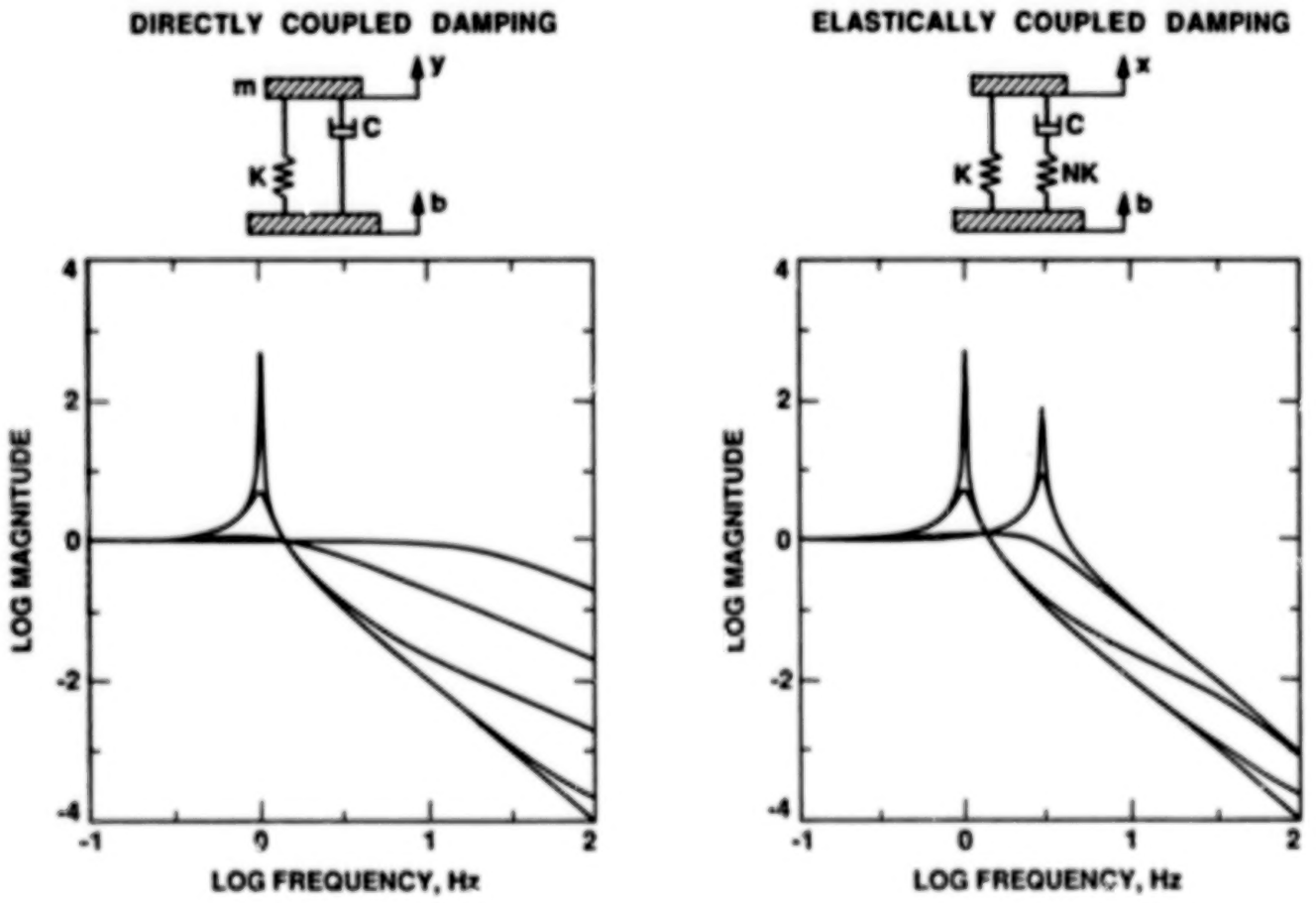
  Active: - Most complex, high performance hardware and software
  - May require extensive, accurate knowledge of the whole system

- Vibration Compensation:
  - May require complex software
  - Requires accurate knowledge of the whole system
  - No new hardware, but must have high performance

- Vibration Isolation:
  - Does not require extensive knowledge of the whole system
  - Modular, easily adapted to different situations
  - New hardware, but less strict performance requirements

Examining the transfer function from base body motion to payload motion, at low frequency, the mount should support the payload for the required loads, so the transfer function should start at 1. At high frequency, ideally transmission should be 0. In between, at some frequency the transfer function should roll off. There remains the problem of resonance. Given a directly coupled damping mechanism, reducing the resonance (by increasing the damping c) increases the high frequency response. This can be overcome by clever mount design, for example if the damping mechanism is elastically coupled, the resonance may be damped while maintaining second order rolloff behavior. In this case as c is increased, the resonance decreases to a minimum, and then increases at a higher frequency. The rolloff maintains a second order character.

TRADEOFF BETWEEN LOW FREQUENCY STIFFNESS, DAMPING, HIGH FREQUENCY ISOLATION



Active Isolation

Active isolators allow much more design flexibility than passive systems. In first of the examples shown, the control adds damping only over a limited bandwidth:

$$u = -\left(\frac{\alpha}{s+\alpha}\right) c\, s\, (x_p - x_b).$$

As α is increased, past the natural frequency, the transfer function approaches the passive directly coupled damping case. The control can also cancel the stiffness over high frequencies:

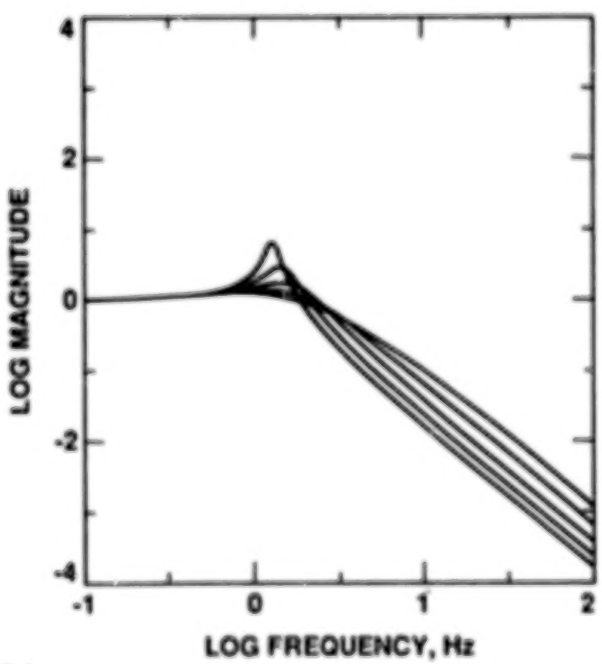
$$u = \left(\frac{s}{s+\alpha}\right) k\, (x_p - x_b).$$

In this case, as α is increased the disturbance rejection is performed at higher and higher frequencies.

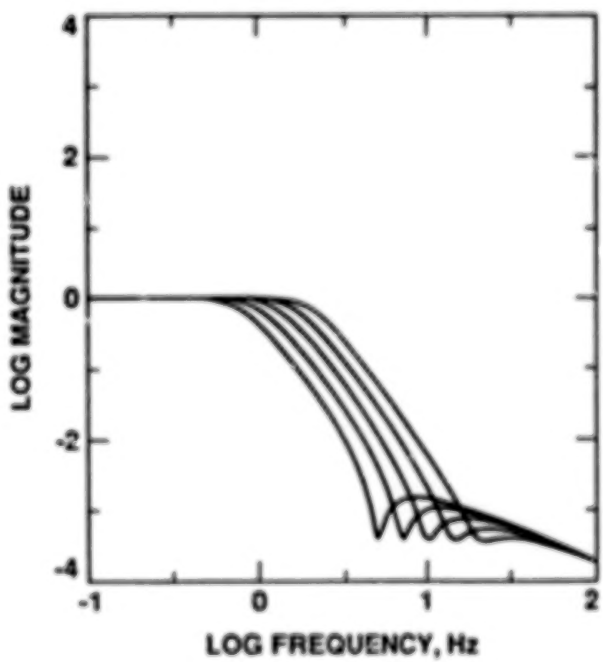
The examples demonstrate some ways in which the frequency response can be tailored to the problem at hand. The spring/damping characteristics can even take on complex nonlinear behavior, for example the stiffness could be set to zero within a deadband, maintaining close to perfect isolation for a limited time. If certain disturbances are predictable, then disturbance compensation techniques can be incorporated into the isolator control to improve performance.

- MORE DESIGN VARIABILITY THAN PASSIVE SYSTEMS
  - FASTER THAN SECOND ORDER HIGH FREQUENCY ROLLOFF
  - NONLINEAR SPRING/DAMPING CHARACTERISTICS
  - CAN INCLUDE COMPENSATION FOR PREDICTABLE DISTURBANCES
  - CAN ADJUST ISOLATION PROPERTIES FOR DIFFERENT CONDITIONS

ACTIVE DAMPING



ACTIVE STIFFNESS CANCELLATION

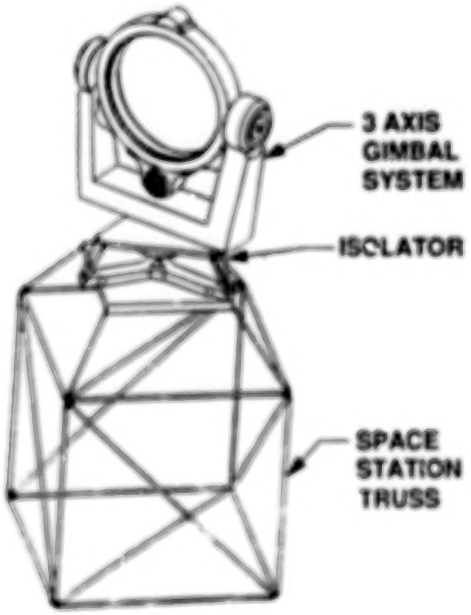


Example Isolator Performance

Passive Soft Mount with Reactuator

One vibration isolation system under study at JPL is a passive soft mount with a reactuator on top. The soft mount consists of 6 struts similar to those used by Honeywell for isolation of the Space Telescope reaction wheels, a passive hydraulic system. The reactuator, for each axis, consists of a powered gimbal system (with axis through the payload center of mass), with an additional motor driving a reaction wheel on the payload. There are thus two motors, one gimbal system, and one reaction wheel per axis. The gimbal motor is driven so as to cancel external torques such as bearing friction and cable windup. The reaction wheel is used for high bandwidth control of payload pointing. The control can be high bandwidth even if the basebody is not known, since the torque acts between the payload and the wheel, and only affects the basebody through the remaining bearing friction and cable torques not eliminated by the outer gimbal motor control.

- **SPACE STATION BASED POINTING SYSTEM**
- **PASSIVE SOFT MOUNT - FLUID FOR DAMPING, 6 STRUTS FOR 6 DOF, EFFECTIVE ISOLATION FREQUENCY 0.02 Hz**
- **CENTER OF MASS MOUNTED GIMBAL**
- **TWO MOTORS PER AXIS:**
  - **LOW FREQUENCY CONTROL REACTS AGAINST SOFT MOUNT**
  - **HIGH FREQUENCY CONTROL REACTS AGAINST REACTION WHEEL**



Example Isolator Performance

Passive Soft Mount with Reactuator

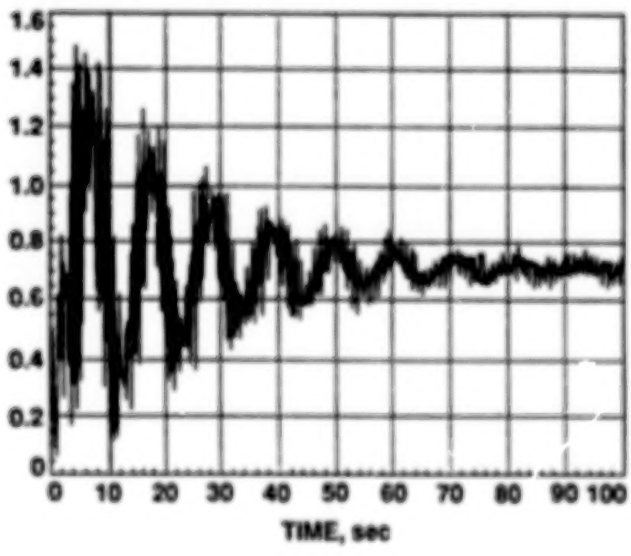
Shown is the Solar Terrestrial Observatory and Solar Instrument Group (STO/SIG) payload on the block 1 Space Station. A hardmount direct drive system is compared to the reactuator on a soft mount. Both systems use gimbals with axes through the payload mass center. The comparison shows the substantial improvement obtained using isolation, even using the same controller.

HARDMOUNT vs ISOLATOR

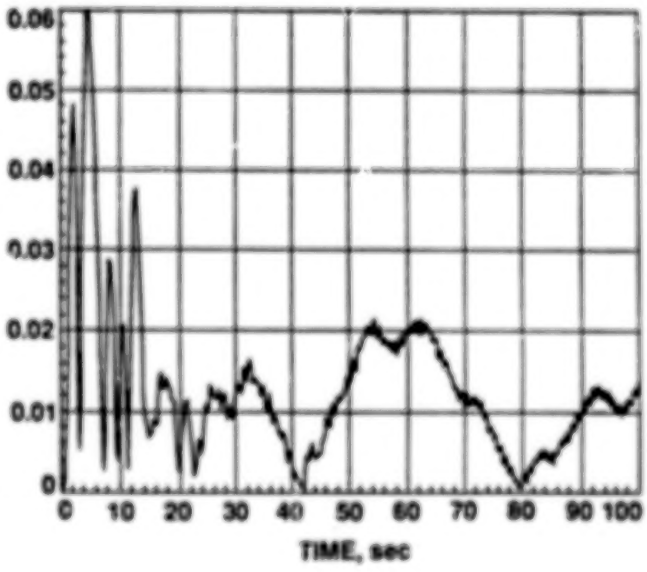
LINE OF SIGHT ERROR IN ARC-SECONDS

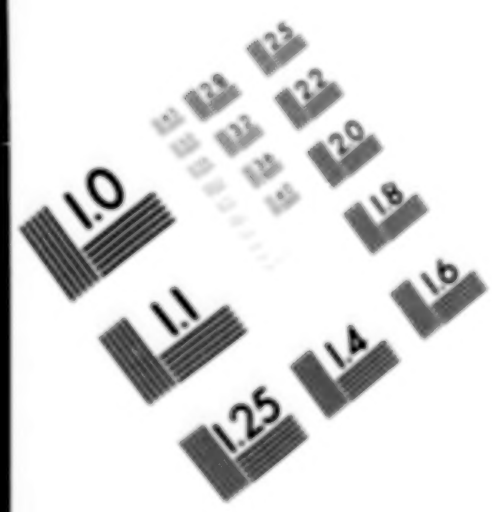
STO/SIG PAYLOAD 45 deg
CONTROLLER: 0.5 Hz INNER 0.1 Hz OUTER 0.01 Hz CMG
FRICTION: LINEAR SPRING OF 4 Nm / 206 arc-sec
DISTURBANCE: 180 lb TREADMILL AT HAB FX TUNED TO 1.125 Hz REASONANCE

HARDMOUNT INTERFACE / DIRECT DRIVE MOTOR



ISOLATOR INTERFACE / REACTIONLESS MOTOR

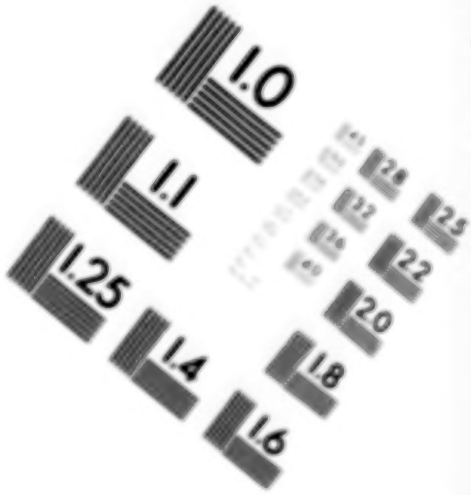




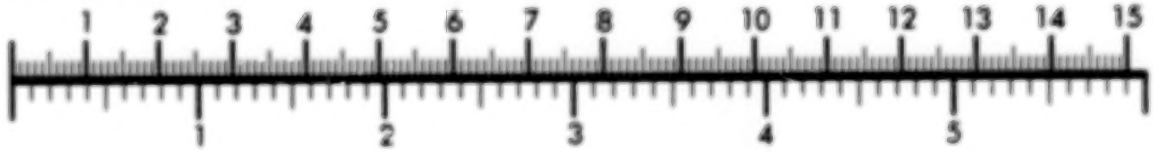


Association for Information and Image Management

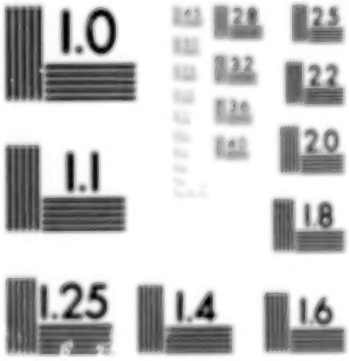
1100 Wayne Avenue, Suite 1100
Silver Spring, Maryland 20910
301/587-8202



Centimeter



Inches





MANUFACTURED TO AIIM STANDARDS
BY APPLIED IMAGE, INC.

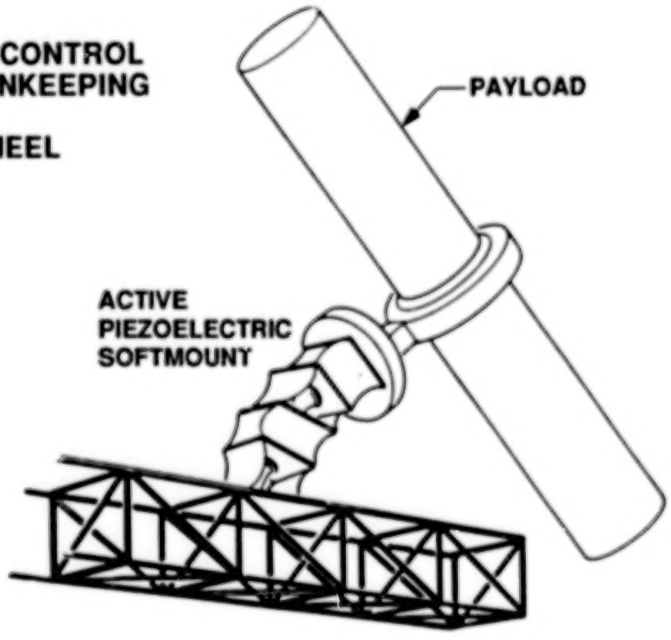


Example Isolator Performance

Soft Mounted Inertially Reacting Pointing System (SIRPNT)

An advanced pointing system concept in development at JPL is SIRPNT. The mount is made of multilayered piezoelectric polymer PVF_2, which is very compliant, but the shape can be controlled (with low authority). A gimbal system is not needed as the polymer can undergo large deformations. While the mount performs vibration isolation and stationkeeping, the primary pointing control consists of reaction wheels (or small CMG's) on the payload itself.

- **SPACE STATION BASED POINTING SYSTEM**
- **ACTIVE 6 DOF SOFT MOUNT - MULTILAYER PIEZOELECTRIC POLYMER (PVDF) CAPABLE OF LARGE DEFORMATION, EFFECTIVE ISOLATION FREQUENCY 0.002 Hz**
- **NO GIMBAL SYSTEM**
  - **LOW FREQUENCY SOFT MOUNT CONTROL TO DAMP RESONANCES, STATIONKEEPING**
  - **HIGH FREQUENCY REACTION WHEEL OR CMG CONTROL**



Example Isolator Performance

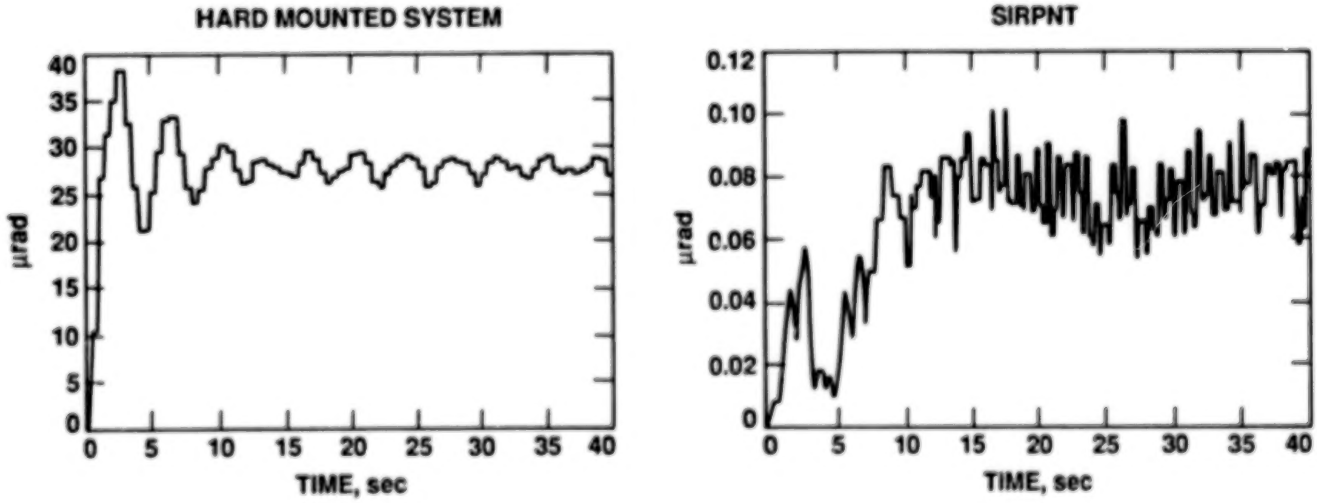
Soft Mounted Inertially Reacting Pointing System (SIRPNT)

Shown is a comparison of a hard mounted, mass center mounted gimbal system with a SIRPNT (with a 2.0 m mass center offset from the attach point). The basebody is the block 1 Space Station, with a treadmill disturbance. The payload is the High Resolution Solar Observatory (HRSO). Pointing stability is a measure of image "smear," the amount the image will be smeared given the instrument exposure time. The stability $s(t)$ over time T is defined in terms of the pointing error e by:

$$s(t) = \max_{\tau<T} \mid e(t+\tau) - e(t) \mid .$$

The controller for the hardmount had a 0.5 Hz bandwidth, while the SIRPNT controller used a 2 Hz bandwidth.

SPACE STATION POINTER STABILITY OVER 1 SECOND



Plans for MPP Work at JPL

Work on Multiple Payload Platforms at JPL will concentrate on vibration isolation methods, building upon previous JPL work in the area of passive and active isolation. We will start with existing simulations, and integrate the isolation and pointing systems from the simulations onto a standard basebody. The basebody used will be the Langley Mission to Earth model, to complement the analytical and experimental work at LaRC. Other, new concepts for isolation systems will be considered for integration into this model. An expanded effort would examine in detail differences between vibration compensation, vibration suppression, and isolation for the MPP problem, but this is beyond the scope of the current effort.

- Concentrate on vibration isolation methods, including previous JPL efforts at passive and active isolation.
- Generate analytical testbed for examining various isolation and compensation designs.
- Complement the analytical and experimental work at LaRC.
- An expanded effort would examine in detail differences between vibration compensation, vibration suppression, and isolation for the MPP problem.

GOES I-M AND BEYOND: SCIENCE REQUIREMENTS AND TECHNOLOGY CHALLENGES

William E. Shenk
NASA/Goddard Space Flight Center
Greenbelt, Maryland

Controls - Structures Interaction Technology Conference - 1989
Third Annual NASA/DoD Conference
January 29 - February 2, 1989

MAJOR EARTH OBSERVATION PARAMETERS MEASURED FROM GEOSYNCHRONOUS SATELLITES

The most significant parameters that are expected to be measured from geosynchronous orbit as a function of spectral region from the ultraviolet through the microwave (≥ 5GHz) are shown below. The spectral regions that are the primary contributors are shown with a "P" and the other regions that contribute in a secondary role are shown with an "S". In every case more than one spectral region is involved with the measurement of each parameter. The most effective measurement system will often combine the data from more than one instrument. Since many of the parameters are used to investigate a scientific event the simultaneous data from numerous instruments is required. Also, these data can be combined with low orbiting measurements to further improve accuracy, resolution, etc. Thus, there will be a requirement to co-locate the measurements from low earth and geosynchronous orbits which will place a high demand on the earth location accuracy from each orbit, usually at the level of the highest spatial resolution used in the analysis.

	SPECTRAL REGION				
PARAMETERS	UV	VISIBLE	REFLECTED IR	EMITTED IR	MICROWAVE (≥5 GHz)
SURFACE TEMPERATURE		S		P	P
TEMPERATURE AND MOISTURE PROFILES		S		P	P
WINDS					
• CLOUD MOTIONS		P		P	S
• MOISTURE MOTIONS				P	
• FROM MASS FIELD		S		P	P
CLOUD PROPERTIES					
• HEIGHT		P		P	
• PHASE (ICE VS. WATER)		P	P		P
• TYPE		P	P	P	S
• AMOUNT		P		P	
PRECIPITATION		P		P	P
LIGHTNING		P			
WATER AND AIR POLLUTION		P	P		
OZONE	P			P	
ICE/SNOW		P	P		P
SOIL MOISTURE			P	P	P
OCEAN COLOR		P			
EARTH RESOURCES		P	P	P	

P - PRIMARY S - SECONDARY

SEVERE LOCAL STORM OBSERVATIONAL GUIDELINES

The table below is a set of observational guidelines for severe local storms that have reached the mature convective phase (i.e. actually producing severe weather conditions like hail, tornadoes, and/or strong surface winds). The guidelines represent what parameters are required and their spatial, temporal, and vertical resolution and accuracy. The guidelines represent what is required to monitor the thunderstorms that are in progress and the surrounding atmosphere within which more storms could be produced. Nearly all of the guidelines have a range of values. Most of the improvements to understanding and prediction of severe local storm events are expected to come as observations move from the low resolution end to the high resolution end of each range. Although observations outside the low resolution limits can still be of benefit, the greatest increase in improvement should come from the observations within the range. Likewise, to improve observational performance beyond the upper limit is not expected to result in much improvement in the basic understanding or the forecasting of these events.

The earth coverage, even at the highest temporal resolution, should be at least 1000x1000 km. Therefore, the combination of resolution, coverage and accuracy will place high demands on the instruments and the rest of satellite system (e.g. navigation, communications).

In general, these guidelines represent the most demanding set that is connected with studying atmospheric processes. When these guidelines are satisfied, then just about all of the guidelines associated with mesoscale and regional scale atmospheric circulations are satisfied including data sets that could be used in atmospheric models. Many guidelines would also be satisfied concerning the diurnal measurement of parameters connected with global change (e.g. clouds). For global change, large areas (e.g. full disk) would be monitored at lower temporal resolution (e.g. 5-60 minutes).

Parameter	Resolution			Absolute Accuracy
	Spatial (km)	Vertical (km)	Temporal (min)	
Temperature:				
o Surface	5-15		10-30	±1-2K[a]
o Profile, General	10-50	1-5[b]	30-120	±1-2K[a]
o Profile, Thunderstorm and Immediate Vicinity	5-25	1-5[b]	1-10	±1-2K[a]
Moisture:				
o Profile, General	10-50	1-5[b]	30-120	±5-15RH
o Profile, Thunderstorm and Immediate Vicinity	5-25	1-5[b]	1-10	±5-15RH
o Lower Tropospheric Moisture Gradient (e.g., dry line)	3-15		5-30	±10-25RH[a]
Surface Pressure:				
o General	10-50		30-120	0.5-1.0 mb[a]
o Thunderstorm and Immediate Vicinity	5-25		1-10	0.5-1.0 mb[a]
Winds:				
o Boundary Layer	5-20	0.2-1	5-30	±1-3m/sec
o Above Boundary Layer	10-50	1-5	15-60	±1-3m/sec
Precipitation:				
o Rate	3-50		3-30	±20-50%
o Type	1-10		1-10	Rain/Hail
o Yes/No	5-50		6-60	
Cloud Top Height	0.5-10	0.25	0.5-15	±250-500m

[a]Relative accuracy is one-half these values

[b]Need 0.2 km vertical resolution for inversions

BEST COPY AVAILABLE

FUTURE GEOSYNCHRONOUS SATELLITES - MAJOR INSTRUMENT REQUIREMENTS

The table on the following page describes the major earth-viewing geosynchronous satellite remote sensing requirements that result from the parameter requirements like what is shown on the previous page. This is the best that we can envision based on the current state of the art. There are still areas where further progress is needed which will be specified later. There are numerous instances in the following table where the remote sensing requirements are different than the parameter requirements. A good example is what is needed to track clouds to infer the winds as contrasted to the actual spatial and temporal resolution of the wind fields. The instrument temporal and spatial resolution requirements are much greater than the wind field resolutions since the instrumental resolutions are dependent on accurately locating and following the progress of small cloud elements to determine the winds.

There are many places in the table where a wide range of resolutions is indicated. This is because a number of uses are expected and the range reflects the resolutions associated with those uses. The principal requirements that are expected to drive instrument and spacecraft system design in the table are as follows:

1) The microwave spatial resolution for precipitation, temperature, and moisture profiles. Even if high frequency microwave window channels (e.g. 150 GHz) were used for precipitation, an antenna size of about 70 m would be needed to achieve 1 km resolution. The use of lower frequencies would require proportionally larger antennas.

2) The combination of spectral and spatial resolution, radiometric resolution and sensitivity, and coverage requirements associated with infrared temperature and moisture profiling.

3) The combination of spatial resolution (particularly infrared), image frequency, and radiometric sensitivity associated with the measurement of surface temperature, cloud properties, and precipitation using visible and infrared imagery.

4) The combination of spatial resolution and sensitivity requirements associated with ocean color and vegetation measurements.

Future Geosynchronous Satellites

Major Instrument Requirements

Parameter	Primary Instrument Type	Resolution: Spatial (km)	Resolution: Temporal (min)	Resolution: Spectral	Nadir Earth Coverage (km)	Typical Sensitivity Values
Temperature						
Surface	o Visible and IR o Imaging	≤1	≤10 (1000x1000 km) ≤60 (full disk)	≤50 nm	1000x1000[1]	≤0.1K NEΔT at 300K (IR channels)
Profiles	o IR Profiling o Microwave (MW) profiling	≤5 (IR) 5-25 (MW)	1-10 (IR) 1-30 (MW) - up to 1000x1000 km	0.2-40 cm^{-1} (IR) 200-500 MHz (MW)	1000x1000[1]	≤0.1K NEΔT -normal scene temperature for a channel (IR) ≤0.25K NEΔT -normal scene temperature for a channel (MW)
Moisture Profiles	o IR Profiling o MW Profiling	≤5 (IR) 5-25 (MW)	1-10 (IR) 1-30 (MW) - up to 1000x1000 km	1-40 cm^{-1} (IR) 1 GHz (MW)	1000x1000[1]	Same as temperature profiles
Ozone	o UV spectrometer o IR Imaging or Profiling	10-50	10-60	2 nm (UV) 0.35-5 cm^{-1} (IR)	1000x1000[1]	1% within 100-600 Dobson units (UV) 0.1 K NEΔT at 200K (IR)
Winds	o Visible, IR and MW imaging o IR and MW Temp. profiling	0.2-2 5-25	1-10 10-180	≥20 nm (IR) Same as temp. profiling	1000x1000[1]	1K NEΔT at 200K (IR) Same as temp. profiles
Precipitation	Visible, IR and MW imaging	0.5-5 (vis & IR) 1-10 (MW)	1-5 (vis & IR) 3-30 (MW)	≥20 nm (vis & IR) 0.5-1 GHz (MW)	500x500[1]	0.5K NEΔT at 200K (IR) 1K NEΔT at 200K (MW)
Cloud Properties (e.g. amount, type, and height)	Visible and IR Imaging	0.2-1	0.25-30	1-50 nm	500x500[1]	0.5 K NEΔT at 200K (IR)
Lightning	Visible and Near IR Imagery	1-10	1 millisecond	1 nm	1000x1000[1]	4.5 μjoules m^{-2} ster
Sulfur Dioxide (volcanic eruption)	UV spectrometer	10-50	10-60	1 nm	1000x1000[1]	≤3 milliatm. cm of SO_2
Ocean Color	Visible and IR Imaging	0.1-0.5	30-60	10-20 nm	100x100 up to 1000x1000	0.003 MW cm^{-2} μ^{-1} $ster^{-1}$
Vegetation	Visible and IR Imaging	0.03-0.5	30-60	10-20 nm	50x50 up to 500x500	0.003 MW cm^{-2} μ^{-1} $ster^{-1}$

[1]Minimum coverage needed--up to full disk required for maximum coverage

BEST COPY AVAILABLE

RAPID CONVECTIVE CELL GROWTH

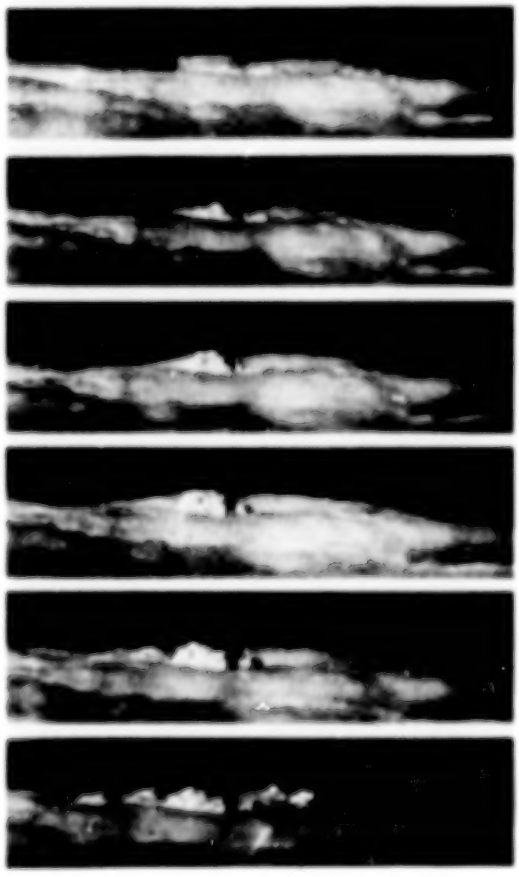
The following series of aircraft photographs of the tops of a violent thunderstorm illustrates the need for extremely frequent imaging to accurately depict what is occurring during an extreme event. It is crucial that we design our satellite instruments to capture extreme events because they are the ones that have the greatest impact. Hail and tornadoes were produced during the lifetime of this convective complex.

These rapidly growing and dissipating domes penetrated into the lower stratosphere in extreme southern Texas on May 12, 1972. From about 90 km away and with the aircraft near the level of the anvil, a dome near the center of each photograph grew rapidly between 2330 and 2331 GMT and had begun to collapse at 2332. At 2331:30 the height of the 7.7 km wide dome was 2.3 km above the cirrostratus anvil. Between 2330 and 2330:30 the vertical growth rate was 27 m sec^{-1} and slowed to 18 m sec^{-1} over the next 30-sec interval. New cells can be seen beginning to grow on both sides of the principal dome near the end of the sequence.

These extreme growth rates and the cell dimensions can provide guidelines for the development of future geosynchronous satellite instrumentation. From the analysis of this case and other similar events, we have concluded that ≤ 1 km visible and infrared imaging resolution is required at 15 second intervals to properly monitor the tops of violent convection.

PHOTOGRAPHED FROM A LEAR JET AT 45,000 FT.

MAY 12, 1972



BEST COPY AVAILABLE

FUTURE GEOSYNCHRONOUS SATELLITE REQUIREMENTS

A. Space System Requirements

1. Absolute Earth Location (3σ)

Within 1 pixel of the highest resolution measurement made on the spacecraft.

2. Imaging Within Image Stability and Image-to-Image Registration (3σ)

Within 30% of the highest resolution measurement made on the spacecraft.

3. Instrument-to-Instrument Alignment Knowledge (3σ)

Within 1 pixel of the highest resolution used in the analyses of measurements from the combined instruments.

4. Absolute Pointing Accuracy - Within 5% of the smallest size area covered from any sensor on the spacecraft.

B. General Instrument Requirements

1. Imaging -

a. Channel-to-channel registration (3σ) - Within 30% of the highest resolution pixel in the instrument. This could be a system requirement if there are very high frequency sources of spacecraft jitter.

b. Knowledge of diffraction effects out to the 99% encircled energy level.

c. System MTF at least to the GOES I-M imager level.

2. IR Profiling

a. Channel-to-channel registration (3σ) - Within 10%

b. Knowledge of diffraction effects out to 99.5% the encircled energy level.

c. High spatial resolution cloud knowledge out to the 99% encircled energy level.

3. Microwave Profiling

a. Same as items 1 and 2 for IR profiling

b. Beam efficiency within Aries disk - ≥97%.

Examples of Major Technological Challenges for the Next 25 Years

System

- o Earth Location Accuracy
- o Image Stability
- o Motion Compensation for Diverse Sensors on Same Spacecraft Implementing Complex Measurement Scenarios
- o Rapid and Accurate Parameter Determination and Widespread Information Dissemination
- o Longer Lifetimes (includes servicing)

Visible and Infrared Imaging and Infrared Profiling

- o Detector Technology - Stability, Sensitivity, Arrays, Spectral Knowledge, etc.
- o Calibration - Large Mirrors
- o Coolers (radiative, refrigerators, cryogen)
- o Pushing Spectral Resolution Limits (filters, interferometers, spectrometers, Fabry-Perot)
- o Scanning Mechanisms - Stability
- o Minimize Diffraction Effects
- o Channel-to-Channel Registration

Microwave Imaging and Profiling

- o Develop and Maintain Antenna Surface Tolerances ($\leq 1/20\lambda$)
- o Earth Coverage of $\geq$1000x1000 km (up to full disk) Within Temporal Limits Using Large Antennas
- o Unfurling Large Antennas and Maintaining Surface Tolerances (e.g. 50 m Antenna Measuring at 220 GHz)
- o Minimize Antenna Movement Effects on the Performance of Other Sensors
- o Synthetic Aperture Microwave

Major Areas for Further Long-Range ($\geq$25 years) Development in Geosynchronous Orbit

- o Active Sensing (e.g. lidar, radar)
  - o Pressure (surface and profiles)
  - o Temperature and moisture profile vertical resolution and accuracy
  - o Precipitation
- o Very Large Microwave Antennas ($\geq$100m) for Low Frequency Measurements ($\leq$40 GHz)
- o Surface Energy Augmentation from Space

CONTROLLED MULTIBODY DYNAMICS SIMULATION FOR LARGE SPACE STRUCTURES

J. M. Housner
NASA Langley Research Center
Hampton, Virginia

S. C. Wu and C. W. Chang
The Comtek Company
Yorktown, Virginia

Third Annual CSI Conference
San Diego, California
January 30 - February 2, 1989

MULTIBODY DYNAMICS DISCIPLINE

The multibody dynamics discipline involves the large relative motions of connected flexible bodies. Thus, the configuration of the multibody system is time-varying, generally resulting in time-varying inertial properties and sometimes in time-varying stiffness properties. Hinge connections between the bodies are necessary to enable the changing relative orientations. Because there are multiple bodies, it is quite likely there will also be multiple control systems with multiple objectives. Multibody dynamics finds application in various fields. Many applications impose constraints on the multibody system and the handling of these is a critical aspect of the discipline.

- o DEFINITION: Interconnected Flexible Body Dynamics With Time Varying Relative Orientations
  - Time Varying Stiffness and Mass
  - Hinge Connections of Various Types
  - Multiple Control Systems
- o APPLICATIONS:
  - Mechanisms
  - Unfolding Deployment/Retraction
  - Articulation
- o CONSTRAINTS
  - Motion Limiters, Mechanical Regulators
  - Connect/Disconnect
  - Lock/Unlock
  - Robotic Hand-Off

THE ROLE OF MULTIBODY DYNAMICS SIMULATION ANALYSIS IN CSI DESIGN

Four roles are here identified for multibody dynamics simulation. Use of this simulation early in the design process can be most effective as it can reveal design shortcomings before commitment to a design concept. Multibody simulation can be used to address performance degradation, constraint violation and stability. Invariably the simulation models are more refined then the design models and can thus be used to judge the suitability of the design models. The simulation models usually incorporate modes left out of the design models, thus addressing "spillover", uncertainties in structure, controller, sensors and actuators, and nonlinearities which are often neglected in design.

o IDENTIFIES TECHNICAL ISSUES EARLY IN DESIGN PROCESS

LESS EXPENSIVE THAN EXPERIMENTATION
CAPABLE OF PARAMETER STUDIES WITH REFINED MODELS

o ESTABLISHES CONTROLLER PERFORMANCE DEGRADATION

MODAL TRUNCATION, UNCERTAINTIES AND NONLINEARITIES

o ESTABLISHES VIOLATION OF CSI DESIGN CONSTRAINTS

STRUCTURAL MEMBER BUCKLING
ACTUATOR OUTPUT EXCEEDANCE

o EXAMINES STABILITY OF DESIGNED SYSTEM

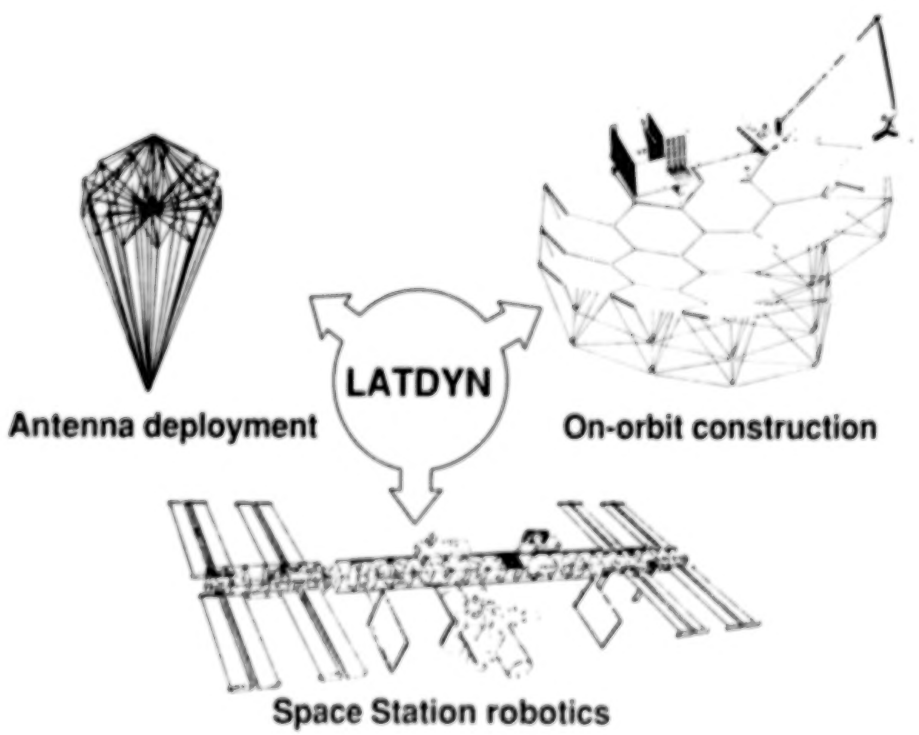
ACTUATOR AND SENSOR PLACEMENT
LINEAR DESIGN ASSUMPTIONS

LATDYN CAPABILITIES

The LATDYN (Large Angle Transient DYNamics) code is a simulation tool for controlled multibody dynamics. The code is finite element based with the present version having a limited element library consisting of mass, spring, damper and beam elements. The user models each body with finite elements, rather than with truncated modes or other function sets which have to be generated outside the multibody program.

Control laws are input through a FORTRAN-based command language which gives the user internal access to the code from an external position. Further details on the program architecture are given in the chart on LATDYN architecture.

Practicalities of control implementation can also be modeled such as actuators, friction and time delay in digital control. Two and three dimensional versions are available and results from these are presented herein. Additional information on the code is available in references 1 - 3.



LATDYN CAPABILITIES

- SIMULATION ANALYSIS TOOL FOR LARGE MOTIONS AND DEFORMATIONS OF CONTROLLED MULTIBODY STRUCTURES FOR,

  ASSEMBLY DYNAMICS, ARTICULATING COMPONENTS, ROBOTIC OPERATIONS

- FINITE ELEMENT BASED STRUCTURAL MODELING

  RIGID OR FLEXIBLE COMPONENTS
  ARBITRARY GEOMETRY

- EXTENSIVE CONTROLS MODELING

  FORTRAN BASED COMMAND LANGUAGE PERMITS SIMPLIFIED USER INPUT OF CONTROL ALGORITHMS

- ACTUATOR AND MOTOR MODELING

  FRICTION AND TIME DELAY

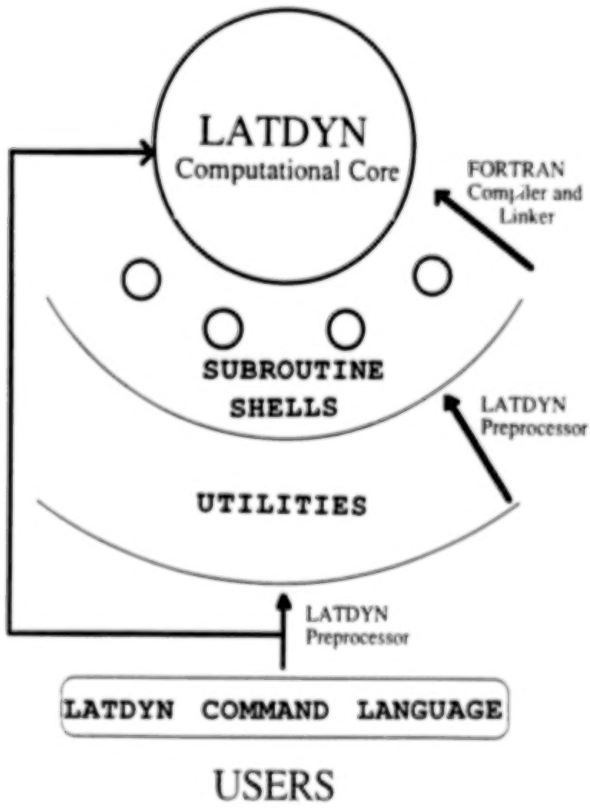
- 2-D VERSION DEVELOPED IN 1986

- 3-D WORKING VERSION OPERATIONAL

LATDYN ARCHITECTURE

For the structural part of the modeling, user commands resembling that of a typical general purpose finite element program are employed. However, for controls, the commands take on a somewhat different character. The user writes the control law equations in FORTRAN within a command statement using a defined protocol to access utilities residing in the LATDYN pre-processor. (Since most users are well acquainted with FORTRAN this is a natural language to use.) The pre-processor generates complete FORTRAN code which is then placed in empty subroutine shells. This resembles the user-written subroutines employed by other programs, but has the distinct advantage of relieving the user of the burden of understanding the complex operations of the code. The user need not be concerned with what subroutines are created, nor how data are transferred within the code. This and many other functions are performed automatically. Finally the generated code is compiled and linked to the LATDYN computational core.

Furthermore, the user can create his own variables and can readily specify logic conditions under which commands are to be activated or deactivated. This is an important aspect for control actuators which are only activated once prescribed conditions are exceeded or can become saturated as in the case of momentum exchange devices.

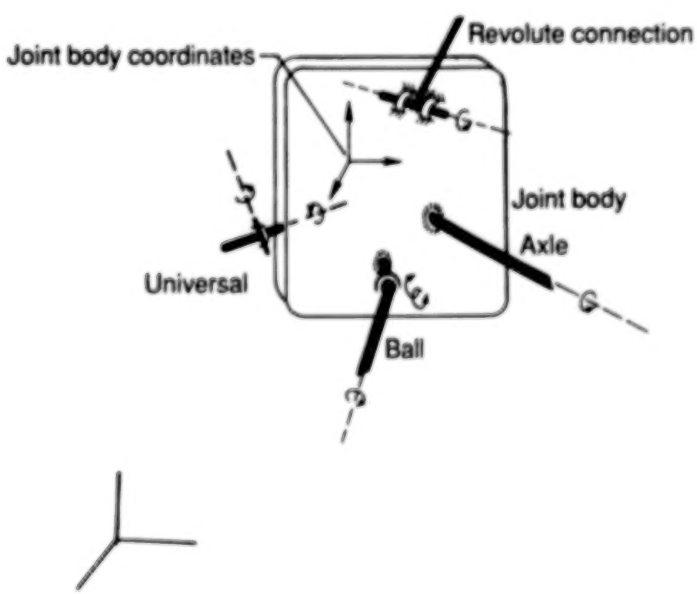


GENERIC JOINT BODY WITH VARIOUS TYPES OF HINGE CONNECTIONS

The class of structures to be treated by this program is joint dominated. That is, the mass of the interconnecting joints between the bodies represents a significant portion of the total mass and the orientation of the joint's hinge lines plays an important role in determining structural behavior. It is thus reasonable to construct the finite element program with the joints as a part of the element connectivity. This avoids numerical problems which can arise due to what might be called "the tail waging the dog" phenomenon. Furthermore, since large angular rotations are not vectors, connectivity relationships could be time varying and quite complex. The use of hinge bodies circumvents these connectivity complications.

A generic hinge body with several members connected to it through various types of joints is depicted in the figure. Accommodations for hinge connections to various members connected to the hinge body are built into the formulation.

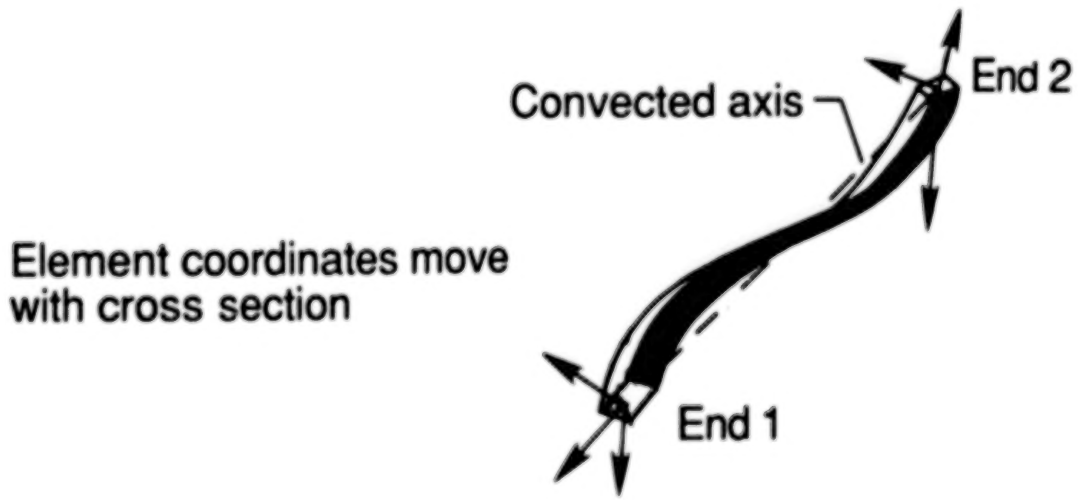
A Cartesian coordinate system is used to measure three translations of a designated point on a hinge body and a transformation matrix provides the orientation of three orthogonal axes embedded into the hinge body. Members are assumed to be hinge-connected to a hinge body. The connecting hinge line is embedded into the hinge body and is related to the hinge body axes through a fixed transformation matrix Γ. The rotation Θ about the hinge line is time varying.



DEFORMED FINITE-ELEMENT AND ELEMENT COORDINATE SYSTEMS

Each structural member is divided into finite elements. A typical deformed element is shown in the figure. The orientation of the element at its ends is monitored by means of a two-element coordinate system, one at each end. These coordinates move with the element. The x-axis of the element system is tangent to the element at its end and the other two orthogonal axes are parallel to the principle axes of the element cross section. The orientation along the length is found from an assumed polynomial shape function as in any finite-element analysis.

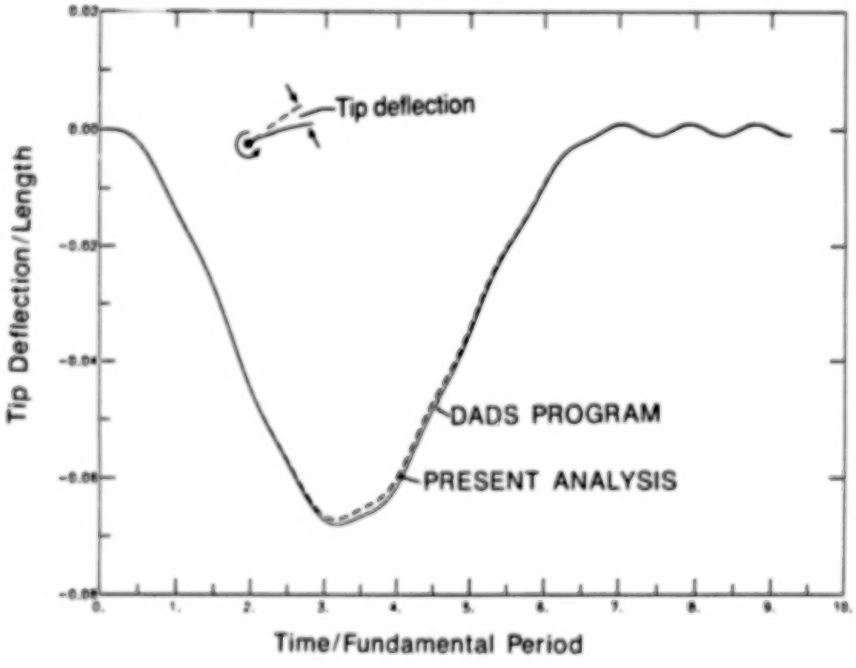
A convected coordinate system is used to define a reference for measuring element flexural deformations. This separates rigid body and deformable motion. As shown in the figure, the convected x-axis connects the end points of element. Its other two orthogonal axes roll with the element.



Deformations are measured from convected axes

COMPARISON OF RESULTS FOR FLEXIBLE BEAM SPIN-UP ON A PLANE

A flexible rotating beam, with a one hertz fundamental frequency is accelerated to a constant angular velocity in six seconds. The results of the LATDYN program are compared with those from a commercial code known as DADS. (See reference 4 for further details on this code.) Results are in excellent agreement with only a slight deviation during the transient region. The LATDYN model uses two finite elements, but one would have sufficed. The DADS result can be found in reference 5.



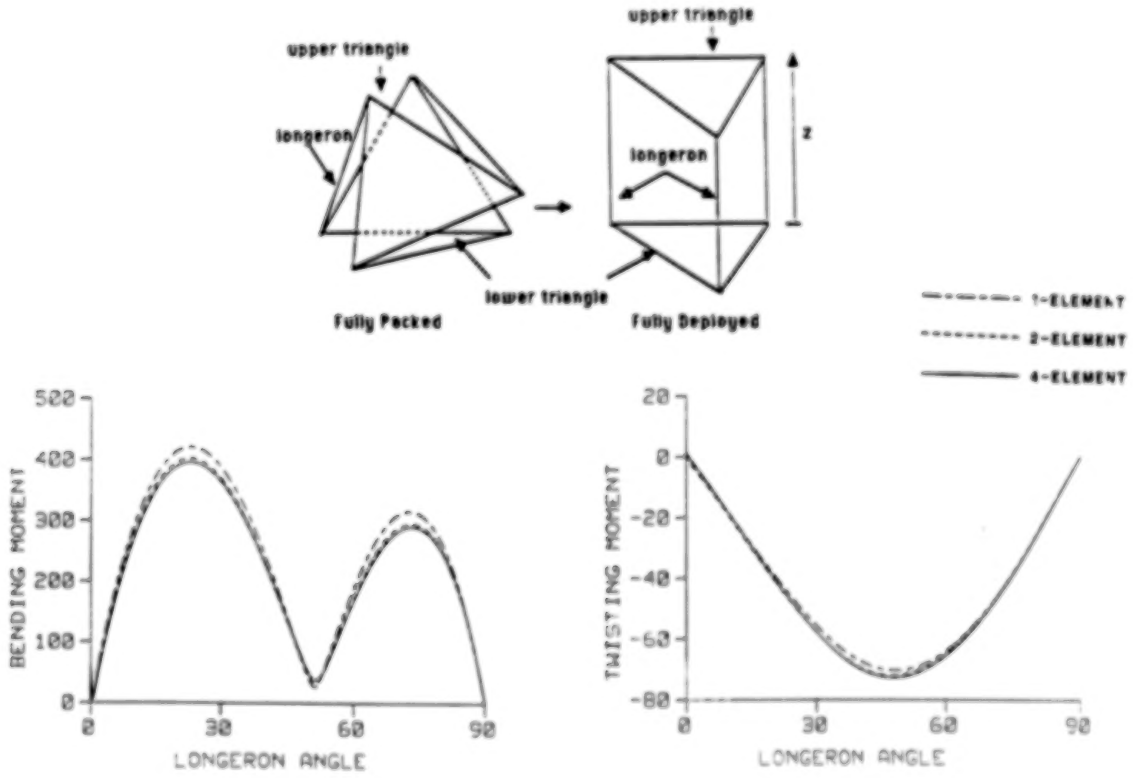
BEST COPY AVAILABLE

MINI-MAST DEPLOYMENT

The Mini-Mast is a 20 meter long, triangular cross-section, three longeron truss. The truss members are of graphite-epoxy and the joints, which contain the hinges between the members, are titanium. Reference 6 provides further details on the truss properties. The Mini-Mast derives its name from the longer 60 meter mast formerly planned as an on-orbit experiment deployed from the Space Shuttle's cargo bay. The Mini-Mast was designed and fabricated by the ASTRO Corporation.

The upper portion of the chart shows a single bay of the truss. Deployment proceeds by rotating the upper triangle 100 degrees counterclockwise about the vertical axis till the longerons are in a vertical orientation. Though not shown in the figure, a diagonal exists on each face of a truss-bay. The diagonal has a folding hinge at its mid-length and locks-up following deployment.

The hinge angles are designed so that when fully packaged, as it would be in the cargo bay, the members are stress free. Also, when fully deployed, the members are stress free. However, during deployment or retraction, the members deform considerably. This is seen in the bottom portion of the chart both in the bending and twisting moments of the longeron.

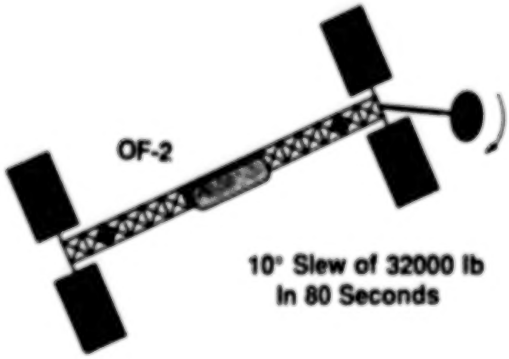


BEST COPY AVAILABLE

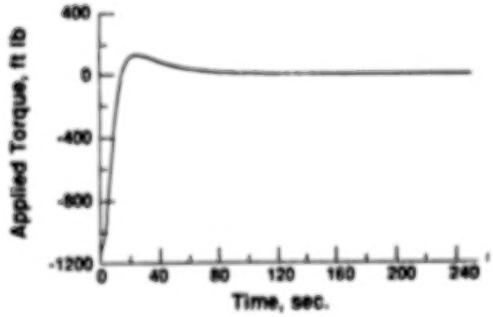
LATDYN Simulation of Controlled Robotic Slewing Operation on Space Station

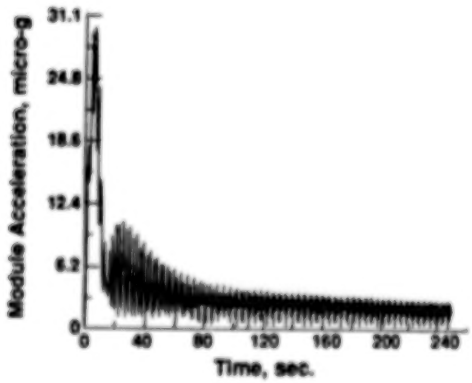
The LATDYN code is used to simulate Space Station response to a 10 degree slew of an RMS-like arm carrying a 32,000 pound payload. The slew operation is performed very slowly, taking 80 seconds. (At this rate a complete 360 degree operation takes about the half an orbit of the station.)

A torque motor at the arm's root drives the operation and, using angular rate feedback, suppresses the arm's vibration. As shown in the figure, the simulation provides the torque history which can then be used to improve the design of the torque motor, gimbal, or truss members. Also provided is the resulting module micro-gravity environment which shows that even though the arm controller suppresses arm vibration, as seen in the torque history, the modules continue to ring for a long time. Clearly more is required if the module micro-gravity environment is to be further reduced.



- Perform 10° slew using RMS-like arm
- Torque motor control law performs slew and suppresses payload vibration
- Generate torque history for future loads analysis
- Examine micro-g environment



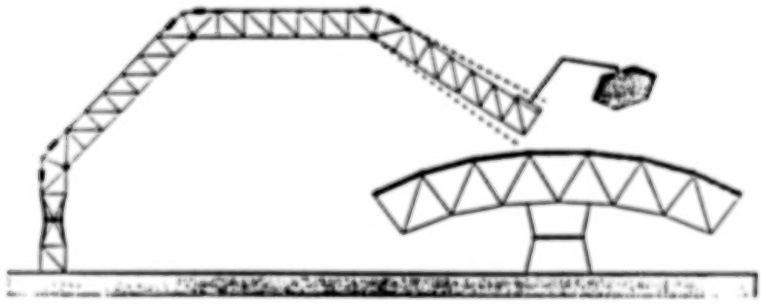


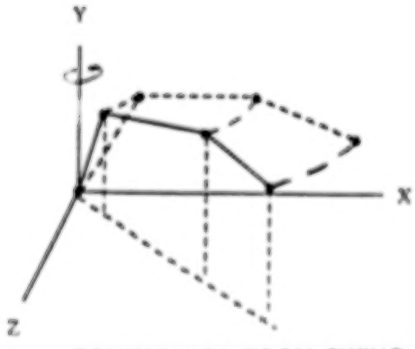
SPACE CRANE CONTROLLED MANIPULATION

In these three figures, results are presented for the simulation of a space crane manipulation. Such a space crane may be used for on-orbit construction.

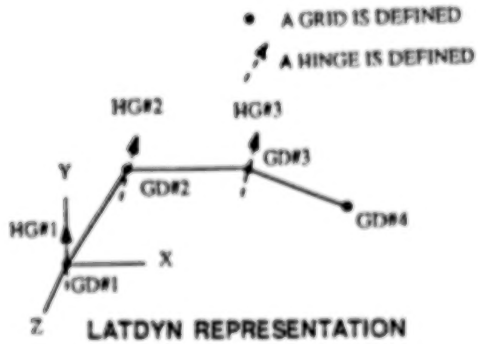
A torque motor rotates the crane 45 degrees about the vertical axis. An angular rate feedback loop is used to help suppress crane vibrations. The crane is modeled using a continuum beam representation of the crane's truss-like components. Three-beam component beams are thus used in the model.

The simulation is used here to identify the maximum rate at which the manipulation can be performed. The criterion used is the structural integrity of the crane. Buckling of truss members occurs at about 50,000 Newton-meters of bending moment on a built-up truss cross section. Results indicate that rotating 45 degrees in 5 seconds (a little faster than a clock's second hand) is about maximum speed. Of course, safety factors must be applied to this, thereby further restricting manipulation speed.





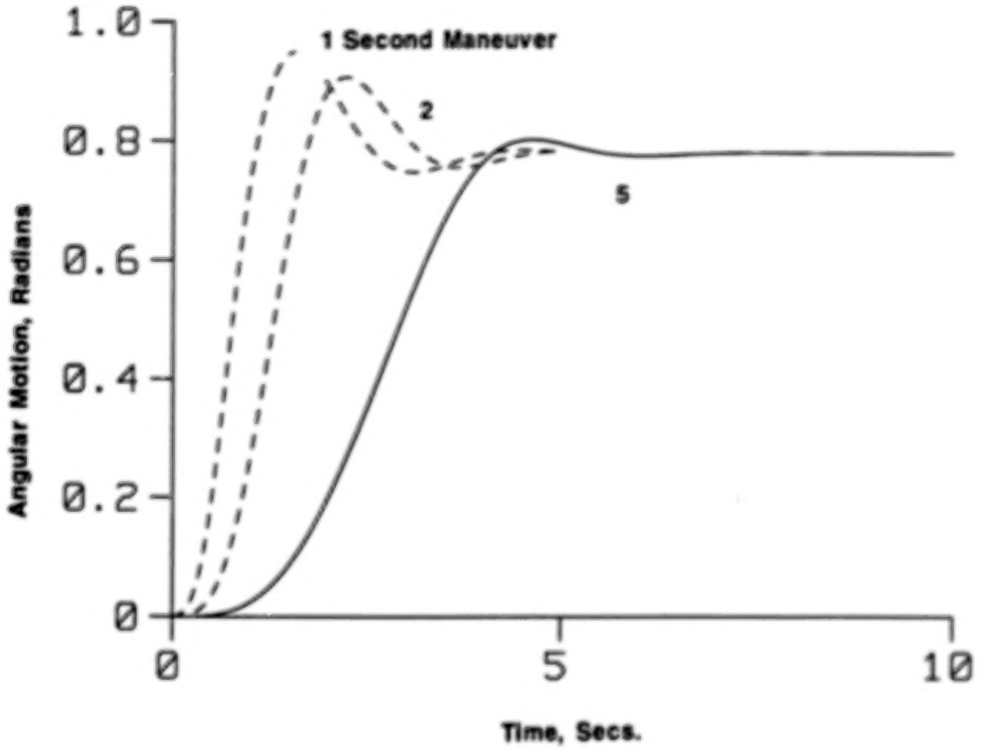
CONTROLLED BOOM SWING



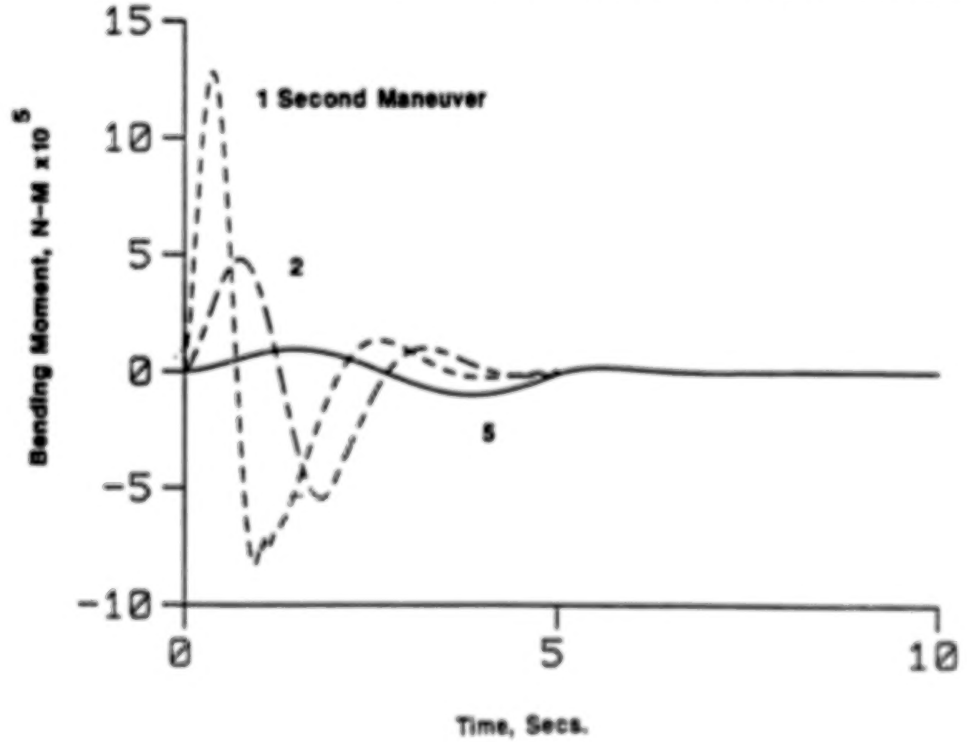
LATDYN REPRESENTATION

BEST COPY AVAILABLE

ANGULAR MOTION OF SPACE CRANE DURING 45 DEG. CONTROLLED SWING



SPACE CRANE ROOT BENDING MOMENT DURING 45 DEG. CONTROLLED SWING



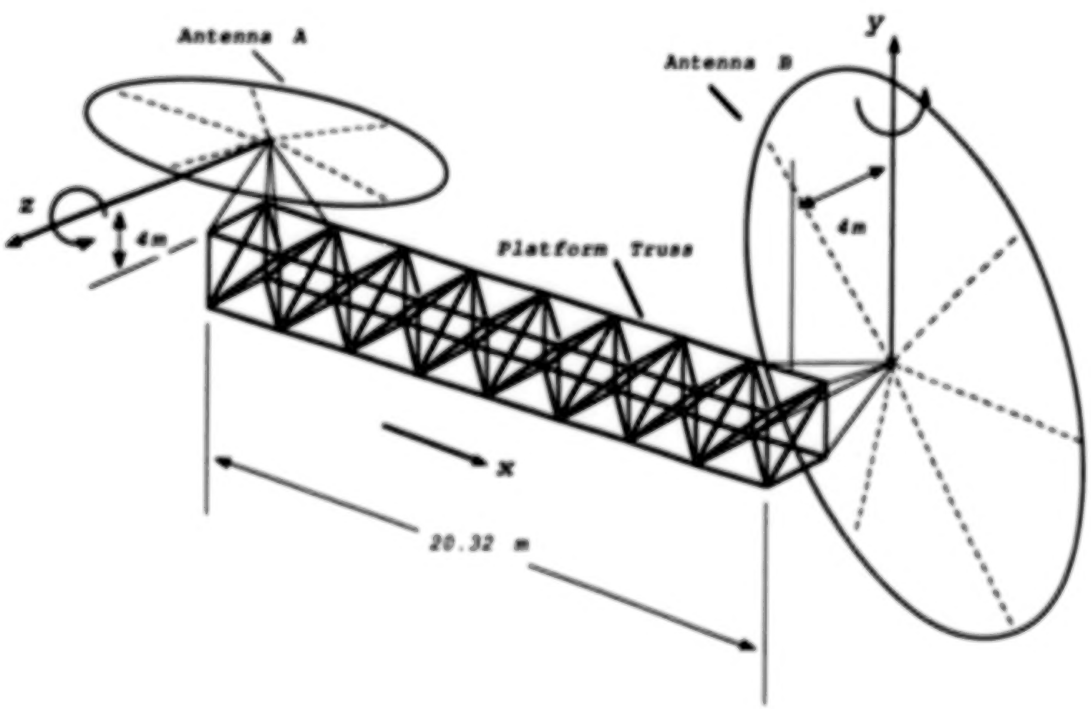
BEST COPY AVAILABLE

Potential CSI Test Article

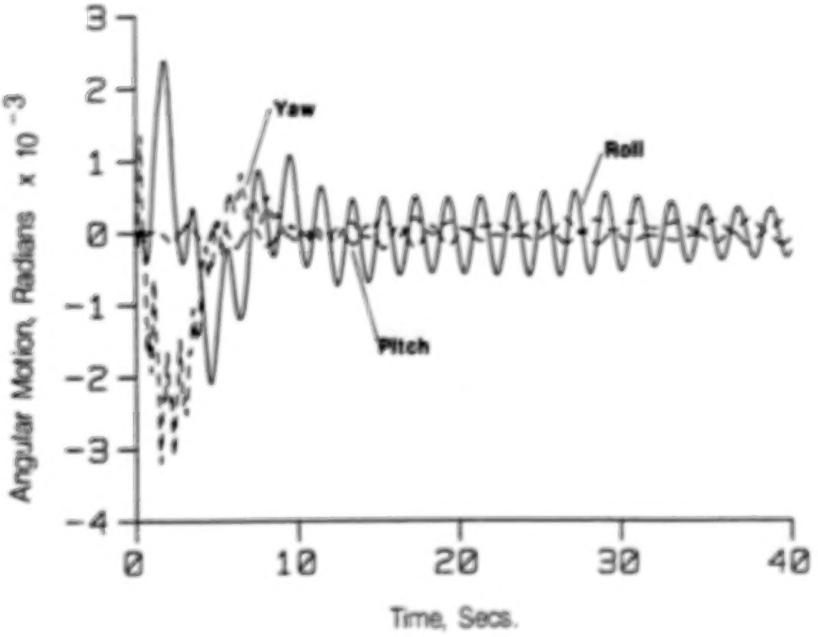
A potential CSI article is depicted in the first of the next three charts. Though not shown to scale, the truss contains ten inch cubic bays. In the LATDYN simulation, the larger antenna, labeled B, is rotated 30 degrees about the vertical y axis (yaw rotation) and the response at the truss center of gravity is studied under two conditions; without an attitude control system and with an attitude control system.

In the absence of an attitude control system, the yawing of the antenna produces a yaw of the spacecraft due to conservation of angular momentum and a roll of the spacecraft due to the offset of the antennas from the truss-beam neutral axis. In addition, gyroscopic effects result in a smaller pitching motion of the craft. Angular feedback control on the motor which drives the antenna yaw helps to suppress some of the ensuing vibrations. Its design being based on rigid body assumptions, it does a poor job of this.

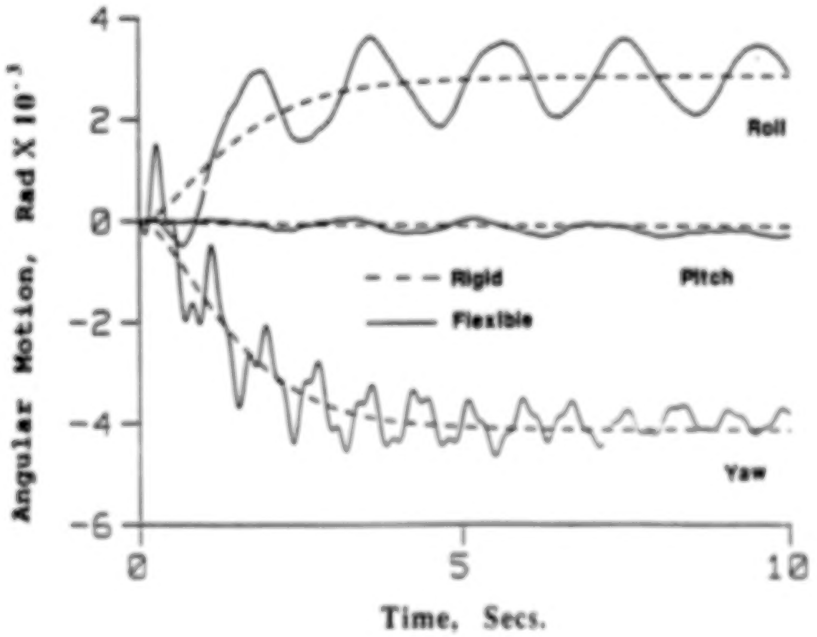
In the presence of an attitude control system, the overall attitude of the spacecraft is kept along its nominal path, but vibrations of the flexible craft are significant. Additional actuators are necessary to reduce these vibrations.



SPACECRAFT RESPONSE AT TRUSS C.G. DUE TO 30 DEG. LARGE ANTENNA YAW - WITH ATTITUDE CONTROL



SPACECRAFT RESPONSE AT TRUSS C.G. DUE TO 30 DEG. LARGE ANTENNA YAW - WITHOUT ATTITUDE CONTROL



Requirements for Multibody Benchmark Experiments

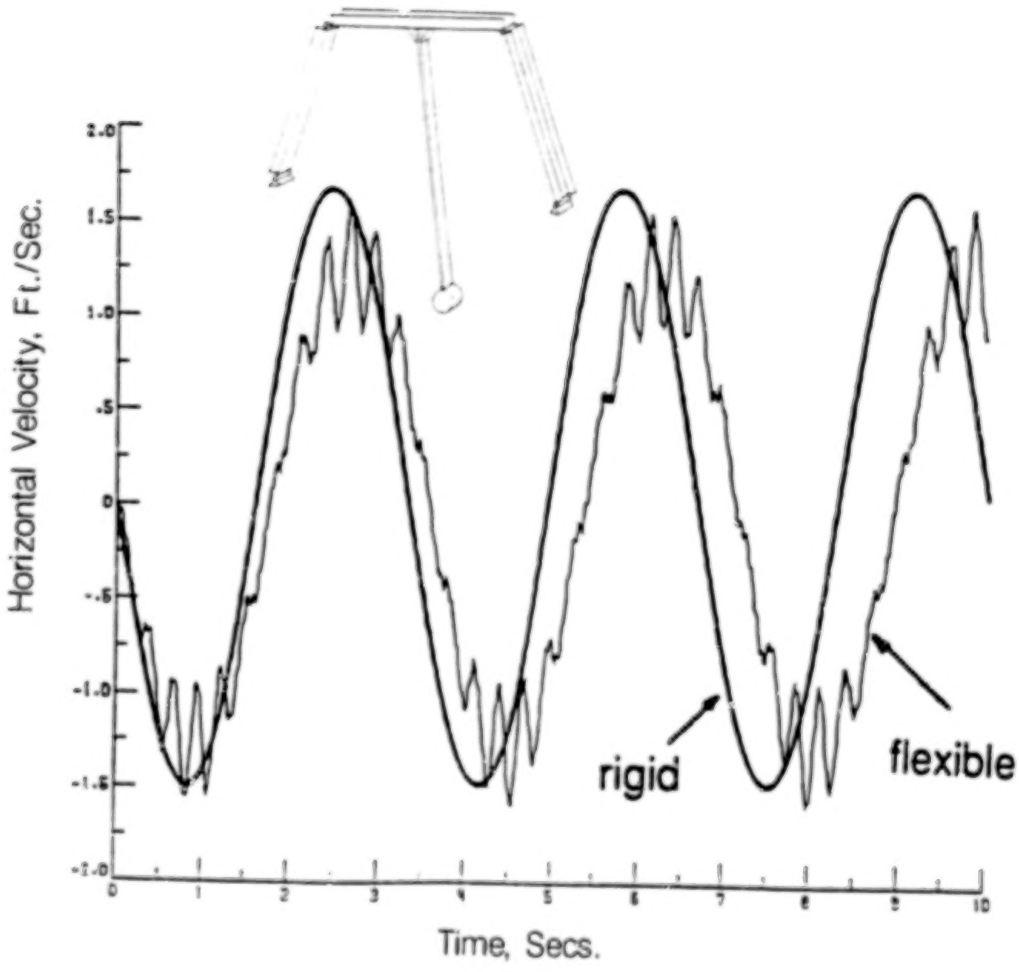
The next two charts address the need for multibody experiments which can be used to determine their accuracy and reliability. Such experiments should be relatively inexpensive and easy to assemble and to change out components. Most importantly their motions when rigid components are used must be significantly different from their motions when flexible components are used.

One such experiment is shown. It consists of three nearly rigid members and one pendular member which can be either rigid or flexible. Response of the pendular member tip is shown both for a flexible and a rigid member. The responses are desirably different, even having a somewhat different fundamental frequency.

The dimensions of the members and the tip mass have been chosen so as to make the device stable, but these can be changed to come as close as desired to instability. This represents an important test for simulation codes, since they may predict stability when the system is unstable or stable when it is not.

- **INEXPENSIVE**
- **EASY TO ASSEMBLE AND CHANGE COMPONENTS**
- **FLEXIBLE MOTION SIGNIFICANTLY DIFFERENT FROM RIGID BODY MOTION**

FLEXIBLE PENDULUM MULTIBODY EXPERIMENT



BEST COPY AVAILABLE

CONCLUDING REMARKS

- **MULTIBODY RIGID/FLEXIBLE COUPLED EXPERIMENTS ARE REQUIRED FOR SIMULATION VALIDATION**

- **THOUGH COST-EFFECTIVE RELATIVE TO EXPERIMENTS, SIMULATION OF SPACE VEHICLE OPERATON REQUIRES EXPENSIVE COMPUTER RUNS**

- **LATDYN VERSION AND DOCUMENTATION SOON TO BE RELEASED AND WORKSHOP TO BE HELD**

REFERENCES

1. Housner, J. M., McGowan, P. E., Abrahamson, A. L., and Powell M. G., The LATDYN User's Manual, NASA TM-87635, January 1986.

2. Housner, J. M.,"Convected Transient Analysis for Large Space Structures Maneuver and Deployment", AIAA/ASME/ASCE/AHS 25th Structures, Structural Dynamics and Materials Conference, AIAA Paper No. 84-1023-CP, Palm Springs, California.

3. Housner, J. M., Wu, S. C., and Chang, C. W.,"A Finite Element Method for Time Varying Geometry in Multibody Structures", Proceeding of the AIAA/ASME/ASCE/AHS 29th Conference, Williamsburg, VA, April 18-20, 1988, pp.187-197.

4. DADS User's Manual, Computer Aided Design Software, Inc., P.O. Box 203, Oakdale, Iowa 52319, 1987.

5. Wu, S. C., and Haug, E. J.,"Geometric Non-linear Substructuring for Dynamics of Flexible Mechanical Systems", International Journal for Numerical Methods in Engineering, Vol. 26, pp.2211-2226, 1988.

6. Adams, L. R.,"Design, Development and Fabrication of A Deployable/Retractable Truss Beam Model for Large Space Structures Application", NASA CR-178287, June 1987.

ELEMENT-SPECIFIC MODAL FORMULATIONS FOR LARGE-DISPLACEMENT MULTIBODY DYNAMICS

R. R. Ryan
Mechanical Dynamics, Inc.
Ann Arbor, Michigan

H. H. Yoo
University of Michigan
Ann Arbor, Michigan

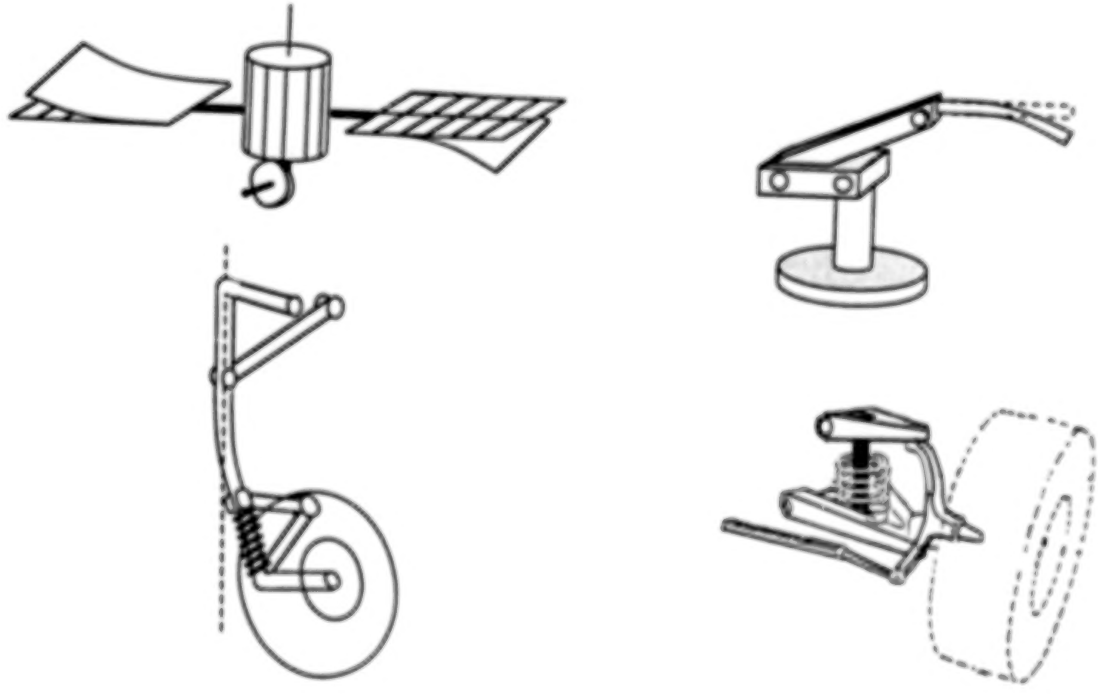
Third Annual NASA/DOD CSI Technology Conference
San Diego, California
January 29 – February 2, 1989

OBJECTIVE

This paper examines large displacement assumed-mode modeling techniques in the context of multibody elastodynamics. The range of both general and element-specific approaches are studied with the aid of examples involving beams, plates, and shells. For systems undergoing primarily structural bending and twisting, with little or no membrane distortion, it is found that fully-linear, element-specific, modal formulations provide the most accurate time history solutions at the least expense. When membrane effects become dominant in structural problems due to loading and boundary conditions, one must naturally resort to a formulation involving a nonlinear stress-strain relationship in addition to nonlinear terms associated with large overall system motion. Such nonlinear models have been investigated here using assumed modes and found to lead to modal convergence difficulties when standard free-free structural modes are employed. A constrained mode formulation aimed at addressing the convergence problem is proposed here.

OVERVIEW

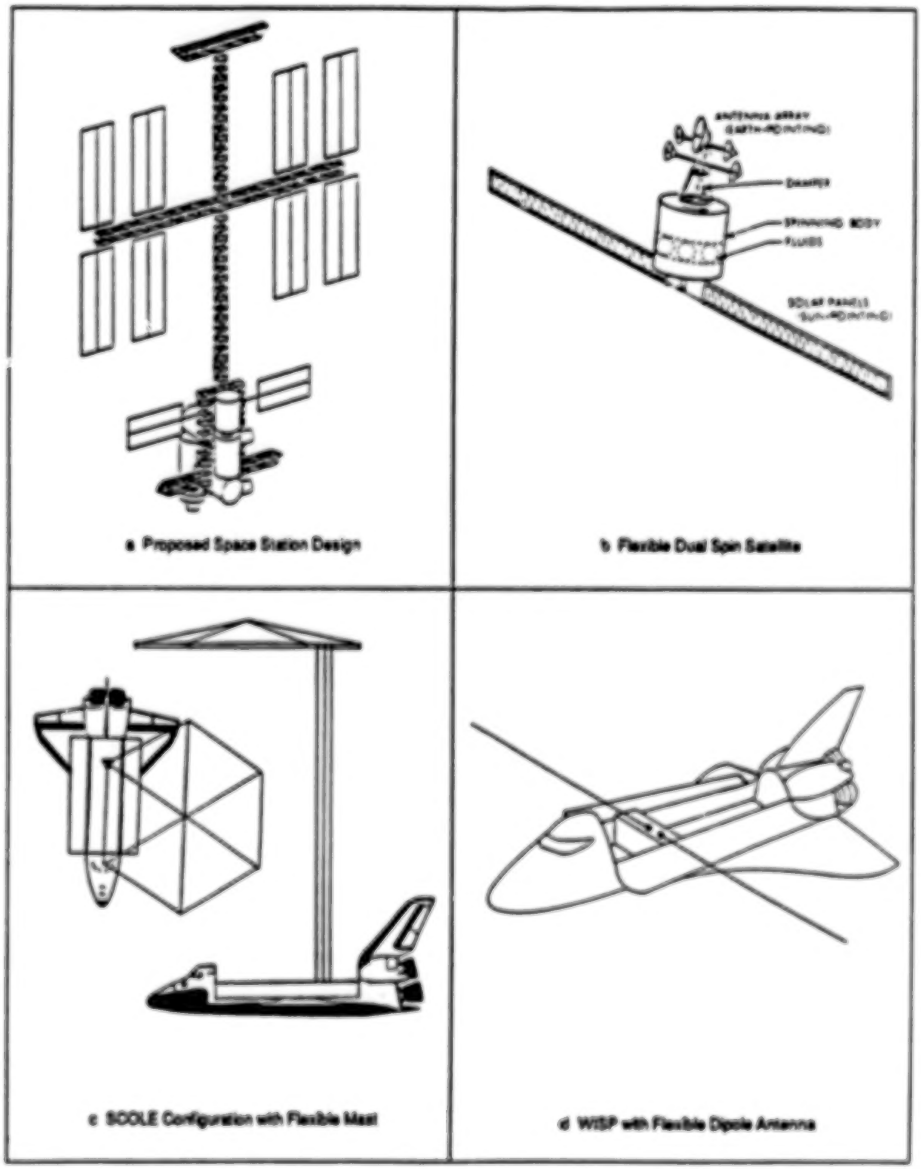
The general design trend for mechanical systems including machines and mechanisms, spacecraft and satellites, robotic manipulators, and large space structures is toward ever lighter, more flexible systems with increasingly faster dynamic response and minimal power requirements. A consequence of the extreme flexibility of structural elements comprising these systems is that elastic deformation of components often occurs during standard operational motions. The deformations interacting with the control law performance can lead to drastic effects on overall motion. These new designs have motivated increased research, such as that summarized here, aimed at producing accurate models of such systems for purposes of simulation, structural verification, dynamic stability determination, and control law design. The role of simulation, in particular, has increased dramatically in importance in recent years due mainly to two factors: (1)for many new aerospace multibody system designs, Earth-based experimental testing in a non-zero gravitational field cannot provide accurate answers concerning the behavior of the system in its actual space environment, and (2)the increased competitiveness of worldwide consumer industries necessitates fewer mechanical prototypes and more reliance on *computational prototyping* procedures. A basic requirement of models intended for general-purpose simulation of these newer designs is that they must be able to account properly for both large overall rotational and translational motions and concurrent small strain elastic deformations of flexible body components as well as accurately include the important coupling effects existing between these two types of dynamic behavior. In particular, full consideration should be given to the variations in flexible body stiffness caused by inertia forces arising from rapid overall motion. In other words, when a component of a multibody system undergoes rotational maneuvers or moderate-to-fast translational accelerations, the resistance of the component to deformation may change considerably; this fact should be incorporated in the system model used for simulation.



SPACECRAFT APPLICATIONS

Although multibody dynamic analysis spans many application areas, including automotive and off-highway vehicles, rail cars, agricultural and construction equipment, consumer products, biomechanical systems, and robotic manipulators, perhaps the most rigorous testing ground for general multibody dynamic analysis techniques occurs in spacecraft applications due to the total freedom of translational and rotational motion, the large amplitude inertia forces, the high flexibility of light-weight aerospace structures, and the complex behavior of the active control systems.

In order to focus our study of multibody elastodynamic techniques on key issues of concern for the majority of space transportation vehicles, space stations, Earth satellites, and complex interplanetary probes, we will limit our investigations to four typical categories of overall system motion, namely: (1)stationkeeping, (2)constant spin rotational motions, (3)*slewing* or repositional maneuvers, and (4)spin-up or spin-down motions.



a Proposed Space Station Design

b Flexible Dual Spin Satellite

c SCOLE Configuration with Flexible Mast

d WISP with Flexible Dipole Antenna

BEST COPY AVAILABLE

OUTLINE

The following discussion begins with a summary of two necessary, but not sufficient, requirements for multibody elastodynamic programs to accurately simulate uncontrolled and actively-controlled systems containing deformable structural elements undergoing large overall rotation and translation as well as small deformation.

This is followed by a brief review of possible modeling techniques and pitfalls to be avoided. Element-specific approaches involving physical discretization, Galerkin finite element discretization, and modal discretization techniques are examined. Advantages and disadvantages of each approach are discussed.

Then, new element-specific linear and nonlinear modal formulations for beams, plates, and shells are introduced and compared to other techniques. Finally, simulation results indicating the effectiveness and accuracy of various methods are presented.

I. Requirements For General Flexible Multibody Formalisms
- Element-Specificity
- Proper Coupling of Deformation/Overall Motion

II. Possible Modeling Approaches
- General Modal Continuum Modeling
- Element-Specific Discrete and Continuous Modeling

III. Linear and Nonlinear Element-Specific Formulations
- Consistently Linearized Beam, Plate, and Shell
- Second-Order Beam and Plate Models

IV. Simulation Results
- Membrane/Bending Problems
- Convergence

REQUIREMENTS

In order to accurately predict motion of joint-connected systems of rigid and deformable bodies undergoing both large overall motion and small deformation, a dynamic formalism must satisfy a number of important criteria. Two of these criteria which will be explicitly discussed here are: (1)the ability of the formalism to model specific element types differently and completely, and (2)to include motion-induced stiffness variations.

I. Treat Structural Element Types Distinctly

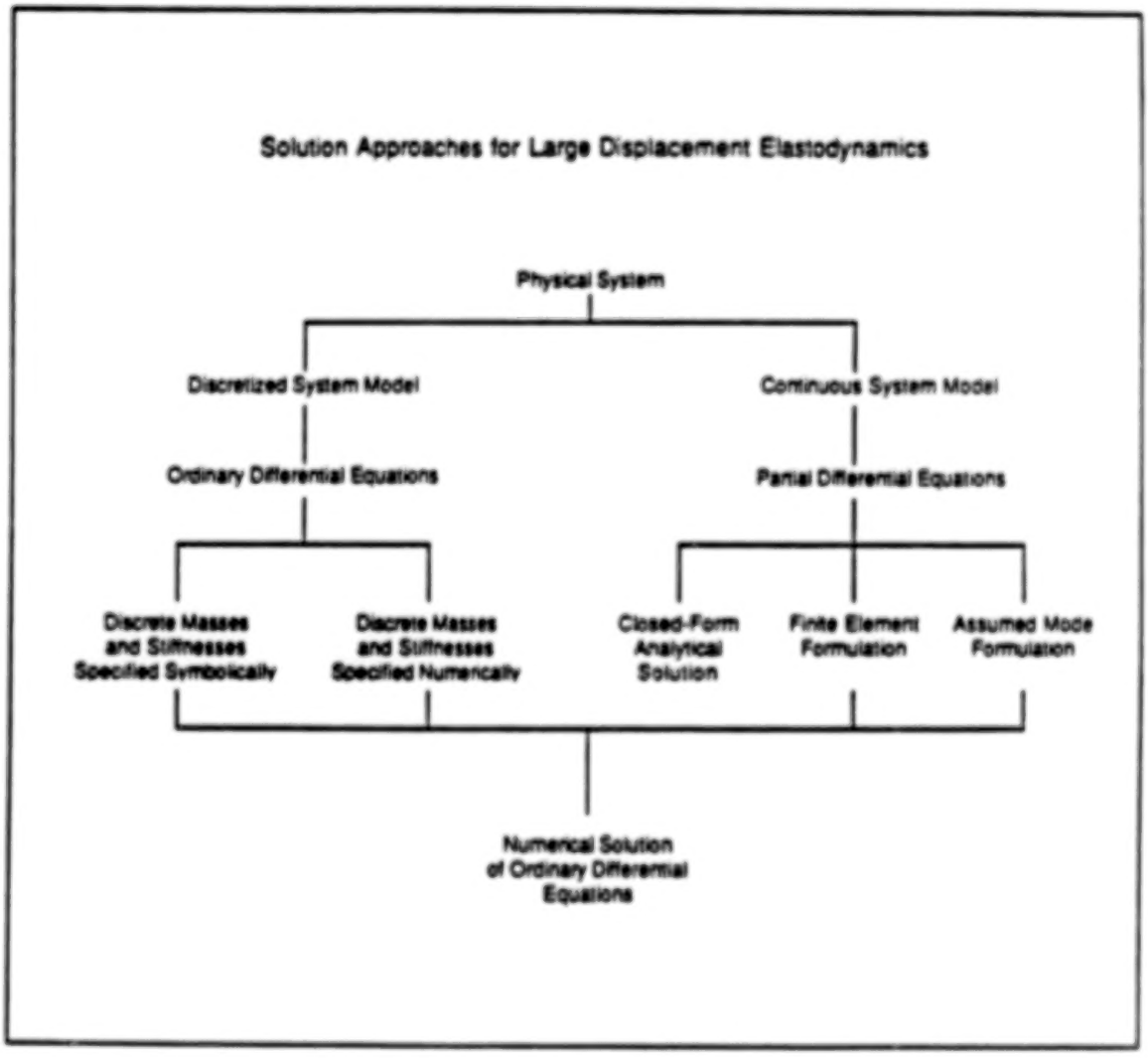
- Different Models for:
  - Beams,
  - Plates,
  - Shells,
  - Solids, etc

II. Model Motion-Induced Stiffness Variations

- Axial Inertial Force Contributions
- Rotational Inertial Force Contributions

MODELING APPROACHES

There are numerous ways to characterize the deformability of elastic bodies in a multibody system. The techniques range from pure physical discretization methods to mathematical discretization procedures involving local (Galerkin finite element) or global (Rayleigh-Ritz assumed mode) shape functions.



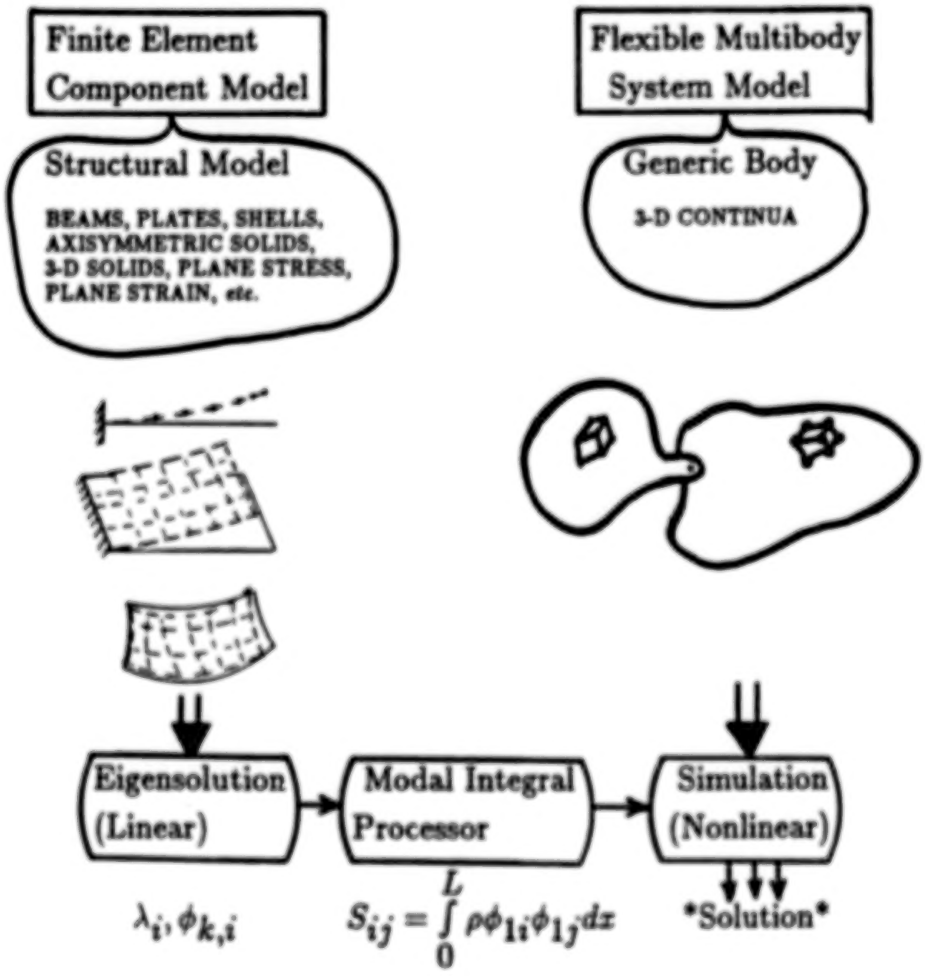
Solution Techniques for Large Displacement Elastodynamics

BEST COPY AVAILABLE

MODELING APPROACHES (CONT'D)

These methods can be further sub-divided according to the manner in which component bodies are treated directly within the multibody formalism in question. Some formalisms model each component body, regardless of its actual composition, as a general three-dimensional continuum whose flexibility is characterized entirely by component modes obtained from a separate finite element analysis wherein the component was modeled in detail using structural elements. However, in order to provide proper model fidelity, it will be shown that the components also must be modeled using structural elements directly within the multibody formalism, even if modes are obtained from a separate detailed structural finite element model.

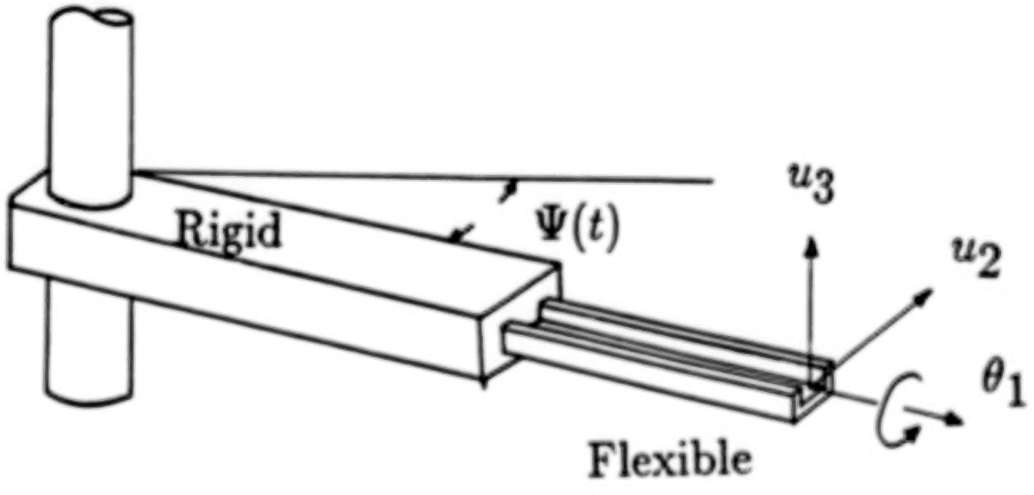
General Modal Linear Continuum Modeling

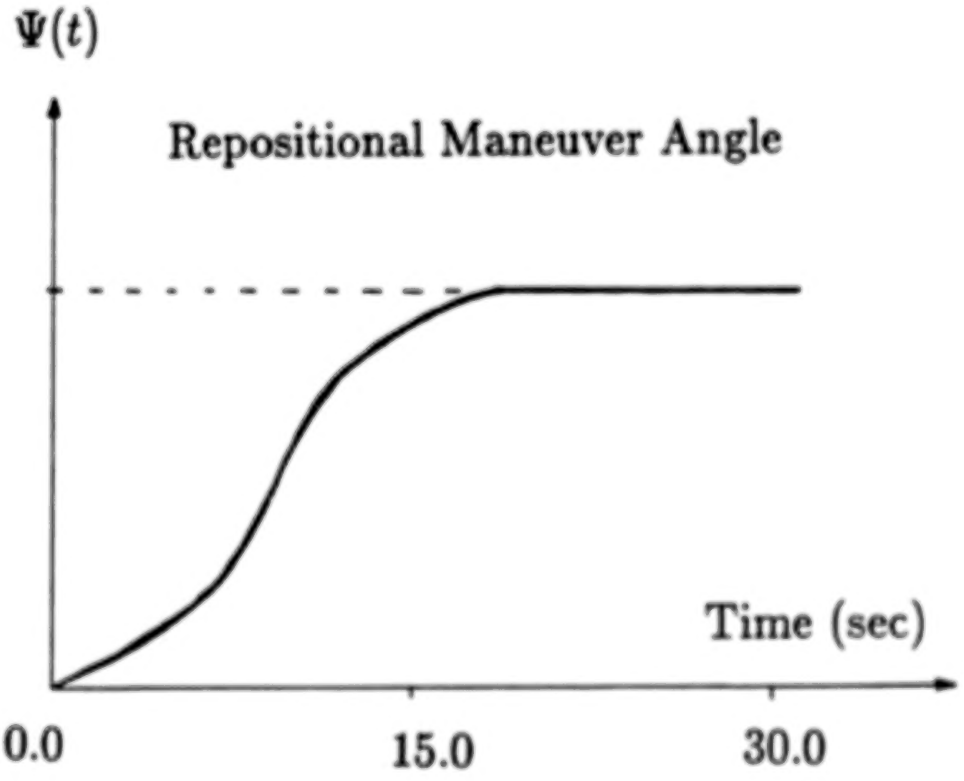


ELEMENT SPECIFICITY PROBLEMS

SLOW REPOSITIONAL MANEUVER OF CHANNEL BEAM

In order to examine differences between formalisms that are element-specific and those that employ general linear continuum modeling, we will use the two methods to predict response of a sample system. Shown below is a flexible channel section beam which is to be repositioned slowly through an angle Ψ of 180°. The time history of the angle Ψ, shown in the sketch, is given below.

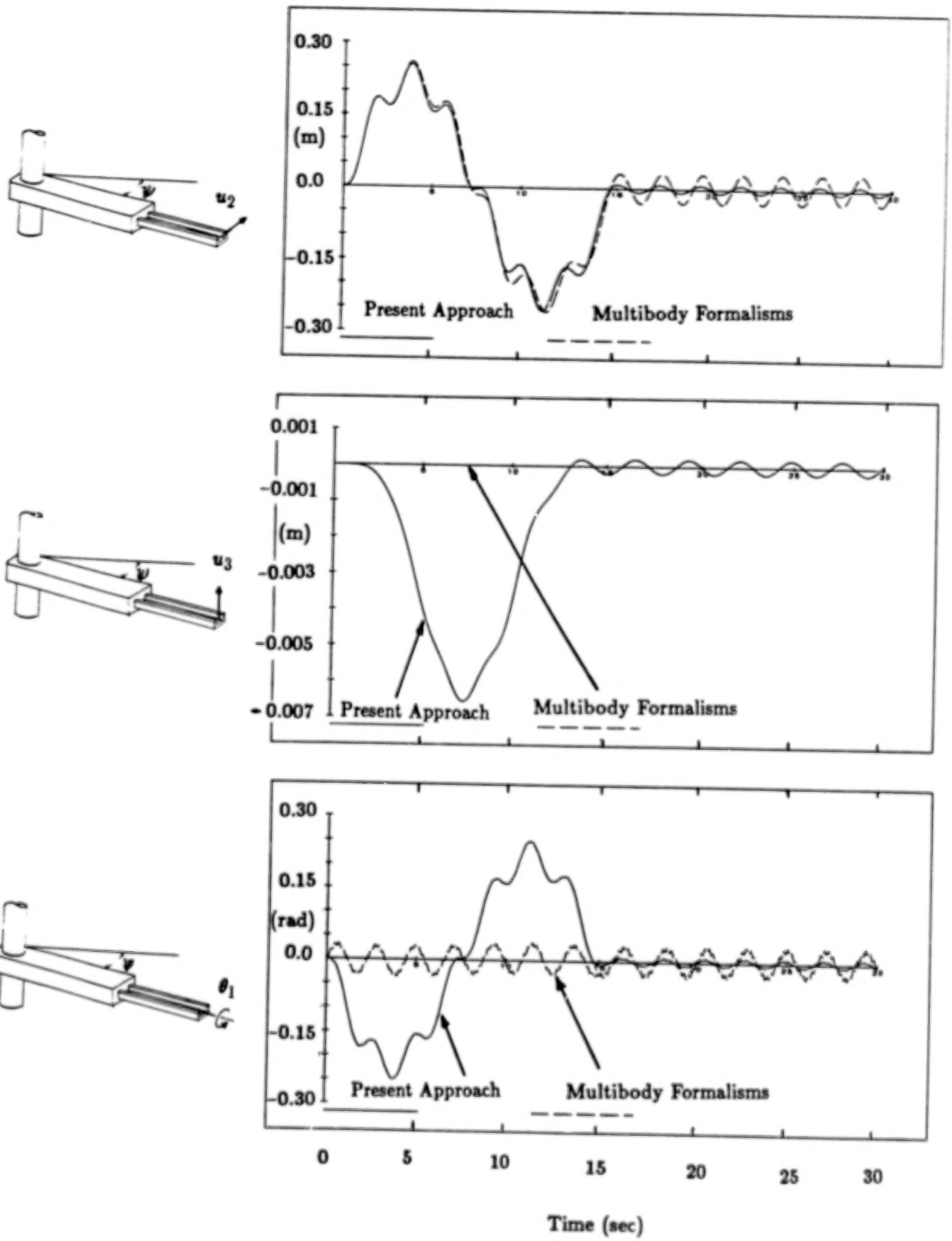




ELEMENT SPECIFICITY PROBLEMS

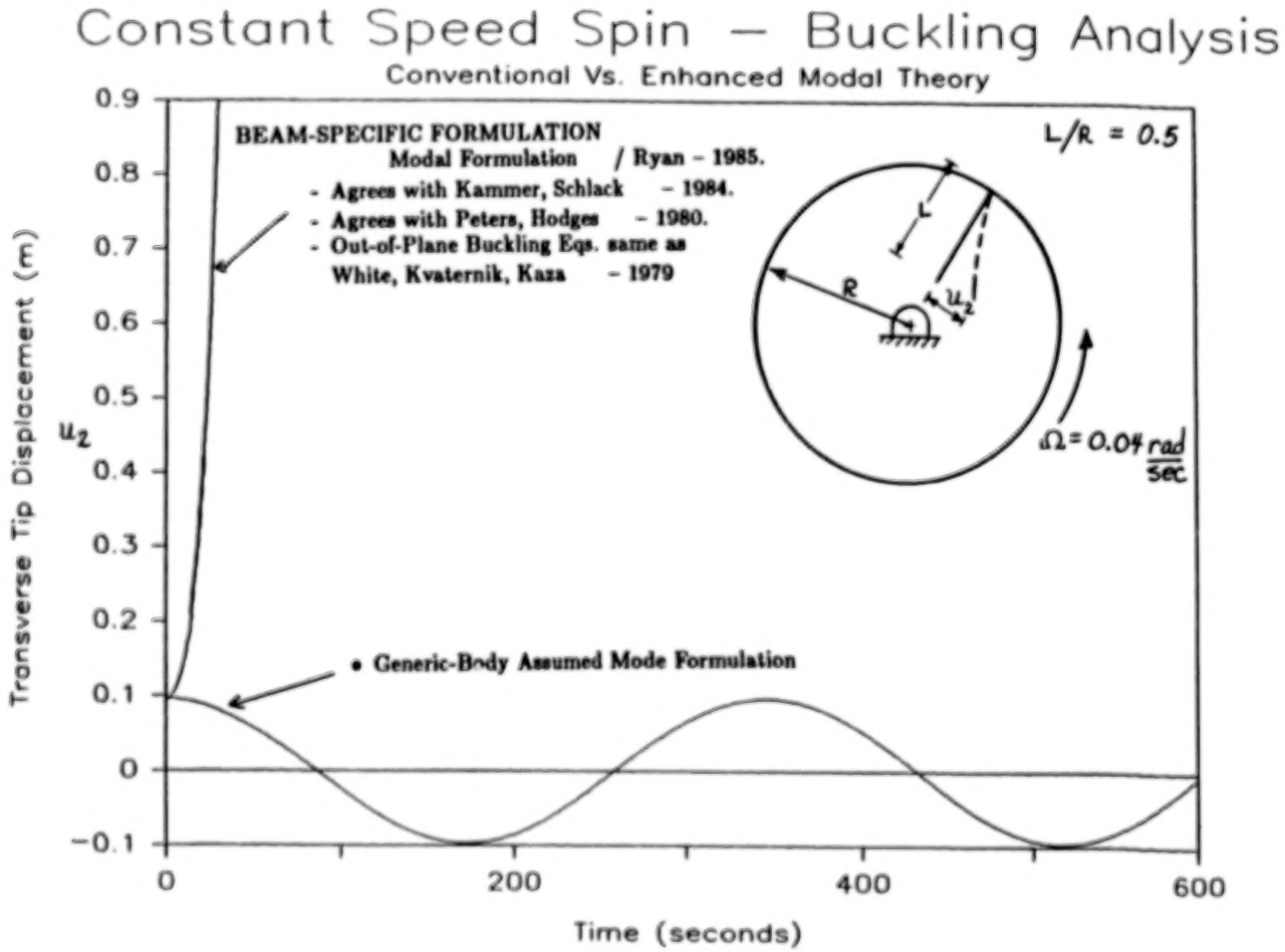
SLOW REPOSITIONAL MANEUVER OF CHANNEL BEAM - RESULTS

The following page shows the predicted values of the displacement of the tip of the channel section beam relative to a point which is fixed on the rigid hub and originally coincident with the beam tip. The results show that the general linear continuum modeling approach and the linear beam-specific approach predict similar in-plane transverse displacements but very dissimilar twist and out-of-plane displacements. The beam-specific approach has been verified by independent use of nonlinear finite element techniques as well as physical discretization. The linear continuum modelling approach is in error due to its inability to provide proper coupling between overall motion and small deformation, even during extremely slow maneuvers. Proper account is not taken of the coupled bending and twisting inherent in a beam of this type.


0.30
0.15
(m)
0.0
-0.15
-0.30
u_2
Present Approach
Multibody Formalisms
0.001
-0.001
(m)
-0.003
-0.005
-0.007
u_3
Present Approach
Multibody Formalisms
0.30
0.15
(rad)
0.0
-0.15
-0.30
θ_1
Present Approach
Multibody Formalisms
0
5
10
15
20
25
30
Time (sec)

MOTION-INDUCED STIFFNESS PROBLEMS

As discussed in many recent publications, it is also extremely important that flexible multibody formalisms be capable of accurately capturing motion-induced stiffness variations. Conventional linear modal continuum models embedded in multibody formalisms cannot do so in general. Shown below is a beam attached to the inside of a rotating rim. Classical theory and element-specific modal approaches predict the beam will buckle; however, the non-element specific approach erroneously predicts stable oscillatory deformation.



LINEAR AND NONLINEAR ELEMENT-SPECIFIC MODAL MODELS

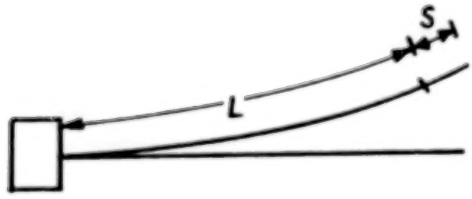
In order to overcome the previously-noted limitations in general continuum-based approaches, two element-specific modal approaches are proposed. Due to the use of modes, these methods provide a high level of efficiency and they provide accurate results over a certain subset of problems.

- Consistently-Linearized Multibody Structural Theories
  - Structural Constraints Modeled Explicitly
  - Equations Linearized in In-Plane Stretch Variables
- Second-Order Nonlinear Multibody Structural Theories
  - Von Karman Strain Meaures Employed

Element Specific
Consistently-Linearized Multibody Structural Theories

- Beam

$$s \stackrel{\triangle}{=} u_1 + \frac{1}{2}\int_0^x [(\frac{\partial u_2}{\partial \sigma})^2 + (\frac{\partial u_3}{\partial \sigma})^2] d\sigma$$



- Plate

$$r \stackrel{\triangle}{=} u_2 + \frac{1}{2}\int_0^y (\frac{\partial u_3}{\partial \eta})^2 d\eta$$

$$s \stackrel{\triangle}{=} u_1 + \frac{1}{2}\int_0^x (\frac{\partial u_3}{\partial \xi})^2 d\xi$$



$$M\ddot{q} + G\dot{q} + (K_I + K_L + K_g)q = F$$

Advantages:

- Excellent Convergence
- Captures Motion-Induced Bending Stiffness Variation
- Ease of Modal Reduction/Controls
- Easily-Implemented – Linear in Deformation

Disadvantages:

- Don't Capture Motion-Induced Membrane Stiffness

Element-Specific
Second-Order Structural Multibody Theories

- Beam

$$U_b = \frac{1}{2}\int_0^\ell E\left\{I_{zz}\left(\frac{\partial^2 u_2}{\partial x^2}\right)^2 + I_{yy}\left(\frac{\partial^2 u_3}{\partial x^2}\right)^2\right\}dx$$

$$U_s = \frac{1}{2}\int_0^\ell EA\left\{\left[\left(\frac{\partial u_1}{\partial x}\right) + \frac{1}{2}\left(\frac{\partial u_2}{\partial x}\right)^2 + \frac{1}{2}\left(\frac{\partial u_3}{\partial x}\right)^2\right]^2\right\}dx$$

- Thin Rectangular Plates:

$$U_b = \frac{1}{2}\int_0^b\int_0^a \beta\left\{\left(\frac{\partial^2 u_3}{\partial x^2} + \frac{\partial^2 u_3}{\partial y^2}\right)^2 - 2(1-\nu)\left[\left(\frac{\partial^2 u_3}{\partial x^2}\right)\left(\frac{\partial^2 u_3}{\partial y^2}\right) - \left(\frac{\partial^2 u_3}{\partial x \partial y}\right)^2\right]\right\}dxdy$$

$$U_s = \frac{1}{2}\int_0^b\int_0^a \gamma\left\{\left(\frac{\partial u_1}{\partial x}\right)^2 + \left(\frac{\partial u_1}{\partial x}\right)\left(\frac{\partial u_3}{\partial x}\right)^2 + \left(\frac{\partial u_2}{\partial y}\right)^2 + \left(\frac{\partial u_2}{\partial y}\right)\left(\frac{\partial u_3}{\partial y}\right)^2 + \frac{1}{4}\left[\left(\frac{\partial u_3}{\partial x}\right)^2 + \left(\frac{\partial u_3}{\partial y}\right)^2\right]^2 + 2\nu\left[\left(\frac{\partial u_1}{\partial x}\right)\left(\frac{\partial u_2}{\partial y}\right) + \frac{1}{2}\left(\frac{\partial u_2}{\partial y}\right)\left(\frac{\partial u_3}{\partial x}\right)^2 + \frac{1}{2}\left(\frac{\partial u_1}{\partial x}\right)\left(\frac{\partial u_3}{\partial y}\right)^2\right] + \frac{(1-\nu)}{2}\left[\left(\frac{\partial u_1}{\partial y}\right)^2 + 2\left(\frac{\partial u_1}{\partial y}\right)\left(\frac{\partial u_2}{\partial x}\right) + \left(\frac{\partial u_2}{\partial x}\right)^2 + 2\left(\frac{\partial u_1}{\partial y}\right)\left(\frac{\partial u_3}{\partial x}\right)\left(\frac{\partial u_3}{\partial y}\right) + 2\left(\frac{\partial u_2}{\partial x}\right)\left(\frac{\partial u_3}{\partial x}\right)\left(\frac{\partial u_3}{\partial y}\right)\right]\right\}dxdy$$

$$M\ddot{q} + G\dot{q} + (K_I + K_L + K_n)q = F$$

Advantages:

- Captures Important Motion-Induced Bending AND Membrane Stiffness Variations for Small Strain

Disadvantages:

- Poor Convergence With Standard Modes
- Order Reduction Results in Very Inaccurate Models
- Very Costly to Incorporate

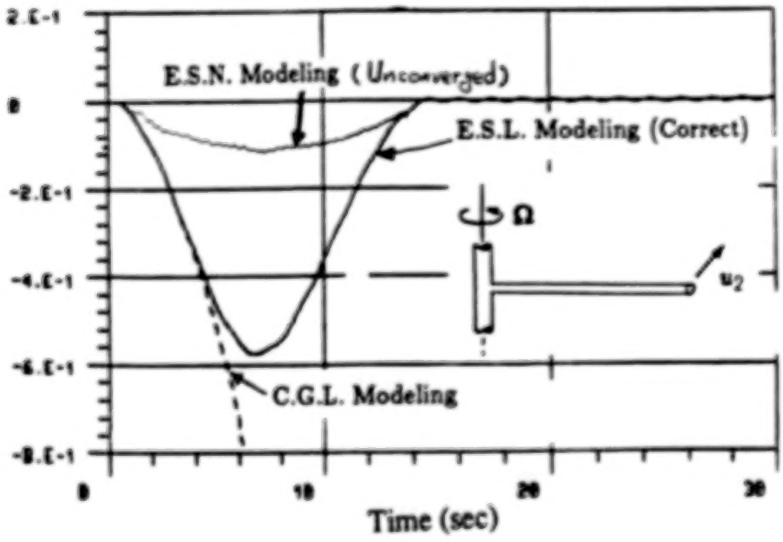
SIMULATION RESULTS

The next two pages depict simulation results predicting the deformational behavior of different structural elements and configurations undergoing prescribed overall motions. Each of these maneuvers involves two phases, including a spin-up transient phase and a steady-state constant spin phase. The first set of results pertains to beams and plates mounted in a cantilever fashion to a rotating hub structure. The second set of results corresponds to structures which are simply-supported to rotating rigid components. Three curves are shown in the plots. The curves labelled C.G.L. denote the solution obtained using conventional general linear modeling and not taking explicit account of element type or structural element constraints. The curves labelled E.S.L. represent results obtained by utilizing the consistently-linearized beam and plate models with explicit structural constraints. Lastly, the curves marked E.S.N. indicate the response predicted by the second-order Von Karman theories.

For all cases, the C.G.L. modeling method is unable to provide intuitively reasonable results, and always predicts softer elastic response than when the structure is stationary. For the cantilever structures, it has been independently proven that the E.S.L. method provides the correct solution with very few standard modal functions. Although one might expect a higher-order model to automatically provide better model fidelity than the linear model, the second-order nonlinear Von Karman model cannot produce the correct solution with a small number of standard modal functions. This conclusion is supported by the curve labelled E.S.N. in the first figure. Using the same number of modal functions as in the E.S.L. method, the E.S.N. method produced the result shown, indicating slow convergence to the true solution. The poor convergence is due to the inability of the standard modes to capture foreshortening effects when structural constraints are not imbedded in the formulation. To correct the problem, one may use interaction modes involving combinations of standard axial and transverse modes to model the true nonlinear transverse response.

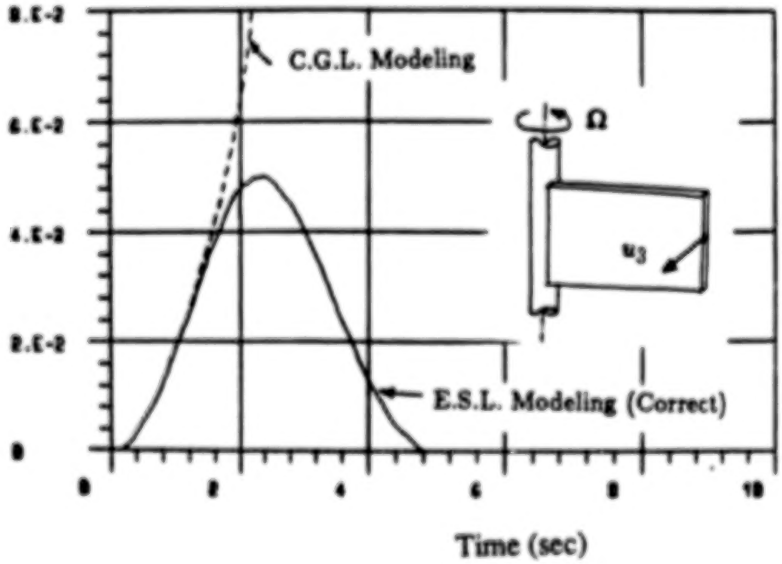
When one studies simply-supported structures, very different results are noticed, as shown in the second set of figures. In these structures, membrane effects are dominant, and foreshortening is of secondary importance. The E.S.N. method provides correct solutions, as verified independently, with very few standard modal functions. There is no need to employ interaction modes in this case, since the bending effects are of secondary importance. The E.S.L. method which efficiently produces the correct solution for cantilever-type structures cannot do so for simply-supported structures undergoing large overall motion due to the inherently nonlinear nature of the problem.

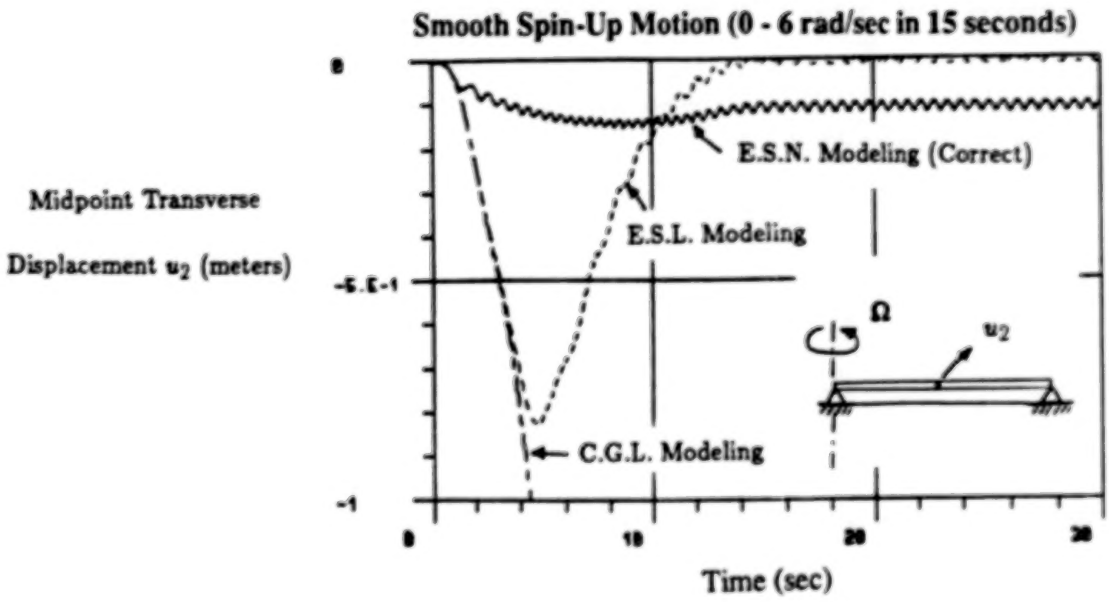
Smooth Spin-Up Motion (0 - 6 rad/sec in 15 seconds)



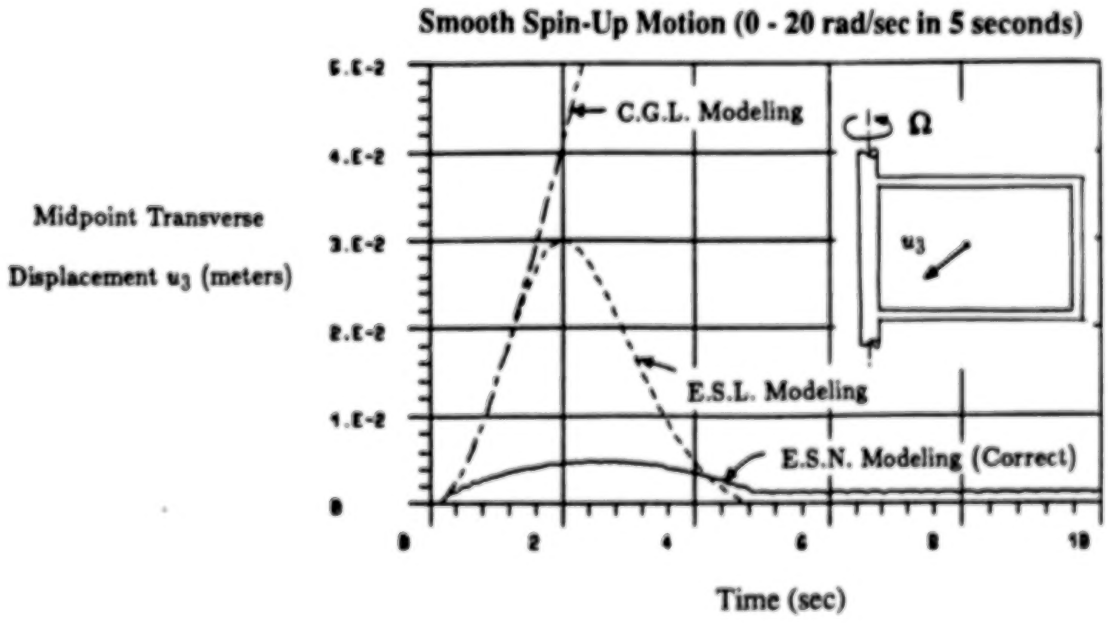
Element Specific Linear Modeling (E.S.L. Modeling)
Element Specific Nonlinear Modeling (E.S.N. Modeling)
Conventional General Linear Modeling (C.G.L. Modeling)

Smooth Spin-Up Motion (0 - 20 rad/sec in 5 seconds)





Element Specific Linear Modeling (E.S.L. Modeling)
Element Specific Nonlinear Modeling (E.S.N. Modeling)
Conventional General Linear Modeling (C.G.L. Modeling)



- Multibody Elastodynamic Formalism Requirements:
  - Ability to Model Element-Specific Behavior
  - Model Motion-Induced Stiffness Variations
- Alternative Approaches:
  - Explicitly Account for Geometric Constraints
  - Use a Nonlinear Strain Measure
- Consistently-Linearized Models:
  - Work Well For Most Problems
  - Cannot Capture Motion-Induced Membrane Stiffness Variations
- Second Order Structural Theories:
  - Account for Membrane-Dominant Motion-Induced Stiffness Variations
  - Converge Slowly With Standard Mode Functions
- Nonlinear Constraint Functions:
  - Serve Well as Modal Functions in Order to Improve Convergence in Second Order Structural Theories.

NONLINEAR AND DISTRIBUTED PARAMETER MODELS OF THE MINI-MAST TRUSS

Lawrence W. Taylor, Jr.
NASA Langley Research Center
Hampton, VA

3rd NASA/DOD
Controls-Structures Interaction
Technology Conference
January 30, 1989

ABSTRACT

Large spacecraft such as Space Station Freedom employ large trusses in their construction. The structural dynamics of such trusses often exhibit nonlinear behavior and little damping which can impact significantly the performance of control systems. The Mini-MAST truss was constructed to research such structural dynamics and control systems. The Mini-MAST truss is an object of study for the Guest Investigator Program as part of NASA's Controls-Structures Interaction Program. The Mini-MAST truss is deployable and about 65 feet long. Although the bending characteristics of the Mini-MAST truss are essentially linear, the angular deflection under torsional loading has exhibited significant hysteresis and nonlinear stiffness. It is the purpose of this study to develop nonlinear and distributed parameter models of the truss and to compare the model dynamics with actual measurements. Distributed parameter models have the advantage of requiring fewer model parameters. A tangent function is used to describe the nonlinear stiffness in torsion, partly because of the convenience of its easily expressed inverse. Hysteretic slip elements are introduced and extended to a continuum to account for the observed hysteresis in torsion. The contribution of slipping to the structural damping is analyzed and found to be strongly dependent on the applied loads. Because of the many factors which affect the damping and stiffness in a truss, it is risky to assume linearity.

INTRODUCTION

Future missions in space require spacecraft which are considerably larger and more flexible than current spacecraft. Large spacecraft such as Space Station Freedom employ large, complex trusses in their construction. The structural dynamics of such trusses often exhibit nonlinear behavior and low structural damping which can impact significantly the performance of control systems. For example, in reference 1, Lallman studies the effect of damping on the performance of the attitude control system of the Space Station Freedom. The Mini-MAST truss was constructed to research the interaction of such structural dynamics and control systems and is an object of study for the Guest Investigator Program as part of NASA's Controls-Structures Interaction Program.

The Mini-MAST truss was designed to be deployable to a length of 66.14 feet when fully extended. The bending characteristics of the Mini-MAST truss are essentially linear. The angular deflection under torsional loading, however, has exhibited significant hysteresis and nonlinear stiffness during laboratory tests.

The complexity of such structures creates a burden to optimal design and to systems identification for upgrading dynamic model parameters by analyzing experimental test data. The large number of model parameters which results if each structural mode is assumed to be independent can be greatly reduced if distributed parameter models are used.

It is the purpose of this study to develop distributed parameter models of the Mini-MAST truss and to compare the model dynamics with the actual dynamic characteristics. A second purpose is to model the nonlinear stiffness and damping properties of this joint-dominated truss. It is hoped that the study results will be useful in designing control systems for large spacecraft (such as Space Station Freedom) which employ similar trusses.

DISCUSSION

Because the Mini-MAST truss is representative of structures that will be used for large spacecraft such as the Space Station Freedom, the study of its structural dynamics is valuable in assuring the dependability and high performance of spacecraft control systems. Figure 1a. pictures the Mini-MAST truss being deployed. The reduction in volume is striking when compared to the deployed truss shown in figure 1b. Reference 2 describes in detail the design of the Mini-MAST. Because of the complexity of the truss it is important to study simplifying models of its dynamics. Figure 2 shows how many modes are required to depict accurately the static deflection of a cantilevered beam. The problem is compounded if the modal parameters are considered to be independent. Because of the resulting complexity there is considerable advantage in using distributed parameter models. Due to the greatly reduced numbers of parameters required for such models as shown in figure 3, the ability to employ systems identification (Reference 3) and optimal design techniques is greatly facilitated. Because of these advantages it is valuable to determine the accuracy with which distributed parameter models can represent the Mini-

MAST truss. For example, can such simple models predict accurately the peaks of the frequency response shown in figure 4? If distributed parameter models represent accurately the dynamics of the Mini-MAST truss, then the model equations can be used to upgrade the model parameters using systems identification. Also the models will be useful in integrated control-structures design because their form provides easy access to global varibles such as the modulus of elasticity.

The Mini-MAST truss, being deployable, requires a large number of joints. The compliance and possible slippage of the joints may affect the overall stiffness of the truss when viewed as an equivalent beam. The action of the joints may also affect the damping of the truss as well. It is important to know accurately the damping of a spacecraft in order to assure reliable and high performance control. It is also important to understand and to model any nonlinear behavior caused by the numerous joints.

Distributed Parameter Bending Model

The Mini-MAST truss is modeled as a cantilevered beam with an added tip mass as depicted in the schematic in figure 5. The partial differential equations (Euler beam equation) and boundary condition equations (Cantilevered and tip mass) are solved thereby determining the modal characteristics. First, the calculated static deformation resulting from a constant 15 pound for applied to the tip is compared to actual test results in figure 6. The value of the stiffness parameter, EI, for an equivalent Euler beam derived from this test is 27.6 x 10^6 pound feet squared. The comparison suggests that the model deformation matches the actual deformation within the measurement error. The resulting modal frequencies in bending are then compared with experimental results and those for a finite element model* in figure 7. The frequencies for the first few bending modes of the distributed parameter model accurately match the actual bending frequencies of the truss. At higher mode numbers, however, the actual modal frequencies are lower than the theoretical values for the Euler beam model. Belvin** showed that the shear deformation of a similar truss cannot be ignored as is done in

*Bailey, James, Finite-Element Model of the Mini-MAST Truss, personal communication, NASA Langley.

**Belvin, W. Keith, Simplified Analysis of NASA's COFS 1 MAST-Beam, personal communication, NASA Langley.

the Euler beam model. Belvin used the techniques of reference 6 in his study. The Timoshenko beam, in contrast, accounts for the shear deformation and more accurately models the frequencies in bending as shown in figure 7.

Figure 7 also shows the accuracy with which the frequencies of a finite element model match the actual frequencies of the truss. The finite element model is reasonably accurate even at high mode numbers. The parameter, EI, used in the finite element model equals 29.8 x 10^6 pound feet squared. In figure 8 the bending mode shapes generated by the same finite element model exhibit shapes similar to Euler beams with one exception. Examination of the third mode reveals that the shear deformation is significant enough to give a change in slope almost at the bottom of the truss. The general contour of the mode shapes in figure 8 compare well with those of the Timoshenko beam (not shown) but the irregularities which show significant local deformation will be missing from the distributed parameter models. It is possible that overlookong such local deformations could cause control system instability.

The effect on the first bending mode frequency of changing the mass at the tip of the equivalent beam is shown in figure 9. The frequency response measurements of figure 4 had a tip mass which weighs 70.125 pounds (mass ratio = .31). The Mini-MAST truss excluding its tip mass weighs 229 pounds. The Euler beam model depicts accurately the change in frequency when the tip mass is removed. The assembly for the active control of the Mini-MAST is expected to weigh in excess of 300 pounds. The frequencies for higher mode numbers will not change as much as that for the first mode because as mode number increases the motion of the tip mass diminishes, thereby approaching a pinned end condition.

Distributed Parameter Torsion Model

Similar to the bending case, the truss is modeled in torsion as a uniform shaft which is fixed at one end and has a tip body attached to the other end. Based on the angular deformation due to an applied moment the torsional parameter GI_{polar} equals 2.16 x 10^6 pound feet squared per radian. The partial differential equations and end conditions are solved and in figure 10 the model's torsional frequencies are compared with experimental results and the finite element model of Bailey's personal communication. The close comparison indicates that the modal frequencies for both the distributed parameter model and the finite element model compare closely with the actual frequencies.

Nonlinear Torsional Stiffness

Because the Mini-MAST truss exhibits significant nonlinear stiffness and hysteretic behavior in torsion, it is necessary to model these characteristics. The nonlinear stiffness model will be discussed first. The hysteretic model will be treated in the next section.

Although the form of the nonlinear stiffness is approximately cubic, a tangent function is used because (1) its form gives the nearly linear plus cubic relationship that is needed, and (2) the tangent has a conveniently express inverse. Figure 11 depicts the tangent model of the nonlinear stiffness in torsion and introduces the parameters, K, and, B, which govern the linear and the cubic contribution, respectively. The parameter, K, then is the usual torsional stiffness.

In figure 12 it is evident that the tangent relationship compares well with the experimental results. The data shown are believed to not involve any slipping as it represents the relaxation from a load having been applied. As the load is increased slipping does take place and will next be considered.

Torsional Slip Model

The torsional hysteretic model is comprised of an infinite number of slip elements. An individual slip element is assumed to slip instantaneously upon reaching a particular moment threshold. A reverse slip is assumed to take place at a moment of equal level but opposite sign as depicted in figure 13. A slip distribution function is introduced which describes the probability density function of the values of moment threshold. The second order exponential form of the function, shown in figure 14, was chosen to fit the experimental data. Effort is under way to link this distribution function to the vertical loading of the joints. The total deflection amplitude consists of (1) the deflection due to compliance without slipping plus and (2) the deflection due to an accumulation of slips due to the applied moment. The expected value of the accumulation of slips is given by the integral of the slip distribution function between the last moment reversal or zero and the current applied moment. The deflection equation is depicted in figure 15.

The total hysteretic model which contains both the nonlinear stiffness and the hysteretic slipping is compared with actual test results in figure 16. The close comparison of the model results and the actual hysteretic behavior gives validity to the model for torsional deflection due to applied moment.

The hysteretic behavior is expected to be dependent on the vertical loading. When the 300 pound plus active control assembly is attached to the top of the Mini-MAST the total angular deflections are not expected to change significantly, but an increase in the moment threshold is expected. Because of the effect of gravity it is difficult to determine the hysteretic behavior in an unloaded condition as in space.

Structural Damping

The damping for the first bending mode is affected by the mass of the tip body as shown in figure 17. The damping ratio which was measured for the truss without tip mass was about 3.3%. This value was about three time the value expected based on the assumption that the dimensional damping of the truss would not change. The damping ratio would be expected to double from the value of about .45% for the 70 pound tip mass. This discrepancy is probably due to slipping being affected by vertical loading, as is the case for torsion.

In torsion it is possible to link slipping to damping by accounting for the loss of energy due to slipping. Figure 18 shows that the expected contribution to damping from slipping for oscillations about the unloaded condition reflect the shape of the slip distribution function. The damping contribution for oscillations in torsion about a loaded condition may be as low as zero because of the complete lack of slipping.

The statically determinant truss to be used on the Space Station Freedom can be expected to involve internal loading. As a result the damping of the truss for small amplitudes is not expected to involve slipping and will consequently exhibit very low damping.

Laboratory tests have revealed a damping ratio for bending modes for the cantilevered truss to be about .0045. The damping ratio will decrease when large bodies are added to the truss. In the absence of air, the damping can be expected to be even smaller, perhaps approaching .002.

Past practices of using a constant damping ratio of .005 for Space Station studies does not represent the worst case. Lower values of damping should be used which reflect mass loading and internal loading effects.

CONCLUDING REMARKS

The Mini-MAST truss has been tested and analyzed for the purpose of understanding the dynamic characteristics, nonlinear stiffness and hysteretic damping of large spacecraft.

It was necessary to use a Timoshenko beam model for bending to account for the shear deformation of the Mini-MAST truss. The modal frequencies of the Euler beam model were higher than the actual values.

A tangent function model of the nonlinear torsional stiffness was developed and its parameters estimated to match experimental results.

A hysteretic slip model for torsion was developed using the experimental test data. The slip distribution function used has a second order, exponential form. The hysteretic behavior is expected to be affected by changes in the vertical loading due to gravity.

The damping contribution in torsion of the hysteretic behavior was deduced by analyzing the torsional slip model. The damping due to slipping was determined to be quite dependent on loading conditions. A steady load, for example, might eliminate slipping and consequently any damping contribution due to slipping.

Future studies of control system performance should use lower values of structural damping than the .005 used in the past, and should consider the nonlinear effects.

REFERENCES

1. Young, John W. and Frederick J. Lallman: Control/Structures Interaction Study of Two 300 KW Dual-Keel Space Station Concepts. NASA Technical Memorandum 87679. May 1986.

2. Adams, Louis R.: Design, Development and Fabrication of a Deployable/Retractable Truss Beam Model for Large Space Structures Application. NASA Contractor Report 178287. June 1987.

3. Taylor, Lawrence W., Jr.: On-Orbit Systems Identification of Flexible Spacecraft. 7th IFAC Symposium on Identification and System Parameter Estimation. York, England. July 2-8, 1985.

4. Noor, A. K., Anderson, M. S. Anderson and W. H. Greene: Continuum Models for Beam- and Platelike lattice Structures. AIAA J., v. 16, no. 12, December 1978.



Figure 1a. The Mini-MAST Truss Being Deployed.

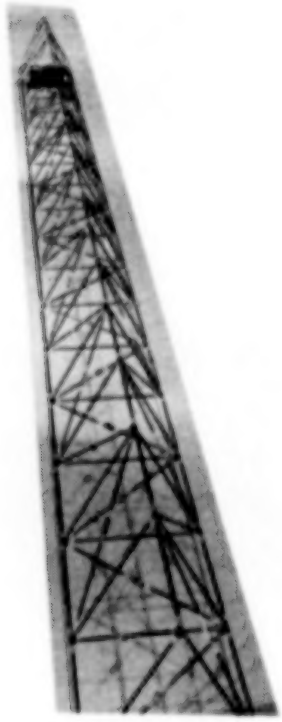


Figure 1b. The Mini-MAST Truss Fully Deployed.

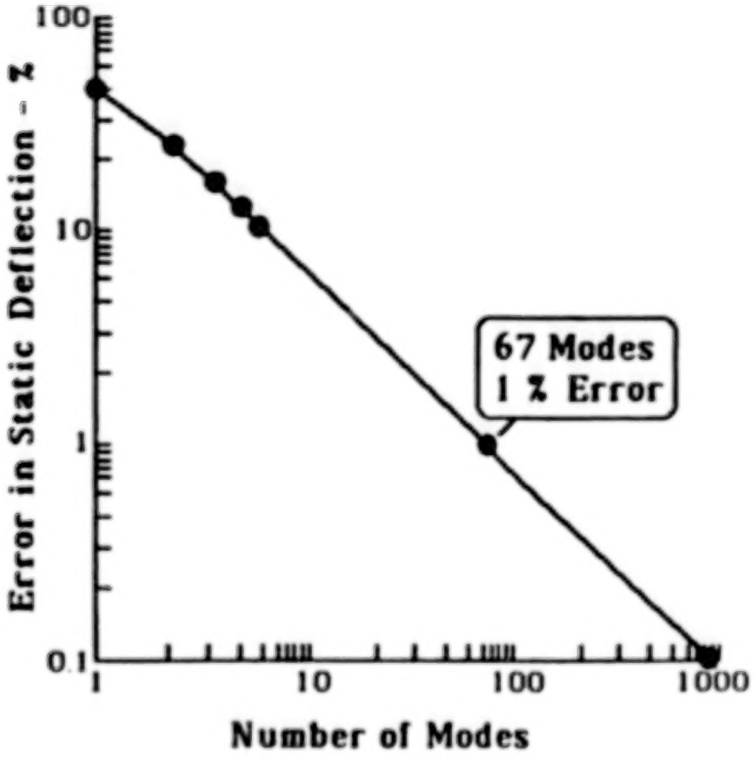


Figure 2. The Number of Modes Required for a Modal Model to Accurately Represent the Static Deflection of a Cantilevered Euler Beam.

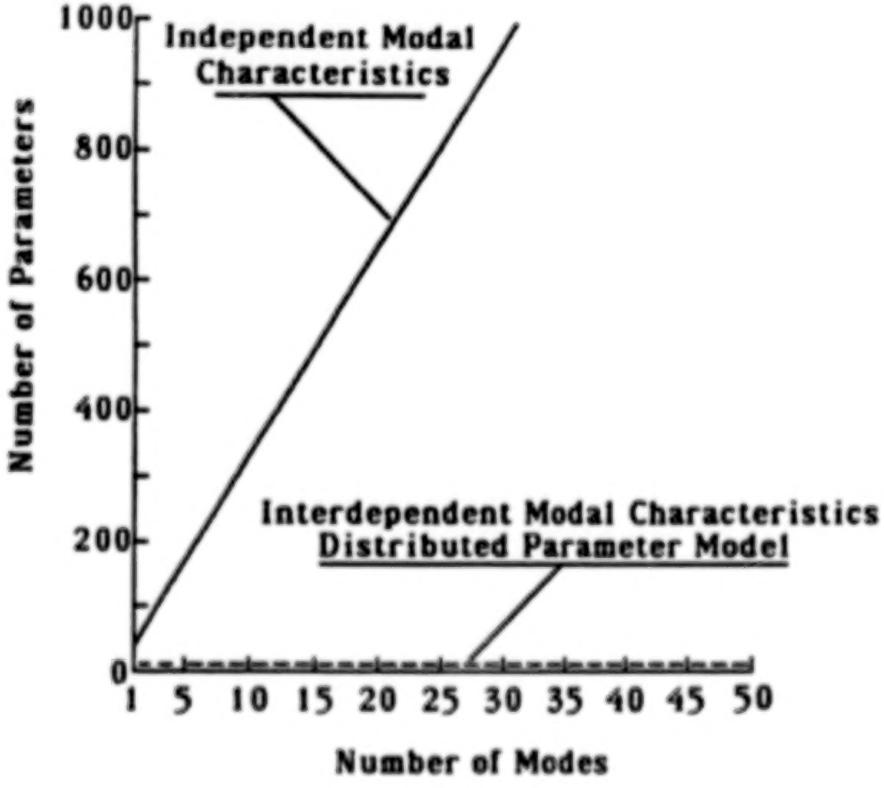


Figure 3. Comparison of the Number of Model Parameters for Modal Models and Distributed Parameter Models.

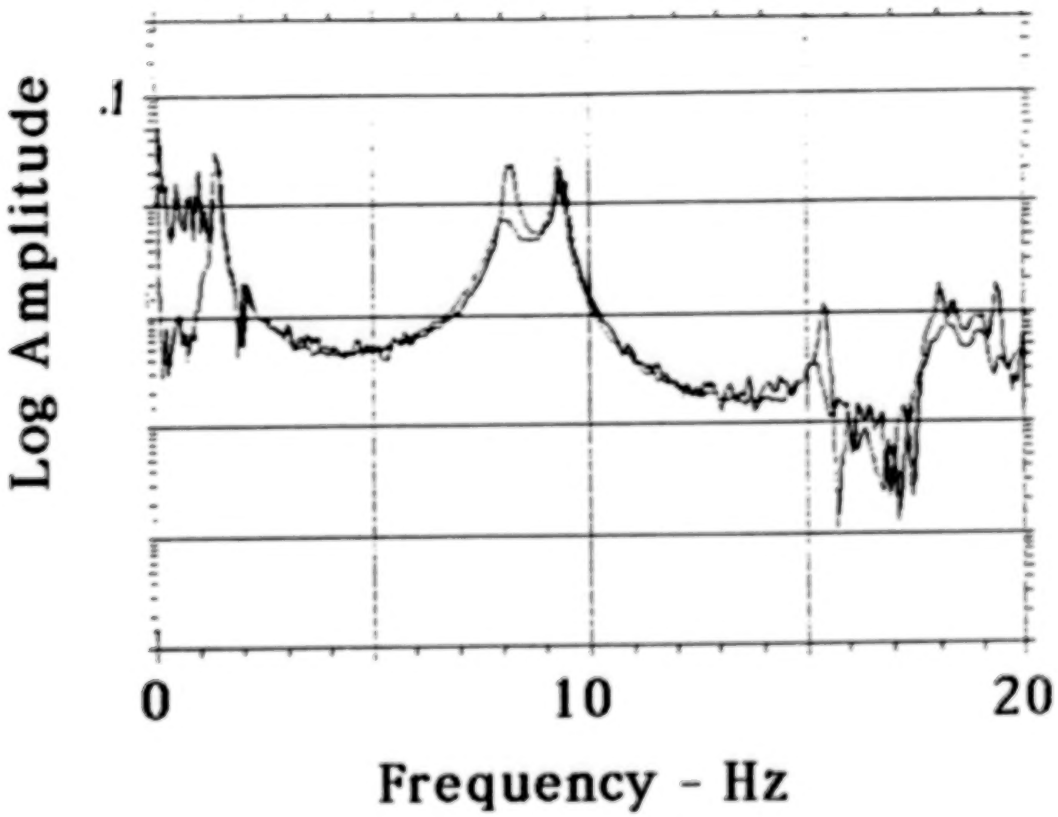


Figure 4a. Frequency Response of the Mini-MAST Truss in Term of Inches of Response per Pound of Input. Frequency from 0 to 20 Hz.

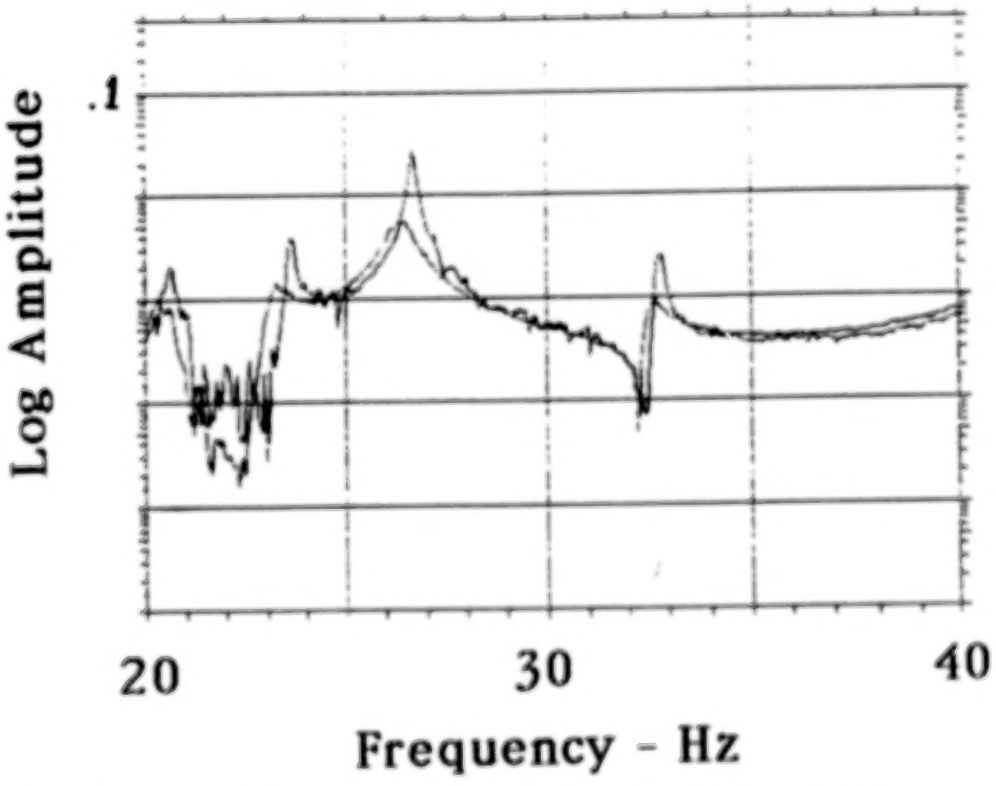


Figure 4b. Frequency Response of the Mini-MAST Truss in Term of Inches of Response per Pound of Input. Frequency from 20 to 40 Hz.

BEST COPY AVAILABLE

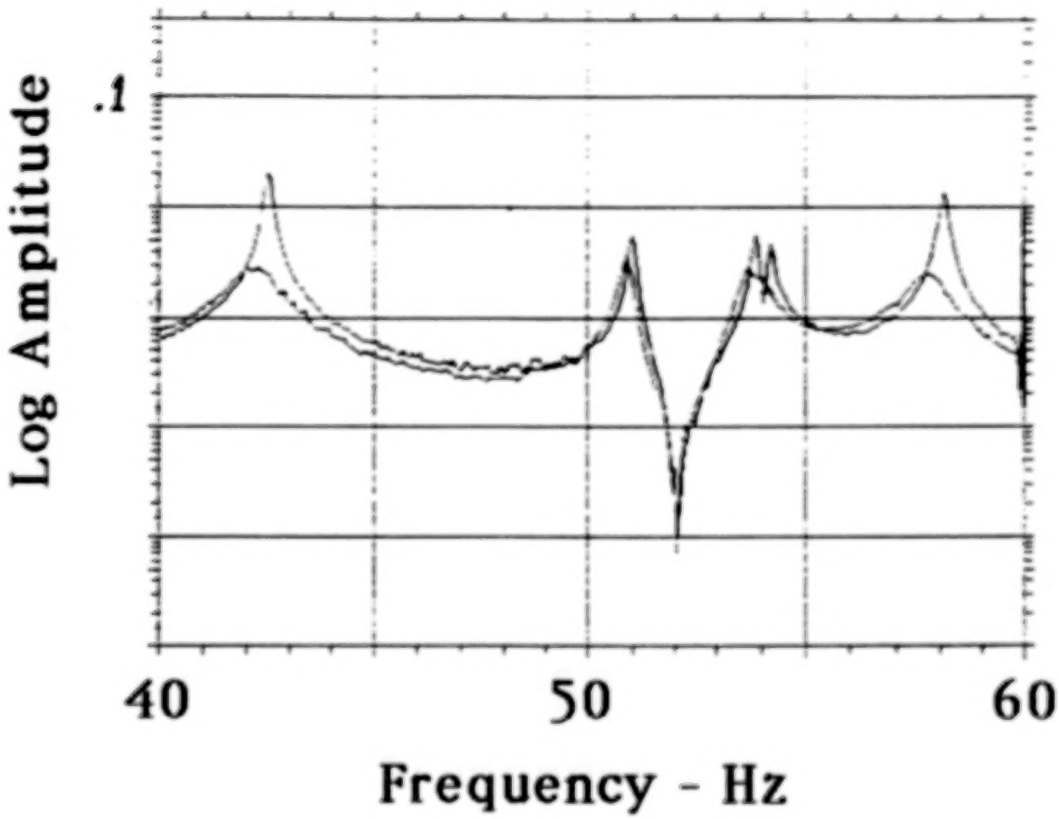


Figure 4c. Frequency Response of the Mini-MAST Truss in Term of Inches of Response per Pound of Input. Frequency from 40 to 60 Hz.

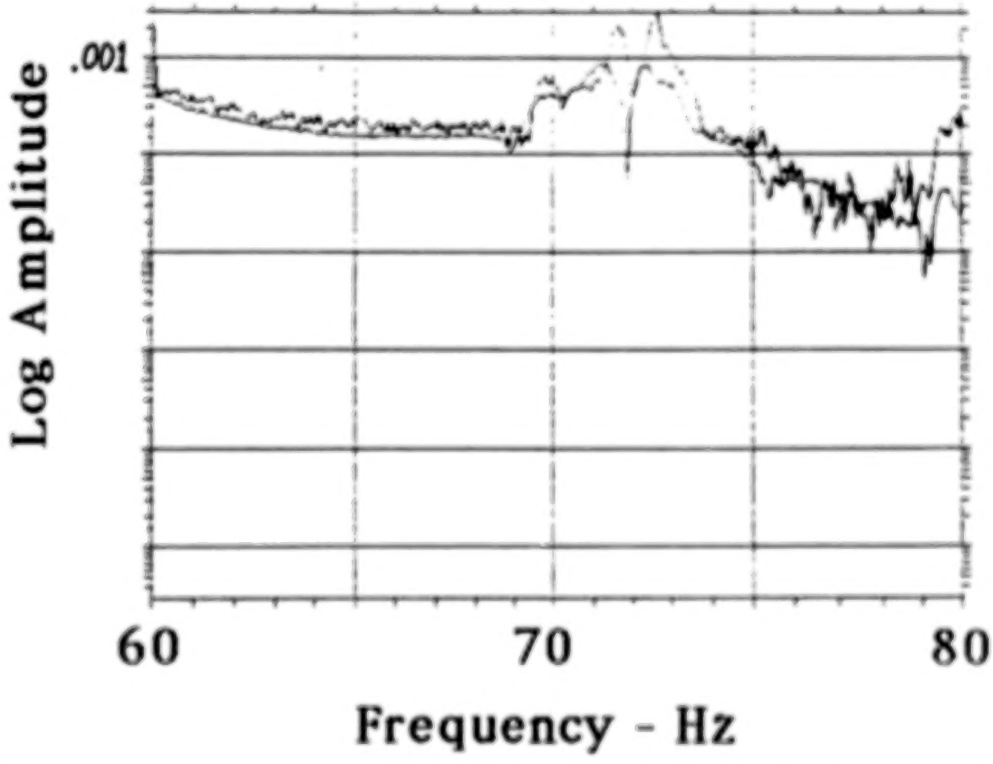


Figure 4d. Frequency Response of the Mini-MAST Truss in Terms of Inches of Response per Pound of Input. Frequency from 60 to 80 Hz.

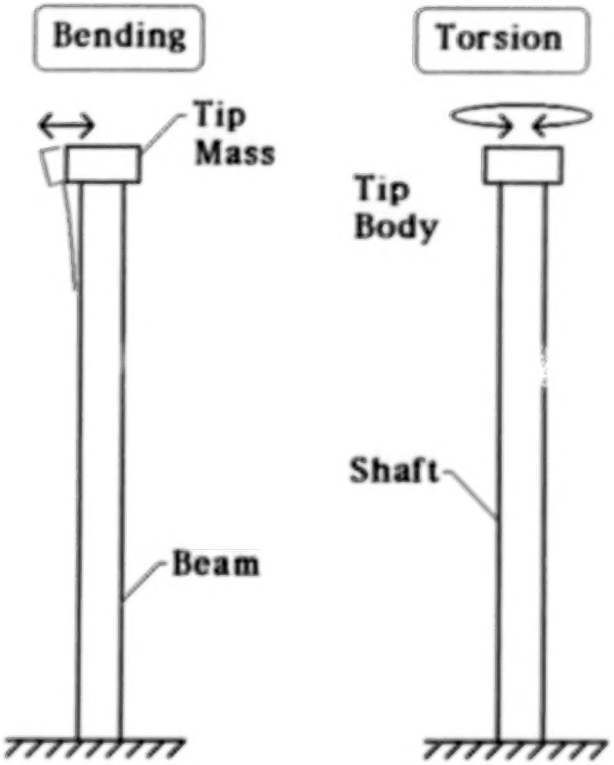


Figure 5. Schematics of Distributed Parameter Models for Bending and Torsion.

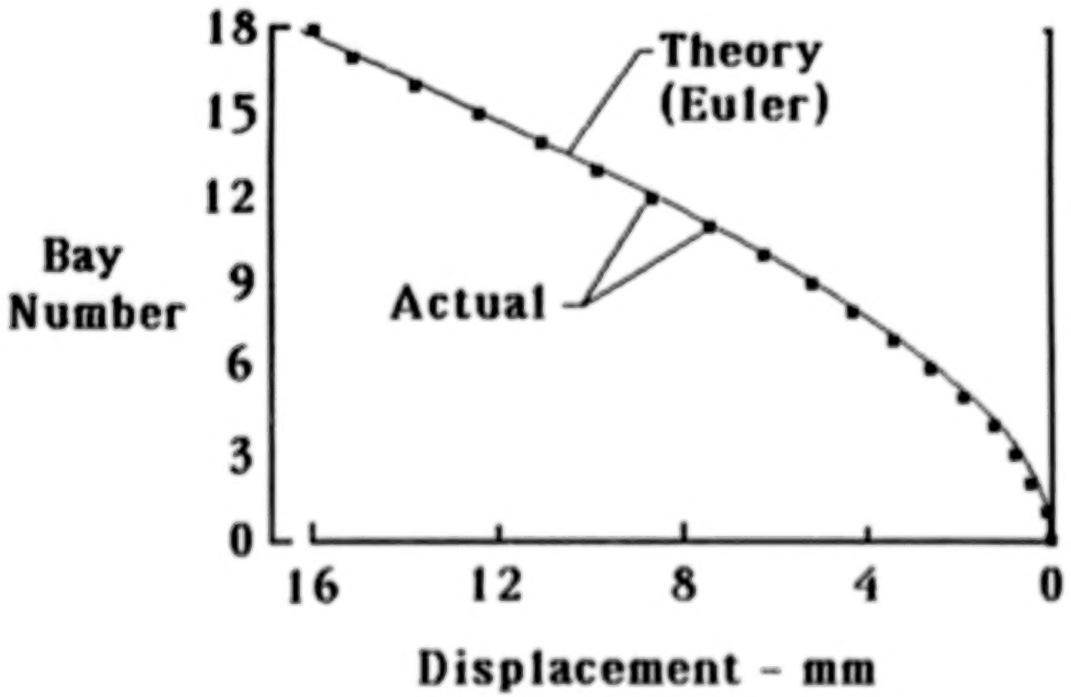


Figure 6. Comparison of the Model and Actual Static Deflection in Bending of the Mini-MAST Truss Subjected to a 15 Pound Force at the Top.

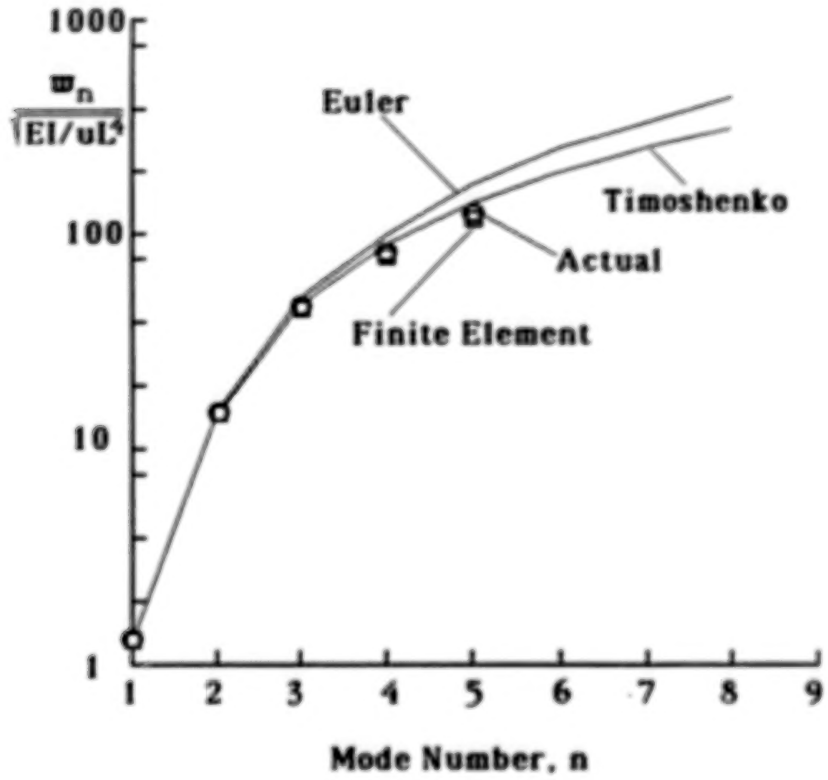


Figure 7. Comparison of Distributed Parameter Model, Finite Element Model and Actual Normalized Bending Frequencies.

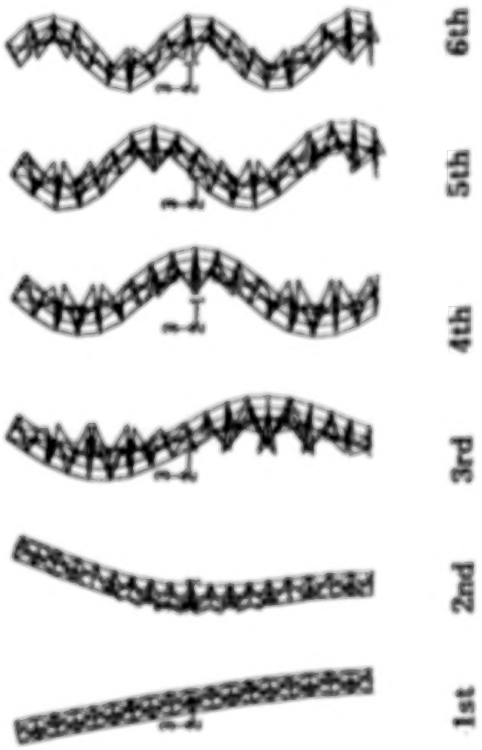


Figure 8. Finite Element Model Mode Shapes for Bending.

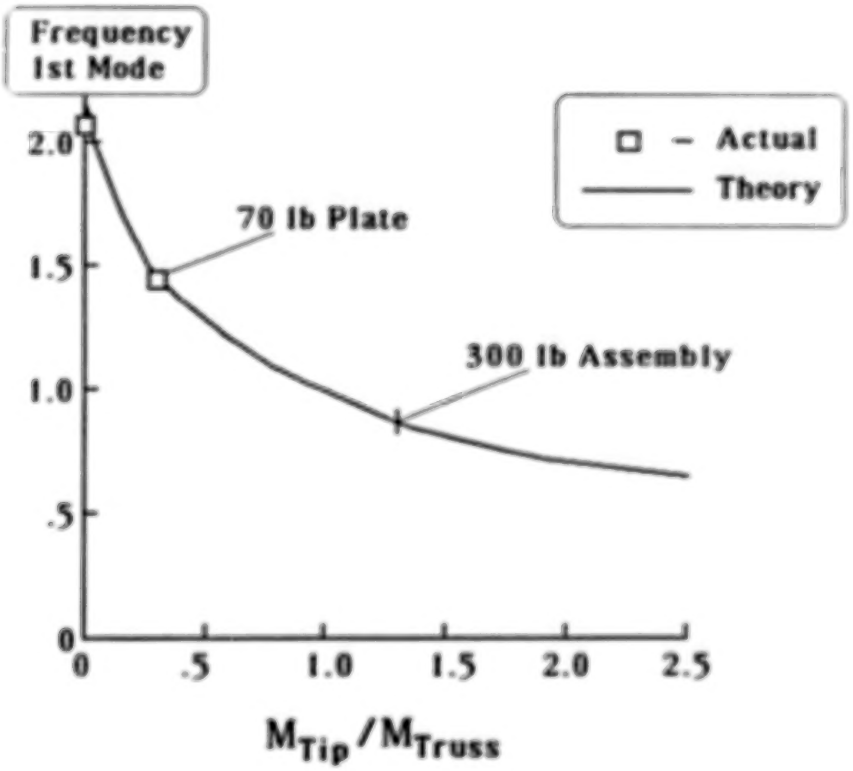


Figure 9. Comparison of the Model and Actual First Mode Bending Frequencies as a Function of Tip Mass to Truss Mass Ratio.

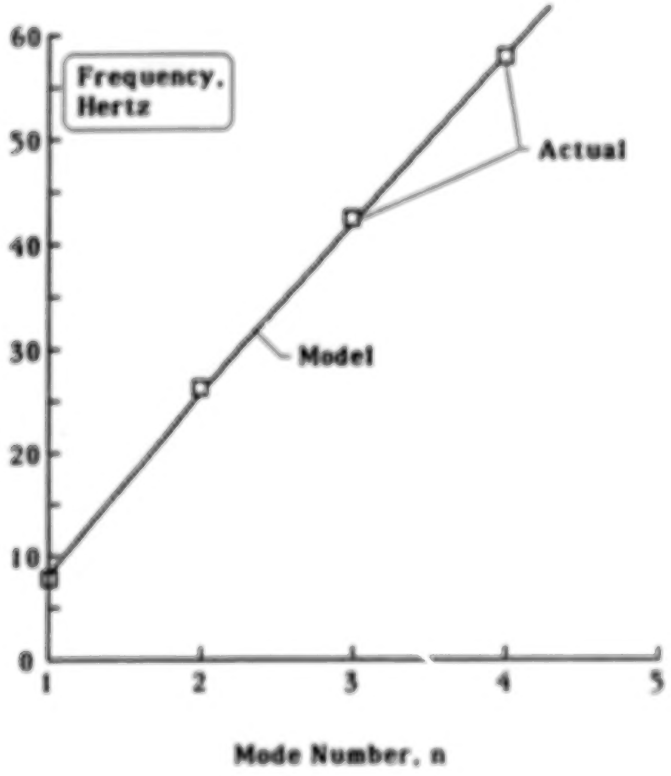
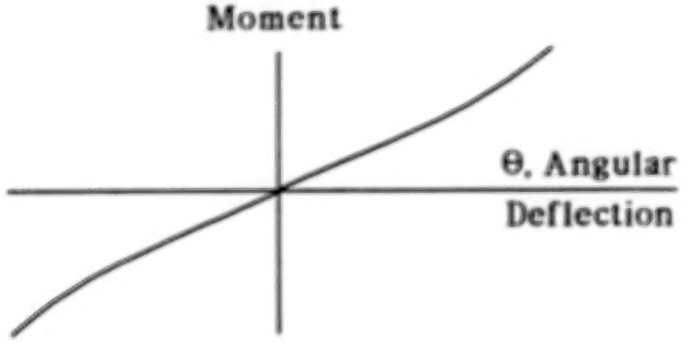


Figure 10. Comparison of Model and Actual Torsion Mode Frequencies.



$$M = \frac{K}{B}\mathrm{Tan}(B\theta) \quad \text{or} \quad \theta = \frac{1}{B}\mathrm{Arctan}\left(\frac{MB}{K}\right)$$

$$\left.\frac{d\theta}{dM}\right|_{M=0} = \frac{1}{K} \qquad \left.\frac{d^3\theta}{dM^3}\right|_{M=0} = \frac{2B^2}{K^3}$$

Linear Cubic

Figure 11. Nonlinear Stiffness Formulation Used for the Torsion Model.

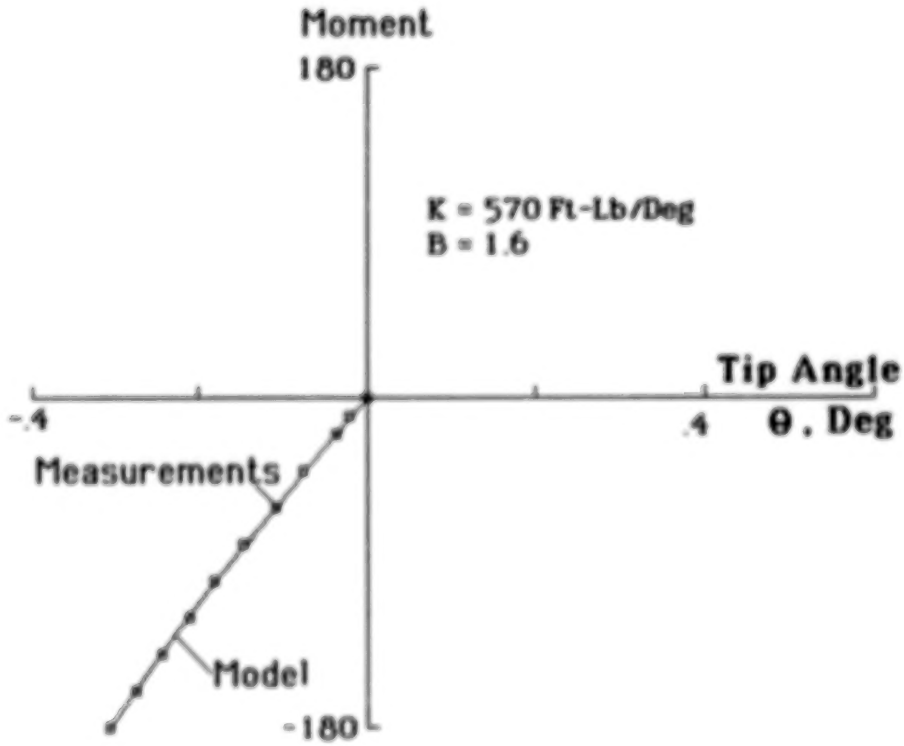


Figure 12. Comparison of Model and Actual Static Deflection in Torsion.

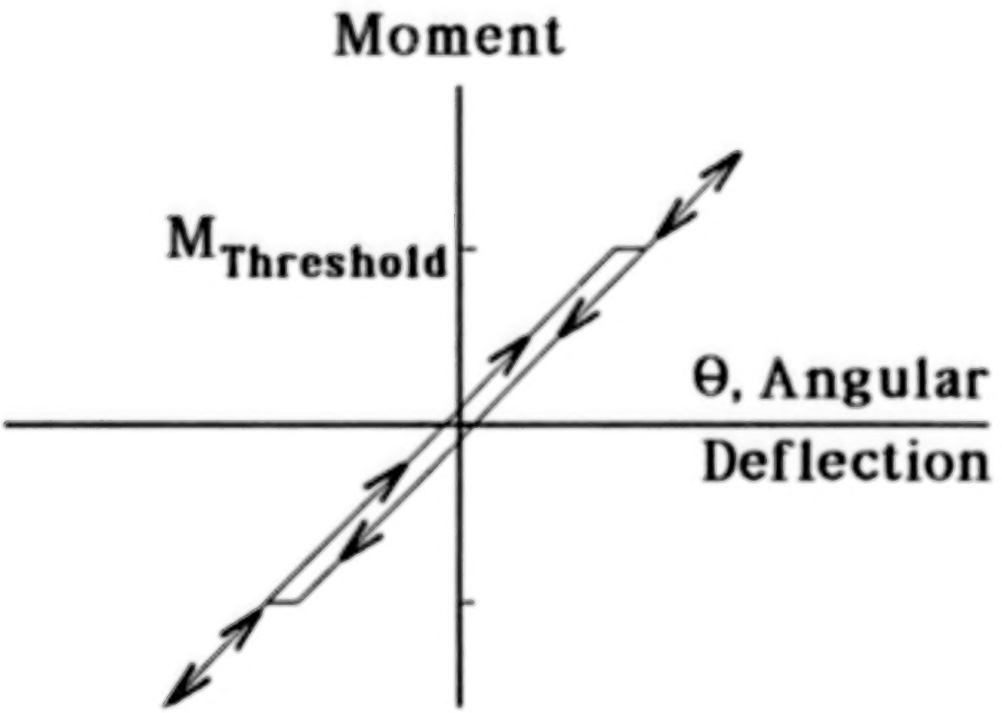
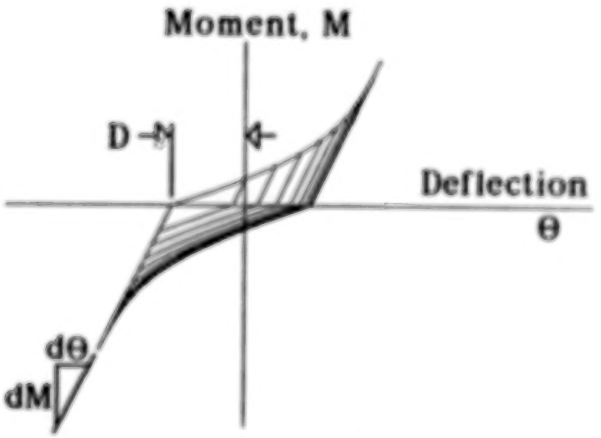


Figure 13. An Individual Nonlinear Slip Element for the Torsion Model.

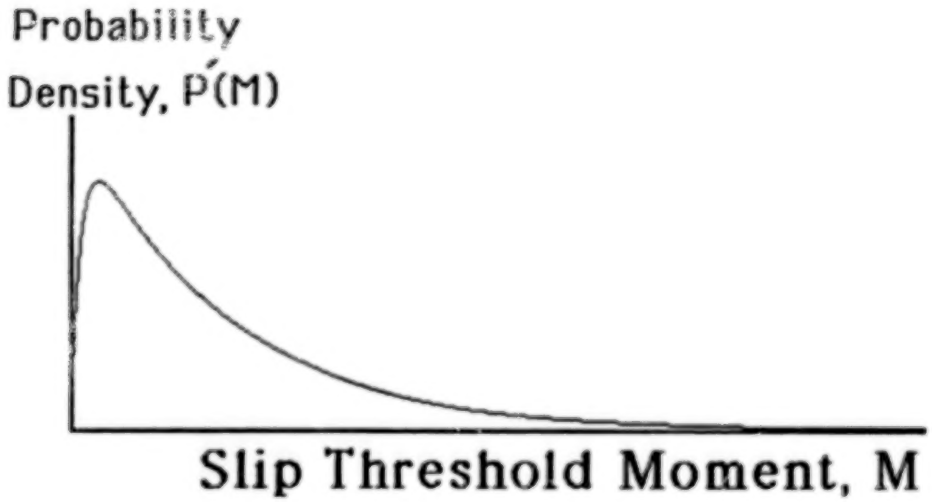


$$\theta = M/K + D\int_{A}^{M} P'(M)\,dM$$

$$A = M_{reversal} \quad \text{if} \quad M_{reversal} > 0$$

$$= 0 \quad \text{if} \quad M_{reversal} < 0$$

Figure 14. Nonlinear Hysteretic Model for Torsion.



$$P'(M) = -\frac{e^{-M/X1}}{X2-X1} + \frac{e^{-M/X2}}{X2-X1}$$

Figure 15. The Slip Distribution Function.

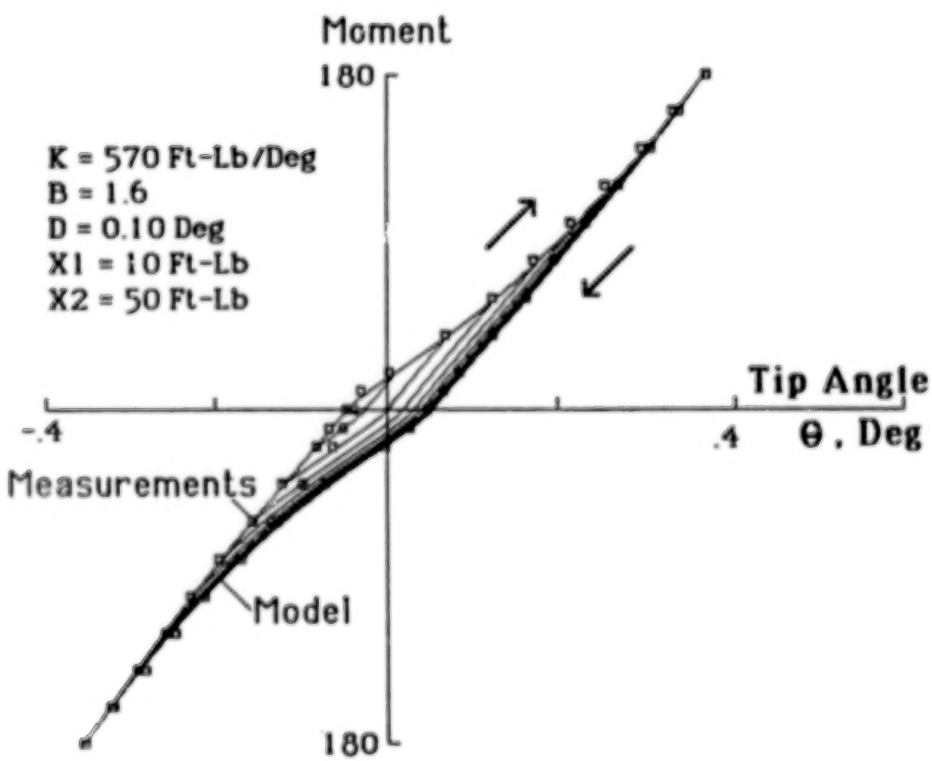


Figure 16. Comparison of Hysteretic Model and Actual Static Deflection in Torsion.

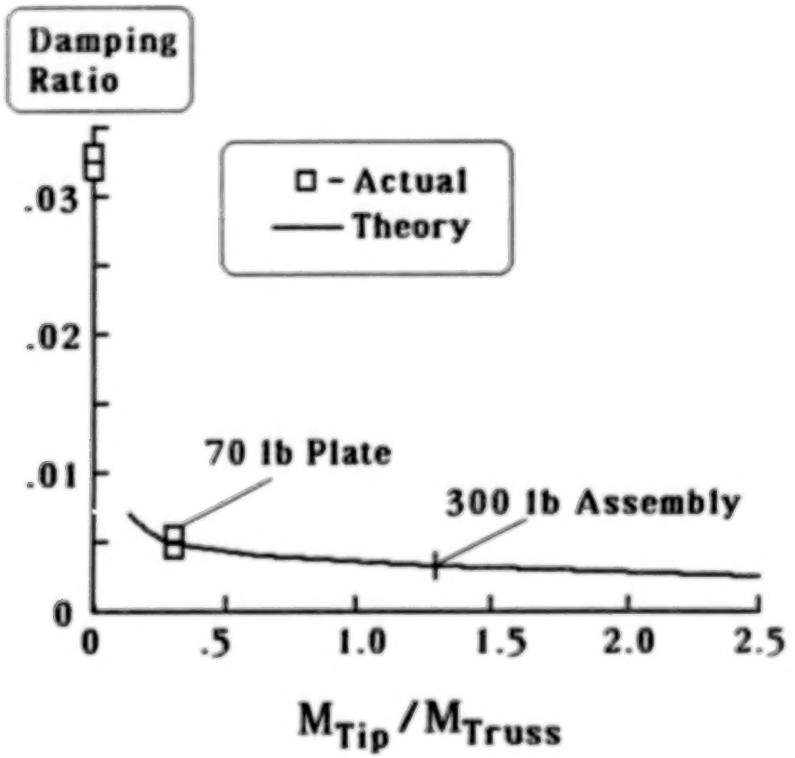


Figure 17. Comparison of Model and Actual Damping Ratios in Bending as a Function of Tip Mass to Truss Mass Ratio.

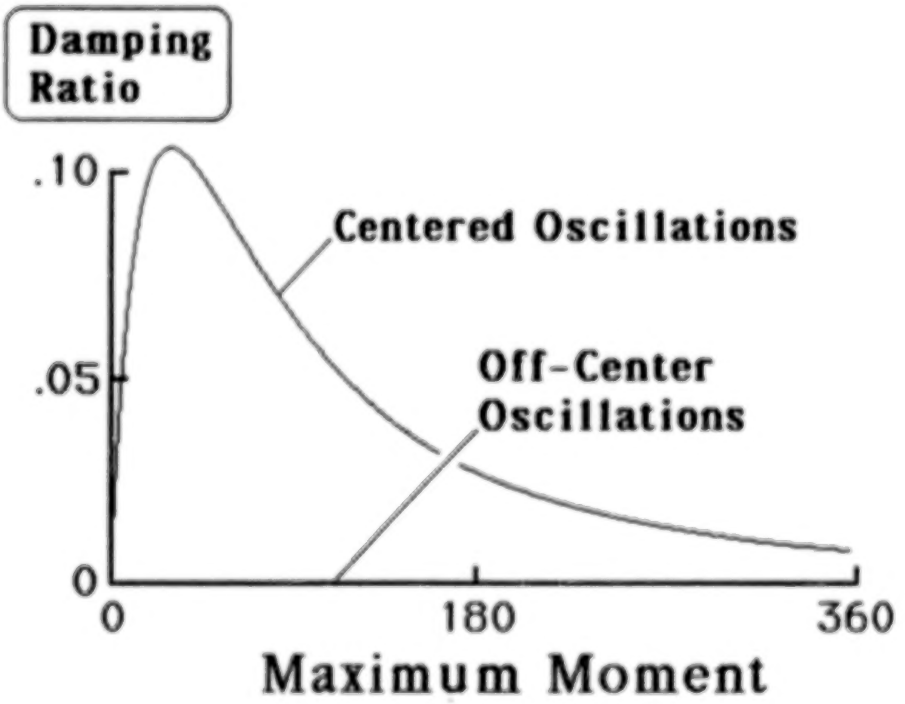


Figure 18. Effect of the Hysteretic Behavior on Damping in Torsion.

A DISTRIBUTED FINITE-ELEMENT MODELING AND CONTROL APPROACH FOR LARGE FLEXIBLE STRUCTURES

K. D. Young
Lawrence Livermore National Laboratory
University of California
Livermore, California

Third Annual NASA/DOD CSI Conference
San Diego, California
January 29 - February 2, 1989

INTRODUCTION

This paper describes an unconventional framework for the design of decentralized controllers for large flexible structures. In contrast to conventional control system design practice which begins with a model of the open loop plant, the controlled plant is assembled from *controlled components* in which the modeling phase and the control design phase are integrated at the component level.

The developed framework is called *Controlled Component Synthesis* (CCS) to reflect that it is motivated by the well developed *Component Mode Synthesis* (CMS) methods which have been demonstrated to be effective for solving large complex structural analysis problems for almost three decades.

The design philosophy behind CCS is also closely related to that of the *Subsystem Decomposition Approach* in decentralized control.

CONTROLLED COMPONENT SYNTHESIS

CCS is a framework for an integrated, component oriented, finite-element modeling and structural control design. Similar to CMS methods, CCS is developed on the premise that a large complex controlled structure is to be built from *controlled components*: The finite element modeling and control design are carried out for the individual components; the model of the large complex structure is assembled from the controlled components only for the purpose of performance evaluation.

The CCS method developed herein adopts the following modeling and control design considerations at the component level: Instead of using either the boundary loading, or the constraint modes approach as in CMS, we introduce a new approach called *Isolated Boundary Loading* for the development of component models. For the design of controllers for the component, an *InterLocking Control* concept is developed to minimize the motion of the nodes that are adjacent to the boundary, thereby suppressing the transmission of mechanical disturbance from component to component in the coupled structure.

The major ideas behind CCS are:

Component modeling using Isolated Boundary loading

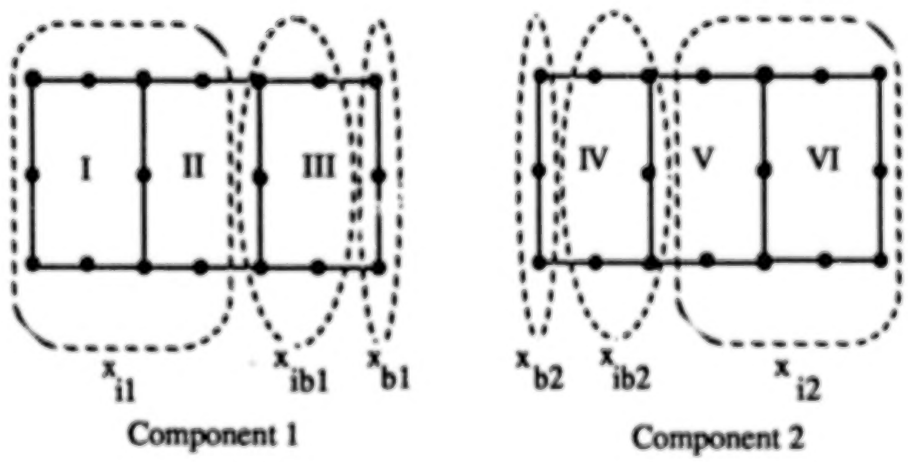
Connections to Overlapping Decomposition

Intelocking Control Concept

COMPONENT MODELING

A two component structure, as shown below, will be used to outline the modeling and design procedure of the CCS method. Each of the structure component is composed of three finite elements. Identified in the figure by Roman numerals are the finite elements, and by solid circles are the element node points.

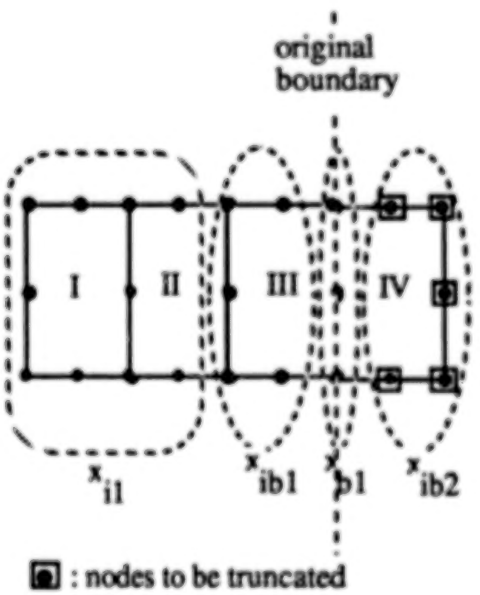
In the **CCS** method, the nodal coordinates of a component are partitioned into three groups: The internal coordinates are subdivided into a group of internal boundary coordinates x_{ibs} and a group of internal coordinates x_{is}. The boundary coordinates x_{bs} remain in a single group. The boundary coordinates are coordinates of the boundary element, such as element III of component 1, which are on the boundary. The remaining coordinates of the boundary element are designated the internal boundary coordinates. The remaining coordinates of the component are the internal coordinates.



A two component structure modeled with finite elements

ISOLATED BOUNDARY LOADING

The component mass and stiffness matrices are obtained from the finite-element modeling of an expanded component, *i.e.*, the original boundary of the component is extended one finite element into the adjacent component. The nodes of the expanded component consist of the original nodes of the component, and the internal boundary coordinates of the adjacent component. The mass and stiffness matrices are obtained from the mass and stiffness matrices of the expanded component by deleting the rows and columns corresponding to the nodes in the expanded portion.

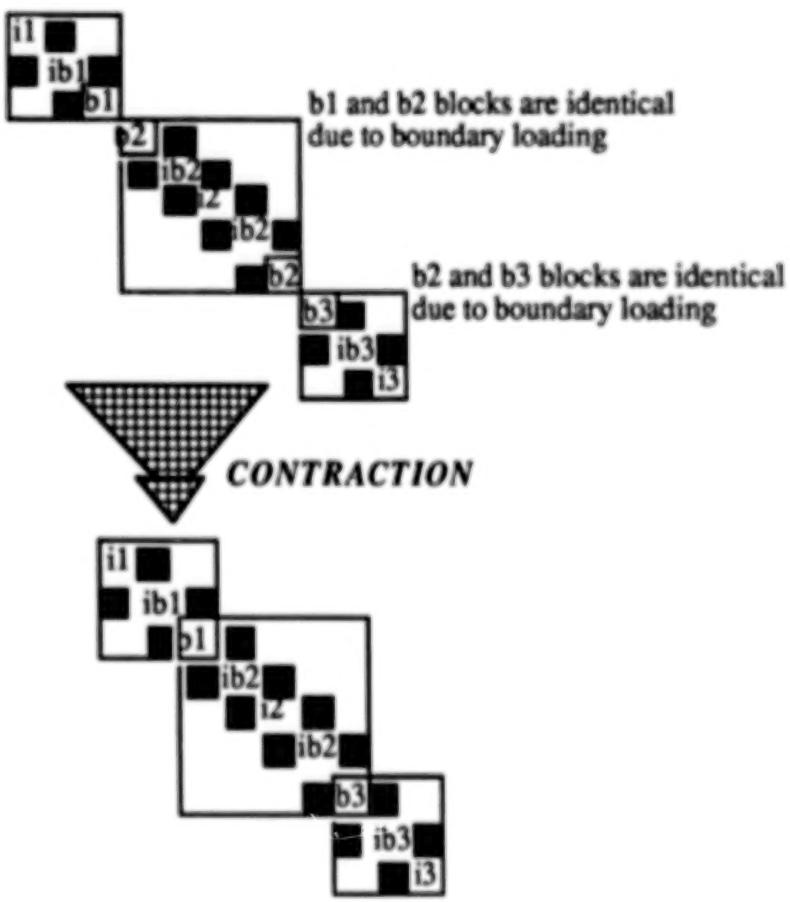


Expanded component 1

CONNECTION TO OVERLAPPING DECOMPOSITION

The component models developed using isolated boundary loading have direct connection with the Subsystem Decomposition Approach. These models are identical to the decoupled subsystem models if an overlapping decomposition is applied to the finite-element model of the coupled structure. This is a key connection which allows the use of tools developed by Siljak[1] and his co-workers for evaluating the performance of the controlled coupled structure, after the controlled component designs have been completed.

The mass and stiffness matrix connectivity is illustrated in the following diagram showing how the component models can be "contracted" to form the coupled structure finite-element model.



Overlapping Decomposition Connection

INTERLOCKING CONTROL CONCEPT

The new insights gained from the developed component modeling approach in turn motivate a new component level control design concept which we call *InterLocking Control* (**ILC**) in which collocated actuator and sensors are placed at the internal boundary degrees of freedom, and the control law is designed, using the developed component model for **CCS**, to minimize the internal boundary coordinate motion.

Such minimization would localize the dynamic interactions of the coupled structure in the components. The component control action is designed to lock up its own internal boundary to realize a boundary condition which better approximates the one assumed in the component modeling of its adjacent components.

A convenient control design technique for this concept is the linear quadratic optimal regulator approach in which the internal boundary coordinates are considered as regulated outputs of the component to be weighted together with the component control inputs in the quadratic performance index. The resulting component control law minimizes this index.

The **ILC** concept translates into a two step component control design process summarized below:

1. For the **sth** component, use the component model

$$\begin{bmatrix} M^s_{ii} & M^s_{ib} & 0 \\ M^s_{bi} & M^s_{b} & M^s_{bb} \\ 0 & M^s_{bb} & M^s_{bb,LL} \end{bmatrix} \begin{bmatrix} \ddot{x}_{i} \\ \ddot{x}_{b} \\ \ddot{x}_{b} \end{bmatrix} + \begin{bmatrix} K^s_{ii} & K^s_{ib} & 0 \\ K^s_{bi} & K^s_{b} & K^s_{bb} \\ 0 & K^s_{bb} & K^s_{bb,LL} \end{bmatrix} \begin{bmatrix} x_{i} \\ x_{b} \\ x_{b} \end{bmatrix} = \begin{bmatrix} 0 \\ u^s \\ 0 \end{bmatrix}$$

$$y^s = x_{b}.$$

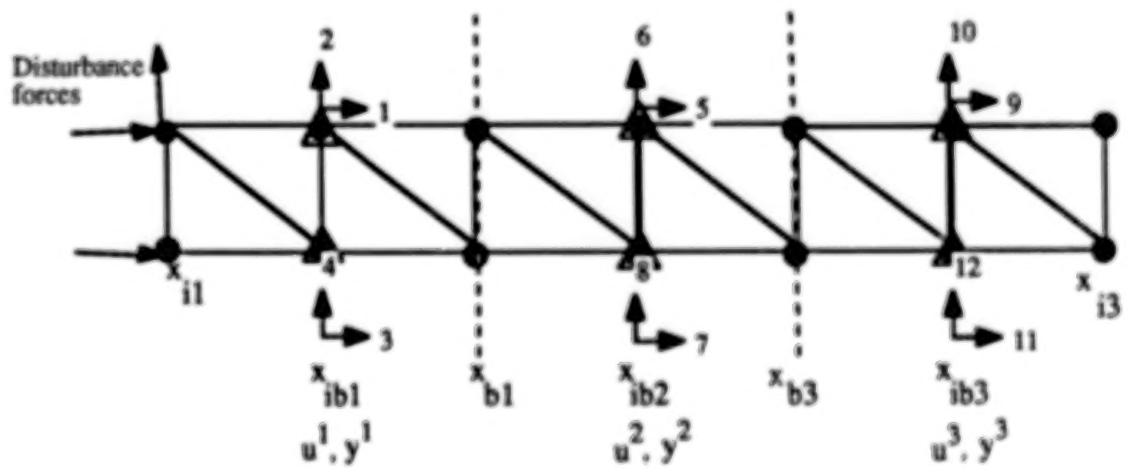
for control system design, where u^s and y^s denotes respectively the control force exerted by the actuators, and the sensor outputs, at the internal boundary coordinates.

2. Derive the component control law by minimizing the performance index,

$$J^s_c = \frac{1}{2}\int_0^\infty (y^{sT} y^s + u^{sT} R^s u^s)\,dt.$$

APPLICATION TO TRUSS STRUCTURE CONTROL

The developed CCS method is applied to the design of structural control laws for a planar truss structure for a preliminary assessment of its feasibility toward solving more complex structural control design problems. This truss structure which is depicted below has six bays, and the nodal coordinates are defined as the vertical and horizontal displacements at the joints.



Planar truss for CCS evaluation

External forces applied at the nodes are decomposed into orthogonal components. The assumptions made are that the truss members are subjected to axial forces alone, and not bending moments; and the members are uniform rods of identical lengths L, mass per unit length m, cross-section area per unit length A and modulus of elasticity E.

The six bay truss can be viewed as a structure that consists of three identical components, namely the left component, the center component, and the right component, which are composed of the left-most, the middle, and the right-most two bays respectively. The six bay/three component truss structure is chosen to capture the essential characteristics of a truss consists of an arbitrary number of identical components, i.e., a truss structure with an arbitarily large number of two bay components is composed of the three same types of components identified in the six bay truss, with the center component duplicated as necessary. Thus, conclusions from the six bay/three component design apply equally well to the design of structural controls for a multiple bay truss.

TRUSS STRUCTURE CONTROL - CCS MODELING

For CCS, the component models are developed using the expanded component introduced in Isolated Boundary Loading. The mass and stiffness matrices of the expanded component are derived using a finite-element method with the Ritz-Rayleigh approximation. The truss member mass and stiffness matrices used in the assembly process are:

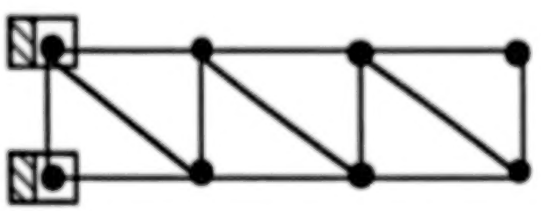
$$K_{member} = \frac{EA}{L}\begin{bmatrix} 1 & -1 \\ -1 & 1 \end{bmatrix} \quad , \quad M_{member} = \frac{mL}{6}\begin{bmatrix} 2 & 1 \\ 1 & 2 \end{bmatrix}$$

The component model is further scaled to remove the effects of the material properties: a new time variable

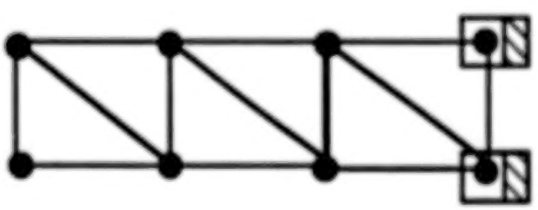
$$\tau = \sqrt{\frac{m}{6EA}}\, Lt$$

is introduced, and the nodal forces are scaled by $L(EA)^{-1}$.

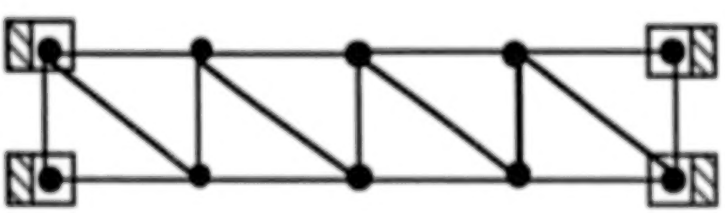
The three expanded components from which the component models are derived are shown below. The internal boundary degrees of freedom at which collocated force actuators and displacement sensors are placed are marked by Δ.



Right-most Component



Left-most Component



Center Component

 : Nodes to be truncated/Degrees of Freedom to be constrained

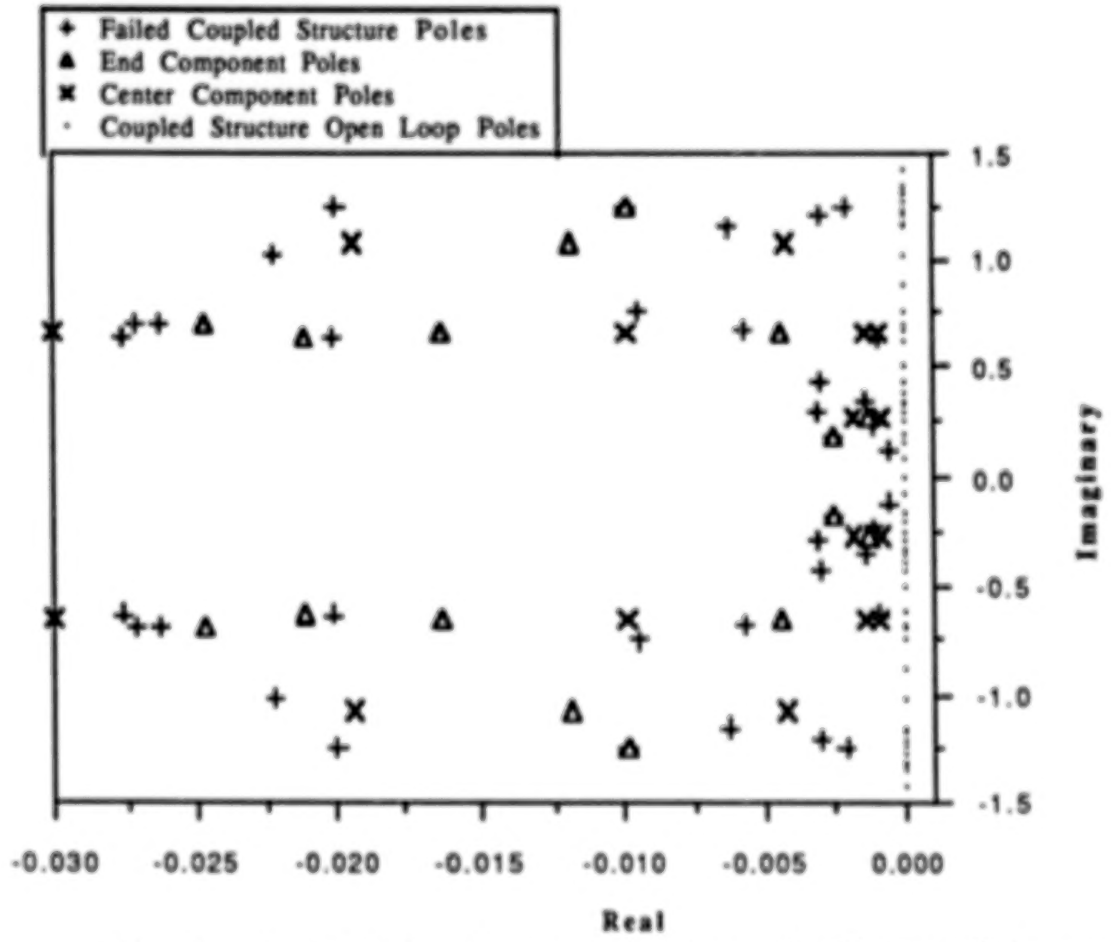
The three expanded component

TRUSS STRUCTURE CONTROL - INTERLOCKING CONTROL DESIGN

The component level control design using the Interlocking Control concept is carried out with a 4 × 4 identical control weighting matrix $R=.001\ I$ for all three components. The control designs for the left-most and right-most components are identical due to symmetry. Therefore, we only need to carry out a center component design and an end component control design.

The controlled components' poles, as well as the poles of the controlled truss structure, are plotted in the figure below. Since the left-most and right-most components are identical, we plot only the poles of one of them which are denoted by End Component Poles in these figures. All the poles of the controlled structure have negative real parts, indicating that the closed-loop system is asymptotically stable.

That the pole locations of the controlled components are close to that of the controlled coupled structure indicates that the component models developed for CCS are effective for this structural control design.

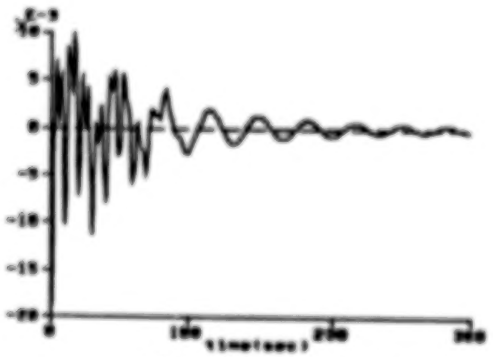


Closed up view of pole location near the imaginary axis of the controlled components and the controlled structure, open loop poles of the coupled structure are inserted for reference

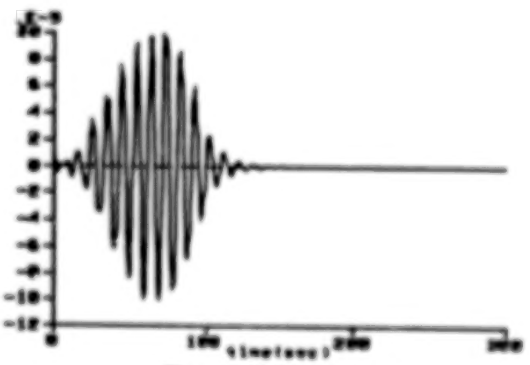
TRUSS STRUCTURE CONTROL - SIMULATION RESULTS

For transient response studies, the response of the controlled structure to three disturbance force pulses of 0.5 seconds is examined, simultaneously applied to the left-most nodes of the truss, as shown in the three expanded component figure. The coupled structure is assumed to be in static equilibrium initially in the simulation, of which samples of the sensor output time responses are shown in the top two figures below. Two of the twelve sensor channels, one horizontal (Channel 1 in the three expanded component figure) and one vertical nodal displacements (Channel 10), are selected. The magnitudes of the displacement response drop by an order of magnitude per component for nodes that are farther away from the disturbances. The delay effect of the force pulses on the displacements shown in the Channel 10 displacement figure below is typical for the right-most component.

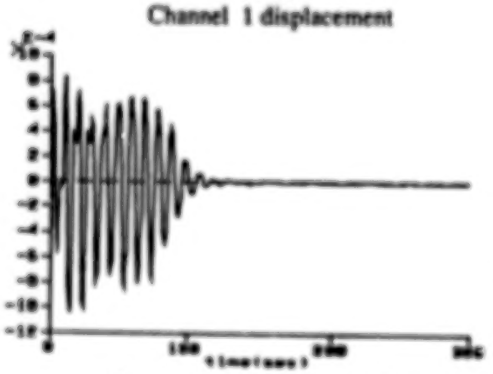
The developed CCS method inherits the capability to withstand system failures from decentralized control developed using the Subsystem Decomposition Approach. The controlled structure, in which the center component controller failed, is simulated for the same disturbances and initial conditions as before. The two bottom figures below show an order-of-magnitude performance degradations for one of the displacements (Channel 5) at the center component. However, despite the center component controller failure, the neighboring components stabilize the vibrations in the center component with interlocking controls.



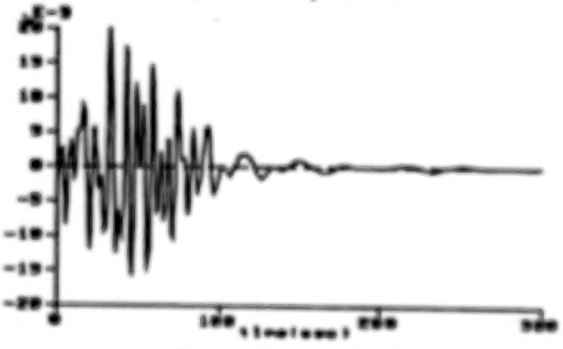
Channel 1 displacement



Channel 10 displacement



Channel 5 displacement, without failure



Channel 5 displacement,
with center component controller failure

BEST COPY AVAILABLE

REFERENCES

1. Siljak, D. D.(1978). *Large-Scale Dynamic Systems*, North-Holland.

BIBLIOGRAPHY

1. Young, K. D. (1983). An Application of Decomposition Techniques to Control of Large Structures. *Proceedings of the Fourth VPI &SU /AIAA Symposium on Dynamics and Control of Large Structures*, Blacksburg, VA, June 6-8, 1983, pp.201-214.
2. Ikeda M. and D. D. Siljak(1980). Overlapping Decompositions, Expansions, and Contractions of Dynamic Systems. *Large Scale Systems*, Vol. 1, pp. 29-38.
3. Ikeda M., D. D. Siljak, and D. E. White(1981). Decentralized Control with Overlapping Information Set. *J. Opt. Theory Appl.*, Vol. 34, pp. 279-310.

EFFECTIVE TECHNIQUES FOR THE IDENTIFICATION AND ACCOMMODATION OF DISTURBANCES

C. D. Johnson
Electrical and Computer Engineering Dept.
Univ. of Alabama in Huntsville
Huntsville, Alabama

Third NASA/DoD Technology Conference for
Controls–Structures Interaction
Jan. 29– Feb. 2, 1989
San Diego, CA

1. Introduction

The successful control of dynamic systems such as space stations, launch vehicles, etc. requires a controller design methodology that acknowledges and addresses the disruptive effects caused by external and internal disturbances that inevitably act on such systems. These disturbances, technically defined as "uncontrollable inputs," typically vary with time in an uncertain manner and usually cannot be directly measured in real time.

Traditionally, control designers have employed two basic techniques for coping with uncertain disturbances. If the disturbance essentially behaves as an unknown constant, the well–known technique of integral–control is quite effective. In those cases where the disturbance behaves like random, erratic noise (radio static, sensor noise, etc.) the technique known as stochastic (statistical) control is often used.

However, in many realistic cases of practical interest today, the significant disturbances are not as simple as "unknown constants" and not as erratic and capricious as "random noise". Moreover several such disturbances, with perhaps dissimilar characteristics, may enter the system at different locations, thus creating a situation of multi–input disturbances. The accurate positioning control of a space station in the face of uncertain crew motions, equipment movements, gravity gradient torques, structural deflections, etc. is an example of the kind of problem we have in mind.

In this paper we will first describe a relatively new non–statistical technique for modeling, and (on–line) identification, of those complex uncertain disturbances that are not as erratic and capricious as random noise. This technique applies to multi–input cases and to many of the practical disturbances associated with the control of space stations, launch vehicles, etc. Then, we describe a collection of new "smart controller" design techniques that allow controlled dynamic systems, with possible multi–input controls, to accommodate (cope with) such disturbances with extraordinary effectiveness. These new "smart controllers" are designed by non–statistical techniques and typically turn out to be unconventional forms of dynamic linear controllers (compensators) with constant coefficients. The simplicity and reliability of linear, constant coefficient controllers is well–known in the aerospace field.

This paper is written in a tutorial style. Derivations and other technical details of the material outlined here are contained in (refs. 1–34) listed at the end of the paper. To help the reader quickly access specific details of interest, an unusually large number of topical citations to those references are given throughout the text.

2. A Critique of Stochastic Control

The uncertain, time–varying nature of typical disturbances encountered by dynamic systems has led many control designers to conclude that such disturbances are best modeled as random processes and should be characterized by the statistics of their long–term average behavior such as: mean–value, variance, power spectral density, higher–order moments, etc. Using this approach, realistic disturbances are often treated as classical random "noise" (white or colored noise with known statistical properties) and designers then employ the mathematical theories of stochastic control to design controllers that yield good long–term "average" performance in the face of such imagined "noisy disturbances". If the actual disturbances really do behave like radio static, wide–band sensor noise, etc., such a controller is usually effective.

The potential trouble with this stochastic approach to disturbance modeling and control is twofold. First, the actual disturbances encountered by the system might not behave like erratic random noise. Second, knowledge of the long–term statistical averages of disturbance behavior, as expressed by mean, variance, etc., may have little, if any, relevance to the problem of making real–time control decisions for fast–acting, high–performance dynamic systems. Thus, a stochastic controller that is "optimal" in the long–term average sense might yield unsatisfactory performance in the face of realistic disturbances and dynamic systems with time–stressed performance requirements, eg. tight set–point or servo–tracking requirements with specified short

settling–times. This latter point is rather subtle and warrants further elaboration.

In order to obtain meaningful numerical values for the statistical mean, variance, etc., of an uncertain disturbance w it is necessary to observe and analyze the disturbance time–behavior w(t) over a sufficiently long window of time $t_o \leq t \leq T_s$ as shown in Figure 1. Otherwise, the computed "mean" $\bar{w}$ (for instance) will vary unpredictably with the length of the observation window and perhaps with the particular sample function w(t) being considered, thereby contradicting the concept of statistical mean. On the other hand, the performance time–window $t_o \leq t \leq T_p$, during which a controller must grapple with the disturbance and accomplish the specified control task, might be significantly shorter than the minimal window $t_o \leq t \leq T_s$ needed to evaluate the disturbance's statistics. In the latter event, knowledge of the disturbance's long–term average mean, variance, etc. would offer little, if any, help in making real–time control decisions; see Figure 1. To make matters even worse, some of the most elementary forms of practical disturbances w(t) (eg. random constant disturbances) do not satisfy the ergodic hypothesis; ie. the hypothesis that ensemble–averages equal time–averages for "almost all" sample functions. This hypothesis forms the foundation upon which most stochastic control principals are based.

3. Essential Disturbance Information for Real–Time Control Decisions

According to the preceding arguments, information about long–term statistical averages of disturbance behavior is of little help in making real–time control decisions over short performance windows. Thus, it is natural to ask: what disturbance information is essential for making "good" control decisions in such cases? The answer is best stated in terms of two subcases.

3.1 The Idealistic Case

It can be shown that in the idealistic case, where the unknown disturbance w(t) is nevertheless a theoretically "completely determined function" over the performance window $t_o \leq t \leq T_p$, the optimum real–time control decision at each $t_o \leq t \leq T_p$ requires complete knowledge of the future disturbance behavior (function) $w(t_f)$ over the remaining performance window $t \leq t_f \leq T_p$. This kind of information is not available in most practical applications. However, the result has certain theoretical importance. A special case of the result was established by Kalman (ref. 14) for linear–quadratic optimal control problems and was extended to a general class of plants and performance criteria in (ref. 5).

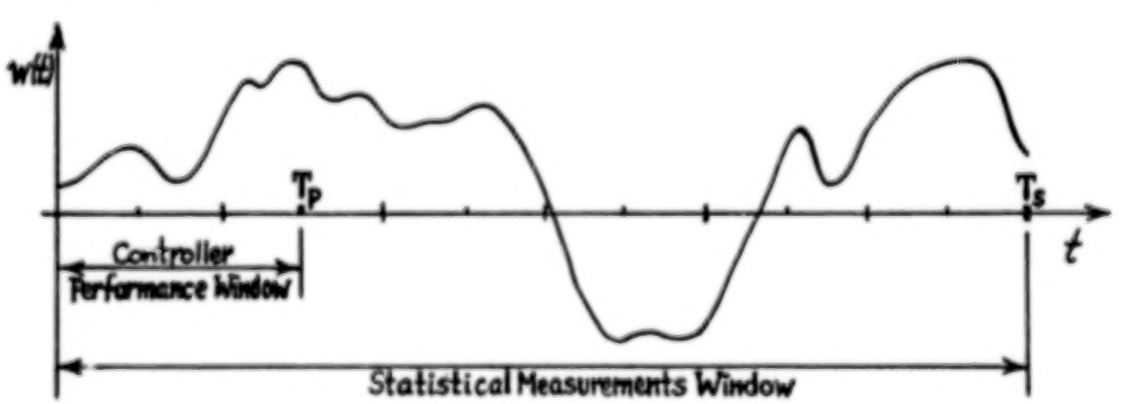


Fig. 1 – Comparison of Time Windows for Statistical Measurements and Controller Performance.

BEST COPY AVAILABLE

3.2 The Practical Case

In most practical cases the unknown disturbance w(t) is not a theoretically "completely determined function" over $t_o \le t \le T_p$ but rather is "determined" only over sequential subsets (cells) $t_i \le t \le t_{i+1}$ which partition the performance interval $t_o \le t \le T_p$ as shown in Figure 2. At the boundaries t_i, t_{i+1} of each cell abrupt indeterminable (a priori) random–like jumps occur in the value of w(t) and/or one or more of its time derivatives. Since these indeterminable jumps occur only at the cell boundaries t_i,t_{i+1}, the unknown function w(t) is said to be theoretically "determined" within the interior $t_i < t < t_{i+1}$ of each cell. In such cases the conditionally optimum real–time control decision for each cell–interior time $t_i < t_{real} < t_{i+1}$ requires complete knowledge of future $w(t_f)$ behavior over the remaining cell length $t_{real} \le t_f < t_{i+1}$; see Figure 2. Here, the term "conditionally optimum" reflects the fact that behavior of the disturbance function w(t) is mathematically indeterminable (a priori) beyond the current (real–time) cell $t_i < t < t_{i+1}$, and therefore in making real–time control decisions within a cell it is desirable but theoretically impossible to account rationally for future disturbance behavior beyond that current cell. This fundamental theoretical handicap to the optimal control decision process is inescapable and cannot be mitigated by any rational procedure. On the other hand, if within a current cell one is willing to gamble on the likely behavior of the indeterminable function w(t) over future cells, it is possible that "luck of the draw" or a "fortuitous guess" can sometimes result in a control decision, for a particular moment of time, that turns out (in retrospect) to be "better" than the rational, conditionally optimum decision described above. This gambling in function spaces is exciting entertainment but is not recommended as a means for improving conditionally optimum control decisions for space stations, launch vehicles, etc.

It would appear that "conditionally optimum" control decisions are themselves physically unrealizable, in general, since they require knowledge of "local" future behavior $w(t_f)$, $t_{real} \le t_f < t_{i+1}$ within each cell, as shown in Figure 2. In the remaining sections of this paper we will describe a new approach to disturbance modeling and estimation that makes it possible to (easily) implement "conditionally optimum" control decisions in practical applications.

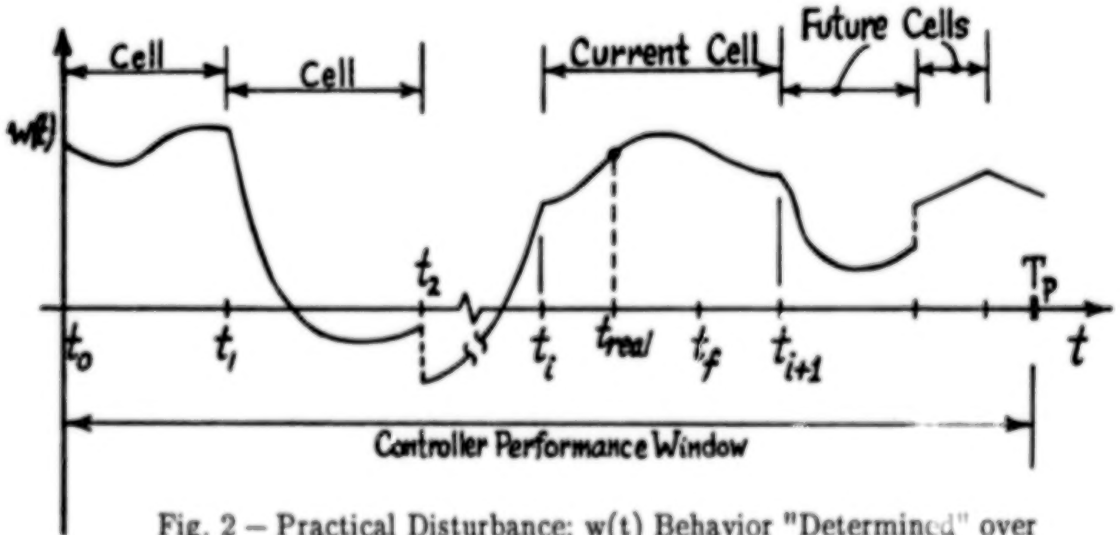


Fig. 2 – Practical Disturbance; w(t) Behavior "Determined" over Sequential Time–Cells, $t_i < t < t_{i+1}$.

BEST COPY AVAILABLE

3.3 The Limiting Case of Random Noise

In the limiting case where the cell–lengths $\ell_i = t_{i+1} - t_i$ all approach zero, the disturbance function w(t) becomes indeterminable for all $t_o \le t \le T_p$ and thus w(t) reduces to a classical "random noise" process. In that event it becomes theoretically impossible to account for the local, real–time behavior of the disturbance w(t) in making real–time control decisions. Consequently for such cases the only determinable information about w(t) is that embodied in the long–term average statistics (mean, variance, etc.) of w(t), as measured a priori. The conventional theory of stochastic control uses those long–term statistical averages of w(t) to arrive at (long–term) optimum control decisions for such limiting cases.

4. The Idea of Waveform Structure and State Models for Uncertain Disturbances

In the remainder of this paper, we will focus attention on the "practical case" of disturbances as described in Section 3.2. In that case we will say the unknown disturbance w(t) has (linear) waveform structure if, over each cell, the function w(t), $t_i < t < t_{i+1}$, can be mathematically modeled by an expression of the form

$$w(t) = c_1 f_1(t) + c_2 f_2(t) + \cdots + c_M f_M(t), \qquad t_i < t < t_{i+1} \tag{1}$$

where the weighting coefficients $\{c_1, c_2, \cdots, c_M\}$ are unknown "constants" that may jump in value at the cell boundaries, and the functions $\{f_1(t), f_2(t), \cdots, f_M(t)\}$ are completely known a priori. The representation (1) is a generalized spline–function model, hereafter called "waveform model," and the $f_k(t)$ are referred to as the basis functions for that spline model.

In practice, one selects the $f_k(t)$ in (1) to closely match the natural waveform modes (waveform patterns) actually observed in representative samples of w(t). For example, if w(t) is observed to be periodic in nature, one would choose the $f_k(t)$ to be the natural harmonic components ($\sin\omega_k t$, $\cos\omega_k t$), k = 1,2,···, of w(t), just as in a Fourier series. In other cases, the natural choices for the $f_k(t)$ might be one or more elements from the set $\{1, t, t^2, \cdots, t^N e^{\alpha t}, te^{\alpha t}, e^{\alpha t}\sin\omega t$, etc.$\}$. In some cases the natural basis functions for w(t) are not clearly defined by the available data. For such cases it is usually effective to use a "polynomial spline" waveform–model of the form

$$w(t) = c_1 + c_2 t + c_3 t^2 + \cdots + c_M t^{M-1}, \quad M = 1,2,\cdots. \tag{2}$$

Practical experience with (2) has shown that M–values in the range $1 \le M \le 4$ are adequate for most disturbances encountered in applications. In the case of multi–variable disturbances a separate descriptor (1), (2) is used for each independent $w_i(t)$.

The idea of modeling unknown disturbances w(t) by spline–type waveform–models (1),(2) was developed in a series of papers published in the period 1968–71, (refs. 1,2,3,4,5). That idea now forms the foundation for a new branch of control theory called Disturbance–Accommodating Control (DAC), (refs. 6,7,8,9,10), which we will discuss in the next section. It should be emphasized that in DAC theory the values of the arbitrary weighting coefficients c_i in (1),(2) are assumed piecewise–constant, with "once–in–a–while" jumps, but otherwise completely unknown. No statistical properties or probabilistic structures are assumed about the time behavior of the c_i. Thus, for instance, the traditional statistical properties of uncertainty such as mean, covariance and power–spectral density of w(t) are assumed completely unknown in (1),(2) and, in fact, are of no

concern in DAC theory. This means that assumptions about the disturbance's ergodic behavior, stationary statistics, etc. are not required in DAC designs using the disturbance models (1),(2).

When an uncertain disturbance has waveform structure, the use of waveform models (1),(2) and DAC design techniques allows the controller to make more effective real–time control decisions than are possible using long–term mean, covariance, etc. statistical properties of w(t).

4.1 State Models of Disturbances with Waveform Structure

The waveform model (1) is the key idea behind our approach to disturbance modeling. However, the "information" reflected in the model (1) must be encoded into an alternative format before it can be used effectively in identification and control design recipes. That alternative format is called a "disturbance state–model" in DAC theory and consists of a differential equation for which (1), with the c_i viewed as constants, is the general solution. In other words, one must solve the following inverse–problem in differential equations: Given the general solution (1), with arbitrary constants c_i, find the (a) differential equation. There are many interesting ramifications to this latter problem (ref. 6; pg. 402,417). However, in practical applications of DAC theory, the basis functions $f_i(t)$ are almost always such that this step leads to a linear differential equation. Consequently, one obtains a state–model of (1) in the form (a.e. means "almost everywhere");

$$\frac{d^{\rho}w}{dt^{\rho}} + \beta_{\rho}(t)\frac{d^{\rho-1}w}{dt^{\rho-1}} + \cdots + \beta_2(t)\frac{dw}{dt} + \beta_1(t)\, w = 0, \qquad \text{a.e.} \tag{3}$$

where the coefficients $\beta_1(t),\cdots,\beta_{\rho}(t)$ in (3) are completely determined by the (known) basis functions $f_1(t),\cdots,f_M(t)$ in (1). That is, the $\beta_i(t)$ are not functions of the (unknown) weighting coefficients c_i in (1). In the case of a multi–variable (vector) disturbance $w(t) = (w_1(t),\cdots,w_p(t))$, a differential equation similar to (3) would be obtained for each independent disturbance component $w_i(t)$. In the latter case, the differential equation for $w_i(t)$ may contain coupling–terms involving the other $w_j(t)$ etc.

The final step in constructing a state–model for (1) is to write the differential equation(s) (3) in the form of a set of simultaneous first–order differential equations, (ref. 6, p. 405,406). The end result, in the general case of a vector disturbance $w = (w_1,\cdots,w_p)$, has the form:

$$w = H(t)z \qquad , \qquad z = (z_1,\cdots,z_{\rho}) \tag{4–a}$$

$$\dot{z} = D(t)z + \sigma(t) \tag{4–b}$$

where H(t), D(t) are completely known matrices and z(t) is a ρ–vector called the "state" of the disturbance w. The elements z_i of z embody the disturbance components $w_1,\cdots,w_p$ and certain of their higher–derivatives. The term $\sigma(t) = (\sigma_1(t),\cdots,\sigma_{\rho}(t))$ is a symbolic representation of a vector sequence of impulses with completely unknown "once–in–a–while" arrival times and completely unknown random–like intensities. Thus, the basis–functions $f_i(t)$ in (1) appear in (4) as the principle mode solutions of the homogeneous disturbance state equation $\dot{z} = D(t)z$ in (4–b). As shown in (refs. 11,6,8,12,17) the disturbance state–model (4) can be generalized to include terms involving the plant state x, the plant control u and conventional noise inputs.

The completely unknown impulses of $\sigma(t)$ in (4) represent the source of the uncertain, once–in–a–while jumps in the values of the piecewise–constant weighting coefficients c_i in (1). In DAC theory it is assumed that adjacent impulses in $\sigma(t)$ are separated by a finite time–spacing (cell–length in Figure 2) not less than μ, where μ is the controller's closed–loop settling–time; i.e.

$\sigma(t)$ consists of a sparsely populated sequence of unknown impulses. If the impulses of $\sigma(t)$ arrive "too fast", the c_i in (1) will jump in value too often and the DAC controller will then be unable to respond properly. In that case we say the disturbance w(t) looses its waveform structure and becomes "noise"; see Section 3.3. In particular, if the impulses arrive arbitrarily close (and are totally uncorrelated) the $\sigma(t)$ sequence then behaves like a vector "while–noise" process (Bode–Shannon realization) and our disturbance state–model (4) then appears similar to the white–noise coloring filters traditionally used in stochastic control. However, note the subtle differences. Namely, in DAC theory the matrices H(t), D(t) in (4) are determined by the disturbance's natural waveform patterns rather than by long–term statistical means, variances, etc. Moreover, the homogeneous part of the DAC disturbance model (4) is not required to satisfy stability conditions. In fact, even though w(t) itself is usually bounded and well–behaved, it is common in DAC applications to find that many of the natural principle mode solutions $f_i(t)$ of the disturbance equation $\dot{z} = D(t)z$ are unstable, (i.e. grow with time in an unbounded fashion). For example, a uniformly bounded, well–behaved disturbance w(t) can have the natural waveform–model $w(t) = c_1e^t + c_2te^{-10t} + c_3t^2$, where the "constants" c_i jump in a strategically correlated manner determined by the physical process that produces w(t). Such behavior of (4) is not permitted of the coloring filters in conventional stochastic control theories. This constitutes a unique and practically important feature of our disturbance modeling technique (1),(3),(4).

5. Real–Time Identification of the State z(t) of a Waveform–Structured Disturbance

As we stated in the Introduction, disturbances w(t) associated with dynamic system control problems usually cannot be directly measured in real–time. It should be mentioned in passing, however, that some noteworthy exceptions to this truism are found in the field of chemical process control. In any event, control engineers have traditionally argued that if the uncertain disturbances w(t) could somehow be directly measured in real–time the system performance could be easily managed by feeding–forward the disturbance measurements to strategic points in the system. This concept seems plausible, but turns–out to be flawed when examined from the scientific viewpoint. Namely, if the uncertain disturbance w(t) has at least some waveform structure (as virtually all realistic disturbances do) then it is not just the real–time value of w(t), but rather the real–time value of the state z(t) of w(t), that is important to the real–time control decision process. This important fact is established in (ref. 5) and can be summarized as the following principle.

The Principle of Optimal Disturbance Accommodation

Suppose a controlled dynamical system is acted upon by uncertain disturbances w(t) that are known to have waveform structure in the sense of (1). Then, for a broad class of performance criteria the corresponding optimal real–time choice for the control $u^o(\cdot)$, at time t, can be expressed in terms of the current plant state x(t) and the current disturbance state z(t); i.e. $u^o(t)$ has the generic "control law" format

$$u^o(t) = \phi(x(t), z(t), t) \quad . \tag{5}$$

Remarks

This principle implies that at each t the current disturbance state z(t) embodies enough information about w(t) to allow a rational scientific choice for the real–time control u(t) --- even though the actual future behavior of w(t) is uncertain (in fact, indeterminable!) beyond the "current" cell in Figure 2.. This result enables the control designer to derive a DAC deterministic control policy (5) for accommodating the presence of uncertain disturbances. Because that control policy is based on the real–time dynamic behavior of z(t) in (4), [not the forecasted long–term mean, variance, etc. of w(t)] it can achieve the conditionally optimum control decisions described

in Section 3.2. In particular the DAC controller automatically adapts control actions to the actual real–time waveform patterns of the disturbance function w(t) as those patterns evolve with time over each cell. In control problems involving set–point or servo "commands," the generic controller (5) will also be a function of the current "state" c(t) of the command signal; see eq. (29) in the next section and also (refs. 4,22).

If, in fact, the disturbance w(t) can be directly measured, this principle shows that one should not "feedforward" only w(t) but rather should feedforward the "state" z(t) of w(t), as obtained from a real–time z(t) estimator described in the next section; see also (ref. 6, p. 431 and 434).

5.1 The Use of Composite Observers to Generate Real–Time Estimates $\hat{x}(t)$, $\hat{z}(t)$

Generally speaking, it is not possible to directly measure x(t) and/or z(t) in practical applications. Therefore, the practical implementation of DAC control laws of the form (5) is accomplished by using a special form of on–line, real–time observer (or Kalman filter) to generate real–time estimates of both the plant state x(t) and disturbance state z(t). That observer, called a composite–state observer, processes the control input measurements u(t) and plant output measurements y(t) to simultaneously generate reliable estimates $\hat{x}(t)$, $\hat{z}(t)$ of the current plant and disturbance states. Those estimates are then used in place of x, z, in (5). The theory and explicit design recipes for DAC composite observers is covered in refs. (6,11,12) for the continuous–time (analog) control case and in (refs. 7,8,13) for the discrete–time (digital) control case; see also (refs. 4,10). These DAC composite observers are typically linear in structure and enjoy all the features one usually associates with conventional state observers and Kalman filters; a DAC composite observer based on Kalman filter ideas is used when some disturbances are truly "noisy" in nature, see (refs. 12,13).

5.2 Example of a Full–Order Composite State Observer for Linear Dynamical Systems

In this section, we will illustrate the DAC technique for real–time identification of the disturbance state z(t) for a waveform–structured disturbance w(t). In particular, we will consider the class of linear dynamical systems (plants)

$$\dot{x} = A(t)x + B(t)u + F(t)w \quad ; \qquad \begin{matrix} x = \text{n–vector plant state} \\ u = \text{r–vector control} \\ w = \text{p–vector disturbance} \end{matrix} \qquad (6\text{–a})$$

$$y = C(t)x \qquad y = \text{m–vector plant output} \qquad (6\text{–b})$$

where each element of the vector uncertain disturbance $w = (w_1, w_2, \cdots w_p)$ is assumed to be independent and have waveform structure in the sense of (1). It is further assumed that the set of natural basis functions $\{f_i(t)\}$ in (1) is such that the associated disturbance state–model has the linear form (4). In that case the composite, time–varying dynamic model of the plant and disturbance states is found by consolidating (4), (6) to obtain

$$\begin{bmatrix} \dot{x} \\ \dot{z} \end{bmatrix} = \left[\begin{array}{c|c} A & FH \\ \hline O & D \end{array}\right] \begin{bmatrix} x \\ z \end{bmatrix} + \begin{bmatrix} B \\ O \end{bmatrix} u + \begin{bmatrix} O \\ \sigma \end{bmatrix} \qquad (7\text{–a})$$

$$y = [C \,|\, O] \begin{bmatrix} x \\ z \end{bmatrix} \qquad (7\text{–b})$$

All matrices shown in (7) are allowed to vary with time in a known manner; see (ref. 10) for the case of uncertain matrices.

Setting $\bar{x} = \begin{bmatrix} x \\ z \end{bmatrix}$ we can write (7) in the compact form

$$\dot{\bar{x}} = \bar{A}(t)\bar{x} + \bar{B}(t)u + \bar{\sigma} \tag{8-a}$$

$$y = \bar{C}(t)\bar{x} \tag{8-b}$$

where the meanings of $(\bar{A},\bar{B},\bar{C},\bar{\sigma})$ are evident from (7). The DAC composite state $\bar{x}$ in (8) is sometimes called the system "metastate".

The composite system (7) is clearly uncontrollable, since $\dot{z}$ does not depend on either x or u. However, this conclusion is not necessarily true for the generalizations of (4) considered in (ref. 5; ref. 6, p. 416; ref. 11, p. 826; ref. 17, eq. (14)). On the other hand, it is common to find that the composite system (7) is completely observable. That is, the pair $(\bar{A},\bar{C})$ in (7), (8) satisfies the Kalman criterion for complete observability (ref. 14). In the time–invariant case $(\bar{A},\bar{C})$ = constant, this implies that, in principle, one can always generate reliable, real–time estimates $\hat{x}(t)$, $\hat{z}(t)$, between arrivals of the "sparse" impulses of $\sigma(t)$, using a conventional full–order state observer for (7), (8). If $(\bar{A},\bar{C})$ are not constant this latter feat is still possible (between $\sigma(t)$ impulses) provided the pair $(\bar{A},\bar{C})$ satisfies a stronger observability condition known as "uniform complete observability," on every positive sub–interval of time between impulses of $\sigma(t)$; see (refs. 14; 4, p. 223). Thus, assuming the appropriate observability condition is satisfied one can generate the real–time estimates $\hat{x}(t)$, $\hat{z}(t)$ by employing a conventional full–order observer for (7), (8). That observer, called a "composite–state" or "metastate" observer in DAC theory, is given by (ref. 5, p. 222)

$$\begin{bmatrix} \dot{\hat{x}} \\ \dot{\hat{z}} \end{bmatrix} = \left[\begin{array}{c|c} A & FH \\ \hline O & D \end{array}\right] \begin{bmatrix} \hat{x} \\ \hat{z} \end{bmatrix} + \begin{bmatrix} B \\ O \end{bmatrix} u - \begin{bmatrix} K_{01} \\ K_{02} \end{bmatrix} (y - C\hat{x}) \tag{9}$$

where (K_{01},K_{02}) are observer gain matrices to be designed. The dynamics of the estimation error $\varepsilon = \begin{bmatrix} x \\ z \end{bmatrix} - \begin{bmatrix} \hat{x} \\ \hat{z} \end{bmatrix}$ associated with (7), (8), (9) is easily shown to be (between impulses of $\sigma(t)$)

$$\dot{\varepsilon} = [\bar{A}(t) + \bar{K}_O(t)\bar{C}(t)]\varepsilon \quad ; \quad \bar{K}_O = \begin{bmatrix} K_{01} \\ K_{02} \end{bmatrix} \tag{10}$$

and thus $\bar{K}_O(t)$ should be designed to make $\varepsilon(t) \to o$ rapidly, between impulses of $\sigma(t)$. Effective recipes for designing such $\bar{K}_O(t)$ are described in (refs. 4,5,6), provided one corrects a recurring sign error therein, as explained in (ref. 15).

In summary, under the assumptions stated the linear dynamical data–processing algorithm (observer) (9) will process the real–time measurements of {u(t),y(t)} to generate reliable, real–time estimates $\hat{x}(t)$, $\hat{z}(t)$ of the plant and disturbance states (between impulses of $\sigma(t)$. Those state estimates can then be used in an appropriate DAC "control law" (5) to achieve optimal accommodation of real–time uncertain disturbances w(t). A diagram of the disturbed plant (6), (4) with generic DAC controller (5), (9) installed is shown in Fig. 3. Note that the DAC controller contains an "internal copy" of the external disturbance process (4). This feature is characteristic of all DAC controllers and was first discussed in a 1970 paper (ref. 2; Fig. 2 and pp. 225, 226); see also (ref. 5; Fig. 2 and p. 229), (ref. 22; Fig. 5). As pointed out in (ref. 5, p. 222), the estimator (9) is valid for arbitrary control inputs u(t). Thus, (9) accurately estimates x(t), z(t) even if $u(t) \equiv 0$, and even if (5) is an arbitrary form of nonlinear control law.

A discrete–time (difference–equation) version of (9) is described in (refs. 7,8,13) for use in digital computer implementations. Also, a reduced–order version of (9) is described in (refs.

4,6,11). The modification of (9) to account for state–dependent disturbances and/or the direct measurement of some of the disturbance components w_i is presented in (ref. 6; p. 431 and 434); see also (ref. 8) for the discrete–time counterparts.

5.3 Real–Time Identification of "Plant Parameter Perturbation" Disturbances Using the DAC Method: A New Approach to Adaptive Control

The waveform–model idea (1), (4) can also be applied to the problem of identifying (and compensating for) internal disturbances in the form of uncertain perturbations in plant parameters. In practice these uncertain parameter perturbations can result from: parameter modeling errors, effects of neglected non–linear terms, reduced–order models, and actual real–time changes in plant parameters caused by operating environment and aging effects. For instance, in the case of a linear dynamical system (6) it may happen that one or more of the coefficients a_{ij} of the matrix A(t) are subject to uncertain perturbations δa_{ij} away from their known nominal values a_{iN}. Thus, A(t) in (6) can be written as

$$A(t) = A_N(t) + [\delta A(t)] \quad ; \quad A_N = \text{known nominal value.} \tag{11}$$

In this case, (6–a) can be written

$$\dot{x} = A_N(t)x + B(t)u + [\delta A(t)]x + F(t)w \tag{12}$$

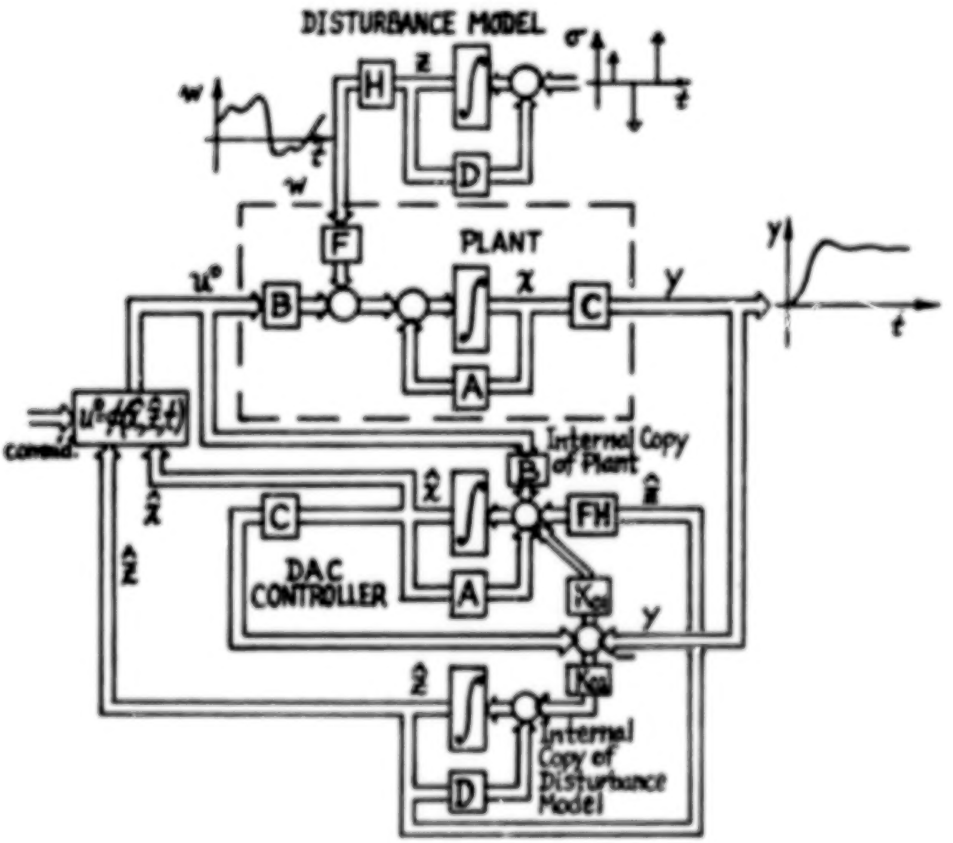


Fig. 3 – General Block-Diagram of Plant and Disturbance (6),(4) with DAC Controller (5),(9) Installed.

BEST COPY AVAILABLE

It is now clear from (12) that the perturbation term

$$w_a(t) = [\delta A(t)]x(t) \tag{13}$$

acts on the plant as an uncertain "disturbance" just like the conventional disturbance term w(t). Moreover, the nature of the practical time–variations in $w_a(t)$ in (13) suggests that $w_a(t)$ should possess "waveform–structure" in the sense of (1).

Thus, it is plausible that the same DAC techniques (1),(4),(5),(9) used for w(t) can also be used to: (i) identify the "state" $z_a(t)$ of $w_a(t)$ in real–time, and, (ii) design a control law (5) to optimally compensate for $w_a(t)$ in real–time. This concept differs radically from conventional approaches to identification and compensation of parameter perturbations. In particular, all conventional approaches first estimate the n^2 elements of [δA], using elaborate nonlinear estimation schemes, and then <u>compose</u> the estimate $\hat{w}_a(t)$ of (13) by setting

$$\hat{w}_a(t) = \widehat{[\delta A]}\hat{x} \,. \tag{14}$$

Our unorthodox approach recognizes that the real "disturbance" in (12) is <u>not</u> [δA] but rather the n–vector (n elements) $w_a = [\delta A]x$. Thus, instead of generating the conventional "product of estimates" (14) we generate the "estimate of the product"

$$\hat{w}_a(t) = \widehat{[\delta A]x} \tag{15}$$

using a DAC state–model for w_a and a special composite observer to generate $\hat{z}_a(t)$. The virtue of (15) is that estimation of the product (15) is much easier and quicker than generating the product of estimates (14). In particular, (15) can be generated by an <u>all–linear</u>, constant coefficient estimation algorithm (observer).

In (ref. 6; pp. 413–415) the DAC approach (11)–(13), (15) to plant parameter "disturbances" was advocated using a polynomial–spline waveform model (2) for each element w_{ai} of the uncertain "disturbance" $w_a(t)$. The model (2) leads to a state–model (3) of the Mth–order integrator type

$$\frac{d^M w_{ai}}{dt^M} = 0 \quad , \quad \text{a.e.} \tag{16}$$

which results in a particularly simple model (4) and disturbance state observer (9); see (ref. 6; eq. (32)). The effectiveness of (16) in identifying $\hat{w}_a(t)$ is quite good --- provided $w_a(t)$ changes slowly. This limitation has now been largely removed by the recent discovery of a more efficient "natural" set of basis functions $\{f_i(t)\}$ for $w_a(t)$ in (13). In particular it has been shown in (refs. 10,16,17,18,19,20) that if x in (12) denotes the "error–state" (refs. 4, art. VI; 6, p. 450; 10, p. 31; 19, p. 2453), and [δA] ≈ constant, then during "ideal–model" response x(t)≈0 each independent element w_{ai} of the n–vector $w_a(t)$ in (13) is closely modeled by a "natural" state–model (3) having the special form [compare with (16)]

$$\frac{d^n w_{ai}}{dt^n} + \beta_n^* \frac{d^{n-1} w_{ai}}{dt^{n-1}} + \cdots + \beta_2^* \frac{dw_{ai}}{dt} + \beta_1^* w_{ai} = 0, \text{ a.e.} \tag{17}$$

where $\{\beta_1^*, \beta_2^*, \cdots, \beta_n^*\}$ are constant, known coefficients defined by

$$\det[\lambda I - A_M] = \lambda^n + \beta_n^* \lambda^{n-1} + \cdots + \beta_2^* \lambda + \beta_1^* = 0 \tag{18}$$

and A_M is the (presumed given, constant) matrix that specifies the desired (ideal–model) error–state response $x(t) \rightarrow 0$ via the expression

$$\dot{x}_{ideal} = A_M x_{ideal} \quad , \quad x = \text{"error–state"}. \tag{19}$$

In other words,the "natural" eigenvalues of (17) correspond to the desired closed–loop poles specified for the plant "error–dynamics" (19). This discovery allows the DAC approach (11)–(13), (15) to be successfully applied to cases in which $w_a(t)$ in (13) changes rapidly. Moreover, even though [δA] itself has been assumed = constant in the theoretical development of (17), it turns–out that significant time–variations in [δA(t)] can be accommodated provided that a polynomial–spline model (2) with M = 2,3 is added to the natural state–model (17), see (refs. 19, p. 2458 and Fig. 7; 10, Fig. 5).

6. A New Family of "Smart" Controllers for Real–Time Accommodation of Disturbances

The fundamental advantage of our waveform–modeling technique (1),(3),(4), compared to conventional long–term averaged statistical models of uncertain disturbances, is that the waveform–model allows one to estimate the actual real–time dynamic behavior (state) of each individual disturbance function w(t) as it evolves in real–time. In other words, to use a term from stochastic control, our waveform–modeling technique allows the DAC controller to recognize and deal–with the unique behavior of each individual disturbance "sample–function" (ref. 4, footnote 8). The conventional stochastic controller has no means of recognizing this actual real–time disturbance behavior and must instead rely on the disturbance's long–term statistical ensemble averages as measured by some earlier experiment. Since at any given moment the current disturbance behavior can differ greatly from the long–term statistical averages measured earlier, it follows that real–time controller decisions based on current disturbance behavior will tend to be smarter and more effective than those based on long–term statistical averages. This advantage can be rather significant in those cases where the controller's performance window $t_o \leq t \leq T_p$ is relatively short compared to the window $t_o \leq t \leq T_s$ used to measure statistical averages of the disturbance. This consideration prompted the original idea for DAC theory (ref. 1, p. 417) and my own experience suggests that, in practice, those cases occur more frequently than (most) control designers and theoreticians realize.

The systematic design of "smart" (DAC) controllers in Figure 3 that can take advantage of real–time disturbance "state" information z(t) is a rather lengthy topic that is covered, in detail, in (refs. 4,5,6,7,8,10,12,13,21). Here,we will only be able to outline the main ideas and final results. For this purpose, it is convenient to sub–divide the discussion into three parts, corresponding to the three fundamental strategies for "accommodating" disturbances.

6.1 Modes of Disturbance–Accommodation; Design Options Unique to DAC Theory

One of the most attractive features of DAC theory is the unique flexibility it offers the control designer in selecting strategies for coping with multi–variable uncertain disturbances. In fact, prior to the introduction of DAC theory control designers used essentially only one strategy (= cancellation) in regard to accommodating disturbances. In DAC theory there are basically three strategies one can choose from, each having several possible variations. Those basic strategies of accommodation can best be illustrated in terms of the well–known multi–variable linear plant model (6) which is repeated here for convenience

$$\dot{x} = A(t)x + B(t)u + F(t)w(t) \; ; \qquad u = (u_1,\cdots,u_r) \qquad w = (w_1,\cdots,w_p) \tag{20–a}$$

$$y = C(t)x \qquad y = (y_1,\cdots,y_m) \tag{20–b}$$

For simplicity, we will assume A, B, F, C are all constant; see (ref. 6) for a treatment of the time–varying case and further generalizations of (20).

The Disturbance Cancellation Mode of Accommodation

The strategy of disturbance–cancellation, sometimes called disturbance–absorption or rejection, consists of designing the control u(t) to completely cancel–out the effects of the disturbance w(t) on the plant behavior. This strategy is prompted by the common attitude that disturbances cause only unwanted disruptions or perturbations in the plant behavior. In terms of the specific plant (20), and disturbance model (4) the disturbance–cancellation design procedure goes like this. First, one agrees to split (allocate) the total control action u(t) into two parts

$$u = u_p + u_d \tag{21}$$

where u_d is responsible for the disturbance–cancellation task and u_p is responsible for accomplishing the primary control task such as stabilization, set–point regulation, servo–tracking, etc. Substituting (21) into (20) yields

$$\dot{x} = Ax + Bu_p + Bu_d + Fw(t); \quad y = Cx \tag{22}$$

In terms of (22) and (4), the task of u_d is to achieve and maintain the condition of complete cancellation:

$$Bu_d(t) = -Fw(t) = -FHz(t), \quad z\varepsilon E^{\rho}, \ t_o \le t \le T . \tag{23}$$

The n.a.s.c. for satisfaction of (23), by some u_d, is

$$\text{rank}[B\,|\,FH] = \text{rank}\,[B] \tag{24}$$

which is called the "complete cancellation" condition of DAC theory. Condition (24) implies $FH = B\Gamma$ for some (possibly non–unique) matrix Γ, in which case the control u_d in (23) can be ideally chosen as

$$u_d(t) = -\Gamma z(t) \tag{25}$$

where for implementation purposes one would use an observer–produced estimate $\hat{z}(t)$ in place of z(t) in (25). Substitution of (25) into (22) yields

$$\dot{x} = Ax + Bu_p \tag{26}$$

so that one can now proceed to design u_p by conventional methods. It is remarked that the technique of splitting (allocating) the total control effort u into task–oriented parts, as illustrated in (21), is a simple but notably effective design idea that appears to be unique to DAC theory, as far as modern state–variable control theories are concerned.

Suppose the designer is concerned about cancelling only that subset of disturbance effects that appear in the plant output y(t) in (20). This is called "output disturbance–cancellation" and is achieved as follows. Let $u_p = Kx + \tilde{u}_p$ and $u_d = \Lambda z$, where K, Λ are to be designed and $\tilde{u}_p$ denotes terms of u_p which do not involve x (such as set–points, etc.). Then, the n.a.s.c. for complete cancellation of disturbances in the output y(t) is:

$$C[\hat{B}\,|\,\bar{A}\hat{B}\,|\,\bar{A}^2\hat{B}\,|\cdots|\,\bar{A}^{(n-1)}\hat{B}] = 0; \qquad \begin{aligned} \hat{B} &= B\Lambda + FH \\ \bar{A} &= A + BK \end{aligned} \tag{27}$$

Thus, one first designs K to satisfy the primary control task and then chooses Λ to satisfy the output

cancellation condition (27). Several such iterations on the design of K, Λ may be required since the solution Λ of (27) depends on K, while the effect of residual disturbances on the primary control task (and therefore on the choice of K) may depend on Λ. Further details are given in (refs. 6,22,23). The condition (27) implies that Λ should be chosen so that the "controllable subspace" of $(\bar{A},\hat{B})$ becomes totally unobservable. In DAC theory the latter subspace is called the "disturbable subspace" [24].

In addition to the "observer–based" disturbance cancellation theory just outlined, there are two other DAC theories for designing disturbance cancellation controllers. Those two alternative theories, known as the "Optimal Control Method" and the "Algebraic/Stabilization Method", are based on different concepts and employ different mathematical procedures. The details are outlined in (ref. 9) where the original references are also given.

The Disturbance–Minimization Mode of Accommodation

Suppose the complete cancellation condition rank [B|FH] = rank [B] fails to be satisfied. Then, there does not exist a control $u_d(t)$ that can satisfy (23). In that event, the designer can invoke the alternative strategy of disturbance–minimization control (DMC) in which the objective is to choose $u_d(t)$ so as to "minimize" the disturbance effects in (22) in some specified sense. There are literally hundreds of variations on this problem, depending on which disturbance effect(s) one chooses to minimize in (22). For example, one natural approximation to (23) is to choose u_d to minimize $\|Bu_d + FHz\|$. The minimum–norm control that solves this latter problem is $u_d^o = B^\dagger FHz$ where $(\cdot)^\dagger$ denotes the Moore–Penrose generalized inverse. Alternatively, one can choose u_d to cancel the effects of certain selected components of $w = (w_1,\cdots,w_p)$ or can choose u_d to cancel the total disturbance effect(s) as they appear on certain selected components of $x = (x_1,\cdots,x_n)$. The latter is called disturbance cancellation for "critical" state–variables, and represents a generalization of the "output cancellation" idea (27) where $y = Cx$ plays the role of a vector of critical variables. Finally, there is the innovative technique called "indirect disturbance cancellation" which can be explored as an option under the disturbance–minimization mode. In that option the control u_d itself doesn't directly counteract the disturbance but rather u_d maneuvers certain noncritical state–variables $x_j(t)$ into such a position that the $x_j(t)$ themselves perform the disturbance cancellation; see [6; pp. 465–468]. Further details of the disturbance–minimization mode may be found in (refs. 4,6,8).

The Disturbance–Utilization Mode of Accommodation

The most intriguing mode of disturbance–accommodation in DAC theory is called disturbance–utilization control (DUC) and is based on the recognition that disturbance effects might not be altogether detrimental to the primary control task(s). In other words, it is conceivable that if the disturbances are pushing in the right direction, at just the right time,they might usefully "assist" the control u in achieving the primary control task(s). If that were the case, it would be foolish and wasteful to apply a control strategy of cancelling or minimizing those "useful" disturbance effects. What one should do in that case is manipulate the control u(t) so as to exploit and take maximal advantage of all useful energy and other beneficial effects in the disturbances. Needless–to–say this latter feat requires extraordinary finesse in making real–time control decisions.

The systematic design of optimum disturbance–utilizing controllers is relatively straightforward using DAC theory. First, one constructs a state–model (4) of the disturbance

$w = (w_1, \cdots, w_p)$. Then, a performance index (functional) J must be chosen with the property that minimization of J with respect to u simultaneously achieves two things: 1) it achieves the primary control task(s), and 2) it makes maximum utilization of the disturbances w(t) to assist in achieving the primary control task(s). One possible candidate for J, which also happens to be computationally attractive, is the familiar error–quadratic performance index

$$J = \varepsilon^T(T_p)S\,\varepsilon(T_p) + \int_{t_o}^{T_p} [\varepsilon^T(t)Q(t)\varepsilon(t) + u^T(t)R(t)u(t)]dt \tag{28}$$

where $\varepsilon(t) = x^*(t) - x(t)$, [or $\varepsilon(t) = y^*(t) - y(t)$], *–denotes desired value, and where (typically) S,Q,R are symmetric, positive–definite weighting matrices chosen by the designer. It is remarked that a rationale and theory for admitting a range of <u>indefinite</u> and <u>negative–definite</u> Q in (28) has recently appeared in (refs. 25,26). The control penalty term u^TRu in (28) automatically encourages u(t) to "let w(t) do the driving" whenever that policy is cost–effective. If the disturbance <u>can</u> provide useful assistance to the control u(t) we say the disturbance has <u>positive</u> "utility". On the other hand if w(t) is only a hindrance to achieving the primary control task(s) we then say the disturbance has <u>negative</u> utility. It is possible to derive a "utility function" $\mathcal{U} = \mathcal{U}(x,z,t,.)$ which actually measures the sign and degree of optimum disturbance utility, (refs. 8,27). During the performance–interval, $t_o \le t \le T_p$, the disturbance utility function $\mathcal{U}$ may change sign back and forth, which is further evidence of the cunningness required in real–time control decisions in order to actually utilize disturbances to maximum advantage.

The DAC method of deriving the optimal disturbance–utilizing control $u^o(t)$ consists of appending (4) to (20), together with a dynamic model of the "commanded" (desired) behavior $x^*(t)$ or $y^*(t)$ of the form [compare with (4)]

$$y^* = y_c = Gc \quad ; \quad G,E = \text{known} \tag{29–a}$$

$$\dot{c} = Ec + \bar{\mu}(t) \ , \tag{29–b}$$

where $\bar{\mu}(t)$ = a sparse sequence of unknown impulses and c is the "state" of the command input $x^*(t)$ or $y^*(t)$. The idea of using a state model of the type (29) to represent uncertain set–points and servo–commands was proposed in (ref. 4, eqs. 40,41); see also (refs. 6,22). Next, one introduces the composite state vector $\tilde{x} = (x|c|z)$ so that $\varepsilon(t)$ in (28) can be expressed as $\varepsilon = [-C|G|0]x$. Then, (28) can be minimized subject to the composite dynamics of $\dot{\tilde{x}} = \tilde{A}\tilde{x} + \tilde{B}u$ by applying standard methods of Linear–Quadratic Optimal Control Theory (ref. 28). The details of this procedure are given in (refs. 4,5,6,8,27). The final form of the optimal disturbance–utilizing control u^o is

$$u^o = -R^{-1}B^T[K_1(t)x + K_2(t)c + K_3(t)z] \tag{30}$$

where the gain matrices $K_i(t)$ are independent of x, c, z, and are determined by off–line solution of an auxiliary system of unilaterally–coupled matrix differential equations with known boundary conditions at $t = T_p$; see (ref. 4; pg. 641; 6; pg. 470).

It is important to note that in designing the disturbance utilizing control u^o in (30) we <u>do not</u> split (allocate) the total control u into parts as was done in (21) for the cancellation and minimization modes of accommodation. Moreover, the disturbance–utilizing control policy (30) continues to yield optimum control decisions <u>even</u> <u>if</u> <u>the</u> <u>disturbances</u> <u>w(t)</u> <u>have</u> <u>no</u> <u>useful</u> <u>effect</u>

(i.e. have only negative utility). In the latter case, the control (30) automatically minimizes the inevitable performance losses (= increase in J) due to "non–useful" disturbances. Thus, the control law (30) is a universally attractive substitute for the traditional Linear–Quadratic Optimal Control Law

$$u_{LQ} = - R^{-1}B^{T}K(t)x, \tag{31}$$

as presented in control textbooks and currently widely used in industry. Such a substitution is easy to implement (graceful upgrading) because the gain matrix K(t) in (31) coincides exactly with the matrix $K_1(t)$ in (30); see (Refs. 4,6). Moreover, the more general "disturbance–utilizing control law" (30) automatically reduces to the traditional Linear–Quadratic control law (31) whenever the disturbance w(t) disappears, [i.e., whenever z(t) becomes zero, assuming c = 0 also]. Note that the term K_2c in (30) represents DAC " feedforward" control of the command state c in (29). The importance of feeding–forward the command state c(t), rather than just the servo–command $y^*(t)$, is underscored throughout DAC theory; see (ref. 22, Figs. 3,4,5) and also (refs. 4,6,29).

The use of a disturbance–utilizing control law can result in significant savings in the consumption of u(t) control energy, without jeopardizing the performance quality of the primary control task. In fact, performance quality may also be significantly improved (refs. 30,31). This capability represents an exciting new domain of control design options and is unique with DAC theory.

Multi–Mode Accommodation of Disturbances

The three primary modes of accommodation just outlined can be blended in various ways to obtain a multi–mode disturbance controller which, for instance, performs disturbance–utilization during the initial phase of the control period and performs disturbance cancellation during the final (terminal) phase of control. This further widens the range of controller design options that DAC provides for coping with disturbances.

7. Summary

The disturbance modeling, identification and accommodation techniques outlined in this paper, collectively known as DAC theory, have attractive performance and design features which make them viable candidates for consideration in stabilization, set–point regulation, servo–tracking and model–reference adaptive control design problems in which uncertain external and internal disturbances play an important role. As such, DAC theory represents an effective alternative to existing stochastic control and adaptive control theories for dynamical systems with uncertain parameters and persistently acting, uncertain external disturbances.

Of course, in real–life control engineering problems, the day–to–day disturbances that act on a controlled system always deviate, to some extent, from the idealistic disturbance model originally used in the controller design. Thus any approach to controller design for disturbances will, of necessity, be less–than–optimal with respect to the actual disturbances. Therefore, in view of this inherent uncertainty in developing disturbance models, it is our opinion that designers should not choose a priori between DAC, stochastic, or other design methods, but rather in each application they should design an assortment of candidate controllers using all reasonable design methods. Then, by exercising each of the candidate controllers against the same family of representative real–life disturbances and parameter perturbations (or simulations thereof) one can decide which candidate controller is "best" for that particular application. In this respect, DAC theory simply provides an additional candidate in the competition for "best".

8. Epilogue

The DAC waveform modeling technique (1)–(4), and disturbance control law design methodologies in Section 6, originated in a small NASA–funded study during the period 1966–67

(refs. 32,33) and has evolved over the past 21 years into an effective general theory for the control of systems with complex, uncertain multivariable disturbances. Some representative applications of that theory, and many additional references, are described in (ref. 9); see also (refs. 21,34). The DAC theory outlined here is now beginning to appear as a standard topic in control engineering texts and university courses. In a few cases, the nomenclature and lineage presented therein differs from that presented here and reflected in the original literature.

9. References Cited

1. C. D. Johnson, "Optimal Control of the Linear Regulator With Constant Disturbances," IEEE Trans. Auto. Cont., AC–13, No. 4, p. 416, 1968.
2. C. D. Johnson, "Further Study of the Linear Regulator With Disturbances; The Case of Vector Disturbances Satisfying a Linear Differential Equation," IEEE Trans. Auto. Cont., AC–15, No. 2, p. 222, 1970.
3. C. D. Johnson, "Comments on 'Optimal Control of the Linear Regulator With Constant Disturbances'", IEEE Trans. Auto. Cont., AC–15, No. 4, p. 516, 1970.
4. C. D. Johnson, "Accommodation of Disturbances in Linear Regulator and Servomechanism Problems," IEEE Trans. Auto. Cont., AC–16, No. 6, p. 635, 1971, (Special Issue on the Linear–Quadratic–Gaussian Problem).
5. C. D. Johnson, "Accommodation of Disturbances in Optimal Control Problems," Proc. 3rd Southeastern Symp. Sys. Theory, Atlanta, Ga., April 1971; see also Int. J. Cont., Vol. 15, No. 2, p. 209, 1972.
6. C. D. Johnson, "Theory of Disturbance–Accommodating Controllers," Chapt. in the book, Control and Dynamic Systems: Advances in Theory and Applications, Vol. 12, edited by C. T. Leondes, Academic Press, Inc., New York, 1976.
7. C. D. Johnson, "A Discrete–Time Version of Disturbance–Accommodating Control Theory with Application to the Digital Control of Missiles," AIAA Jour. of Guidance and Control, Vol. 4, No. 2, p. 116, Mar.–Apr., 1981.
8. C. D. Johnson, "A Discrete–Time, Disturbance–Accommodating Control Theory for Digital Control of Dynamical Systems," Chapt. in the book: Control and Dynamic Systems: Advances in Theory and Applications, Vol. 18, Academic Press, N.Y., 1982.
9. C. D. Johnson, "Disturbance–Accommodating Control; An Overview," Proc. 1986 Amer. Control Conf., Seattle, Wash., Vol. 1, pp. 526–536, June, 1986.
10. C. D. Johnson, "A New Approach to Adaptive Control," Chapt. in the book, Advances in Control and Dynamic Systems, Vol. 27, (Ed. by C. T. Leondes), Academic Press, 1988.
11. C. D. Johnson, "On Observers for Systems with Unknown Inaccessible Inputs," International Jour. of Control, Vol. 21, No. 5, pp. 825–831, 1975.
12. C. D. Johnson, "Disturbance–Utilizing Control for Noisy Measurements and Disturbances, Part I, The Continuous–Time Case," International Journal of Control, Vol. 39, No. 5, pp. 859–868, 1984.
13. C. D. Johnson, "Disturbance–Utilizing Control for Noisy Measurements and Disturbances,Part II, The Discrete–Time Case," International Journal of Control, Vol. 39, No. 5, pp. 869–877, 1984.
14. R. E. Kalman, "Contributions to the Theory of Optimal Control," Bol. Soc. Math. Mex., Vol. 5, pp. 102–119, 1960.
15. C. D. Johnson, "Correction to 'Accommodation of External Disturbances in Linear Regulator and Servomechanism Problems'", IEEE Trans. on Auto. Control, Vol. AC–18, No. 3, June, 1973.
16. C. D. Johnson, "Adaptive Controller Design Using Disturbance–Accommodation Techniques," Intern'l. Jour. of Control, Vol. 42, No. 1, p. 193, 1985.
17. C. D. Johnson, "Linear Adaptive Control; A New Result in Model–Error Compensation Design," Proc. of the First IFAC Workshop on Model–Error Concepts and Compensation (book), Boston, 1985; Publ. by Pergamon Press, Oxford, England, 1986.
18. C. D. Johnson, "Linear Adaptive Control via Disturbance–Accommodation; Same Case Studies," Proc. 1986 Amer. Control Conf., Seattle, Wash., Vol. 1, p. 542, 1986.

19. C. D. Johnson, "Applications of a New Approach to Adaptive Control," Proc. 1988 Amer. Control Conf., Vol. 3, p. 2452, Atlanta, Ga., June, 1988; to appear, Inter. Jour. of Adaptive Control and Signal Processing, 1989.
20. C. D. Johnson, "A Singular Condition in Linear Adaptive Control Theory," Inter. Jour. of Control, Vol. 48, No. 2, p. 817, 1988.
21. C. D. Johnson, "Control of Dynamical Systems in the Face of Uncertain Disturbances," Chapt. in the book Stochastic Problems in Mechanics, Univ. of Waterloo Press, SM Study No. 10, Waterloo, Ontario, Canada, June, 1974.
22. C. D. Johnson, "Algebraic Solution of the Servomechanism Problem With External Disturbances," ASME Trans. J. Dynamic Sys., Measurements and Cont., Series G., Vol. 96, No. 1, p. 25, 1974.
23. C. D. Johnson, "An Improved Computational Procedure for 'Algebraic Solution of the Servomechanism Problem with External Disturbances'", ASME Trans. J. Dynamic Sys., Measurements and Cont., Series G., Vol. 97, No. 2, p. 161, 1975.
24. C. D. Johnson, "Algebraic Solution of the Servomechanism Problem With External Disturbances," Proc. 1973 ASME Winter Ann. Meet., Detroit, Michigan, Paper No. 73–WA/Aut–7, Nov. 11–15, 1973.
25. C. D. Johnson, "Limits of Propriety for the Linear–Quadratic Regulator Problem," Inter. Jour. of Control, Vol. 45, No. 4, p. 1835, 1987; see also, ibid., Vol. 48, No. 2, p. 827; 1988.
26. C. D. Johnson, "The 'Unreachable Poles' Defect in LQR Theory; Analysis and Remedy", Inter. Jour. of Control, Vol. 47, No. 3, p. 697; 1988.
27. C. D. Johnson, "Utility of Disturbances in Disturbance–Accommodating Control Problems," Proc. 15th Annual Meeting, Society of Engineering Science, Session 4B, p. 347, Univ. of Fla.; Dec. 1978.
28. R. E. Skelton, Dynamic Systems Control (book) John Wiley, N.Y., 1988.
29. C. D. Johnson, "Discussion of the Paper 'Experimental Evaluation of Optimal Multivariable Regulatory Controllers with Model Following Capabilities,'" Jour. Automatica, Vol. 9, pp. 137–138, 1973.
30. W. C. Kelly, "Homing Missile Guidance with Disturbance–Utilizing Control, "Proceedings of the 12th Southeastern Symposium on System Theory, Virginia Beach, Va.; pp. 260–268, May 1980.
31. W. C. Kelly, "Optimal Utilization of Gravity in a Homing Missile Problem," Proceedings of the AMSAA 2nd Meeting of the Coordinating Group on Modern Control, Part I, Aberdeen Proving Ground, Md., p. 177, Dec. 1980.
32. C. D. Johnson, "Optimal Control of the Disturbed Linear Regulator," Chapt. 3 in Final Report, Contract NAS8–18008, Convair Div. of General Dynamics, Huntsville Operations, GDC Rpt. No. DDF67–003, 1967.
33. C. D. Johnson, "Disturbance–Accommodating Control: A History of Its Development," Proc. 15th Annual Meeting, Society of Engineering Science, Session 4B, p. 331; Univ. of Fla.; Dec. 1978.
34. "Special Issue on Disturbance–Accommodating Control Theory," Jour. of Interdisciplinary Modeling and Simulation, Vol. 3, No. 1, 1980.

Modeling and Control of Flexible Space Platforms with Articulated Payloads

Philip C. Graves
Vigyan Research Associates
Hampton, Va.

Suresh M. Joshi
NASA Langley Research Center
Hampton, Va.

Third Annual NASA/DoD CSI Conference
San Diego, Ca.
January 29 - February 2, 1989

Abstract

The first steps in developing a methodology for spacecraft control–structure interaction (CSI) optimization are identification and classification of anticipated missions, and the development of tractable mathematical models in each mission class. A mathematical model of a generic large flexible space platform (LFSP) with multiple, independently pointed rigid payloads (representative of "Class II" CSI missions) is considered. The objective here is not to develop a general purpose numerical simulation, but rather to develop an analytically tractable mathematical model of such composite systems. The equations of motion for a single payload case are derived, and are linearized about zero steady-state. The resulting model is then extended to include multiple rigid payloads, yielding the desired analytical form. The mathematical models developed clearly show the internal inertial/elastic couplings, and are therefore suitable for analytical and numerical studies. A simple decentralized control law is proposed for fine pointing the payloads and LFSP attitude control, and simulation results are presented for an example problem. The decentralized controller is shown to be adequate for the example problem chosen, but does not, in general, guarantee stability. A centralized dissipative controller is then proposed, requiring a symmetric form of the composite system equations. Such a controller guarantees robust closed-loop stability despite unmodeled elastic dynamics and parameter uncertainties.

Outline

- CSI Mission Classification
- Mathematical Model of LFSP/ Single Payload
- Extension to Multi-Payload Systems
- Decentralized Control Law
- Simulation Results for Space Station/Articulated Payloads
- Centralized Dissipative Controller
  - guarantees closed-loop stability
  - requires symmetric form of eqns. of motion
- Concluding Remarks

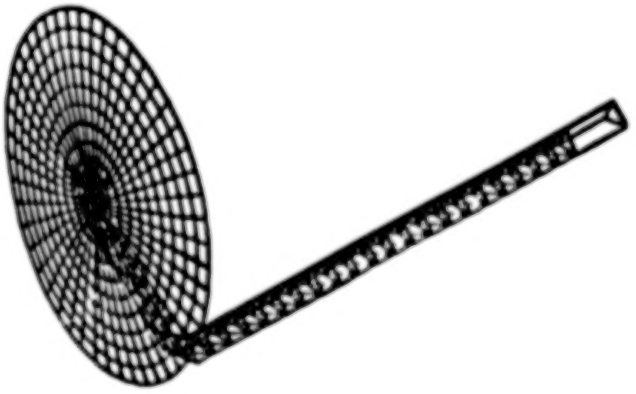
CSI Mission Classification

Anticipated missions involving control–structure interaction (CSI) can be broadly divided into four classes. Class I missions are those which require fine-pointing of the overall spacecraft as well as vibration suppression. There are no articulated substructures, and because of small elastic and rigid-body motion, the modeling and control problem is essentially linear. There may, however, be actuator and sensor nonlinearities. Examples of this mission class include large space antenna concepts such as the hoop-column and wrap-rib antennas. The controller must satisfy the performance specifications, which include fine-pointing (rigid plus flexible rotational motion), reflector surface distortion, and defocus errors caused by feed and base elastic motion. The control system must be capable of performing in the presence of significant elastic motion.

- **Class I :** Single-Body Flexible Spacecraft (Linear)
  - fine-pointing and vibration suppression
  - surface shape distortion and defocus errors



hoop-column antenna concept

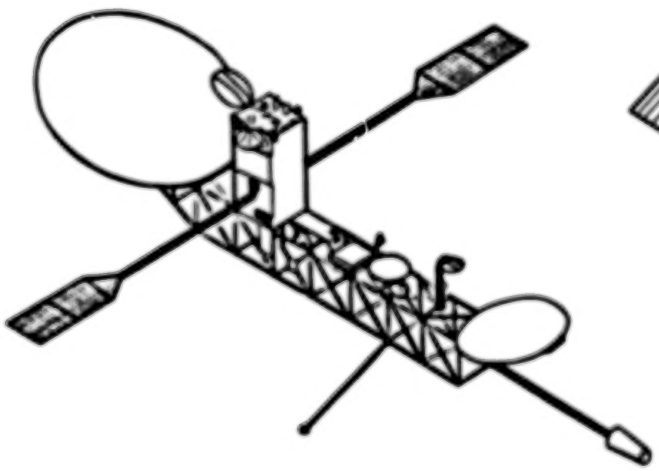


wrap-rib antenna concept

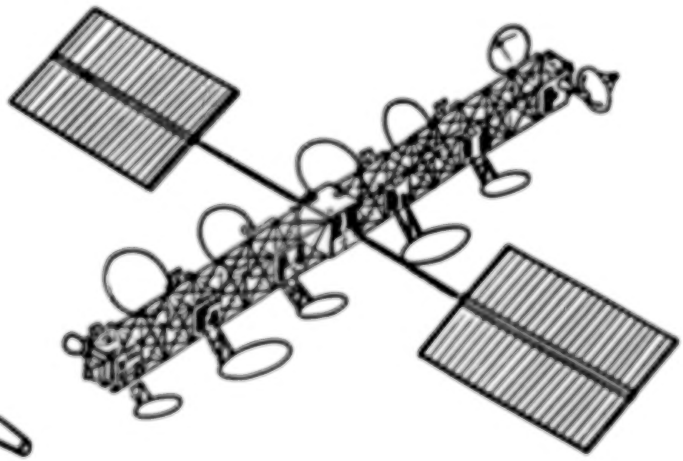
CSI Mission Classification (cont.)

Class II missions represent an extension of Class I missions with articulated payloads mounted on the flexible spacecraft. This important class of missions includes many types of low-earth and geosynchronous platforms. The composite system consists of a large flexible space platform (LFSP) to which a number of rigid or elastic appendages are mounted. The objectives of the controller are precision attitude control of the spacecraft, fine-pointing of each of its payloads, and vibration suppression. The problem is still linear, but the elastic and rigid-body motions between bodies are coupled.

- **Class II :** Flexible Spacecraft with Articulated Appendages (Linear)
  - includes rigid and elastic appendages (payloads)
  - fine-pointing of all rigid and elastic components
  - vibration suppression to improve payload performance



Earth Observation System (EOS)



geosynchronous platform

BEST COPY AVAILABLE

CSI Mission Classification (cont.)

Class III and IV missions are essentially the nonlinear counterparts to the Class I and II missions previously discussed. Class III missions will require large angle maneuvers of the entire structure (without articulated appendages) while simultaneously minimizing the effects of elastic motion induced by nonlinear internal couplings and external disturbances. Although this problem has been studied numerically for specific flexible spacecraft, generic models do not exist.

Class IV missions have the inherent difficulty of the nonlinear Class III problems, but include the additional complexity of the articulated appendages of their linear Class II counterparts. Such missions may require large-angle maneuvering of the flexible structure while simultaneously and independently pointing various payloads to their own respective targets in the presence of elastic motion. There is rigid/elastic coupling between all of the various components. Furthermore, payloads may be repositioned, or the spacecraft reconfigured by commanded motions of the various appendages. Examples of this mission class include LFSPs with articulated payloads and robotic arms allowing translational degrees of freedom.

The purpose of this paper is to develop a generic mathematical model and control laws for an LFSP with multiple articulated payloads representative of Class II missions suited to CSI optimization.

- **Class III :** Single-Body Flexible Spacecraft (Nonlinear)
  - Precision large angle maneuvers for retargeting or tracking
  - Vibration suppression during maneuvers
- **Class IV :** Flexible Spacecraft with Articulated Appendages (Nonlinear)
  - Large angle rotational motion of spacecraft and appendages
  - Robotic manipulators allowing spacecraft reconfiguration

BEST COPY AVAILABLE

Mathematical Model for LFSP/Single Payload

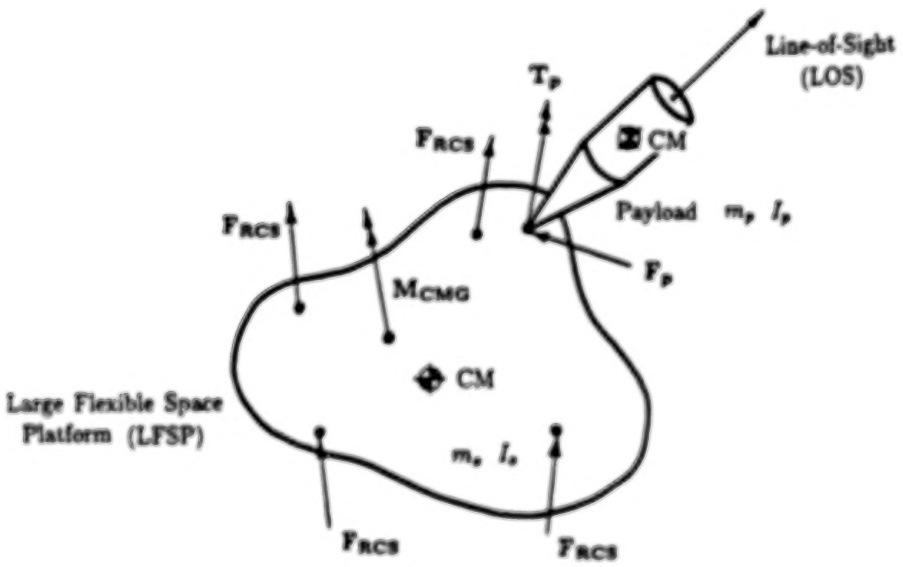
In developing the equations of motion, the single payload composite system will first be described in terms of its various coordinate systems, position vectors, etc. The equations of motion for each component comprising the composite system, including LFSP rigid and elastic motion as well as payload rigid-body motion, will then be presented. By removing the constraint force between the LFSP and payload, these equations will then be coupled, and presented in matrix form. This generic model will then be extended to the multi-payload case.

A large flexible central body with a single attached articulated rigid payload is considered first. The mass/inertia properties of both bodies are assumed known. The modal solution (frequencies and displacement vectors) for n modes of the flexible body (LFSP) is also assumed known. This modal solution is usually obtained using finite element codes such as NASTRAN or EAL, wherein the effects of the payloads are taken into account by representing them as point masses and inertias on the LFSP model. The present analysis requires the values of LFSP mode shapes and mode slopes at the points of application of forces and torques, respectively. Both are required at the payload attachment point. The attitude control system for the LFSP is assumed to utilize reaction control system (RCS) thrusters, and control moment gyro (CMG) torques. The payload pointing mechanism is idealized as a three-axis point torque acting at the attachment gimbal. The objective is to control the payload line-of-sight and LFSP attitude in the presence of elastic motion.

Overall Configuration

- LFSP with single rigid payload
- Control objectives:
  - attitude control of LFSP
  - fine-pointing of payload

- Data required for model
  - payload and LFSP masses and inertias
  - modal frequencies
  - mode shapes for forces (e.g.: RCS thrusters)
  - mode slopes for moments (e.g.: CMG moments)

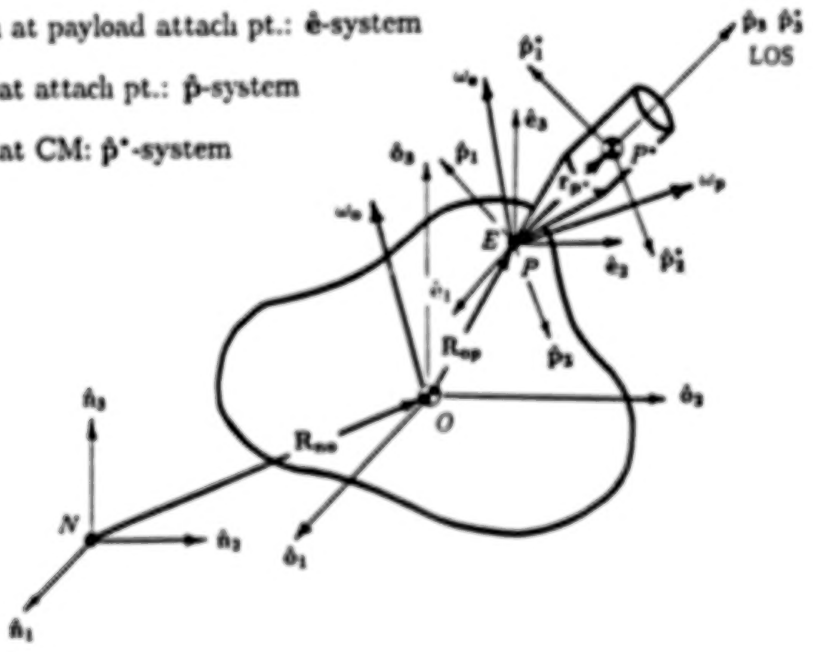


Coordinate Systems

The LFSP has two coordinate systems associated with it. One, designated the $\hat{\mathbf{o}}$-system, is fixed to the nominal center of mass (CM), and in conjunction with the nominally zero Euler angles (ϕ_o, θ_o, ψ_o), describes the rigid-body orientation. The other coordinate system, designated the $\hat{\mathbf{e}}$-system, is fixed to the payload attach point ("point P") on the LFSP, thus rotating and translating with the rigid and elastic LFSP motion at that point. This system is nominally parallel to the $\hat{\mathbf{o}}$-system axes. The orientation of the elastic axis system ($\hat{\mathbf{e}}$-system) with respect to the $\hat{\mathbf{o}}$-system axes is described by Euler angles (ϕ_e, θ_e, ψ_e) (i.e., the rotational elastic displacements), which are nominally zero. The origin of the LFSP $\hat{\mathbf{o}}$-system is located in the reference inertial coordinate system (denoted the $\hat{\mathbf{n}}$-system), by the position vector $\mathbf{R_{no}} = X\hat{\mathbf{n}}_1 + Y\hat{\mathbf{n}}_2 + Z\hat{\mathbf{n}}_3$. The payload attachment point P for the undeformed spacecraft is located from the LFSP CM, the $\hat{\mathbf{o}}$-system origin, by position vector $\mathbf{R_{op}} = x_p\hat{\mathbf{o}}_1 + y_p\hat{\mathbf{o}}_2 + z_p\hat{\mathbf{o}}_3$.

The rigid payload is described by a body-fixed $\hat{\mathbf{p}}$-system originating from the attachment point, but fixed to the payload. The $\hat{\mathbf{e}}$- and $\hat{\mathbf{p}}$-system origins are coincident. Orientation with respect to the elastic axes is described by Euler angles (ϕ_p, θ_p, ψ_p). These are the payload pointing mechanism "gimbal angles". The desired nominal orientation is defined by user-specified gimbal angles. Thus the angular orientation of the payload may be determined from the orientation of the $\hat{\mathbf{p}}$-system with respect to the $\hat{\mathbf{e}}$-system; the $\hat{\mathbf{e}}$-system with respect to the $\hat{\mathbf{o}}$-system (due to elastic deformation); and the orientation in inertial space of the $\hat{\mathbf{o}}$-system. Expressing a vector in terms of components in the various coordinate systems requires transformations using a 1-2-3 Euler sequence of rotations. The angular velocity vectors (body rates) of the various coordinate frames are ω_o, ω_e, and ω_p for the LFSP rigid frame, LFSP elastic frame, and the payload frame, respectively. The body rates must be transformed into Euler rates prior to linearization.

- inertial reference: $\hat{\mathbf{n}}$-system
- LFSP (rigid) body axes: $\hat{\mathbf{o}}$-system
- elastic system at payload attach pt.: $\hat{\mathbf{e}}$-system
- payload axes at attach pt.: $\hat{\mathbf{p}}$-system
- payload axes at CM: $\hat{\mathbf{p}}^*$-system



Nonlinear Model

The nonlinear equations of motion for the composite system are developed next. The bodies are each assumed to have constant mass and mass distribution, and to possess only rotational freedom with respect to each other. All terms in the equations represent inertial quantities which are to be expressed in the $\hat{\mathbf{o}}$-system, nominally parallel to the inertial frame. It should be noted that " $\frac{d}{dt}$ " denotes differentiation with respect to the inertial frame, and so angular velocity cross-products appear, whereas an overdot "$\dot{}$" indicates a local time derivative inside a particular frame. Appropriate coordinate transformations in terms of Euler angles, using a 1-2-3 sequence, are required.

First consider the LFSP equations of motion. Beginning with the translational equation of motion, writing Newton's law gives equation (1). Here m_o is the LFSP mass, $\mathbf{F_p}$ is the internal constraint (reaction) force exerted on the LFSP by the payload, and there are n_F external forces $\mathbf{F_{oi}}$ acting on the body (e.g., RCS thrusters).

Next the nonlinear rotational equation of motion of the LFSP is given by equation (2). $\mathbf{I_o}$ is the LFSP inertia matrix about the CM, $\mathbf{T_p}$ is the pointing system reaction torque, and there are n_M moments $\mathbf{M_{oi}}$ acting on the LFSP (e.g., CMG moments). The position vector $\mathbf{R_{op}} = x_p\hat{\mathbf{o}}_1 + y_p\hat{\mathbf{o}}_2 + z_p\hat{\mathbf{o}}_3$ locates the payload attachment point, and the position vector $\mathbf{r_{oi}} = x_{oi}\hat{\mathbf{o}}_1 + y_{oi}\hat{\mathbf{o}}_2 + z_{oi}\hat{\mathbf{o}}_3$ locates the i^{th} external force $\mathbf{F_{oi}}$ acting on the LFSP. Here the "prime" notation with $\mathbf{R'_{op}}$ and $\mathbf{r'_{oi}}$ indicates the (3×3) matrix cross-product form.

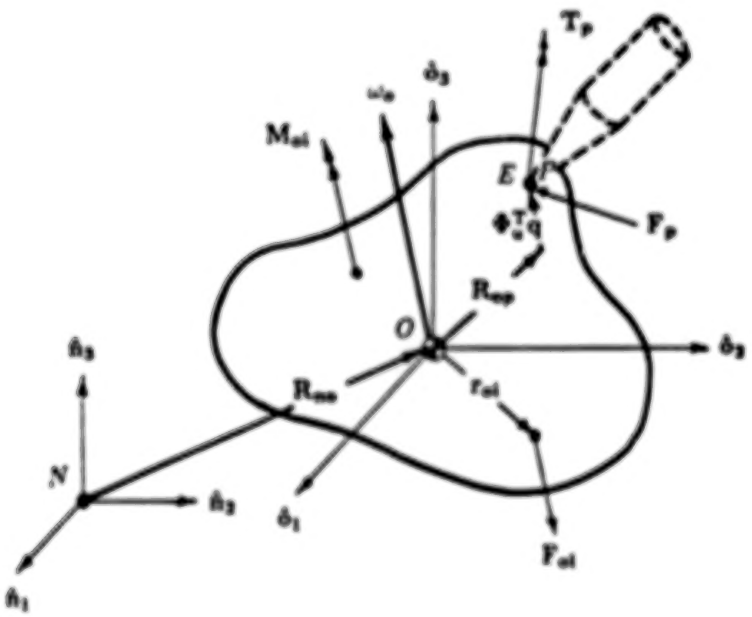
LFSP Eqns. of Motion

- LFSP translation:

$$m_o\ddot{\mathbf{R}}_{no} = -\mathbf{F_p} + \sum_{i=1}^{n_F} \mathbf{F_{oi}} \tag{1}$$

- LFSP rotation:

$$\mathbf{I_o}\dot{\boldsymbol{\omega}}_o + \boldsymbol{\omega}_o \times \mathbf{I_o}\boldsymbol{\omega}_o = -\mathbf{R_{op}} \times \mathbf{F_p} - \mathbf{T_p} + \sum_{i=1}^{n_M} \mathbf{M_{oi}} + \sum_{i=1}^{n_F} \mathbf{r_{oi}} \times \mathbf{F_{oi}} \tag{2}$$



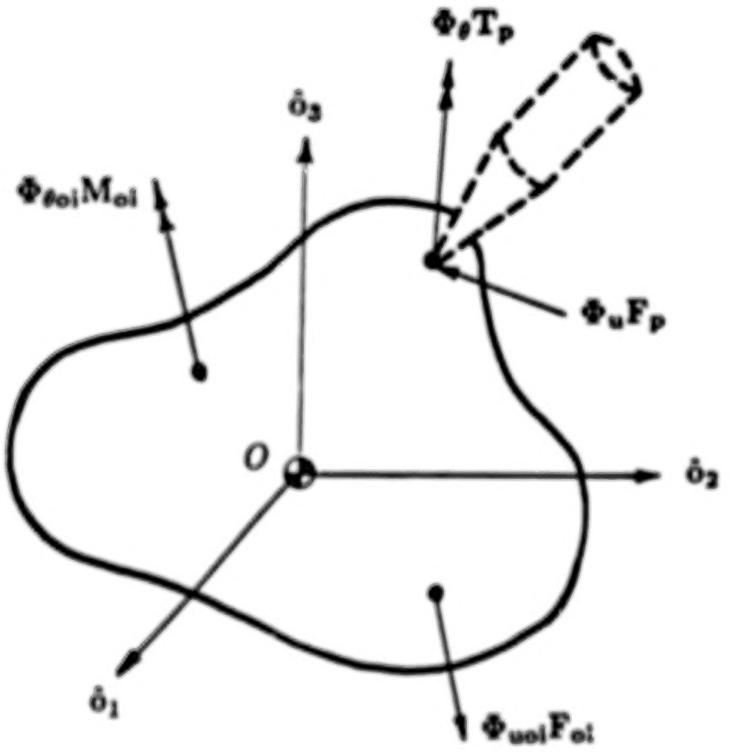
BEST COPY AVAILABLE

Nonlinear Model (cont.)

The LFSP elastic motion is assumed to be decoupled from the LFSP rigid-body motion (valid for small motion), so that inertial/elastic coupling terms arise from payload interactions with the platform at the attachment point. Thus the elastic motion of the LFSP may be described by equation (3), the modal equation of motion. The $(n \times 1)$ vector $\mathbf{q}$ contains the modal coordinates, where n is the number of modes used to describe the elastic motion. The modal coordinates and their corresponding time derivatives will comprise $2n$ components of the system state vector. The matrix $\mathbf{D}$ is a diagonal matrix with terms $2\zeta_i\omega_i$, where ζ_i and ω_i are the damping ratio and frequency, respectively, for elastic mode i. Matrix $\mathbf{\Lambda}$ is a diagonal matrix of ω_i^2. The $\mathbf{\Phi}$'s consist of mode slopes at the point where a moment is applied, or mode shapes at force application points. The modal matrices $\mathbf{\Phi}$ are dimensioned $(n \times 3)$. The right-hand side of the expression represents modal forces and moments.

LFSP Elastic Motion

$$\ddot{\mathbf{q}} + \mathbf{D}\dot{\mathbf{q}} + \mathbf{\Lambda}\mathbf{q} = -\mathbf{\Phi}_u\mathbf{F}_p - \mathbf{\Phi}_\theta\mathbf{T}_p + \sum_{i=1}^{n_M} \mathbf{\Phi}_{\theta oi}\mathbf{M}_{oi} + \sum_{i=1}^{n_F} \mathbf{\Phi}_{uoi}\mathbf{F}_{oi} \qquad (3)$$



Nonlinear Model (cont.)

Next consider the payload equations. The payload CM location, point P*, for the deformed spacecraft with respect to the inertial reference is given by vector $\mathbf{R}_{\mathbf{np}^*}$ in (4) below. The acceleration of the payload CM is sought. Consider time derivatives of the position vector $\mathbf{R}_{\mathbf{np}^*}$ with respect to the inertial frame, that is, take "$\frac{d}{dt}$" of the right-hand side of $\mathbf{R}_{\mathbf{np}^*}$. This gives the velocity of the payload CM, $\dot{\mathbf{R}}_{\mathbf{np}^*}$. Taking another time derivative, again including terms due to the relative rotations between coordinate systems, yields the inertial acceleration of the payload CM, $\ddot{\mathbf{R}}_{\mathbf{np}^*}$. The only external force acting on the payload is the constraint force at the attachment point. Writing Newton's law gives the nonlinear translational equation of motion, equation (5).

Lastly, the nonlinear payload rotational equation of motion (about the payload CM) is given by equation (6). $\mathbf{I}_\mathbf{p}$ is the payload centroidal inertia matrix for the $\hat{\mathbf{p}}^*$-system, and $\mathbf{M}_\mathbf{p}$ is the total moment about the payload CM. Taking appropriate time derivatives and characterizing the moment $\mathbf{M}_\mathbf{p}$ acting on the payload results in equation (7).

Nonlinear Payload Equations of Motion

- Payload CM translation:

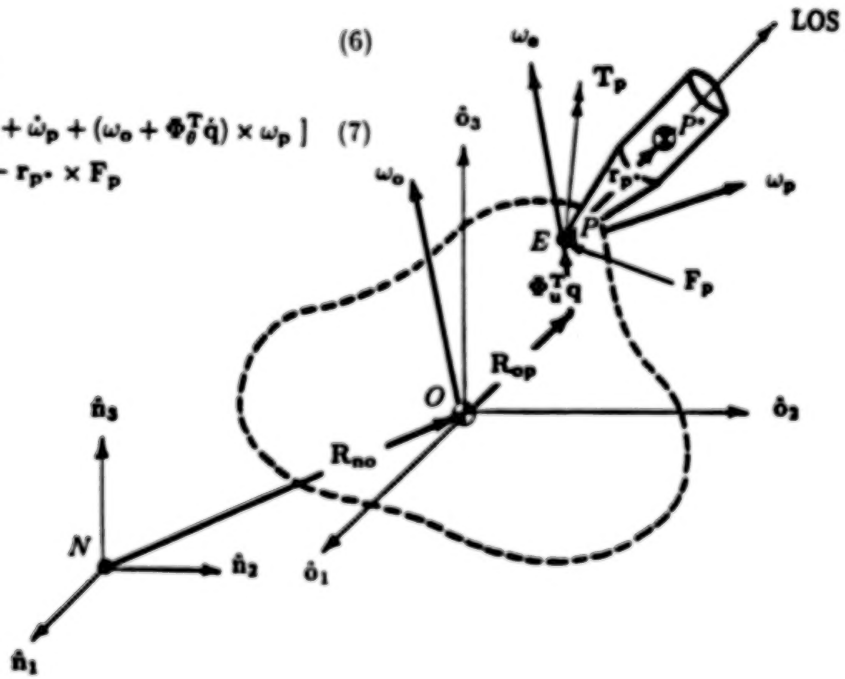
$$\mathbf{R}_{\mathbf{np}^*} = \mathbf{R}_{\mathbf{no}} + \mathbf{R}_{\mathbf{op}} + \Phi_\mathbf{u}^\mathbf{T}\mathbf{q} + \mathbf{r}_{\mathbf{p}^*} \tag{4}$$

$$m_p\ddot{\mathbf{R}}_{\mathbf{np}^*} = \mathbf{F}_\mathbf{p} \tag{5}$$

- Payload rotation:

$$\mathbf{I}_\mathbf{p}\,\frac{d}{dt}(\omega_\mathbf{o} + \omega_\mathbf{e} + \omega_\mathbf{p}) = \mathbf{M}_\mathbf{p} \tag{6}$$

$$\mathbf{I}_\mathbf{p}\,[\,\dot{\omega}_\mathbf{o} + \Phi_\theta^\mathbf{T}\ddot{\mathbf{q}} + \omega_\mathbf{o} \times \Phi_\theta^\mathbf{T}\dot{\mathbf{q}} + \dot{\omega}_\mathbf{p} + (\omega_\mathbf{o} + \Phi_\theta^\mathbf{T}\dot{\mathbf{q}}) \times \omega_\mathbf{p}\,] = \mathbf{T}_\mathbf{p} - \mathbf{r}_{\mathbf{p}^*} \times \mathbf{F}_\mathbf{p} \tag{7}$$



Linearized Model

Consider now transformation of all the inertial quantities to $\hat{\mathbf{o}}$-system components, linearization of the nonlinear equations, and the introduction of perturbations (to nominal values). Note that the $\hat{\mathbf{o}}$-system is nominally parallel to the inertial frame. Upon linearization, system variables may be thought of as being comprised of a nominal value plus a perturbation quantity, for example some variable $y = y_0 + \delta y$. The prefix "δ" will be used to denote departure values from the equilibrium (nominal) state. The nominal attitude of the LFSP is $\mathbf{a_o} = (\phi_o, \theta_o, \psi_o)^\mathbf{T} = \mathbf{0}$, the nominal angular elastic deformation at the payload attach point is $\mathbf{a_e} = (\phi_e, \theta_e, \psi_e)^\mathbf{T} = \mathbf{\Phi}_\theta^\mathbf{T} \delta\mathbf{q} = \mathbf{0}$, and the nominal gimbal angles are $\mathbf{a_p} = (\phi_p, \theta_p, \psi_p)^\mathbf{T} = (\bar{\phi}_p, \bar{\theta}_p, \bar{\psi}_p)^\mathbf{T}$. Furthermore, the modal coordinates used to describe the elastic motion are nominally zero, as are the forces and moments acting on the system.

The angular velocities of the various coordinate systems may be expressed in general as $\omega = \omega_\mathbf{0} + \delta\omega$. However, the nominal angular rates are zero, and $\delta\omega = \delta\dot{\mathbf{a}}$, with $\mathbf{a} = (\phi\ ,\ \theta\ ,\ \psi)^\mathbf{T}$, the Euler angle vector. The elastic deformation angular rate may be written in terms of the mode slopes and modal coordinates as follows: $\delta\dot{\mathbf{a}}_\mathbf{e} = \mathbf{\Phi}_\theta^\mathbf{T} \delta\dot{\mathbf{q}}$.

- "Variable" = "Nominal" + "Perturbation", $y = y_0 + \delta y$
- Nominal Values:
  - LFSP attitude, $\mathbf{a_o} = (\phi_o, \theta_o, \psi_o)^\mathbf{T} = \mathbf{0}$
  - modal coordinates, $\mathbf{q} = \mathbf{0}$
  - gimbal angles, $\mathbf{a_p} = (\bar{\phi}_p, \bar{\theta}_p, \bar{\psi}_p)^\mathbf{T}$

Linearized Model (cont.)

The linearized perturbation equations of motion are given below. The prime notation denotes the matrix cross-product form. $\bar{\mathbf{C}}_{\mathbf{ep}}$ is the transformation from the $\hat{\mathbf{e}}$-system to the $\hat{\mathbf{p}}$-system for the nominal gimbal angles $\bar{\mathbf{a}}_{\mathbf{p}} = (\bar{\phi}_p, \bar{\theta}_p, \bar{\psi}_p)^{\mathbf{T}}$. Also, $\mathbf{I}_{\mathbf{po}} = \bar{\mathbf{C}}_{\mathbf{ep}}^{\mathbf{T}} \mathbf{I}_{\mathbf{p}} \bar{\mathbf{C}}_{\mathbf{ep}}$ is the payload centroidal inertia matrix $\mathbf{I}_{\mathbf{p}}$ (expressed in the $\hat{\mathbf{p}}^*$-system) transformed into the $\hat{\mathbf{o}}$-system. $\mathbf{I}_{\mathbf{po}}$ premultiplies the payload inertial angular acceleration.

- LFSP translation:

$$m_o \delta \ddot{\mathbf{R}}_{\mathbf{no}} = -\delta \mathbf{F}_{\mathbf{p}} + \sum_{i=1}^{n_F} \delta \mathbf{F}_{\mathbf{oi}} \tag{8}$$

- LFSP rotation:

$$\mathbf{I}_{\mathbf{o}} \delta \ddot{\boldsymbol{\phi}}_{\mathbf{o}} = -\mathbf{R}'_{\mathbf{op}} \delta \mathbf{F}_{\mathbf{p}} - \delta \mathbf{T}_{\mathbf{p}} + \sum_{i=1}^{n_M} \delta \mathbf{M}_{\mathbf{oi}} + \sum_{i=1}^{n_F} \mathbf{r}'_{\mathbf{oi}} \delta \mathbf{F}_{\mathbf{oi}} \tag{9}$$

- LFSP elastic motion:

$$\delta \ddot{\mathbf{q}} + \mathbf{D} \delta \dot{\mathbf{q}} + \boldsymbol{\Lambda} \delta \mathbf{q} = -\boldsymbol{\Phi}_{\mathbf{u}} \delta \mathbf{F}_{\mathbf{p}} - \boldsymbol{\Phi}_{\boldsymbol{\theta}} \delta \mathbf{T}_{\mathbf{p}} + \sum_{i=1}^{n_M} \boldsymbol{\Phi}_{\boldsymbol{\theta}\mathbf{oi}} \delta \mathbf{M}_{\mathbf{oi}} + \sum_{i=1}^{n_F} \boldsymbol{\Phi}_{\mathbf{uoi}} \delta \mathbf{F}_{\mathbf{oi}} \tag{10}$$

- Payload CM translation:

$$\begin{aligned} m_p \{ \delta \ddot{\mathbf{R}}_{\mathbf{no}} - [\mathbf{R}'_{\mathbf{op}} + (\bar{\mathbf{C}}_{\mathbf{ep}}^{\mathbf{T}} \mathbf{r}_{\mathbf{p}\bullet})'] \delta \ddot{\mathbf{a}}_{\mathbf{o}} + [\boldsymbol{\Phi}_{\mathbf{u}}^{\mathbf{T}} - (\bar{\mathbf{C}}_{\mathbf{ep}}^{\mathbf{T}} \mathbf{r}_{\mathbf{p}\bullet})' \boldsymbol{\Phi}_{\boldsymbol{\theta}}^{\mathbf{T}}] \delta \ddot{\mathbf{q}} \\ - (\bar{\mathbf{C}}_{\mathbf{ep}}^{\mathbf{T}} \mathbf{r}_{\mathbf{p}\bullet})' \bar{\mathbf{C}}_{\mathbf{ep}}^{\mathbf{T}} \delta \ddot{\mathbf{a}}_{\mathbf{p}} \} = \delta \mathbf{F}_{\mathbf{p}} \end{aligned} \tag{11}$$

- Payload rotation:

$$\mathbf{I}_{\mathbf{po}} (\delta \ddot{\mathbf{a}}_{\mathbf{o}} + \boldsymbol{\Phi}_{\boldsymbol{\theta}}^{\mathbf{T}} \delta \ddot{\mathbf{q}} + \bar{\mathbf{C}}_{\mathbf{ep}}^{\mathbf{T}} \delta \ddot{\mathbf{a}}_{\mathbf{p}}) = \delta \mathbf{T}_{\mathbf{p}} - (\bar{\mathbf{C}}_{\mathbf{ep}}^{\mathbf{T}} \mathbf{r}_{\mathbf{p}\bullet})' \delta \mathbf{F}_{\mathbf{p}} \tag{12}$$

Linearized Model (cont.)

The final equations of motion can be coupled by substituting for the constraint force $\delta\mathbf{F_p}$ given by equation (11) into the remaining equations (8, 9, 10, and 12), thus eliminating the expression for payload translation. The LFSP translational, rotational, and elastic equations, and the payload rotational equation may be expressed in the form of equation (13). Here **A** is a (4×4) block matrix of overall dimension $(n + 9)$ square. Matrices **B** and **C** are essentially null except for n diagonal terms corresponding to the elastic motion. The vector $\delta\eta$ is $(n + 9) \times 1$, and is given by equation (14).

The expression for matrix **A** is given by (15). Various terms comprising matrix **A** are given by equation (16). The expressions for matrices **B** and **C** are given by equation (17). The matrices **D** and **Λ** were given previously. The mathematical structure of this generic model includes the internal couplings between payload rigid-body motion and LFSP rigid and elastic motion.

- Model form:

$$\mathbf{A}\delta\ddot{\eta} + \mathbf{B}\delta\dot{\eta} + \mathbf{C}\delta\eta = \mathbf{E}\delta\mathbf{u} \tag{13}$$

- Vector of system variables:

$$\delta\eta = \delta(X, Y, Z; \phi_o, \theta_o, \psi_o; q_1, \ldots, q_n; \phi_p, \theta_p, \psi_p)^T \tag{14}$$

- Matrices **A**, **B**, and **C**:

$$\mathbf{A} = \begin{bmatrix} (m_o + m_p)\mathbf{I_{3\times3}} & -m_p\bar{\mathbf{R}}' & m_p\bar{\Phi} & -m_p\bar{\mathbf{r}}'\bar{\mathbf{C}}_{\mathbf{ep}}^{\mathbf{T}} \\ m_p\mathbf{R}'_{\mathbf{op}} & \mathbf{I_o} - m_p\mathbf{R}'_{\mathbf{op}}\bar{\mathbf{R}}' & m_p\mathbf{R}'_{\mathbf{op}}\bar{\Phi} & -m_p\mathbf{R}'_{\mathbf{op}}\bar{\mathbf{r}}'\bar{\mathbf{C}}_{\mathbf{ep}}^{\mathbf{T}} \\ m_p\Phi_{\mathbf{u}} & -m_p\Phi_{\mathbf{u}}\bar{\mathbf{R}}' & \mathbf{I_{n\times n}} + m_p\Phi_{\mathbf{u}}\bar{\Phi} & -m_p\Phi_{\mathbf{u}}\bar{\mathbf{r}}'\bar{\mathbf{C}}_{\mathbf{ep}}^{\mathbf{T}} \\ m_p\bar{\mathbf{r}}' & \mathbf{I_{po}} - m_p\bar{\mathbf{r}}'\bar{\mathbf{R}}' & \mathbf{I_{po}}\Phi_\theta^{\mathbf{T}} + m_p\bar{\mathbf{r}}'\bar{\Phi} & (\mathbf{I_{po}} - m_p\bar{\mathbf{r}}'\bar{\mathbf{r}}')\bar{\mathbf{C}}_{\mathbf{ep}}^{\mathbf{T}} \end{bmatrix} \tag{15}$$

where:

$$\bar{\mathbf{r}}' = (\bar{\mathbf{C}}_{\mathbf{ep}}^{\mathbf{T}}\mathbf{r}_{\mathbf{p}^*})' \qquad \bar{\mathbf{R}}' = (\mathbf{R}'_{\mathbf{op}} + \bar{\mathbf{r}}') \qquad \bar{\Phi} = (\Phi_{\mathbf{u}}^{\mathbf{T}} - \bar{\mathbf{r}}'\Phi_\theta^{\mathbf{T}}) \tag{16}$$

$$\mathbf{B} = \begin{bmatrix} \mathbf{0_{6\times6}} & & \\ & \mathbf{D_{n\times n}} & \\ & & \mathbf{0_{3\times3}} \end{bmatrix}, \qquad \mathbf{C} = \begin{bmatrix} \mathbf{0_{6\times6}} & & \\ & \mathbf{\Lambda_{n\times n}} & \\ & & \mathbf{0_{3\times3}} \end{bmatrix} \tag{17}$$

Linearized Model (cont.)

Now consider the right-hand side of equation (13). The vector of control inputs is given by (18). Matrix $\mathbf{E}$ is made up of n_F block-columns corresponding to forces $\delta\mathbf{F_{oi}}$, n_M block-columns for moments $\delta\mathbf{M_{oi}}$, and a single block-column multiplying the payload torque. The overall dimensions of matrix $\mathbf{E}$ are $(n+9) \times (3n_F + 3n_M + 3)$, and $\mathbf{E}$ as a partitioned matrix is given by equation (19). Each of the three partitioned matrices comprising $\mathbf{E}$ are given in (20). It is clear that $\mathbf{E_1}$ corresponds to external force inputs to the LFSP, $\mathbf{E_2}$ to external moment inputs, and finally $\mathbf{E_3}$ corresponds to the payload gimbal torque.

- Vector of control inputs:

$$\delta\mathbf{u} = (\delta\mathbf{F}_{\mathbf{o1}}^{\mathbf{T}}, \ldots, \delta\mathbf{F}_{\mathbf{on_F}}^{\mathbf{T}}; \delta\mathbf{M}_{\mathbf{o1}}^{\mathbf{T}}, \ldots, \delta\mathbf{M}_{\mathbf{on_M}}^{\mathbf{T}}; \delta\mathbf{T}_{\mathbf{p}}^{\mathbf{T}})^{\mathbf{T}} \tag{18}$$

- Partitioned form of matrix $\mathbf{E}$:

$$\mathbf{E} = [\ \mathbf{E}_{\mathbf{1}(n+9)\times(3n_F)}\ ,\ \mathbf{E}_{\mathbf{2}(n+9)\times(3n_M)}\ ,\ \mathbf{E}_{\mathbf{3}(n+9)\times 3}\ ] \tag{19}$$

$$\mathbf{E_1} = \begin{bmatrix} \mathbf{I_{3\times3}} & \cdots & \mathbf{I_{3\times3}} \\ \mathbf{r'_{o1}} & \cdots & \mathbf{r'_{on_F}} \\ \mathbf{\Phi_{uo1}} & \cdots & \mathbf{\Phi_{uon_F}} \\ \mathbf{0_{3\times3}} & \cdots & \mathbf{0_{3\times3}} \end{bmatrix}, \mathbf{E_2} = \begin{bmatrix} \mathbf{0_{3\times3}} & \cdots & \mathbf{0_{3\times3}} \\ \mathbf{I_{3\times3}} & \cdots & \mathbf{I_{3\times3}} \\ \mathbf{\Phi_{\theta o1}} & \cdots & \mathbf{\Phi_{\theta on_M}} \\ \mathbf{0_{3\times3}} & \cdots & \mathbf{0_{3\times3}} \end{bmatrix}, \mathbf{E_3} = \begin{bmatrix} \mathbf{0_{3\times3}} \\ \mathbf{-I_{3\times3}} \\ \mathbf{-\Phi_\theta} \\ \mathbf{I_{3\times3}} \end{bmatrix} \tag{20}$$

Decentralized Control Law

The matrix equation (13) may be put into state variable form by allowing $\mathbf{x_1} = \delta\eta$, as given in (14), and $\mathbf{x_2} = \delta\dot{\eta}$. Thus one obtains the expressions in (21), which may in turn be written as equation (22). The matrices $\bar{\mathbf{A}}$ and $\bar{\mathbf{B}}$ are given by equation (23), with each sub-block of $\bar{\mathbf{A}}$ and $\bar{\mathbf{B}}$ dimensioned $(9+n)$ square.

The approach considered herein is a decentralized control strategy using simple proportional plus rate feedback with collocated actuators and sensors for both payload pointing and LFSP attitude hold. Only applied moments are considered, with LFSP attitude control effected by moment input $\delta\mathbf{M_o}$, and payload pointing accomplished by an applied gimbal torque $\delta\mathbf{T_p}$. The sensed LFSP attitude and attitude rate at the CMG location are given by (24). The LFSP attitude is the sum of the central body rigid angles, and the elastic rotations at the CMG location. The sensed attitude and attitude rate of the payload are given by (25). The payload attitude is the sum of the central body rigid angles, the elastic rotation angles at the payload attach point, and the gimbal angles.

- State-space Form

$$\begin{aligned}\dot{\mathbf{x}}_1 &= \mathbf{x_2} \\ \dot{\mathbf{x}}_2 &= \mathbf{A}^{-1}[\mathbf{Eu} - \mathbf{Bx_2} - \mathbf{Cx_1}]\end{aligned} \tag{21}$$

$$\dot{\mathbf{x}} = \bar{\mathbf{A}}\mathbf{x} + \bar{\mathbf{B}}\mathbf{u} \tag{22}$$

$$\bar{\mathbf{A}} = \begin{bmatrix} \mathbf{0} & \mathbf{I} \\ -\mathbf{A}^{-1}\mathbf{C} & -\mathbf{A}^{-1}\mathbf{B} \end{bmatrix} \qquad \bar{\mathbf{B}} = \begin{bmatrix} \mathbf{0} \\ \mathbf{A}^{-1}\mathbf{E} \end{bmatrix} \tag{23}$$

- Sensor Outputs

  - LFSP attitude and attitude rate:

$$\begin{aligned}\delta\mathbf{a_{os}} &= \delta\mathbf{a_o} + \boldsymbol{\Phi}_{\theta\mathbf{o}}^{\mathbf{T}}\delta\mathbf{q} \\ \delta\dot{\mathbf{a}}_{\mathbf{os}} &= \delta\dot{\mathbf{a}}_{\mathbf{o}} + \boldsymbol{\Phi}_{\theta\mathbf{o}}^{\mathbf{T}}\delta\dot{\mathbf{q}}\end{aligned} \tag{24}$$

  - Payload attitude and attitude rate:

$$\begin{aligned}\delta\mathbf{a_{ps}} &= \delta\mathbf{a_o} + \boldsymbol{\Phi}_{\theta}^{\mathbf{T}}\delta\mathbf{q} + \bar{\mathbf{C}}_{\mathbf{ep}}^{\mathbf{T}}\delta\mathbf{a_p} \\ \delta\dot{\mathbf{a}}_{\mathbf{ps}} &= \delta\dot{\mathbf{a}}_{\mathbf{o}} + \boldsymbol{\Phi}_{\theta}^{\mathbf{T}}\delta\dot{\mathbf{q}} + \bar{\mathbf{C}}_{\mathbf{ep}}^{\mathbf{T}}\delta\dot{\mathbf{a}}_{\mathbf{p}}\end{aligned} \tag{25}$$

Decentralized Control Law (cont.)

The decentralized control laws for LFSP attitude control and payload pointing are given by equations (26) and (27), respectively. Consider the LFSP attitude control system. If the gain matrices $\mathbf{K}_{\mathbf{a}_o}$ and $\mathbf{K}_{\dot{\mathbf{a}}_o}$ are chosen as in (28), the resulting closed-loop system (assuming no coupling) would have a damping ratio of ρ_o, and a bandwidth of Ω_o rad/sec. Similar expressions for the payload gimbal controller may be written by replacing $\mathbf{A_{22}}$ with $\mathbf{A_{44}}$ as in equation (29), giving a closed-loop system with damping ratio ρ_p and bandwidth Ω_p.

- Control Law
  - LFSP attitude:

$$\delta\mathbf{M_o} = -[\mathbf{K}_{\mathbf{a}_o}\delta\mathbf{a}_{os} + \mathbf{K}_{\dot{\mathbf{a}}_o}\delta\dot{\mathbf{a}}_{os}] \tag{26}$$

  - Payload Gimbal Torquer:

$$\delta\mathbf{T_p} = -[\mathbf{K}_{\mathbf{a}_p}\delta\mathbf{a}_{ps} + \mathbf{K}_{\dot{\mathbf{a}}_p}\delta\dot{\mathbf{a}}_{ps}] \tag{27}$$

  - LFSP Gain Matrices:

$$\begin{aligned} \mathbf{K}_{\mathbf{a}_o} &= -\mathbf{A_{22}}\mathrm{diag}(\Omega_o^2) \\ \mathbf{K}_{\dot{\mathbf{a}}_o} &= -\mathbf{A_{22}}\mathrm{diag}(2\rho_o\Omega_o) \end{aligned} \tag{28}$$

  - Payload Gain Matrices:

$$\begin{aligned} \mathbf{K}_{\mathbf{a}_p} &= -\mathbf{A_{44}}\mathrm{diag}(\Omega_p^2) \\ \mathbf{K}_{\dot{\mathbf{a}}_p} &= -\mathbf{A_{44}}\mathrm{diag}(2\rho_p\Omega_p) \end{aligned} \tag{29}$$

Extension to Multi-Payload Case

The equations of motion for multi-payload configurations may be written in the form of equation (30). The vector $\delta\eta$ is dimensioned $(6 + n + 3n_p) \times 1$, and is given by (31). The vector of force and moment inputs $\delta\mathbf{u}$ is dimensioned $(3n_F + 3n_M + 3n_p) \times 1$, and is written as in (32), where $\delta\mathbf{F_{oi}}$, $\delta\mathbf{M_{oi}}$, and $\delta\mathbf{T_i}$ are external LFSP forces and moments, and payload gimbal torques, respectively. The coefficient matrices appearing in equation (30) are given in Appendix A.

- matrix form of eqns.:

$$\mathbf{A}\delta\ddot{\eta} + \mathbf{B}\delta\dot{\eta} + \mathbf{C}\delta\eta = \mathbf{E}\delta\mathbf{u} \tag{30}$$

- vector of system variables:

$$\delta\eta = \delta(\, X,\, Y,\, Z;\, \phi_o,\, \theta_o,\, \psi_o;\, q_1,\, \ldots\,,\, q_n;\, \phi_1,\, \theta_1,\, \psi_1;\, \ldots\,;\, \phi_{n_p},\, \theta_{n_p},\, \psi_{n_p}\,)^T \tag{31}$$

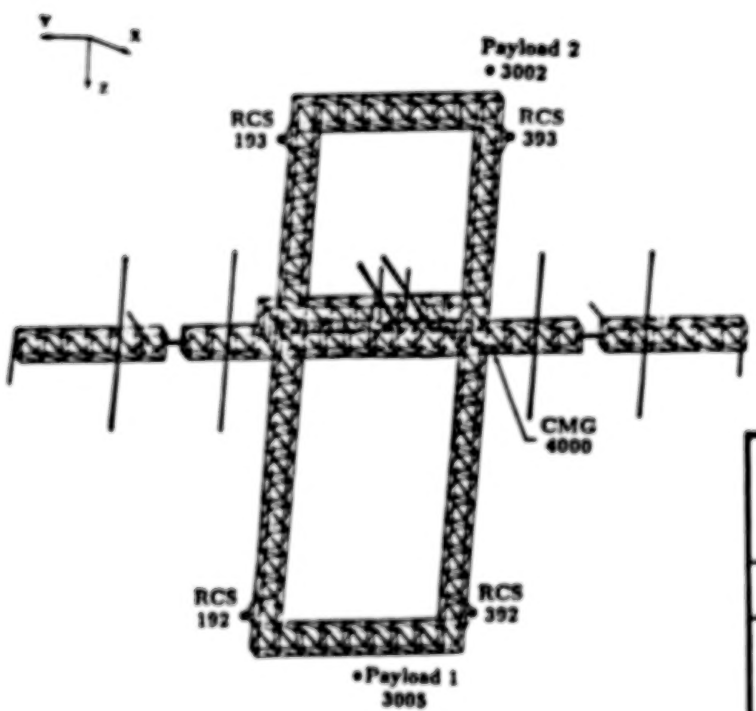
- vector of control inputs:

$$\delta\mathbf{u} = \delta(\, \mathbf{F_{o1}^T},\, \ldots\,,\, \mathbf{F_{on_F}^T};\, \mathbf{M_{o1}^T},\, \ldots\,,\, \mathbf{M_{on_M}^T};\, \mathbf{T_1^T},\, \ldots\,,\, \mathbf{T_{n_p}^T}\,)^{\mathbf{T}} \tag{32}$$

Simulation Results for an Example Problem

In order to demonstrate the modeling and control methods developed, the dual-keel space station ISS04 reference configuration with individually pointed payloads was considered. Mass, inertia, and other parameters for the station are summarized in the table below. Many different simulation scenarios were considered in exercising the space station model, however only a two–payload study comparing the effects of end-mounting versus CM-mounting will be presented herein. Attitude control moment input to the station was provided by a three-axis CMG near the station CM, while three-axis gimbal torquers acted at each of the two payload attachment points. In this study, the "worst-case" station rigid-body initial conditions were chosen based on the most severe anticipated maneuver, re-boosting to higher orbit. Initial modal coordinates were obtained from the steady-state elastic deformation resulting from the firing of RCS thrusters. The decentralized controller must drive the station rigid-body angles and payload pointing errors to zero in the presence of elastic motion.

ISS04 Configuration



c.m. location: (ft)	$X = -9.1667$ $Y = -5.4167$ $Z = -21.333$
mass: (slug)	$m_o = 17757.76$
inertias w.r.t. CM: (slug-ft^2)	$I_{xx} = 2.15670 \times 10^8$ $I_{xy} = 2.15450 \times 10^7$ $I_{xz} = 3.27812 \times 10^5$ $I_{yy} = 1.20342 \times 10^8$ $I_{yz} = 1.06323 \times 10^6$ $I_{zz} = 1.19695 \times 10^8$
RCS nodes: CMG node:	192, 193, 392, 392 4000

BEST COPY AVAILABLE

Simulation Results (cont.)

The 12 vibrational modes that were actually used in the simulation studies, and their corresponding modal frequencies, are tabulated below. These 12 modes were chosen because they represent major truss-structure bending and torsional deformations, as opposed to mere appendage modes. The elastic modes were assumed to have a damping ratio of 0.005. Payload data are also summarized below. Given are the payload attachment points, and the masses and inertias. The first rigid payload was mounted on the lower keel, and the second payload on the upper keel. For the control systems, the desired closed-loop damping ratios were assumed to be 0.707, and the desired bandwidths were 10.0 rad/sec and 0.1 rad/sec for the two payloads and the space station, respectively.

Model Data

mode #	frequency (rad/sec)
7	1.37236
8	1.39753
9	1.50451
20	2.01425
21	2.24925
22	2.68481
36	4.09370
37	4.74973
38	4.87077
39	5.86502
40	6.51971
41	7.26311

Modes Included in Composite System Model

Payload Data

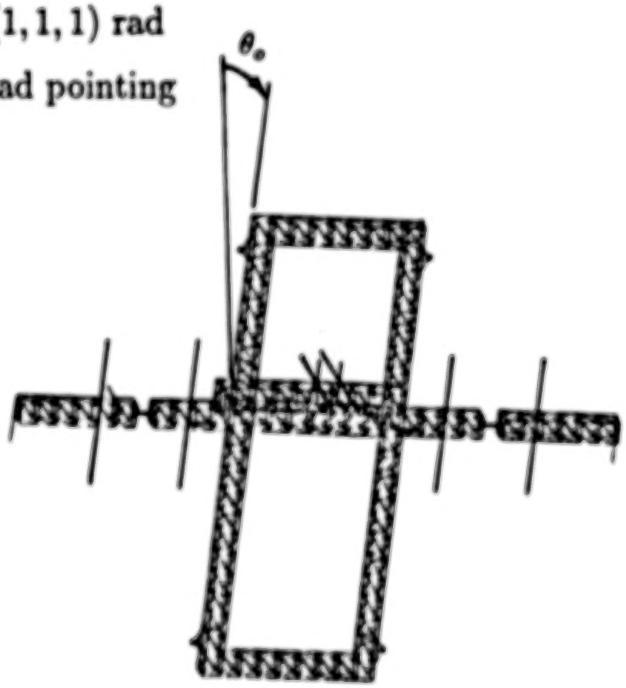
	payload 1	payload 2
ISS04 gimbal node	3005	3002
position vectors from CM (ft)	$x = 8.3333$ $y = 5.4167$ $z = 230.223$	$x = 9.1667$ $y = -60.202$ $z = -142.708$
payload mass (slug)	100.0	100.0
payload inertias (slug-ft^2)		
I_{xx}	1250.0	1250.0
I_{xy}	0.0	0.0
I_{xz}	0.0	0.0
I_{yy}	1250.0	1250.0
I_{yz}	0.0	0.0
I_{zz}	1500.0	1500.0

BEST COPY AVAILABLE

Simulation Results (cont.)

The steady-state (limit cycle) station rigid-body pitch and pitch rate encountered in a reboost maneuver simulation study were 0.02187 rad (1.25 deg) and 0.0008727 rad/sec (0.05 deg/sec), respectively. The present simulation used these values as initial angular displacements and velocities about each of the station axes. The initial modal coordinates were calculated by assuming the space station had reached steady-state conditions after the the firing of the four RCS thrusters in the x-direction at 75 lb_f each. This assumed maneuver serves only to provide a reasonable initial deformed state. There are no thruster inputs after the start of the simulation. The payload gimbal Euler angles and the remaining states are initially zero. The desired gimbal angles for both payloads are $\bar{\mathbf{a}}_{\mathbf{1,2}} = 0.1(1,1,1)$ rad. It was desired to return the station to its nominal orientation, i.e. the Euler angles $(\phi_o,\ \theta_o,\ \psi_o) = \mathbf{0}$, while driving the payload pointing error to zero, in the presence of nonzero initial conditions and any induced elastic deformation. Two cases were compared as a result of studying the equations of motion: an end-mounted case with nonzero distance between the gimbals and the CM, $\mathbf{r_{p^*}} = (0,\ 0,\ 6)^{\mathbf{T}}$ ft, and a CM-mounted case where $\mathbf{r_{p^*}} = (0,\ 0,\ 0)^{\mathbf{T}}$.

- Initial Conditions
  - each axis: angle = 1.25 deg, angular rate = 0.05 deg/sec
  - initial elastic deformation due to thruster firing (steady-state)
  - initial gimbal angles are all zero
- desired gimbal angles: $\mathbf{a_{p1}} = \mathbf{a_{p2}} = 0.1\ (1,1,1)$ rad
- station stabilization, simultaneous payload pointing
- two cases:
  - end-mounted payload
  - CM-mounted payload

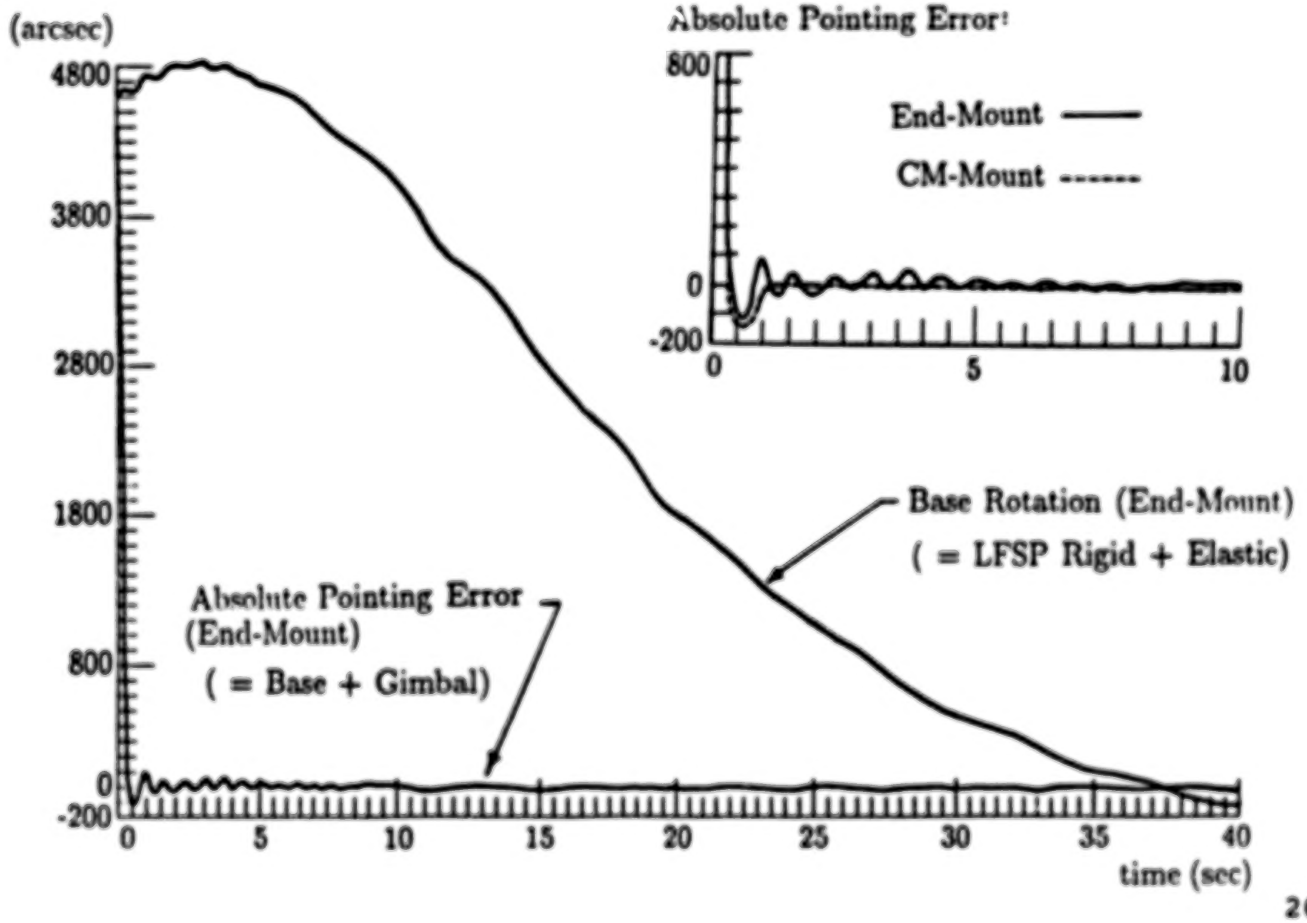


Simulation Results (cont.)

The results given below are for Payload 2 on the upper keel, about the pitch axis (the x and z motions are analogous, as are the results for the payload on the lower keel). The figure shows the "base" motion, that is, the sum of the space station rigid-body orientation angles and the elastic rotation at the payload attachment point, for an end-mounted payload. This motion must be compensated for by the payload gimbal torquer so that the payload remains on target. The large rigid-body motion about the y-axis masks the much smaller elastic motion. The absolute payload pointing error for the end-mounted case is also shown below. The absolute pointing error is the sum of the base motion and the payload gimbal angles, and should be driven to zero by the payload controller.

The inset figure compares the absolute pointing error for the CM- and end-mounted cases. Note that the absolute error for the end-mounted case is significantly more oscillatory than the CM-mounted case. The end-mounted case has a maximum overshoot of -136.49 arcsec. This response remains oscillatory with a magnitude on the order of 10 arcsec. The CM-mounted case yields the desired error response (i.e., perfect second-order system response) about the y-axis (and x and z axes as well) because the payload rotational motion is completely uncoupled from the LFSP motion. Here the overshoot is -194.22 arcsec, with the absolute error dropping below 0.001 arcsec in 2.32 sec.

- Results for Payload 2, angles about pitch axis (i.e.: "$\delta\theta$")



Alternate Dissipative Controller

The decentralized controller described previously was found to give satisfactory performance for the space station example. However, coupling between rigid and elastic motion was not severe, as the masses and inertias of the payloads were small compared to the station values, and the station represents a nearly rigid spacecraft. Decentralized control does not guarantee stability for the general case of a highly flexible LFSP with large inertial payload/LFSP coupling, as control system interactions can be destabilizing. An alternate method is to utilize a dissipative controller which requires that the matrix "**A**" in the second order vector equation (33) be symmetric. Development of the symmetric form of the equations of motion may be found in Appendix B. By redefining the system variables "$\delta\eta$" as in (35), it can be shown that the resulting "**A**" matrix is always positive definite. Using the sensor outputs as in (36) and the control law as in (37), it can be proven that the system is asymptotically stable (in the sense that all rotational and elastic motion tends to zero as time goes to infinity). The stability is guaranteed regardless of errors in the system parameters or ignored (unmodeled) elastic motion. Research is presently in progress on this type of controller.

- Symmetric Form of Equations

$$\mathbf{A}\delta\ddot{\eta} + \mathbf{B}\delta\dot{\eta} + \mathbf{C}\delta\eta = \mathbf{E}\delta\mathbf{u} \tag{33}$$

where:

$$\mathbf{A}^T = \mathbf{A} > 0$$

$$\mathbf{B}^T = \mathbf{B} \geq 0$$

$$\mathbf{C}^T = \mathbf{C} \geq 0$$

$$\mathbf{E} = \left[\begin{array}{c|c} 0_{3\times 3} & \\ I_{3\times 3} & 0_{[(6+n)\times 3n_p]} \\ \Phi_{\theta o(n\times 3)} & \\ \hline 0_{3\times 3} & \\ \vdots & I_{(3n_p\times 3n_p)} \\ 0_{3\times 3} & \end{array}\right] \tag{34}$$

$$\delta\eta = \left(\delta\mathbf{R}_{no}^T,\ \delta\mathbf{a}_o^T,\ \delta\mathbf{q}^T,\ \delta\mathbf{a}_{1o}^T,\ \ldots\ ,\ \delta\mathbf{a}_{n_po}^T\right)^T \tag{35}$$

$$\mathbf{y} = \mathbf{E}^T\eta = \left[\begin{array}{c} \text{station attitude (rigid + flexible), at CMG location} \\ \text{transformed gimbal angles, payload 1} \\ \vdots \\ \text{transformed gimbal angles, payload } n_p \end{array}\right] \tag{36}$$

- Control Law

$$\delta\mathbf{u} = -\mathbf{G}_p\delta\mathbf{y} - \mathbf{G}_r\delta\dot{\mathbf{y}}\ ; \quad \mathbf{G}_p^T = \mathbf{G}_p > 0,\ \ \mathbf{G}_r^T = \mathbf{G}_r^T > 0 \tag{37}$$

- Closed-loop system asymptotically stable, i.e.:

$$(\delta\mathbf{a}_o, \delta\mathbf{q}, \delta\mathbf{a}_{1o}, \delta\mathbf{a}_{2o}, \ldots, \delta\mathbf{a}_{n_po}) \to 0 \text{ as } t \to \infty \tag{38}$$

- Research presently in progress

Concluding Remarks

The problem of dynamic modeling and control of composite systems consisting of a central flexible space platform and articulated rigid payloads was considered. Generic linearized equations of motion were derived for a single rigid payload mounted on such a platform using a three-degree-of-freedom gimballing mechanism. This generic large flexible space platform (LFSP) model was then extended to the case of multiple independently pointed payloads. A simple decentralized control law was proposed for platform attitude control and payload pointing. Simulation results were obtained for an example problem with a single payload, and also with two payloads, attached to the space station. The results demonstrate the effects of dynamic couplings in the composite system, and also indicate that the control law used provides satisfactory payload pointing and platform stabilization for the example problem.

An alternate centralized dissipative control law, which uses a symmetric form of the equations of motion, was also proposed. This control law guarantees stability regardless of modeling erros and unmodeled modes. Further research is in progress on that topic. The model obtained herein is mathematically tractable, and yet has an accurate structure that includes all internal dynamic couplings. This model offers a suitable tool for analytical and numerical investigation of the dynamics and control of an important class of missions arising in the Control-Structure Interaction (CSI) program.

- Developed nonlinear math models for LFSP/ articulated payload system
- Extended to multi-payload systems
- Obtained linearized equations
- Simulation results for an example problem
  - indicates satisfactory performance for decentralized control law
- Proposed a centralized dissipative control law
  - provides robust stability
  - development in progress
- Further investigation:
  - extension to flexible articulated appendages
  - automated "FEM-type" model assembly
  - incorporation in CSI optimization problem

Appendix A: Equations for Multi-Payload Case

The equations for an LFSP supporting multiple payloads will be derived from the linearized equations (8) through (12). Here a large flexible space platform described in part by n known elastic modes, is acted on by n_F external forces and n_M moments exclusive of the torques required to point the n_p payloads.

The translational expression is:

$$m_o \delta \ddot{\mathbf{R}}_{\mathbf{no}} = \sum_{i=1}^{n_F} \delta \mathbf{F}_{\mathbf{oi}} - \sum_{i=1}^{n_p} \delta \mathbf{F}_{\mathbf{i}} \tag{A1}$$

The expression for the rigid-body rotation of the LFSP becomes:

$$\mathbf{I}_{\mathbf{o}} \delta \ddot{\mathbf{a}}_{\mathbf{o}} = \sum_{i=1}^{n_M} \delta \mathbf{M}_{\mathbf{oi}} + \sum_{i=1}^{n_F} \mathbf{r}'_{\mathbf{oi}} \delta \mathbf{F}_{\mathbf{oi}} - \sum_{i=1}^{n_p} \mathbf{R}'_{\mathbf{oi}} \delta \mathbf{F}_{\mathbf{i}} - \sum_{i=1}^{n_p} \delta \mathbf{T}_{\mathbf{i}} \tag{A2}$$

Again the "prime" notation with $\mathbf{R}'_{\mathbf{oi}}$ and $\mathbf{r}'_{\mathbf{oi}}$ indicates the (3×3) matrix cross-product form of the vectors $\mathbf{R}_{\mathbf{oi}} = x_i \hat{\mathbf{o}}_1 + y_i \hat{\mathbf{o}}_2 + z_i \hat{\mathbf{o}}_3$ and $\mathbf{r}_{\mathbf{oi}} = x_{oi} \hat{\mathbf{o}}_1 + y_{oi} \hat{\mathbf{o}}_2 + z_{oi} \hat{\mathbf{o}}_3$. The linearized equation for the elastic motion of the platform is:

$$\delta \ddot{\mathbf{q}} + \mathbf{D} \delta \dot{\mathbf{q}} + \mathbf{\Lambda} \delta \mathbf{q} = \sum_{i=1}^{n_M} \mathbf{\Phi}_{\theta \mathbf{oi}} \delta \mathbf{M}_{\mathbf{oi}} + \sum_{i=1}^{n_F} \mathbf{\Phi}_{\mathbf{uoi}} \delta \mathbf{F}_{\mathbf{oi}} - \sum_{i=1}^{n_p} \mathbf{\Phi}_{\mathbf{ui}} \delta \mathbf{F}_{\mathbf{i}} - \sum_{i=1}^{n_p} \mathbf{\Phi}_{\theta \mathbf{i}} \delta \mathbf{T}_{\mathbf{i}} \tag{A3}$$

Next are the rigid payload equations. There will be a translational and a rotational equation for each of the n_p payloads. The CM of the i^{th} payload ("point i^*") from the inertial reference for the deformed spacecraft is given by:

$$\mathbf{R}_{\mathbf{ni}\bullet} = \mathbf{R}_{\mathbf{no}} + \mathbf{R}_{\mathbf{oi}} + \mathbf{\Phi}^{\mathbf{T}}_{\mathbf{ui}} \mathbf{q} + \mathbf{r}_{\mathbf{i}\bullet} \tag{A4}$$

Differentiating this equation twice results in the inertial acceleration of the i^{th} payload CM in the form of equation (7). Noting that the only external force acting on the payload is the constraint force, and linearizing gives:

$$\begin{aligned} m_i \{ \delta \ddot{\mathbf{R}}_{\mathbf{no}} - [\mathbf{R}'_{\mathbf{oi}} + (\bar{\mathbf{C}}^{\mathbf{T}}_{\mathbf{ei}} \mathbf{r}_{\mathbf{i}\bullet})'] \delta \ddot{\mathbf{a}}_{\mathbf{o}} + [\mathbf{\Phi}^{\mathbf{T}}_{\mathbf{ui}} - (\bar{\mathbf{C}}^{\mathbf{T}}_{\mathbf{ei}} \mathbf{r}_{\mathbf{i}\bullet})' \mathbf{\Phi}^{\mathbf{T}}_{\theta \mathbf{i}}] \delta \ddot{\mathbf{q}} \\ - (\bar{\mathbf{C}}^{\mathbf{T}}_{\mathbf{ei}} \mathbf{r}_{\mathbf{i}\bullet})' \bar{\mathbf{C}}^{\mathbf{T}}_{\mathbf{ei}} \delta \ddot{\mathbf{a}}_{\mathbf{i}} \} = \delta \mathbf{F}_{\mathbf{i}} \end{aligned} \tag{A5}$$

$\bar{\mathbf{C}}_{\mathbf{ei}}$ is the nominal transformation between the elastic and some i^{th} payload axes. The payload rotational equation of motion becomes:

$$\mathbf{I}_{\mathbf{io}} (\delta \ddot{\mathbf{a}}_{\mathbf{o}} + \mathbf{\Phi}^{\mathbf{T}}_{\theta \mathbf{i}} \delta \ddot{\mathbf{q}} + \bar{\mathbf{C}}^{\mathbf{T}}_{\mathbf{ei}} \delta \ddot{\mathbf{a}}_{\mathbf{i}}) = \delta \mathbf{T}_{\mathbf{i}} - (\bar{\mathbf{C}}^{\mathbf{T}}_{\mathbf{ei}} \mathbf{r}_{\mathbf{i}\bullet})' \delta \mathbf{F}_{\mathbf{i}} \tag{A6}$$

Here $\mathbf{I_{io}} = \bar{\mathbf{C}}_{\mathbf{ei}}^{\mathbf{T}}\ \mathbf{I_i}\ \bar{\mathbf{C}}_{\mathbf{ei}}$ is the i^{th} payload inertia matrix transformed into the $\hat{\mathbf{o}}$-system. This inertia matrix multiplies the absolute inertial angular acceleration of the i^{th} payload.

Using summations over the n_p payloads, equation (A5) can be used to remove $\sum \delta \mathbf{F_i}$ terms from the LFSP equations (A1, A2, and A3). Furthermore, $\delta \mathbf{F_i}$ may be removed from the i^{th} payload rotational equation (A6), yielding n_p additional equations. This system of equations may then be assembled in the following matrix form:

$$\mathbf{A}\delta\ddot{\eta} + \mathbf{B}\delta\dot{\eta} + \mathbf{C}\delta\eta = \mathbf{E}\delta\mathbf{u} \tag{A7}$$

The vector $\delta\eta$ is dimensioned $(6 + n + 3n_p) \times 1$, and is given by:

$$\delta\eta = \delta(\ X,\ Y,\ Z;\ \phi_o,\ \theta_o,\ \psi_o;\ q_1,\ \cdots,\ q_n;\ \phi_1,\ \theta_1,\ \psi_1;\ \cdots;\ \phi_{n_p},\ \theta_{n_p},\ \psi_{n_p}\ )^T \tag{A8}$$

The vector of force and moment inputs $\delta\mathbf{u}$ is dimensioned $(3n_F + 3n_M + 3n_p) \times 1$, and is written as follows:

$$\delta\mathbf{u} = \delta(\ \mathbf{F_{o1}}^{\mathbf{T}},\ \cdots,\ \mathbf{F_{on_F}}^{\mathbf{T}};\ \mathbf{M_{o1}}^{\mathbf{T}},\ \cdots,\ \mathbf{M_{on_M}}^{\mathbf{T}};\ \mathbf{T_1}^{\mathbf{T}},\ \cdots,\ \mathbf{T_{n_p}}^{\mathbf{T}}\ )^{\mathbf{T}} \tag{A9}$$

where $\delta\mathbf{F_{oi}}$, $\delta\mathbf{M_{oi}}$, and $\delta\mathbf{T_i}$ are external LFSP forces and moments, and payload gimbal torques, respectively.

The coefficient matrices $\mathbf{A}$, $\mathbf{B}$, and $\mathbf{C}$, dimensioned $(6 + n + 3n_p)$ square, and $\mathbf{E}$, dimensioned $(6 + n + 3n_p) \times (3n_F + 3n_M + 3n_p)$, are given below. Matrix $\mathbf{A}$ is essentially a "mass/inertia" matrix given by:

$$\mathbf{A} = \begin{bmatrix} \mathbf{A_{1[(6+n)\times(6+n)]}} & \mathbf{A_{2[(6+n)\times 3n_p]}} \\ \mathbf{A_{3[3n_p\times(6+n)]}} & \mathbf{A_{4(3n_p\times 3n_p)}} \end{bmatrix} \tag{A10}$$

The blocks comprising matrix $\mathbf{A}$ are:

$$\mathbf{A_1} = \begin{bmatrix} \left(m_o + \sum_{i=1}^{n_p} m_i\right)\mathbf{I_{3\times 3}} & -\sum_{i=1}^{n_p} m_i \bar{\mathbf{R}}_{\mathbf{i}}' & \sum_{i=1}^{n_p} m_i \bar{\mathbf{\Phi}}_{\mathbf{i}} \\ \sum_{i=1}^{n_p} m_i \mathbf{R}_{\mathbf{oi}}' & \mathbf{I_o} - \sum_{i=1}^{n_p} m_i \mathbf{R}_{\mathbf{oi}}' \bar{\mathbf{R}}_{\mathbf{i}}' & \sum_{i=1}^{n_p} m_i \mathbf{R}_{\mathbf{oi}}' \bar{\mathbf{\Phi}}_{\mathbf{i}} \\ \sum_{i=1}^{n_p} m_i \mathbf{\Phi}_{\mathbf{i}} & -\sum_{i=1}^{n_p} m_i \mathbf{\Phi}_{\mathbf{i}} \bar{\mathbf{R}}_{\mathbf{i}}' & \mathbf{I_{n\times n}} + \sum_{i=1}^{n_p} m_i \mathbf{\Phi}_{\mathbf{i}} \bar{\mathbf{\Phi}}_{\mathbf{i}} \end{bmatrix} \tag{A11a}$$

$$\mathbf{A_2} = \begin{bmatrix} -m_1 \bar{\mathbf{r}}_1' \mathbf{C}_{\mathbf{e1}}^{\mathbf{T}} & \cdots & -m_{n_p} \bar{\mathbf{r}}_{\mathbf{n_p}}' \mathbf{C}_{\mathbf{en_p}}^{\mathbf{T}} \\ m_1 \mathbf{R}_{\mathbf{o1}}' \bar{\mathbf{r}}_1' \mathbf{C}_{\mathbf{e1}}^{\mathbf{T}} & \cdots & m_{n_p} \mathbf{R}_{\mathbf{on_p}}' \bar{\mathbf{r}}_{\mathbf{n_p}}' \mathbf{C}_{\mathbf{en_p}}^{\mathbf{T}} \\ -m_1 \mathbf{\Phi}_1 \bar{\mathbf{r}}_1' \mathbf{C}_{\mathbf{e1}}^{\mathbf{T}} & \cdots & -m_{n_p} \mathbf{\Phi}_{\mathbf{n_p}} \bar{\mathbf{r}}_{\mathbf{n_p}}' \mathbf{C}_{\mathbf{en_p}}^{\mathbf{T}} \end{bmatrix} \tag{A11b}$$

$$\mathbf{A_3} = \begin{bmatrix} \bar{\mathbf{r}}'_1 m_1 & \mathbf{I}_1 - m_1 \bar{\mathbf{r}}'_1 \bar{\mathbf{R}}'_1 & \mathbf{I}_1 \boldsymbol{\Phi}^{\mathbf{T}}_{\theta 1} + m_1 \bar{\mathbf{r}}'_1 \bar{\boldsymbol{\Phi}}_1 \\ \vdots & \vdots & \vdots \\ \bar{\mathbf{r}}'_{\mathbf{n_p}} m_{n_p} & \mathbf{I}_{\mathbf{n_p}} - m_{n_p} \bar{\mathbf{r}}'_{\mathbf{n_p}} \bar{\mathbf{R}}'_{\mathbf{n_p}} & \mathbf{I}_{\mathbf{n_p}} \boldsymbol{\Phi}^{\mathbf{T}}_{\theta \mathbf{n_p}} + m_{n_p} \bar{\mathbf{r}}'_{\mathbf{n_p}} \bar{\boldsymbol{\Phi}}_{\mathbf{n_p}} \end{bmatrix} \tag{A11c}$$

$$\mathbf{A_4} = \begin{bmatrix} (\mathbf{I}_1 - m_1 \bar{\mathbf{r}}'_1 \bar{\mathbf{r}}'_1) \mathbf{C}^{\mathbf{T}}_{\mathbf{e1}} & \cdots & \mathbf{0_{3\times 3}} \\ \vdots & \ddots & \vdots \\ \mathbf{0_{3\times 3}} & \cdots & (\mathbf{I}_{\mathbf{n_p}} - m_{n_p} \bar{\mathbf{r}}'_{\mathbf{n_p}} \bar{\mathbf{r}}'_{\mathbf{n_p}}) \mathbf{C}^{\mathbf{T}}_{\mathbf{e n_p}} \end{bmatrix} \tag{A11d}$$

where:

$$\bar{\mathbf{r}}'_{\mathbf{i}} = (\mathbf{C}^{\mathbf{T}}_{\mathbf{ei}} \mathbf{r}_{\mathbf{i}\bullet})' \qquad \bar{\mathbf{R}}'_{\mathbf{i}} = (\mathbf{R}'_{\mathbf{oi}} + \bar{\mathbf{r}}'_{\mathbf{i}}) \qquad \bar{\boldsymbol{\Phi}}_{\mathbf{i}} = (\boldsymbol{\Phi}^{\mathbf{T}}_{\mathbf{ui}} - \bar{\mathbf{r}}'_{\mathbf{i}} \boldsymbol{\Phi}^{\mathbf{T}}_{\theta \mathbf{i}}) \tag{A12}$$

Matrices **B** and **C** are for the most part null except for diagonal blocks multiplying the n modal coordinates. **B** and **C** are then modal damping and modal stiffness matrices written as:

$$\begin{aligned} \mathbf{B} &= \text{diag}[\mathbf{0}_{(6\times 6)},\ \mathbf{D}_{(n\times n)},\ \mathbf{0}_{(3n_p \times 3n_p)}] \\ \mathbf{C} &= \text{diag}[\mathbf{0}_{(6\times 6)},\ \boldsymbol{\Lambda}_{(n\times n)},\ \mathbf{0}_{(3n_p \times 3n_p)}] \end{aligned} \tag{A13}$$

where:

$$\begin{aligned} \mathbf{D} &= [\text{diag}(2\zeta_i \omega_i)]_{(n\times n)} \\ \boldsymbol{\Lambda} &= [\text{diag}(\omega_i^2)]_{(n\times n)} \end{aligned} \tag{A14}$$

The coefficient matrix **E** is written as:

$$\mathbf{E} = \begin{bmatrix} \mathbf{E}_{1[(6+n)\times 3n_F]} & \mathbf{E}_{2[(6+n)\times 3n_M]} & \mathbf{E}_{3[(6+n)\times 3n_p]} \\ \mathbf{0}_{(3n_p \times 3n_F)} & \mathbf{0}_{(3n_p \times 3n_M)} & \mathbf{I}_{(3n_p \times 3n_p)} \end{bmatrix} \tag{A15}$$

where the first row of blocks in **E** are given by:

$$\mathbf{E_1} = \begin{bmatrix} \mathbf{I_{3\times 3}} & \cdots & \mathbf{I_{3\times 3}} \\ \mathbf{r}'_{\mathbf{o1}} & \cdots & \mathbf{r}'_{\mathbf{on_F}} \\ \boldsymbol{\Phi}_{\mathbf{uo1}} & \cdots & \boldsymbol{\Phi}_{\mathbf{uon_F}} \end{bmatrix}, \quad \mathbf{E_2} = \begin{bmatrix} \mathbf{0_{3\times 3}} & \cdots & \mathbf{0_{3\times 3}} \\ \mathbf{I_{3\times 3}} & \cdots & \mathbf{I_{3\times 3}} \\ \boldsymbol{\Phi}_{\theta \mathbf{o1}} & \cdots & \boldsymbol{\Phi}_{\theta \mathbf{on_M}} \end{bmatrix}, \quad \mathbf{E_3} = \begin{bmatrix} \mathbf{0_{3\times 3}} & \cdots & \mathbf{0_{3\times 3}} \\ -\mathbf{I_{3\times 3}} & \cdots & -\mathbf{I_{3\times 3}} \\ -\boldsymbol{\Phi}_{\theta 1} & \cdots & -\boldsymbol{\Phi}_{\theta n_p} \end{bmatrix} \tag{A16}$$

Appendix B: Symmetric-Form Equations for Single and Multi-Payload Cases

A symmetric form of the composite system equations of motion will now be derived from the linearized asymmetric form. The linearized LFSP translation, rotation, and elastic equations of motion, as well as the payload rotational equations follow:

$$(m_o + m_p)\mathbf{I_{3\times 3}}\delta\ddot{\mathbf{R}}_{\mathbf{no}} - m_p\bar{\mathbf{R}}'\delta\ddot{\mathbf{a}}_{\mathbf{o}} + m_p\bar{\mathbf{\Phi}}\delta\ddot{\mathbf{q}} - m_p\bar{\mathbf{r}}'\bar{\mathbf{C}}^{\mathbf{T}}_{\mathbf{ep}}\delta\ddot{\mathbf{a}}_{\mathbf{p}} = \sum_{i=1}^{n_F}\delta\mathbf{F}_{\mathbf{oi}} \tag{B1}$$

$$\begin{aligned} m_p\mathbf{R}'_{\mathbf{op}}\delta\ddot{\mathbf{R}}_{\mathbf{no}} + [\mathbf{I}_{\mathbf{o}} - m_p\mathbf{R}'_{\mathbf{op}}\bar{\mathbf{R}}']\delta\ddot{\mathbf{a}}_{\mathbf{o}} + m_p\mathbf{R}'_{\mathbf{op}}\bar{\mathbf{\Phi}}\delta\ddot{\mathbf{q}} - m_p\mathbf{R}'_{\mathbf{op}}\bar{\mathbf{r}}'\bar{\mathbf{C}}^{\mathbf{T}}_{\mathbf{ep}}\delta\ddot{\mathbf{a}}_{\mathbf{p}} \\ = \sum_{i=1}^{n_F}\mathbf{r}'_{\mathbf{oi}}\delta\mathbf{F}_{\mathbf{oi}} + \sum_{i=1}^{n_M}\delta\mathbf{M}_{\mathbf{oi}} - \delta\mathbf{T}_{\mathbf{p}} \end{aligned} \tag{B2}$$

$$\begin{aligned} m_p\mathbf{\Phi}_{\mathbf{u}}\delta\ddot{\mathbf{R}}_{\mathbf{no}} - m_p\mathbf{\Phi}_{\mathbf{u}}\bar{\mathbf{R}}'\delta\ddot{\mathbf{a}}_{\mathbf{o}} + [\mathbf{I}_{\mathbf{n\times n}} + m_p\mathbf{\Phi}_{\mathbf{u}}\bar{\mathbf{\Phi}}]\delta\ddot{\mathbf{q}} - m_p\mathbf{\Phi}_{\mathbf{u}}\bar{\mathbf{r}}'\bar{\mathbf{C}}^{\mathbf{T}}_{\mathbf{ep}}\delta\ddot{\mathbf{a}}_{\mathbf{p}} \\ = \sum_{i=1}^{n_F}\mathbf{\Phi}_{\mathbf{uoi}}\delta\mathbf{F}_{\mathbf{oi}} + \sum_{i=1}^{n_M}\mathbf{\Phi}_{\theta\mathbf{oi}}\delta\mathbf{M}_{\mathbf{oi}} - \mathbf{\Phi}_{\theta}\delta\mathbf{T}_{\mathbf{p}} \end{aligned} \tag{B3}$$

$$\begin{aligned} m_p\bar{\mathbf{r}}'\delta\ddot{\mathbf{R}}_{\mathbf{no}} + [\mathbf{I}_{\mathbf{po}} - m_p\bar{\mathbf{r}}'\bar{\mathbf{R}}']\delta\ddot{\mathbf{a}}_{\mathbf{o}} + [\mathbf{I}_{\mathbf{po}}\mathbf{\Phi}^{\mathbf{T}}_{\theta} + m_p\bar{\mathbf{r}}'\bar{\mathbf{\Phi}}]\delta\ddot{\mathbf{q}} \\ + (\mathbf{I}_{\mathbf{po}} - m_p\bar{\mathbf{r}}'\bar{\mathbf{r}}')\bar{\mathbf{C}}^{\mathbf{T}}_{\mathbf{ep}}\delta\ddot{\mathbf{a}}_{\mathbf{p}} = \delta\mathbf{T}_{\mathbf{p}} \end{aligned} \tag{B4}$$

where:

$$\bar{\mathbf{r}}' = (\bar{\mathbf{C}}^{\mathbf{T}}_{\mathbf{ep}}\mathbf{r}_{\mathbf{p}\bullet})' \qquad \bar{\mathbf{R}}' = (\mathbf{R}'_{\mathbf{op}} + \bar{\mathbf{r}}') \qquad \bar{\mathbf{\Phi}} = (\mathbf{\Phi}^{\mathbf{T}}_{\mathbf{u}} - \bar{\mathbf{r}}'\mathbf{\Phi}^{\mathbf{T}}_{\theta}) \tag{B5}$$

A symmetric form of the equations of motion may now be obtained by removing $\delta\mathbf{T}_{\mathbf{p}}$ from equations (B2) and (B3) using (B4), yielding:

$$\begin{aligned} m_p\bar{\mathbf{R}}'\delta\ddot{\mathbf{R}}_{\mathbf{no}} + (\mathbf{I}_{\mathbf{o}} + \mathbf{I}_{\mathbf{po}} - m_p\bar{\mathbf{R}}'\bar{\mathbf{R}}')\delta\ddot{\mathbf{a}}_{\mathbf{o}} + (\mathbf{I}_{\mathbf{po}}\mathbf{\Phi}^{\mathbf{T}}_{\theta} + m_p\bar{\mathbf{R}}'\bar{\mathbf{\Phi}})\delta\ddot{\mathbf{q}} \\ + (\mathbf{I}_{\mathbf{po}} - m_p\bar{\mathbf{R}}'\bar{\mathbf{r}}')\bar{\mathbf{C}}^{\mathbf{T}}_{\mathbf{ep}}\delta\ddot{\mathbf{a}}_{\mathbf{p}} = \sum_{i=1}^{n_F}\mathbf{r}'_{\mathbf{oi}}\delta\mathbf{F}_{\mathbf{oi}} + \sum_{i=1}^{n_M}\delta\mathbf{M}_{\mathbf{oi}} \end{aligned} \tag{B6}$$

$$m_p\bar{\Phi}^{\mathbf{T}}\delta\ddot{\mathbf{R}}_{\mathbf{no}} + (\Phi_\theta \mathbf{I}_{\mathbf{po}} - m_p\bar{\Phi}^{\mathbf{T}}\bar{\mathbf{R}}')\delta\ddot{\mathbf{a}}_{\mathbf{o}} + (\mathbf{I}_{n\times n} + \Phi_\theta \mathbf{I}_{\mathbf{po}}\Phi_\theta^{\mathbf{T}} + m_p\bar{\Phi}^{\mathbf{T}}\bar{\Phi})\delta\ddot{\mathbf{q}}$$
$$+ (\Phi_\theta \mathbf{I}_{\mathbf{po}} - m_p\bar{\Phi}^{\mathbf{T}}\bar{\mathbf{r}}'\bar{\mathbf{C}}_{\mathbf{ep}}^{\mathbf{T}}\delta\ddot{\mathbf{a}}_{\mathbf{p}} = \sum_{i=1}^{n_F}\Phi_{\mathbf{uoi}}\delta\mathbf{F}_{\mathbf{oi}} + \sum_{i=1}^{n_M}\Phi_{\theta\mathbf{oi}}\delta\mathbf{M}_{\mathbf{oi}} \qquad (B7)$$

A matrix form of equations (B1, B6, B7, and B4) may be assembled as follows:

$$\mathbf{A}\delta\ddot{\eta} + \mathbf{B}\delta\dot{\eta} + \mathbf{C}\delta\eta = \mathbf{E}\delta\mathbf{u} \qquad (B8)$$

Here $\mathbf{A}$ is a (4×4) block matrix of overall dimension $(n + 9)$ square. Matrices $\mathbf{B}$ and $\mathbf{C}$ are essentially null except for n diagonal terms corresponding to the elastic motion. The vector $\delta\eta$ of system parameters is $(n + 9) \times 1$, and is given by:

$$\delta\eta = \delta(\mathbf{R}_{\mathbf{no}}^{\mathbf{T}}; \mathbf{a}_{\mathbf{o}}^{\mathbf{T}}; \mathbf{q}^{\mathbf{T}}; \mathbf{a}_{\mathbf{po}}^{\mathbf{T}})^{\mathbf{T}} \qquad (B9)$$

The transformed payload angles $\delta\mathbf{a}_{\mathbf{po}} = \bar{\mathbf{C}}_{\mathbf{ep}}^{\mathbf{T}}\delta\mathbf{a}_{\mathbf{p}}$ must appear in the vector of system parameters for symmetric equations to result. The vector of control inputs is:

$$\delta\mathbf{u} = (\delta\mathbf{F}_{\mathbf{o1}}^{\mathbf{T}}, \ldots, \delta\mathbf{F}_{\mathbf{on_F}}^{\mathbf{T}}; \delta\mathbf{M}_{\mathbf{o1}}^{\mathbf{T}}, \ldots, \delta\mathbf{M}_{\mathbf{on_M}}^{\mathbf{T}}; \delta\mathbf{T}_{\mathbf{p}}^{\mathbf{T}})^{\mathbf{T}} \qquad (B10)$$

The equations for an LFSP supporting multiple payloads will be given as obtained from the linearized equations (B1, B6, B7, and B4). Here a large flexible space platform described in part by n known elastic modes, is acted on by n_F external forces and n_M moments exclusive of the torques required to point the n_p payloads.

The equations of motion for multi-payload configurations may be written in the following form:

$$\mathbf{A}\delta\ddot{\eta} + \mathbf{B}\delta\dot{\eta} + \mathbf{C}\delta\eta = \mathbf{E}\delta\mathbf{u} \qquad (B11)$$

The vector $\delta\eta$ is dimensioned $(6 + n + 3n_p) \times 1$, and is given by:

$$\delta\eta = \delta(\mathbf{R}_{\mathbf{no}}^{\mathbf{T}}; \mathbf{a}_{\mathbf{o}}^{\mathbf{T}}; \mathbf{q}^{\mathbf{T}}; \mathbf{a}_{\mathbf{1o}}^{\mathbf{T}}, \ \ldots\ , \mathbf{a}_{\mathbf{n_po}}^{\mathbf{T}})^{\mathbf{T}} \qquad (B12)$$

The vector of force and moment inputs $\delta\mathbf{u}$ is dimensioned $(3n_F + 3n_M + 3n_p) \times 1$, and is written as follows:

$$\delta\mathbf{u} = \delta(\ \mathbf{F}_{\mathbf{o1}}, \ \ldots\ , \mathbf{F}_{\mathbf{on_F}};\ \mathbf{M}_{\mathbf{o1}}, \ \ldots\ , \mathbf{M}_{\mathbf{on_M}};\ \mathbf{T}_1, \ \ldots\ , \mathbf{T}_{n_p}\ ) \qquad (B13)$$

where $\delta\mathbf{F}_{\mathbf{oi}}$, $\delta\mathbf{M}_{\mathbf{oi}}$, and $\delta\mathbf{T}_{\mathbf{i}}$ are external LFSP forces and moments, and payload gimbal torques, respectively.

The coefficient matrices **A**, **B**, and **C**, dimensioned $(6+n+3n_p)$ square, and **E**, dimensioned $(6+n+3n_p) \times (3n_F+3n_M+3n_p)$, are given below. Matrix **A** is essentially a "mass/inertia" matrix given by:

$$\mathbf{A} = \begin{bmatrix} \mathbf{A_{1[(6+n)\times(6+n)]}} & \mathbf{A_{2[(6+n)\times 3n_p]}} \\ \mathbf{A_{3[3n_p\times(6+n)]}} & \mathbf{A_{4(3n_p\times 3n_p)}} \end{bmatrix} \tag{B14}$$

The blocks comprising matrix **A** are:

$$\mathbf{A_1} = \begin{bmatrix} \left(m_o + \sum_{i=1}^{n_p} m_i\right)\mathbf{I_{3\times 3}} & -\sum_{i=1}^{n_p} m_i \bar{\mathbf{R}}_i' & \sum_{i=1}^{n_p} m_i \bar{\mathbf{\Phi}}_i \\ \sum_{i=1}^{n_p} m_i \bar{\mathbf{R}}_i' & \mathbf{I_o} - \sum_{i=1}^{n_p} \left(\mathbf{I_{io}} - m_i \bar{\mathbf{R}}_i' \bar{\mathbf{R}}_i'\right) & \sum_{i=1}^{n_p} \left(\mathbf{I_{io}} + m_i \bar{\mathbf{R}}_i' \bar{\mathbf{\Phi}}_i\right) \\ \sum_{i=1}^{n_p} m_i \bar{\mathbf{\Phi}}_i^{\mathbf{T}} & -\sum_{i=1}^{n_p} \left(\mathbf{\Phi}_{\theta i}\mathbf{I_{io}} - m_i \bar{\mathbf{\Phi}}_i^{\mathbf{T}} \bar{\mathbf{R}}_i'\right) & \mathbf{I_{n\times n}} + \sum_{i=1}^{n_p} \mathbf{\Phi}_{\theta i}\mathbf{I_{io}}\mathbf{\Phi}_{\theta i}^{\mathbf{T}} \\ & & + \sum_{i=1}^{n_p} m_i \bar{\mathbf{\Phi}}_i^{\mathbf{T}} \bar{\mathbf{\Phi}}_i \end{bmatrix} \tag{B15a}$$

$$\mathbf{A_2} = \begin{bmatrix} -m_1 \bar{\mathbf{r}}_1' & \cdots & -m_{n_p} \bar{\mathbf{r}}_{n_p}' \\ \mathbf{I_{1o}} - m_1 \bar{\mathbf{R}}_1' \bar{\mathbf{r}}_1' & \cdots & \mathbf{I_{n_p o}} - m_{n_p} \bar{\mathbf{R}}_{n_p}' \bar{\mathbf{r}}_{n_p}' \\ \mathbf{\Phi}_{\theta 1}\mathbf{I_{1o}} - m_1 \bar{\mathbf{\Phi}}_1^{\mathbf{T}} \bar{\mathbf{r}}_1' & \cdots & \mathbf{\Phi}_{\theta n_p}\mathbf{I_{n_p o}} - m_{n_p} \bar{\mathbf{\Phi}}_{n_p}^{\mathbf{T}} \bar{\mathbf{r}}_{n_p}' \end{bmatrix} \tag{B15b}$$

$$\mathbf{A_3} = \begin{bmatrix} m_1 \bar{\mathbf{r}}_1' & \mathbf{I_{1o}} - m_1 \bar{\mathbf{r}}_1' \bar{\mathbf{R}}_1' & \mathbf{I_{1o}}\mathbf{\Phi}_{\theta 1}^{\mathbf{T}} + m_1 \bar{\mathbf{r}}_1' \bar{\mathbf{\Phi}}_1 \\ \vdots & \vdots & \vdots \\ m_{n_p} \bar{\mathbf{r}}_{n_p}' & \mathbf{I_{n_p o}} - m_{n_p} \bar{\mathbf{r}}_{n_p}' \bar{\mathbf{R}}_{n_p}' & \mathbf{I_{n_p o}}\mathbf{\Phi}_{\theta n_p}^{\mathbf{T}} + m_{n_p} \bar{\mathbf{r}}_{n_p}' \bar{\mathbf{\Phi}}_{n_p} \end{bmatrix} \tag{B15c}$$

$$\mathbf{A_4} = \begin{bmatrix} \mathbf{I_{1o}} - m_1 \bar{\mathbf{r}}_1' \bar{\mathbf{r}}_1' & \cdots & \mathbf{0_{3\times 3}} \\ \vdots & \ddots & \vdots \\ \mathbf{0_{3\times 3}} & \cdots & \mathbf{I_{n_p o}} - m_{n_p} \bar{\mathbf{r}}_{n_p}' \bar{\mathbf{r}}_{n_p}' \end{bmatrix} \tag{B15d}$$

where:

$$\bar{\mathbf{r}}_i' = (\mathbf{C}_{ei}^{\mathbf{T}} \mathbf{r}_{i\bullet})' \qquad \bar{\mathbf{R}}_i' = (\mathbf{R}_{oi}' + \bar{\mathbf{r}}_i') \qquad \bar{\mathbf{\Phi}}_i = (\mathbf{\Phi}_{ui}^{\mathbf{T}} - \bar{\mathbf{r}}_i' \mathbf{\Phi}_{\theta i}^{\mathbf{T}}) \tag{B16}$$

Matrices $\mathbf{B}$ and $\mathbf{C}$ are for the most part null except for diagonal blocks multiplying the n modal coordinates. $\mathbf{B}$ and $\mathbf{C}$ are then modal damping and modal stiffness matrices written as:

$$\begin{aligned} \mathbf{B} &= \text{diag}[\mathbf{0}_{(6\times6)},\ \mathbf{D}_{(n\times n)},\ \mathbf{0}_{(3n_p\times 3n_p)}] \\ \mathbf{C} &= \text{diag}[\mathbf{0}_{(6\times6)},\ \mathbf{\Lambda}_{(n\times n)},\ \mathbf{0}_{(3n_p\times 3n_p)}] \end{aligned} \tag{B17}$$

where:

$$\begin{aligned} \mathbf{D} &= [\text{diag}(2\zeta_i\omega_i)]_{(n\times n)} \\ \mathbf{\Lambda} &= [\text{diag}(\omega_i^2)]_{(n\times n)} \end{aligned} \tag{B18}$$

The coefficient matrix $\mathbf{E}$ is written as:

$$\mathbf{E} = \begin{bmatrix} \mathbf{E}_{1[(6+n)\times 3n_F]} & \mathbf{E}_{2[(6+n)\times 3n_M]} & \mathbf{0}_{[(6+n)\times 3n_p]} \\ \mathbf{0}_{(3n_p\times 3n_F)} & \mathbf{0}_{(3n_p\times 3n_M)} & \mathbf{I}_{(3n_p\times 3n_p)} \end{bmatrix} \tag{B19}$$

where $\mathbf{E_1}$ and $\mathbf{E_2}$ are given by:

$$\mathbf{E_1} = \begin{bmatrix} \mathbf{I_{3\times3}} & \cdots & \mathbf{I_{3\times3}} \\ \mathbf{r'_{o1}} & \cdots & \mathbf{r'_{on_F}} \\ \mathbf{\Phi_{uo1}} & \cdots & \mathbf{\Phi_{uon_F}} \end{bmatrix},\quad \mathbf{E_2} = \begin{bmatrix} \mathbf{0_{3\times3}} & \cdots & \mathbf{0_{3\times3}} \\ \mathbf{I_{3\times3}} & \cdots & \mathbf{I_{3\times3}} \\ \mathbf{\Phi_{\theta o1}} & \cdots & \mathbf{\Phi_{\theta on_M}} \end{bmatrix} \tag{B20}$$

DETECTION OF POTENTIAL SPACE STATION*CONTROL/STRUCTURE INTERACTION WITH CO-ST-IN

Kelly Carney
Ron Graham
Doug Kyr
NASA Lewis Research Center
Cleveland, Ohio

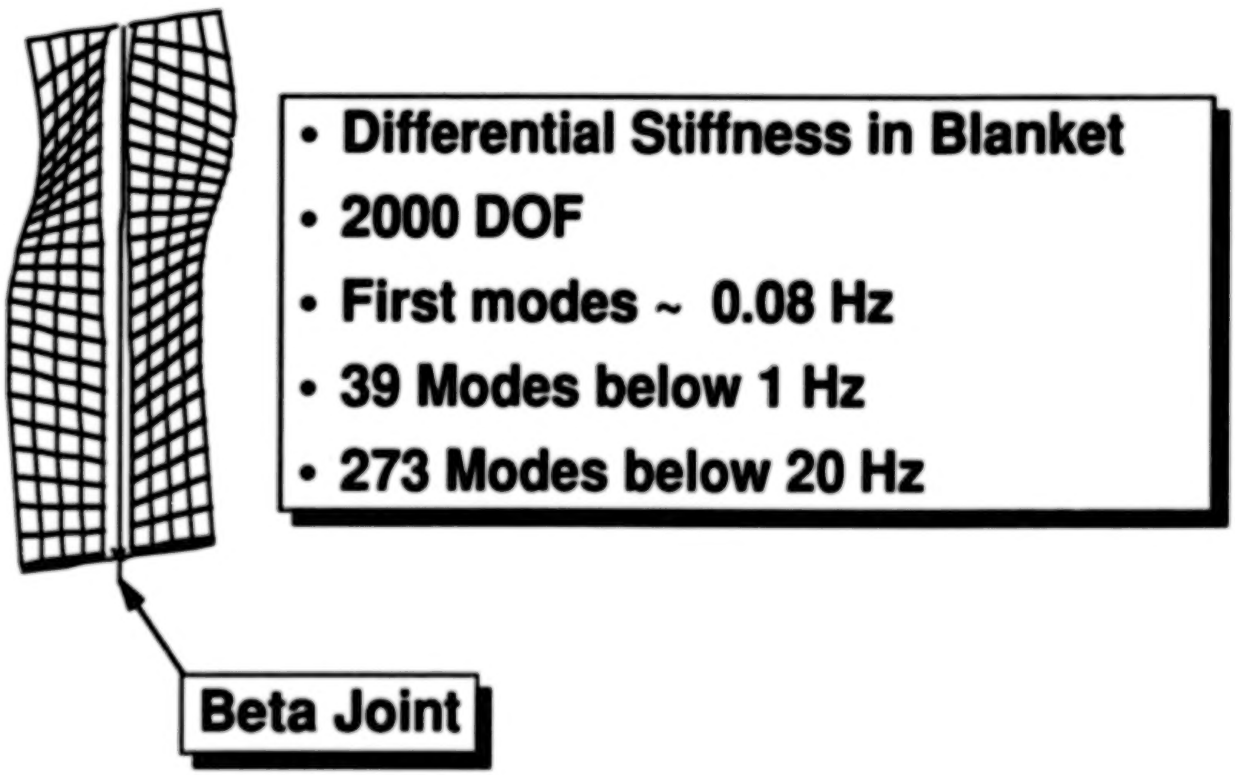
Paul Blelloch
SDRC WRO
San Diego, California

3rd Annual NASA/DoD CSI Conference
January 29 - February 2, 1989

*Space Station Freedom

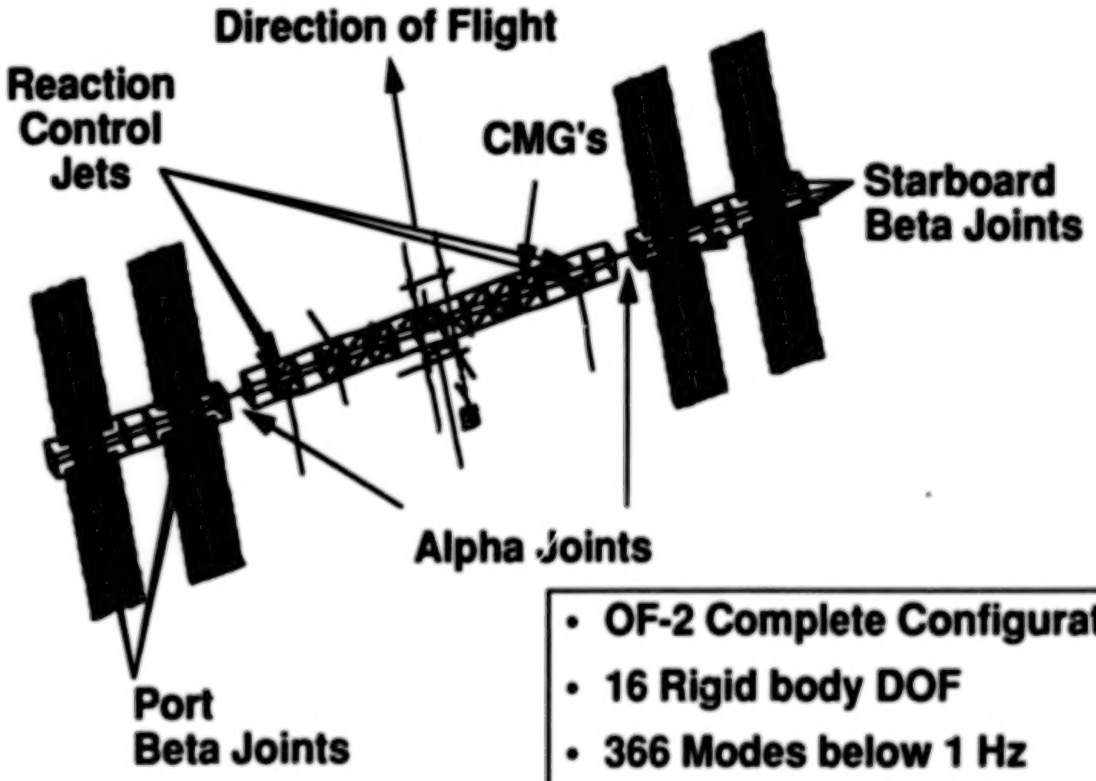
SOLAR POWER PROVIDED BY EIGHT PV ARRAYS

The electrical power for Space Station Freedom is generated by eight large photovoltaic (PV) arrays. Lockheed Missiles and Space Company's proposal defines an array which is 113.7 feet long and 33.8 feet wide, and weighs about 1,200 lbs. The eight solar arrays represent a significant portion of the structural weight and inertia of the Space Station outboard of the central modules. A detailed finite element model of the array was generated using 2,000 degrees of freedom (DOF). The array's stiffness is partially created by stretching the photovoltaic cell substrate using a differential stiffness method. The verification of the method to analyze the differential stiffness effect will be presented at the AIAA SDM conference in April. The predicted array first bending and first torsion mode frequencies are both at approximately 0.08 Hz. Each solar array has 39 modes of vibration under 1 Hz and 273 modes of vibration under 20 Hz.



OVERALL SPACE STATION MODEL IS VERY LARGE

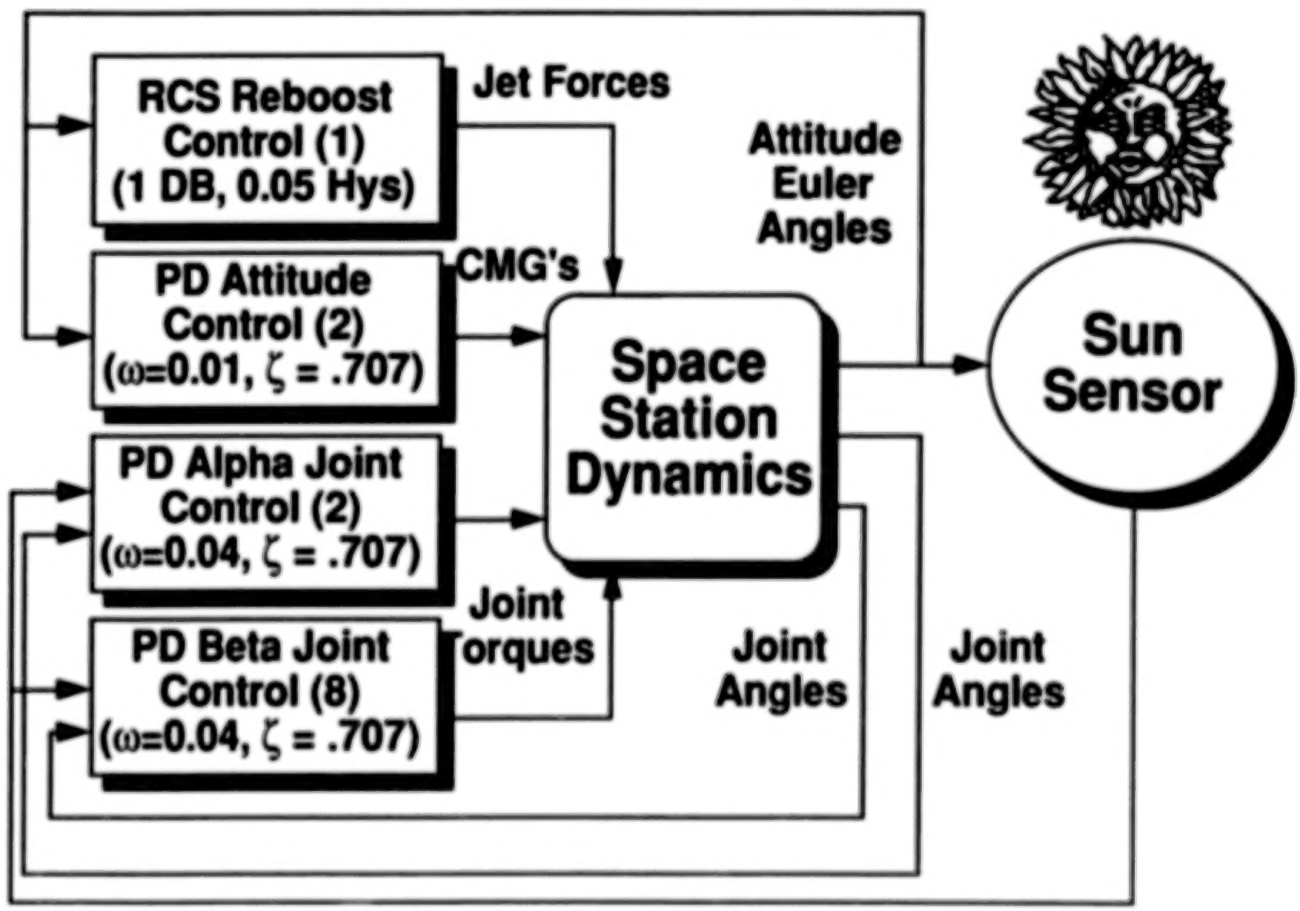
A Craig-Bampton dynamic component model of the photovoltaic array was formed as described in the previous slide, duplicated eight times and coupled to the overall Space Station model. The Space Station model used was the Microgravity Study, OF-2, assembly complete configuration. A finite element model of the beta joint was also created and included in the synthesized station model. Both the alpha joint and the beta joint were freed to rotate when system modes were generated, resulting in sixteen rigid body modes. There are a total of 366 normal modes under 1 Hz. Without any further model reduction at the component level, we would expect to find between 3,000 and 4,000 modes below 20 Hz. A modal ordering algorithm, described later, was used to select 99 modes of the 366 below 1 Hz for the controls analysis.



- OF-2 Complete Configuration
- 16 Rigid body DOF
- 366 Modes below 1 Hz
- 99 Modes selected for analysis
- 3000-4000 Modes below 20 Hz

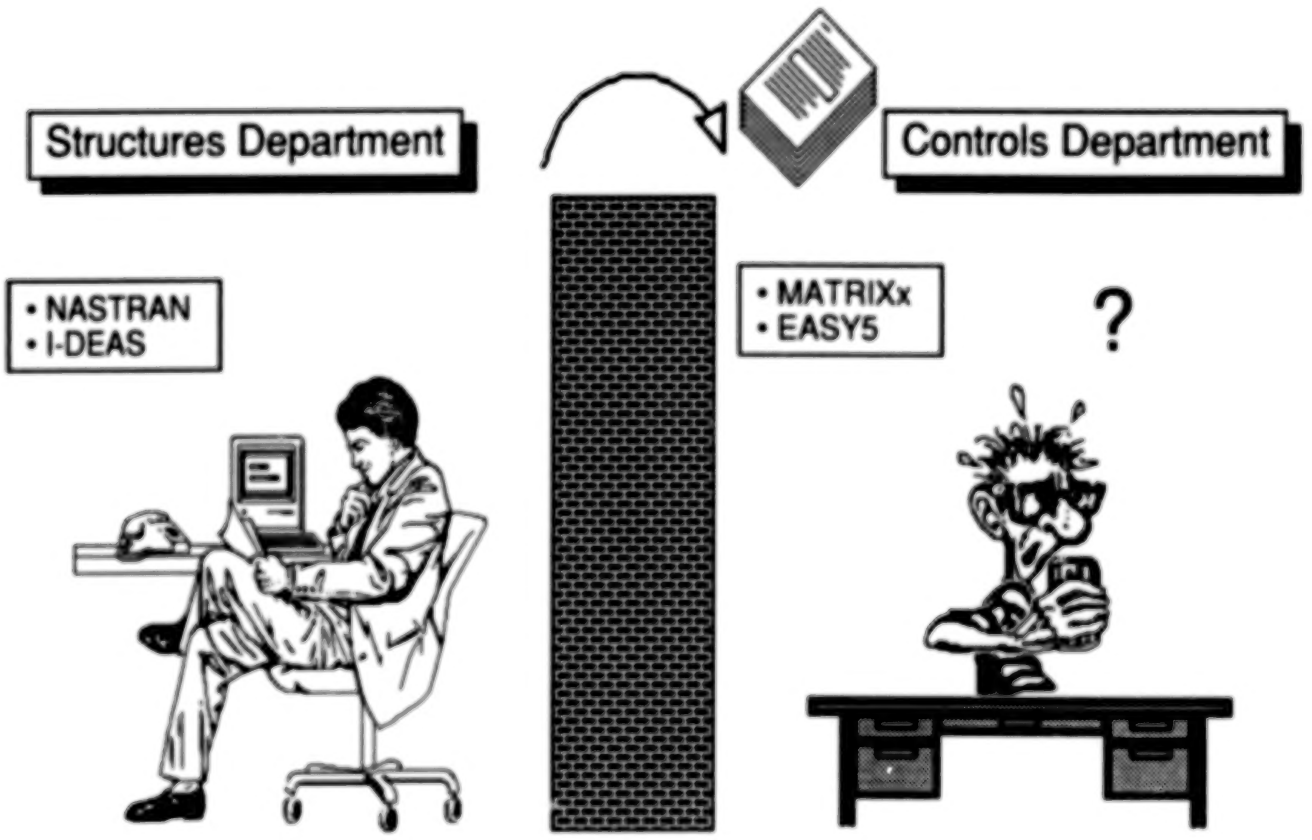
FOUR CONTROL SYSTEMS SIMULATED

Four control systems were simulated for this initial study. The first is three axis Proportional-plus-Derivative (PD) attitude control. Variations from commanded attitude are sensed at an avionics platform co-located with the Control-Moment-Gyros (CMG's) which apply a restoring torque to the Station. Control gains are chosen to result in control frequencies of 0.01 Hz and damping ratios of 0.707 about each axis. The second control system is a simplified model of the Reaction Control System (RCS) during reboost. In this model the RCS accelerates the station in the direction of flight (x) and controls attitude in pitch (θ_y) only. The pitch axis PD controller is deactivated during reboost, though roll and yaw controllers reamin active. The jet firing logic is based on a deadband of 1.0° and a hysteresis of 0.05°, where the error signal is the sum of the pitch rotation and rotational velocity. The final two control systems control the two alpha joints and the eight beta joints. These are PD controllers with control frequencies of 0.04 Hz and damping ratios of 0.707. The rotation of both the alpha and beta joints is commanded by a sun-sensor mounted on the avionics platform, resulting in a co-located inner loop, but a non co-located outer loop.



CONVENTIONAL APPROACH: MANUAL TRANSFER OF DATA

The conventional approach for control/structure interaction studies is undertaken by two separate departments. A finite element model is typically developed by a structures department and solved for some number of normal modes. Some subsets of these modes are then transferred (often manually) to a controls department where they are used to develop a structural dynamic model which is coupled to control systems for analysis. If structural loads are required, input forces are usually extracted from the coupled analysis and returned to the structures department which runs through a load cycle. Even if we side step the issue of developing truly coupled software to perform both the structural and control system analyses, a number of issues remain in the transfer of data between structural dynamic and control system analysis software. The emphasis of our development efforts at the NASA Lewis Research Center have been to retain current software tools in each of the two disciplines (MSC/NASTRAN for structural dynamics and BCS/EASY5 for control system analysis), while carefully examining the issue of data transfer.

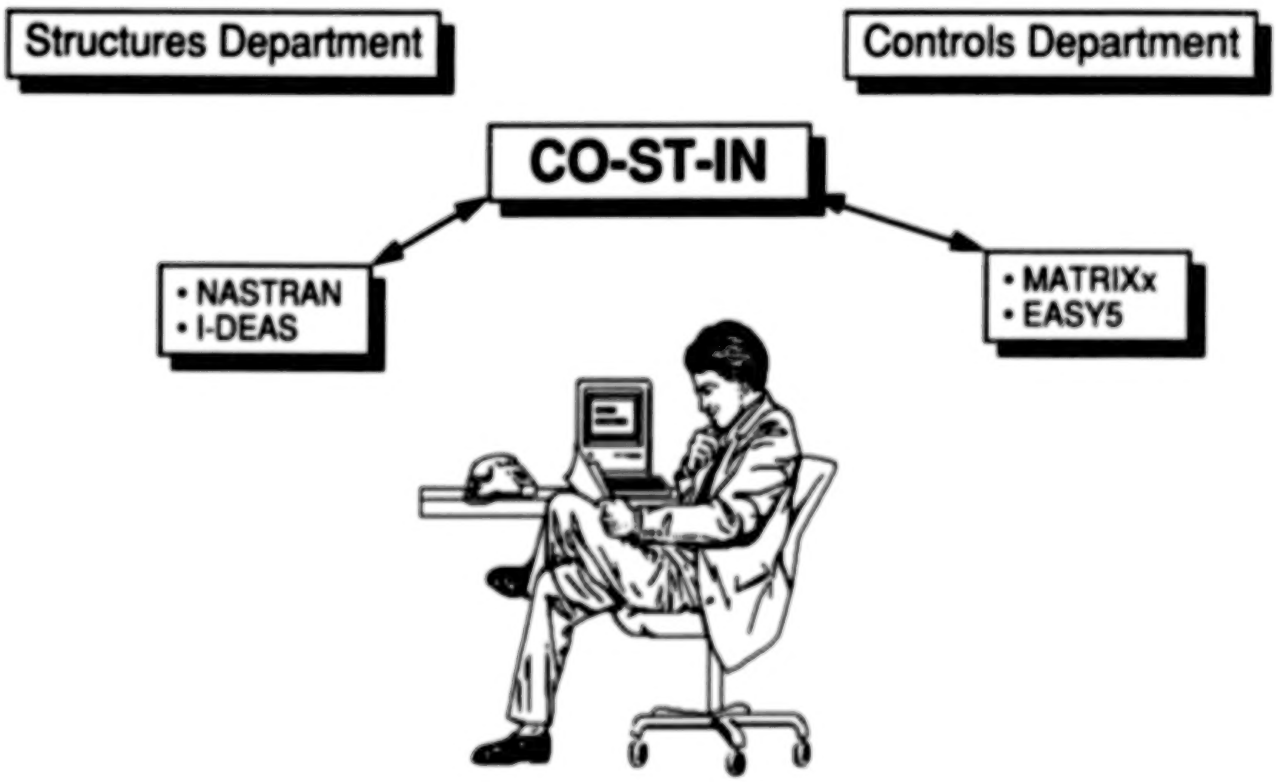


AUTOMATED APPROACH UNIFIES PROBLEM

The outcome of this development has been a software program called CO-ST-IN (COntrol-STructure-INteraction). The structural model is still developed and solved in MSC/NASTRAN, while control system analyses are performed in BCS/EASY5. CO-ST-IN simply acts to transfer data between the two programs, provided an efficient platform for coupled analyses. The emphasis in developing CO-ST-IN has been on the type of data to be transferred and how best to do this transfer. Some of the issues which we have considered are listed below:

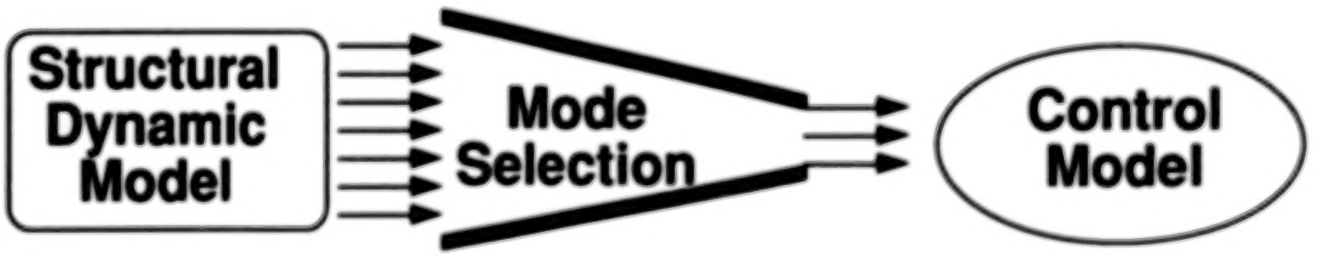
- Modal selection as a method of model reduction.
- Most efficient methods for recovering accurate internal loads and stresses.
- Alternate modal representations resulting in more accurate closed-loop models using fewer modes.

Each of these is discussed in greater detail in following slides.



MODAL ORDERING REDUCES MODEL SIZE

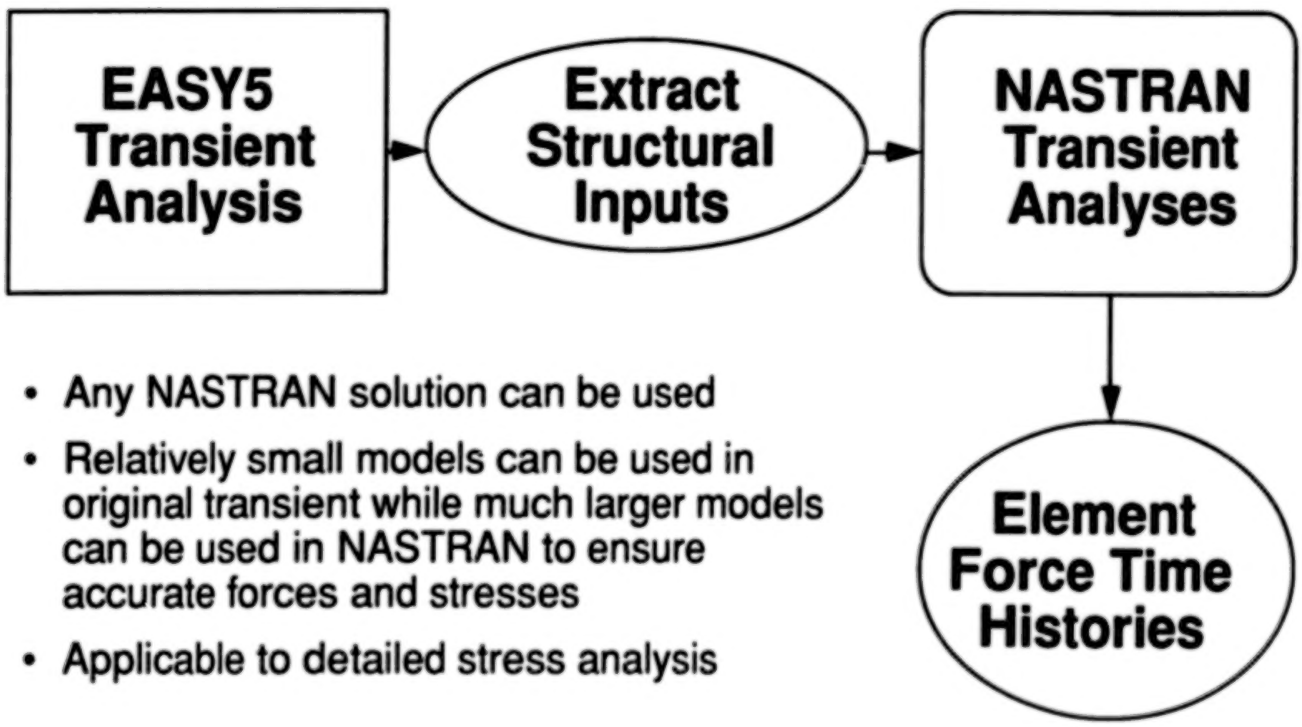
One of the largest discrepancies between typical structural dynamic and control system models is model size. The Phase I Space Station model presented here, for instance, has 366 modes below Hz. While this model can be handled effectively using structural dynamic software such as MSC/NASTRAN, it is too large for effective control system analysis using currently available software. While many methods of model reduction can be found in the literature, most methods based on state-space representations (such as internal balancing, component cost analysis and optimal Hankel-norm approximations) reduce to modal selection under the assumptions of light damping and sufficiently separated frequencies. This suggests that modal selection provides an especially powerful method of model reduction for lightly damped flexible structures. CO-ST-IN implements three algorithms in order to select modes. The first is approximate balanced singular value based on Moore's internal balancing, the second is the modal cost based on Skelton's component cost analysis and the final algorithm measures each mode's contribution to the static deflection of the structure. In order to implement meaningful modal selection algorithms we have found it essential to be able to group modes with equal or nearly equal frequencies and also to scale inputs and outputs so as to reflect their relative importance.



- Three algorithms used:
  - (1) Approximate Balanced Singular Values
  - (2) Modal Cost
  - (3) Contribution to Static Deflection
- Modes grouped by frequency
- Inputs and outputs scaled to reflect relative importance

CONVENTIONAL INTERNAL LOADS AND STRESSES CALCULATION

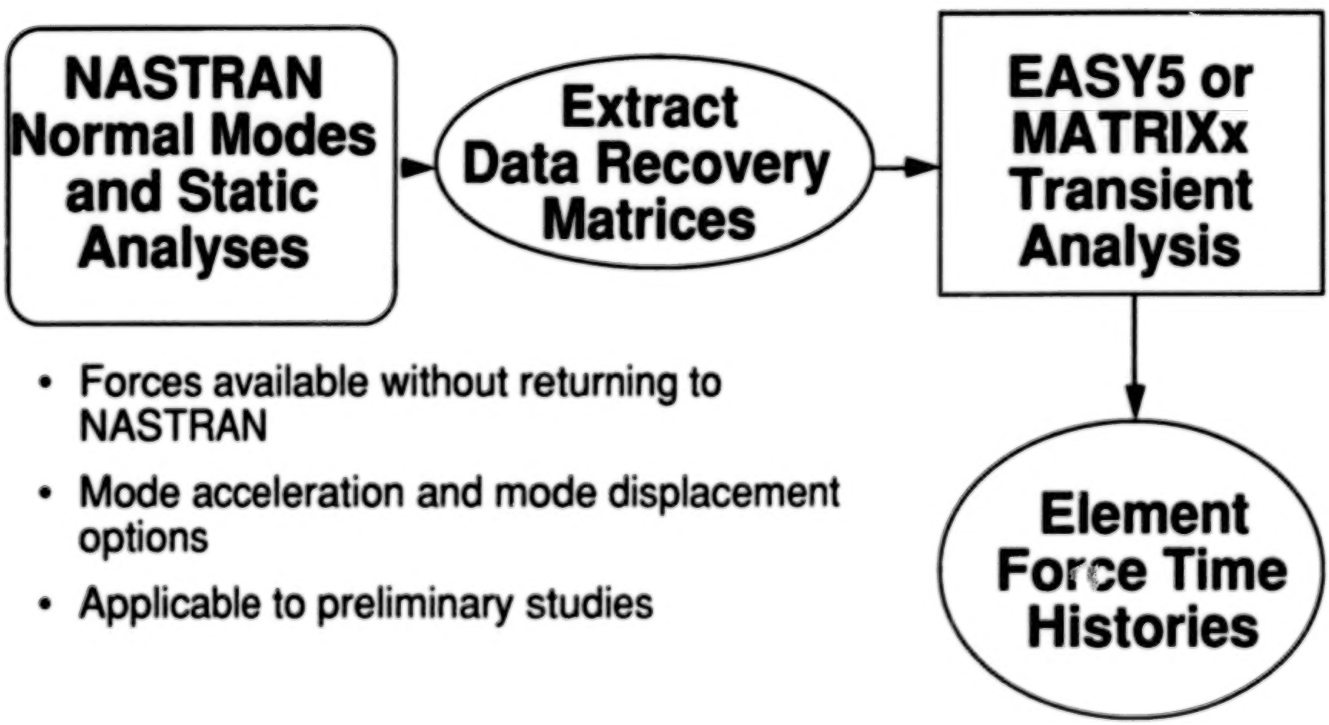
The conventional method for recovering internal loads and stresses is to extract structural input loads from the coupled control system simulation and apply these to the structural dynamic model. This approach offers a number of advantages when compared to methods which depend on the number of modes represented in the coupled simulation. The first is that structural dynamic software such as MSC/NASTRAN can effectively handle very large amounts of data, and structural engineers have the tools and expertise to reduce this data. A more fundamental advantage is that the number of modes used in the coupled simulation must only be large enough to calculate accurate input loads, but this is typically much smaller than the number of modes required to calculate accurate internal loads and stresses. This approach then allows the analyst to choose the model size which is most appropriate for each analysis, thereby greatly reducing the number of modes required in the control analysis. CO-ST-IN facilitates the implementation of this conventional approach by searching EASY5 output data for structural inputs and writing these as dynamic input data for NASTRAN.



- Any NASTRAN solution can be used
- Relatively small models can be used in original transient while much larger models can be used in NASTRAN to ensure accurate forces and stresses
- Applicable to detailed stress analysis

INTERNAL FORCES AND STRESSES CALCULATED IN CONTROL SIMULATION

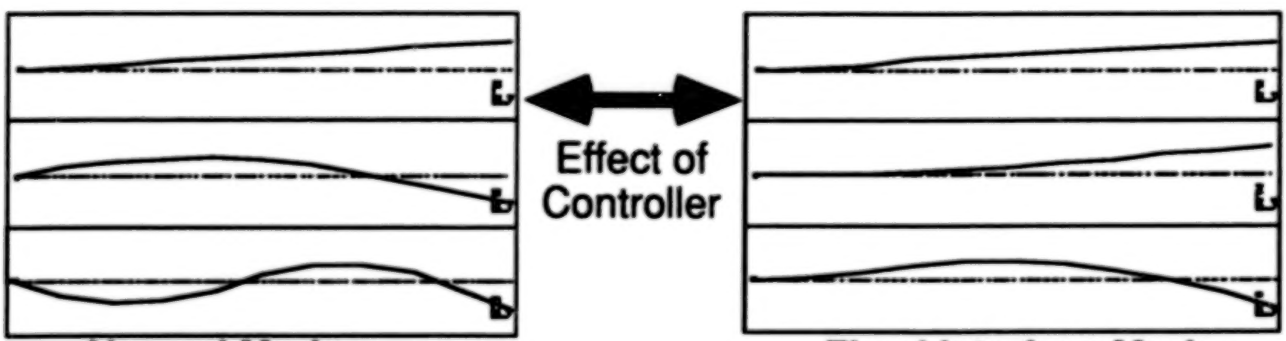
While the conventional approach described in the previous slide can be very powerful, it can also be somewhat cumbersome in situations where a quick turnaround of results is desired. This is because it is necessary to transfer loads back to the structural dynamic model after each dynamic simulation. Turnaround time for the analyses can be greatly reduced by extracting "data recovery matrices" from the structural dynamic routine and using these to calculate internal loads and stresses directly during the coupled simulations. Data recovery matrices are used by the structural dynamic routine to calculate internal loads and stresses given information on the modal displacements and additionally the input loads if a mode acceleration method is used. CO-ST-IN allows the user to extract these matrices from MSC/NASTRAN and transfer them to EASY5. Either the mode displacement or the mode acceleration methods can be used. The mode acceleration method adds a static correction (direct feedthrough) term to modal data, resulting in improved accuracy with a given number of modes. The mode acceleration method is particularly recommended in this case since the number of modes in the coupled analysis is typically limited.



- Forces available without returning to NASTRAN
- Mode acceleration and mode displacement options
- Applicable to preliminary studies

FIXED INTERFACE REPRESENTATIONS CAN BE MORE ACCURATE

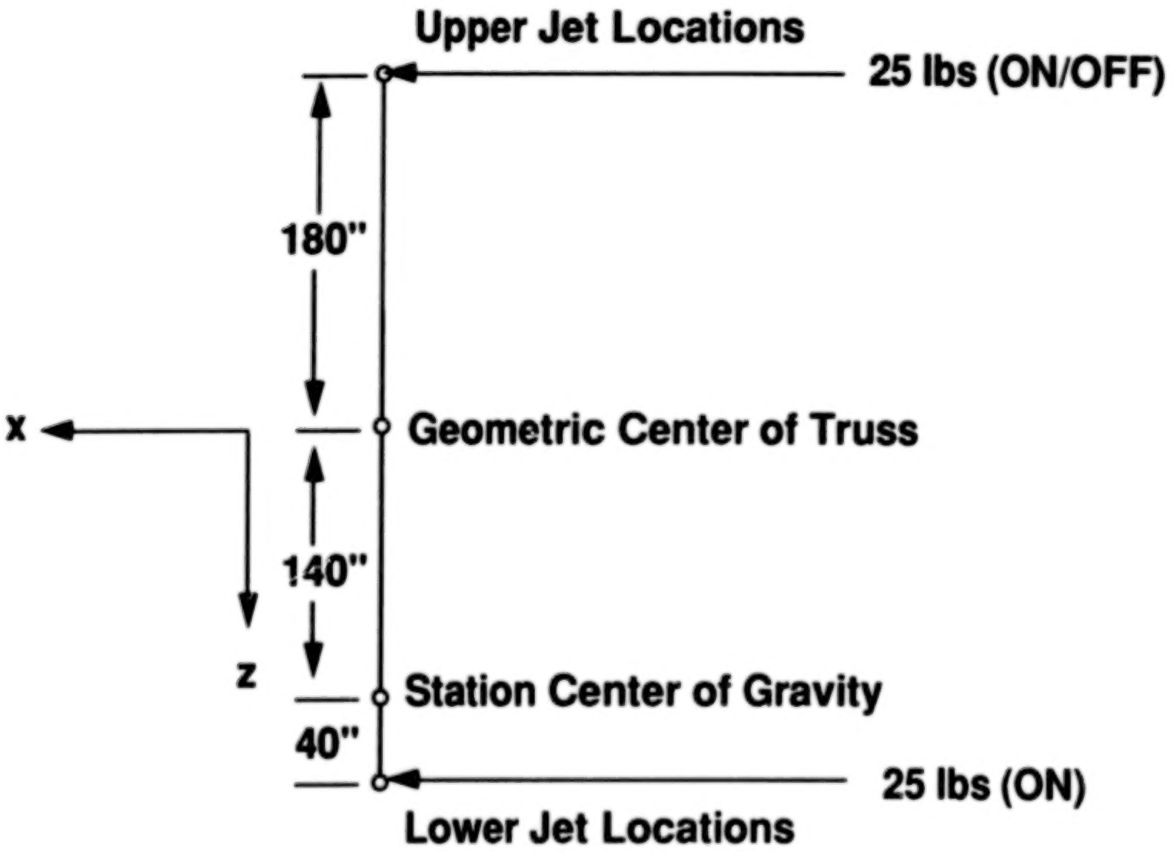
While the use of normal modes as a structural representation offers a number of advantages, these modes are calculated with all controlled DOF (i.e., DOF at which control actuators apply forces and moments) left free. This implies, in some cases, that a large number of modal DOF may be required in order to calculate an accurate closed-loop model. One method for circumventing this problem is to use a Craig-Bampton representation, based on the calculation of modes with controlled DOF held fixed. The actual effect of the controller lies somewhere between these two extremes, but we have found that even with relatively soft controllers, the Craig-Bampton representation results in more accurate closed-loop models. We have developed a simple procedure for calculating and extracting Craig-Bampton models using MSC/NASTRAN's superelement capability. Since we only transfer modal data, many of the advantages of the normal modes representation are retained.



- Fixed Interface Modes result in more accurate closed-loop poles and closed-loop frequency response when sensors and actuators are collocated.
- The improvement is large for "stiff" controllers, but still exists for "soft" controllers
- Fixed Interface Modes Result in Off-Diagonal Mass Terms
- Fixed Interface Representations are simple to calculate in MSC/NASTRAN and only normal mode data need to be transfered

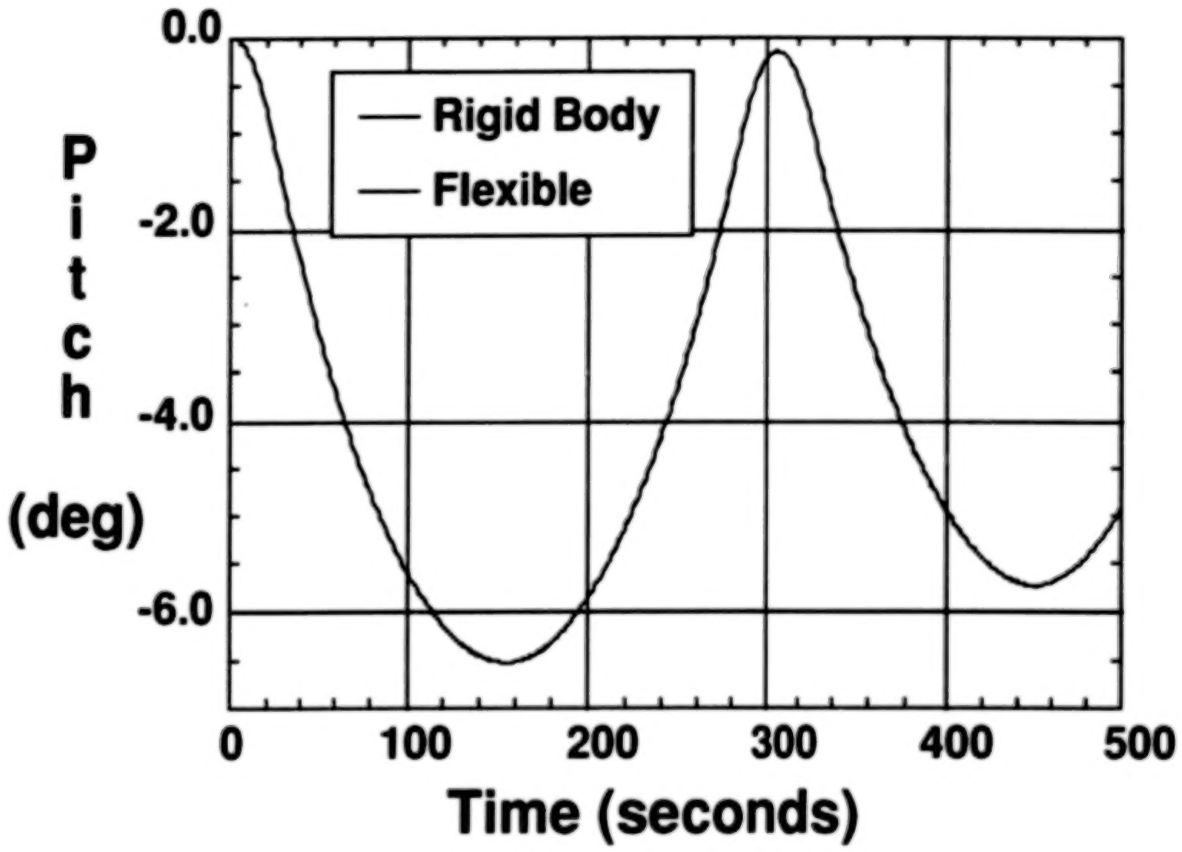
REBOOST JETS USED FOR PITCH CONTROL

We examined the response of the Space Station during a reboost maneuver where the Station is accelerated in the direction of flight (x-axis). In this case roll and yaw attitude are controlled by CMG's, while pitch is controlled by the four reboost jets, each firing with a force of 25 lbs. Because the module cluster lies below the boom, the Station center of mass is approximately 140" below the center of boom, so with all four jets firing the top of the station pitches forward. The pitch angle plus a rate gain times the pitch rate is fed back to the Reaction Control System (RCS). Once this error signal exceeds the deadband plus hysteresis the upper jets turn off and the Station rotates back until the error drops below the deadband at which time the upper jets switch back on and the procedure is repeated. Since the moment arm with all four jets firing is much larger than with only the lower jets firing, the station will initially exhibit a large overshoot as the lower jets turn it back around. This overshoot can be reduced by increasing the rate gain which adds an effective lead compensation to the control system.



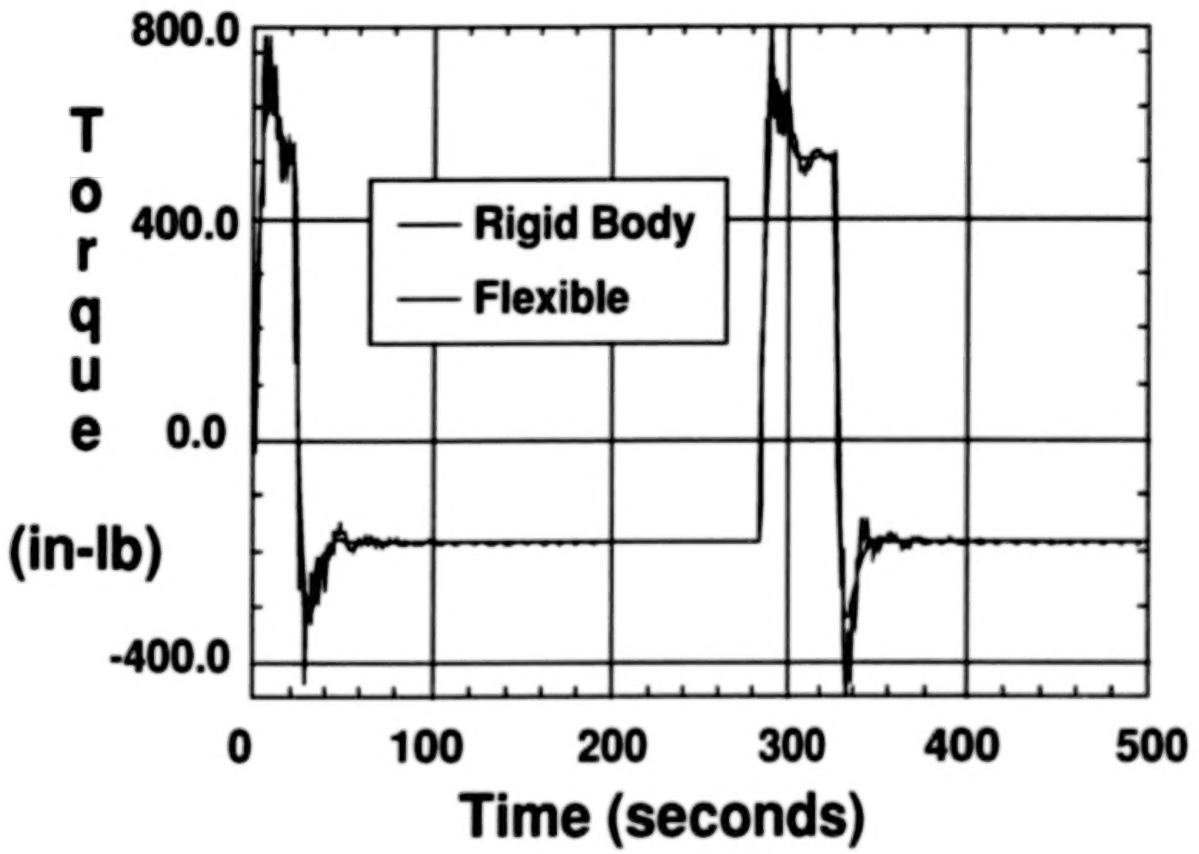
STATION PITCH RESPONSE TO REBOOST
(Rate Gain = 1.0, Hysteresis = 0.05°)

With a rate gain of 1.0, a deadband of 1° and hysteresis of 0.05°, the pitch response exhibits an initial transient with an 500% overshoot and it does not settle into a steady state limit cycle within the 500 second simulation. This is a relatively benign excitation from a structural point of view and the effect of flexible modes on the pitch response is very small.



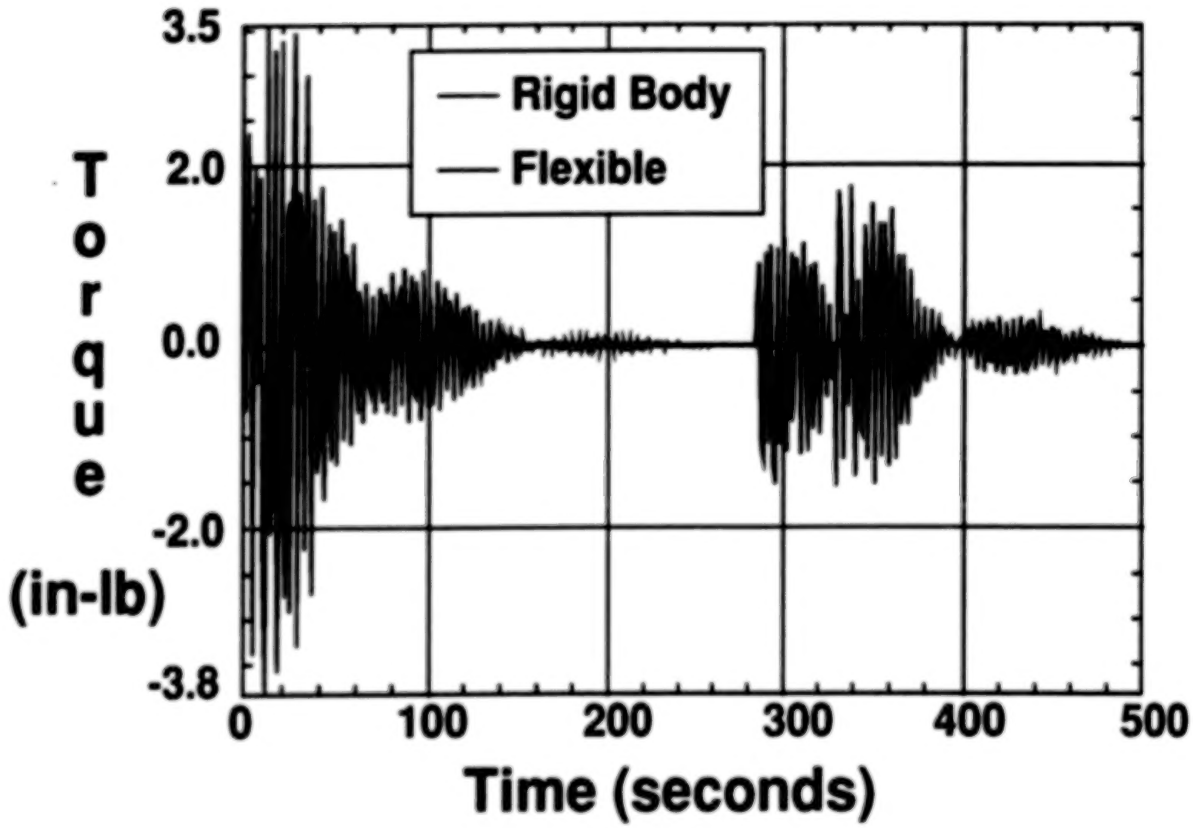
ALPHA JOINT TORQUE RESPONSE TO REBOOST
(Rate Gain = 1.0, Hysteresis = 0.05°)

One way to examine the model for potential control/structure interaction is to compare the response of control systems with and without the presence of flexible modes. In this case we examine the response of the alpha joint controllers which are acting to maintain the relative rotation at the alpha joints. The response with and without flexible modes is very similar, though the effect of flexible motion is clearly visible. Even with this relatively benign excitation, the structural dynamic response of the station outboard of the alpha joints will vary depending on whether it is excited by the forces calculated with flexible modes or those calculated with rigid body modes only.



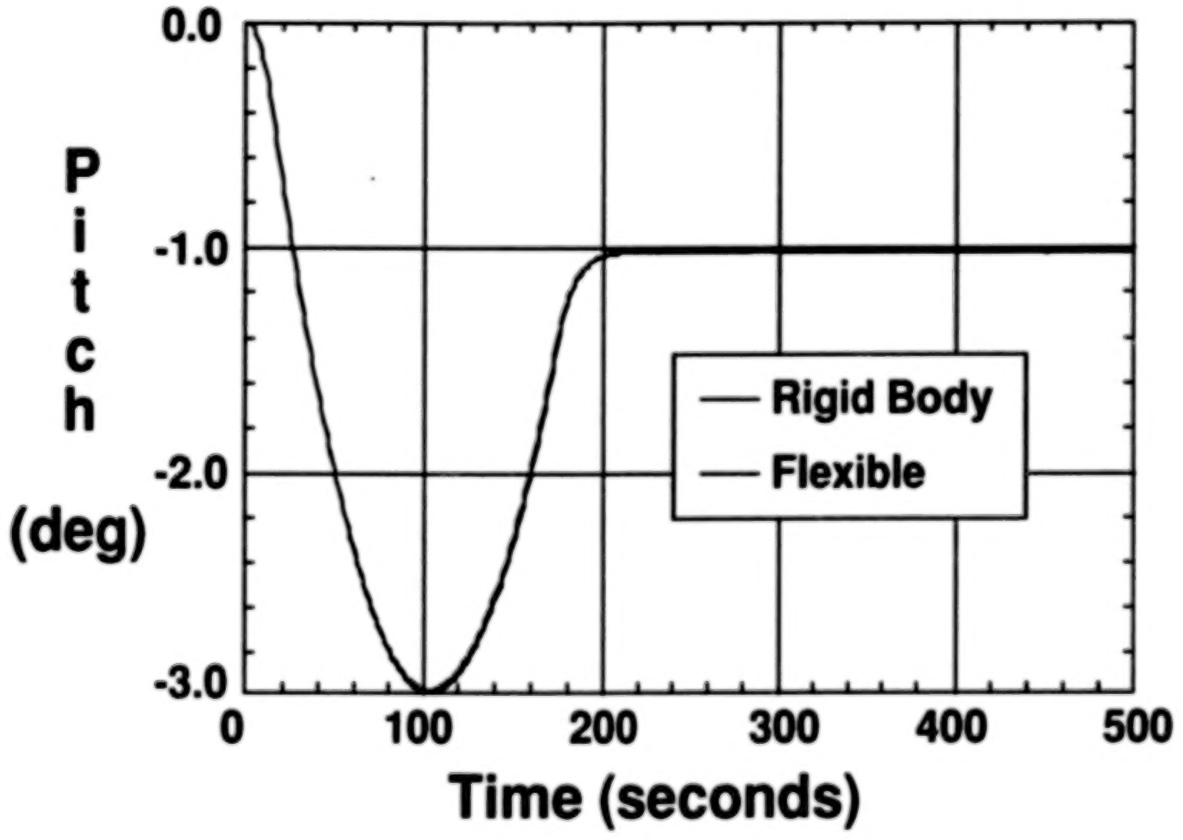
BETA JOINT TORQUE RESPONSE TO REBOOST
(Rate Gain = 1.0, Hysteresis = 0.05°)

While the alpha joints are strongly excited by the rigid body pitching of the Space Station, the beta joints are not. The response of the beta joint controllers to RCS jet firing is essentially zero with rigid body modes only, but increases to peak of near 4 in-lbs with the addition of flexible modes. While this is still a small response it does illustrate the effect of flexible modes.



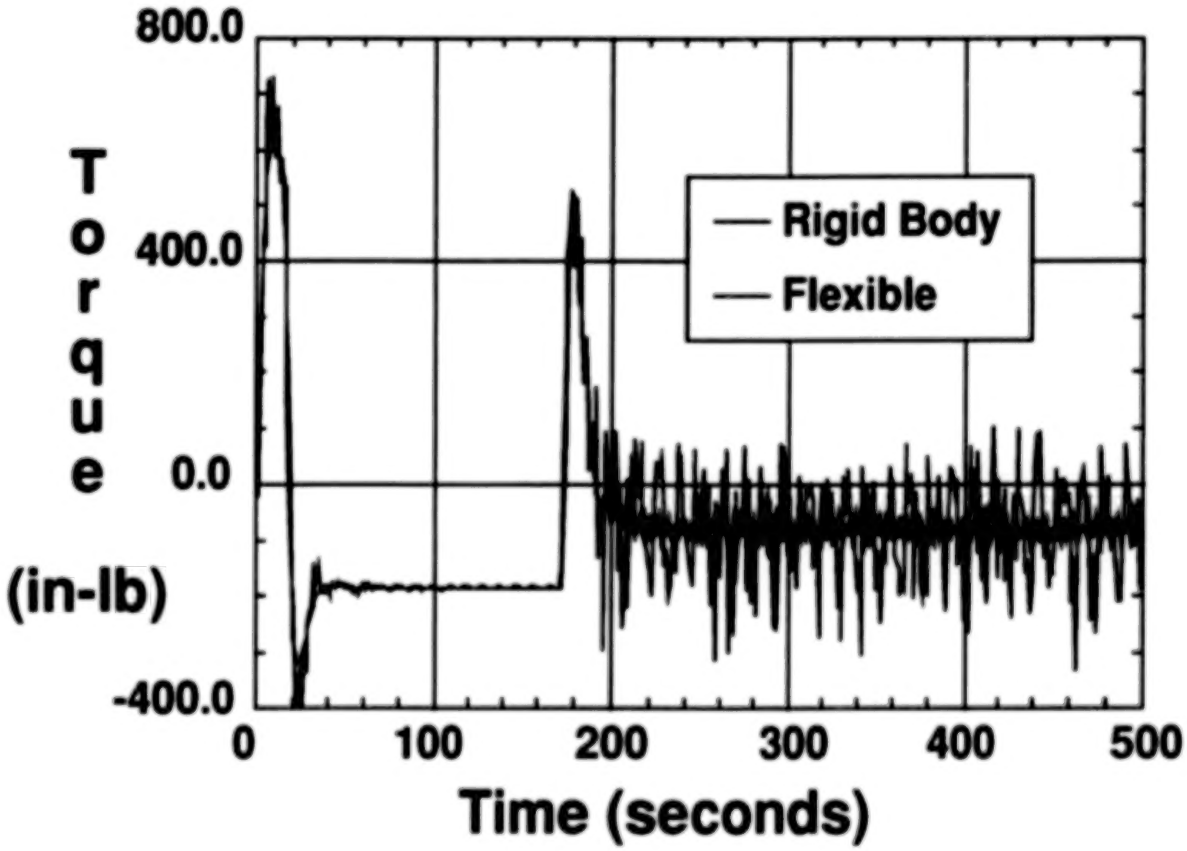
STATION PITCH RESPONSE TO REBOOST
(Rate Gain = 10.0, Hysteresis = 0.01°)

Now consider a variation in the control parameters to improve rigid body response. Increasing the rate gain reduces overshoot, while decreasing the hysteresis reduces the effect of limit cycling. As expected the response does improve. The overshoot is reduced to 200% and the pitch angle attains a constant steady state value after the initial 200 second transient. The response with flexible modes is offset slightly, though it is still very similar. The cost paid for the improved performance is that the upper RCS jets are now switching on and off at a much higher rate, possibly reducing efficiency and increasing the potential for excitation of structural modes.



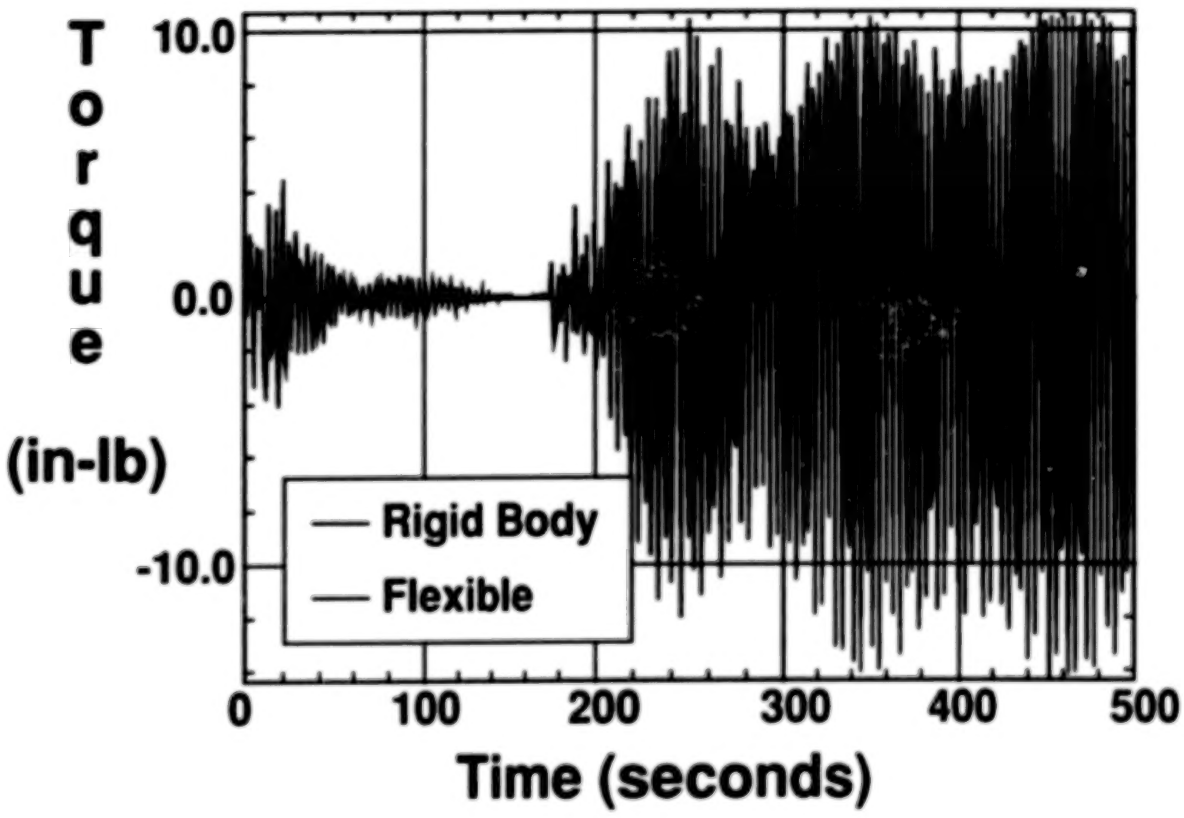
ALPHA JOINT TORQUE RESPONSE TO REBOOST
(Rate Gain = 10.0, Hysteresis = 0.01°)

Once again examine the torque response of the alpha joint controllers in order to identify any potential for control/structure interaction. In this case the rigid body response of the alpha joints undergoes two initial transients and then settles close to a steady state value. The flexible response follows a similar pattern, but the peak moments generated during the initial transient are significantly higher and the amplitude of the steady state response is close to an order of magnitude higher than with rigid body modes only. It is clear that with this choice of control parameters, there is a significant control/structure interaction. It is also clear that variation of control parameters and possibly filtering of the alpha joint control signals can reduce this effect, though careful analysis of the results will be necessary.



BETA JOINT TORQUE RESPONSE TO REBOOST
(Rate Gain = 10.0, Hysteresis = 0.01°)

With the increase in rate gain and decrease in hysteresis, the response of the beta joint controllers with a rigid body model is still near zero, but with a flexible modes peak torques of more than 10 in-lbs are observed. The response of the beta joint controllers, in this case is almost entirely due to the coupling effect of the flexible modes of vibration.



SUMMARY

The NASA Lewis Research Center is concerned with the potential of interaction between space station controllers and the solar PV array structures. The models required to handle this problem are very large, and we have developed automated methods for the transfer of data between structural dynamic and control system analysis software. These methods emphasize the need to achieve accurate coupled analysis results while using as small a model as possible. Specific tools which help the analyst in this regard include modal order techniques, the use of mode acceleration to calculate internal loads and stresses and the transfer of Craig-Bampton components to reduce problems associated with modal sufficiency. These techniques were applied to a space station model with 366 modes below 1 Hz. Attitude control, and alpha and beta joint control were simulated. The inclusion of alpha and beta joint controllers is important when examining overall space station dynamics. An initial choice of control parameters does indicate a potential for control/structure interaction during reboost. As expected this is exacerbated by increasing the rate gain and decreasing the hysteresis of the Reaction Control System (RCS) in order to improve rigid body performance.

- **CSI analysis of Space Station involves large models**
- **PV arrays are very flexible and can have a significant effect on station dynamics**
- **Selected Data Transfer Facilitates Analysis**
- **Alpha/Beta joint controllers are important**
- **Potential for CSI exists depending on control parameters**

OPTIMIZATION OF THE STRUCTURAL AND CONTROL SYSTEM FOR LSS WITH REDUCED-ORDER MODEL

N. S. Khot
Air Force Wright Aeronautical Laboratories (AFWAL/FDSR)
Wright-Patterson Air Force Base, Ohio

Third NASA/DOD Controls-Structures Interaction (CSI) Technology Conference
San Diego Princess
San Diego, California
January 30 - February 2, 1989

INTRODUCTION

The objective of this study is the simultaneous design of the structural and control system for space stuctures. The minimum weight of the structure is the objective function, and the constraints are placed on the closed-loop distribution of the frequencies and the damping parameters. The controls approach used is linear quadratic regulator with constant feedback. In the present investigation a reduced-order control system is used. The effect of uncontrolled modes is taken into consideration by the model error sensitivity suppression (MESS) technique which modifies the weighting parameters for the control forces. For illustration, an ACOSS-FOUR structure is designed for a different number of controlled modes with specified values for the closed-loop damping parameters and frequencies. The dynamic response of the optimum designs for an initial disturbance is compared.

OBJECTIVES

- MINIMUM WEIGHT DESIGN
- SIMULTANEOUS STRUCTURAL AND CONTROL DISCIPLINES
- CLOSED-LOOP DAMPING AND EIGENVALUE REQUIREMENTS
- REDUCED ORDER CONTRUL MODEL
- EFFECT OF NUMBER OF MODES CONTROLLED ON THE DESIGN
- DYNAMIC RESPONSE OF OPTIMUM DESIGNS

OPTIMIZATION PROBLEM

Minimize W, the weight of the structure, such that the constraints on the closed-loop frequencies, $\tilde{\omega}_i$, and the closed-loop damping, $\tilde{\xi}_i$, are satisfied. This optimization problem was solved by using the NEWSUMT-A program which is based on the extended interior penalty function method with Newton's method of unconstrained minimization.

Structure/Control Optimization Problem

Minimize weight

$$W = \sum \rho_i A_i l_i \tag{1}$$

Such that

$$g_j(\tilde{\omega}_i) \leq 0 \tag{2}$$

$$g_j(\xi_i) = 0 \tag{3}$$

$$g_j(A_i) \geq 0 \tag{4}$$

Where

$$g_j(\tilde{\omega}_i) = \tilde{\omega}_i - \overline{\tilde{\omega}}_i \tag{5}$$

$$g_j(\xi_i) = \xi_i - \overline{\xi}_i \tag{6}$$

$$g_j(A_i) = A_i - \overline{A}_i(\text{min}) \tag{7}$$

MODEL ERROR SENSITIVITY SUPPRESSION

The control problem is defined in Eqs. 1 and 2, where $\{x\}_c$ and $\{x\}_s$ are the controlled and suppressed states. The model error sensitivity suppression technique involves setting a singular perturbation on the $\dot{x}$ system which implies that the derivatives $\dot{x}$ be set identically to zero. This condition when applied to the suppressed states yields Eq. 3. This algebraic equation now can be solved for the suppressed states as given in Eq. 4. Using Eqs. 1 and 4 a new performance index can be written as given in Eq 5.

REDUCED ORDER MODEL

$$PI = \int_0^\infty (\{x\}_c^T [Q]_c \{x\}_c + \{x\}_s^T [Q]_s \{x\}_s + \{f\}^T [R] \{f\}) dt \qquad (1)$$

Subject to

$$\begin{bmatrix} \dot{x}_c \\ \dot{x}_s \end{bmatrix} = \begin{bmatrix} A_c & 0 \\ 0 & A_s \end{bmatrix} \begin{bmatrix} x_c \\ x_s \end{bmatrix} + \begin{bmatrix} B_c \\ B_s \end{bmatrix} \{f\} \qquad (2)$$

Singular perturbation of suppressed system

$$0 = [A]_s \{x\}_s + [B]_s \{f\} \qquad (3)$$

Solve for

$$\{x\}_s = -[A]_s^{-1} [B]_s \{f\} \qquad (4)$$

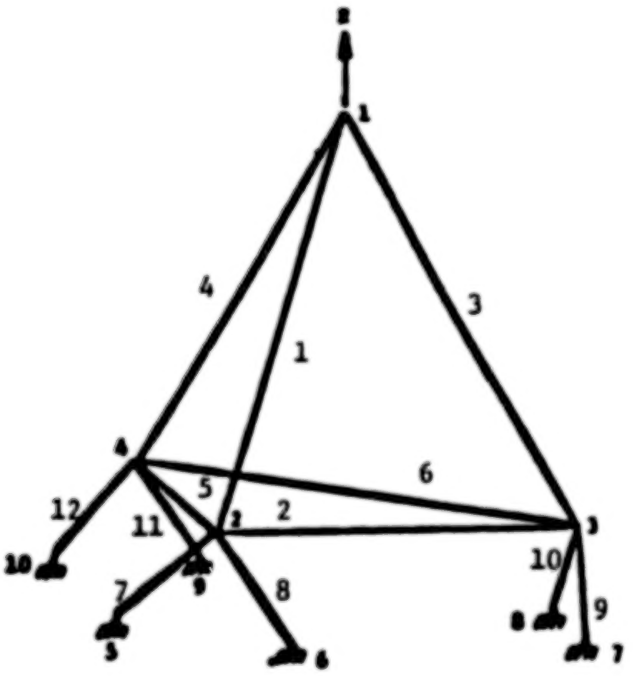
Substitute for $\{x\}_s$ in PI

$$PI = \int_0^\infty \left(\{x\}_c^T [Q]_c \{x\}_c + \{f\}^T \left[R + [B]_s^T [A]_s^{-T} [Q]_s [A]_s^{-1} [B]_s \right] \{f\} \right) dt \qquad (5)$$

PROBLEM DESCRIPTION

The finite element model of the ACOSS-FOUR is shown in this figure. The edges of the tetrahedron are 10 units long. The structure has twelve degrees of freedom and four nonstructural masses of 2 units each are attached at nodes 1 through 4. The dimensions of the structure and the elastic properties are defined in unspecified consistent units. The collocated actuators and sensors are located in six bipods. The objective of the control system is to control the line of sight (LOS) error which is the displacement of node 1 in the $X - Y$ plane due to some initial disturbance.

ACOSS FOUR (ELEMENT NUMBERS)



CONSTRAINTS

The nominal design was used as the initial design for optimization. The cross-sectional areas of this design are given in the second table. The weight of the structure for this design was 43.69 units. The imaginary parts of the closed-loop eivenvalues and the damping parameters associated with the lowest two frequencies are given below on the left side. The constraints imposed on the optimum design are given below on the right side. In the optimum design the specified damping parameters are twice those of the nominal design. The weighting matrix $[Q]$ for the state variables is a function of the square of the structural frequencies. The weighting matrix $[R]$ is the identity matrix.

NOMINAL DESIGN	CONSTRAINTS ON OPTIMUM DESIGN
weight $= 43.69$	
$\bar{\omega}_1 = 1.341$	$\bar{\omega}_1 \geq 1.341$
$\bar{\omega}_2 = 1.666$	$\bar{\omega}_2 \geq 1.6$
$\bar{\xi}_1 = 0.061169$	$\bar{\xi}_1 = 0.122$
$\bar{\xi}_2 = 0.07822$	$\bar{\xi}_2 = 0.156$

NUMERICAL RESULTS

This table gives the closed-loop damping parameter associated with different modes. The numbers under the first column are for the initial nonoptimum design. The second column contains the damping parameters for an optimal design where all the twelve modes were controlled. Subsequent columns contain damping parameters for different optimum designs with the number of controlled modes given in the first row. It is seen that the damping parameters associated with the first two modes for all optimum designs are the same. These were the constraints on the optimum design.

CLOSED-LOOP DAMPING PARAMETERS

# modes	12†	12‡	10‡	8‡	5‡	3‡
	0.062	0.122	0.122	0.122	0.126	0.122
	0.078	0.156	0.156	0.156	0.143	0.156
	0.097	0.164	0.148	0.165	0.143	0.164
	0.106	0.123	0.146	0.123	0.159	
	0.112	0.056	0.127	0.054	0.144	
	0.117	0.077	0.082	0.077	0.124	
	0.105	0.079	0.083	0.082		
	0.099	0.047	0.073	0.049		
	0.048	0.040	0.038			
	0.041	0.046	0.036			
	0.029	0.028				
	0.009	0.037				

† Non–Optimum
‡ Optimum

NUMERICAL RESULTS (CONT)

This table gives the cross-sectional areas of the members and the weights of all the designs. The initial weight or the weight of the nominal design was 43.69 units while the optimum design weights varied between 32.89 to 36.92. Even though there is not too much variation in the weights of the optimum designs, the relative values of the cross-sectional areas of the members are not the same.

AREA OF MEMBERS

ELE	12†	12‡	10‡	8‡	5‡	3‡
1	1000	607	614	588	654	572
2	1000	652	804	652	214	637
3	100	155	206	184	667	175
4	100	680	770	688	337	669
5	1000	192	175	168	780	174
6	1000	748	852	748	392	727
7	100	45	118	44	929	46
8	100	517	625	524	129	511
9	100	41	42	42	45	43
10	100	448	41	406	49	407
11	100	168	57	155	52	128
12	100	46	67	45	58	46
wt	43.69	33.94	36.92	33.74	34.06	32.89

† Initial Design
‡ Number of Controlled Modes

NUMERICAL RESULTS (CONT)

This table gives the square of the structural frequencies for all designs. The band of frequencies for an optimum design with twelve modes controlled is minimum. The frequencies associated with the first and second modes are nearly equal for all the designs. This is due to the constraints imposed on the closed-loop frequencies.

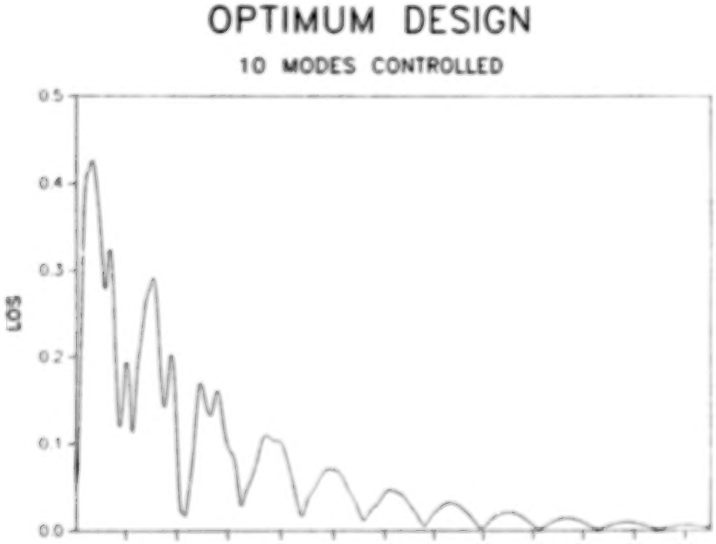
STRUCTURAL FREQUENCIES (ω_j^2)

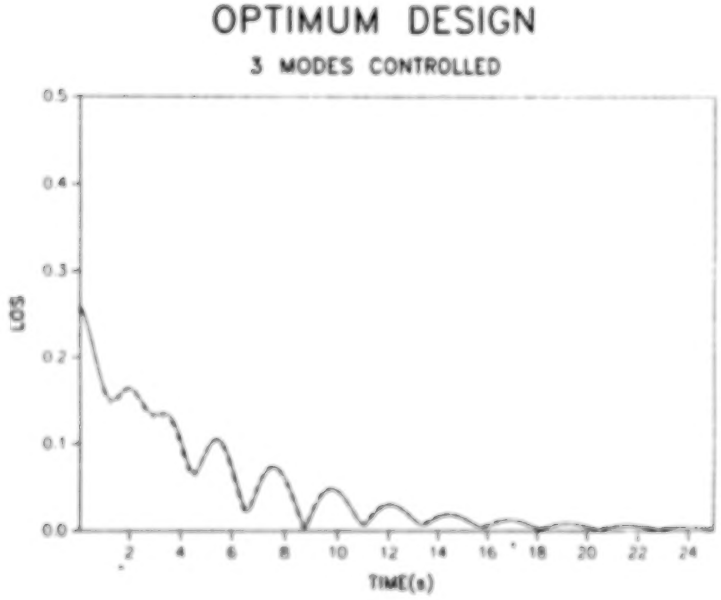
# modes	12†	12‡	10‡	8‡	5‡	3‡
	1.80	1.80	1.79	1.79	1.98	1.79
	2.77	2.56	2.56	2.56	2.56	2.56
	8.35	7.63	5.15	6.34	5.68	6.40
	8.74	9.31	6.59	8.42	6.56	8.21
	11.55	13.19	12.10	10.64	11.83	10.40
	17.68	26.41	18.67	24.84	20.63	22.78
	21.73	27.78	21.64	26.35	29.51	25.33
	22.61	34.33	31.84	51.68	33.86	50.62
	72.92	40.32	69.89	66.42	47.05	64.25
	85.57	44.70	81.73	93.66	72.19	92.60
	105.8	46.32	124.9	109.1	110.8	105.9
	166.5	50.10	133.7	116.6	185.9	113.4

† Non–Optimum
‡ Optimum

TRANSIENT RESPONSE

These two figures show the dynamic response of the designs with ten modes and three modes controlled. The transient response was simulated for a period of 25 seconds at a time interval t = 0.05 secs. The magnitude of the LOS is given by the square root of the sum of the squares of the X and Y components of the displacements at node 1. The dash line is for the case where unmodeled modes are also included in the calculation of the transient response. For the design with ten modes controlled the two curves coincide. In the case of 3 modes controlled a small difference in the response is observed.





BEST COPY AVAILABLE

CONCLUSIONS

This presentation included the results of an investigation to design a minimum weight structure by taking into consideration a reduced order control system. The reduced order approach was based on the model error sensitivity suppression technique. It was found that the weights of the structures with a different number of modes controlled were not substantially different. The work done by the actuators was found to be reduced with a less number of contolled modes. The transient response of the different designs was not the same. There was not much difference in the LOS when unmodelled modes were included in calculating the response.

- Simultaneous structural and control with closed–loop damping and eigenvalue requirements
- NEWSUMT — An optimizer for solving the problem
- Control design based on reduced order model
- The transient response for designs with different number of modes controlled was not the same

Computational Architecture for Integrated Controls and Structures Design

W. Keith Belvin
NASA Langley Research Center
and
K. C. Park
University of Colorado

Third Annual NASA/DOD CSI Conference

San Diego, CA

January 29 - February 2, 1989

Abstract

To facilitate the development of Control-Structure Interaction (CSI) design methodology, this paper presents a computational architecture for interdisciplinary design of active structures. The emphasis of the computational procedure is to exploit existing sparse matrix structural analysis techniques, in-core data transfer with control synthesis programs, and versatility in the optimization methodology to avoid unnecessary structural or control calculations. The architecture is designed such that all required structure, control and optimization analyses are performed within one program. Hence, the optimization strategy is not unduly constrained by "cold" starts of existing structural analysis and control synthesis packages.

Design of Closed-Loop Spacecraft Dynamics

Conventional attitude and station keeping control system design, which maintain bandwidth separation between rigid-body controllers and flexible-body dynamics, cannot meet the performance goals of future science missions. Thus, both the rigid and flexible-body closed-loop dynamics of the spacecraft must be concurrently designed. The interdisciplinary design of controller and structure dynamics can be studied most easily through computer simulation. To this end, a computational software testbed has been designed and implemented to test new ideas and algorithms for future spacecraft design.

The software testbed consists of three in-core modules: a structural modeling and analysis module, a control synthesis processor, and a versatile optimization package. Key features of the software include in-core data transfer between the control, structure, and optimization modules and a sparse matrix utility. Both features facilitate new implementations of solution algorithms and control strategies.

The software testbed has been applied as a research tool to study CSI partitioned analysis procedures[1], suboptimal second order observers[2], and a number of truss design problems. The discussion herein emphasizes use of the software architecture to reduce the computational burden of CSI analysis, synthesis, and/or simulation. By reducing burdensome data transfer among separate analysis packages and by increasing the computational efficiency, more freedom is allowed to explore closed-loop spacecraft dynamics design methodology. A description of the architecture and its implementation in a prototype code are discussed. Examples of active truss designs are also presented.

COMPUTATIONAL ARCHITECTURE FOR INTEGRATED CONTROLS AND STRUCTURES DESIGN

OBJECTIVE:

Develop a computational architecture for the study of CSI that reduces data handling and thus promotes more study of design methodology.

APPROACH:

Assemble public domain software into a single program for in-core data transfer between structures, controls and optimization analysis software.

Benefits of Interdisciplinary Design

Several tangible benefits usually result from an integrated design approach for controlled structures. These include minimizing structural mass, decreasing the amount of controller energy, and increasing system robustness.[3-7] These benefits are usually the first and sometimes the only benefits considered from the integrated design approach. There exist, however, intangible benefits that must not be overlooked. The interaction of engineers and scientists from controls and structures disciplines produces new insight into active structure design. Specifically, the implications that changes in one discipline have on another discipline are better understood. This leads to physical insight into CSI and permits the portion of the design relegated to the computer to be minimized.

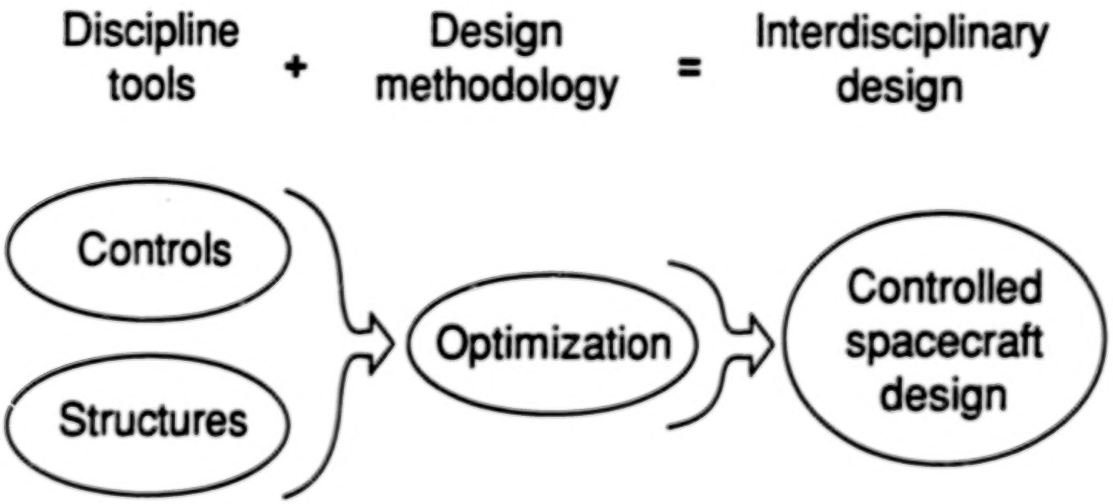
Developing physical insight into the interrelationship of the structure and control system will enable substantial improvements in spacecraft design. Most importantly, increased physical insight will aid the systems level decision process which ultimately determines the viability of a mission from both cost and technical considerations. Physical insight into interdisciplinary CSI design has motivated the present computational approach.

- TANGIBLE
  - Minimization of mass
  - Reduced controller energy
  - Enhanced robustness
- INTANGIBLE
  - Physical insight into CSI
  - Better informed decisions

Optimization - A Tool for Studying Design Methodology

Significant advances in the use of optimization as a design tool for interdisciplinary problems were presented at a recent Symposium on Multidisciplinary Analysis and Optimization.[8] Methods for determining objective function and constraint sensitivities for both control and structure design variables are becoming more analytic in nature. Data base systems for managing shared structure and control data are being used to link analysis software.[9,10] Unfortunately, formulating the correct objectives and constraints for interdisciplinary problems still remains a subject of research.

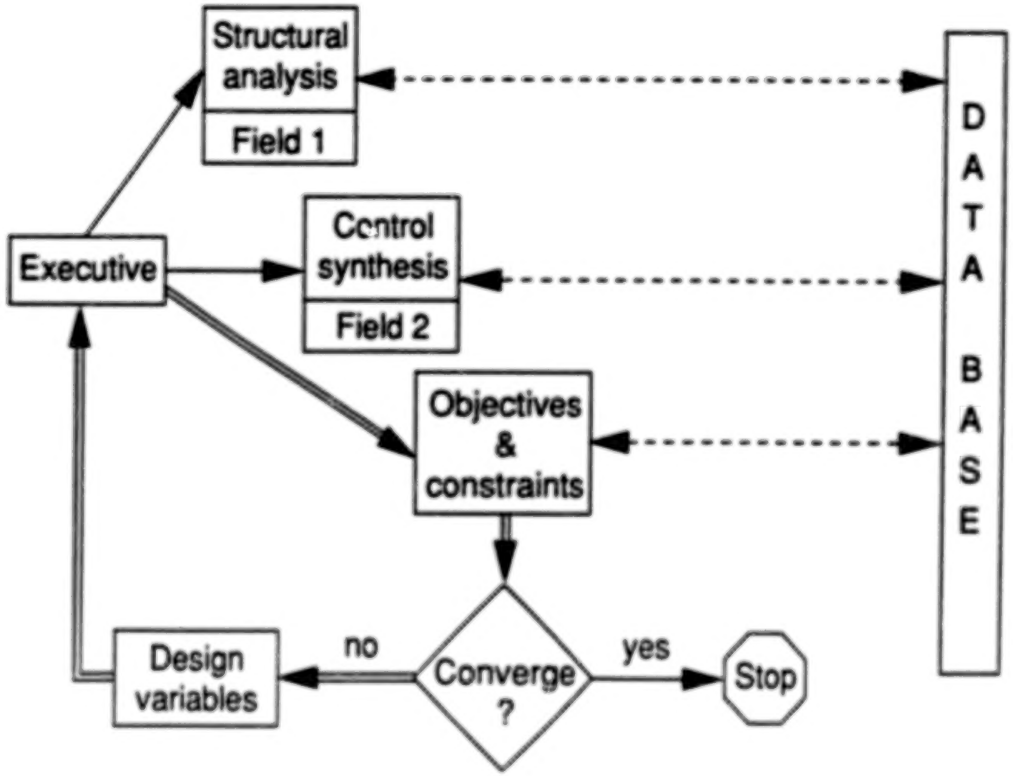
Optimization can be used as a tool for studying the effects of different objectives and constraints. From experience the designer gains insight into appropriate formulations of the problem. Sensitivity calculations, which are an integral part of optimization analysis, yield physical insight. Hence, optimization can be a tool for studying design methodology. It is in this context that optimization will play a key role in CSI technology development.



Conventional Architecture for Coupled-Field Problems

To date, most designs which consider both the controller and structure as design variables have been performed using an ad hoc collection of discipline specific software modules. Such software tools were originally developed for the solution of single-field problems (e.g. control law synthesis, finite element structural modeling). The use of these tools has required specialized interfaces to be developed which must transfer data from one module to the next as shown below.

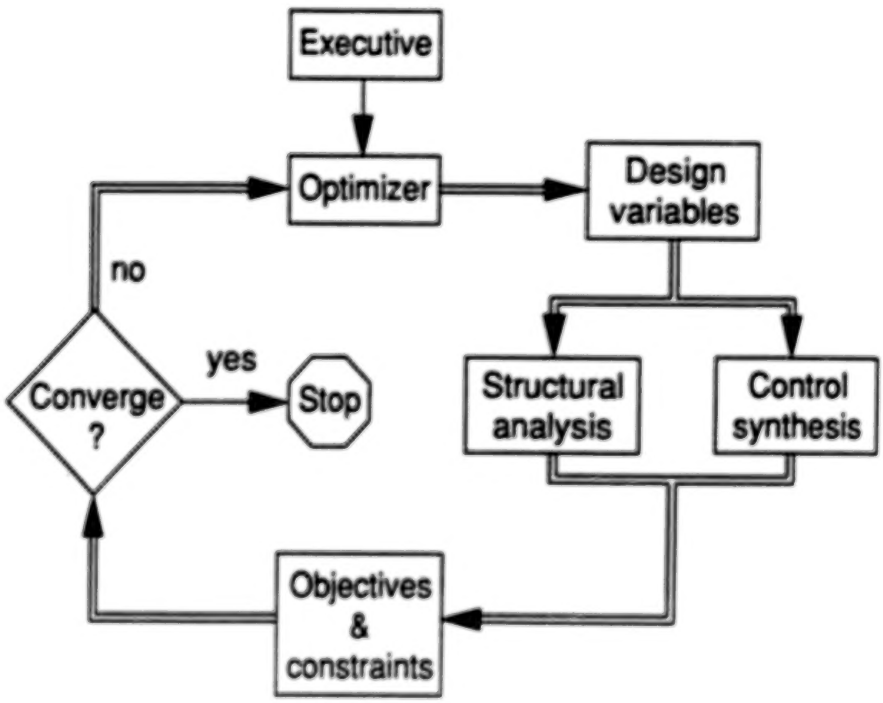
Integration of such single-field analysis codes by means of a common data base manager yields an executive-type program. It provides for immediate usage of existing software. However, the executive program is usually hardwired to a few design methods thereby losing versatility. Moreover, the high cost associated with 'cold' starts of structural analysis or control synthesis packages discourages asking "What if?" The use of loosely coupled single-field programs also masks the physics associated with CSI. Hence, the need for a new architecture for the coupled-field optimization problem is indicated.



Proposed Architecture for Coupled-Field Problems

To alleviate some of the computational problems associated with integrated design of structures and controllers, an in-core architecture is proposed as shown below. The objectives of the procedure are to exploit sparse matrix structural analysis procedures, in-core data transfer with control synthesis algorithms, and to maintain versatility in the optimization methodology. The architecture is designed so that all required structure, control and optimization analyses are performed within one executable program.

Although the available memory (virtual memory) of new computers has grown dramatically in recent years, some very large problems must still be solved out-of-core. Data-base type design codes will continue to be needed to handle very large problems for the foreseeable future. The proposed architecture is targeted for research studies of design methodology for small to moderate size problems (1000 structural degrees of freedom). The benefits of this approach are described next.



Benefits of the Proposed Integrated Design Architecture

Several advantages exist in using the proposed architecture versus the conventional data base approach. First, the computational speed can be improved using in-core data transfer (i.e. common blocks instead of data bases). Coupling the Input/Output time savings with algorithms that exploit matrix sparsity and the second order form of structures equations enables moderate size problems to be solved routinely. Second, the new architecture requires engineers and scientists from both controls and structures disciplines to work more closely. Since they both use the same software tool, a conducive software environment exists for exploring interdisciplinary problems. Finally, the in-core architecture permits much more flexibility in asking 'What if?' questions.

If optimization will be used as the tool for studying the physics of CSI, it becomes imperative to provide as much freedom as possible to study different design methodologies. In particular, there should be a great deal of freedom in selecting objective functions and constraints. By connecting the essential software in one executable program, the proposed architecture reduces the computational burden which permits the researcher more time to study methodology and problem formulation.

- Increased speed
  - Sparse matrix procedures
  - Fewer repeat calculations
- Encourages interdisciplinary design
- Freedom to ask, "What if?"

Prototype Code - Controlled Structure Simulation Software (CS^3)

A prototype code called CS^3 has been developed using public domain software to implement the proposed architecture. The key feature sought in choosing the software is the availability of source code which could be modified to permit in-core data transfer among the different programs. There exist many other possible choices for the optimizer, structural analysis and control synthesis than the ones presented herein.

The executive program is simply one that tests input data to determine whether analysis or optimization is to be performed. If optimization is to be performed, the program flow is governed by the optimizer.

The optimization path uses the Automated Design Synthesis (ADS)[11] system of subroutines written by Dr. Gary Vanderplatts. A number of solution strategies may be chosen within the ADS system. Currently objective and constraint sensitivities are performed by finite differences; however, analytic and semi-analytic sensitivity modules will be added to CS^3.

Structural finite element modeling, real-symmetric eigenvalue analysis, and transient response calculations are performed with a code called Linear Analysis of Sparse Structures (LASS). LASS has been written and/or collected by the NASA Langley Research Center and the University of Colorado.

Control synthesis is performed using the Optimal Regulator Algorithms for the Control of Linear Systems (ORACLS)[12] library of linear algebra subroutines. ORACLS is a system for Linear-Quadratic-Gaussian control law design developed by Dr. E. S. Armstrong.

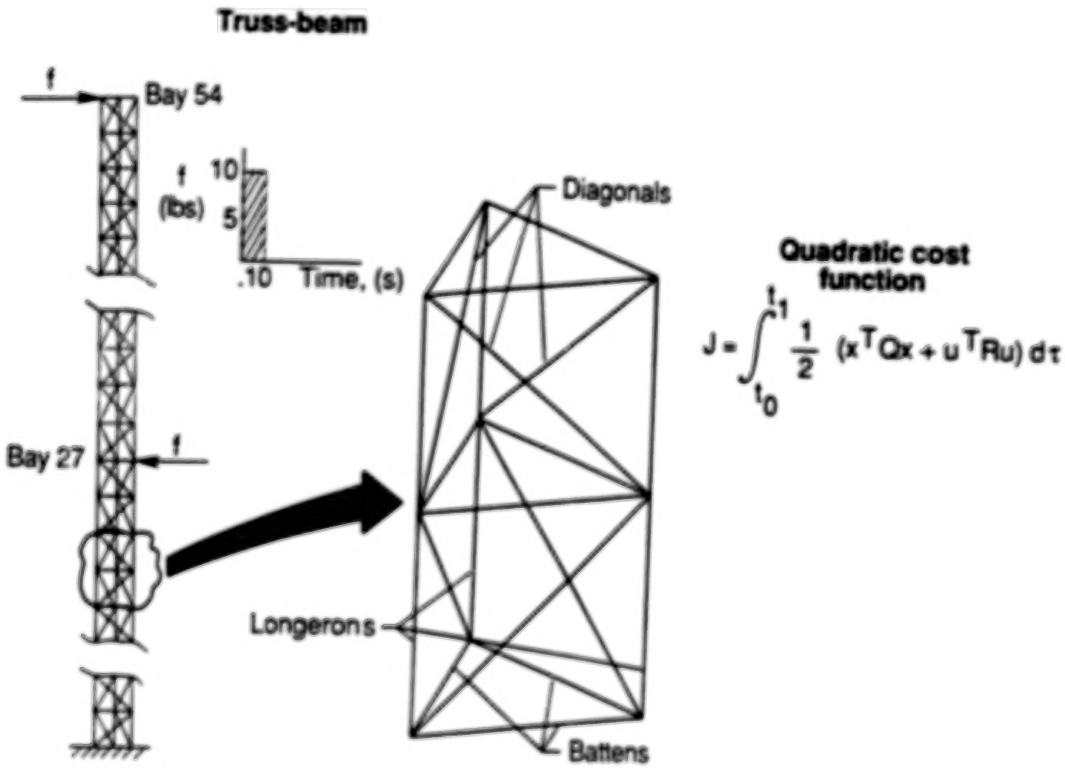
PROTOTYPE CODE - CS^3
CONTROLLED STRUCTURE SIMULATION SOFTWARE

- Executive - User supplied
- Optimization - ADS (Vanderplatts)
- Structures - LASS (NASA LaRC, University of Colorado)
- Controls - ORACLS (NASA LaRC)

Truss-Beam Design Example

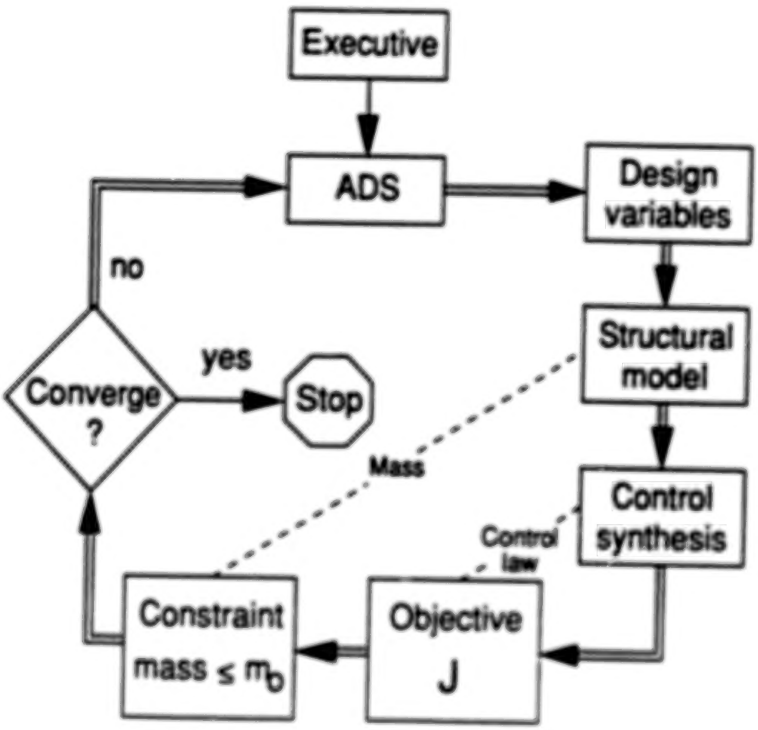
The truss-beam shown below has been used to demonstrate the use of CS^3. The three-longeron, single-laced truss was modeled by finite elements with one beam element from joint-to-joint. The model had 165 nodes and 990 degrees of freedom. More detailed information is presented in reference 13. Three design variables were chosen: the outside diameters of the batten, diagonal and longeron. All members were tubular with the inside diameter equal to 75 percent of the outer diameter.

The objective was to minimize a quadratic cost function by tailoring the structure. Seven modes were used in the control law design. Weighting matrices in the cost function which influence the control law were implicit functions of the design variables. Constraints consisted of forcing the total mass of the structure not to exceed the nominal design mass, and a restriction on local beam vibration frequencies.



CS³ Flowchart For Truss-Beam Design

The flowchart below shows the steps used to tailor the truss-beam to minimize the quadratic cost function. All data were transferred in-core (virtual memory) on a SUN 3 workstation. Problem dependent objective and constraint evaluation subroutines enable virtually unlimited freedom in formulating the problem. Data transfer among subroutines through common blocks permits intermediate results computed in one calculation to be used in another computation, even when the second computation occurs in a different subroutine. This greatly enhances the computational speed of the design process.

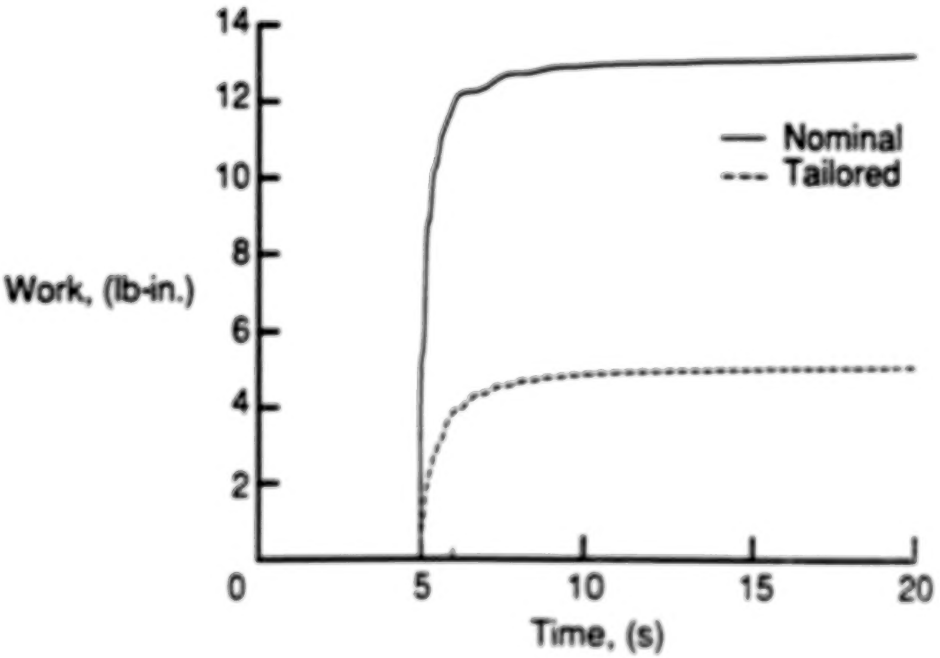


Truss-Beam Optimized Design

The table below lists the nominal and optimized tube diameters. The optimal design was obtained in 18 iterations with each iteration taking about 10 minutes. Note that considerable time savings are possible if analytic derivatives rather than finite differences were used to compute sensitivities. The figure below shows the actuator work for the nominal and optimized beam subjected to the same performance requirement of reducing the tip vibration amplitude below 0.025 in. within 10 seconds. The optimized beam requires 56 percent less actuator work.

Outside tube diameter, in.	Nominal	Tailored
Longeron	0.789	1.717
Diagonal	1.707	1.284
Batten	0.918	0.640

Truss beam actuator work



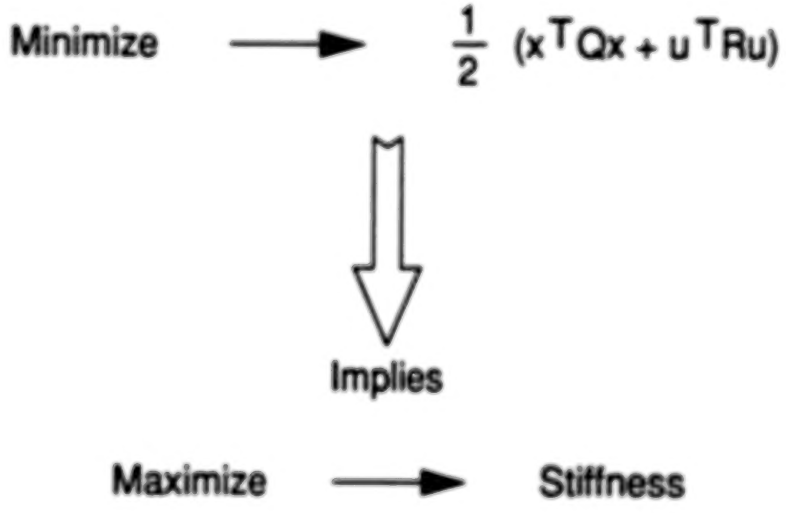
Physical Insight Into Truss-Beam Design

The results of the truss-beam optimization have been noted to involve maximizing a quantity related to the stiffness of the structure[13]. The truss-beam optimization used the following weighting matrices:

$$\mathbf{Q} = \begin{bmatrix} \mathbf{K} & 0 \\ 0 & \mathbf{M} \end{bmatrix} \qquad \mathbf{R} = \left[\mathbf{D}^T\mathbf{K}^{-1}\mathbf{D}\right]$$

where, $\mathbf{K}$ is the stiffness matrix, $\mathbf{M}$ is the mass matrix and $\mathbf{D}$ is the actuator location matrix.

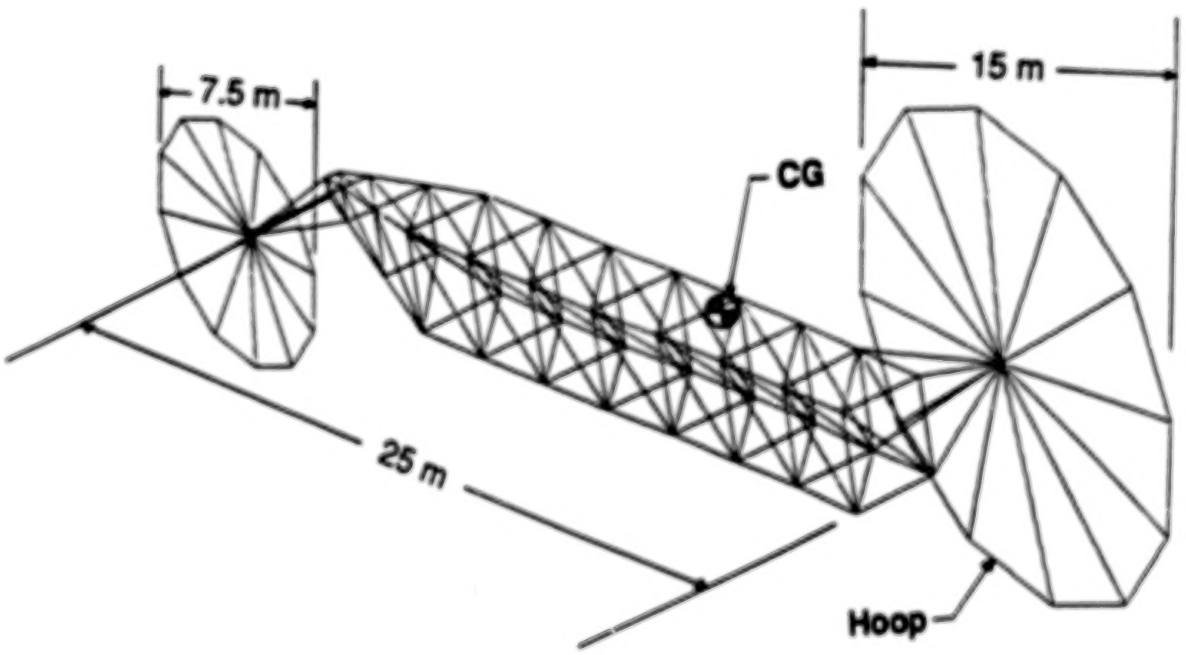
To minimize this quadratic measure of the energy, subject to a constraint on total mass, it is found that the optimal solution is one that maximizes a measure of the structural stiffness. Thus, the question arises, what is the proper way to pose the integrated structure and control design problem to give a balanced solution between structures and controls? That is, a solution is desired which does not imply making the structure as stiff as possible within a mass budget. This remains an open question for research, and will be addressed through the next example problem.



Earth Pointing Satellite Design Problem

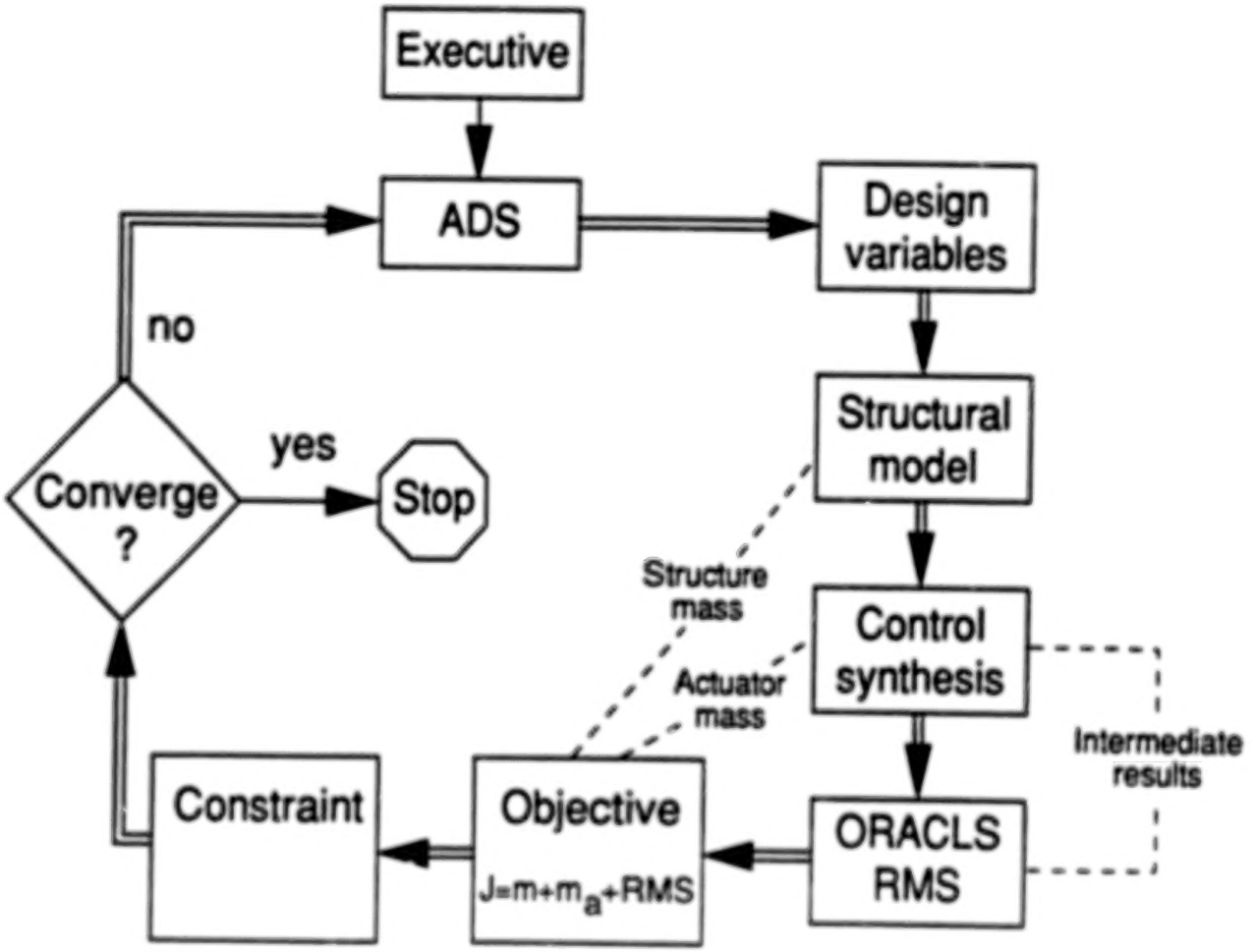
The Earth Pointing Satellite (EPS), shown below, is a derivative of the proposed platforms for study of Earth Observation Sciences (EOS).[14] This class of structure is receiving considerable attention for future missions involving remote sensing of the Earth's environment and resources. The CSI Analytical Design Methods team at the NASA Langley Research Center is planning studies of the EPS to test various methodologies for integrated controls and structures design.

To address the problem formulation mentioned on the previous page, an objective function has been examined which includes structural mass, controller mass and a pointing performance measure. It is believed that this objective, with proper weighting of the objective parts, will yield a great deal of insight into the controls and structures trade-off. The next chart shows the ease with which CS^3 can be modified to handle this problem formulation.



CS³ Flowchart for the EPS Design Problem

Evaluating the objective function for the EPS design problem requires structural and control analyses plus calculation of a stochastic measure of the rms pointing error. Because CS³ can share data easily, the computation of the objective is quite straightforward. The structural mass is obtained from the finite element model. Actuator mass is a function of the control gains, hence, the control law synthesis must be performed first. Subsequently, the rms pointing error, which uses numerous intermediate calculations performed in the control law synthesis, is carried out. Thus, CS³ can be readily changed to study different formulations of the integrated design. Conventional design approaches, which use data base systems, would require either new information to be written to the data base or 'cold' starts of program modules when the problem formulation drastically changes.



Future Modifications to CS^3

A number of enhancements are envisioned to CS^3. These include plotting capabilities, new elements in the finite element library, additional control synthesis techniques and better user interfaces. In addition, new algorithms for vectorization and perhaps parallelization will be included. The code will remain a tool for studying CSI and designing linear time-invariant controlled structures. The main purpose of the architecture is to alleviate the computational burden from the researcher to enhance the study of design methodology.

There are other classes of problems which involve time-variant and/or nonlinear systems. At the present time, CS^3 cannot address these problems. However, the architecture proposed herein should be exploited for these classes of problems when possible.

It is recognized that this architecture does not lend itself well to big problems on small computers. Hence, there needs to be continued development of data-base type design codes. Hopefully, future data-base type software will more closely couple the control and structure disciplines and thereby promote as much interdisciplinary research as possible.

- Pre & post processing
  - User interfaces
  - Graphics
- Additional capabilities
  - More structural elements
  - More control synthesis methods
- Faster algorithms
  - Vectorization

Concluding Remarks

A computational architecture has been implemented for preliminary controlled structure design which greatly enhances the researchers freedom in formulating integrated design problems. By incorporating codes from separate disciplines within a single executable program, optimization of the control-structure coupled-field problem can be solved as easily as a single-field optimization problem. A prototype code called CS³ has been described which demonstrates the flexibility of the architecture. Example problems show the architecture to be amenable to design methodology studies.

It is the authors' hope that by eliminating some of the computational burden associated with CSI, the proposed architecture will permit increased research into the underlying physics of CSI.

- The proposed in-core architecture greatly reduces user data management.
- By incorporating structures, controls and optimization into one program, interdisciplinary design is encouraged.
- A prototype code called CS^3 which uses the in-core architecture, has been successfully applied to CSI design problems.

REFERENCES

1. Park, K. C.; and Belvin, W. K.: Stability and Implementation of Partitioned CSI Solution Procedures. AIAA 89-1238, AIAA/ASME/ASCE/AHS 30th Structures, Structural Dynamics, and Materials Conference, Mobile, Alabama, April 3-5, 1989.

2. Belvin, W. K.; and Park K. C.: On the State Estimation of Structures With Second Order Observers. AIAA 89-1241, AIAA/ASME/ASCE/AHS 30th Structures, Structural Dynamics, and Materials Conference, Mobile, Alabama, April 3-5, 1989.

3. Haftka, R. T.; Martinovic, Z. N.; and Hallauer, W. L.: Enhanced Vibration Controllability by Minor Structural Modifications. AIAA Journal, Vol. 23, pp. 1260-1266, Aug. 1985.

4. Hale, A. L.; Lisowski, R. J.; and Dahl, W. E.: Optimal Simultaneous Structural and Control Design of Maneuvering Flexible Spacecraft. Journal of Guidance, Control and Dynamics, Vol. 8, pp. 86-93, Jan-Feb. 1985.

5. Hanks, B. R.; and Skelton, R. E.: Designing Structures for Reduced Response by Modern Control Theory. AIAA 83-0815, AIAA/ASME/ASCE/AHS 24th Structures, Structural Dynamics, and Materials Conference, Lake Tahoe, Nevada, May 1983.

6. Khot, N. S.; and Venkayya, V. B.; Oz, H.; Grandhi, R. V.; and Eastep, F. E.: Optimal Structural Design with Control Gain Norm Constraint. AIAA-87-0019, AIAA 25th Aerospace Sciences Meeting, Reno, Nevada, Jan. 12-15, 1987.

7. Becus, G. A.; Lui, C. Y.; Venkayya, V. B.; and Tischler, V. A.: Simultaneous Structural and Control Optimization via Linear Quadratic Regulator Eigenstructure Assignment. NASA CP-2488, Oct. 1987, pp.225-232.

8. Barthelemy, J.-F. M. (editor): Recent Advances in Multidisciplinary Analysis and Optimization. NASA CP-3031, April 1989.

9. Cooper, P. A.; Young, J. W.; and Sutter, T. R.: Multidisciplinary Analysis of Actively Controlled Large Flexible Spacecraft. First NASA/DOD CSI Technology Conference, NASA CP-2447, 1986.

10. Baker, M.; et. al.: Space Station Multidisciplinary Analysis Capability —— IDEAS^2 AIAA/ASME/ASCE/AHS 27th Structures, Structural Dynamics and Materials Conference, AIAA 86-0954, San Antonio, TX, May 19-21, 1986.

11. Vanderplatts, G. N.: ADS - A Fortran Program for Automated Design Synthesis - Version 1.10. NASA CR 177985, Sept. 1985.

12. Armstrong, E. S.: ORACLS-A System for Linear-Quadratic-Gaussian Control Law Design. NASA TP 1106, 1978.

13. Belvin, W. K.; and Park, K. C.: Structural Tailoring and Feedback Control Synthesis: An Interdisciplinary Approach. AIAA 88-2206, AIAA/ASME/ASCE/AHS 29th Structures, Dynamics and Materials Conference, Williamsburg, VA, April 18-20, 1988.

14. Ramler, J.; and Durrett, R. : NASA's Geostationary Communications Platform Program, Proceedings of the AIAA 10th Communications Satellite Systems Conference, AIAA 84-0702, Orlando, FL, March 4, 1984.

Controller Reduction for Effective Interdisciplinary Design of Active Structures

Mark J. Balas
Ralph Quan

Center for Space Structures and Controls and
Department of Aerospace Engineering Sciences
Campus Box 429
University of Colorado
Boulder, Colorado

Acknowledgment: This research was partially supported by the NASA Center for Space Construction at the University of Colorado – Boulder.

Introduction:

Control problems of large aerospace structures are intrinsically interdisciplinary and require strategies which address the complete interaction between flexible structures, electromechanical actuators and sensors, and feedback control algorithms. In this paper we would like to survey our current research and future directions which will require an interdisciplinary team effort in dynamics, control and optimization of such structures.

It is generally agreed that the dynamics of space structures require large-scale discrete modeling, resulting in thousands of discrete unknowns. Proven control strategies, on the other hand, employ a low-order controller that is based on a reduced-order model of structures. Integration of such low-order controllers and large-scale dynamics models often leads to serious deterioration of the closed-loop stability margin and even instability. To alleviate this stability deterioration while low-order controllers remain effective, we have investigated the following approach:

(a) Retain low-order controllers based on reduced-order models of structures as the basic control strategy;

(b) Introduce a compensator that will directly account for the deterioration of stability margin due to controller-structure integration;

(c) Assess overall performance of the integrated control-structure system by developing measures of suboptimality in the the combination of (a) and (b).

The benefits of this approach include:

(1) Simplicity in the design of basic controllers, thus facilitating the optimization of structure-control interactions;

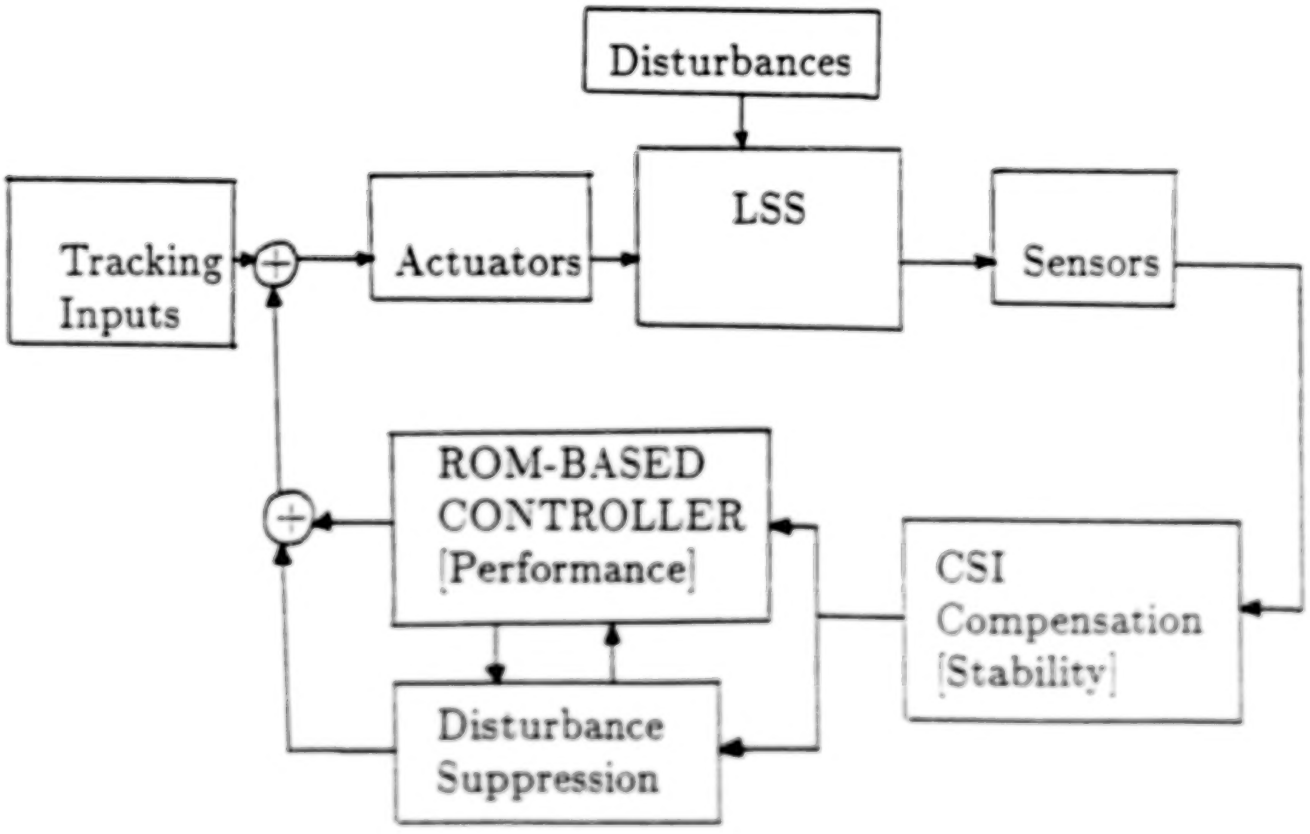
(2) Increased understanding of the roles of the compensator so as to modify the structure as well as the basic controller, if necessary, for improved performance;

(3) Adaptability to localize controllers by viewing the compensator as a systems integration filter.

We have demonstrated the above approach in the active control design of a simulation of a three-dimensional truss beam structure. Future research will focus on the use of these ideas for local control of partially assembled structures. In particular, it is natural to simulate large structures by partitioning them into simpler substructures, integrating the substructure dynamics on parallel processors. We plan to develop local controllers along the same lines using substructure-controller optimization and alleviating the deterioration of stability margin due to controller-structure interaction by introducing an appropriate compensator.

Current Research

- ⊙ Distributed Parameter System Theory for Model Reduction and Low-Order Controller Design
- ⊙ CSI Compensation By Residual Mode Filters
- ⊙ Numerically Well-Conditioned Methods for Structure/Controller Redesign to Reduce Detrimental CSI



Large Space Structure (Finite Element) Model:

LSS: $M_0\ddot{q} + D_0\dot{q} + K_0 q = B_0 u$

Sensor Outputs: $y = C_0 q + E_0 \dot{q}$

M_0, D_0, K_0 symmetric matrices

(change variables and take $M_0 = I$)

State Space Form:

$$x = \begin{bmatrix} q \\ \dot{q} \end{bmatrix}$$

$$\begin{cases} \dot{x} = Ax + Bu \\ y = Cx \end{cases}$$

$$A = \begin{bmatrix} 0 & I \\ -K_0 & -D_0 \end{bmatrix} \qquad B = \begin{bmatrix} 0 \\ B_0 \end{bmatrix}$$

$$C = [\, C_0 \quad E_0 \,]$$

First - Order State Estimators

(A, C) observable if and only if $A - KC$ has arbitrary poles

$$\begin{cases} \dot{\hat{x}} = A\hat{x} + Bu + K(y - \hat{y}) \\ \hat{y} = C\hat{x} \end{cases}$$

Take $\hat{x} = \begin{bmatrix} \hat{q} \\ \dot{\hat{q}} \end{bmatrix}$ & $K = \begin{bmatrix} K_1 \\ K_2 \end{bmatrix}$

Then

$$\begin{cases} \dot{\hat{q}} = \hat{\dot{q}} + K_1(y - \hat{y}) \\ \dot{\hat{\dot{q}}} + D_0\hat{\dot{q}} + K_0\hat{q} = B_0u + K_2(y - \hat{y}) \\ \hat{y} = C_0\hat{q} + E_0\hat{\dot{q}} \end{cases}$$

NOTE: If $K_1 = 0$, then $\hat{\dot{q}} = \dot{\hat{q}}$ and

$$\begin{cases} \ddot{\hat{q}} + D_0\dot{\hat{q}} + K_0\hat{q} = B_0u + K_2(y - \hat{y}) \\ \hat{y} = C_0\hat{q} + E_0\dot{\hat{q}} \end{cases}$$

"Natural" Second - Order State Estimators

$$\begin{cases} \ddot{\tilde{q}} + D_0\dot{\tilde{q}} + K_0\tilde{q} = B_0u + K_3(y - \tilde{y}) \\ \tilde{y} = C_0\tilde{q} + E_0\dot{\tilde{q}} \end{cases}$$

Example:

$$\begin{cases} \ddot{\tilde{q}} + q = u \\ y = q \end{cases}$$ No velocity measurement

First - Order State Estimator:

$$A = \begin{bmatrix} 0 & 1 \\ -1 & 0 \end{bmatrix} \qquad B = \begin{bmatrix} 0 \\ 1 \end{bmatrix} \qquad C = [1 \quad , \quad 0]$$

$$\begin{cases} \dot{\hat{q}} = \hat{\dot{q}} + K_1(y - \hat{y}) \\ \dot{\hat{\dot{q}}} + \hat{q} = u + K_2(y - \hat{y}) \\ \hat{y} = \hat{q} \end{cases}$$

(A, C) observable; so above converges arbitrarily fast by choice of gains K_1 and K_2

Second - Order "Natural" State Estimator:

$$\begin{cases} \ddot{\hat{q}} + \hat{q} = u + K_3(y - \hat{y}) \\ \hat{y} = \hat{q} \end{cases}$$

Does **not** converge for any choice of gain K_3

K. Belvin: "If **any** velocity measurement is available anywhere, then a second-order natural state estimator can be built to converge."

Result: (Balas - Quan)

Assume (a) No damping ($D_0 = 0$)

(b) $K_e \equiv K_0 + (C_p^0)^T Q_p C_p^0$ positive definite for some Q_p

(c) (K_e, C_v^0) observable

where $y_p = C_p^0 q$, $y_v = C_v^0 \dot{q}$, and $y = \begin{bmatrix} y_p \\ y_v \end{bmatrix}$.

Then there is **always a convergent** "natural" second-order state estimator:

$$\ddot{\hat{q}} + K_0 \hat{q} = B_0 u + K_p(y_p - \hat{y}_p) + K_v(y_v - \hat{y}_v)$$

$$\hat{y}_p \equiv C_p^0 \hat{q} \quad \text{and} \quad \hat{y}_v \equiv C_v^0 \dot{\hat{q}}$$

where $K_p \equiv (C_p^0)^T Q_p$ and $K_v \equiv (C_v^0)^T Q_v$ with Q_p, Q_v any positive definite matrices.

Example: (Balas - Quan)

$$\begin{cases} \ddot{q}_1 + 2q_1 - q_2 = 0 \\ \ddot{q}_2 - q_1 + q_2 = 0 \\ y_v = \dot{q}_2 \qquad \text{velocity of second mass} \end{cases}$$

NOTE: $K_0 = \begin{bmatrix} 2 & -1 \\ -1 & 1 \end{bmatrix}$ and $C_v^0 = [0 \quad 1]$

First Order Observer:

No damping $(D_0 = 0)$

(K_0, C_v^0) observable if and only if (A, C) observable

therefore, arbitrarily fast convergence.

Second - Order "Natural" Observer:

$K_e = K_0$ positive definite and (K_0, C_v^0) observable

$$\begin{cases} \ddot{\hat{q}}_1 + 2\hat{q}_1 - \hat{q}_2 = 0 \\ \ddot{\hat{q}}_2 - \hat{q}_1 + \hat{q}_2 = Q_v(y_v - \dot{\hat{q}}_2) \; ; \quad Q_v \text{positive.} \end{cases}$$

This converges, but the maximum rate is $e^{-0.4t}$

Question: Can every first-order state estimator for a LSS be rewritten as a second-order state estimator ?

Answer: Yes, but not a "natural" one (Balas - Quan).

Non - Natural Second - Order State Estimators:

$$\begin{cases} \tilde{\zeta} + D_0\dot{\zeta} + K_0\zeta = B_0\tilde{u} + K_3(y - \tilde{y}) + \gamma_c \\ \tilde{y} = C_0\zeta + E_0\dot{\zeta} \end{cases}$$

where $\hat{q}$ and $\hat{\dot{q}}$ are **linear** functions of available signals and the corrector term γ_c is also.

Example: $\begin{cases} \tilde{q} + q = u \\ y = q \end{cases}$ No "Natural" Convergent Second - Order State Estimator

Non - Natural Second - Order State Estimator:

$$\begin{cases} \tilde{\zeta} + \zeta = \tilde{u} + K_1(y - \tilde{y}) + \gamma_c \\ \tilde{y} = \dot{\zeta} \end{cases}$$

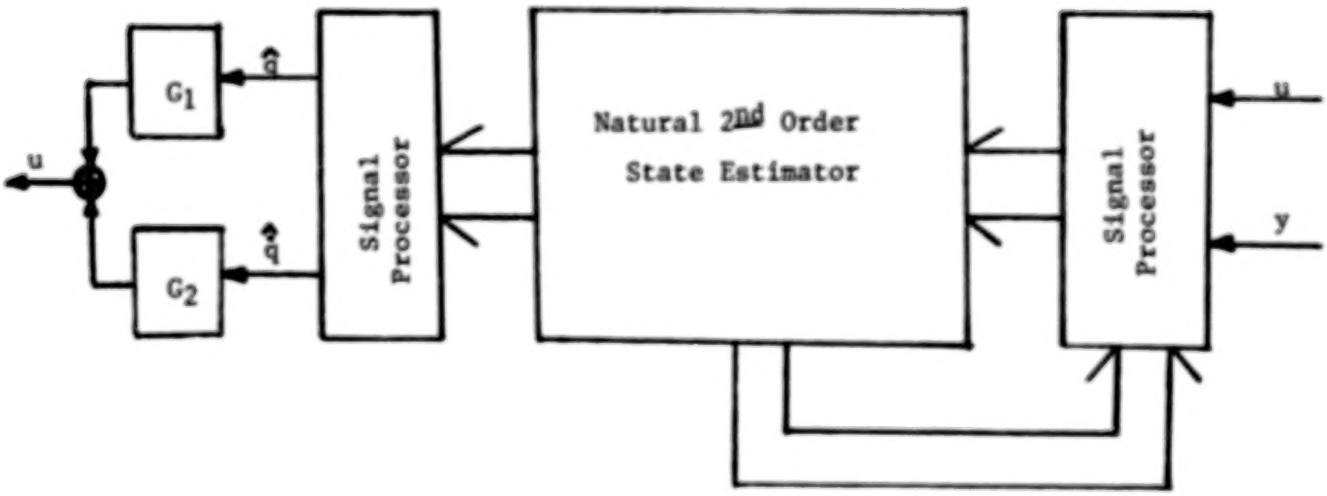
where $\gamma_c \equiv K_2(v - \zeta)$; $\dot{v} + \epsilon v = y$; $\dot{\tilde{u}} + \epsilon\tilde{u} = u$; $\hat{q} = \dot{\zeta}$; $\hat{\dot{q}} = -\zeta + \tilde{u} + \gamma_c$; $\epsilon > 0$.

This converges arbitrarily fast.

Conclusion:

LSS: $\begin{cases} \ddot{q} + D_0\dot{q} + K_0 q = B_0 u \\ y = C_0 q + E_0 \dot{q} \end{cases}$

Controller: $u = G_1\hat{q} + G_2\dot{\hat{q}}$



Advantages:

- ⊙ Controller Based on Second - Order Computer Architecture
- ⊙ Model Reduction Based on Physical Co-ordinate Finite Element Structure Model
- ⊙ Controller Designed for Performance in Physical Co-ordinates; Compensation for CSI induced instabilities added-on, e.g. Residual Mode Filters.

RECENT EXPERIENCE IN SIMULTANEOUS CONTROL-STRUCTURE OPTIMIZATION

M. Salama, R. Ramaker, and M. Milman
Jet Propulsion Laboratory
California Institute of Technology
Pasadena, CA

Third Annual NASA/DoD CSI Conference
San Diego, CA
January 29-February 2, 1989

MOTIVATIONS: The optimization of a structure and its control system has traditionally proceeded along two separate but sequential paths. First, the structure is optimized by selecting a set of member sizes $\underset{\sim}{a}^*$ which minimize a structural criterion $J_s(\underset{\sim}{a})$, subject to constraints $h_s(\underset{\sim}{a})$, Eq (1). Then having specified the optimal structure, one may use the control theory to determine an optimal set of control variables $\underset{\sim}{u}^*$ that optimize a control criterion J_c subject to constraints $h_c(\underset{\sim}{u})$, Eq. (2). This two-step optimization procedure is the so-called separate optimizatcn and is equivalent to finding the linear sum of two separate minima, Eq. (3). The question arises then as to whether it is possible to achieve a superior combined optimum ($\underset{\sim}{a}^{**}$, $\underset{\sim}{u}^{**}$) over ($\underset{\sim}{a}^*$, $\underset{\sim}{u}^*$) had one combined the two problems before, Eq. (4), rather than after, Eq. (3), the minimization. Intuitively, the answer to this question is affirmative, Eq. (5), since the minimum of the sum is less than the sum of the minima.

- SEPARATE OPTIMIZATION

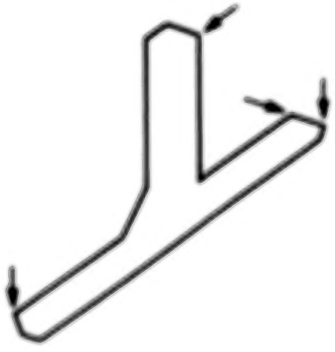
$$J_s(\underset{\sim}{a}^*) = \min_{\underset{\sim}{a}} J_s(\underset{\sim}{a}) \quad (1)$$

$$h_s(\underset{\sim}{a}) \geq 0 \ , \underset{\sim}{a}^* \in \underset{\sim}{a}$$

$$J_c(\underset{\sim}{a}^*, \underset{\sim}{u}^*) = \min_{\underset{\sim}{u}} J_c(\underset{\sim}{a}^*, \underset{\sim}{u}) \quad (2)$$

$$h_c(\underset{\sim}{u}) \geq 0 \ , \underset{\sim}{u}^* \in \underset{\sim}{u}$$



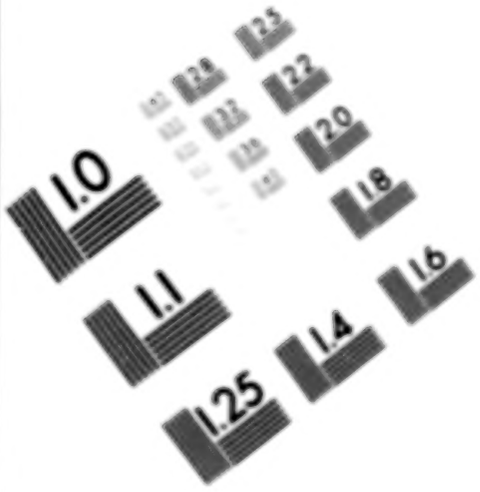


$$J(\underset{\sim}{a}^*, \underset{\sim}{u}^*) = J_s(\underset{\sim}{a}^*) + J_c(\underset{\sim}{a}^*, \underset{\sim}{u}^*) = \min_{\underset{\sim}{a}} J_s + \min_{\underset{\sim}{u}} J_c \quad (3)$$

- SIMULTANEOUS OPTIMIZATION

$$J(\underset{\sim}{a}^{**}, \underset{\sim}{u}^{**}) = \min_{\underset{\sim}{a}, \underset{\sim}{u}} [J_s(\underset{\sim}{a}) + J_c(\underset{\sim}{a}, \underset{\sim}{u})] \quad (4)$$

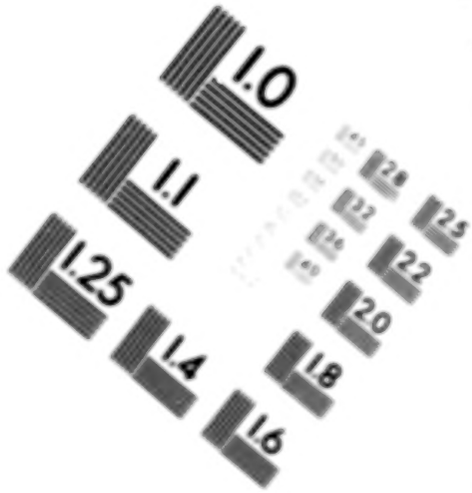
$$J(\underset{\sim}{a}^{**}, \underset{\sim}{u}^{**}) \leq J(\underset{\sim}{a}^*, \underset{\sim}{u}^*) \quad (5)$$



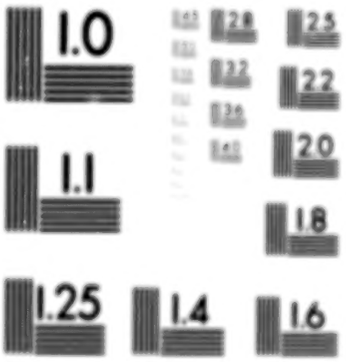


Association for Information and Image Management

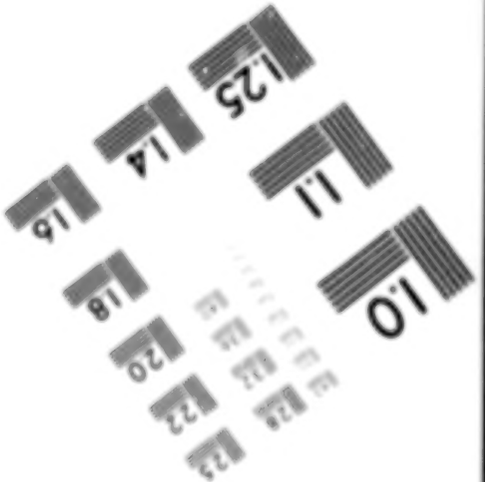
1100 Wayne Avenue, Suite 1100
Silver Spring, Maryland 20910
301/587-8202











MANUFACTURED TO AIIM STANDARDS
BY APPLIED IMAGE, INC.

DEFINITIONS: A common starting point for most approaches begins with the second order dynamical equation, Eq. (6), in n_s degrees of freedom (d.o.f.). The $\underset{\sim}{M}$, $\underset{\sim}{D}$, $\underset{\sim}{K}$ matrices are the mass, damping, and stiffness. $\underset{\sim}{G}_1$ = the disturbance influence matrix, $\underset{\sim}{G}_2$ = control influence matrix, $\underset{\sim}{a}$ = structure design variables, $\underset{\sim}{u}$ = control variables, w = disturbance vector, and v = physical d.o.f.

Let $\underset{\sim}{x} = (\underset{\sim}{v}, \dot{\underset{\sim}{v}})^T$ = state variables, then the equation of state is given by (7), with output consisting of controlled states $\underset{\sim}{z}$ and measured states $\underset{\sim}{y}$, both related to $\underset{\sim}{x}$ by Eq. (8). Where $\underset{\sim}{A}$, $\underset{\sim}{B}_1$, $\underset{\sim}{B}_2$, $\underset{\sim}{C}_1$ and $\underset{\sim}{C}_2$ are defined by Eq. (9).

$$\underset{\sim}{M}(\underset{\sim}{a})\,\ddot{\underset{\sim}{v}} + \underset{\sim}{D}(\underset{\sim}{a})\,\dot{\underset{\sim}{v}} + \underset{\sim}{K}(\underset{\sim}{a})\,v = \underset{\sim}{G}_1\,\underset{\sim}{w} + \underset{\sim}{G}_2\,\underset{\sim}{u} \tag{6}$$

$$\underset{\sim}{x} = (\underset{\sim}{v}, \dot{\underset{\sim}{v}})^T$$

$$\dot{\underset{\sim}{x}} = \underset{\sim}{A}(\underset{\sim}{a})\,\underset{\sim}{x} + \underset{\sim}{B}_1(\underset{\sim}{a})\,w + \underset{\sim}{B}_2(a)\,\underset{\sim}{u} \tag{7}$$

$$\text{CONTROLLED STATES} \quad \underset{\sim}{z} = \underset{\sim}{C}_1\,\underset{\sim}{x} \tag{8}$$

$$\text{MEASURED STATES} \quad \underset{\sim}{y} = \underset{\sim}{C}_2\,\underset{\sim}{x}$$

$$\underset{\sim}{A} = \left(\begin{array}{c|c} 0 & I \\ \hline -\underset{\sim}{M}^{-1}\underset{\sim}{K} & -\underset{\sim}{M}^{-1}\underset{\sim}{D} \end{array}\right); \quad \underset{\sim}{B}_1 = \left(\begin{array}{c} 0 \\ \hline -\underset{\sim}{M}^{-1}\underset{\sim}{G}_1 \end{array}\right); \quad \underset{\sim}{B}_2 = \left(\begin{array}{c} 0 \\ \hline -M^{-1}G_2 \end{array}\right)$$

$$\underset{\sim}{C}_1 = (C_{11}, C_{12}) \; ; \; \underset{\sim}{C}_2 = (C_{21}, C_{22}) \tag{9}$$

FORMULATION: Herein, we focus on LQ-based formulation as a natural one to generalize to the simultaneous control-structure optimization. Two types of controllers are considered; state feedback and output feedback. For both of these, the control criterion J_c is taken as a quadratic function of the structural response and control energy, Eq. (10). For the structural criterion, we assume one that depends only on the structural variables $\underset{\sim}{a}$. As will become clear later, this simplifies the derivations considerably. An example of such structural criteria is the mass of the structure, M(a).

The simultaneous optimization problem consists of finding the structure and control variables ($\underset{\sim}{a}^{**}$, $\underset{\sim}{u}^{**}$) that minimize the combined criterion (11), subject to any behavioral constraints (12), and/or side constraints (13) providing upper and/or lower bounds on the design variables ($\underset{\sim}{a}$, $\underset{\sim}{u}$). Since the terms in (11) do not have the same units, the scalar α and matrices $\underset{\sim}{Q}$ and $\underset{\sim}{R}$ can be chosen on computational and physical grounds.

- STATE FEEDBACK
- OUTPUT FEEDBACK
- INDIVIDUAL CRITERIA:

$$\text{CONTROL:} \quad J_c(\underset{\sim}{a}, \underset{\sim}{u}) = \int_0^\infty (\underset{\sim}{x}^T \underset{\sim}{Q} \underset{\sim}{x} + \underset{\sim}{u}^T \underset{\sim}{R} \underset{\sim}{u}) dt$$

$$\text{STRUCTURE:} \quad J_s(\underset{\sim}{a}) = M(\underset{\sim}{a}) \qquad (10)$$

- COMBINED CRITERION: FIND $(\underset{\sim}{a}^{**}, \underset{\sim}{u}^{**})$, $\underset{\sim}{a}^{**} \in \underset{\sim}{a}$, $\underset{\sim}{u}^{**} \in \underset{\sim}{u}$

$$J(\underset{\sim}{a}, \underset{\sim}{u}) = \min_{\underset{\sim}{a}, \underset{\sim}{u}} [\alpha M + \int_0^\infty (\underset{\sim}{x}^T \underset{\sim}{Q} \underset{\sim}{x} + \underset{\sim}{u}^T \underset{\sim}{R} \underset{\sim}{u}) dt] \qquad (11)$$

$$\text{SUBJECT TO:} \quad h_j(\underset{\sim}{a}, \underset{\sim}{u}) \geq 0 \qquad (12)$$

$$\underline{a} \leq a_i \leq \bar{a}, \; \underline{u} \leq u_i < \bar{u} \qquad (13)$$

STATE FEEDBACK: With the assumption that the structural objective M is dependent upon $\underset{\sim}{a}$ only, Eq. (11) simplifies to (14) and then to (15). This allows the familiar analytical solution for the optimal control u^{**} in (18) and its companion equations (16) and (17). The necessary conditions for the minimum of (15) subject to the constraint (17) and the constraints imposed by (12) can be derived by first forming an auxiliary Lagrangian function, then setting its partial derivatives at the local minimum to zero. This yields conditions (19), (20) and (21), from which the optimal $\underset{\sim}{a}^{**}$ can be computed iteratively. For a given $\underset{\sim}{a}$, Eqs. (21) and (22A) are solved for P and $P_{,a}$. With these, Eq. (19) is solved for an updated $\underset{\sim}{a}$, and (20) is evaluated to check the constraints.

- $J(a,u) = \min_{\underset{\sim}{a}}\left[\alpha M(a) + \min_{\underset{\sim}{u}} \int (\underset{\sim}{x}^T \underset{\sim}{\underset{\sim}{Q}} \underset{\sim}{x} + \underset{\sim}{u}^T \underset{\sim}{\underset{\sim}{R}} \underset{\sim}{u}) dt\right]$ (14)

$$= \min_{\underset{\sim}{a}}\left[\alpha M(a) + Tr(PQ_o)\right] \quad (15)$$

$$\underset{\sim}{\underset{\sim}{Q}}_o = \underset{\sim}{\underset{\sim}{B}}_1 \underset{\sim}{\underset{\sim}{B}}_1^T \quad \text{IF DIST W IS UNIT IMPULSE}$$
$$= \underset{\sim}{x}_o \underset{\sim}{x}_o^T \quad \text{IF DIST IS INITIAL COND } \underset{\sim}{x}(o) = x_o \quad (16)$$

$$\text{P SATISFIES} \quad A^T P + PA + Q - P(B_2 R^{-1} B_2^T)P = o \quad (17)$$

$$u^{**} = -R^{-1} B_2^T P X \quad (18)$$

- CONDITIONS OF OPTIMALITY

$$\hat{J}_{a_i} = \alpha M_{,a_i} + Tr(PQ_{o,a_i} + P_{,a_i} Q_o) + \sum_j \ell_j h_{j,a_i} = o \quad (19)$$

$$\ell_j h_j = o \quad (20)$$

$$A^T P + PA + Q - PB_2 R^{-1} B_2^T P = o \quad (21)$$

$$A_c^T P_{,a_i} + P_{,a_i} A_c + [A_{,a_i}^T P + PA_{,a_i} - P(B_2 R^{-1} B_2^T)_{,a_i} P + Q_{a_i}] = o \quad (22)A$$

$$A_c = A - B_2 R^{-1} B_2^T P$$

OUTPUT FEEDBACK: To avoid the state reconstruction necessary to implement the full state feedback control design, the static output feedback approach requires only the output of the measured states $\underset{\sim}{y}$. With a controller of the form of Eq. (22B), in which the gain $\underset{\sim}{F}$ is assumed to stabilize the structure, the combined criterion in (11) reduces to (23). Equation (23) is similar to its counterpart, Eq. (15) for the state feedback, except now the output feedback gain $\underset{\sim}{F}$ may be considered as an optimization variable in addition to $\underset{\sim}{a}$. Furthermore, $\underset{\sim}{P}(\underset{\sim}{a},\underset{\sim}{F}) = \underset{\sim}{P}^T(\underset{\sim}{a},\underset{\sim}{F})>0$ satisfies the Lyapunov Eq. (24).

Here again, the necessary conditions for the minimum of Eq. (23), subject to the constraints of Eqs. (24) and (12), can be found by forming the auxiliary Lagrangian function and setting its partial derivatives at the local minimum to zero. This leads to Eqs. (25) to (29), which must be solved iteratively. For a given ($\underset{\sim}{a}$, $\underset{\sim}{F}$), Eqs. (27), (28) and (29), respectively, allow the solution of $\underset{\sim}{P}$, the Lagrangian matrix multiplier $\underset{\sim}{L}$ and the scaler Lagrangians $\ell_j \geq 0$ for each behavioral constraint h_j. With these, Eqs. (25) and (26) yield an improved ($\underset{\sim}{a}$, $\underset{\sim}{F}$), and so on.

- ASSUMES $\underset{\sim}{u} = \underset{\sim}{F}\underset{\sim}{y}$ (F STABILIZES STRUCTURE) (22)B

- FIND MIN. OF $J(\underset{\sim}{a}, \underset{\sim}{u}) = \min_{\underset{\sim}{a},\,\underset{\sim}{F}} [\alpha \underset{\sim}{M} + \mathrm{Tr}(\underset{\sim}{P}\underset{\sim}{Q}_o)]$ (23)

  WHERE $P(\underset{\sim}{a}, \underset{\sim}{F})$ SATISFIES $\underset{\sim}{A}_c^T\underset{\sim}{P} + \underset{\sim}{P}\underset{\sim}{A}_c + \underset{\sim}{Q}_c = 0$ (24)

$$\underset{\sim}{A}_c = \underset{\sim}{A} + \underset{\sim}{B}_2\underset{\sim}{F}\underset{\sim}{C}_2$$

$$\underset{\sim}{Q}_c = \underset{\sim}{Q} + \underset{\sim}{C}_2^T\underset{\sim}{F}^T\underset{\sim}{R}\underset{\sim}{F}\underset{\sim}{C}_2$$

- CONDITIONS OF OPTIMALITY

$$\alpha \underset{\sim}{M}, a_i + \mathrm{Tr}[\underset{\sim}{P}\underset{\sim}{Q}_{o,a_i} + 2\underset{\sim}{L}\underset{\sim}{P}\underset{\sim}{A}_{c,a_i} + \underset{\sim}{L}\underset{\sim}{Q}_{c,a_i}] + \sum_j \ell_j h_{j,a_i} = 0 \quad (25)$$

$$\mathrm{Tr}[2\underset{\sim}{L}\underset{\sim}{P}\underset{\sim}{A}_{c,F} + \underset{\sim}{L}\underset{\sim}{Q}_{c,F}] + \sum_j \ell_j h_{j,F} = 0 \quad (26)$$

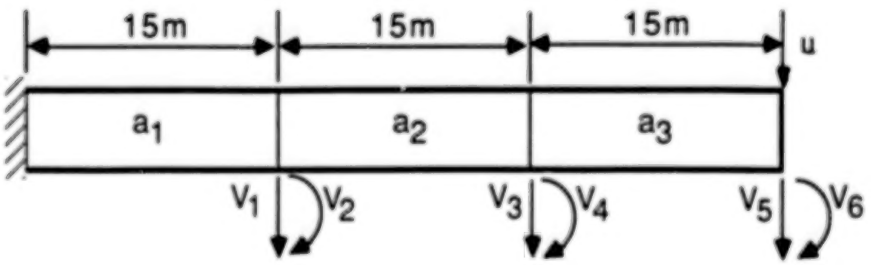
$$\underset{\sim}{A}_c^T\underset{\sim}{P} + \underset{\sim}{P}\underset{\sim}{A}_c + \underset{\sim}{Q}_c = 0 \quad (27)$$

$$\underset{\sim}{L}\underset{\sim}{A}_c^T + \underset{\sim}{A}_c\underset{\sim}{L} + \underset{\sim}{Q}_o = 0 \quad (28)$$

$$\ell_j h_j = 0 \quad (29)$$

EXAMPLE 1: STATE FEEDBACK (Ref. 1)

The cantilever beam shown is modeled by three finite elements with cross-sectional areas $\underset{\sim}{a} = (a_1, a_2, a_3)^T$, and has six d.o.f. An initial deformation vector at the six d.o.f. $x(0) = x_o$ is specified, and a control force u is applied at the free tip. The areas $\underset{\sim}{a}$ and control u are to be determined so as to minimize Eq. (11) while maintaining a fundamental open-loop frequency $\omega > 0.10$ rad/sec. Rather than a first order minimization, it was found necessary for faster convergence to use a second order scheme based on modified Newton-Raphson iterations. For this purpose, the design variables $\underset{\sim}{a}$ and multiplier ℓ are obtained iteratively from the recursive relations in Eq. (30).



$\underset{\sim}{x}_o = (0.011, 0.00135, 0.037, 0.002, 0.0688, 0.00216)^T$

$\omega \geq 0.10$ rad/sec. (i.e. $h = \omega^2 - (0.10)^2 \geq o$)

$E = 9.56\,10^{10} N/m^2$, $\rho = 1660\ Kg/m^3$

DAMPING = 0.5% CRITICAL

$$\begin{Bmatrix} \underset{\sim}{a} \\ \ell \end{Bmatrix}_{r+1} = \begin{Bmatrix} \underset{\sim}{a} \\ \ell \end{Bmatrix}_{r} - S \left[\begin{array}{c|c} J_{,\underset{\sim}{a}\underset{\sim}{a}} + \sum_j \ell_j h_{j,\underset{\sim}{a}\underset{\sim}{a}} & h_{j,\underset{\sim}{a}} \\ \hline h_{j,\underset{\sim}{a}} & o \end{array} \right]_r^{-1} \begin{Bmatrix} J_{,\underset{\sim}{a}} + \sum_j \ell_j h_{j,\underset{\sim}{a}} \\ \hline h_j \end{Bmatrix}_r \quad (30)$$

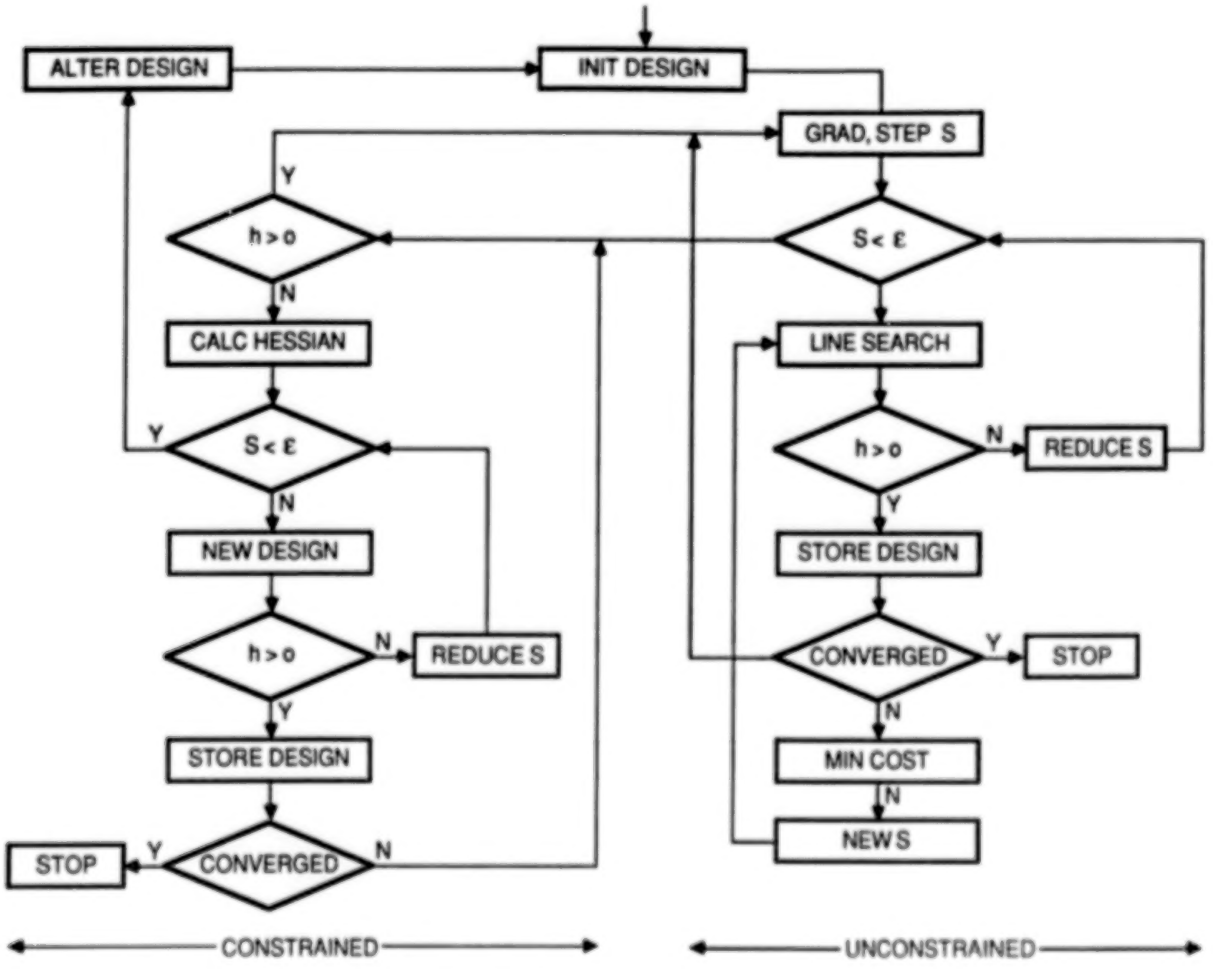
ALGORITHM: The algorithm begins with a feasible initial design and a step length s with which a line search in the direction of negative gradient is performed. This is continued until the minimum is reached, or until the constraint is violated. If the latter occurs, constrained minimization is employed with an initial estimate of the multiplier $\underset{\sim}{\ell}$ from

$$\underset{\sim}{\ell} = -[\underset{\sim}{H}^T\underset{\sim}{H}]^{-1}\underset{\sim}{H}^T\underset{\sim}{J}_{,\underset{\sim}{a}}$$

where

$$H = [h_{1,\underset{\sim}{a}} \cdots h_{n,\underset{\sim}{a}}]$$

With this Eq. (30) is used. The constraint is checked continually. If the design moves away from the constraint, unconstrained minimization is reverted to. Thus the minimization process alternates between iterations which involve unconstrained minimization and iterations which involve constrained minimization as outlined below.



EXAMPLE 1 - RESULTS: The numerical results of this example are displayed in the table below, in which the same initial design is optimized using two approaches; the traditional separate optimization and the simultaneous optimization. The numerical values for the weighting factors are $\alpha = 0.01$, $\underset{\sim}{Q} = \underset{\sim}{R}$ = identity.

The results of this example confirm that the simultaneous optimization of $(\alpha J_s + J_c)_{min}$ produces a combined design which is 50% superior over that produced by the separate optimization of $[(\alpha J_s)_{min} + (J_c)_{min}]$.

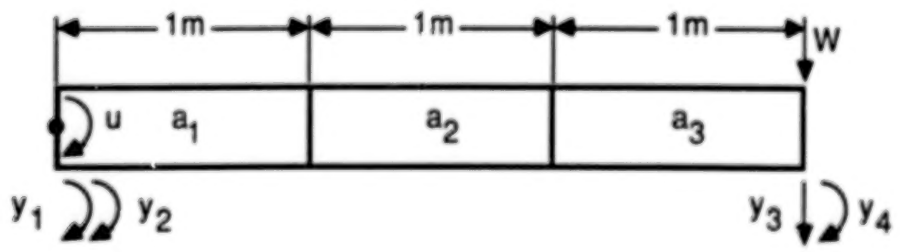
EXAMPLE 1: COMPARISON OF SEPARATE AND SIMULTANEOUS OPTIMIZATION

	INITIAL DESIGN			SEPARATE OPTIMIZATION			SIMULTANEOUS OPTIMIZATION		
	a_1	a_2	a_3	a_1	a_2	a_3	a_1	a_2	a_3
AREAS	0.001	0.001	0.001	0.318-4	0.211-5	0.133-5	0.849-4	0.625-6	0.149-6
ω	0.11853			0.10042			0.14799		
MASS (αJ_s)	(1.0)			(0.012)			(0.029)		
CONTROL INDEX (J_c)	(1.0)			(0.932)			(0.222)		
($\alpha J + J_c$)	(1.0)			(0.053)			(0.037)		

( ) = NORMALIZED TO INITIAL VALUE

EXAMPLE 2: OUTPUT FEEDBACK (Ref. 2)

In this example, an active disturbance force is applied to the free end of the beam in the figure below. At the other end the beam is pinned and a control torque is applied there. The measurements consist of angular deformation and angular velocity at the free end. The design variables for minimization are the cross-sectional areas $\underset{\sim}{a} = (a_1, a_2, a_3)^T$ and the gains $\underset{\sim}{F} = (F_1, \ldots F_4)^T$. No behavioral constraints are imposed. Other parameters of the problem are listed below. Since there are no constraints, the minimization algorithm is essentially similar to the unconstrained gradient search portion of the algorithm described previously.



$E = 800\ N/m^2, \rho = 100\ Kg/m^3$

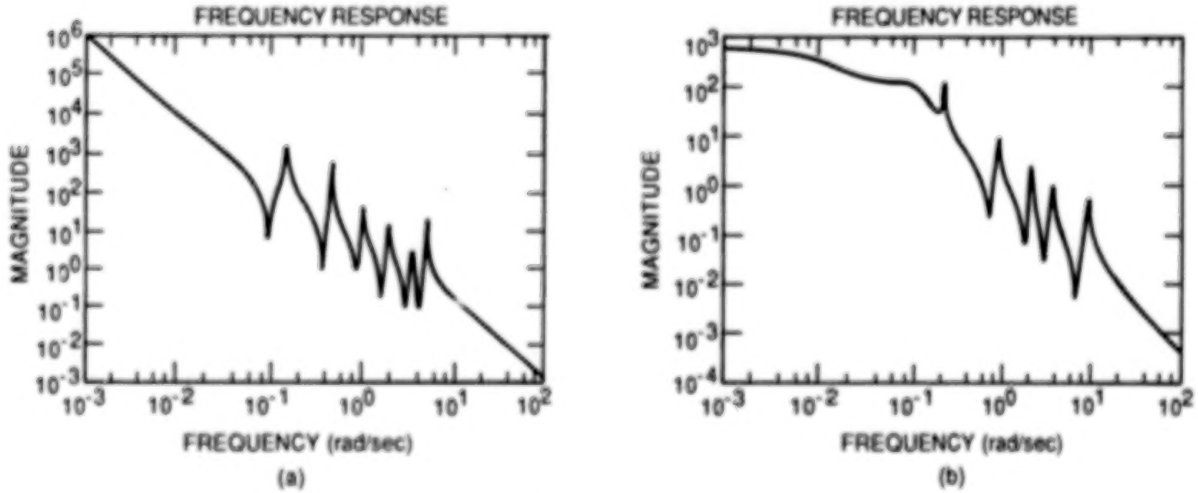
$R = 10, Q = c_1^T c_1, \alpha = 1000$

DAMPING = 0.5% CRITICAL

EXAMPLE 2 - RESULTS: The numerical results in the table below compare $\underset{\sim}{a}$ and $\underset{\sim}{F}$, and the resultant mass and combined index J for the initial design and optimized design. A factor of three reduction in J is realized as a consequence of simultaneous optimization over $\underset{\sim}{a}$ and $\underset{\sim}{F}$. In the accompanying plots, the transfer functions of the initial and optimum design from disturbance to the controlled output show three orders of magnitude reduction in response.

SIMULTANEOUS OPTIMIZATION

	INITIAL DESIGN				SIMULTANEOUS OPTIMIZATION			
AREAS	a_1	a_2	a_3		a_1	a_2	a_3	
	0.1	0.1	0.1		0.02308	0.01654	0.03572	
GAINS	F_1	F_2	F_3	F_4	F_1	F_2	F_3	F_4
	-1.0	-1.0	0.0	0.0	-0.0306	-1.2872	-1.2387	+0.1136
MASS	30.0				7.4			
$\hat{J}_{min}$	3.06×10^4				9.20×10^3			



FREQUENCY RESPONSE OF (a) INITIAL DESIGN AND (B) OPTIMUM DESIGN

CONCLUDING REMARKS: To show the feasibility of simultaneous optimization as design procedure, we have used low-order problems in conjunction with simple control formulations. The numerical results indicate that simultaneous optimization is not only feasible - but also advantageous. Such advantages come at the expense of introducing complexities beyond those encountered in structure optimization alone, or control optimization alone. Examples include: larger design parameter space, optimization may combine continuous and combinatoric variables, and the combined objective function may be nonconvex.

Future extensions to include large order problems, more complex objective functions and constraints, and more sophisticated control formulations will require further research to ensure that the additional complexities do not outweigh the advantages of simultaneous optimization. Some areas requiring more efficient tools than currently available include: multiobjective criteria and nonconvex optimization. We also need to develop efficient techniques to deal with optimization over combinatoric and continuous variables, and with truncation issues for structure and control parameters of both the model space as well as the design space.

- SIMPLE FORMULATIONS USED WITH LOW-ORDER PROBLEMS
- RESULTS SHOW SIMULTANEOUS OPTIMIZATION FEASIBLE AND ADVANTAGEOUS
- ADDITIONAL COMPLEXITIES:
  - LARGER PARAMETER SPACE
  - POSSIBLE NONCONVEXITY OF OBJECTIVE FN.
  - MIXTURE OF CONTINUOUS AND COMBINATORIC VARIABLES
- FURTHER EXTENSIONS:
  - LARGER PROBLEMS
  - OTHER OBJECTIVE FNs, CONSTRAINTS, MORE SOPHISTICATED CONTROL FORMULATIONS
  - MORE EFFICIENT TOOLS TO DEAL WITH ABOVE COMPLEXITIES
  - UNIFIED TRUNCATION METHODOLOGY FOR CONTROL & STRUCTURE PARAMETERS OF MODEL SPACE & DESIGN SPACE

REFERENCES:

1. Salama, M., Garba, J., and Demsetz, L., "Simultaneous Optimization of Controlled Structures," Journal of Computational Mechanics, Vol. 3, 1988, pp. 275-282.

2. Ramaker, R., "Integrated Structural/Controller Optimization Using Output Feedback," Engineering Memorandum 347-88-254, 1988, Jet Propulsion Laboratory, Pasadena, CA.

A Survey of Experiments and Experimental Facilities for Active Control of Flexible Structures

Dean W. Sparks, Jr.
Garnett C. Horner
Jer-Nan Juang
NASA Langley Research Center
Hampton, VA

Gerhard Klose
Jet Propulsion Laboratory
Pasadena, CA

Third NASA/DoD CSI Technology Conference
San Diego, CA
January 30 - February 2, 1989

MOTIVATION

We wish to identify large space structures (LSS) ground test experiments and facilities, both past and current, for comparison with the planned Langley Research Center's (LaRC) Control/Structures (CSI) Program's experiments and facility. This will give a better perspective of the ground testing work to be performed at LaRC.

TO IDENTIFY LSS GROUND TEST EXPERIMENTS AND FACILITIES, BOTH PAST AND PRESENT, TO PUT THE CSI TEST PLANS INTO PERSPECTIVE

INTRODUCTORY COMMENTS

NASA's future space missions will involve advanced space systems, such as the Hubble Space Telescope and the Mission to Earth platform. These systems will be comprised of large, flexible structures of complex, multi-body designs. They will also have increased on-orbit performance capabilities, such as large angle (non-linear) slewing, in order to accomplish their missions.

It is envisioned that new interdisciplinary (CSI) design methods will be required to tackle the challenges stated above. These new design and analysis methods will inevitably result in new concepts that must be validated via thorough ground testing. Ground experimentation will be required for (1) concept development - the testing of new configurations and concepts for space structures, optimized in terms of both controls and structures and (2) analysis verification - verifying new control algorithms or structural identification techniques in the laboratory. Both of these must be checked out in the most realistic scenarios as feasible. This will include advanced suspension systems and in testing in special controlled environments.

- **NASA FUTURE SPACE MISSIONS WILL INVOLVE:**

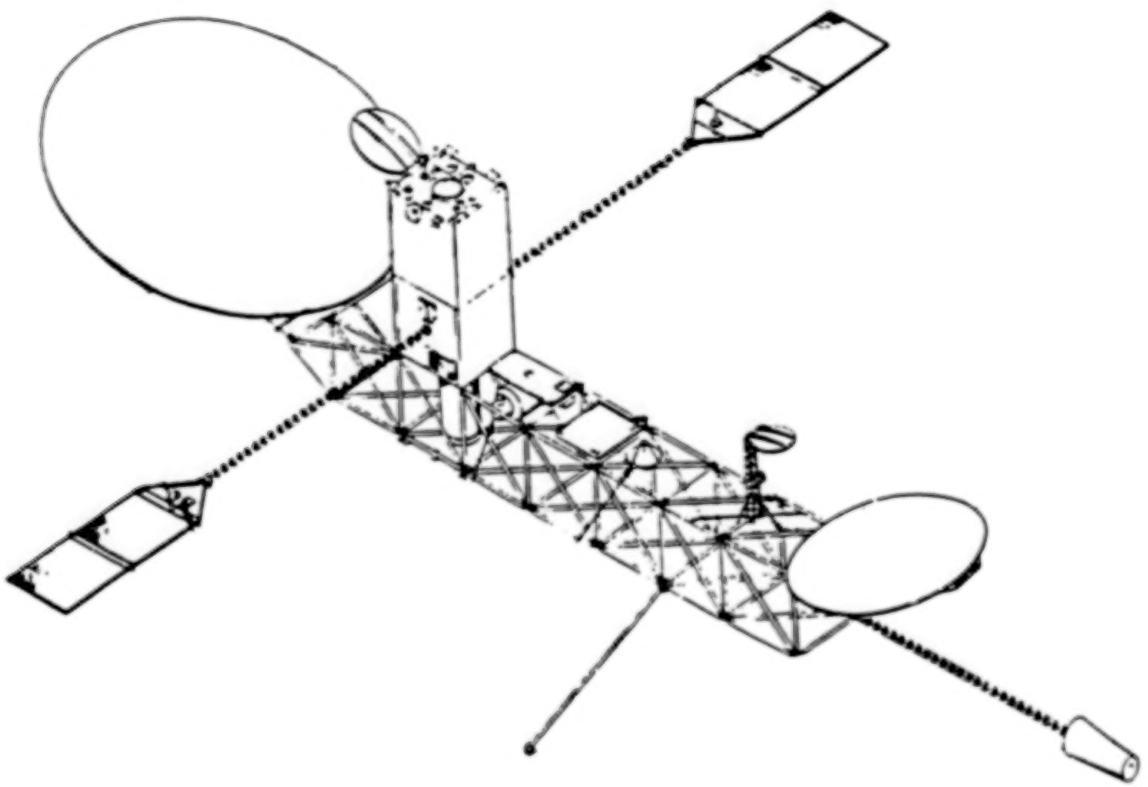
  LARGE, FLEXIBLE STRUCTURES
  COMPLEX, MULTI-BODY DESIGNS
  LARGE ANGLE (NON-LINEAR) MANEUVERS

- **NEW INTERDISCIPLINARY DESIGN METHODS WILL BE REQUIRED TO MEET THESE CHALLENGES**

- **GROUND TESTING WILL BE REQUIRED FOR:**

  CONCEPT DEVELOPMENT
  ANALYSIS VERIFICATION
  REALISTIC SIMULATION

MISSION TO EARTH PLATFORM



OUTLINE

This survey will cover large space structure ground testing in the following order: (1) the pre 1982 experiments, the last survey was conducted in 1982 and this paper will take up from that point, (2) post 1982 experiments and facilities, those recently concluded or are still ongoing, and (3) the planned future experimental facilities, concentrating on Langley's CSI ground test program. In the descriptions of each experimental set-up, pertinent components of the test article and/or test procedures that address flexible spacecraft issuses (e.g., vibration suppression, slewing and pointing control) will be emphasized.

The paper only reports on U.S. experimental programs (with the sole exception of one test bed from Canada). Also, even with the increased work in flexible robots, the topic of robotics is not included in this survey. It is felt that it should be treated as a separate issue.

- **PRE 1982 EXPERIMENTS**
- **POST 1982 EXPERIMENTS & FACILITIES**
- **FUTURE EXPERIMENTAL FACILITIES**
- **SUMMARY**

PRE 1982 EXPERIMENTS

The following chart, taken directly from an Air Force Rocket Propulsion Laboratory (AFAL) report [1], shows the ground experiments pertaining to large space structures studies undertaken up to 1982. They were relatively simple test articles, being beams or plates, as compared to present structures. None were specifically tailored to control-structure interaction studies.

One interesting note: the general types of actuators (torquers, proof masses, piezoelectrics, ...) and sensors (rate gyros, lasers, accelerometers, ...) used then were pretty much the same as today's. There is certainly an opportunity to develop and test new types of these devices in the CSI program.

Company	Type	Description	Sensor	Actuator	Demonstration
Draper	Beam	Fixed-free 1/4" X 1" X 60" Aluminum	Piezoelectric Accelerometers	Electrodynamic Shaker	Observation/control spillover modern modal control
Lockheed	Beam	Fixed-free 40" Magnesium	Optical rate sensor	Proof-mass	Low authority control
	I-Beam	Fixed-free 25' X 18" (400lbs) Aluminum	Optical rate sensor	Single gimbal CMG	Low authority control
	Vertical Beam	Fixed-free 6' Aluminum lead tip masses	Accelerometers, quad-detector photodiodes	Pivoted proof-mass	Low authority control System identification
	Circular plate	Suspended, 2 meter diameter, Aluminum	Multi-channel micro-phase optics	Pivoted proof-mass	Low authority control Low/High authority control System identification
	POC *	Suspended, 4.5 meter boom, 3 meter reflector, Aluminum	Accelerometers, rate gyros, laser	CMG, proof mass	Classical & modern control of vibration & slew
	Toysat	Suspended rigid body 1.6 m cantilever beams Aluminum	Accelerometers, LVDT velocity pickoffs	Electrosesis actuators	Open loop torque profile high authority control
Convair	Plate	Fixed-free 68" X 103" Aluminum 4" X 5/16" welded beams	Rate gyros	Torque wheels	Modern error sensitivity suppression
JPL	Beam	Pinned-free 150" X 6" X 1/32" stainless steel	Eddy current position sensor	Brushless d.c. torque motor	Modern modal control
LaRC	Beam	Suspended 12' X 6" X 3/16" Aluminum	Noncontacting deflection sensor, load sensor	Electrodynamic shaker	
TRW	Plate	Clamped 1.73 m X 1.22 m X 1.66 mm Aluminum	Rate sensors, accelerometers	Bending moment actuator	Vibration suppression and damping augmentation

* Lockheed's Proof of Concept (POC) experiment, for ACOSS support, is the most sophisticated test article on this chart. It was tested from 1981 to 1983.

POST 1982 EXPERIMENTS

The following charts show the flexible structures experiments of the present day. The catagories are broken into four parts: (1) experiment name, the responsible organization and a contact name, (2) the general description, (3) actuator and sensor types used, and (4) the main goal(s) of the experiment. This list is certainly not all inclusive but does provide a good sample of experiments recently concluded or ongoing. This list was compiled through direct contacts with researchers in the large space structures community and by literature search [2-17].

There are several experiments in this chart that are of particular interest, in terms of CSI. The Harris Plate Experiment is especially interesting since one of its test objectives is the study of actuator and sensor placement. This important issue is one of the basic concerns in the CSI Program (not only the placement of hardware, but possibly the development of new types).

The Spacecraft Control Laboratory Experiment (SCOLE) is a good test article for rigid-body slewing and vibration suppression testing. The fault detection tests performed on SCOLE are very important, since real spacecraft hardware failures are inevitable. This issue will be studied carefully in the CSI Program.

POST 1982 EXPERIMENTS

EXPERIMENT	DESCRIPTION	ACTUATORS/SENSORS	TEST OBJECTIVE
Advanced Beam Experiment (ABE) - AFWAL [Robert W. Gordon]	71 in. aluminum beam, vertically hung, cantilevered at top	Proof mass actuators, accelerometers	active vibration suppression
12 m Truss Control AFWAL [Robert W. Gordon]	Aluminum truss, vertically oriented, cantileverd at base	Proof mass actuators, accelerometers, photodiode	active & passive damping
TRW Truss Experiment [Maribeth Roesler]	115 X 55 in. truss box	optical sensor	active & passive damping
Compound Pendulum Harris Corp. [John Shipley]	2 beams, connected at middle and bottom end	Harris Linear DC motor, accelerometers	testing of Harris LDCM on lightly damped structure
Plate Experiment Harris Corp. [John Shipley]	4 sq. ft., 1/8 in. thick plate, suspended vertically	microshakers, accelerometers	surface roughness control, sensor/ actuator placement studies
Multi-Hex Prototype Experiment (MHPE) Harris Corp. [John Shipley]	10 ft diameter, 7 graphite epoxy panel segmented test bed	Harris Linear Precision Actuators (LPACTS), piezoelectrics, optical sensor	generic testing of large segmented reflectors, surface shape control
Air Force Planar Truss Experiment USAFA-AFOSR [William L. Hallauer]	23.3 ft, 20 bay truss, horizontal on bearing	thrusters, proof mass actuators, accelerometer	actuator-structure interaction studies
Beam Cable - VPI [William L. Hallauer]	80 in. vertical steel beam, with aluminum cross beam, hung by cables	force actuators, velocity sensors	active damping, theoretical/ experimental comparisons
2-D Pendulous Plane Grid VPI [William L. Hallauer]	Aluminum grid with steel top beam		
Slewing Grid - VPI [William L. Hallauer]	Aluminum plane grid, pivots about steel shaft	reaction wheels, servo accelerometers	active rigid body slewing and vibration suppression

POST 1982 EXPERIMENTS (CON'T)

EXPERIMENT	DESCRIPTION	ACTUATORS/SENSORS	TEST OBJECTIVE
Hoop-column antenna Langley [Thomas Campbell]	15 m mesh antenna, supported by outer graphite hoop, a 13 m column in center	accelerometers, proximity probes	deployment, electromagnetic, structural tests
Three-body rapid maneuvering experiment Langley [Jer-Nan Juang]	two flexible, horizontal panels, one on each side of a rigid hub, hub rotates in horizontal plane	gearmotor, strain gauges, potentiometers	rapid slewing experiments
Multi-body maneuvering experiment - Langley [Jer-Nan Juang]	1 m flexible panel, projecting out from a cart, cart travels on a horizontal 3 m beam	gear box motor, direct drive motor, tachometer, potentiometer, strain gauges	rapid translational & rotational control of flexible panel, can be mini-test article for CSI
Daisy Test bed Dynacon Enterprises [P.C. Hughes]	central rigid hub, 10 equally spaced rods projecting out total diameter 19 ft.	thrusters, reaction wheels, accelerometers, digital angular motion encoders	generic test bed for flexible spacecraft studies
Ohio State University Control Research Lab [Ü. Özgüner]			
Free-Free Beam	1.8 m horizontally suspended aluminum beam	proof mass actuators, accelerometers, strain gauges	system ID, vibration suppression
Slewing Beam	40 in. horizontal aluminum beam, attached at end to hub, counter-weight attached at opposite side of hub	direct drive motor, motor encoders, accelerometers, tachometer	slewing control and vibration suppression
Smart Structures Lab VPI [Harry Robertshaw]			
Variable Geometry Truss	2 module variable configuration truss, with beam suspended vertically in center	electric motors, linear potentiometers, strain gauges	truss configuration, beam control
Planar Truss	1 bay truss, contrained on one side, horizontal on table	jack screws, strain gauges	vibration and slewing control
Free-Free Planar Truss	1 bay truss, free to move horizontally on table	jack screws, strain gauges, linear potentiometers	

293

BEST COPY AVAILABLE

POST 1982 EXPERIMENTS (CON'T)

EXPERIMENT	DESCRIPTION	ACTUATORS/SENSORS	TEST OBJECTIVE
Flexible Satellite Slew Test bed - AFAL/CSDL [P. Madden]	hub with 4 horizontal arms (9 ft total diameter), suspended on air table	cold gas jets, proof mass actuators, angle resolver, accelerometers	active vibration suppression, rigid body slewing control
MIT Space Systems Lab [Ed Crawley]	composite beam, horizontally hung by wire	embedded piezoceramic actuators, strain gauges	active vibration suppression
	25 ft. brass beam, horizontally suspended by wire	shaker, accelerometer	traveling wave experiments
	horizontal truss on soft springs	piezoceramic actuators, PCB structcel accelerometers	active structural member studies
Aluminum Beam Expander Structure (ABES) AFWL [David Founds]	SBL Beam Expander Model 9 m tripod, 6 m base	shakers, triaxial accelerometers	system identification
Spacecraft Control Laboratory Experiment (SCOLE) - Langley [Raymond Montgomery]	rigid platform, with 10 ft beam with a 40 in. diameter offset reflector frame, all suspended by steel cable	cold gas jets, reaction wheels, control moment gyros, rate gyros, optical sensors, accelerometers	slewing and pointing experiments, with vibration suppression, system identification tests, failure detection and reconfiguration tests
Advanced Structures/ Controls Integrated Experiment (ASCIE) Lockheed [Ken Lorell]	truss supporting a 2 m diameter, 7 hexagonal aluminum plate, segmented mirror	proportional electro-mechanical flexure levers, optical sensor	control test bed for segmented reflectors
Space Integrated Controls Experiment (SPICE) - AFWL [Capt. Robert Hunt]	SBL test model	active suspension (SAVI) and passive	
Passive and Active Control of Space Structures (PACOSS) AFWAL/MMDA	Dynamic Test Article (DTA) various components		Active and passive control
Joint Optics Structure Experiment (JOSE) AFAL-TRW-Litton-ITEK [Capt. Robert Hunt]	Primary/secondary reflector optical truss - Halo structure	proof mass actuators	

BEST COPY AVAILABLE

POST 1982 EXPERIMENTS (CONC)

EXPERIMENT	DESCRIPTION	ACTUATORS/SENSORS	TEST OBJECTIVE
SUNY - Buffalo [Daniel Inman]	vertically oriented aluminum beam, cantilevered, active hinge connecting beam with second flexible beam	torque motor, strain gauges, tachometer (active hinge)	slewing/vibration suppression control
	cantilevered composite beam	proof mass actuators	transverse vibration control, actuator/sensor interaction tests
	horizontally cantilevered beam	torque motor	eigenfunction based slewing control
	planar truss structure	proof mass actuator	periodic trusses modeling
	cantilevered beam and truss	electric motors	slewing/vibration control, actuator/sensor interaction tests
	horizontal beam, hinged at end, suspended at other end	active track/cart system	active suspension tests
Vibration Control of Space Structures (VCOSS) MSFC-AFWAL-LMSC-TRW [Henry B. Waites]	13 m Astromast with asymmetric cruciform at base, vertically oriented, cantilevered at top	linear momentum exchange devices, LVDT, accelerometers	pre-cursor to ACES
Active Control Technique Evaluation for Spacecraft (ACES) - MSFC [Henry B. Waites]	13 m Astromast with 3 m offset antenna, vertically oriented, cantilevered at top	linear momentum exchange devices, accelerometers, laser	general test article, vibration suppression, system ID
Mini-Mast - Langley [Richard Pappa]	vertically oriented, 20 m, 18 bay truss, cantilevered at base	reaction wheels, proof mass actuators, position sensors, accelerometers	vibration damping and system ID, general test structure

295

BEST COPY AVAILABLE

AIR FORCE PLANAR TRUSS EXPERIMENT

The following experiment was built to study the interactions between a structure's flexible modes and the dynamics of the structure's proof mass actuator used for vibration suppression. This important work will look into these interactions and how they may be taken advantage of when designing control systems. The test article is a 20 bay, 23.3 ft. long planar truss resting horizontally on ball bearings. A pair of air thrusters for low frequency vibration suppression and the proof mass actuator for high frequency vibrations serve as actuators. An accelerometer is used as a sensor.

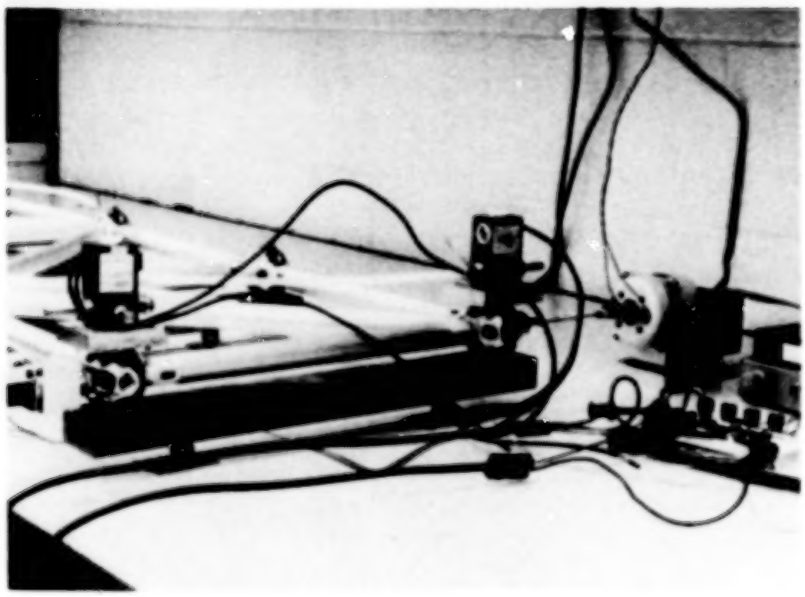
Attachments will be added to this planar truss to build up an article that better mimics more elaborate space structures after the above study is completed. This interactions work will continue on the more complex dimensional test structure. Futhermore, various types of proof mass actuators, their locations and their mountings on the structure will be examined.

The work is currently sponsored by the Air Force and is being conducted at the Air Force Academy. The principal investigators are Steven Lamberson, William Hallauer, John Duke and David Wagie.

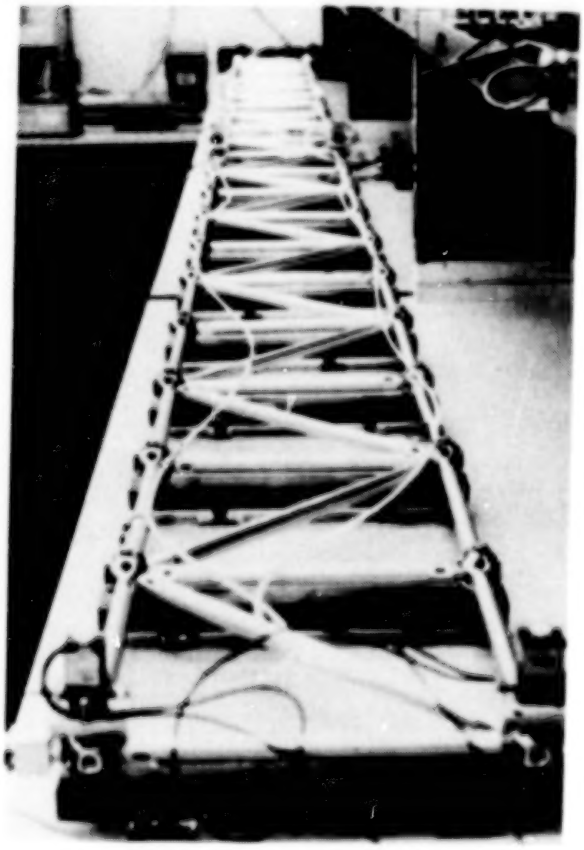
- **EXAMINES ACTUATOR & STRUCTURE INTERACTION**

- **INCLUDES INTERACTION EFFECTS IN CONTROL SYSTEM DESIGN**

- **PROVIDES BACKGROUND FOR MORE COMPLEX TEST ARTICLES**



Truss Tip Instrumentation



Photograph of Planar Truss

MULTI-BODY MANEUVERING EXPERIMENT

A test article for studying rapid translational and rotational motion control of a flexible panel has been built at NASA Langley. This structure consists of the following parts: 1 m flexible panel projecting out from a cart which can travel along a straight, horizontal 3 m beam. The flexible panel is also oriented horizontally, but is at a right angle with respect to the beam. A direct drive motor on one end of the beam moves the cart along the beam, while a gearmotor on the cart provides moments at the end of the flexible panel. Strain gauges attached to the flexible panel and a potentiometer on the cart give sensor measurements.

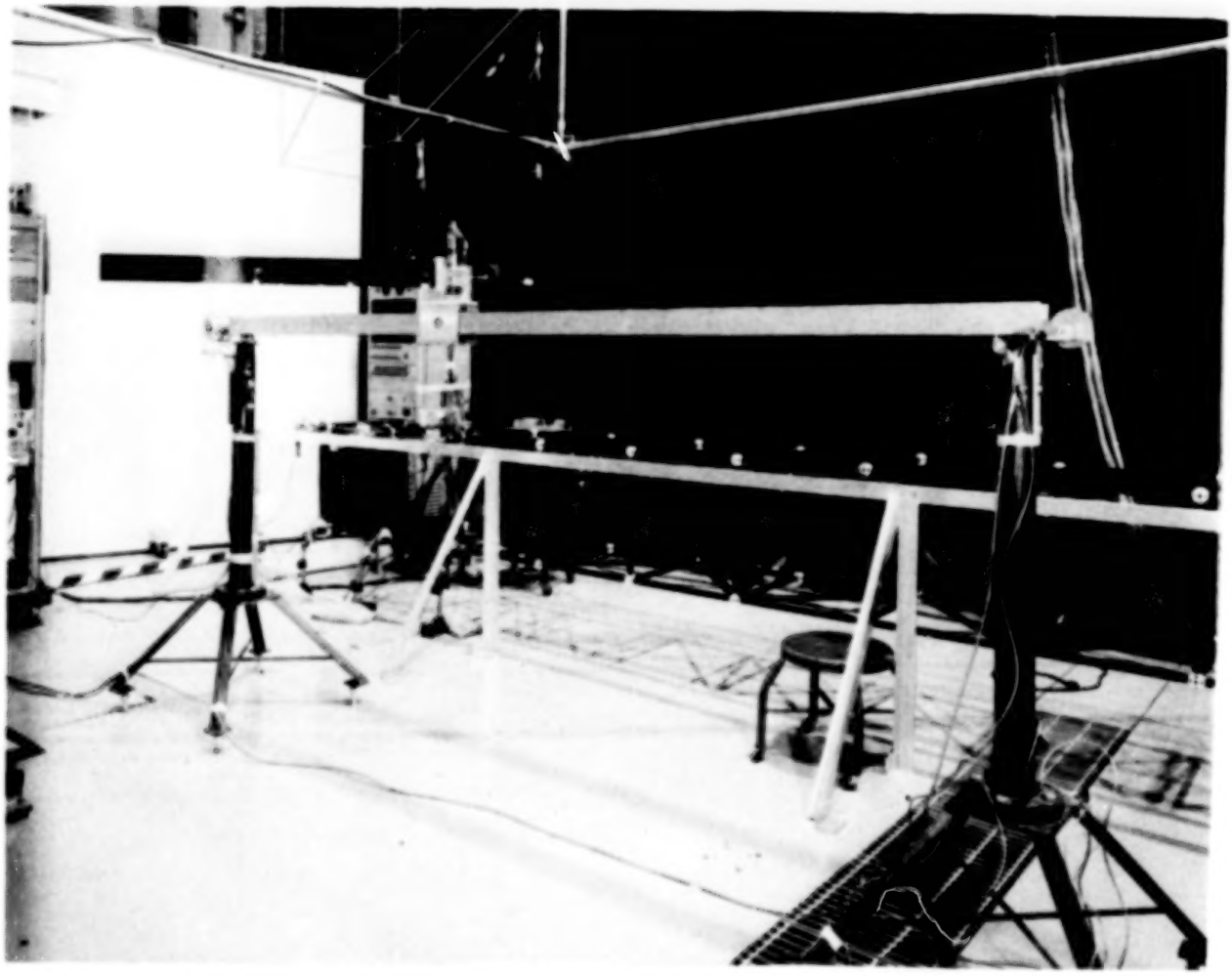
This is an on-going experiment that addresses rapid maneuvering of payloads. However, its small size precludes it from becoming a full test article for the CSI Program. It is hoped that this particular article can be used to perform initial control tests before placing the same control algorithms on the full size CSI test model.

- **RAPID TRANSLATIONAL & ROTATIONAL MOTION CONTROL OF A FLEXIBLE PANEL**

- **ADDRESSES RAPID PAYLOAD MANEUVERING PROBLEMS**

- **TOO SMALL FOR FULL SIZE CSI TEST ARTICLE, CAN BE USED FOR PRELIMINARY CONTROL ALGORITHM VERIFICATION**

PHOTOGRAPH OF LANGLEY'S MULTI-BODY MANEUVERING EXPERIMENT



HARRIS MULTI-HEX PROTOTYPE EXPERIMENT

Harris Corporation has built the Multi-Hex Prototype Experiment (MHPE) to act as a test bed for control/structure interaction studies. The test article represents a generic large, deployable segmented antenna or mirror. It is made up of seven graphite epoxy panels, resulting in a total diameter of 10 feet. This test article will address several issues: vibration suppression, pointing control and the important surface shape control. Harris developed linear proof mass actuators, called Linear Precision Actuators (LPACTS), and piezoelectric actuators will be used, as well as an optical measurement system for sensing.

Currently, system identification work is being performed on the MHPE. It is planned to use an optical quality surface, wavefront sensors, additional piezoelectrics and a pointing system to complete the MHPE test article set-up. The test bed can also serve as a platform for the development and testing of new actuators and sensors.

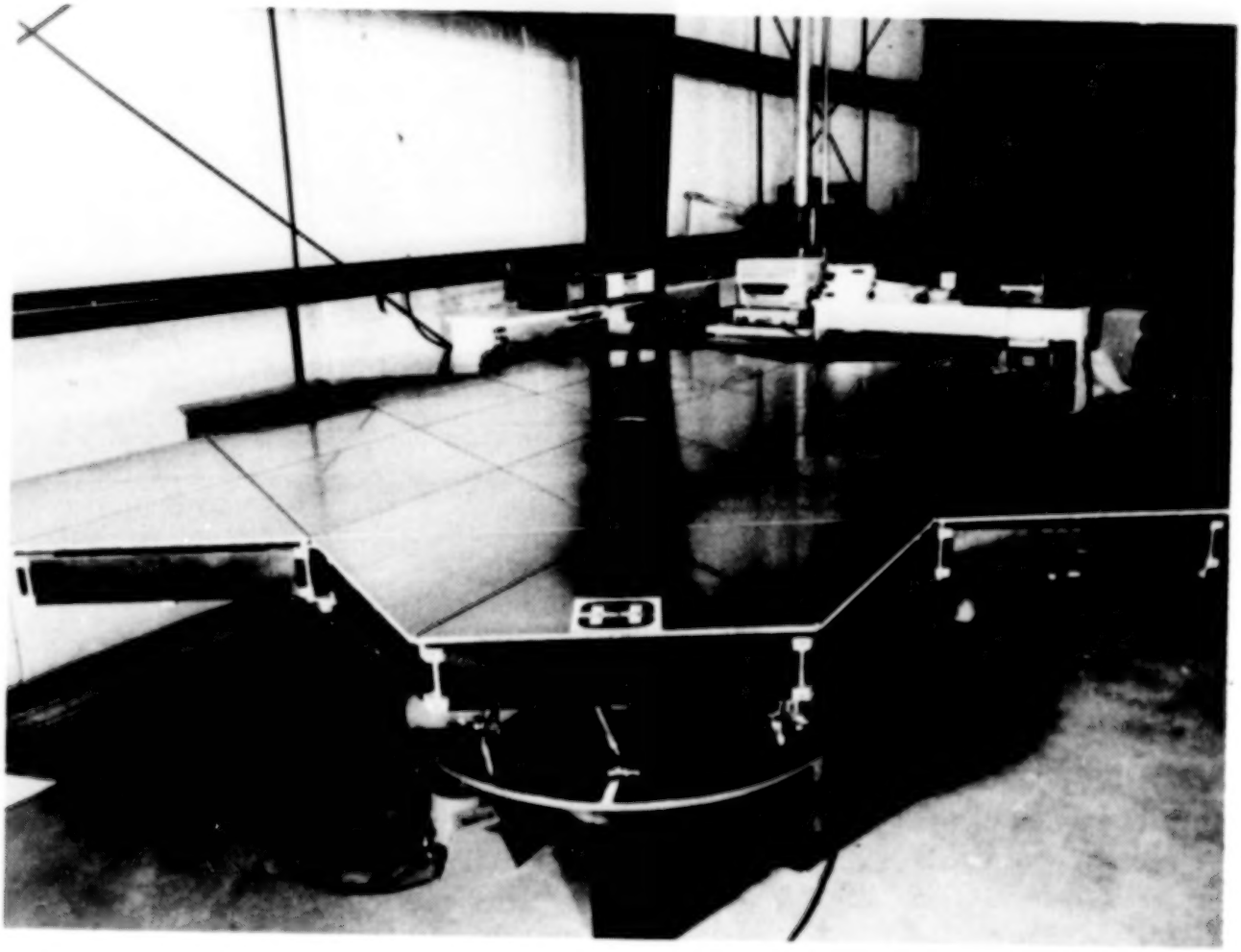
- **TEST BED FOR GENERIC LARGE SEGMENTED MIRROR OR ANTENNA STUDIES**

- **VARIOUS CONTROL FUNCTIONS WILL BE TESTED:**

  VIBRATION SUPPRESSION
  POINTING CONTROL
  SURFACE SHAPE CONTROL

- **CAN BE USED AS PLATFORM FOR NEW ACTUATOR AND/OR SENSOR DEVELOPMENT**

PHOTOGRAPH OF THE HARRIS MULTI-HEX PROTOTYPE EXPERIMENT



POST 1982 FACILITIES

The attached chart shows current large structure research facilities. The facility, in this survey, includes the test article on which the experiment is being performed, the computer systems and other necessary equipment to support the test work.

The catagories for the facilities chart are as follows: (1) the facility name, (2) general description, both of the experiment and the laboratory, (3) the computer and data acquisition systems used, (4) the actuator and sensor hardware on the test article(s), and (5) the test objective(s) of the facility.

The Large Space Structure - Ground Test Facility (LSS-GTF), the Advanced Space Structure Technology Research Experiment (ASTREX) facility, the JPL Testbed Facility and Langley's Large Component Test Laboratory (LCTL) are all dedicated to CSI experimentation. The AFAL ASTREX facility supports DoD CSI tests while the facilities at MSFC and JPL support NASA's CSI programs. The LCTL currently houses a Space Station truss article for structural dynamics testing. In a short time, a CSI dedicated test structure will also be placed in this laboratory.

POST 1982 FACILITIES

EXPERIMENT	DESCRIPTION	COMPUTER SYSTEM	ACTUATORS/SENSORS	TEST OBJECTIVE
Large Space Structure - Ground Test Facility (LSS-GTF) - MSFC [Henry B. Waites]	currently houses ACES - I, has Single Structure Control (SSC) Lab. future plans: Pinhole Occulter Facility (POF), Multi-Payload Pointing Mount (MPPM), Unobtrusive Sensor and Effector (USE) Lab, Robot Enchancement Lab and Vacuum/ Thermal Chambers. 5m x 5m x 36m	HP 9000 - 9200	advanced gimbal system (AGS), base excitation system (BET), linear momentum exchange devices (LMED), rate gyros, laser system, accelerometers	facility to test LSS articles
Large Space Systems Lab (LSS Lab) - AFAL [Alok Das]	currently houses 25 sq. ft. aluminum grid structure	ISI Max 100	accelerometers, load cells, proximity sensors	system identification
Advanced Space Structures Technology Research Exp. (ASTREX) Lab - AFAL [Alok Das]	40 ft x 40 ft x 40 ft lab space for Space Based Laser (SBL) model	VAX 8600, MicroVAX III	control moment gyros, gas jets, proof mass actuators, rate gyros, accelerometers	specific control-structures studies
Control Technology Verification Facility (CTVF) - JPL [Dan Eldred]	40 ft diameter, 26 ft tall space, houses 19 ft diameter rigid hub structure with 12 equally spaced ribs projecting out.	DEC VAX II/ STD bus based with 80B8 microprocessor	force actuators, position sensors, optical sensor, RVDT angular sensor	facility for control studies, system ID

303

BEST COPY AVAILABLE

POST 1982 FACILITIES (CONC)

EXPERIMENT	DESCRIPTION	COMPUTER SYSTEM	ACTUATORS/SENSORS	TEST OBJECTIVE
MIT Apparatus for Structural Testing & Research on On-orbit Vibration & Control [Ed Crawley]	10 ft diameter vacuum chamber (10**-6 to 10**-8 torr.), 14 ft in height	IBM PC, Microvax, Lecroy and custom built A/D, D/A	strain gauges	free fall tests in a vacuum
JPL Testbed facility [Jim Fanson]	Lab is 1966 sq ft and 20 ft ceiling	PDP 11/73	shakers, piezoelectric actuators, accelerometers, laser	active structure control, system ID, CSI support
Modified Astromast	5 ft fiberglass model of Astromast, vertical, cantileverd at bottom			
Precision Truss	6 ft, 6 bay truss, vertical, cantilevered at base			
Free-Free Truss	13 bay truss, horizontal, cantilevered or suspended in center			
Large Component Test Lab - Langley [Jer-Nan Juang]	80 ft x 80 ft X 80 ft building, currently houses Space Station Truss model	CAMAC - Cyber 175		facility for CSI tests, Space Station modelling

BEST COPY AVAILABLE

JPL TEST BED FACILITY

The JPL Test bed facility was built primarily for testing active control structures, though system identification work can also be done. Currently, this facility supports the CSI program.

There are three test articles in this facility, they are:

Modified Astromast - This structure is a 5 foot, 3 longeron, fiberglass segment of the Astromast. Its base is designed such that the supporting system is statically determinate. The structural elements can be easily replaced, either by active structural members or sensors. Also, the top has a steel plate on which masses can be added or removed as desired.

Precision Truss - This test article is a 6 foot, 6 bay, 4 longeron truss with special joints which allow for the changing of structural elements and masses. Thus, the dynamic properties of the test truss can be varied for study. The lowest frequency is approximately 8 Hz and lowest damping ratio value is .04%.

Free - Free Truss - This test structure is like the precision truss in that the structural members and masses are changeable. The 13 ft. free - free truss consists of 13 bays and 3 longerons and can be either cantilevered or suspended (free-free) at the center of the truss.

There are various excitors (2 - 150 lbs) and accelerometers available, as well as a laser interferometer system and piezoelectric actuators (50 lb) as active structural components.

The most important aspect of these test articles is the fact that their structural members are changeable, lending themselves to control systems/structures effects studies.

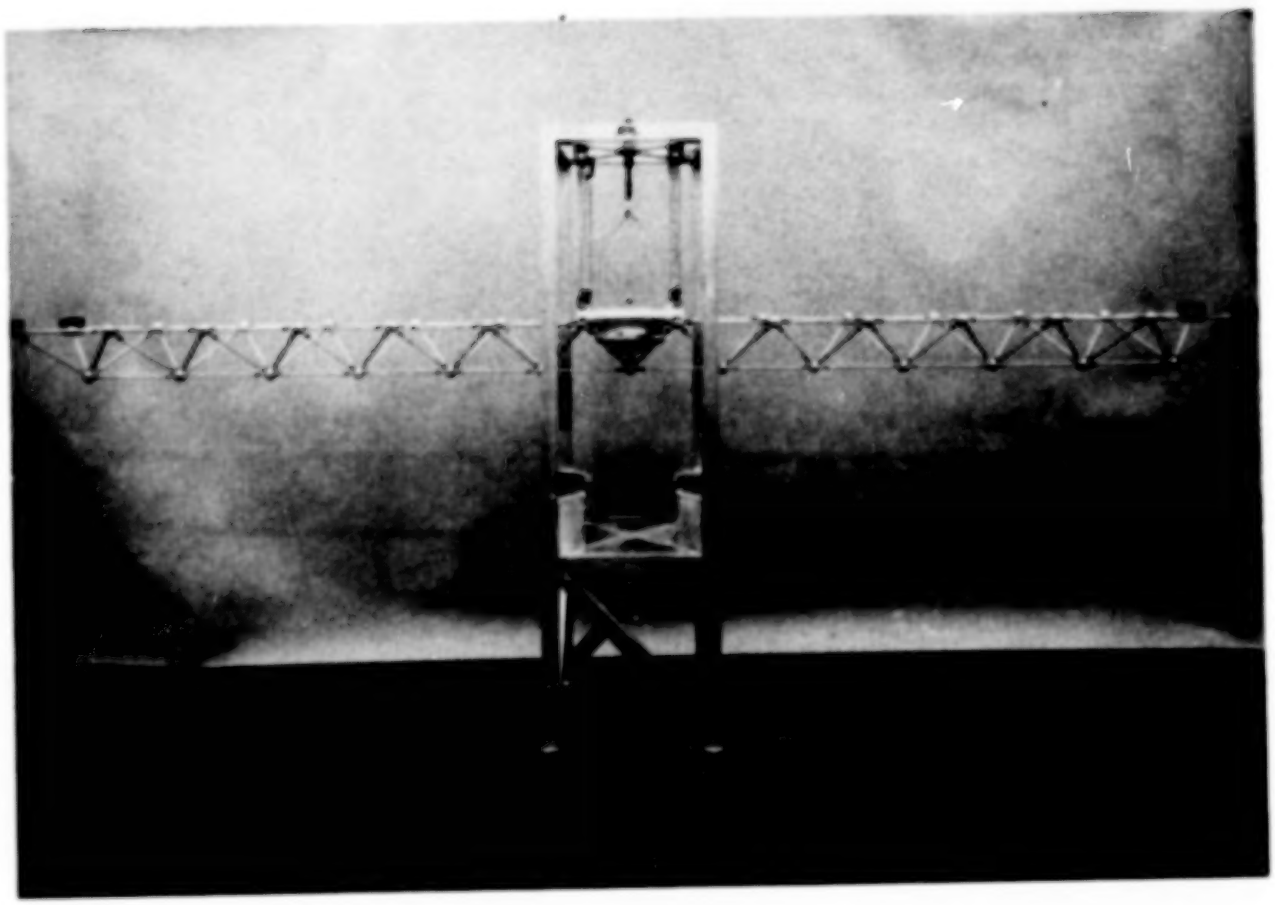
- ACTIVE STRUCTURAL MEMBERS TESTING, IN SUPPORT OF CSI PROGRAM

- THREE TEST ARTICLES IN USE :

  MODIFIED ASTROMAST
  PRECISION TRUSS
  FREE - FREE TRUSS

- STRUCTURAL MEMBERS ARE CHANGEABLE ON THE THREE TEST ARTICLES

PHOTOGRAPH OF JPL FREE-FREE TRUSS



NEED FOR NEW FACILITIES

The pre 1982 experimemts were mostly simple structures, being either beams or plates. The testing performed on those were vibration suppression and/or small angle slewing. The post 1982 experiments, though using larger, more complex structures, still are chiefly vibration suppression and small angle slewing tests.

With newer, more advanced facilities, we can address the space structure design challenges brought out earlier in the paper. Larger facilities are required because the test articles will be larger (by using larger structures, up to full size, the problems with dynamic scaling can be reduced). Also, room must be available to perform large angle slewing motion tests, both for any pointing substructures and of the structure itself.

These facilities must have the state of the art in computer and data acquisition systems, and other support equipment to properly test the new control/structure optimized configurations and their advanced systems. More sophistication in control algorithms and system identification techniques will need better computing power to be fully exploited for CSI.

- **PRE-1982 EXPERIMENTS:**

  MAINLY SIMPLE TEST ARTICLES
  VIBRATION SUPPRESSION/SMALL ANGLE SLEWING

- **POST 1982 EXPERIMENTS:**

  MORE COMPLEX, LARGER STRUCTURES
  STILL CHIEFLY VIBRATION SUPPRESSION &
  SMALL ANGLE SLEW TESTING

- **MORE ADVANCED TESTING IN LARGER, BETTER EQUIPPED FACILITIES IS NEEDED**

FUTURE EXPERIMENTAL FACILITIES

Several facilities are being expanded to improve their capabilities for LSS ground testing. The MSFC's LSS-GTF, AFAL's ASTREX and JPL's Test bed facilities each have their respective plans for adding new equipment in support of CSI.

As NASA's lead in CSI, Langley will also expand their CSI LCTL facility. We are currently in the process of purchasing advanced computer and data acquisition systems, instrumentation and support hardware and expanding and modifying the LCTL area for the CSI evolutionary test model. We will continue to share this laboratory with the Space Station people.

Another LaRC facility, the Large Spacecraft Laboratory (LSL), has been proposed. If constructed, it will house full scale spacecraft models for testing in a controlled environment. The building will be 310 feet in diameter and 150 feet tall at its apex. However, unlike the LCTL, which will be fully operational in the very near future, the LSL is still in the proposal stage at this point.

SEVERAL FACILITIES HAVE EXPANSION PLANS FOR THEIR GROUND TEST PROGRAMS:

LSS - GTF

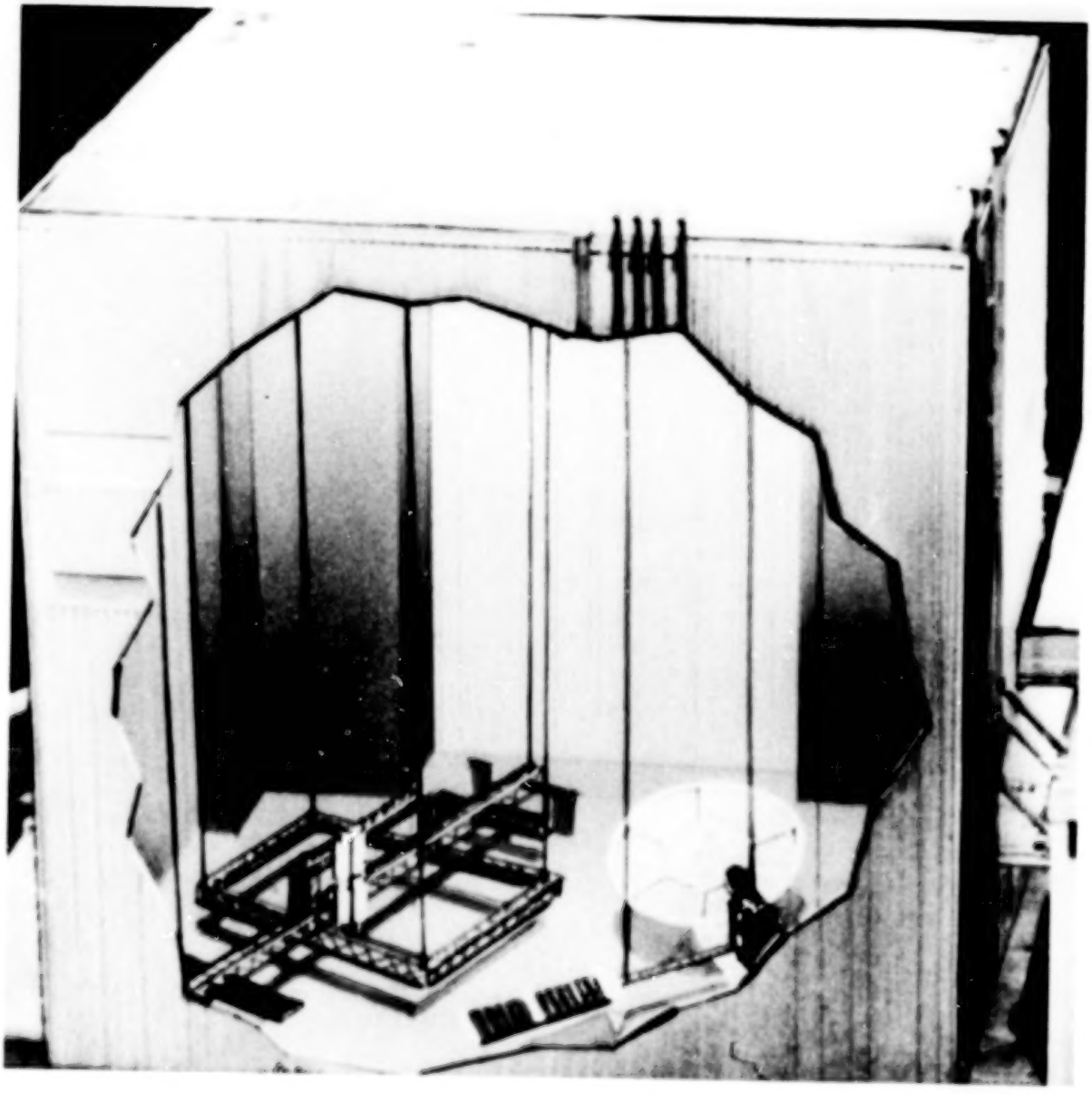
ASTREX

JPL

LaRC LARGE COMPONENT TEST LAB

LaRC LARGE SPACECRAFT LAB

ARTIST'S CONCEPTION OF LANGLEY'S LARGE COMPONENT TEST LABORATORY



INITIAL CSI GROUND TEST PLAN

The ground test team is responsible for all experimental test work to be conducted under Langley's CSI Program. The team's initial plans are as follows:

(1) Support of the Mini-Mast Guest Investigators Program. The Mini-Mast test article is situated in our laboratory area and we will be providing the computer and data acquisition systems, hardware and technical support to the visiting investigators to allow them to perform their respective experiments. In addition, the ground test team will also be conducting their own tests on the Mini-Mast.

(2) Work on the CSI Evolutionary Test Model. This model is called 'evolutionary' because it is being built specifically for CSI experimental testing. In its initial phase, it will be a simplified version of a Mission to Earth spacecraft. It will consist of a 55 ft truss and will be comprised of 10 inch bays, with a 12-16 ft offset antenna frame at one end. The test work on this structure will be performed in two steps:

   (a) Modal Testing - System identification, including static and dynamic testing of the structure and its subcomponents.

   (b) Control Testing - Initial plans call for vibration suppression, suspension system studies (a permanent suspension system has not been decided upon) and small angle slewing testing, in that order. We will then proceed to a more complex verison of this test article and perform antenna pointing and large angle slewing control studies.

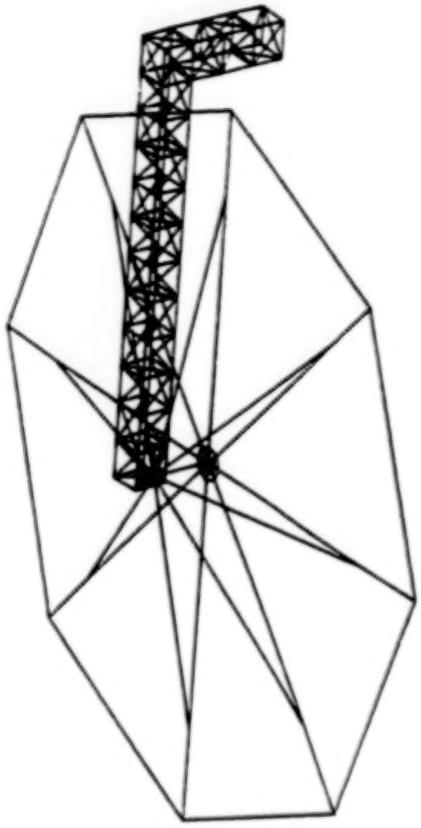
- SUPPORT MINI-MAST GI PROGRAM

- BEGIN WORK ON CSI TEST MODEL, TO BE PERFORMED IN TWO PARTS:

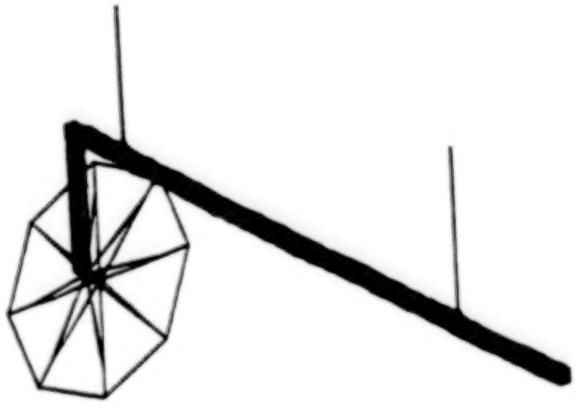
MODAL TESTING - SYSTEM ID

CONTROL TESTING - VIBRATION SUPPRESSION
SUSPENSION STUDIES
SMALL ANGLE SLEWING

GENERIC GEO SPACECRAFT
INITIAL TEST MODEL



TRUSS LENGTH **55 FT**
ANTENNA DIAMETER **12-16 FT**



SUMMARY

A brief survey of large space structure control related experiments and facilities has been presented. This survey covered experiments performed before and up to 1982, and those of the present period (1982 -...). Finally, the future planned experiments and facilities in support of the CSI Program were reported.

It has been stated that new, improved ground test facilities are needed to verify the new CSI design techniques that will allow future space structures to perform planned NASA missions.

PRE & POST 1982 EXPERIMENTS AND FACILITIES SURVEY INDICATES THAT:

TESTING MAINLY ON VIBRATION SUPPRESSION & SMALL ANGLE SLEWING

IMPROVED GROUND TEST EXPERIMENTS & FACILITIES NEEDED TO SUPPORT FUTURE NASA SPACE SYSTEMS

ACKNOWLEDGMENTS

The authors wish to thank the following for their contributions of information on their respective experiments and/or facilities: J.N. Aubrun (Lockheed), Gary Blackwood (MIT alumnus), John Garba (JPL), Robert W. Gordon (AFAL), William L. Hallauer (VPI&SU/USAFA), P.C. Hughes (U. of Toronto), Daniel Inman (SUNY-Buffalo), Ken Lorell (Lockheed), Maribeth Roesler (TRW), John W. Shipley (Harris Corp.), and Yeung Yam (JPL).

REFERENCES

1. Strunce, R., Motyka, P., Schley, B., et. al., *An Investigation of Enabling Technologies for Large Precision Space Structures*, AFRPL-TR-82-074, vol. III, September 1982.

2. Juang, J.N., Turner, J.D., *Research in Slewing and Tracking Control*, First NASA/DoD Control Structures Interaction Conference, NASA CP 2447 part II, November 1986.

3. Rice, S.C., Jones, V.L., Waites, H.B., *Emulating a Flexible Space Structure: Modeling*, Second NASA/DoD Control Structures Interaction Technology 1987, AFWAL-TR-88-3052, November 1987.

4. Das, A., *Experiment in Modeling and Parameter Estimation of Flexible Structures*, Second NASA/DoD Control Structures Interaction Technology 1987, AFWAL-TR-88-3052, November 1987.

5. Quartararo, R., Harris, J., *ASTREX - A Facility for Integrated Structures and Control Research*, Second NASA/DoD Control Structures Interaction Technology 1987, AFWAL-TR-88-3052, November 1987.

6. Eldred, D., Vivian, H., *A Facility for Control Structure Technology Validation*, Second NASA/DoD Control Structures Interaction Technology 1987, AFWAL-TR-88-3052, November 1987.

7. Sincarsin, G.B., Sincarsin, W.G., Hughes, P.C., Reynaud, A.H., *Daisy - A Laboratory Facility to Study the Control of Large Flexible Spacecraft*, Proceedings of Sixth VPI&SU/AIAA Dynamics and Control of Large Structures Symposium, Jun 29 - Jul 1, 1987.

8. Madden, P., *Slewing and Vibration Suppression for Flexible Structures*, Second NASA/DoD Control Structures Interaction Technology 1987, AFWAL-TR-88-3052, November 1987.

9. Waites, H.B., Jones, V.L., *Cost Effective Development of a National Test Bed*, Second NASA/DoD Control Structures Interaction Technology 1987, AFWAL-TR-88-3052, November 1987.

10. Gordon, R., *Large Space Structures Technology Program (LSSTP)*, Second NASA/DoD Control Structures Interaction Technology 1987, AFWAL-TR-88-3052, November 1987.

11. Ghosh, D., Montgomery, R.C., *Problems Associated with Reaction Mass Actuators Used in Conjunction with LQG Control on the Mini-Mast*, Second NASA/DoD Control Structures Interaction Technology 1987, AFWAL-TR-88-3052, November 1987.

12. Mercadal, M., Vander Velde, W.E., *Experimental Failure Detection Results Using the SCOLE Facility*, Second NASA/DoD Control Structures Interaction Technology 1987, AFWAL-TR-88-3052, November 1987.

13. Rogers, L.C., Richards, Jr., K.E., *PACOSS Program Overview and Status*, First NASA/DoD Control Structures Interaction Conference, NASA CP 2447 part I, November 1986.

14. Founds, D., *Joint Optics Structures Experiment (JOSE)*, First NASA/DoD Control Structures Interaction Conference, NASA CP 2447 part II, November 1986.

15. Das, A., Thompson, R., *Experimental Facilities for System Identification*, USAF/NASA Model Demonstration for Large Space Structures, JPL D-5574, March 22-24, 1988.

16. Briggs, Mankins, *Space Station Technology Development Mission Experiment Definition Study*, JPL D-3893, December 1986.

17. Özgüner, Ü, Yurkovich, S., Martin, J., Kotnik, P., *A Laboratory Facility for Flexible Structure Control Experiments*, Proceedings of Sixth VPI&SU/AIAA Dynamics and Control of Large Structures Symposium, Jun 29 - Jul 1, 1987.

NASA CSI Suspension Methods Overview

Stanley E. Woodard and Victor M. Cooley
Spacecraft Dynamics Branch
Structural Dynamics Division
NASA Langley Research Center
Hampton, Virginia

Third Annual NASA/DOD CSI Conference
San Diego, California
January 29 - February 2, 1989

Introduction

New suspension techniques will be necessary for ground testing the flexible spacecraft anticipated in NASA's future space activity. The most complex spacecraft involve nonlinear maneuvering (i.e. large angle slewing) with articulating substructures such as remote manipulating systems. The NASA CSI Ground Test Method team has begun researching and developing methodology to suspend the future class of spacecraft. This overview describes the work completed thus far.

As indicated in the outline below the research objective and technical approach will be presented first. Second, will be a suspension device overview followed by an assessment of existing hardware. Two different mechanical zero-spring-rate mechanisms will be compared for optimal performance. Next, will be a description of how existing hardware can be evolved to meet more general suspension requirements. A comparison of suspending articulating structures overhead vs underneath will follow. After a few experimental results from the zero-spring-rate mechanism/air suspension cart will be concluding remarks and future work.

Outline

- Objective
- Technical Approach
- Suspension Device Overview
- Assessment of Existing Hardware
- Zero-Spring-Rate Mechanism Optimization
- Suspension Device Evolution
- Suspending Articulating Systems
  - Overhead vs Underneath
- Zero-Spring-Rate Mechanism/Air Suspension Cart
  - Experimental Results
- Concluding Remarks/Future Work

Research Objective

The ultimate goal of advanced suspension system research is to simulate flight boundary conditions for ground testing flexible space structures. To achieve such a goal a suspension system must counteract gravity loads while allowing a structure to have unconstrained motion. The research objective is to develop and demonstrate suspension systems for CSI **ground testing**. The suspension problem concerns developing suspension systems for vibratory motion superimposed on large rigid body motion. These large rigid body motions could be large angle slewing or articulating substructures such as a remote manipulating system. Vibratory motion is inherent in the flexible spacecraft under consideration.

A suspension system must be considered as an integral part of the structure itself. However, it should be designed such that the dynamics of the system are dominated by the structure and not the suspension (i.e very soft suspension.) It is therefore desirable to minimize the effective mass, stiffness, damping and friction contributions from the suspension to the overall system.

Develop and demonstrate suspension systems for CSI ground testing

- Vibratory
- Rigid body
- Articulating

Technical Approach

The technical approach in this research is to evolve from simple devices into combinations of devices which will be suitable for general suspension requirements. Leading candidates for suspension devices are zero-spring-rate mechanisms (ZSRMs.) Various ZSRMs have been studied (1-4)* for stiffness reduction or vibration isolation. Their use, however, is restricted to vibratory motion. The CSI suspension problem concerns itself with vibratory as well as nonlinear types of motion. Air bearings are possible candidates for use with ZSRMs.

Spherical and translational air bearings offer almost friction-free surfaces. These devices could be incorporated into structures with large translational and rotational motions. However, their mass coupling with that of the structure becomes a concern. Although it is desirable to use passive systems, active system use becomes inescapable for structures which have both vibratory and large rigid body motion. Development of active suspension should, when possible, be built upon passive devices. Mass coupling, friction, and increased stiffness due to nonlinearity require active systems to reduce or eliminate their effects.

* Gold, R.R.; Reed, W.H.: "Preliminary Evaluation of Suspension Systems for 60-Meter Mast Flight System," prepared for the NASA Langley Research Center, Report No. C2602-008, February 1967.

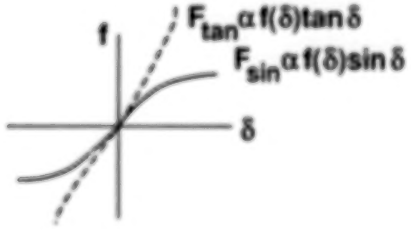
Simple ⇒ Complex

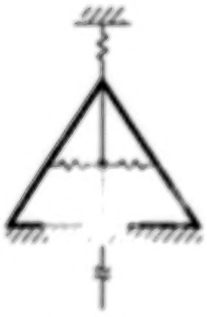
Passive ⇒ Active

Suspension Device Overview

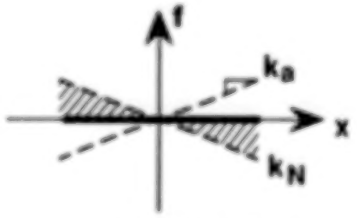
Two leading suspension devices screened by NASA Langley's Dynamic Scale Modeling Technology research were a mechanical ZSRM and a pneumatic ZSRM. There are several implementations of the mechanical ZSRMs. All consist of a main spring which supports the weight of a test article and members in compression which behave as negative springs. The device can support a wide load range by changing the main spring or main spring prestretch. Compressive side members provide force components which act in a sense opposite to the main spring force. The load in the side members, $f(\delta)$, is dependent upon deflection from some initial position. These devices differ from one another by how the vertical component of the compressive forces varies with deflection. Force-deflection curves for two types of devices are illustrated below. On one curve the force varies with the tangent of deflection. Because the tangent curve is increasing as compared with the increasing/ decreasing nature of the sine curve the tangent type device is less nonlinear than the sine type.

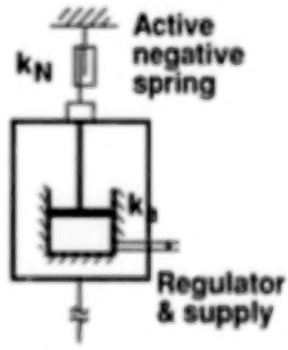
The pneumatic ZSRM has a passive pneumatic main spring which is a piston/ cylinder arrangement. The load carrying capacity can be varied by changing the pressure in the cylinder. This device is inherently linear as illustrated in the force-deflection curve below. A DC servomotor provides a negative spring rate via active control based on the vertical position of the piston. The effective spring rate of the active motor is also linear. Combining the passive pneumatic spring rate and that of the DC servomotor produces a zero spring rate. The active system is remotely tuned to vary load capacity and spring rate.





- Wide load range
- Several implementations
- F_{tan} less nonlinear than F_{sin}





- Remotely tuned
  - Stiffness
  - Load
- Wide load range
- Noncontacting

Assessment of Existing Hardware

Three suspension devices were considered for application to CSI ground testing. A sine type ZSRM was developed at NASA Langley. This device has an effective stiffness which varies with the sine of deflection. The pneumatic Zero-g and the Mechanical lever ZSRM were developed under the Dynamic Scale Modeling Technology (DSMT) research at NASA Langley. DSMT requirements for the two devices were that the suspension frequency be 0.10-0.25 Hz, each device carry 50-500 lbs (290 lbs nominal), frictional force remain less than 0.1 lbf and the devices be remotely controlled for load balancing and tuning.

The table below assesses the three devices for criteria necessary for structures undergoing vibratory as well rigid body motion. All three devices were within the DSMT frequency range. However, because low stiffness structures are considered for some anticipated NASA missions the stiffness of the devices was compared. Because of air piston leaks the pneumatic device was not suitable for vacuum chamber usage. Cart suspension will be necessary of large rigid-body motion. All devices were suitable for cart suspension, however, the mechanical lever ZSRM is more compact. The mechanical lever ZSRM is assessed to be more suitable for all suspension configurations and environments.

Criterion	Pneumatic zero-G	Mechanical lever ZSRM (tangent type)	Sine type
Linearity	+	+	○
Remote tuning	+	Planned	Unplanned
Payload (lbs)	24 - 284	120 - 330	2 - 20
Stiffness (lbs/in.)	0 - 5.000	0.47	0.2700
Damping %	2.3	3.30	2.7000
Breakaway friction, lbf	0.002	0.01	0.0003
Vacuum chamber usage	-	+	+
Suitability for cart suspension	+	+	+

Mechanical lever ZSRM ⇒ all suspension configurations and environments

+ = desirable
○ = limited
- = undesirable

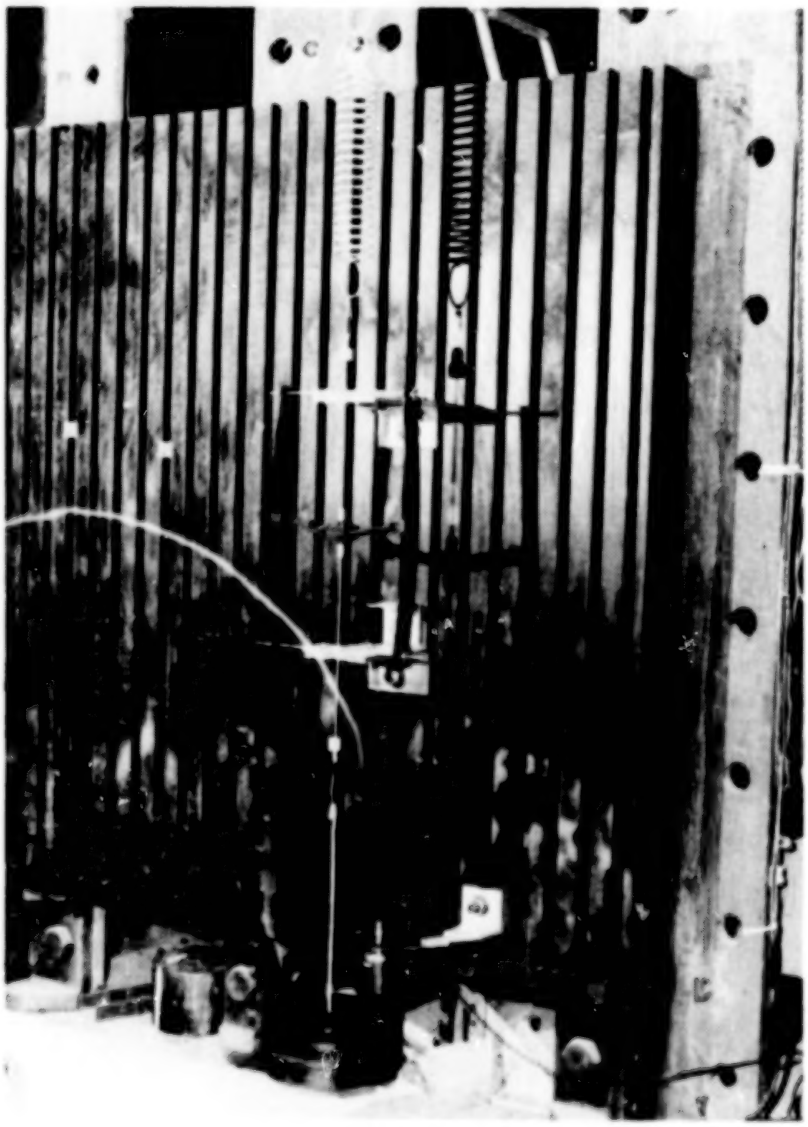
D. Keinholz
J. Gooding
CSA Engineering

Marc Cronet, LMSC
Ed Crawley, MIT
David Keinholz, CSA

V. Cooley
NASA/ Langley

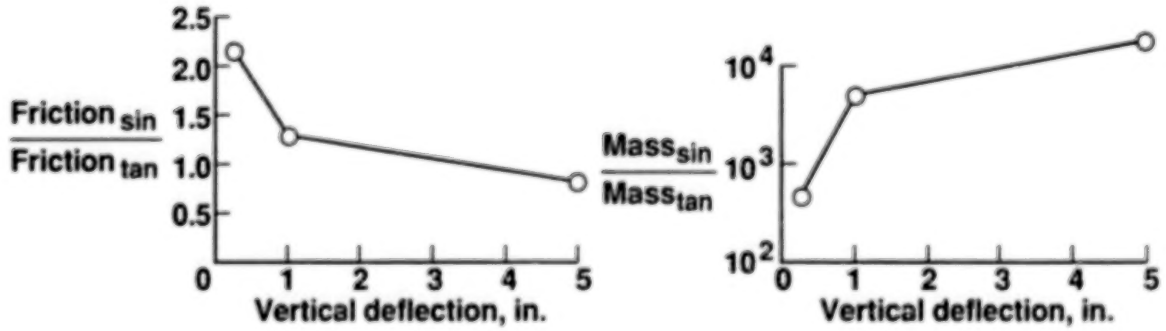
Sine-type Zero-Spring-Rate Mechanism

The figure below illustrates a sine-type ZSRM. The compressive force, $f(\delta)$, is provided by two beams in bending. Sandwiched spring steel compressive side members reduce the friction of the device. A tension spring supports the suspended weight.



Zero-Spring-Rate Mechanism Optimization

Two mechanical ZSRMs were considered in an optimization study which had objectives of minimizing friction and coupled mass. One ZSRM had a force proportional to the sine of the vertical deflection of its side members. Similarly, the other had force proportional to the tangent of deflection. In both designs members are loaded in compression, so a buckling constraint was applied to the optimization analysis. The results of the analysis show that for small deflections the tangent type device has less friction than the sine type. Only for large deflections ($\approx$ 3.0 in) does the sine type device design become slightly advantageous. The two devices have substantial differences in the mass coupling characteristics. The sine type device would require a thousand times more mass than the tangent type to satisfy the same linearity constraint. Because the sine type device is inherently more nonlinear it requires much larger dimensions to have the linearity characteristic.

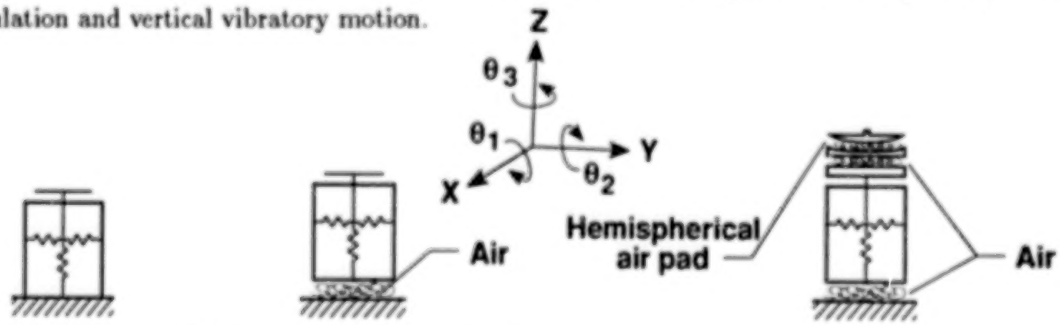


- **Minimum effective mass**
- **Constraints on: linearity**
  bending stress f.s.
  buckling f.s.
- **Assumed solid rectangular x-sections**
- **Flexible suspension modes not examined**

Evolution of Suspension Devices

Existing zero-spring-rate-mechanisms are one degree of freedom devices which support the weight of a test article with a low vertical stiffness. If possible, more complex suspension systems should evolve from simpler ones. A device combining some type of cart and a ZSRM would seem to be the next appropriate stage in suspension device evolution. The type of cart under consideration is an air bearing. Air bearings provide a translational load carrying capability with very low friction. A ZSRM/air bearing combination allows a structure to have unconstrained horizontal degrees of freedom necessary for large horizontal rigid body motion and vertical vibratory motion. Because this device is attached to the supported structure its mass couples horizontally with the structure. A device such as this is suitable for structures undergoing slewing (i.e pointing control). However, because of the horizontal mass coupling this is not suitable for lightweight articulating structures.

The next progression for suspension systems is to augment the ZSRM/air bearing with active control. To eliminate the mass coupling problem the proximity suspension device illustrated below could be used. The proximity device consists of the ZSRM/air bearing combination mentioned above, an air table atop this device, and a concave hemispherical air bearing atop the air table. A convex hemisphere, constructed of lightweight material, will be attached to the test article. The hemispherical air bearing is added to unconstrain the roll and pitch degrees of freedom. The air table that the hemispherical bearing rests on will make it possible to use open-loop active control. When structures and/or the appendages move in ground testing the trajectory of their rigid body motion is known a priori. However, the subsequent vibratory motion is not known. Active control (i.e. DC motor and pulleys) will be provided so that the suspension device synchronously follows the same trajectory of the rigid-body motion attachment point. The air table allows the structure to have horizontal vibratory motion in proximity to the rigid-body motion attachment point. The active system and air table decouple all the horizontal mass except for that of the hemispherical air bearing. This device is suitable for all suspension requirements of large horizontal rigid body motion and/or articulation and vertical vibratory motion.





Z softened

X, Y, θ_3 unconstrained
Z softened
Pointing, vib, sup
no articulation

Proximity suspension:
Active system
follows trajectory
of suspended structure
I_1, I_2, I_3, M_X, M_Y uncoupled
X, Y, θ_1, θ_2, θ_3 unconstrained
Z softened
Pointing, vib, sup with
articulation
General nonlinear
motion with robotics

Suspending Articulating Systems:
Underneath versus Overhead

Much of this paper has focused on suspension devices; however, it is also necessary to consider suspension configurations for articulating systems. The basic consideration is whether structures will be supported overhead or underneath. The charts below illustrate the advantages and disadvantages of each. Overhead supension is usually done with cables. These are broadly used, their overall vertical stiffness can be reduced with ZSRMs and they offer simplicity for ground testing of structures undergoing only vibratory motion. Cable suspension produces pendular and axial stiffness. The necessary controls and hardware will be complex for rapid slewing or articulation.

Suspending articulating structures underneath can be done with the air bearing/ZSRM concepts mentioned earlier. With underneath suspension overhead height is not a factor (i.e. to reduce pendular and axial stiffness.) The air bearing/ZSRM combination is a passive means for suspending articulating structures; however, the mass of the suspension hardware couples horizontally with the structure. The proximity suspension device mentioned earlier could eliminate the horizontal mass coupling.

Overhead

Advantages

- Broad use
- Soft systems/ vibratory motion → cable/ZSRM
- Simple

Underneath

Advantages

- Overhead height not a factor (i.e. vacuum chamber)
- All DOF's unconstrained with proximity suspension
- Vibratory and large rigid body motion (i.e. slewing, telescope)
- Simple open-loop control for proximity suspension
- Safety

SUSPENDING ARTICULATING SYSTEMS
Underneath versus overhead

Overhead

Disadvantages

- Constrained DOF's due to pendular and cable axial stiffness
- Control complexity for rapid slewing/articulation
- String modes
- 82 ft overhead height for pend freq < 0.1 HZ
- Added weight to test configuration
- Tensioned cables may behave as tuned mass dampers

Underneath

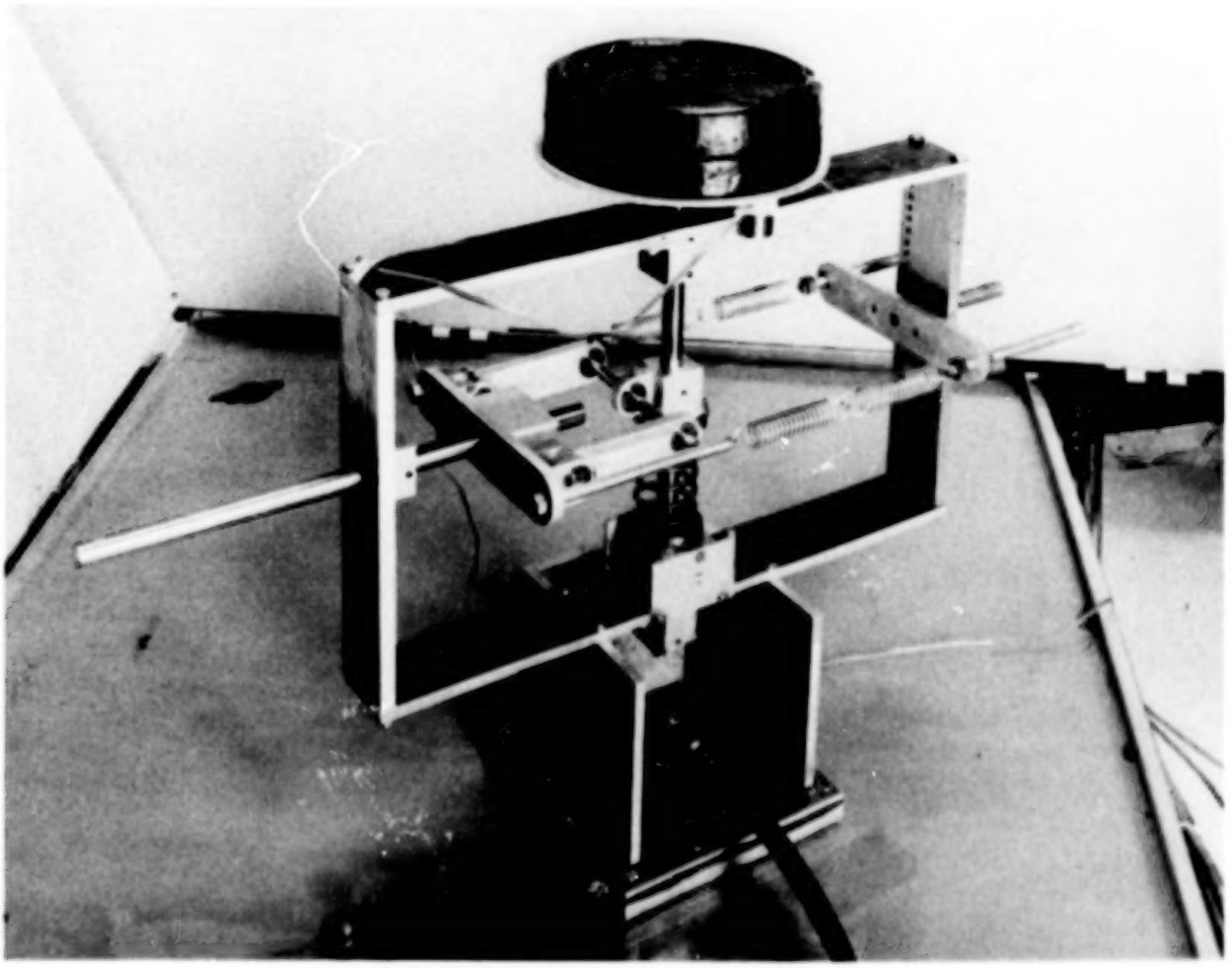
Disadvantages

- Mass coupling in vertical direction (all other eliminated by active control)
- Inverted pendulum stability

Bottom suspension more suitable for structures with large rigid body motion and/or articulating motion

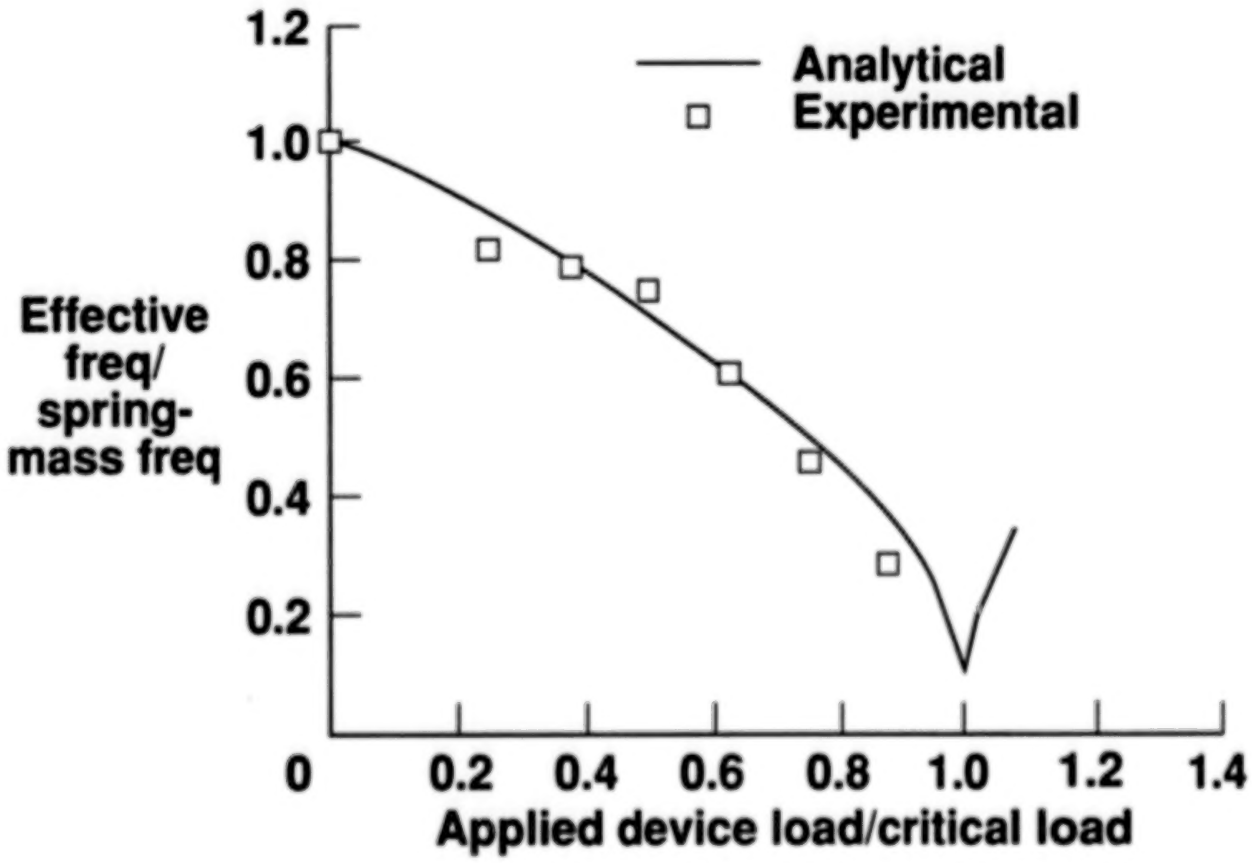
Zero-Spring-Rate Mechanism/Air Suspension Cart

The figure below illustrates a zero-spring-rate mechanism atop an air bearing. This device is for suspending structures undergoing large horizontal rigid body motion concurrently with vertical vibratory motion. A compressive spring supports the weight of the lumped mass.



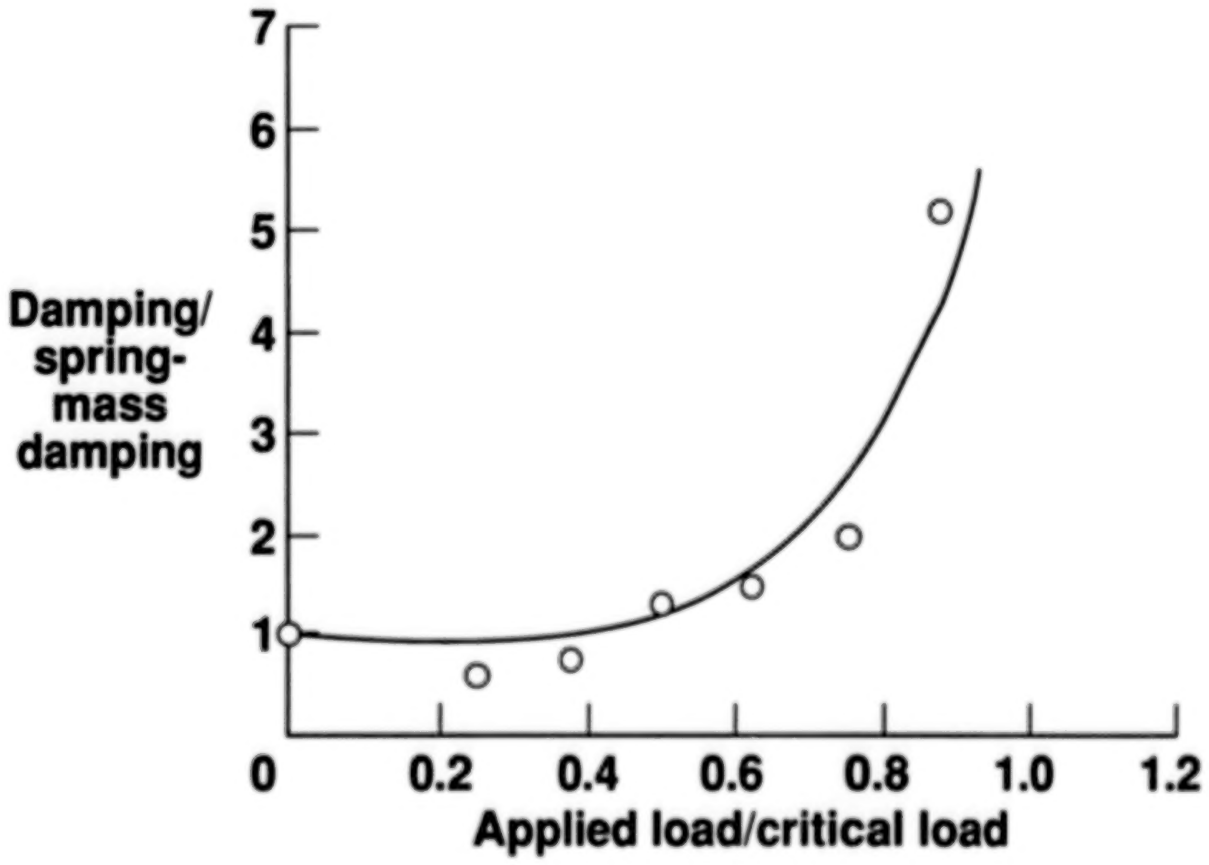
Frequency Variation with Applied Load

The experimental and analytical frequency variation with applied load of the ZSRM used as part of the ZSRM/Air Suspension Cart has been characterized in the figure below. The applied load is normalized with the compressive load (critical load) which would result in a spring rate of zero for linear deflections. Effective frequency is normalized with the frequency of a system containing only the main spring and the lumped mass. As load increases the frequency decreases, which is the essence of the zero- spring-rate device. The minimum frequency occurs at the critical load. However, the frequency is nonzero because the system is nonlinear. For linear systems the effective frequency is independent of initial conditions. The effective frequency of a nonlinear system is dependent upon initial deflection and velocity. The minimum experimental frequency was due to friction in the device.



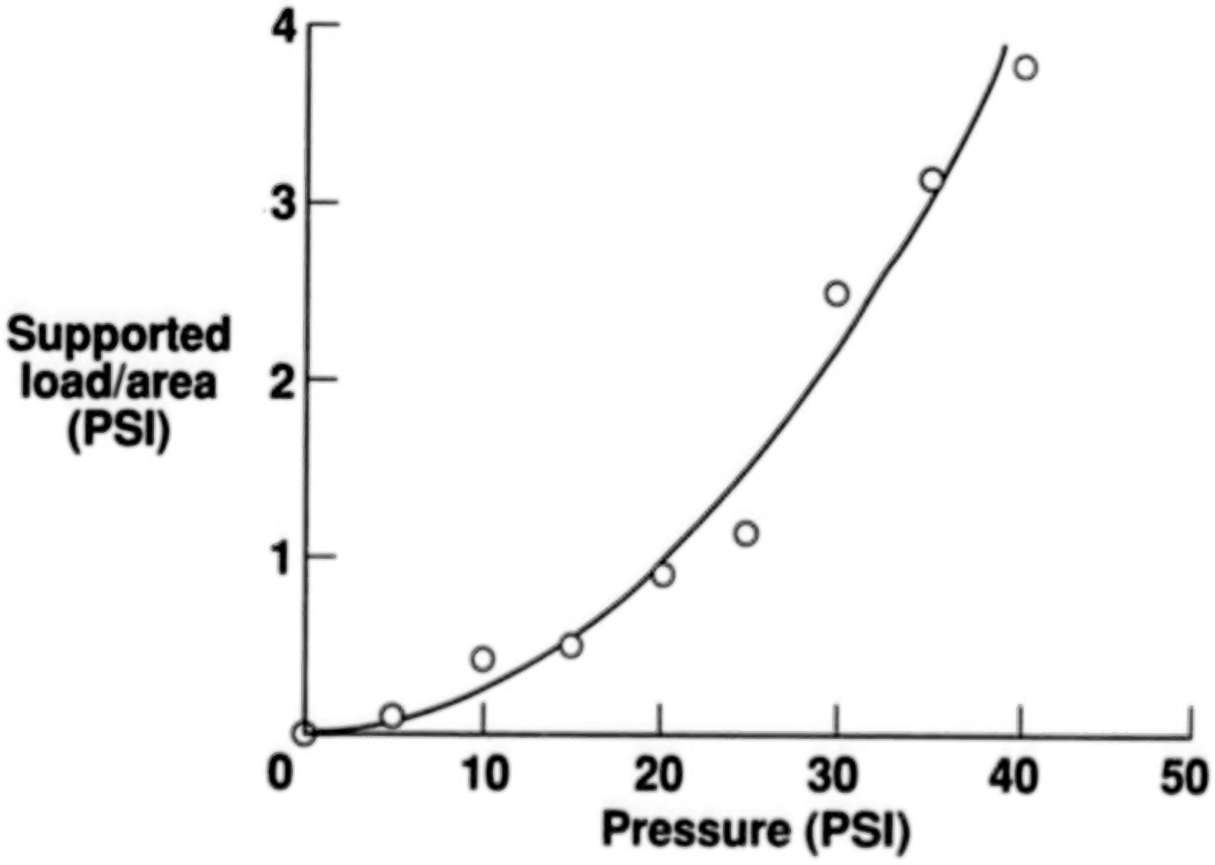
Damping Variation with Applied Load

The experimental damping variation with applied load of the ZSRM used as part of the ZSRM/Air Suspension Cart has been characterized in the figure below. The applied load is normalized with the compressive load (critical load) which would result in a spring rate of zero for linear deflections. Damping is normalized with the damping of a system containing only the main spring and the lumped mass. As load increases the damping increases. The friction in the device is proportional to the horizontal component of the applied load but is not constant when the device is in operation. During the cycle of motion the frictional force is highest when the side members are in the horizontal position and lowest when the deflection is peaked. As illustrated in the previous figure the use of the device can be limited by friction.



Supported Load Variation with Line Pressures

The load carrying capability of the air bearing used as part of the ZSRM/Air Suspension Cart has been characterized in the figure below. The air bearing has an area of 64.0 sq. in. Because the air bearing is capable of supporting a load of approximately 250.0 lbs. with less than 50 psi of supplied pressure it is feasible for suspending heavy structures in most ground test facilities. For most structures it is envisioned that at least two ZSRM/Air Suspension Carts will be used.



Concluding Remarks: Future Work

The problem of suspending flexible structures undergoing large rigid body motion as well as vibratory motion will require new suspension techiques and hardware. It has been shown that existing suspension hardware can be evolved to solve some of the future suspension demands. Passive systems should, if possible, be augmented with active control to eliminate their shortcomings (i.e. mass coupling and increase stiffness due to nonlinearity.) Proximity suspension can be used for structures undergoing large horizontal rigid body motion and/or articulation with vertical and horizontal vibratory motion. By combining air bearings, spherical air bearings and zero-spring-rate mechanisms a structure can be supported while its degrees of freedom remain unconstrained. Much work needs to be done in testing and validation of these concepts.

Future work will consist of a zero-spring-rate mechanism/air suspension cart slewing experiment. A flexible beam will be hinged at one end. On the other end will be an attached zero-spring-rate mechanism/ air suspension cart. This passive device serves as a prelude to a proximity suspension device. The beam will be slewed through large angles. During the slewing motion the structure will be excited so that it will have large rigid body motion as well as vibratory motion. The experiment will validate the use of air bearings and zero-spring-rate mechanisms for flexible structures undergoing large rotations.

- Proximity suspension: promising method for structures with vibratory as well as large rigid body and/or articulating motion
- Active/ZSRM/air suspension supports test article while leaving all DOFs unconstrained
- Passive $\Rightarrow$ Active

References

1. Gayman, W.H.; Trubert, M.R, Abbott, P.W.: "Measurement of Structural Transfer Functions Significant to Flight Stability of the Surveyor Spacecraft," NASA Technical Memorandum 33-389, May 1, 1969.

2. Rogers, L.C., Richards, K.E.: "PACOSS Program Overview and Status," Proceedings of the 1st NASA/DOD Control/Structures Interaction Technology Conference, Norfolk, Virginia, November 1986.

3. Cooley, V.M.; Juang, J.N.; Ghaemmaghami, P.: "Design of Ground Test Suspension Systems for Verification of Flexible Space Structures," Proceedings of the 6th Dynamics and Control of Large Structures Conference, Blackburg, Virginia, June 1987.

5. Woodard, S.E.; Housner, J.M.: "The Nonlinear Behavior of a Passive Zero-Spring-Rate Suspension System," AIAA/ASME/ASCE/AHS 29th Structures, Structural Dynamics, and Materials Conference, Williamsburg, Virginia, April 1988.

AN AIR-BEARING WEIGHT OFFLOAD SYSTEM FOR GROUND TEST OF HEAVY LSS STRUCTURES

R. B. Rice
Martin Marietta Astronautics Group
Denver, Colorado

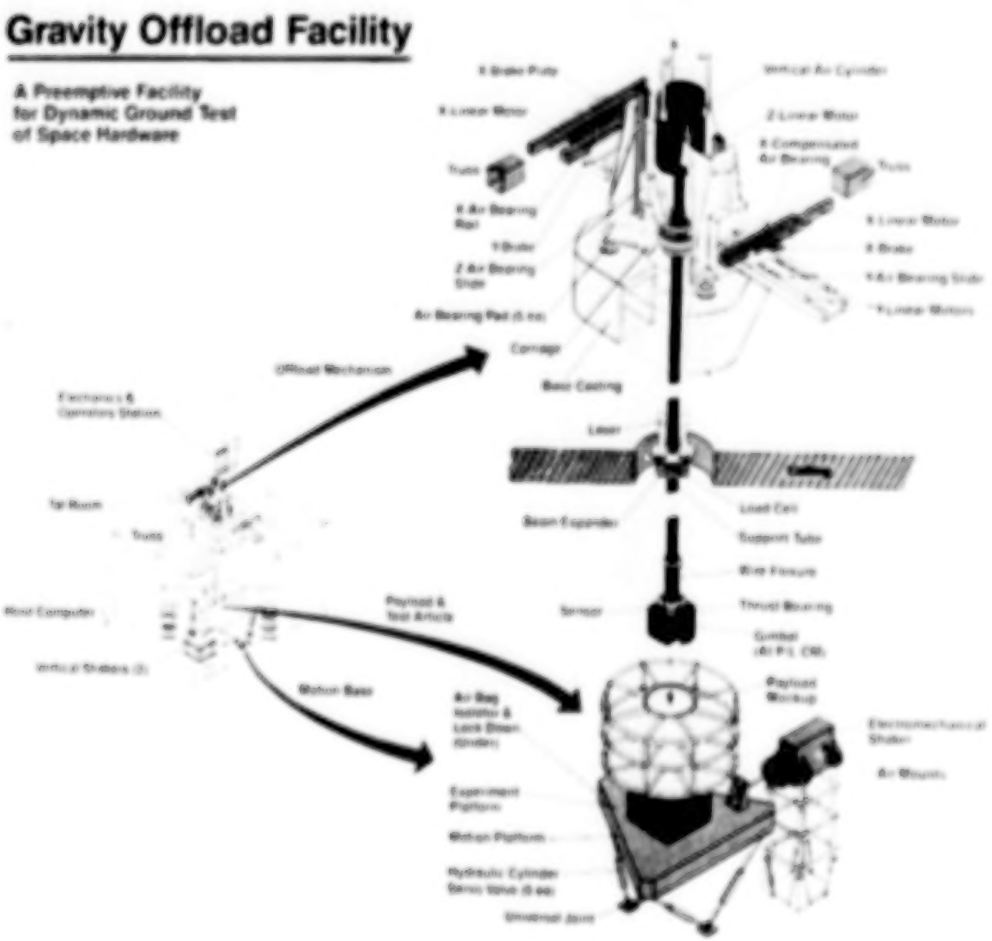
Third NASA/DOD Controls-Structures
Interaction Conference, San Diego, Calif.
Jan. 30 - Feb. 2, 1989

GRAVITY OFFLOAD OVERVIEW

The Gravity Offload Facility (GOF) is a Martin Marietta Capital funded laboratory facility intended for testing of heavy, compact payloads which require up to 6 degrees of freedom (DOF) motion. The primary use is to suspend a payload such as a sensor package or SBL* optical mirror above a delicate isolation or pointing mount which is the object of the test. The payload with its mass and inertia is allowed to move freely under the influence of the mount under test but must not burden it with its weight in the 1 g field.

Design and build of the facility occurred mainly over the calendar year 1987 at the MMAG Inertial Guidance Laboratory in Waterton (Denver), Colorado. The project was highly developmental in nature, due to the heavy weight, frictionless operation and 6 degree of freedom requirements. Several unique components were custom designed and fabricated by outside vendors, but the main design and development was accomplished in-house.

*space-based laser (SBL)



BEST COPY AVAILABLE

FACILITY CAPABILITY

The overhead air bearing assembly is designed for suspension of up to 10,000 LB. It allows frictionless 4 degree of freedom operation by using air bearings in the load path and guide rails. Two more degrees of angular freedom are accomplished at the payload CG by using either a two axis flexure mount for small angle applications or a spherical air bearing for large angles.

The payload is free to travel bounded by a cylinder 18 inches in diameter and 18 inches tall. Depending on which CG gimbal mount is used, angular travel can be up to 60 degrees in pitch and roll and is free to rotate about the vertical axis. Great care has been taken to minimize jitter or noise contamination of the payload from the suspension.

The motion base can provide 6 degree of freedom motion input for a 3000 LB dynamic (or a 10,000 LB static) load over a travel of 24 inches in all directions with a bandwidth up to a few Hz. Beyond this, individual electro-dynamic shakers can be attached to provide vibration inputs up to 2000 Hz at about the 100 LB force level. The system was intended to simulate the vibration and motion environment of the shuttle bay or an SBL aft body.

Suspended Load 6 DOF, Ultra Quiet

- Up to 10,000 lb
- 18 Inch Travel in X Y & Vertical
- Angular Travel Dependent on CG Gimbal
  - Flexure: ±7°, ±15° about Vertical
  - Spherical AB: ±30° Lateral, Free about Vertical

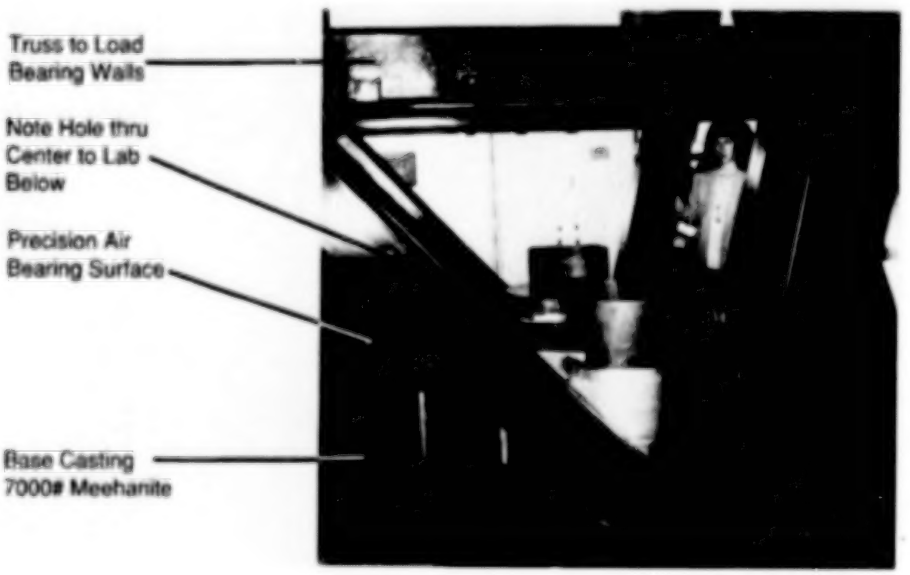
Motion Base 6 DOF

- Load 10,000 lb Static, 3,000 lb Dynamic
- Travel 24 Inch All Directions
- DC to 2000 Hz (Limited) Any Axis

TRUSS AND BASE CASTING

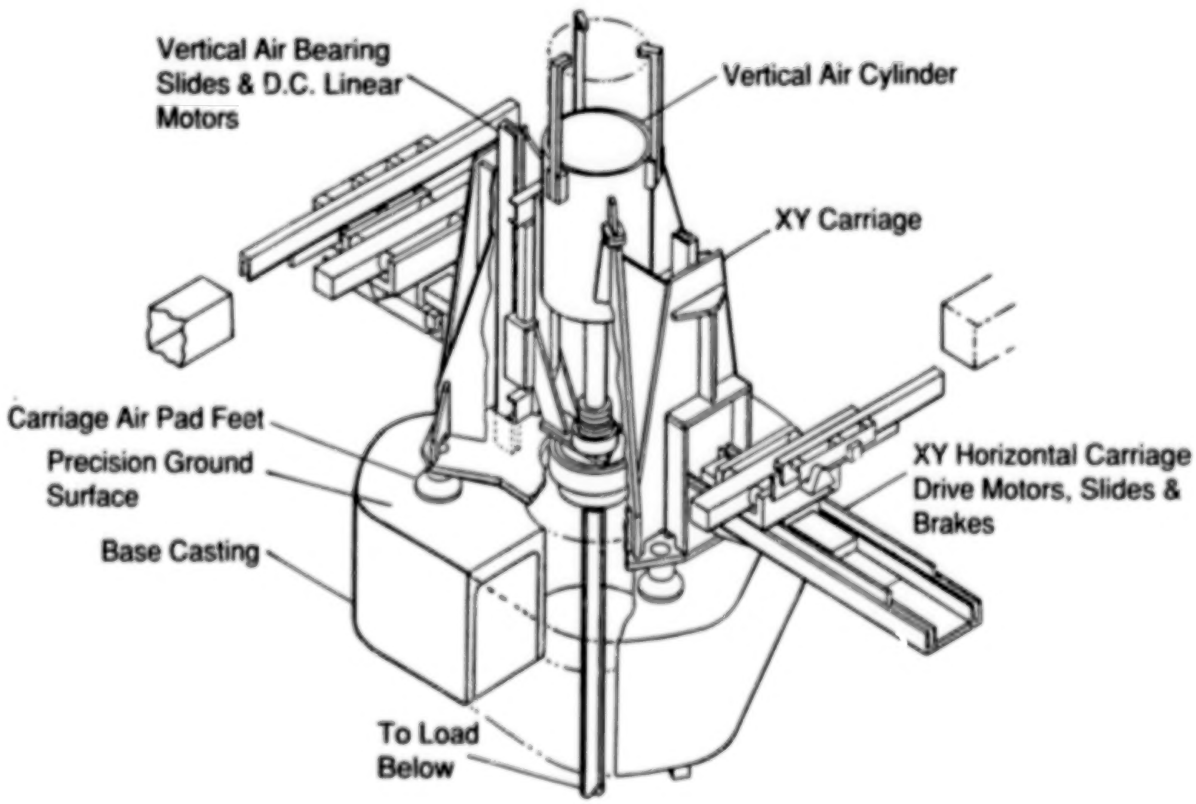
The truss which supports the base casting is sized to minimize angular tipping of the horizontal bearing face as the carriage moves from side to side. The vertical bounce natural frequency goal was to be above 50 hz. The truss is supported on load bearing walls (as opposed to a ceiling mount) to minimize vibration transmission. The casting mount is a 3 point suspension.

A large 7000 LB Meehanite one piece ribbed casting was chosen for backing the horizontal air bearing face. A weldment was considered unsuitable since it would probably not hold tight tolerances after grinding. A granite slab was found unsuitable due to the weight. A great deal of trouble was encountered trying to obtain a high quality air bearing surface due to the large size involved, and the requirements of better than a 10 microinch surface finish and a planarity of better than 50 microinches.



CARRIAGE ASSEMBLY

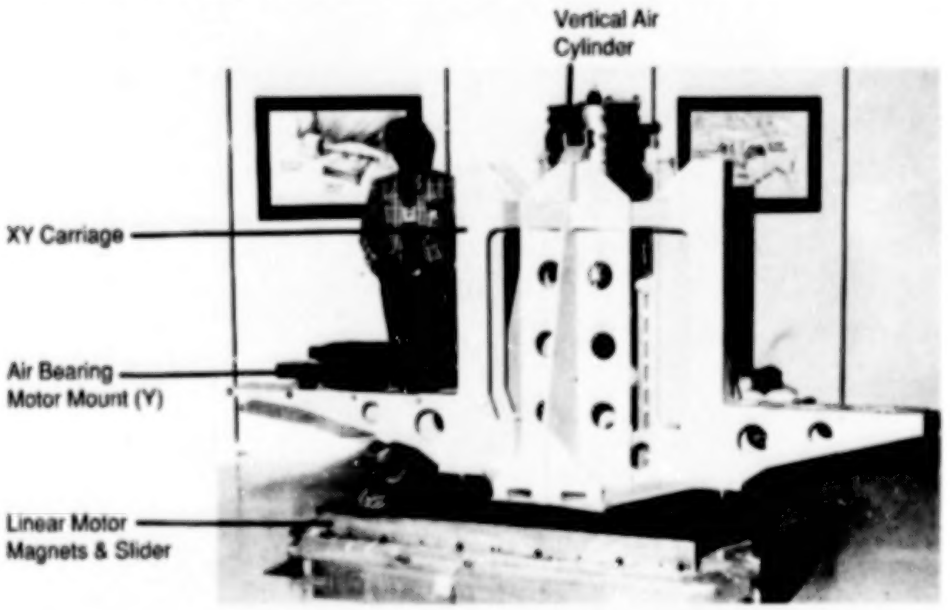
The carriage provides the X Y lateral freedom thrust bearing for the overhead suspension. It rides on six self aligning air bearing feet which travel over the base casting precision surface. It was sized for the 10,000 LB maximum load, and carries the X Y linear motors, slides and sensors. The vertical lift cylinder also rides in the center and provides the vertical degree of freedom. An air bearing gimbal is used to allow angular freedom of the piston rod about the vertical axis. The load path connects directly from the payload up the pipe to the piston. The vertical motors and sensors are connected to the vertical pipe through the gimbal bearing but they ride on their own air slides.



CARRIAGE WELDMENT

The X Y carriage is shown here before assembly. It is constructed from a weldment on which precision points were machined as a final step. One of the six linear motors is shown which provides control of the 3 translational degrees of freedom. These unique motors provide a direct drive frictionless control force without cogging or ripple. Two motors per axis are mounted each on their own air slides with a linear position sensor. Each motor may exert up to 150 LB which yields 300 LB per axis.

Carriage before Assembly above Casting

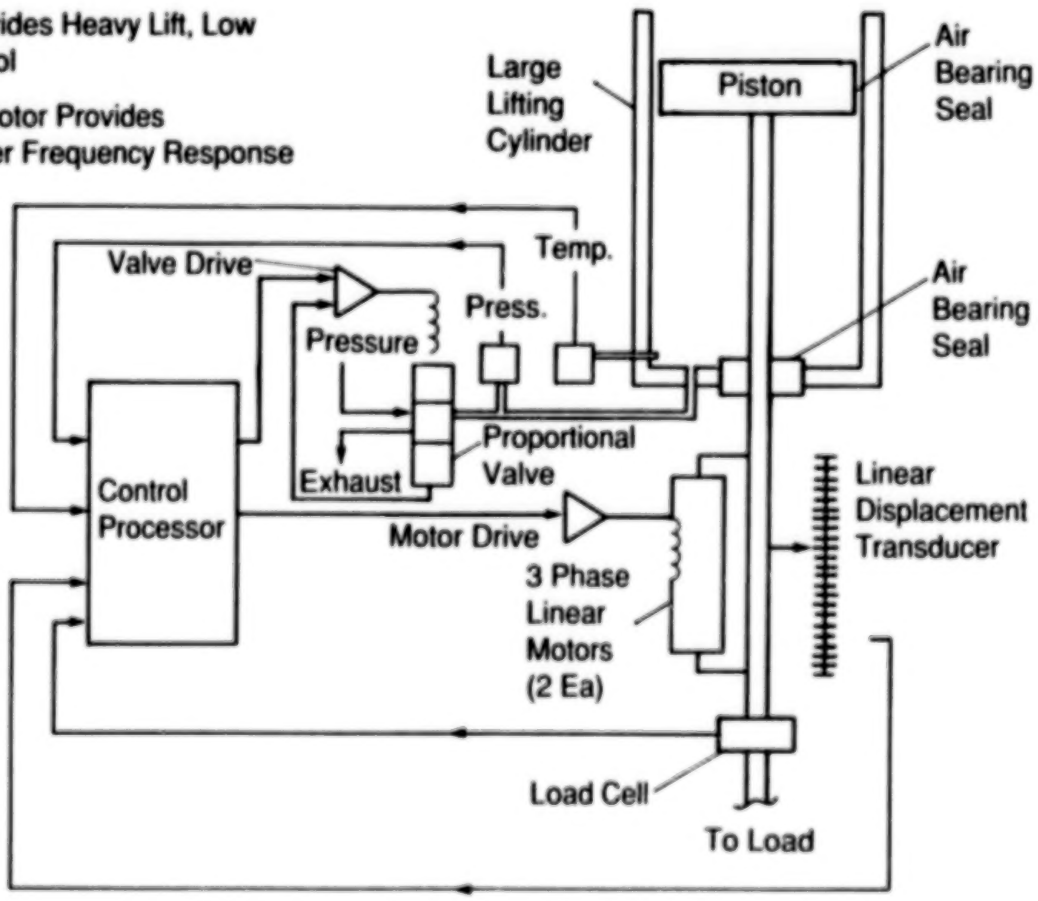


VERTICAL LIFT AXIS CONTROL

The vertical degree of freedom proved to be the most difficult to design. The large air cylinder is used to support the overall payload weight but provides only low frequency support. Two parallel linear motors are used to provide control and damping. A large diameter proportional valve is used to control the cylinder air pressure. Pressure, temperature, load and position are all fed back to control the cylinder. The valve position has its own control loop with sensor and actuator.

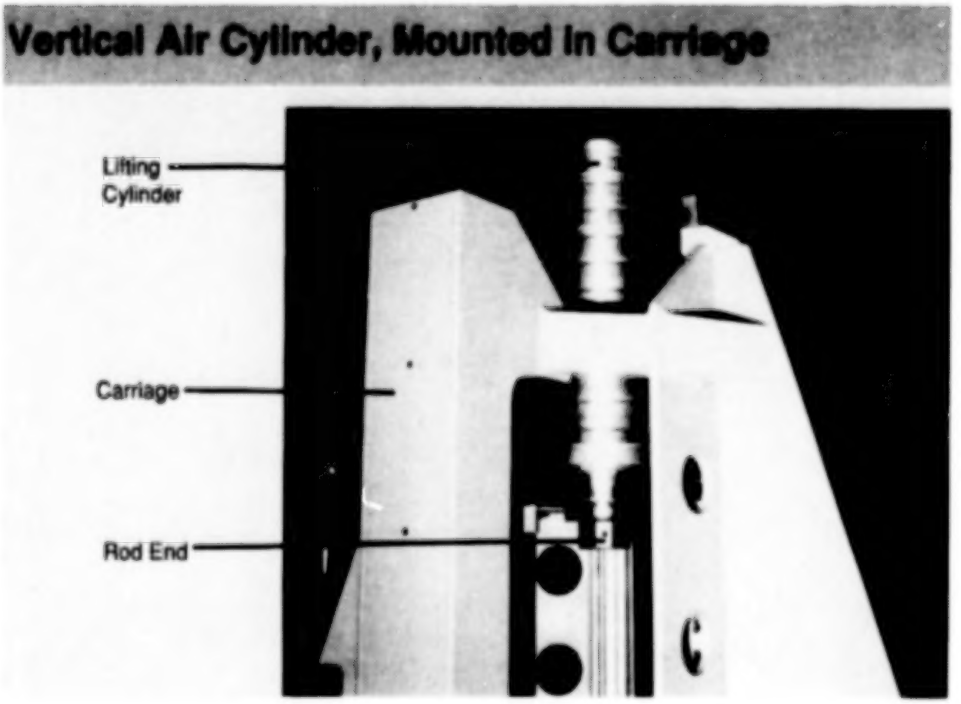
During the design phase extensive use was made of a time domain simulation of the valve, cylinder and gas dynamics. Non-linear compensation was designed to compensate for the wide range of loads and cylinder volumes using this tool. The blend of linear motor versus valve control influence was also defined using this simulation.

- Air Cylinder Provides Heavy Lift, Low Bandwidth Control
- Parallel Linear Motor Provides Damping & Higher Frequency Response



LIFTING CYLINDER

The vertical lifting cylinder is shown here prior to assembly. To maintain frictionless operation, the cylinder rod seal and piston had to be designed using air bearings. Team Corp. of El Monte, Ca. took on the job of developing and building this cylinder. The combination of large bore and deep stroke presented a great deal of trouble in fabrication due to the extremely tight tolerances needed for the air bearing surfaces over the full travel. The tradeoff was between frictionless operation and minimal air consumption. The air gap had to be held to less than 400 microinches over the travel and range of pressures.



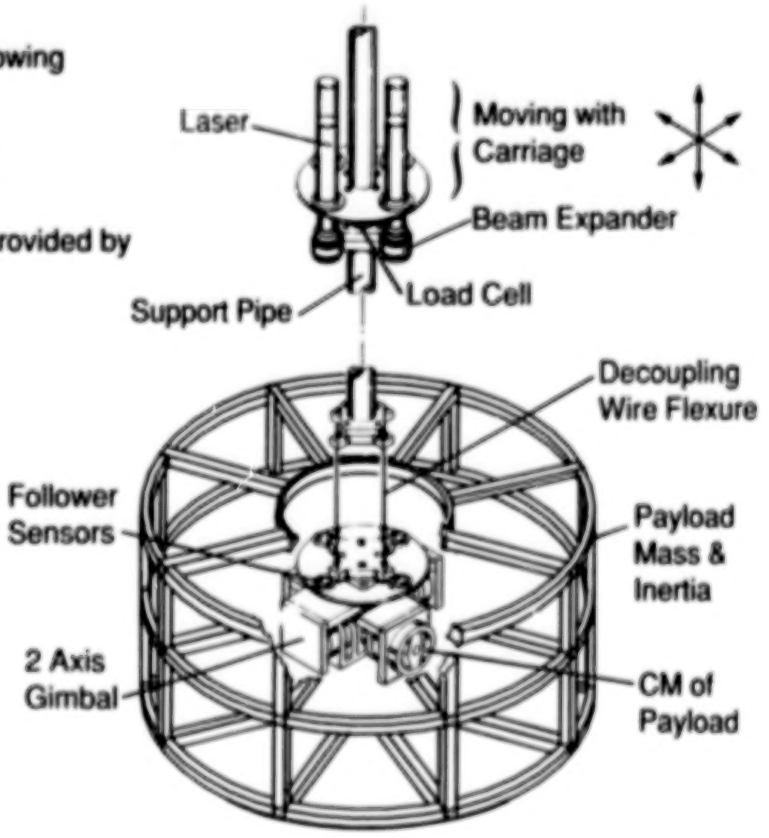
PAYLOAD FOLLOWER AND PAYLOAD GIMBAL

To minimize the effects of the carriage mass, the X, Y and θ_Z axes use a servo to follow the payload motion. Lasers with converging optics are mounted beneath the carriage. Their light spots impinge on sensors mounted just above the payload. Any error is sensed and the linear motors re-align the X Y carriage and the vertical rotation.

The payload angular degree of freedom in pitch and roll is accomplished using a two axis gimbal located at the payload center of gravity. For small angle applications flex pivots are used. For larger angles a spherical air bearing may be used.

Dynamic decoupling of the payload from the overhead suspension is accomplished using a four wire flexure located above the payload gimbal point. This decouples the X Y and θ_Z axes.

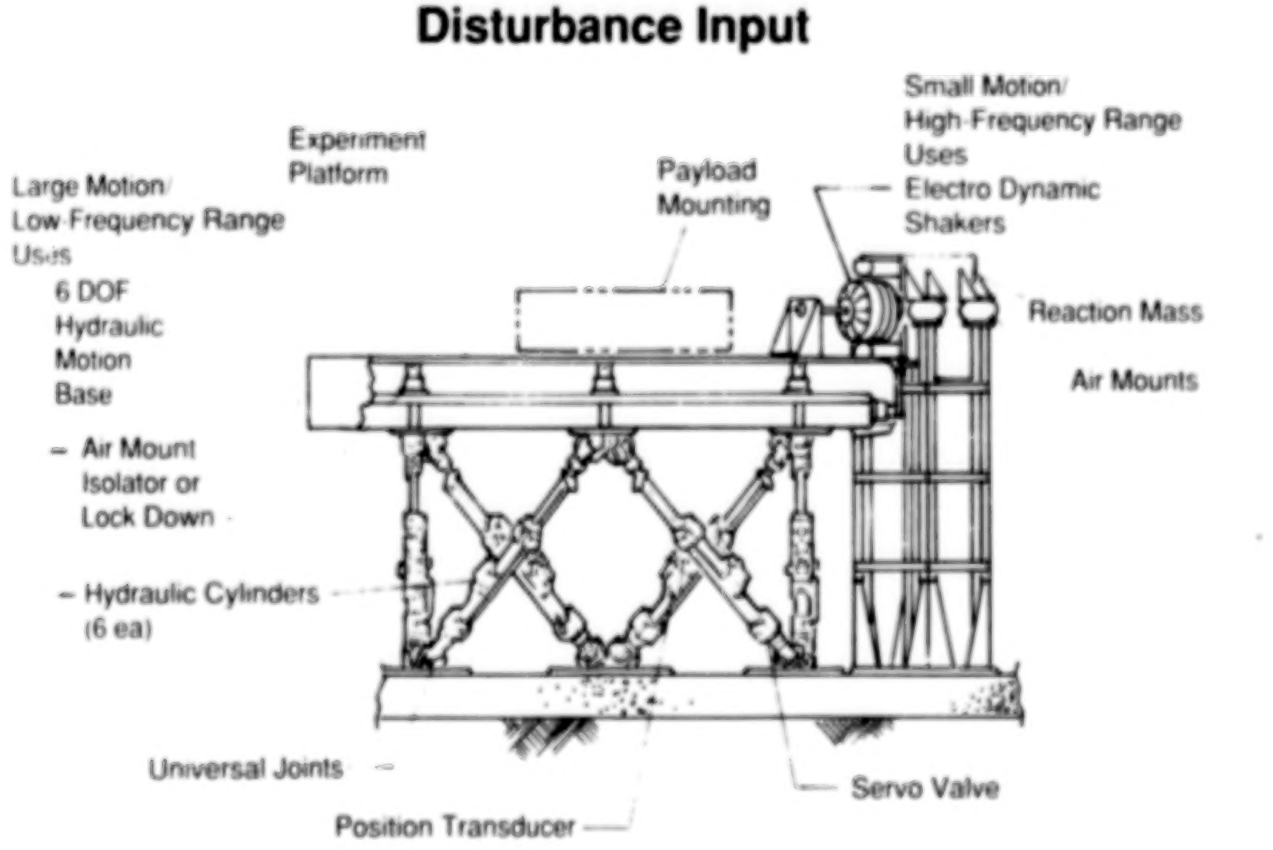
- Carriage Follows Payload Closely:
  - Vertically Following Load Cell
  - Horizontally & Rotationally Following Optical Sensors
- Gimbal Pivots about Payload CM
- Small Motion Vibration Isolation Provided by In-Line Wire Flexure



MOTION BASE LAYOUT

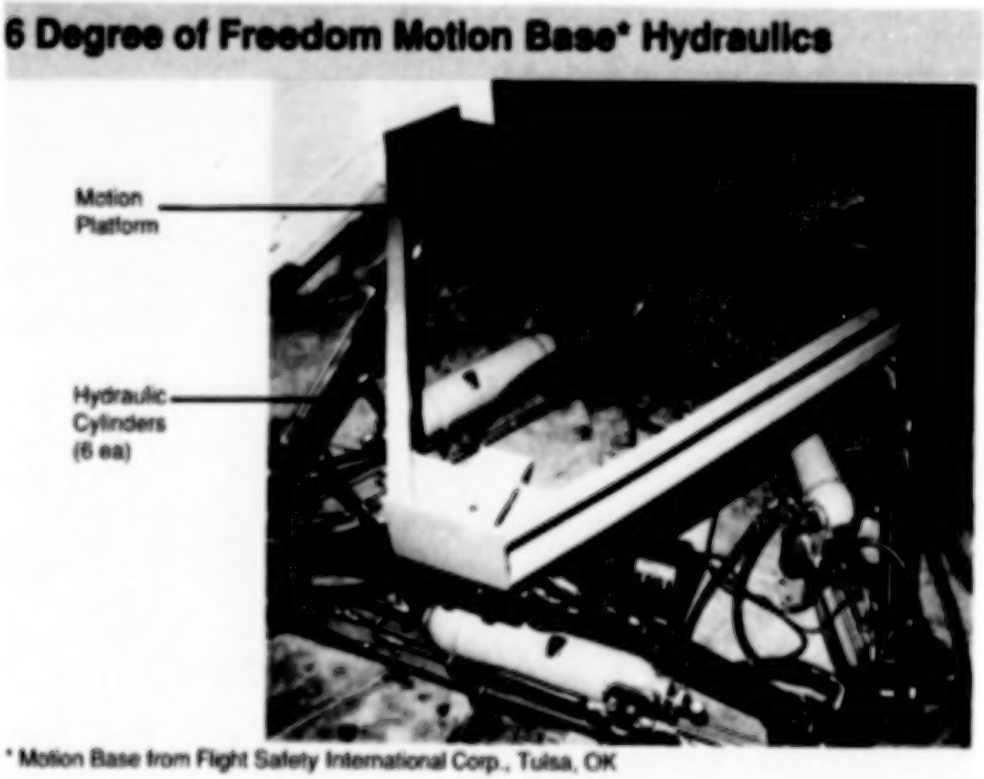
A realistic vibration disturbance environment which simulates that experienced in the shuttle bay or that found on the aft body of an SBL is the goal. Low frequency, large, 6 degree of freedom motion is generated using the hydraulic hexapod. High frequency, small motion inputs are obtained by judicious connection of electro dynamic shakers.

The hydraulic hexapod chosen is a unit routinely used for aircraft simulator crew training. When only large motion is required the experiment platform is clamped to the motion base. When only small-motion high frequency is required, the experiment based is isolated on air mounts and fixed at some orientation, then the electro dynamic shakers are attached. For combined motion, the shakers may ride on the motion base and shake the experiment while the hexapod goes through its maneuvers.



MOTION BASE

The 6 degree of freedom hydraulic motion base is built by Flight Safety International of Tulsa, Ok. Six skewed hydraulic cylinders are arranged in a hexapod connected by special U joints. The cylinders have hydrostatic bearings and seals to minimize friction. The valves are precision proportional Moog valves similar to those used on launch vehicles. Very fine control and minimal jitter is achieved. The motion base slew rate is 23 inches per second in any direction and the small signal bandwidth is in the range of 5 Hz.

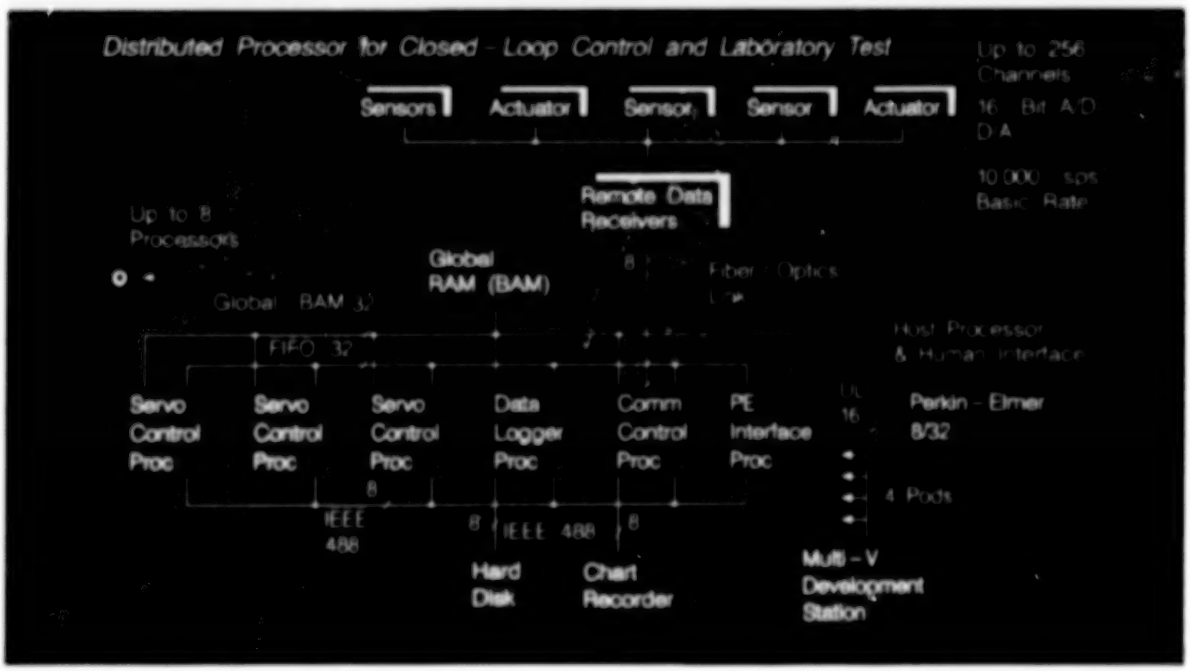


* Motion Base from Flight Safety International Corp., Tulsa, OK

CONTROL PROCESSOR

The control processor is required to simultaneously perform real time closed loop control of the 6 suspension axes, collect data from the experiment sensors, and must also be modular to allow for future expansion and the modifications usually required by each new experiment. An architecture was chosen which is ideally suited to this task. Since a great deal of the operation has to do with distribution of data, one whole processor and special interface hardware were designed for this task. Experiment data collection was assigned to a second processor and the human interface to a third. This leaves up to 5 more processors available for process control. The bus structure was designed to eliminate data transfer bottle necks. Memory has been allocated such that each processor has its own local memory for program code plus some local dynamic use. Also, a global memory is available for common usage between processors. As far as the control function is concerned, input and output is automatic at the basic RTI rate of 10 KSPS, thus data transfer to the hardware does not slow the computation algorithm. Each processor with its co-processor can perform approximately 400K FLOP.

Custom Distributed Processor for Closed-Loop Control and Laboratory Test



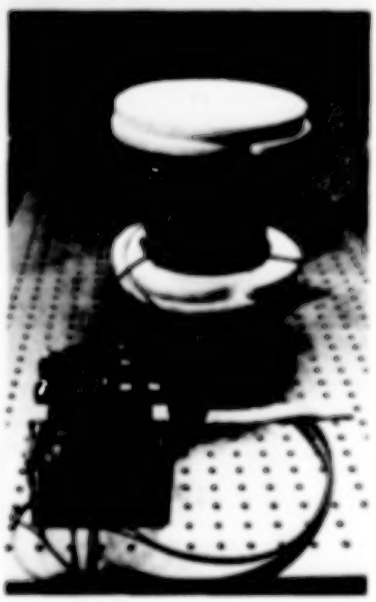
HARDWARE & EXPERIMENT DATA LINK

The combination of multiple channel, high data rate, high resolution, and low noise requirements drove the design to fiber optic data links between the hardware and the processor. Hardware A/D and D/A interfaces are close to the experiment. Cross talk and noise usually associated with long lines are eliminated and mechanical vibration transmission due to heavy cable drops is minimized due to the fiber's small size.

Three prototype builds were required for the electronics which interfaces the computers to the fiber optics. Layout proved to be extremely critical due to the high frequencies involved.

Fiber Optic Data Link between Experiment and Processor

- Minimize Mechanical Noise Transmission
- Eliminate Cross Talk & Noise between Motor Drives & Sensor Channels
- Multiplex Many Channels



FACILITY USES

The COF facility was originally designed to support testing of the Space Active Vibration Isolation (SAVI), hardware and also provide a hardware development capability leading to the Zenith Star Laboratory test. Other interesting uses for the test facility are: close rendezvous and dock between two bodies, manipulator studies and fine pointing experiments. The common characteristic of the applications seems to be that one body is dynamically orientable in 6 DOF, and the other is free to move in a quiet environment, again in 6 DOF.

1. Space Active and Passive Vibration Isolators
2. Gimbal Mounts
3. Fine Pointing Experiments
4. Rendezvous and Dock
5. Retargeting Experiments

ASCIE: AN INTEGRATED EXPERIMENT TO STUDY CSI IN LARGE SEGMENTED OPTICAL SYSTEMS

Jean-Noel Aubrun and Kenneth R. Lorell
Lockheed Palo Alto Research Laboratory
Palo Alto, California

3rd Annual NASA/DoD CSI Conference
Jan 29 - Feb 2, 1989

LARGE SEGMENTED REFLECTOR SYSTEMS

The use of a segmented primary mirror is one of the major design concepts for the new generation of large ground and space-based telescopes. The W. M. Keck Ten-Meter Telescope (TMT), whose structural model is shown on Fig. 1 , or NASA's planned Large Deployable Reflector (LDR) are typical examples of this approach. In a segmented reflector the mechanical rigidity and geometric accuracy are supplied solely by the support structure. Imperfections in the manufacturing process, deformations due to gravity loads, thermal gradients, slewing and tracking dynamics, and structural vibrations make it imperative that the positions of the segments be actively controlled. For example, the TMT segment alignment system requires 162 sensors, 108 actuators, and a special control system to align its 36 segments.

An important characteristic of such systems is that the supporting truss is very light (even for ground-based telescopes like the TMT), thus very flexible, with usually low natural damping. As a result, interactions between the segment alignment control system and the structural dynamics are expected to occur.

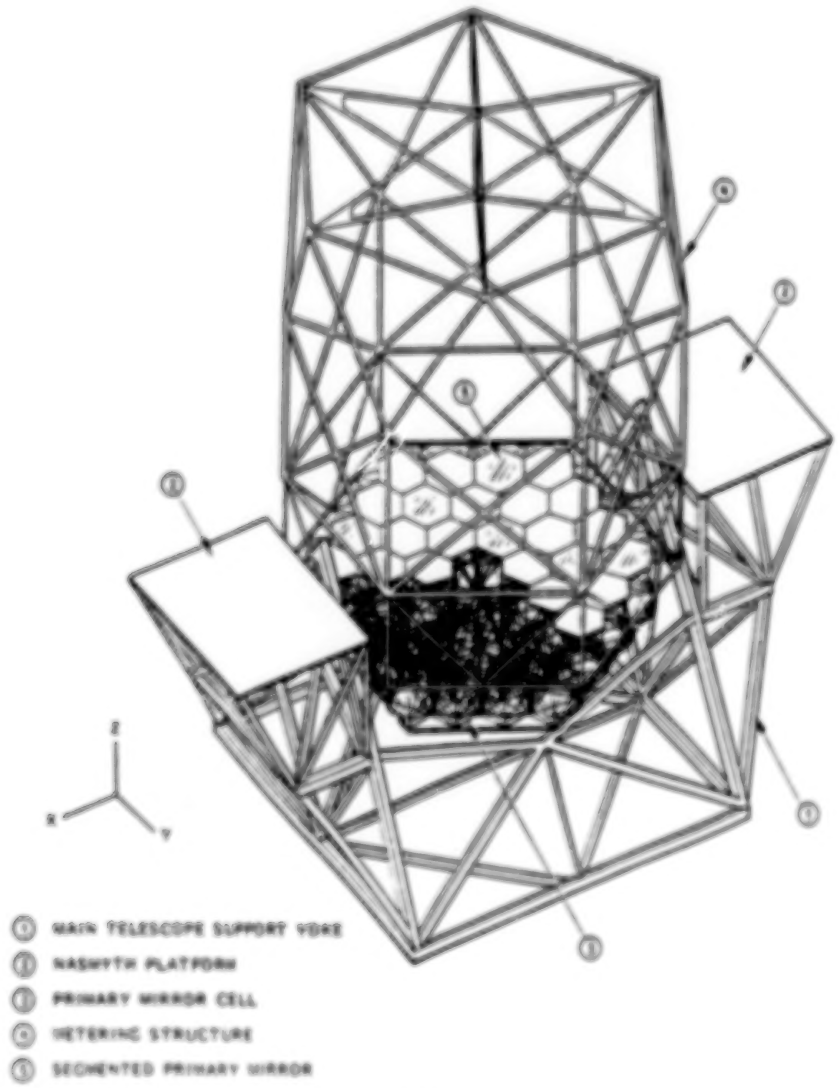


Figure 1

BEST COPY AVAILABLE

MOTIVATION FOR THE DEVELOPMENT OF AN INTEGRATED EXPERIMENT

The interaction between the control system actuators and sensors with the dynamics of the support structure seriously limits the performance of the system. A recent analytical study done by Lockheed [refs 1, 2 and 3] of the TMT that modelled the full structure, actuator and sensor set, and control system operation showed that control system stability was seriously affected by dynamic coupling between the segments through the support structure. Tests performed on a single segment and support cell conducted at the Lawrence Berkeley Laboratory failed to predict this phenomenon because they did not account for the effects of collective motion and coupling in the full system. While analysis can be very effective in predicting major behavior, there are numerous practical problems that must be solved and tested with real hardware. Moreover, the design and implementation of a multi-actuator, multi-sensor control system for large flexible segmented reflectors (LFSR) has never been experimentally validated. There was thus a need to develop a test bed that could support strong interdisciplinary studies to develop and validate the emerging LFSR technology.

ASCIE OBJECTIVES

A unique ground experiment called the Advanced Structures/Controls Integrated Experiment (ASCIE) has been conceived and developed as a means of performing meaningful laboratory experiments for the design, implementation, and validation of control strategies for large flexible systems with distributed optical elements, and in particular for large segmented telescopes. The ASCIE test bed has been designed to support a number of interdisciplinary studies that address major technical challenges of LFSRs. One of the immediate objectives of this project concerns the study of structures/controls interaction in LFSRs. However the scope of ASCIE is of a more general nature. Topics such as structural control (e.g. active damping, vibration suppression, disturbance alleviation) or pointing and slewing techniques for LFSRs will also be addressed using the ASCIE system.

The near-term goal for the ASCIE is to demonstrate in the laboratory a fully operating TMT-like segment alignment control system with a level of performance comparable to that required for a real telescope. This study will provide a means to investigate the CSI phenomenon in a real structure and compare it to analytical predictions. Longer term goals include substantial improvements in bandwidth and disturbance rejection through the use of advanced control techniques.

ASCIE FEATURES

The ASCIE structure shown in Fig. 2 consists of a 2-meter, 7-segment, actively controlled primary mirror supported by a light, flexible truss structure. The optical system emulates that of an f/1.25 Cassegrain telescope and utilizes an actively controlled secondary mirror. The six peripheral segments are controlled in three degrees of freedom using specially developed precision actuators. Segment alignment is obtained through the use of edge sensors whose signals are processed by the control system which then generates the commands for the actuators. One of the unique features of the ASCIE is its optical scoring and calibration system which eliminates the requirement that the segments have real optical surfaces. Small optical flats combined with a special faceted secondary mirror reflect laser beams onto an array of linear position-sensing photodetectors.

The active control of the secondary mirror is necessary to provide correct initial alignment of the primary segments. It will also be used to improve image stability and to simulate a chopping secondary, a feature found in all infrared astronomical telescopes [Refs 4 and 5]. Controlling the secondary mirror to stabilize the image at the focal plane is another example of a non-collocated system where CSI pays an important role [Ref 6].

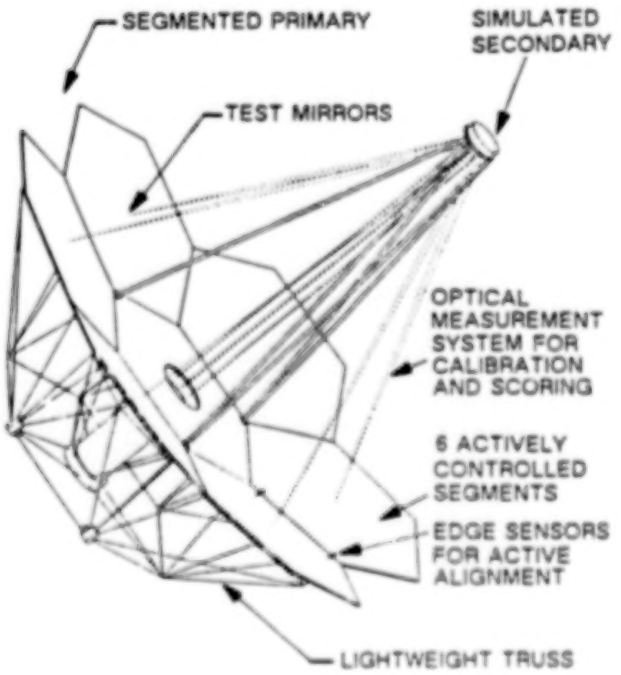
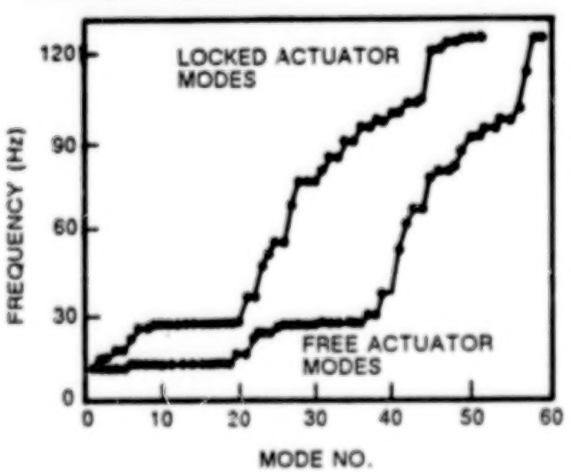


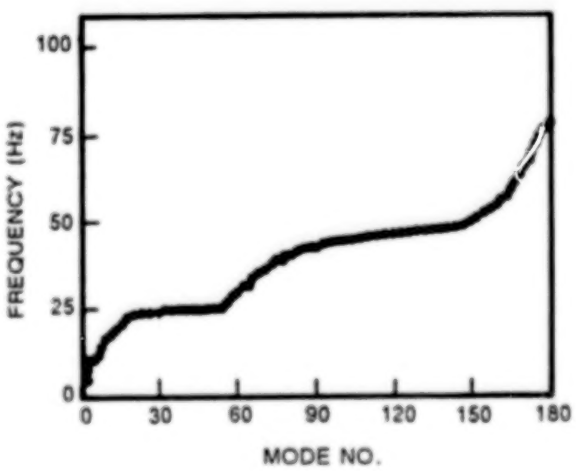
Figure 2

ASCIE STRUCTURE DYNAMICS PROPERTIES

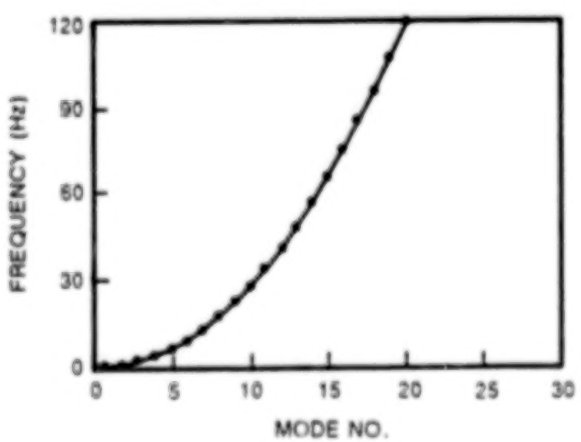
The ASCIE structure was designed to replicate the complex dynamic behavior that characterizes large segmented systems. Typical of such systems is the modal grouping due to the high degree of symmetry of the structure. For a perfectly rigid support structure, the segments and their supporting mechanism (e.g. subcell and actuators) have almost identical dynamic properties and thus can be viewed as N identical oscillators at the same frequency. For ASCIE 18 modes of vibration related to the segments will occur at more or less the same frequency. However, because the support structure is in reality quite flexible, coupling between the grouped oscillators produces two results. First, the resonant frequencies tend to spread slightly by moving away from each other [Ref 7]. The second, and more significant effect in terms of CSI, is the creation of global, or collective modes in which the segments as a whole behave as a continuous sheet rather than as individual pieces. These modes effectively couple one part of the mirror to another, creating adverse interactions that did not exist when considering individual segment dynamics. Fig. 3 shows a comparison between the modal frequency histograms of ASCIE and of the Keck telescope. A great similarity can be observed. This behavior is quite different from that of a beam-like structure as also shown on the figure. In addition the ASCIE structure was tuned to have its significant modes around 12-15 Hz to be relevant to larger systems.



a. ASCIE



b. Histogram of TMT Modal Frequencies



c. Cantilever Beam

Figure 3

COMPARISON WITH KECK TELESCOPE

Table I below shows a comparison between the principal parameters of ASCIE and the Keck telescope. Although of considerable difference in weight and size, the modal frequencies and the overall performance are very similar. With 18 actuators and 24 sensors, the control system is complex enough to be a valid test bed for the type of problems found in larger systems.

	ASCIE	KECK
PRIMARY MIRROR DIAMETER	2 m	10 m
NUMBER OF SEGMENTS	7	36
SEGMENT DIAMETER	0.6 m	1.9 m
NUMBER OF ACTUATORS	18	108
NUMBER OF EDGE SENSORS	24	168
TOTAL MASS	75 Kg	200,000 Kg
FIRST MODE FREQUENCY	7.2 Hz	5 Hz
FIRST CRITICAL MODE FREQUENCY	12 Hz	18 Hz
EXPECTING PHASING ERROR	30 nm	30 nm
EXPECTED TILT ERROR	0.1 arcsec	0.03 arcsec

Table I

ASCIE CONTROL SYSTEM PRINCIPLE

The segment alignment control system is similar to that of the Keck telescope. It utilizes a self-referenced system of edge sensors providing a set of error signals that are processed through a special algorithm to obtain the piston and tilt errors for each individual segment. Corrections based upon these errors are applied, through proper electronic compensation, to the actuators controlling position and tilt of each segment (Fig. 4). In such a centralized control system where the actuators are driven by signals from all the sensors, structural dynamics can couple back the actuators to all the sensors through global modes of vibration, thus resulting in potential instability.

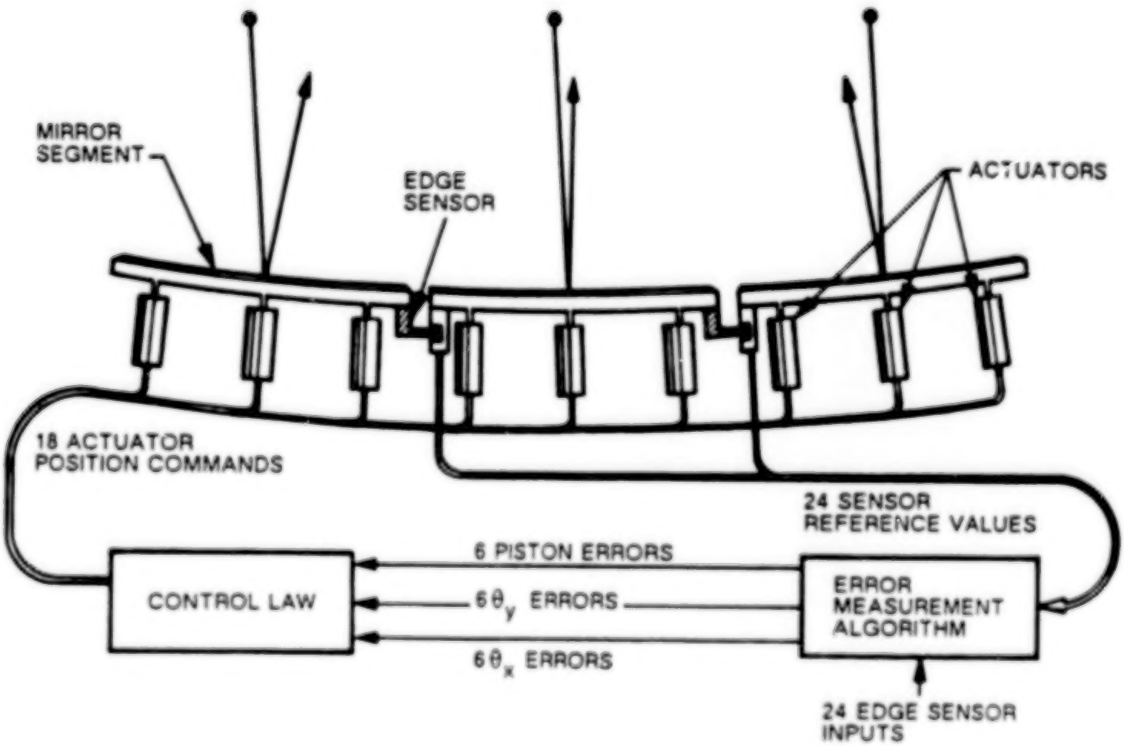


Figure 4

ASCIE EDGE SENSOR SYSTEM

The edge sensors used for ASCIE are small inductive position sensors as shown in Fig. 5a. This type was preferred to the capacitive sensors used for the Keck telescope because of their commercial availability, price and performance characteristics. Also they are very rugged and easy to use. The sensors are mounted on tabs attached to the segments, thus directly measuring the relative edge displacement. Each segment is surrounded by six sensors (2 per edge) as shown in Fig 5b. The offset from the true edge is a very important factor for the full observability of the system and it must be optimized in order to obtain the best sensitivity and noise performance. The redundancy (24 sensors to measure 18 degrees of freedom) also helps to reduce noise, is important for reliability, and will permit fault detection and accommodation studies. Since these measurements are relative, a reference must be chosen to relate them to the absolute axis of the telescope. In ASCIE, the central segment is taken as the reference.

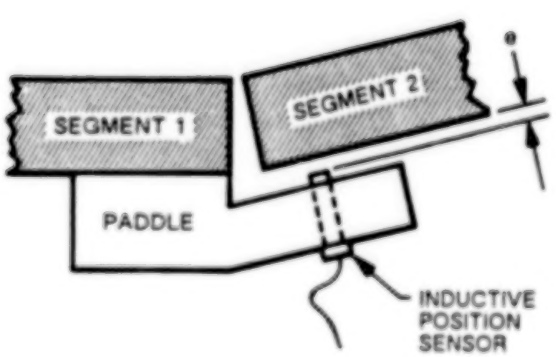


Figure 5a

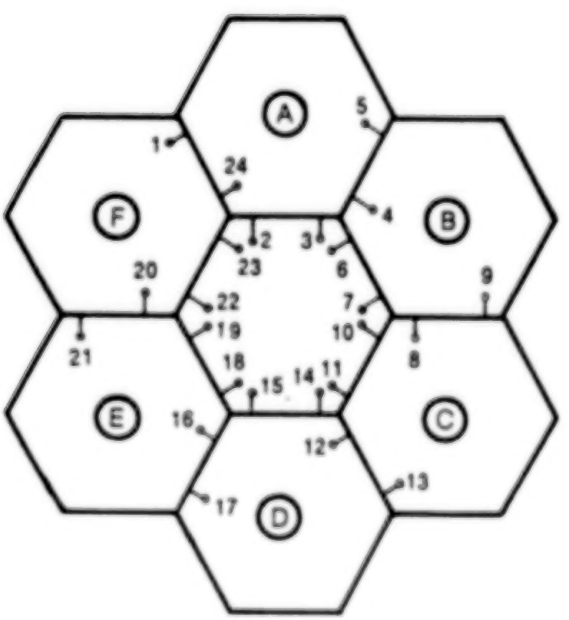


Figure 5b

ASCIE OPTICAL CALIBRATION AND SCORING SYSTEM PRINCIPLE

Fig. 6 shows the principle of an optical system that directly measures the tilt errors associated with each segment. It emulates a more complex wavefront sensor based on holographic patches, for example. The laser beam coming from the central tube reference is split into six equal beams by a special faceted secondary mirror. Each of the beams reflects on a small flat mounted on the corresponding segment reflects back on the same facet of the secondary mirror and finally focuses on a two-axis photodetector. The photodetector provides two electrical signals directly proportional to the position of the laser spot in two orthogonal directions. This optical system has a sensitivity of 0.1 arcsecond and is used to initially align the segments. After this operation the control system remembers the set points of all the edge sensors and maintains them in the presence of disturbances. The optical system is not a part of the control loop but can be used as an independent scoring system to evaluate the performance of the segment alignment control system.

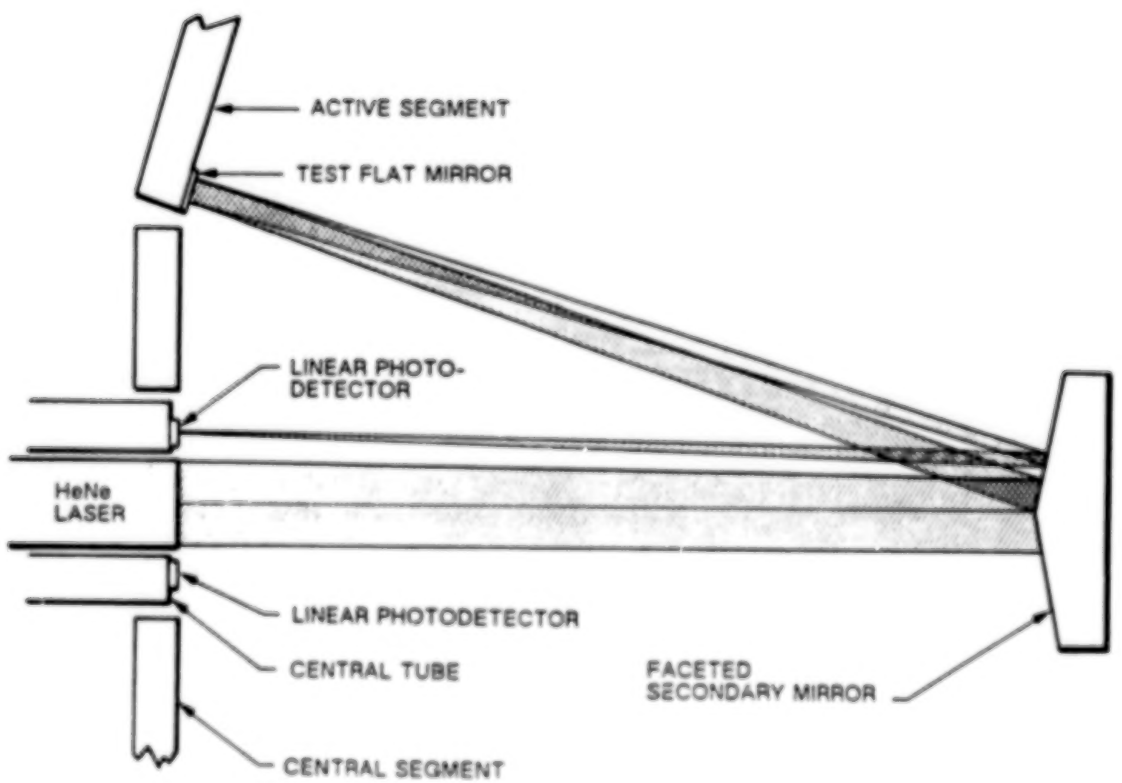


Figure 6

ASCIE DATA ACQUISITION AND CONTROL SYSTEM

The ASCIE system is shown schematically in Fig. 7. The central part is an electronic interface and control console. It contains the analog electronics that controls the actuators and conditions the signals from the sensors. It sends the conditioned edge sensor signals to the Array Processor (A/P) where the segment alignment control laws are implemented. This interface electronics can be operated directly or through a Personal Computer (PC). The PC has also a two-way communication system with the host processor (HARRIS-800). The host processor is used to perform control design, analysis, and data processing, and to control the A/P (downloading control gains, acquiring data from the sensors, the command channels and the internal states of the A/P, and starting and stopping the A/P). In addition to controlling the operations (automated procedures are implemented to power up or shut down the system, to establish various control modes, etc.), the PC is used to display all the important variables involved in the segment alignment control, i.e., edge sensor signals, commands to the actuators, and actual tilt and piston errors for each segment. This display gives the operator a complete view of the system operation and performance.

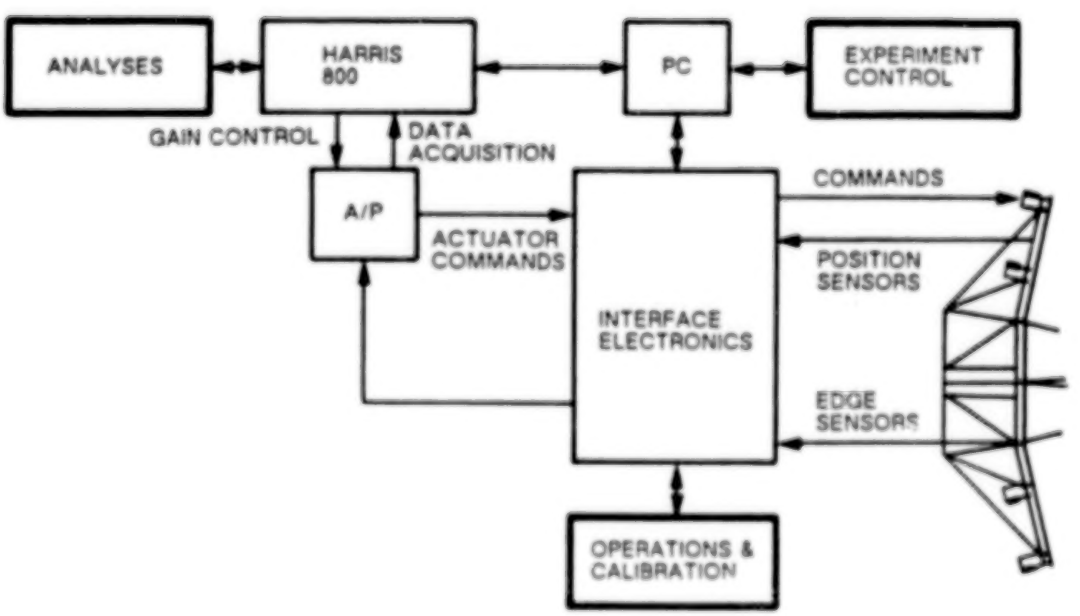


Figure 7

ASCIE HARDWARE

Fig. 8 is a view of the actual ASCIE hardware showing the active secondary mirror on the left, the focal plane sensor mounted in the center of the primary mirror, the small flat mirrors attached to the six peripheral segments near the central segment, and the truss structure supporting the segment actuators. These actuators were specially design in the Lockheed Palo Alto Research Laboratory and have a range of +/- 1 mm with an rms noise of 30 nm. They contain a position servo-loop and are capable of running at a bandwidth greater than 100 Hz. The segments are directly attached to the actuators by special flexures that passively constrain lateral and rotational motions but allow the actuators to position them in the remaining three degrees of freedom (piston and tilts). In its present configuration the structure is cantilevered from the back of the central tube, but can be mounted either horizontally (as in the photograph), or vertically.

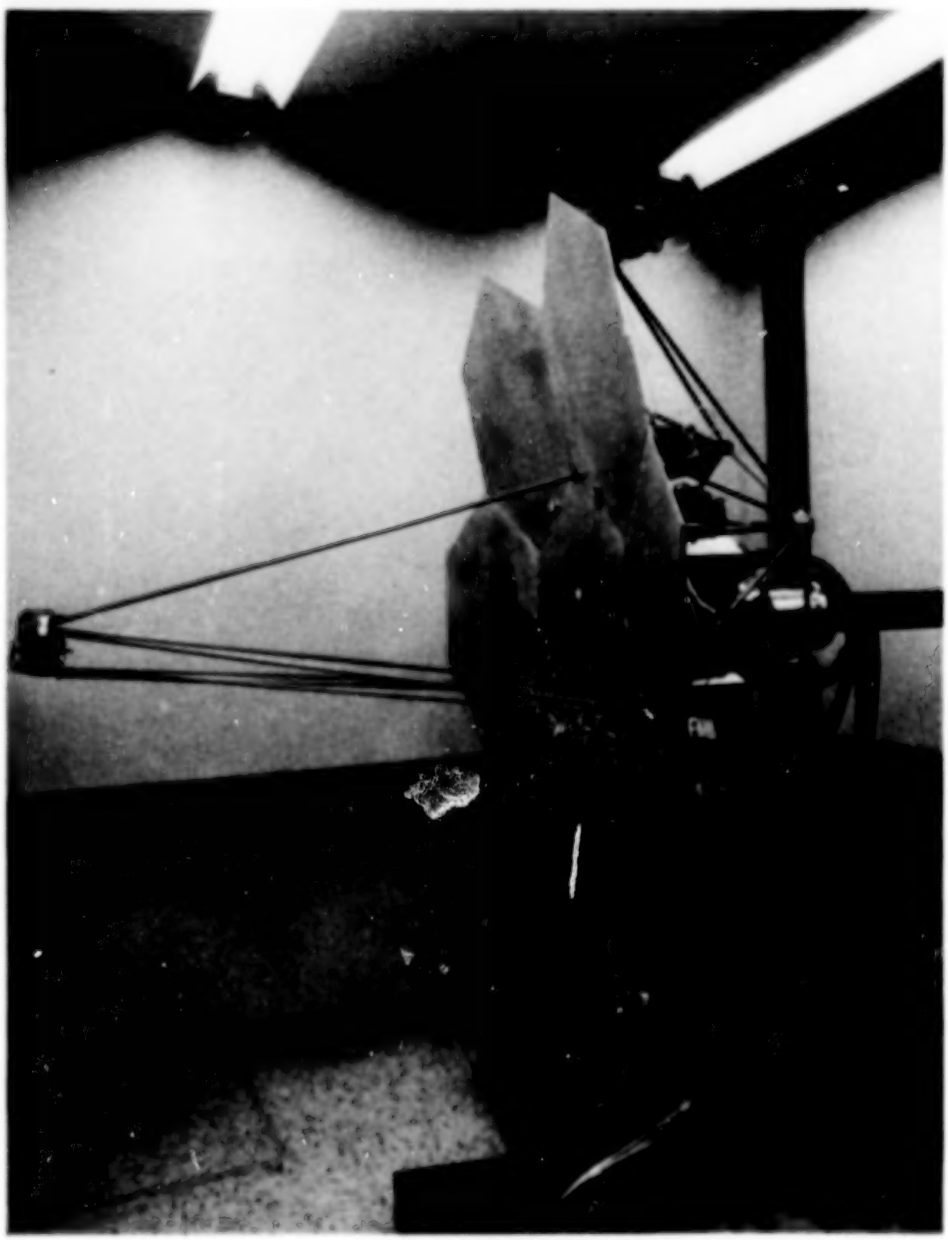


Figure 8

ASCIE PRELIMINARY TEST RESULTS

The objective of the experiments conducted at the Lockheed Palo Alto Research Laboratory is to predict and demonstrate the CSI phenomenon, and develop and test new control approaches to circumvent this problem. One of the main objectives of this research is to obtain results traceable to actual systems. Thus it was essential to design ASCIE for a level of performance comparable to that of optical systems. Preliminary tests were conducted by closing the loop on one segment, while the five others were passively restrained by their own actuator/flexure system.

The loop was closed successfully at a 5 Hz bandwidth. Preliminary analyses had indicated that with the simple integral control scheme used in this case, the CSI effect will limit the bandwidth to about 11 Hz. The traces shown in Fig. 9 are the actual displacements of the three control actuators while the loop is closed on the edge sensors. This 5-second run shows 300 nm (about 1/3 of a micron) motion due principally to thermal distortion in the support structure (the experiment was conducted in a typical laboratory environment). The actuator motions were commanded by the control system so as to maintain the correct alignment of the controlled segment with respect to its neighbors at all times. The corresponding piston and tilt errors are shown in the next plot (Fig. 10).

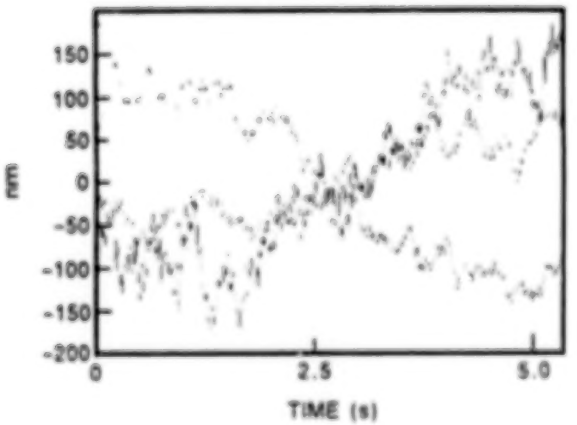


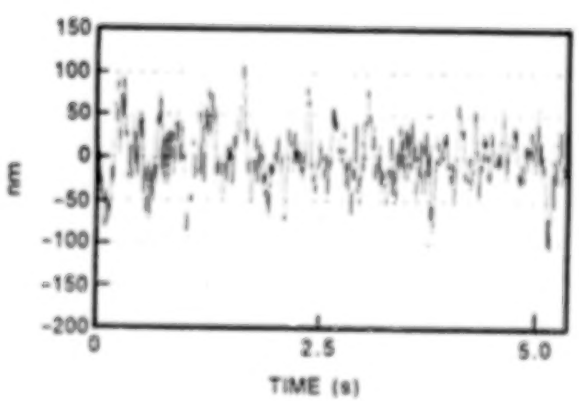
Figure 9

ASCIE SINGLE SEGMENT ALIGNMENT TEST (PISTON AND TILT ERRORS)

The segment aligment errors during closed-loop operations are shown in Fig. 10a for piston, and in Fig. 10b for the two tilt axes ("Petal" denotes a folding motion of the segments toward the optical axis). The residual error is due essentially to seismic and sensor noise. By contrast with the previous plot, the traces are here perfectly centered, i.e., the thermal drift has been completely eliminated. The level of performance that has been achieved (about 30-nm rms in piston and less than 0.05 arcsecond in tilt) is comparable to that of the Keck telescope requirements and thus represents a major step in validating the technology for large flexible segmented optical systems.

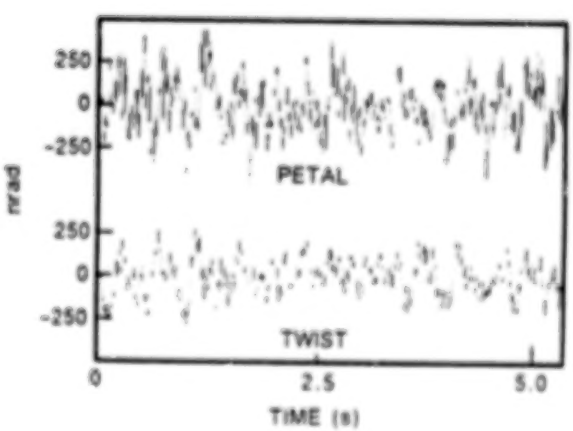
CONCLUSIONS

This paper has presented a description of the ASCIE experimental setup, a generic test bed for several essential technologies. In particular its multi-input, multi-output, non-collocated control system and its complex structural dynamics, characteristic of large segmented systems make it an ideal test bed for CSI experiments. The high accuracy of its measurement system will make it possible to investigate the dynamics of microvibrations and its implication for the CSI phenomenon.



Piston error

Figure 10a



Tilt error

Figure 10b

REFERENCES

1. Aubrun, J-N, Lorell, K.R., Havas, T.W., and Henniger, W.C.: An Analysis of the Segment Alignment Control System for the W. M. Keck Observatory Ten Meter Telescope. Final Report. Keck Observatory Report Number 143, Dec 1985

2. Aubrun, J-N., Lorell, K.R., Mast, T.S., and Nelson, J.E.: Dynamic Analysis of the Actively Controlled Segmented Mirror of the W. M. Keck Ten Meter Telescope. IEEE Control Systems Magazine, Vol. 7, No. 6, Dec 1987

3. Aubrun, J-N, Lorell, K.R., Havas, T.W., and Henniger, W.C.: Performance Analysis of the Segment Alignment Control System for the Ten-Meter Telescope. AUTOMATICA, Vol. 24, No. 4, Jul 1988

4. Sridhar, B., Lorell, K.R., and Aubrun, J-N.: Design of a Precision Pointing Control System for the Space Infrared Telescope Facility. IEEE Control Systems Magazine, Vol. 6, No. 1, Feb. 1986

5. Lorell, K.R. and Aubrun, J-N.: Active Image Stabilization for Shuttle-Based Payloads. Proceedings of the 1986 American Control Conference, June 18-20, Seattle, Washington

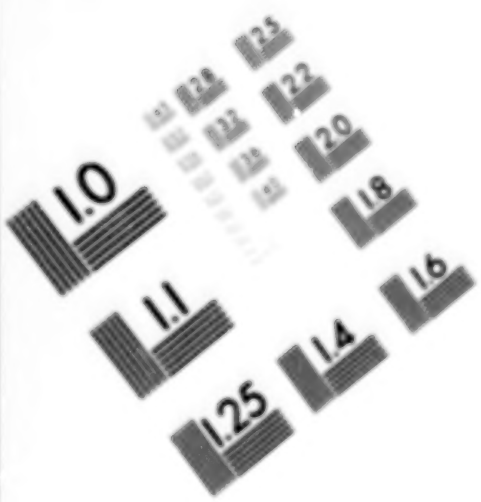
6. Parsons, E.K.: The Jitter Beam: an Experiment Demonstrating Pointing Control on a Flexible Structure. 1988 American Control Conference (Atlanta, Georgia), June 1988

7. Sridhar, B., Aubrun, J-N., and Lorell, K.R.: Analytical Approximation of the Dynamics of a Segmented Optical System. Proceedings of the International Federation of Automatic Control 4th Symposium on Distributed Parameter Systems, June 30 - July 2, 1986, UCLA, Los Angeles, California

CSI Sensing and Control: Analytical and Experimental Results

J. L. Junkins, T. C. Pollock, and
Z. H. Rahman
Texas A&M University
College Station, Texas

3rd Annual NASA/DoD Controls/Structures Interaction Conference
San Diego, CA
January 29 - February 2, 1989



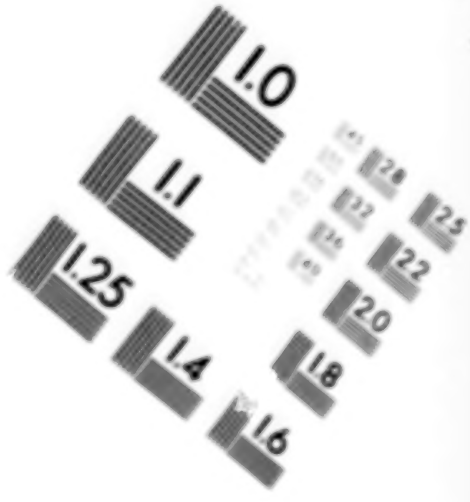


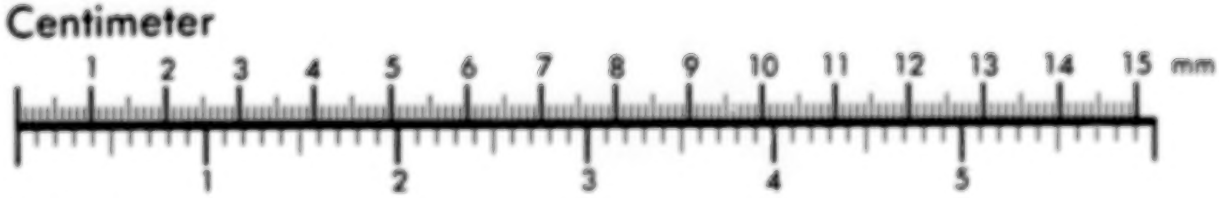
AIIM

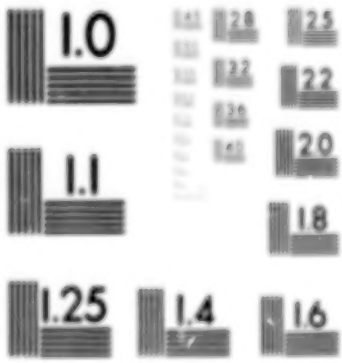
Association for Information and Image Management

1100 Wayne Avenue, Suite 1100
Silver Spring, Maryland 20910

301/587-8202











MANUFACTURED TO AIIM STANDARDS
BY APPLIED IMAGE, INC.

Preface

We present here some of our recent work on structural identification and large-angle maneuvers with vibration suppression. Our recent work has sought to balance structural and controls analysis activities by involving the analysts directly in the validation and experimental aspects of the research. We have successfully implemented some new sensing, actuation, system identification, and control concepts. An overview of these results is given herein.

Acknowledgments

The following graduate research assistants made significant contributions to the analytical, numerical, and experimental results reported herein: G. James, III, S. Morgan, Y. Kim, R. Byers, D. Anderson, and M. McVay. This research is supported by the Air Force Office of Scientific Research and the Texas Advanced Technology Research Program. The liaison of Dr. A. K. Amos is appreciated.

We distinguish between modal and model identification. In modal identification, we seek to extract the natural frequencies, damping factors, and mode shapes from (typically) a free decay response to impulsive initial conditions. In model identification, we seek the estimates of a particular set of physical parameters contained in our best available model of the structure, so that our computed (free or forced) response of the system is in best agreement with the measured response.

In our approach to model identification (see next page for roadmap figure), we utilize modal identification as a preprocessor. That is, we consider the $\{\omega$'s, ξ's, and ϕ's$\}$ determined from free vibration measurements as additional measurements to our model identification process wherein we seek to fit the measured input/output behavior by the frequency response from our model of the system. See reference 1 for details.

OUTLINE

- TAMU Flexible Grid Experiments
  - Structural Identification
  - Test Article, Sensors, and Actuators
  - Stereo-Triangulation Deflection Measurements
  - Measured Response Results
  - Creamer/Junkins Method for System Identification
  - Modeled, Measured, and Identified Frequencies & Mode Shapes
- Large Angle Maneuver Experiment
  - Configuration Description and Dynamical Model
  - Torque-Shaped, Near-Minimum-Time Maneuvers
  - Liapunov-Stable Feedback Control
  - Experimental Results
- Concluding Remarks

A Novel Approach to Structural Identification

STRUCTURAL MODEL IDENTIFICATION

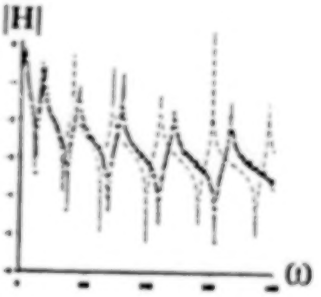
Estimation of the best-fitting linear structural model via Creamer/Junkins substructuring

best fitting linear system:

$$M\ddot{x} + C\dot{x} + Kx = Bu$$

FREQUENCY RESPONSE IDENTIFICATION

Estimation of the frequency response function via Creamer's algorithm



MODAL IDENTIFICATION

Determination of natural frequencies & mode shapes via Juang/Pappa Eigenstructure Realization Algorithm (ERA)

measured natural frequencies & mode shapes

$\omega_i \ \phi_i \ , i = 1,2, \ldots , n$

INERTIAL TARGET TRAJECTORIES

Compute inertial time history of each target's coordinates via stereo ray intersection

FOCAL PLANE TRAJECTORIES

Connect successive image coordinates to form focal plane trajectories, for each of two (or more) focal planes

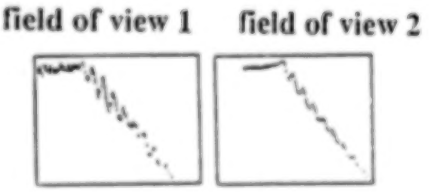
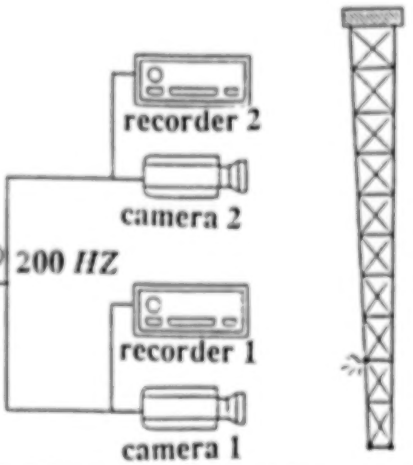


IMAGE CENTROID CALCULATION

From the synchronized cameras' digitized image boundaries, determine the centroids of each image

VIDEO PROCESSING

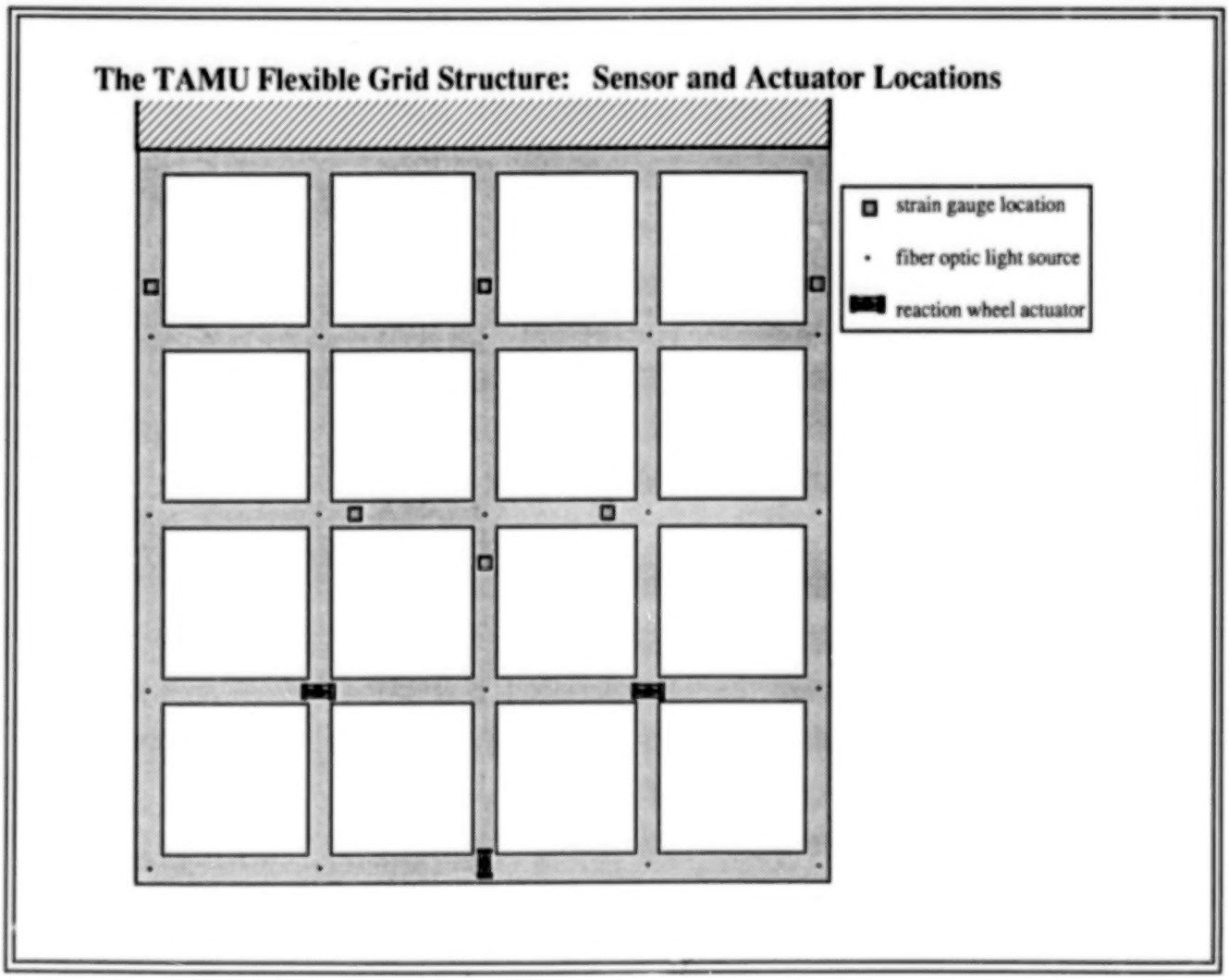
Locate and digitize the image boundaries via Motion Analysis' edge detection processor



This is a sketch of a 5 ft by 5 ft aluminum grid we've been using for a structural identification and vibration control experimental test article. The grid is cantilevered in the vertical plane. We cut this grid from a single sheet of aluminum, so it is jointless. However, a lap joint grid of identical geometry has been developed and is the subject of a similar experimental program by Alok Das et al. at AFAL.

Note that we have 20 optical targets on the grid. Presently these targets are actively illuminated by fiber optic light guides, but we have also successfully used passive targets made from reflective tape ("scotchlite" made by 3M). These optical targets are visible in two video cameras (200 or 60 frames per second); stereo triangulation of centroided image coordinates leads to measured inertial trajectories for each target. We also have six strain gauges mounted on the back of the grid at the stations shown, and we utilize three piezo-electric accelerometers that can be mounted at any three of the grid locations.

Excitation is provided by three grid-mounted reaction wheels (driven by Clifton Precision motors) with their torque axis in the plane of the grid in the directions shown (±20 oz-in. over the bandwidth from 0 to 40 Hz). We also utilize an impulse hammer to impart calibrated initial impulse excitation at any station.



We summarize the geometric equations governing triangulation of video camera imagery. With reference to the left figure, the image coordinates (x,y), measured in the positive focal plane of a single lens camera, are related (ref. 2) to the object space coordinates (X,Y,Z) of the imaged point, the camera's principal point (X_C,Y_C,Z_C), orientation angles (ϕ,θ,ψ), principal point offset (x_o,y_o), and focal length (f), by the colinearity equations

$$x = x_o - f\left[\frac{C_{11}(X-X_c)+C_{12}(Y-Y_c)+C_{13}(Z-Z_c)}{C_{31}(X-X_c)+C_{32}(Y-Y_c)+C_{33}(Z-Z_c)}\right] \equiv F(X,Y,Z;X_c,Y_c,Z_c;\phi,\theta,\psi;x_o,y_o,f)$$

$$y = y_o - f\left[\frac{C_{21}(X-X_c)+C_{22}(Y-Y_c)+C_{23}(Z-Z_c)}{C_{31}(X-X_c)+C_{32}(Y-Y_c)+C_{33}(Z-Z_c)}\right] \equiv G(X,Y,Z;X_c,Y_c,Z_c;\phi,\theta,\psi;x_o,y_o,f)$$

$$\begin{bmatrix} C_{11} & C_{12} & C_{13} \\ C_{21} & C_{22} & C_{23} \\ C_{31} & C_{32} & C_{33} \end{bmatrix} = \begin{bmatrix} 1 & 0 & 0 \\ 0 & \cos\psi & \sin\psi \\ 0 & -\sin\psi & \cos\psi \end{bmatrix} \begin{bmatrix} \cos\theta & 0 & -\sin\theta \\ 0 & 1 & 0 \\ \sin\theta & 0 & \cos\theta \end{bmatrix} \begin{bmatrix} \cos\phi & \sin\phi & 0 \\ -\sin\phi & \cos\phi & 0 \\ 0 & 0 & 1 \end{bmatrix} \tag{1}$$

We adopt a double subscript notation for eqs. (1) to denote the image coordinates of the i^{th} point measured in the j^{th} camera's image space as

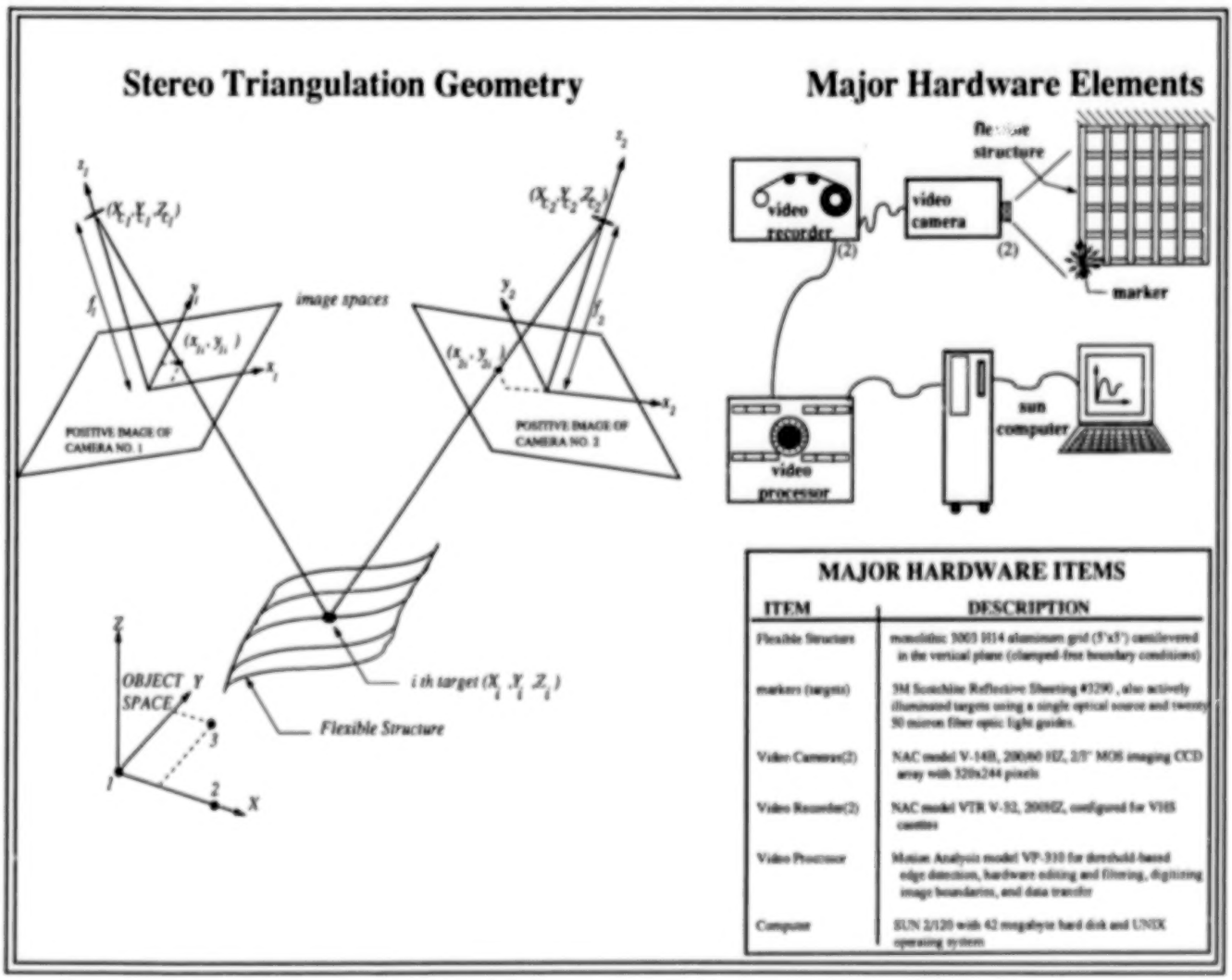
$$\begin{aligned} x_{ij} &= F(X_i,Y_i,Z_i;\ X_{c_j},Y_{c_j},Z_{c_j};\ \phi_j,\theta_j,\psi_j;\ x_{o_j},y_{o_j},f_j) \\ y_{ij} &= G(X_i,Y_i,Z_i;\ X_{c_j},Y_{c_j},Z_{c_j};\ \phi_j,\theta_j,\psi_j;\ x_{o_j},y_{o_j},f_j) \end{aligned}, \quad j=1,2;\ i=1,2,\ldots N \tag{2}$$

In the event that the camera position, orientation, and calibration constants are considered known, measurement of image coordinates of object space points at unknown locations, eqs. (2) provide four equations for the three unknown coordinates of each point. Equations (2) can be inverted by least squares to determine the object space coordinates. Dynamic triangulation must be preceded by a static calibration to determine the camera calibration constants, and for the case of fixed cameras, the position coordinates of the cameras. The calibration should use at least three fixed targets that will subsequently be visible in the dynamic experiments. These three points serve to define the object space coordinate system. The points are numbered in some arbitrary fashion. We use Point 1 as an arbitrary origin: $(X_1,Y_1,Z_1) = (0,0,0)$. Point 2 is used to define the X axis: $(X_2,Y_2,Z_2) = (X_2,0,0)$. Point 3 is used to define the X,Y plane: $(X_3,Y_3,Z_3) = (X_3,Y_3,0)$. Thus the first three points have a total of three unknowns (X_2,X_3,Y_3), and each additional point introduces three unknowns (X_i,Y_i,Z_i) for a total of 3N - 6 unknown object space coordinates. Notice that each object space point has four associated measurements (two measured coordinates in each of the two image planes). Thus, in the most general case, we have the 3N - 6 unknown object space coordinates plus the 18 unknowns associated with the cameras $(X_{c_i},Y_{c_i},Z_{c_i};\ \phi_i,\theta_i,\psi_i;\ x_{o_i},y_{o_i},f_i;$ for i = 1.2). We conclude that we have a total of 4N eqns. and 3N + 12 unknowns; if N > 12 conjugate images are measured, we have enough equations to determine all of the 3N object space coordinates and the 18 camera position, orientation, and calibration parameters.

Also of significance, when using Charged Coupled Device (CCD) focal plane arrays (as in the present application), the effective focal length is different for the x and y axes (actually, there is a ratio of the x and y dimensions of the array as a consequence of the rectangular pixels, which can be absorbed into effective focal lengths to be determined during calibration) thereby increasing the number of unknowns by one for each camera and one additional object space point is required. We have found this calibration process to be very well behaved and can be routinely accomplished in 15 minutes of real time.

The calibration process is strengthened, of course, by making redundant measurements and using other a priori measurements of object space points and/or camera calibration parameters. The precision of the results is dependent most heavily upon the accuracy with which the image coordinates are measured and, of course, the geometric strength of the triangulation process. Upon completing a satisfactory static calibration, the subsequent dynamic triangulation process need consider only four of eqs. (2) at a time to sequentially accomplish the least-squares solution for the object space coordinates (X_i, Y_i, Z_i) of the points imaged on the flexible structure.

The major hardware elements are sketched below and described briefly in the table.



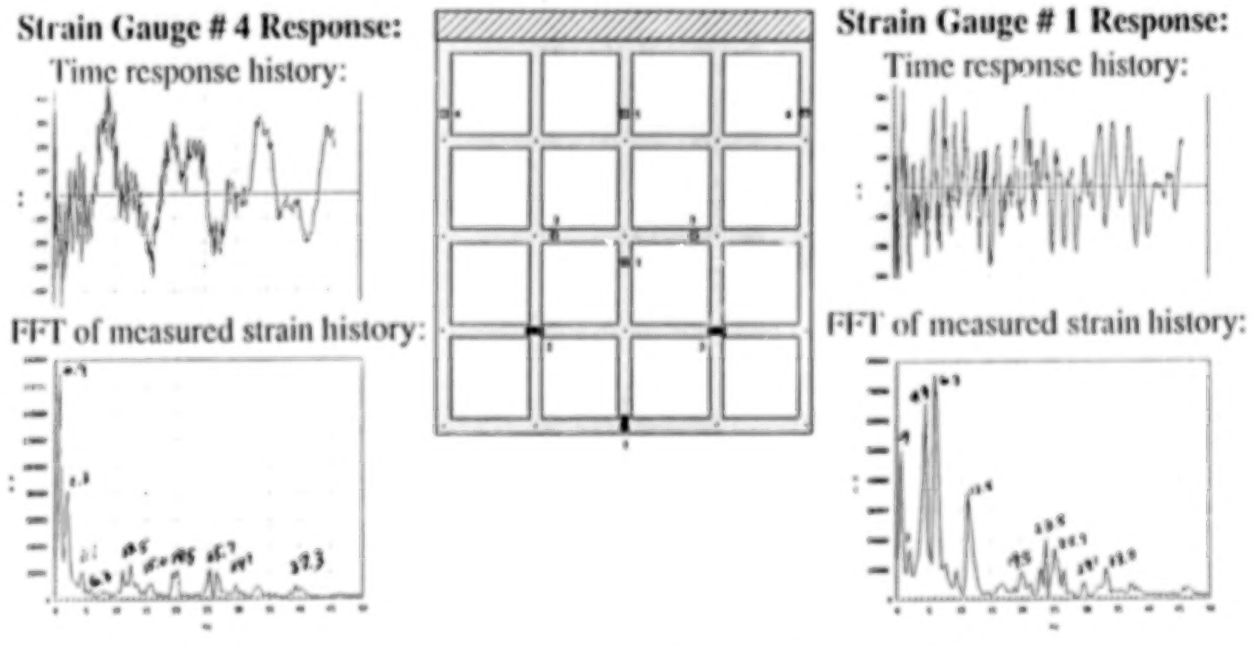
MAJOR HARDWARE ITEMS

ITEM	DESCRIPTION
Flexible Structure	monolithic 3003 H14 aluminum grid (5'x3') cantilevered in the vertical plane (clamped-free boundary conditions)
markers (targets)	3M Scotchlite Reflective Sheeting #3290, also actively illuminated targets using a single optical source and twenty 50 micron fiber optic light guides
Video Cameras(2)	NAC model V-14B, 200/60 HZ, 2/3" MOS imaging CCD array with 320x244 pixels
Video Recorder(2)	NAC model VTR V-32, 2005IZ, configured for VHS cassettes
Video Processor	Motion Analysis model VP-310 for threshold-based edge detection, hardware editing and filtering, digitizing image boundaries, and data transfer
Computer	SUN 2/120 with 42 megabyte hard disk and UNIX operating system

Here we show two typical measured strain histories at two stations in response to impulsive excitation via the impulse hammer. The time span of these records is 2.5 seconds; the sample rate was 700 Hz. An initial impulse was applied at the lower left corner of the grid. Notice from the fast Fourier transform (FFT) of strain gauge #4 that the response is dominated by the first two modes, but significant excitation was imparted to most of the modes below 40 Hz. On the other hand, strain gauge #1 has a large contribution by modes 3 and 4. This is not surprising, because it is intuitively clear that the first torsion mode (mode 2, with nominally zero strain in the center member) even though excited has near zero strain at station #1, but the second cantilever mode (mode 3) and the first "bow" mode (mode 4) are heavily excited by an impulse at the lower left corner, and these modes have significant strain at station #1. Based upon these and similar experiments, we conclude that the strain gauges provide excellent sensitivity to all modes below 50 Hz, for impulsive excitation, and simultaneously using strain measurements at the six stations shown provide excellent observability for all modes below 40 Hz.

As evident in the next figure, however, we have encountered some signal-to-noise difficulties when using the strain gauges to measure response to the reaction wheel excitation.

Response of the Grid to Impulsive Excitation



Below we show two typical measured strain histories at two stations in response to harmonic excitation by reaction wheel #1. A 2-Hz harmonic torque is applied to the structure at the center of the bottom member, about a nominally vertical axis. The torque was applied for approximately 2 minutes to allow a steady state to be achieved before we acquired the above 2.5 seconds of data.

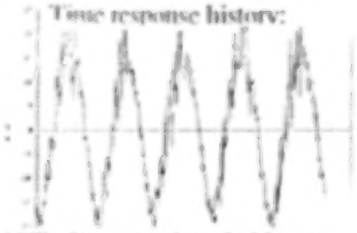
Our experiments indicated that the Clifton Precision motors deliver very clean harmonic excitation, so the high-frequency variations evident in the strain-gauge response are virtually all due to noise. Strain gauge #4 gives data with a satisfactory signal-to-noise ratio. It is evident however that the much smaller strain levels and their closer proximity to the electrical disturbance of the actuator resulted in much noisier data from strain gauge #1. In both cases, the physically dominant steady-state response at 2.0 Hz obviously dominates the strain measurements. However, it is obvious that the "noise modes" are almost negligible in strain gauge #4, whereas they are very significant in strain gauge #1 output. Note the cluster at 60 Hz in the FFT of strain gauge #1's response. This is a near-certain indication that electrical noise from the motor is generating a significant part of the problem. We anticipate that better grounding of the motor will reduce this noise source, but there is the difficulty that locally small strains (which are associated with certain motions) are the fundamental cause of the poor signal-to-noise ratio when using strain gauges as distributed vibration sensors.

These data indicate that the strain gauge is potentially useful in the present application, but other sensing approaches should be explored to eliminate signal-to-noise difficulties. As is evident from the impulsive response in the figure below, the optical sensing methods yield very clean deflection measurements of the low-frequency vibration (<20 Hz), and are therefore very well suited to the present application. We also show below a typical accelerometer record and its FFT. We have found the accelerometer data accurate between 2 Hz and 100 Hz, but very poor below 1 Hz. Our present optical system and triangulation deflection measurements are not compatible with real time. Thus the optical system as we have it presently configured and implemented is suitable for system identification but not feedback control measurements.

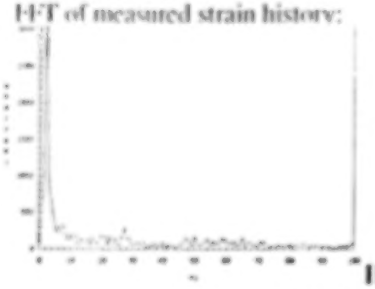
Response of the Grid to Harmonic Excitation

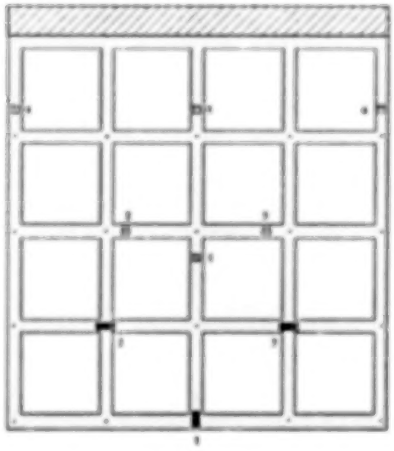
Strain Gauge # 4 Response:

Time response history:



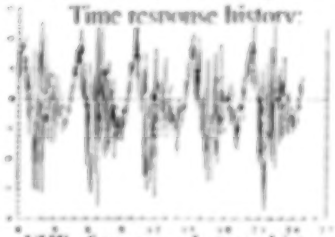
FFT of measured strain history:



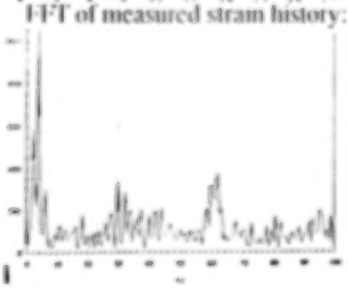


Strain Gauge # 1 Response:

Time response history:

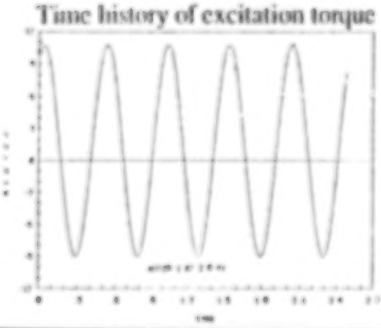


FFT of measured strain history:

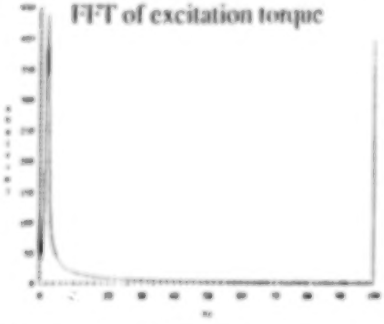


Harmonic Excitation Torque by Reaction Wheel # 1

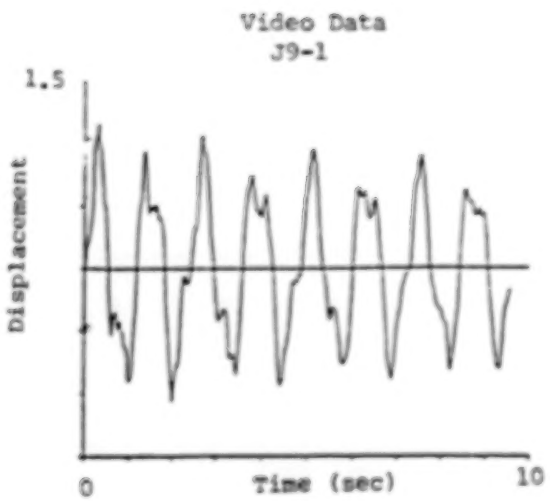
Time history of excitation torque

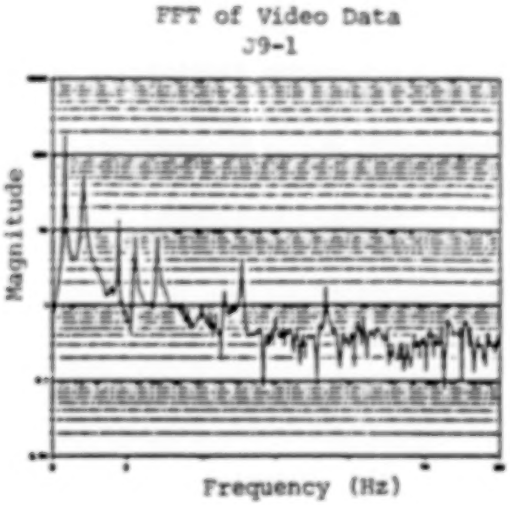


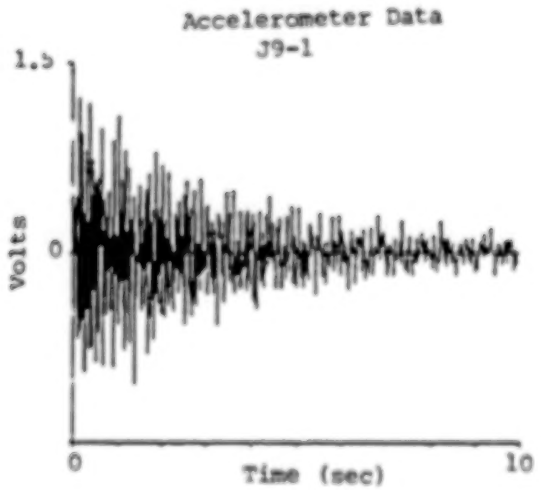
FFT of excitation torque

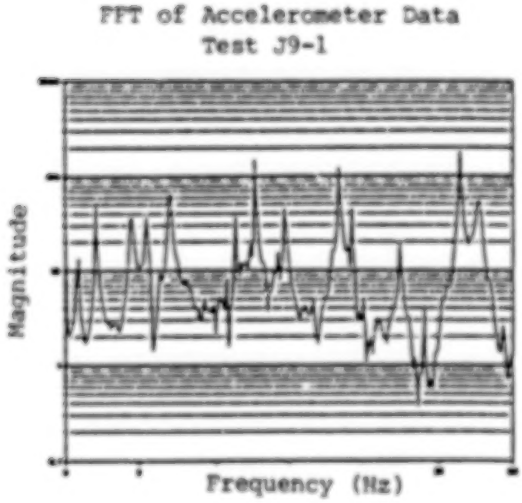


Comparison of Video-Derived Position Measurements with Accelerometer Measurements









The graphs shown above provide some insight into the advantages and disadvantages of the camera system versus an accelerometer. The video data is very useful at the low frequency large amplitude end of the spectrum. The accelerometer response is most reliable at the high frequency end of the spectrum. This data was taken on the AFAL structural identification test article which is similar to the TAMU structure. The video data was taken with a TAMU RCA TC2811 60 Hz video camera. An AFAL Endevco model 7751-500 accelerometer was also used.

Our structural identification approach is based upon the following observations:

- The input/output behavior is uniquely captured by the system transfer function (or frequency response function) matrix, whereas an infinity of structural models has the same transfer function.
- The most important necessary condition of a good model (for control purposes) is that we accurately model the actual system's frequency response over the frequency range of interest.
- Of all the models (realizations) we might use, the most comfortable approach is to modify in some "intelligent" way the model that grew out of our modeling effort (e.g., a finite-element model of the structure).

It is desirable that both free response and forced response behavior be accurately captured by the identified model.

Basic System Realization Concepts

Linear Autonomous System

$$\dot{x} = Ax + Bu$$
$$y = Cx$$

Time Response

$$x(t) = e^{At}\, x(t_0)\mathrm{I} + \int_{t_0}^{t} e^{A(t-\tau)} Bu(\tau) d\tau$$
$$y(t) = C\, e^{At}\, x(t_0)\mathrm{I} + \int_{t_0}^{t} Ce^{A(t-\tau)} Bu(\tau) d\tau$$

Laplace Transform

$$x(s) = (sI - A)^{-1} Bu(s)$$
$$y(s) = Cx(s) = C(sI - A)^{-1} Bu(s)$$
$$y(s) = G(s)\, u(s)$$

Transfer Function

$$G(s) = C(sI - A)^{-1} B$$

Freq. Response Function

$$G(j\omega) = C(j\omega I - A)^{-1} B$$

Notes

The triple (A,B,C) is not unique.

But $G(s)$ is unique.

(A_1, B_1, C_1) and (A_2, B_2, C_2) are said to be **equivalent** if any of the following statements are true:

- The transfer functions are equal:
  $G_1(s) = G_2(s)$, for all s
- The weighting patterns are the same:
  $C_1 e^{A_1 t} B_1 = C_2 e^{A_2 t} B_2$
- $C_1 A_1^k B_1 = C_2 A_2^k B_2$, for all k.

$\Rightarrow$ **Any** (A,B,C) which produces the correct transfer function $G(s) = C(sI - A)^{-1} B$ is said to be a "realization" of the system.

Consider the case that a force or moment is applied at a point, but the response at many measurement stations is available. For this case, B and therefore $G(j\omega)$ are vectors. Suppose that the frequency response function (vector) is measured over a frequency range $\{\omega_{min} < \omega < \omega_{max}\}$ at the frequencies $\{\omega_1, \omega_2, \ldots, \omega_m\}$. Use the notation:

$$\tilde{G} = \begin{Bmatrix} \tilde{G}(\omega_1) \\ \vdots \\ \tilde{G}(\omega_m) \end{Bmatrix} = \textit{measured}\ \text{FRF},\quad G(p) = \begin{Bmatrix} G(\omega_1, p) \\ \vdots \\ G(\omega_m, p) \end{Bmatrix} = \textit{computed}\ \text{FRF using model vector } p \tag{3}$$

and

$$\tilde{\Omega} = \{\tilde{\Omega}_1\ \tilde{\Omega}_2\ \ldots\}^T = \textit{measured}\ \text{free vibration}\ \Omega\text{'s},\quad \Omega(p) = \{\Omega_1\ \Omega_2\ \ldots\}^T = \textit{computed}\ \Omega\text{'s using } p. \tag{4}$$

We seek the optimal estimate of the model parameter vector p which minimizes

$$J = \frac{1}{2}\int_{\omega_{min}}^{\omega_{max}} \Delta G^T(p,\omega) W_G(\omega) \Delta G(p,\omega)\, d\omega + \frac{1}{2}\Delta\Omega^T W_\Omega \Delta\Omega\ ,\quad \Delta G(p,\omega) \equiv \tilde{G}(\omega) - G(\omega, p),\ \Delta\Omega \equiv \tilde{\Omega} - \Omega(p) \tag{5}$$

For FRF measurements available at discrete frequencies, the integral can be replaced by a discrete summation; we seek to minimize a weighted sum square of the residuals between all measured and modeled FRF's and Ω's:

$$\Delta G \equiv \begin{Bmatrix} \tilde{G}(\omega_1) - G(\omega_1, p) \\ \vdots \\ \tilde{G}(\omega_m) - G(\omega_m, p) \end{Bmatrix} = \text{FRF residuals},\quad \Delta\Omega \equiv \begin{Bmatrix} \tilde{\Omega}_1 - \Omega_1(p) \\ \tilde{\Omega}_2 - \Omega_2(p) \\ \vdots \end{Bmatrix} = \text{free vib. frequency residuals} \tag{6}$$

and we are led to the least-squares differential correction algorithm:

$$\begin{Bmatrix} \Delta G \\ \Delta\Omega \end{Bmatrix} = A\Delta p + \ldots \Longrightarrow \quad \Delta p = A^\dagger \begin{Bmatrix} \Delta G \\ \Delta\Omega \end{Bmatrix},\ \text{where}\ A \equiv \begin{bmatrix} \frac{\partial G}{\partial p} \\ \frac{\partial \Omega}{\partial p} \end{bmatrix},\ \text{and}\ p_{new} = p_{old} + \Delta p \tag{7}$$

Potential trouble. This approach works great, but only if: (i) the model is "good" and (ii) p_{start} is "close" to p.

Creamer's Three Step Identification Process

Step 1: Identify a subset of the measured frequencies and mode shapes which correlate well with the corresponding modeled frequencies and mode shapes, do a least square correction correction of the stiffness parameterization to improve correlation if necessary.

Step 2: Find the normalization of the eigenvectors (mode shapes) which results in the best least square fit for the FRF, i. e., find $\{a_0, a_1, a_2, \ldots a_{m+1}\}$ to minimize

$$\int_{\omega_{min}}^{\omega_{max}} \left(\tilde{H}_{pq}(j\omega) - H_{pq_{model}}(j\omega)\right)^2 d\omega \;, \quad or \quad \sum_{\omega_{min}}^{\omega_{max}} \left(\tilde{H}_{pq}(j\omega_k) - H_{pq_{model}}(j\omega_k)\right)^2$$

where

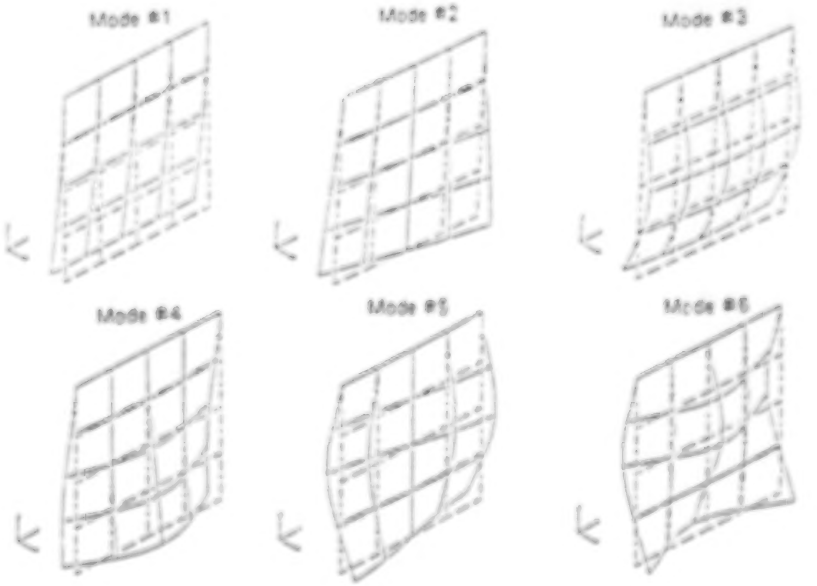
$$H_{pq_{model}}(j\omega) = \frac{a_0}{\omega^2} + \sum_{r=1}^{m} \frac{\tilde{\phi}_{pr}\tilde{\phi}_{qr}}{\tilde{\omega}_r^2 - \omega^2} a_r + a_{m+1}$$

Step 3: Estimate values for the linear mass and stiffness parameterization to satisfy the orthonormality conditions in a least square sense; this leads to the following pair of linear equations for μ_r, *and* κ_r *in* $M = M_o + \Sigma_i \mu_i M_i$, $K = K_o + \Sigma_i \kappa_i K_i$:

Here we show the first five free vibration mode shapes. In the table, we list the a priori finite-element model prediction of the first five natural frequencies, the values recovered from using the Eigenstructure Realization Algorithm to reduce an impulse response of the grid as measured by the stereo triangulation process. As is evident, the agreement is generally good with the most significant prediction errors in the higher modes as might be expected. Applying substructure scale factors to the members contribution to the mass and stiffness matrices resulted in an identified structure with near-identical measured and modeled natural frequencies and mode shapes. The measured modes differed most significantly in that the first mode was observed to have a slight degree of torsion whereas the modeled first mode was a pure cantilever mode. The discrepancy was traced to a slight bend near the upper right of the structure, apparently this occurred when the structure was being mounted.

Using only the optical data, we have demonstrated that the free response and input/output behavior of this structure can be accurately identified using the stereo triangulation system and the methodology we have developed. The presently implemented system works well only for frequencies below approximately 15 Hz. The difficulty at higher frequencies is not a consequence of the camera frame speed (200 frames/sec), but rather because the limited spatial resolution of our cameras cannot "see" the small amplitude vibrations associated with the higher modes.

Modeled, Measured and Identified Modes of the Grid

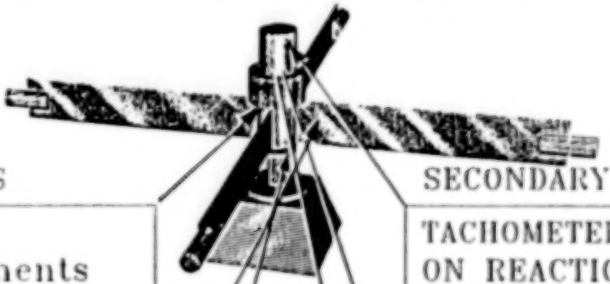


Mode No.	Modeled Value	Measured Value	Identified Value
1	.90 Hz	.92 Hz	.91 Hz
2	2.34	2.32	2.32
3	4.85	4.93	4.93
4	6.05	6.38	6.38
5	7.78	7.27	7.25

BEST COPY AVAILABLE

The appendage/hub structure was designed, fabricated, and assembled so as to produce a structure that is symmetric with respect to physical and geometric parameters and that is also subject to a minimal dynamic asymmetry. Phasing problems that exist between appendages are apparent only after free vibrations are allowed to continue for several minutes. This permits free and forced vibration data to be recorded for a structure that exhibits an initial dynamic symmetry.

TAMU Maneuver and Vibration Suppression Experiment



PRIMARY SENSORS

TORQUE SENSOR
Sensor Developments
custom unit with
signal conditioner

STRAIN GAGES
Micromeasurements Div.
Measurements Group
Std. metal film

ANGLE ENCODER
Teledyne Gurley 8708
36000 counts / rev
C-TEK counter
mod. LIN-101-5021418E

SECONDARY SENSORS

TACHOMETER
ON REACTION WHEEL
PMI Motion Technologies

MOTOR CURRENT MONITOR
hard wired to
A/D board

MOTOR VOLTAGE MONITOR
hard wired to
A/D board

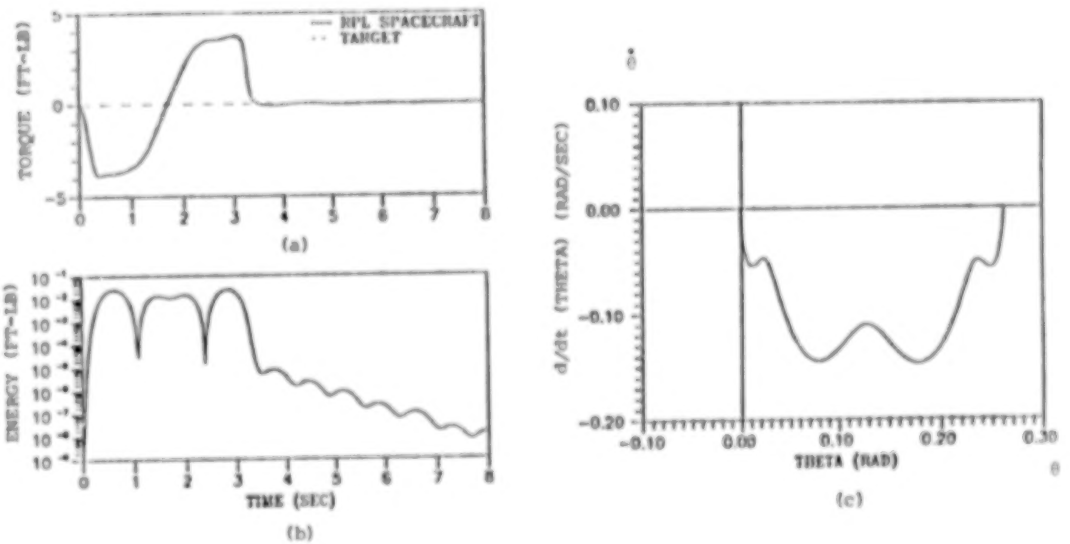
The below maneuver is from a student (Robert Byers') recent M. S. thesis (ref. 3). Byers implemented a variable-structure feedback control law that roughly approximates a smoothed bang-bang near-minimum-time maneuver, but also exhibits good vibration suppression characteristics as is evident. The variable-structure approach is one of several robust control concepts we have studied in recent months, and we are engaged in an experimental effort to parallel and support our analytical activities.

As an alternative approach, we show below an output feedback control law that is based upon a PDE description of the system dynamics, and we prove global stability using Lyapunov's second method. This method is found to be very robust and, since it does not require a state estimator and since no spatial discretization approximations are introduced, it does not suffer from spillover; we feel this is a very attractive approach. We have shown that a near-minimum-time torque-shaped open-loop maneuver can be introduced and the Liapunov based method leads to a tracking-type feedback control that is theoretically globally stable and is, in fact, very robust with respect to modeling and implementation errors. It is this latter idea upon which we have based our early experiments; we will therefore go over the key ideas underlying this approach.

Texas A&M Maneuverable Space Structure Experiment

15° Rest-to-Rest Maneuver

$T_1 = .35$ sec, $\alpha = .93$, $\beta = .97$, $\psi = \varphi = 0$



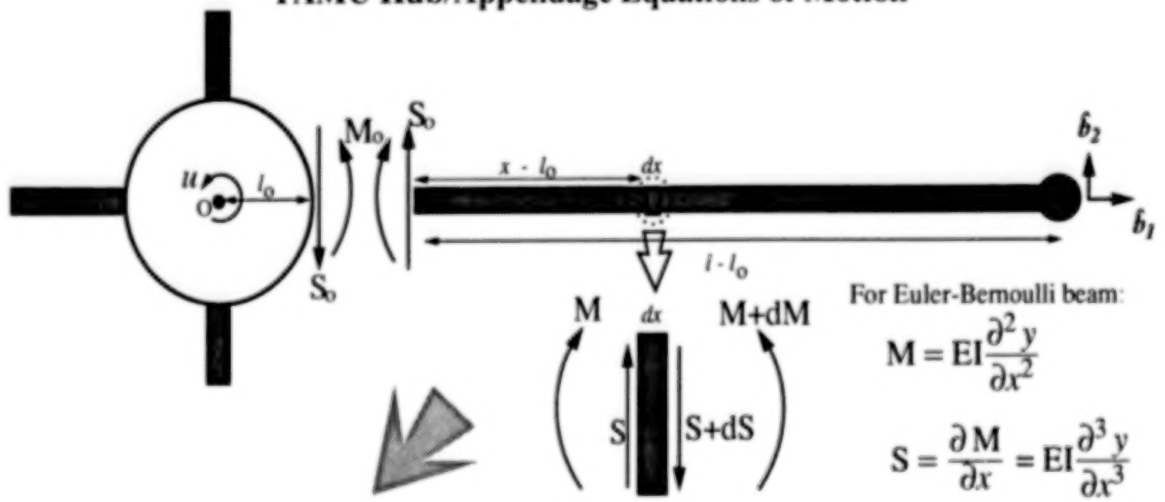
(a) control profile, (b) flexible mode energy,
(c) state space trajectory

BEST COPY AVAILABLE

The figure below shows an overview of the formulation leading to the coupled differential equations of vibratory and rotational motion. Notice that we are taking a distributed parameter approach. The hub rotational dynamics are dictated by the instantaneous control torque u(t) and the root shear and bending moment. The root shear and bending moment must in turn equal the instantaneous time rate of change of the beams' angular momentum. Finally, summing forces and moments on a typical mass element in the beam lead to the generalized Euler beam PDE. HOT refers to higher order terms to account for rotational stiffening, shear deformation, etc.

We will now outline how to derive a globally stable output feedback law without introducing spatial approximations and the associated issues of truncation and spillover.

TAMU Hub/Appendage Equations of Motion



For Euler-Bernoulli beam:

$$M = EI\frac{\partial^2 y}{\partial x^2}$$

$$S = \frac{\partial M}{\partial x} = EI\frac{\partial^3 y}{\partial x^3}$$

Equations of motion:

$$I_{hub}\frac{d^2\theta}{dt^2} = u + 4(M_o - S_o l_o)$$

$$-(M_o - S_o l_o) = \int_{l_o}^{l} \rho x\left(\frac{\partial^2 y}{\partial t^2} + x\frac{d^2\theta}{dt^2}\right)dx + ml\left(l\frac{d^2\theta}{dt^2} + \frac{\partial^2 y}{\partial t^2}|_l\right) + HOT$$

$$\rho\left(\frac{\partial^2 y}{\partial t^2} + x\frac{d^2\theta}{dt^2}\right) + EI\frac{\partial^4 y}{\partial x^4} = 0 + HOT$$

Boundary conditions:

$$at\ x = l_o:\ y = \frac{\partial y}{\partial x} = 0$$

$$at\ x = l:$$

$$(moment)\ \frac{\partial^2 y}{\partial x^2} = 0$$

$$(shear)\ \frac{\partial^3 y}{\partial x^3} = \frac{m}{EI}\left(l\frac{d^2\theta}{dt^2} + \frac{\partial^2 y}{\partial t^2}|_l\right)$$

The control law:

$$u = -\left[g_1(\theta - \theta_o) + g_2\dot{\theta} + g_3(l_o S_o - M_o)\right], \quad g_i \geq 0 \tag{8}$$

for stability is very attractive because it is linear and controls the distributed system without requiring distributed sensing. This law has been experimentally demonstrated by Fujii (ref. 4) and in our work at Texas A&M (ref. 5).

It is of significance that this law maintains its globally stabilizing character even when the above Euler/Bernoulli formulation is generalized to include the non-linear effects of rotational stiffening and Coriolis effects (kinematic/inertial non-linearities) aerodynamic damping/drag as well as a more general accounting for the linear effects of modifications of the formulation to include shear deformation and rotary inertia finite inertia of the tip mass. In short, closed-loop stability using this law is very forgiving of modeling assumptions!

In Search of a Judicious Liapunov Function & a Stabilizing Control Law ...

Motivated by the total system energy

$$2E = 2(T+V) = I_{hub}(\frac{d\theta}{dt})^2 + 4\left[\int_{l_o}^{l}\rho(\frac{\partial y}{\partial t} + x\frac{d\theta}{dt})^2 dx + \int_{l_o}^{l} EI(\frac{\partial^2 y}{\partial x^2})^2 dx + m(l\frac{d\theta}{dt} + \frac{\partial y}{\partial t}|_l)^2\right]$$

and the recent work of Fujii, we "investigate the wisdom" of the candidate Liapunov fct.:

$$2U = a_1 I_{hub}\dot{\theta}^2 + a_2(\theta - \theta_o)^2 + 4a_3\left[\int_{l_o}^{l}\rho(\frac{\partial y}{\partial t} + x\dot{\theta})^2 dx + \int_{l_o}^{l} EI(\frac{\partial^2 y}{\partial x^2})^2 dx + m(l\dot{\theta} + \frac{\partial y}{\partial t}|_l)^2\right] \tag{9}$$

It is obvious by inspection that choosing $a_i>0$ guarantees that U>0, and that U=0 is the desired state. Differentiation, substitution of the Eqs of motion & some calculus lead to

$$\dot{U} = \frac{dU}{dt} = \dot{\theta}\left[a_1 u + a_2(\theta - \theta_o) + 4(a_3 - a_1)(l_o S_o - M_o)\right] \tag{10}$$

Since we require that $\dot{U}<0$ to guarantee stability, we choose the control torque u as

$$u = -\frac{1}{a_1}\left[a_2(\theta - \theta_o) + a_4\dot{\theta} + 4(a_3 - a_1)(l_o S_o - M_o)\right]$$

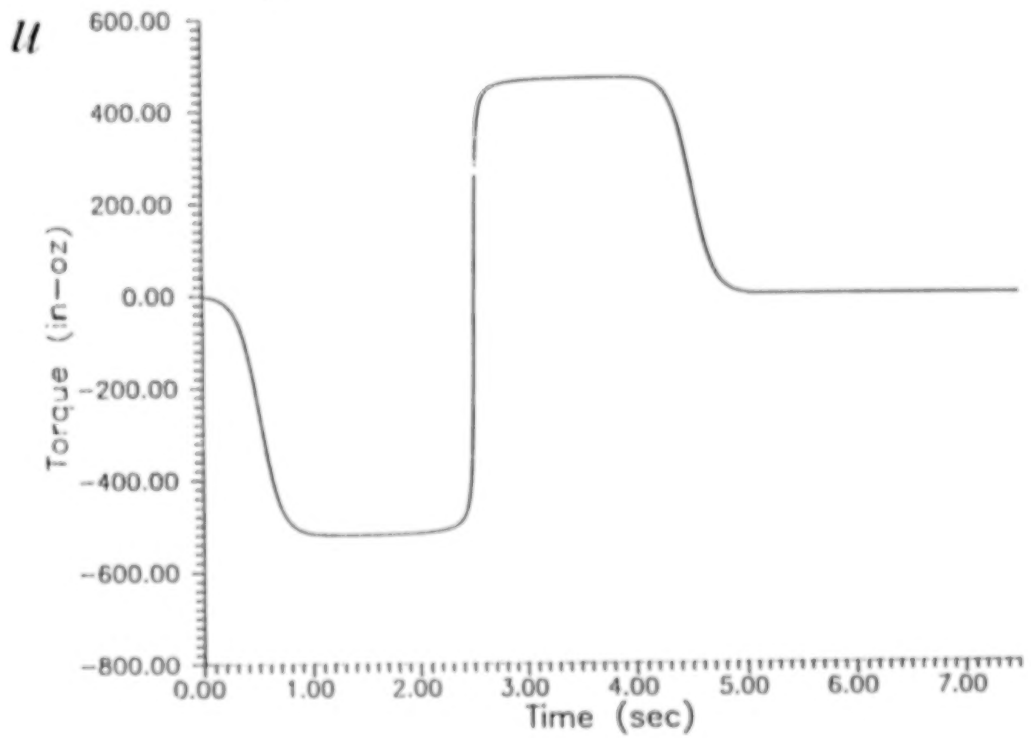
or, we see that the following *linear*, *discrete* feedback law globally stabilizes this system:

$$u = -\left[g_1(\theta - \theta_o) + g_2\dot{\theta} + g_3(l_o S_o - M_o)\right], \quad g_i \geq 0 \text{ for stability} \tag{11}$$

The below figure shows a torque-shaped, near-minimum-time control for the flexible hub derived using the methods of Roger Thompson et al. (ref. 6). This maneuver served as a nominal open-loop control. We used a generalization of the Liapunov control approach to develop a tracking like a globally stable feedback control law to null errors in the event of non-nominal initial conditions, model errors, and control implementation errors. The open-loop maneuver is designed in such a fashion that the maneuver time is about 20-percent longer than a strict bang-bang maneuver of a rigid structure having the same undeformed inertia. However the residual energy of vibration (without feedback) of the flexible structure is theoretically reduced by about 5 orders of magnitude by using the torque-shaped maneuver in lieu of a bang-bang profile. Thus the open-loop control is designed to incur small vibrations during and upon completion of the maneuver, and the feedback control is designed to suppress residual vibrations which arise from whatever physical origin.

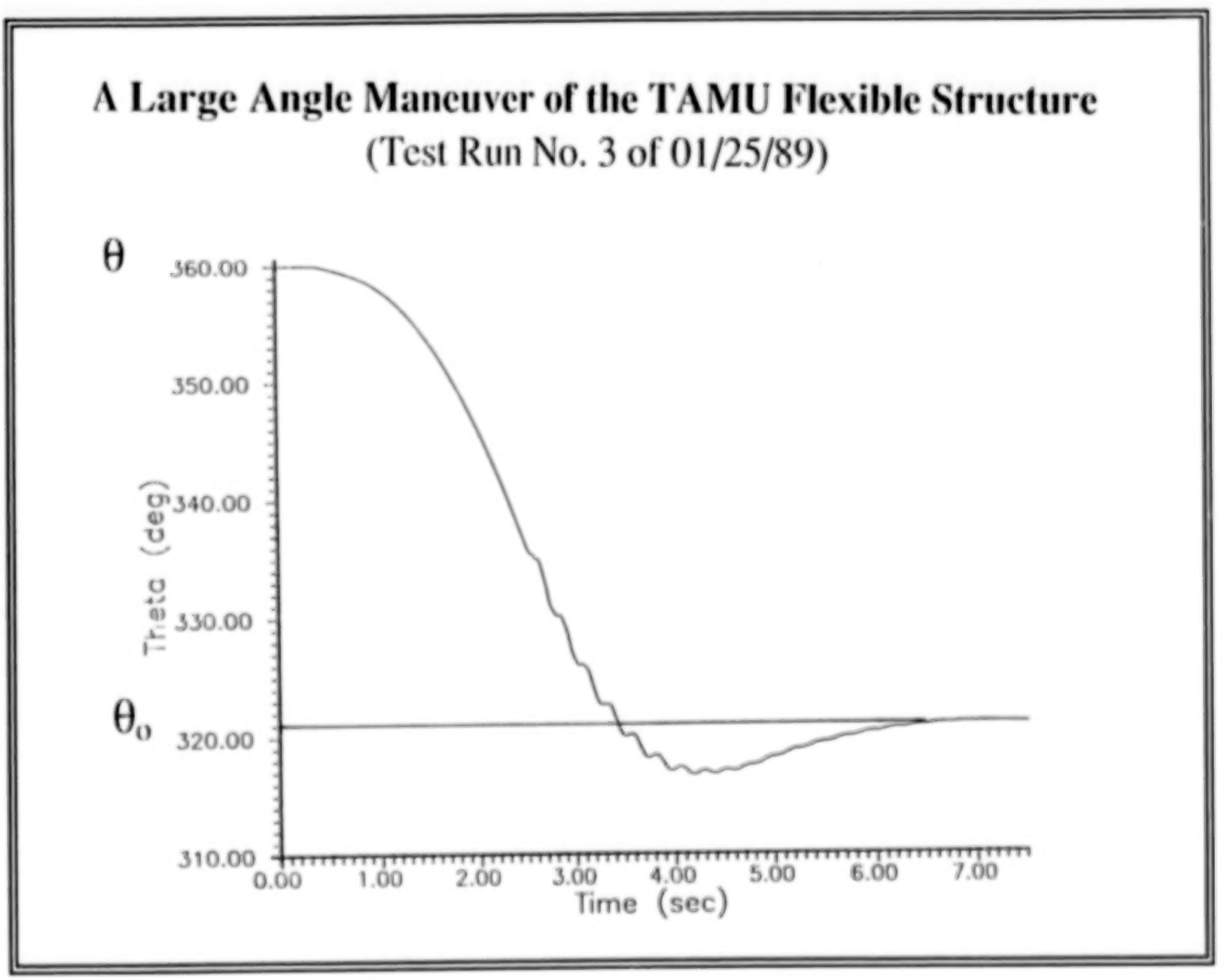
A Torque-Shaped Near-Minimum Time Maneuver of the TAMU Fexible Structure

(Test Run No. 3 of 01/25/89)



The below figure shows the experimentally achieved hub rotation angle as a function of time for a 40° near-minimum time maneuver. The first half of the maneuver was almost identical to the corresponding simulation (slight lag developed due to a lag in the compensator circuit of our power supply). However a large transient occurred at precisely the instant (maneuver mid-point) the commanded current reversed to initiate the breaking phase of the maneuver. This is because our low-budget power supply was unable to accurately generate the commanded current in the face of the variable load presented by the motor near torque reversal. During the last half of the maneuver, the power supply compensation circuits and control commands combined to arrest rotation and vibration with a moderate overshoot.

While the problems with our power supply are evident, we feel pleased with this first implementation of our approach and anticipate substantially improved results in future experiments.



Concluding Remarks

- **Novel Vibration Sensing and System Identification Methods have been Developed and Demonstrated**
- **Large Angle, Near-Minimum-Time, Feedback Control for Flexible Body Maneuvers have been Developed and Successfully Demonstrated**
- **Both of the Above are in a Preliminary State of Development, but Our Results to Date are Significant**

References

1. Creamer, N. G. and Junkins, J. L., Identification Method for Lightly Damped Situations. AIAA Journal of Guidance, Control, and Dynamics, vol. 11, no. 6, Nov.-Dec. 1988, pp. 571-576.

2. Manual of Photogrammetry, Chapter 17, 4th ed., published by the American Society of Photogrammetry, Falls Church, VA, 1980.

3. Byers, R. M., Feedback Control for Smooth, Near-Minimum Time Rotational Maneuvers of Flexible Spacecraft, MS Thesis, Texas A&M University, Department of Aerospace Engineering, August 1987.

4. Fujii, H., Ohtauka T., and Udou, S., Mission Function Control for Slew Maneuver Experiments, AIAA J. of Guidance, Control, and Dynamics, 1989.

5. Rahman, Z., Junkins, J. L., Pollock, T. C., and Bang, H., Large Angle Maneuvers with Vibration Suppression: Analytical and Experimental Results, Paper presented at 7th VPI and SU Symposium on Dynamics and Control of Large Structures, May 1989.

6. Thompson, R. C., Junkins, J. L., and Vadali, S. R.: Near-Minimum Time Open-Loop Slewing of Flexible Vehicles, AIAA Journal of Guidance, Control, and Dynamics, vol. 12, no. 1, Jan.-Feb. 1989, pp. 82-88.

Experimental Evaluation of Active-Member Control of Precision Structures

James Fanson, Gary Blackwood, and Cheng-Chih Chu
Jet Propulsion Laboratory
California Institute of Technology
Pasadena, California

NASA/DOD CSI Conference
January 29-February 2, 1989

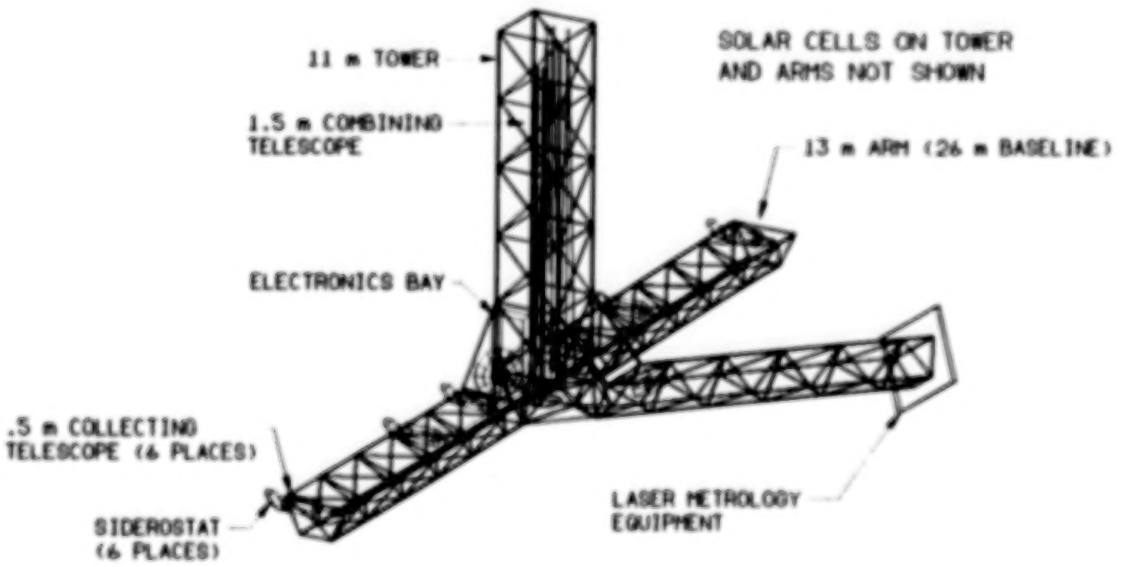
TECHNOLOGY OBJECTIVES

This paper describes the results of closed-loop experiments that use piezoelectric active-members to control the flexible motion of a precision truss structure. These experiments are directed toward the development of high-performance structural systems as part of the Control/Structure Interaction program at JPL. The focus of CSI activity at JPL is to develop the technology necessary to accurately control both the shape and vibration levels in the precision structures from which proposed large space-based observatories will be built. Structural error budgets for these types of structures will likely be in the sub-micron regime; optical tolerances will be even tighter. In order to achieve system level stability and local positioning at this level, it is generally expected that some form of active control will be required.

- **STATIC STRUCTURAL PERFORMANCE**
  - Order-of-magnitude improvement in geometric shape control over passive structures (Micron Level)
  - Active compensation for thermal gradient distortion
- **DYNAMIC STRUCTURAL PERFORMANCE**
  - Order-of-magnitude improvement in dynamic stability over passive structures
- **ON-ORBIT ADAPTABILITY**
  - Ease requirements on ground tests
  - Enable a versatile structural *system* that can adapt its characteristics to meet changing mission requirements
- **SYSTEM IDENTIFICATION**
  - Enable a means of on-orbit system identification and modal testing

JPL CSI FOCUS MISSION: INTERFEROMETER

One application of precision controlled structures, which has become the focus mission for the JPL CSI program, is an orbiting interferometer telescope[1]. The interferometer works by precisely positioning small aperture telescopes separated by large baselines, thereby synthesizing a larger effective aperture and enabling greater imaging resolution. In order to function, the path lengths traversed by starlight striking the various component telescopes must be held constant to a small fraction of the wavelength of light being observed. For an ultraviolet interferometer, this corresponds to path length stability on the order of a few nanometers over distances of tens of meters of relatively lightweight and possibly flexible spacecraft structure.



FMI CONFIGURATION

ACTIVE STRUCTURES APPROACH

One approach to controlling the elastic deflections of truss structures is to use active-members--structural elements with actuators and sensors built into them. A control system can be designed around these active-members to provide "intelligent structure" performance beyond that achievable for conventional structures of comparable weight. Piezoelectric actuators are employed in the JPL active-member design. Previous experiments in active-member control include the use of voice-coil type actuators in one and two bay trusses at TRW and Caltech.[2,3] PID* controllers have also been implemented on a similar structure in Japan.[4] Early work on the use of piezoelectrics for structural control concentrated on the use of flat piezoelectric crystals to control the vibrations of uniform beams.[5,6,7,8] More recent work at MIT has concentrated on the use of piezoelectrics embedded in structural truss members and passively shunted to introduce damping.[9] Concurrent active-member research at JPL in support of the Precision Segmented Reflector program is reported elsewhere.[10]

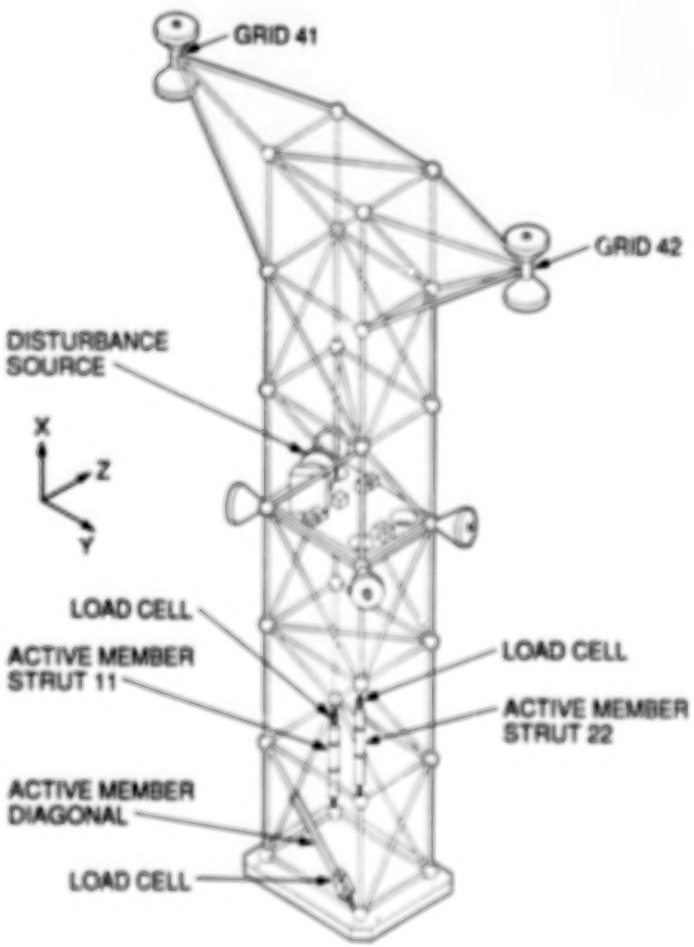
*proportional integral differential

PIEZOELECTRIC ACTIVE-MEMBERS

ADVANTAGES	CHALLENGES
Stiff Structural Members	Close Pole/Zero Pairs
Low Current	High Voltage
Operate Statically	Hysteresis
High Bandwidth	Nonlinearity
Large Force	Small throw
Non-inertial Reacting	
Nanometer Precision	

DIAGRAM OF PRECISION TRUSS TEST BED

The subject of this research is the control of a truss structure called the Precision Truss. The Precision Truss has been designed to exhibit many of the salient features of structures that will form key components of next generation spacecraft. Specifically, the truss is stiff and statically indeterminate, the fundamental vibrational mode occurs below 10 Hz, the lower modes are closely spaced and coupled, and the structure possesses low inherent damping. Repeatable disturbances are injected into the truss by a small shaker mounted to a plate at the center bay of the truss.



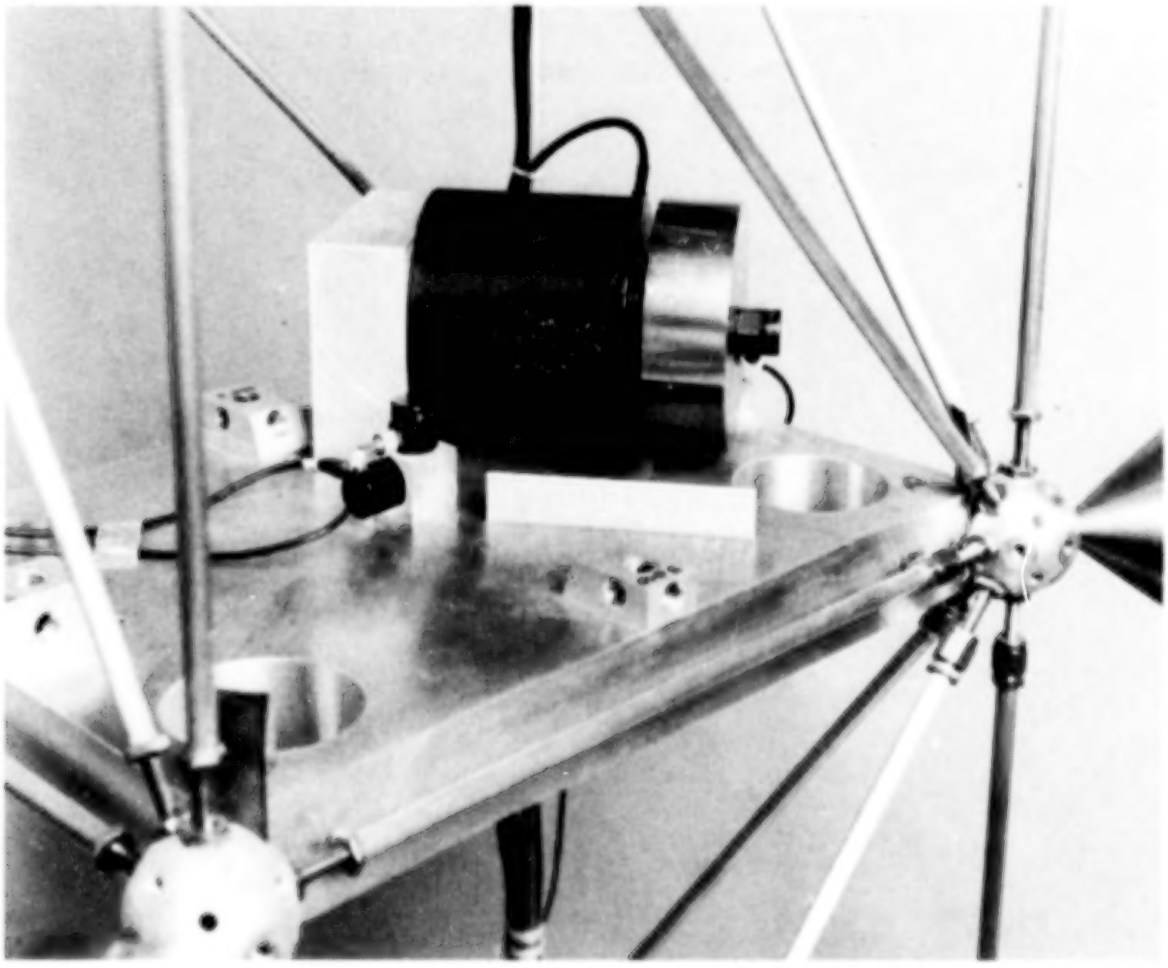
FREQUENCIES AND DAMPING COEFFICIENTS OF THE OPEN-LOOP STRUCTURE

The table lists the increase in passive damping of the structure with active-members compared to the structure without the active-members. The increase is due to the large level of hysteresis in the actuators. Shown are the first three modes--modes one and two are cantilever bending in two directions, the third mode is torsion. Higher modes appear at about 34 Hz. These data are from a modal survey of the Precision Truss using external exciation and active-member excitation[11].

Mode	No Active-Members		With Active-Members	
	f (Hz)	ζ (%)	f (Hz)	ζ (%)
1	8.11	0.036	8.28	0.436
2	10.4	0.051	10.78	0.997
3	11.5	0.031	11.45	0.101

DISTURBANCE SOURCE

The center bay of the truss contains a rigid plate. Mounted to this plate is a 2.25 lbf electromagnetic shaker which is used to inject a repeatable disturbance into the structure. The shaker is oriented at an angle and offset from the center of symmetry so that it can excite not only bending modes in the y and z directions but also torsion along the vertical (x) axis. A 2 lb concentrated mass added to the armature of the shaker provides sufficient inertia for force to be applied to the truss at low frequency without requiring excessive armature motion.

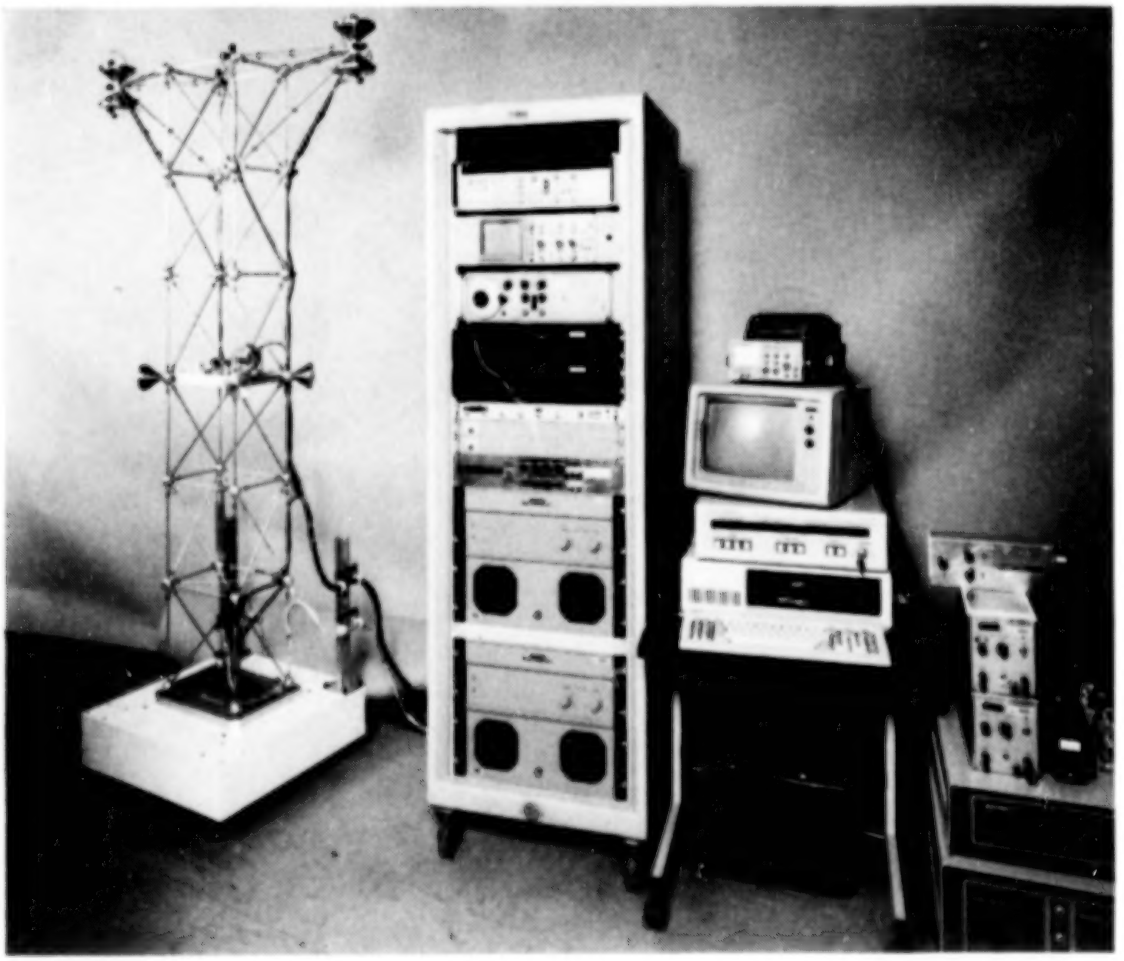


EXPERIMENTAL TEST SETUP FOR CLOSED-LOOP CONTROL

The photograph depicts the experimental setup used for closed-loop control tests. Apart from the active-members, which function as both sensors and actuators for the closed-loop control, the most significant hardware component is the Systolic Systems PC1000 digital array processor. The PC1000 digitizes analog signals at 2000 Hz, implements discrete state space control algorithms utilizing up to 32 states and 16 input signals, and commands up to 16 control outputs through a zero order hold. Variable amplifiers and an output smoothing filter are also used in the closed loop.

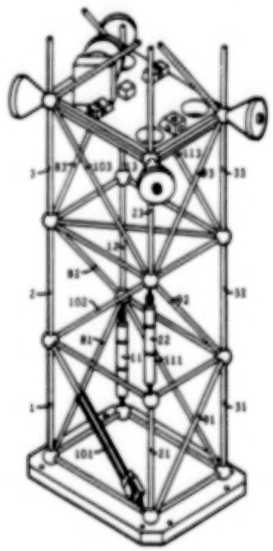
The ultimate objective of the phase 1 control experiments is to stabilize the motion of outrigger 41 subject to a narrowband disturbance at the midbay plate, while utilizing active-members in the lower three bays of the truss. The locations of the three active-members have been optimized for this control objective. The first controllers we have implemented are simple low order SISO* designs; more sophisticated control designs utilizing all three active-members are planned for the coming year. An attempt will be made to later extend the level of control to the submicron regime.

*single-input, single-output



ACTUATOR PLACEMENT SELECTION

Three active-members were available for placement in the Precision Truss structure. The lower bays are an intuitive place to locate the active-members because most of the strain energy for the lower modes occurs near the cantilevered end. A methodology for selecting the optimal locations considers a stationary colored noise disturbance (20 Hz bandwidth) entering at the midbay plate. Performance was defined as $\gamma \| y \|_2 + \| u \|_2$, where y is measured at outrigger 41, u is control effort, and γ is a scaling parameter. For any set of locations, this leads to a well posed $\mathcal{H}_2$ -optimization problem[12]. In order to reduce the number of possible locations to a more tractable set, a preliminary selection was performed by first solving the $\mathcal{H}_2$-optimization problem assuming that an active-member could be placed in all possible locations simultaneously. From the solution to this optimization, the total energy in each control input was computed and ranked. The heuristic argument is that the active-member locations which perform the most work are superior locations for control. A subset of locations with the highest control input energy was selected for subsequent combinatorial optimization. The result of this process for the Precision Truss suggested that the optimal locations were two longerons in the first and second bays and one diagonal in the first bay.



Number Scheme for Longerons and Diagonals in Lower Three Bays

Control Effort for Actuators for Preselection of Candidate Locations

Actuator #	Element #	$\|u_i\|_2$
3	11	10.92815
6	21	8.47903
10	22	8.47496
2	101	7.22583
12	12	6.23132
20	13	6.22398
21	103	5.84743
15	82	5.79099
9	2	5.05582
18	23	4.15259
24	83	4.13487
13	42	3.79535
5	111	3.35653
4	81	3.27266
7	31	3.23416
8	91	3.07798
11	32	2.84030
23	113	2.62724
16	112	2.48088
17	3	2.31858
22	93	2.25864
1	1	2.17953
14	92	2.13915
19	33	1.77798

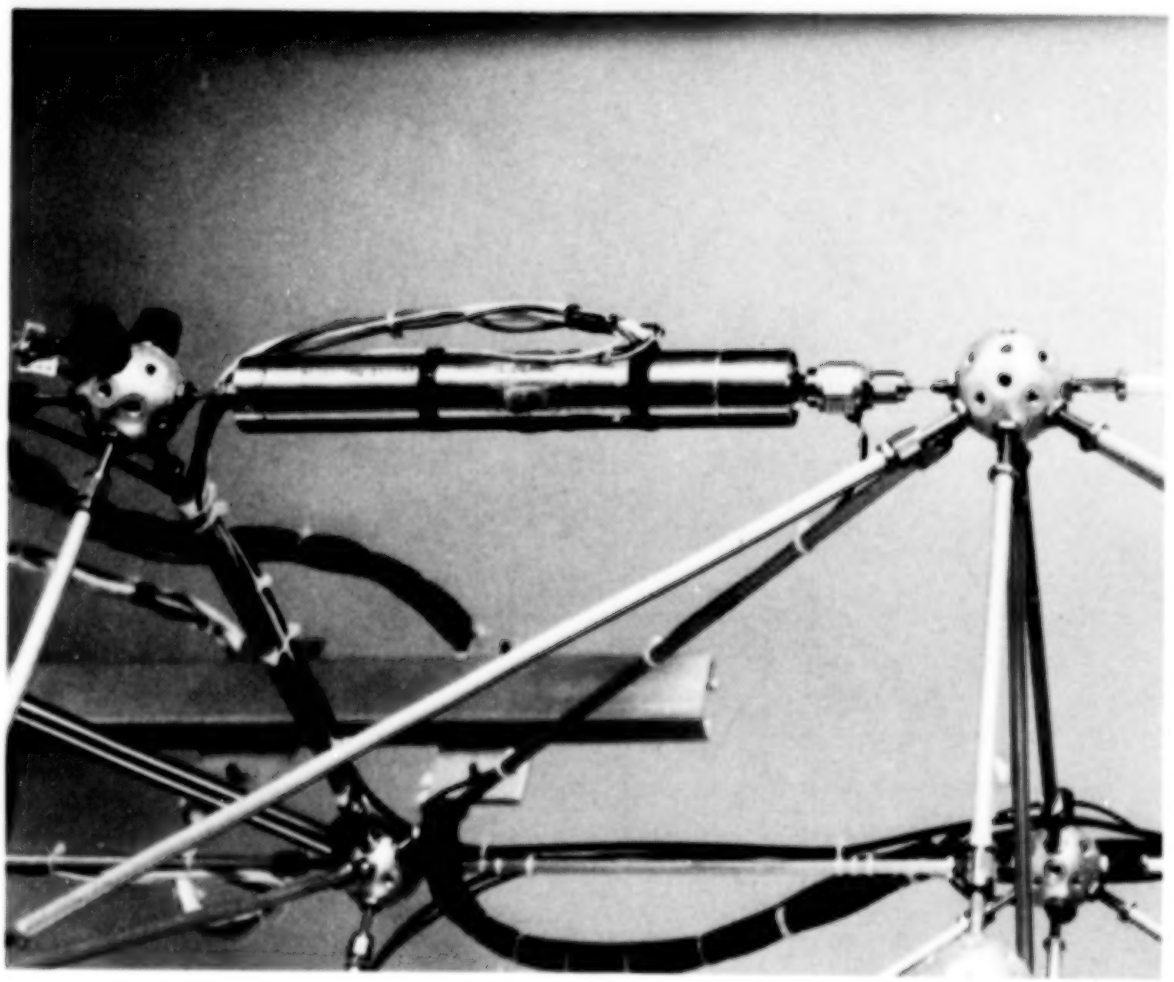
Ranking of Actuator Selection Pairs

Element #	Cost	$\|u\|_2$	$\|y\|_2$	$\frac{\|y\|_2}{\|u\|_2}$	$\frac{\|y\|_2}{\|y_{open}\|_2}$
101, 11, 21	6.87284e+01	5.08403e+01	4.62478e-03	9.09668e-05	1.42634e-02
101, 11, 22	6.87336e+01	5.08466e+01	4.62487e-03	9.09573e-05	1.42637e-02
101, 11, 12	7.15809e+01	5.39124e+01	4.70879e-03	8.73416e-05	1.45226e-02
101, 11, 13	7.15896e+01	5.39231e+01	4.70890e-03	8.73263e-05	1.45229e-02
101, 21, 22	7.56169e+01	5.46423e+01	5.22699e-03	9.56584e-05	1.61207e-02
101, 21, 12	7.92828e+01	5.84258e+01	5.35928e-03	9.17280e-05	1.65287e-02
101, 21, 13	7.92953e+01	5.84392e+01	5.35967e-03	9.17136e-05	1.65300e-02
101, 22, 12	7.92965e+01	5.84367e+01	5.36012e-03	9.17252e-05	1.65313e-02
101, 22, 13	7.93090e+01	5.84501e+01	5.36051e-03	9.17108e-05	1.65325e-02
101, 12, 13	8.66331e+01	6.34581e+01	5.89776e-03	9.29395e-05	1.81895e-02
11, 21, 22	8.26441e+01	4.44797e+01	6.96534e-03	1.56596e-04	2.14821e-02
11, 21, 13	8.41313e+01	4.68191e+01	6.99002e-03	1.49298e-04	2.15582e-02
11, 21, 12	8.41299e+01	4.68096e+01	6.99050e-03	1.49339e-04	2.15596e-02
11, 22, 13	8.41427e+01	4.68172e+01	6.99153e-03	1.49337e-04	2.15628e-02
11, 22, 12	8.41414e+01	4.68077e+01	6.99201e-03	1.49377e-04	2.15643e-02
11, 12, 13	8.68547e+01	4.89402e+01	7.17537e-03	1.46615e-04	2.21298e-02
21, 22, 13	1.02464e+02	5.23094e+01	8.81057e-03	1.68432e-04	2.71730e-02
21, 22, 12	1.02488e+02	5.22436e+01	8.81723e-03	1.68772e-04	2.71935e-02
22, 12, 13	1.06296e+02	5.59834e+01	9.03585e-03	1.61402e-04	2.78678e-02
21, 12, 13	1.06314e+02	5.59464e+01	9.04031e-03	1.61589e-04	2.78815e-02

BEST COPY AVAILABLE

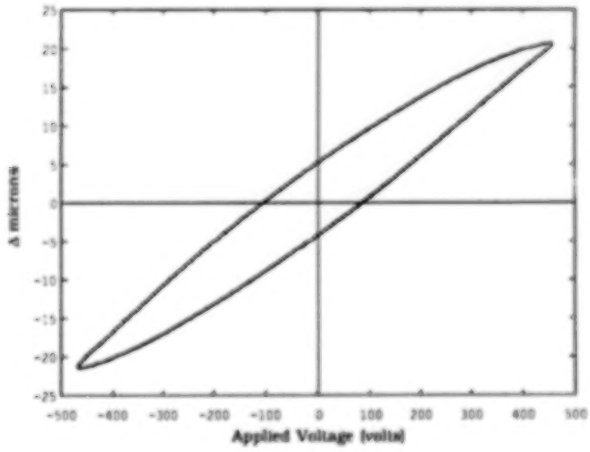
PIEZOELECTRIC ACTIVE MEMBERS

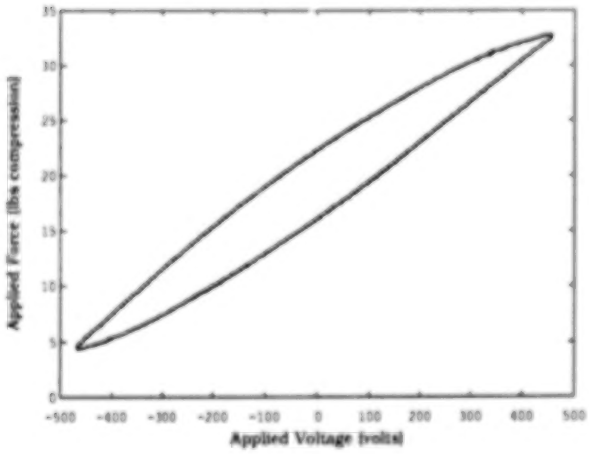
Two types of piezoelectric active-members are used in the truss. The first type is a low voltage piezoelectric actuator ordinarily used for fine positioning of optics. This device has a throw of 106 microns at 150 volts. The device has a relatively low stiffness of 23,300 lb/in which leads to a clamped force of 97 lb. The second type of active-member is a constant length strut (CLS) built to JPL specifications by Kaman Instrumentation Inc. This device makes use of a high voltage piezoelectric wafer stack in series with a stainless steel tube extension. The piezoelectric stack expands and contracts with applied voltage producing a relative motion between the two ends of the strut. A quartz reference rod (selected for low coefficient of thermal expansion) is attached rigidly to the moving end (armature) and extends down the length of the strut along the centerline. A differential eddy-current proximity sensor is built into the opposite end of the strut. This sensor measures the motion of a target disc attached to the reference rod, thereby measuring the change in the length of the strut. This sensor has a resolution of 1 nanometer.



HYSTERESIS OF ACTIVE MEMBERS

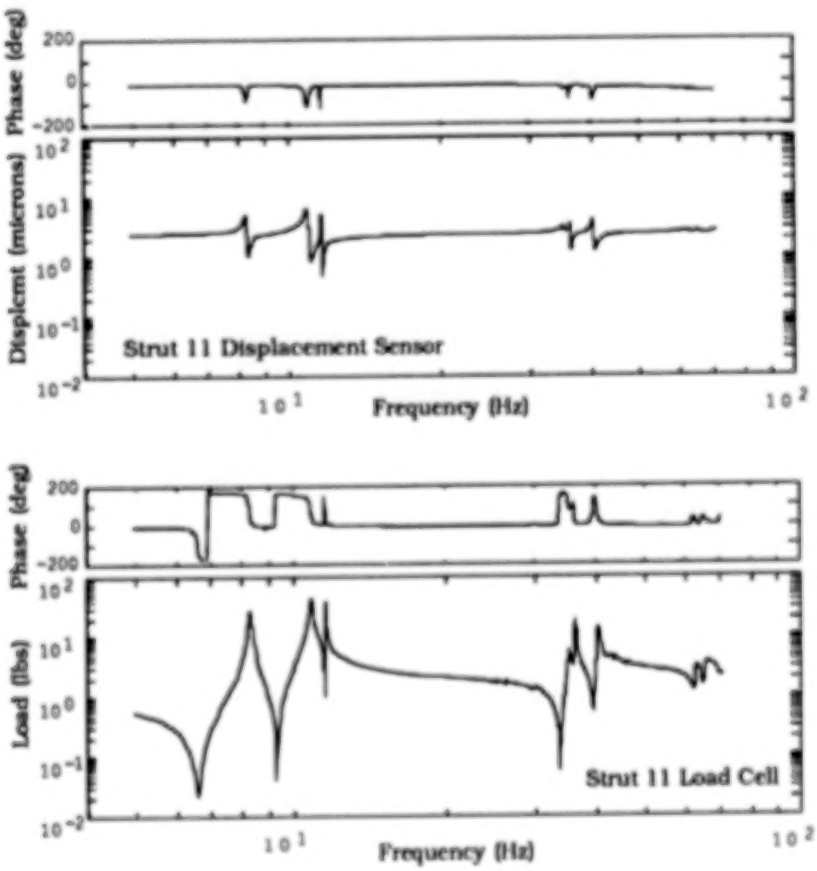
Each active-member was tested in a calibration fixture. The Kaman CLS struts were found to exhibit approximately 20% hysteresis, due to the piezoelectric material used in the actuators.





OPEN-LOOP STRUCTURE--MEASURED DATA

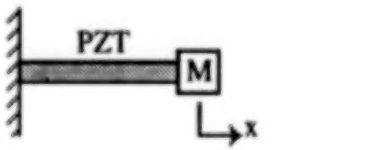
The active-member in the longeron of the first bay (strut 11) was selected as the sole actuator for the initial single-input-single-output control tests. For feedback measurements, it was convenient to use signals from the strut internal displacement sensors. Input-output transfer functions from strut 11 to the two internal displacements were measured using a stepped-sine test and are shown in the figure. Close pole-zero spacing is very pronounced for the collocated transfer function, due to a large feedthrough term corresponding to the residual flexibility of the structure at that actuator location. The feedthrough term was not present for the noncollocated displacement or for either load cell in series with the active-members.

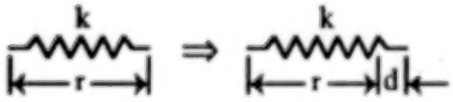


ACTIVE-MEMBER PHENOMENOLOGY

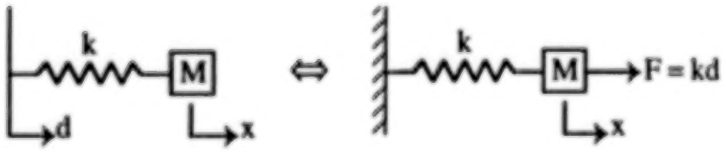
The observed close pole-zero spacing warranted further investigation into the behavior of the active-members. A model was developed for active-members in structures that makes use of externally applied forces at physical degrees of freedom. Were the active-member perfectly linear, it could be modelled as a structural element of length r and stiffness k which, if unconstrained, changes length by an amount d which is proportional to the electric field applied across the piezoelectric. As far as the dynamics of mass M are concerned, the variable length strut is equivalent to a moving boundary on a passive strut of stiffness k. The corresponding differential equation can be rearranged to produce the familiar equation of motion. Thus, the effect of the active-member on the dynamics of mass M can be modelled as an externally applied force kd applied to the interface point between the active-member and mass M.

- PHENOMENOLOGY





$$d = d_{33}\, E_f\, r \sim (100\mu\text{m})$$

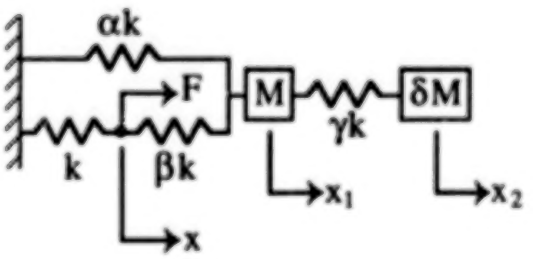


$$M\ddot{x} = k(d - x) \quad \Longleftrightarrow \quad M\ddot{x} + kx = kd$$

$$kd_{\max} = \text{clamped force} \sim (100\text{lb})$$

MODEL OF ACTIVE MEMBER IN STRUCTURE

An interesting phenomenon of close pole/zero pairs occurs when collocated displacement sensors are used in conjunction with active-members. Consider the simplified two degree of freedom model of the Precision Truss shown in the figure. A single active-member is represented as spring k, and the force F models the effect of the active-member on the structure. The collocated transfer function from d to x is computed. The parameter β represents the ratio of the input point stiffness to the active-member stiffness, and in general is less than unity. We see that as $\beta \to 0$ the poles and zeros quickly approach each other. Furthermore, as $s \to \infty$ the transfer function x/d does not approach zero, but rather approaches a constant value $1/(1+\beta)$. This represents a sizable feedthrough term.



$$kd = F, \omega = k/m, \epsilon = 1/\delta$$

$$\frac{x}{d} = \frac{s^4 + s^2(\alpha+\beta+\gamma+\gamma\epsilon)\omega^2 + (\alpha+\beta)\gamma\epsilon\omega^4}{[s^4 + s^2(\alpha+\beta+\gamma+\gamma\epsilon)\omega^2 + (\alpha+\beta)\gamma\epsilon\omega^4](1+\beta) - (s^2+\gamma\epsilon\omega^2)\omega^2\beta^2}$$

$$s \to 0 \qquad \frac{x}{d} \to \frac{1}{1+\frac{\alpha\beta}{\alpha+\beta}}$$

$$s \to \infty \qquad \frac{x}{d} \to \frac{1}{1+\beta}$$

$$\dot{\xi} = A\xi + Bd$$
$$\dot{x} = C\xi + Dd$$

POLE-ZERO SPACING OF MODEL

Solving for the system eigenvalues, the pole-zero spacing is found to be a function of the stiffness ratio β. The smaller the β (corresponding to a large actuator stiffness relative to the structure), the closer is the pole-zero spacing. Pole-zero spacing is small even for β= 1.

$a = (\alpha + \beta + \gamma + \gamma\epsilon), b = (\alpha + \beta)$

for $\beta \ll 1$

zeros:

$$s^2 = -\frac{1}{2}a\omega^2 \pm \omega^2\sqrt{\frac{1}{4}a^2 - b\gamma\epsilon}$$

poles:

$$s^2 = -\frac{1}{2}a\omega^2 \pm \omega^2\sqrt{\frac{1}{4}a^2 - b\gamma\epsilon}\left[1 + \frac{\frac{1}{2}(\gamma\epsilon - \frac{1}{2}a)\beta^2\omega^2}{\frac{1}{4}a^2 - b\gamma\epsilon}\right] + \frac{1}{2}\beta^2\omega^2$$

EXAMPLE

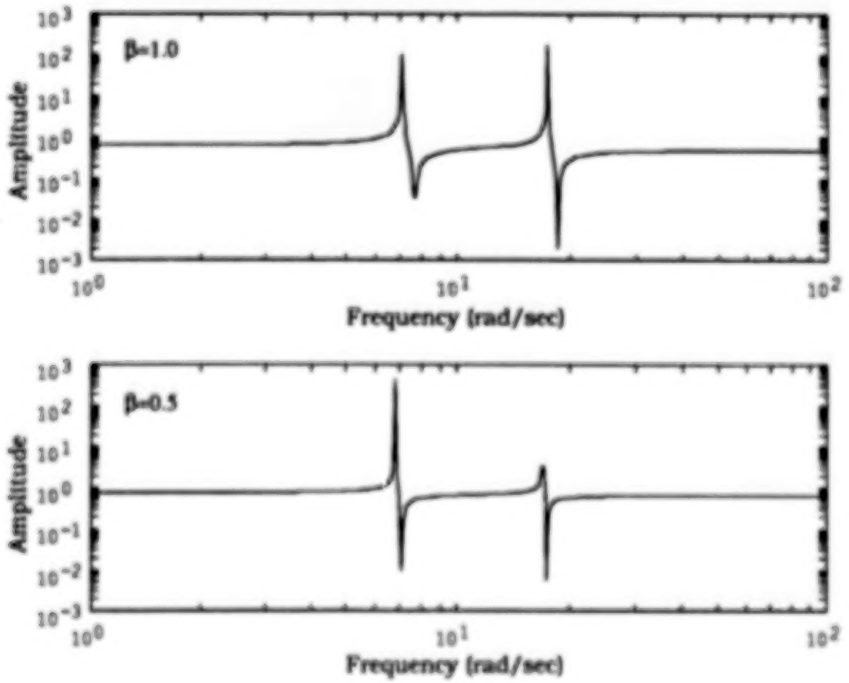
$k = \alpha = \beta = \delta = \gamma = 1$

$M = 0.01, \omega = 10$

$$\text{poles} = \pm j\,7.07, \quad \pm j\,17.32$$
$$\text{zeros} = \pm j\,7.68, \quad \pm j\,18.50$$

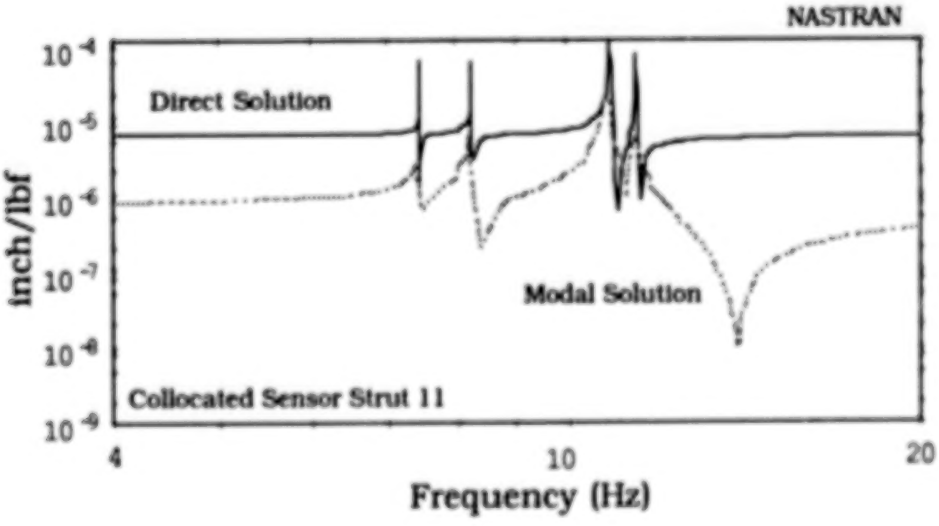
COLLOCATED TRANSFER FUNCTION OF MODEL

Collocated transfer functions of the active-member/structural model are shown for two values of the stiffness ratio β. The near pole-zero cancellation is readily seen. This phenomenon is not restricted to active-member applications but will occur any time a collocated measurement is made at a location where the structure is compliant with respect to the applied force.



COMPARISON OF NASTRAN DIRECT AND MODAL SOLUTIONS

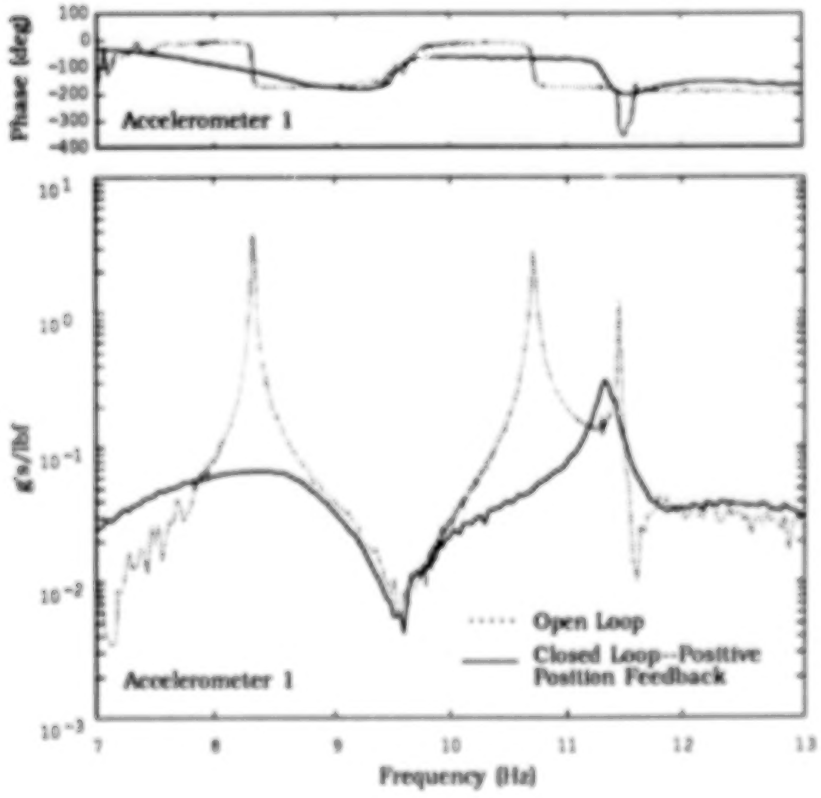
Care must be taken when obtaining the collocated transfer functions of the Precision Truss and other models via finite element models. The figure shows the collocated transfer function for strut 11 produced by NASTRAN. The solid curve is the result of a direct solution utilizing the system mass and stiffness matrices. The dashed curve is the same transfer function obtained by modal solution retaining the first 30 structural modes. There is substantial error in the modal solution both in the feedthrough term and in the transmission zero locations. Modal truncation, even as high as 30 modes, results in nearly complete loss of the residual flexibility between sensor and actuator.



CLOSED-LOOP CONTROL--POSITIVE POSITION FEEDBACK

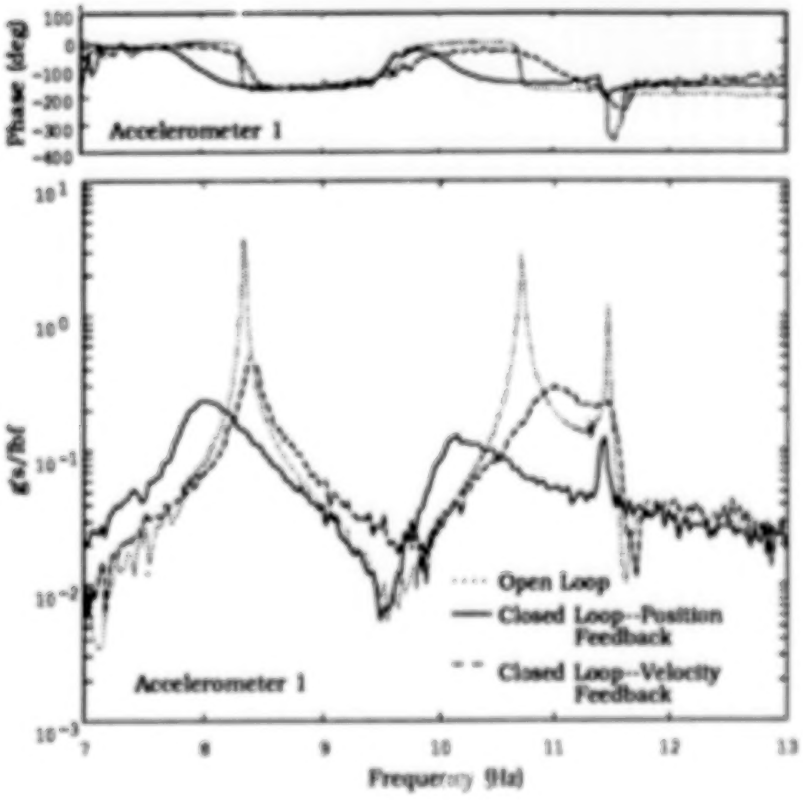
Four single-input-single-output controllers were designed for implementation using the digital array processor. Because the sampling rate of 2000 Hz was high relative to the control bandwidth, controllers were first designed in the continuous domain and were later discretized by a zero order hold approximation. Active-member 11 in the longeron of the first bay was chosen as the sole actuator for this study. The collocated and noncollocated displacement sensors in the longerons were selected as feedback measurements; accelerometer measurements at the outrigger provide a reference point for controller performance. Controllers were designed using Bode and root locus analysis.

The figure depicts a measured stepped-sine transfer function between the shaker disturbance and an accelerometer on the outrigger station 41 for both the open and closed loop cases. The positive position feedback design[13] trades stiffness for damping and reduces the first mode amplitude by 35 dB. The third (torsional) mode displays some attenuation but is otherwise barely observable or controllable from longeron 11.



CLOSED-LOOP CONTROL--OUTPUT AND VELOCITY FEEDBACK

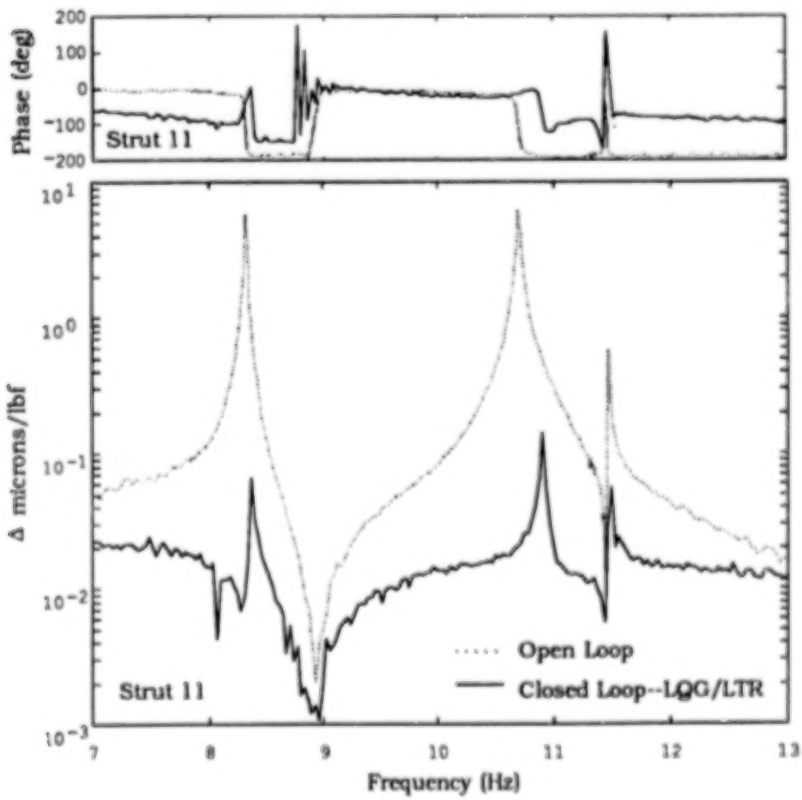
Output and velocity feedback designs were also implemented using the noncollocated internal displacement sensor from strut 22. Positive output feedback had the effect of softening the structure. Velocity feedback was implemented digitially by a second-order compensator with a 30 Hz rolloff. Spillover instability in the high modes limited the performance of each of these designs.



CLOSED-LOOP CONTROL--LQG/LTR

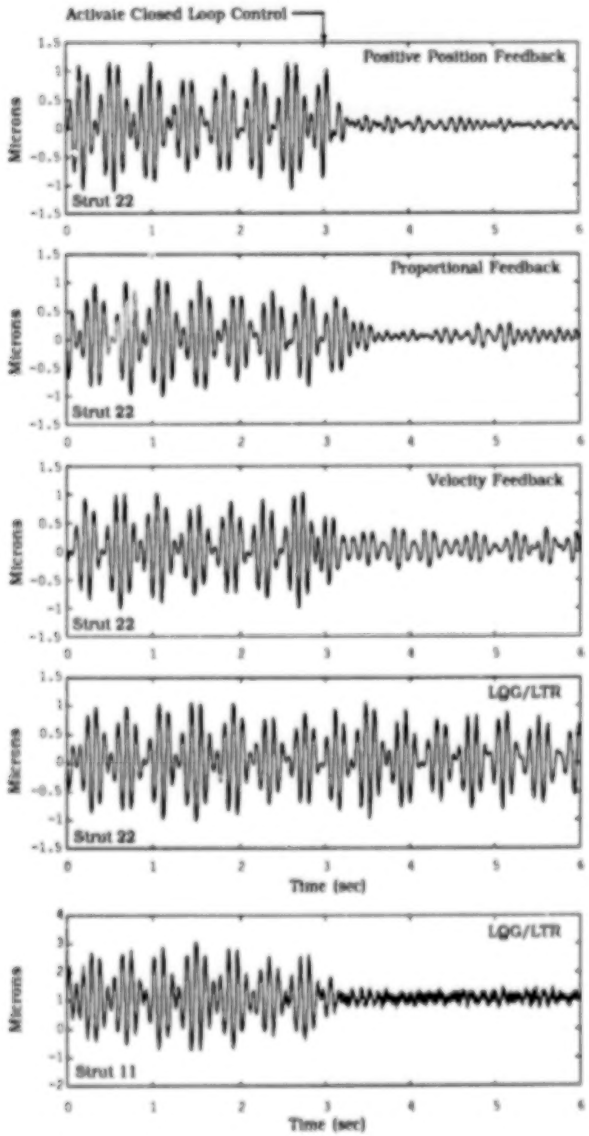
A sixth-order LQG/LTR* controller was implemented for the collocated internal displacement at strut 11. The figure shows the closed-loop transfer function at the design point, and demonstrates that while significant attenuation is achieved at this point, system damping is essentially unchanged. The resonances in the LQG/LTR closed-loop frequency response are due to the inaccuracies in a preliminary disturbance model used in the control design.

*linear quadratic Gaussian/loop transfer recovery



CLOSED-LOOP RESPONSE--NARROWBAND EXCITATION

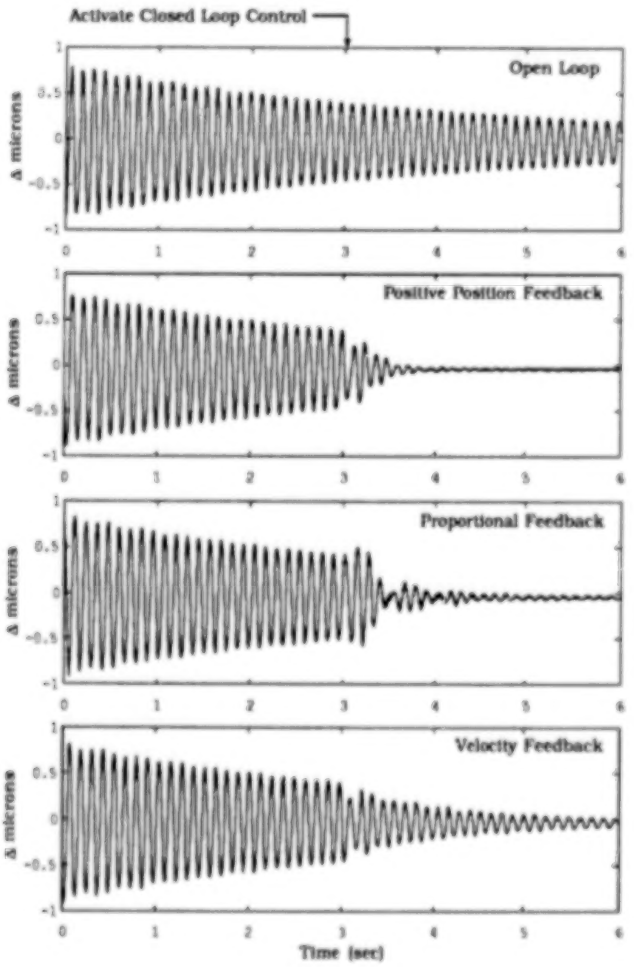
A second set of performance measurements was obtained by injecting a 5 to 15 Hz narrowband random excitation, using the shaker on the midbay plate, and observing the open and closed-loop steady-state response. The time histories are plotted in the figure for the response of the strut 22 internal sensor, the SISO design point. The beating pattern in the open-loop time histories is the result of the close coupling between the second (bending) and third (torsional) modes. The dramatic difference between LQG/LTR controller performance at strut 22 and the design point 11 further illuminates the localized nature of this controller.



FREE DECAY OF FIRST MODE

The third measurement of performance involves turning on the controllers midway through the free decay of the first (bending) mode. Positive Position Feedback*provides the best performance by increasing the damping from the open loop value of 0.436% to an estimated 8%. The PPF design was the most stable of the four designs implemented; the three others tended to drive some higher mode unstable at high loop gain. At high gain the PPF design leads to a static instability which results in saturation of the actuator. This type of instability is relatively benign compared to the potentially destructive effects of a dynamic instability.

*ppf



CONCLUSIONS

The objectives of this study were to close a digital control loop around a piezoelectric active-member in a representative truss structure and achieve improved performance over the open loop structure. These objectives have been achieved. A method for optimal actuator placement was implemented that makes use of a heuristic preselection process that greatly reduces the combinatorial possibilities of candidate actuator locations. The single-input-single-output control designs implemented were relatively simple and no attempt was made to extract optimal performance from these systems. Nevertheless, the response of the first two bending modes of the structure was attenuated by more than 35 dB and damping was increased by a factor of 20 to eight percent.

We have observed and explained analytically that high feedthrough terms are likely to exist in collocated measurements of active members, terms which correspond to the quasi-static "residual flexibility" of higher modes. The feedthrough terms result in close pole-zero pairs which complicate the control design.

Future research will explore the use of more sophisticated multivariable control methodologies for improved performance.

REFERENCES

1. Laskin, R. A., "A Spaceborn Imaging Interferometer - The JPL CSI Mission Focus," presented at the Third NASA/DOD Controls Structures Interaction Technology Conference, San Diego, CA, January 29 -- February2, 1989.

2. Dailey, L. R., and Lukich, M., "Recent Results in Identification and Control of Flexible Truss Structure," *Proceedings of the American Control Conference,* Atlanta GA, June 1988. pp. 1468--1473.

3. Balas, G. J., and Doyle, J. C., "On the Caltech Experimental Large Space Structure on and Control of Flexible Truss Structure," *Proceedings of the American Control Conference,* Atlanta GA, June 1988. pp. 1701--1702.

4. Natori, M., Motohashi, S., Takahara, K., and Kuwao, F., "Vibration Control of Truss Beam Structures Using Axial Force Actuators," *Proceedings of the 29th AIAA SDM Conference,* Williamsburg, VA, April 18 -- 20, 1988. pp. 491--499.

5. Crawley, E. F., and de Luis, J., "Use of Piezo-Ceramics as Distributed Actuators in Large Space Structures," *Proceedings of the 26th AIAA SDM Conference,* 1985.

6. Hanagud, S., Obal, M. W., and Meyyappa, M., "Electronic Damping Techniques and Active Vibration Control," *Proceedings of the 26th AIAA SDM Conference,* 1985.

7. Bailey, T. L., and Hubbard, J. E., "Distributed Piezoelectric Polymer Active Vibration Control of a Cantilever Beam," *Journal of Guidance, Control, and Dynamics,* Vol. 8, Sept.--Oct. 1985, pp. 605--611.

8. Fanson, J. L., and Chen J-C., "Vibration Suppression by Stiffness Control," *Proceedings of the Workshop on Structural Dynamics and Control Interaction of Flexible Structures,* Marshall Space Flight Center, April 22-24, 1986.

9. Hagood, N. W., and Crawley, E. F., "Development and Experimental Verification of Damping Enhancement Methodologies for Space Structures," MIT SSL#18-88, September, 1988.

10. Chen, G-S, Lurie, B. J., and Wada, B. K., "Experimental Studies of Adaptive Structures for Precision Performance," AIAA paper 89-1327, 1989.

11. Chen, J-C., and Fanson, J. L., "System Identification Test Using Active-Members," AIAA paper 89-1290, 1989.

12. Doyle, J. C., Glover, K., Khargonekar, P., and Francis B. A., "State-Space Solutions to Standard H_2 and H_∞ Control Problems," 1988 American Control Conference, Atlanta, GA.

13. Fanson, J. L., and Caughey, T. K., "Positive Position Feedback Control for Large Space Structures," *Proceedings of the 28th AIAA Dynamics Specialists Conference,* Monterey, CA, April 9--10, 1987. pp. 588--598.

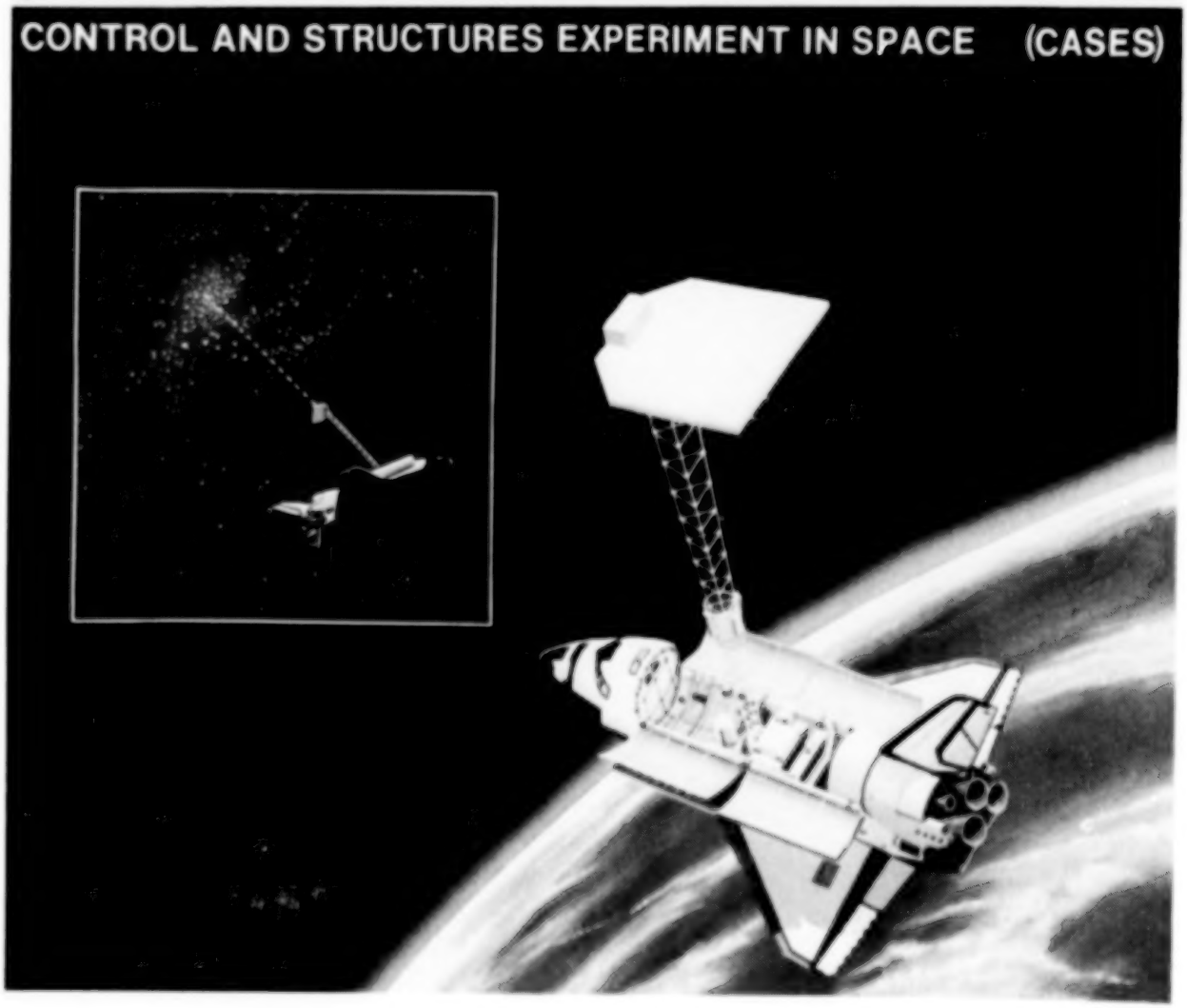
CONTROLS, ASTROPHYSICS, AND STRUCTURES EXPERIMENT IN SPACE (CASES)

Henry B. Waites and John P. Sharkey
NASA Marshall Space Flight Center, AL.

NASA/DOD CSI Conference
January 29-February 2, 1989

ABSTRACT

As the size and performance requirements of future NASA and DoD spacecrafts and payloads tend to increase, the associated control systems that must effect these requirements tend to interact with the vehicle's structural dynamics. Some of the Control Structure Interaction (CSI) issues are being addressed in a flight experiment which is entitled CASES (Controls, Astrophysics and Structures Experiment in Space). As one of the first CSI flight experiments, the main emphasis for CASES is to provide a test bed for validating CSI developments and, simultaneously, to pave the way for subsequent CSI experiments and science missions by establishing precedents for flight qualifying Large Space Structures (LSS)-class spacecraft. In addition, CASES provides an opportunity to obtain data bases for in-space controls and structures experiments and, at the same time, to gather hard X-ray data from pertinent galactic sources.



INTRODUCTION

The CASES will investigate critical control technology applicable to stabilizing and pointing large flexible structures in space. To fully understand and control LSS, the ability to identify and characterize system parameters in space must be demonstrated. To perform system identification the experiment on-orbit modal tests must be conducted to determine natural frequencies and mode shapes. System parameters will then be used to modify control gains used in closed-loop tests. These tests will verify both CSI controller design methodologies and parameters predictive techniques. Such verification is impossible on the ground because of gravity, seismic, and atmospheric effects.

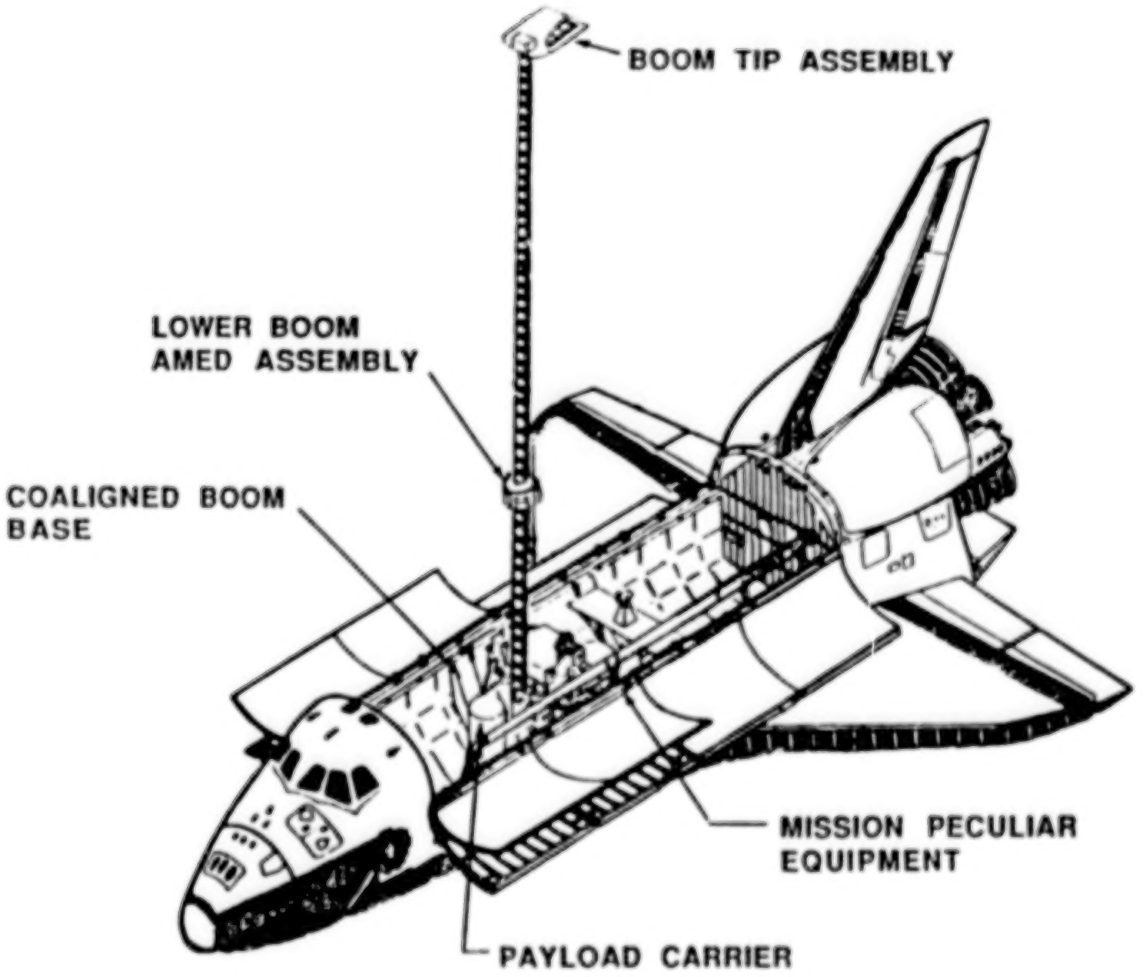
The control of a 32-m extendable boom, as used in the Solar Array Flight Experiment (SAFE) program, will be performed using small cold gas thrusters for pointing and Angular Momentum Exchange Devices (AMEDs) for active damping to suppress vibrations. Since the boom is rigidly attached to the orbiter, the orbiter/boom system can be pointed to a predetermined target for periods of at least 30 minutes. In addition,tracking and slewing of the orbiter at small angular rates by the tip-mounted thrusters will be demonstrated.

The CASES will provide accommodations for an Astrophysics/Solar Physics Hard X-ray Imaging experiment. This experiment will address important issues in high-energy astronomy (in particular, the identification of thc energy source seem at the galactic center and determination of the energy release mechanics in solar flares). The high-energy imaging is made possible by aperture plates mounted on the tip of the boom. They provide both coded aperture and Fourier-transform imaging on position sensitive, proportional counter arrays placed in the cargo bay (at the base of the boom). High spatial resolution is made possible by the large separation between masks and detectors afforded by the boom.

At this time it is envisioned that funding for the CASES definition phase study will be available in FY 1989 with actual work starting in the beginning of CY 1989. Development (phase C/D) program start is planned in FY 1990 with the CASES flight occurring in late CY 1993.

The CASES program is sponsored jointly by the office of Space Science and Applications and the Office of Aeronautics and Space Technology. Marshall Space Flight Center (MSFC) will manage the overall program. Langley Research Center will support MSFC in experiment definition and conduct the Guest Investigators Program. Johnson Space Center will assess the operational aspects of the program relative to the orbiter systems.

CONTROL, ASTROPHYSICS, AND STRUCTURES EXPERIMENTS IN SPACE



CSI Experiment Objectives

The CASES will provide an on-orbit test bed for demonstrating the flight readiness of several key aspects of CSI technology. Since the proposed CSI control concepts represent a significant departure from conventional control methods, the emphasis will be on the ability to accurately predict, based upon analytical models and ground test methods, the on-orbit open- and closed-loop performance of a beam-like LSS, and then to successfully verify the implementation of these CSI methods in orbit. The success of this mission will enable future missions, which may require CSI technology but which are too large for full-scale ground tests, to be safely operated in-orbit with control systems derived from analytic models alone.

- Determination of the degree to which theory and ground tests can predict open- and closed-loop performance of large, flexible deployable structures in space.
- Evaluation of system identification and state estimation algorithms in the space environment.
- Analysis of deployment dynamics and structural damping in space.
- Ground and flight demonstration of Multiple Input/Multiple Output (MIMO) control laws, and robustness of such control laws to model uncertainties and perturbations.
- Demonstration of pointing and tracking control of a LSS using linear Bidirectional Thrusters (BLT's) acting over a long flexible moment arm.
- Evaluation of the operational use of unobtrusive sensor technology for measuring low-frequency, low-amplitude motions of LSS.
- Demonstration of real-time MIMO control law reconfiguration and fine tuning in orbit.
- Achievement of well-defined (sub-arcminute) pointing and stability requirements in support of the X-ray imaging experiments that necessitate the use of CSI technology.

CASES

CSI EXPERIMENT OBJECTIVES

SYSTEM IDENTIFICATION TECHNIQUES

- o ON-ORBIT APPLICATIONS
  - OPEN LOOP
  - CLOSED LOOP
- o SENSITIVITY AND PERTURBATION METHODS
- o UNOBTRUSIVE MEASUREMENT TECHNIQUES

STRUCTURES

- o MECHANISM DEMONSTRATIONS
- o CHARACTERIZATION
- o VALIDATION OF ANALYTICAL AND GROUND TEST METHODS
- o DEPLOYMENT DYNAMICS
- o INVESTIGATION OF STATIC DEFORMATIONS

CONTROLS

- o POINTING OF FLEXIBLE BODIES
- o VIBRATION SUPPRESSION
- o TRACKING AND SLEWING OF FLEXIBLE BODIES
- o SENSOR/EFFECTOR APPLICATIONS
- o REAL-TIME CONTROL CHANGES AND UPDATES
- o SENSITIVITY AND ROBUSTNESS CHECKS
- o DEVELOPMENT OF MISSION OPERATIONS FOR INTERACTIVE CONTROL EXPERIMENTS
- o PERFORMANCE GOALS COMPATIBLE WITH SCIENCE OBJECTIVES (SUB-ARCMINUTE)

SCIENTIFIC OBJECTIVES

Hard X-ray emission is the signature of energetic processes which, through the release of large amounts of energy, accelerate charged particles to high energies. Although these processes appear to be quite common throughout the universe, an exact physical description of the acceleration mechanism still eludes us. On the local scale the Sun is the source of such events. Here we believe that magnetic fields emerging from the solar surface are forced into unstable configurations by the motion of the solar atmosphere. Reconnection of the magnetic lines of force to form a new configuration, with a lower potential energy, results in a rapid release of energy, much of which goes into the acceleration of charged particles. This energy release is observed as a solar flare. Magnetic activity in stars is quite commonplace and in many instances gives rise to considerably more energetic events than we observe on our Sun.

Within our galaxy we believe that hard X-rays are emitted by material which is accelerated to high velocities as it falls into the gravitational potential of extremely dense, compact objects such as neutron stars, or through nuclear processes that occur explosively within these objects. On an even larger scale are the unknown processes that drive the energy release mechanisms in quasars and the nuclei of galaxies. It is speculated that this energy may be released by the infall of material into supermassive black holes or from frequent collisions within a dense cluster of neutron stars or stellar black holes at the galactic center.

Our understanding of the processes involved in the acceleration and propagation of the high-energy particles can be advanced, in both the solar and extra-solar environments, by tying down the location of the emission so that the hard X-ray signature can be related to the conditions existing before and during the release of energy and by allowing the phenomena to be observed with different instruments capable of specialized diagnostic observations over a wider spectral range. At the present time one of the roadblocks to improved understanding has been the wide disparity between the angular resolution of the hard X-ray observations and those in other wavebands. The CASES will be a major step in eliminating these disparities. The large separation between the ends of the boom makes possible angular resolutions of one to two arcsec, an improvement of between one and two orders of magnitude over past observations. This is achieved without having to exceed the current performance of detectors or aspect systems.

Two specific studies have been selected as the strawman objectives for the CASES. The selection was based both on their inherent scientific interest and for their compatibility with the proposed instrument performance.

SCIENCE OBJECTIVES FOR CONTROL ASTROPHYSICS STRUCTURES EXPERIMENT IN SPACE (CASES)

SOLAR OBSERVATIONS

DETERMINE THE HIGH TEMPORAL AND SPATIAL CHARACTERISTICS OF HARD X-RAY EMISSIONS FROM SOLAR FLARES AND MICRO FLARES.

USING THESE DATA INVESTIGATE THE NATURE OF ENERGY RELEASE, TRANSFORMATION, AND SOURCES IN THE SUN'S ATMOSPHERE.

GALACTIC OBSERVATIONS

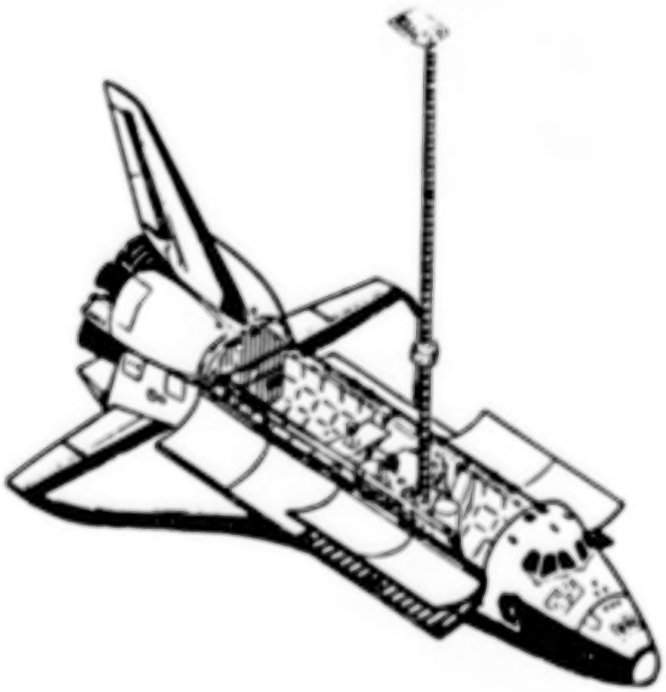
DETERMINE THE EMISSION CHARACTERISTICS AND CELESTIAL POSITION OF HARD X-RAY EMISSIONS AT THE GALACTIC CENTER.

USING THESE DATA CORRELATE THE X-RAY EMISSION WITH INFRARED AND RADIO SOURCES AND DIFFERENTIATE BETWEEN EMISSION MODELS OF BLACK HOLES AND RECENT STAR BURST FORMATION AT THE GALACTIC CENTER.

CASES MISSION AND EXPERIMENT REQUIREMENTS

The mission and experiment requirements for this experiment are summarized below. The mission requirements are an altitude of 200-300 nmi, inclination of 28.5°, and mission duration of 6 days.

The experiment requirements for the Astrophysics and Guest Investigators include minimum operation time from 8 hours to 3 days.



MISSION REQUIREMENTS

- O 200-300 Nautical Miles
- O 28.5° Inclination
- O 6 Days of Orbit Operation
  - 1 Day for Experiment Alignment
  - 2 Days of Operation for the Hard X-Ray Imaging Experiment
  - 3 Days for Guest Investigators to run their experiments

EXPERIMENT REQUIREMENTS

HARD X-RAY IMAGING EXPERIMENT

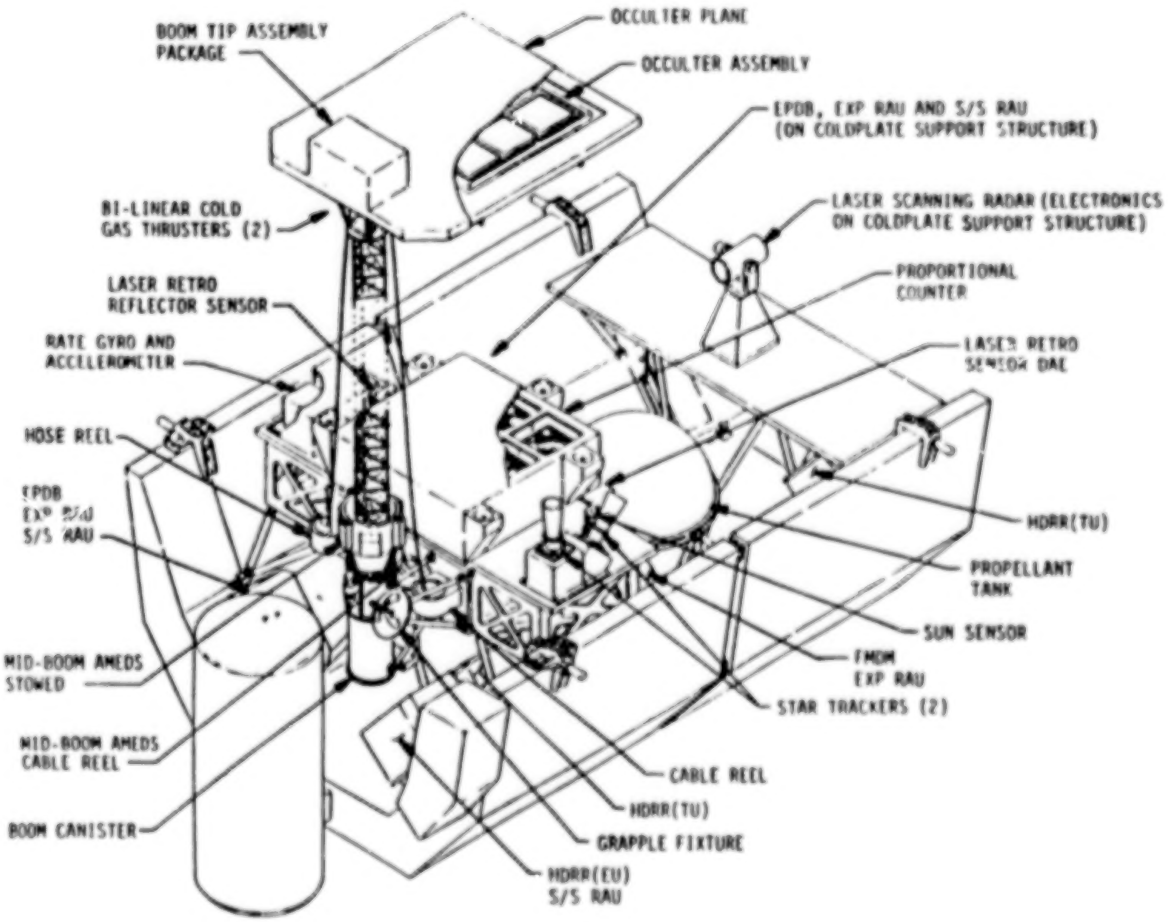
- O Needs a translation table that can move the mask ±6 inches in the X-Y orbiter plane. Also ± 1° in pitch and yaw.
- O The mask cannot tilt more than >.25°
- O Need 8 hours minimum but 48 hours of operation preferred.

CASES EXPERIMENT CONFIGURATION

The configuration for the CASES experiment is shown below. All the major components of the experiment are labeled. The proposed CASES configuration uses as much of the Spacelab equipment as possible to reduce costs. As can be seen, CASES uses two Spacelab Pallets and an Igloo in which reside three AP101SL flight computers. The undefined acronyms in the figure are as follows:

FMDM - Flexible Multiplexer DeMultiplexer
HDRR - High Data Rate Recorder
EPDB - Electrical Power Distribution Box
RAU - Remote Acquisition Unit
S/S - Subsystem
EU - Electronic Unit
TU - Telemetry Unit

CASES EXPERIMENT ON SPACELAB PALLETS



CASES

MODAL ANALYSIS

The model analysis follows.

* The first mode (lowest cyclic frequency) has a cyclic frequency of 0.0345 Hz (28.98 sec/cycle). This is the lowest natural frequency of the system and results in the largest tip displacements.

* The third mode is the first torsional mode of the structure and has a cyclic frequency of 0.1306 Hz. This is the lowest torsional mode and results in large angular displacements (twist) of the tip mass.

* Modes 1 and 2 are bending modes in the xz and yz plane, respectively, and result in large tip displacements. Mode 1 also develops rotation about the z axis because of the tip C.G. offset.

* Mode 3 is the first torsional mode (about the z axis). Bending is also present during this mode because of the C.G. offset.

* Modes 4 and 5 represent the second set of bending modes in the xz and yz planes, respectively. At these modes the tip mass displacement is relatively small and acts as a node.

* Modes 6 and 7 are more complex bending modes, also in the xz and yz planes. The displacement of a point just ahead of the mid-boom assembly is very small, as is the displacement of the tip. Both the tip and the point ahead of the mid-boom assembly act as nodes.

CASES

MODAL ANALYSIS

MODE #	EIGENVALUE	CYCLIC FREQUENCY (Hz)
1	0.04707	0.03453
2	0.04768	0.03475
3	0.67314	0.13058
4	10.1710	0.50758
5	10.3799	0.51277
6	89.0345	1.50176
7	96.3628	1.56234

MODES 1 & 2
pure bending



MODE 3
torsion



MODES 4 & 5
bending



MODES 6 & 7
bending



POINTING REQUIREMENTS

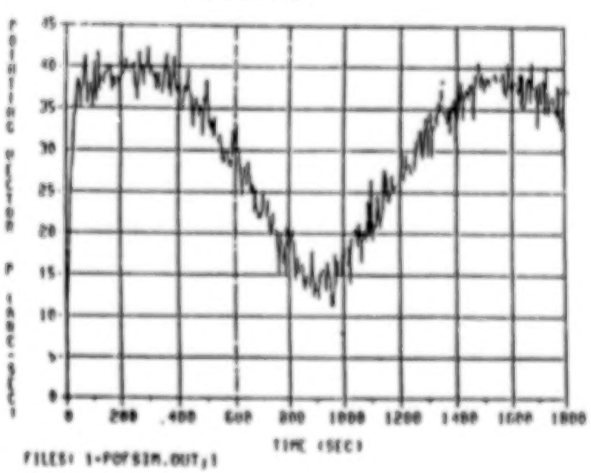
The hard X-ray images are built up by photon counting rather than by integration. Consequently, provided it is possible to develop, post facto, an accurate aspect solution, the requirements on the pointing system are not particularly severe. They are expressed in terms of the pointing error that is defined as a vector equal to the difference between unit vectors along the internal and pointing axes. The internal axis is a line joining corresponding points on the upper and lower grids and the pointing axis is the line from a reference point on the lower grid directed toward the target. The requirements that we have established are:

- Accuracy: The pointing error shall not exceed 2.0 arc min. This is set by field-of-view considerations.
- Stability: The jitter in the pointing error shall be less than 4 arc sec per sec. This requirement is derived from the frequency with which the star tracker can be sampled.
- Roll: Drift in roll shall be maintained within 2° in any one-hour period, and the system shall be capable of acquiring new roll positions with a frequency of once per orbit and an accuracy in the initial position of 1°.

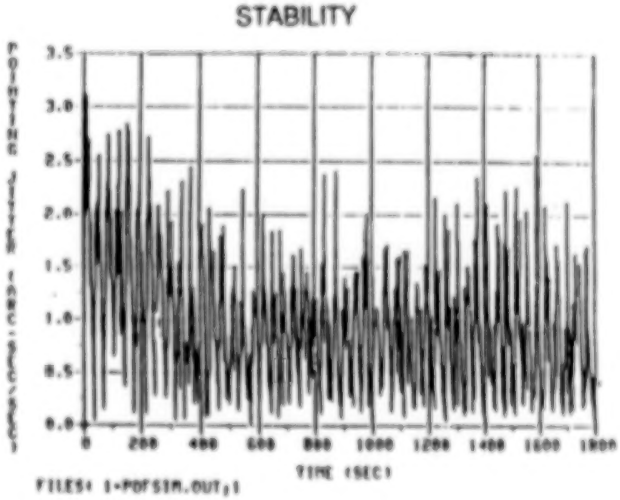
The performance of the control system has been modelled using several different control algorithms. Results for accuracy and stability, typical of worst-case conditions, are reproduced in the chart. The models include the effect of crew motion and gravity gradient and aerodynamic torques. The results are based on ground test and inflight data and provide a high level of confidence in our ability to control the boom with a precision that is adequate for the scientific observations.

POINTING SIMULATIONS

ACCURACY



STABILITY



ATTITUDE CONTROL EQUIPMENT LIST

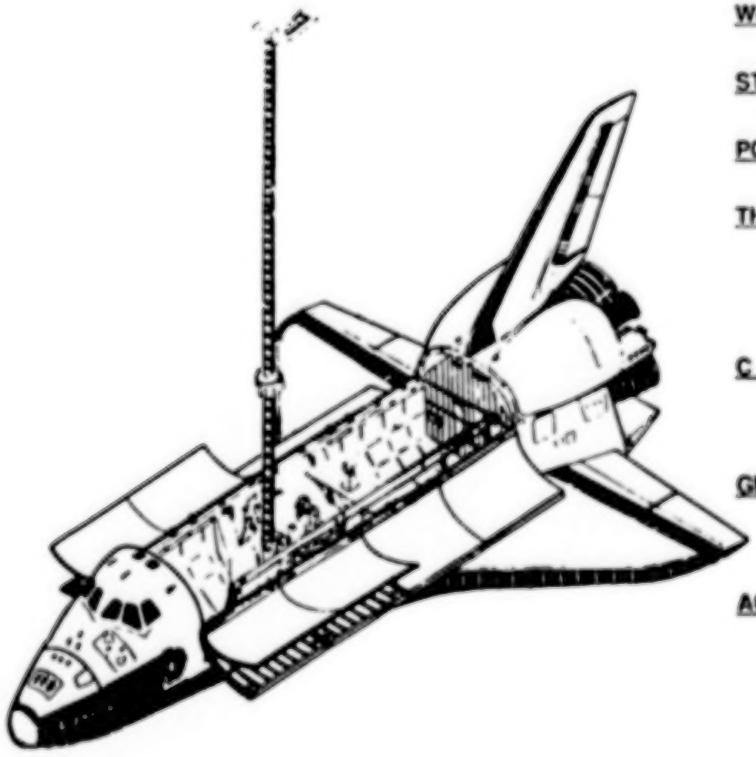
This figure consists of an equipment list for the GN&C subsystem that will meet the experiment requirements. The power and weight for each component are shown. The orbiter GN&C system is also used during this experiment. The components are broken down into the components on the base, components on the boom and components on the tip of the boom. The Bidirectional Linear Thrusters (BLTs) are used for fine pointing and also slewing and vibration suppression. The Angular Momentum Exchange Devices (AMEDs) are used for vibration suppression and distributed control of the boom. The star trackers and fine Sun sensor are used for pointing direction knowledge, and the rate gyros give deviations from this desired pointing over time. The laser scanning radar is used for system identification.

EQUIPMENT	NUMBER	POWER (W)	WEIGHT (LBS)
BASE			
STAR TRACKERS	2	20	88
FINE SUN SENSOR	1	25	22
RATE GYROS	2	20	42
ACCELEROMETERS	3		
RFT	1	55	50
LASER SCANNING RADAR	1	150	200
BOOM			
AMEDS	3		
PLUS ELECTRONICS		15	25
RATE GYROS	2		
TIP			
AMEDS	3		
PLUS ELECTRONICS		15	25
RATE GYROS	2		
BLT	2	5	6
ROLL TORQUE MOTOR	1	5	10.5
PARAMETER MODIFICATION SYSTEM	1	10	40

CONCLUSIONS

There are no technical or safety issues resulting from preliminary studies that are without resolution. The preferred configuration for this experiment is a two Spacelab Pallet train with Igloo. The Spacelab AP101SL computers will be used and housed in the Igloo. There are ample volume, power, weight, and crew time for payload sharing to help utilize extra pallet space. This figure is a summary of the configuration and the subsystems represented in this experiment.

The general control of the Space Shuttle using the CASES experiment will need to be validated through vigorous ground simulations. These simulations will be performed in the CSI ground facility that will be located at MSFC and will be called the CASES Advanced Development Facility.



WEIGHT:	13600 LBS
STRUCTURE:	Boom Length 105 ft.
POWER:	Total Power 3236 W
THERMAL:	Standard Spacelab Thermal Protection System (inc. cold-plates)
C & DH:	Overall rate of 2 MBS On-board Storage Periodic Downlink
GNC:	Stability should be within 3 $\widehat{\text{sec/sec}}$ Pointing within 1 $\widehat{\text{min}}$
ACS:	500 lbs High Pressure Gaseous Nitrogen (GN_2) 1.5 lb Bi-linear Thrusters

BEST COPY AVAILABLE

LACE FLIGHT DYNAMICS EXPERIMENT

Shalom Fisher
Naval Research Laboratory
Washington, D. C.

Third NASA/DOD CSI Technology Conference
San Diego, California
January 29 - February 2, 1989

ABSTRACT

The Low Power Atmospheric Compensation Experiment (LACE) is scheduled for launch in late 1989 into a 556 km altitude circular orbit of 43^0 inclination. The LACE flight dynamics experiment, described in this report, is an experiment secondary to the primary LACE mission. The purpose of the experiment is to provide on-orbit systems identification of the LACE spacecraft. The structure of the LACE spacecraft is of special interest to the CSI community. It incorporates 3 deployable/retractable booms of maximum length 45.72 m (150 ft) mounted on a rectangular parallelepiped bus of mass 1,200 kg. The zenith directed gravity gradient boom is mounted on the top of the bus; the retroreflector boom is mounted forward and deployed along the velocity vector; the balance boom is mounted and pointed aft. Attitude stabilization is accomplished by means of gravity gradient torques and by a momentum wheel. The LACE flight dynamics experiment is designed to measure modal frequencies, damping ratios, and oscillation amplitudes of the LACE spacecraft, as well as the vibration intensity generated by boom deployments and retractions. It is anticipated that this experiment will provide an opportunity for improvements in the accuracy of computer simulations of flexible structures and multibody dynamics.

DESIGN OF LACE FLIGHT DYNAMICS EXPERIMENT

The Low Power Atmospheric Compensation Experiment (LACE) is scheduled for launch in late 1989 into a 556 km altitude circular orbit of 43^0 inclination, as illustrated in figure 1. The LACE flight dynamics experiment, described in this report, is an experiment secondary to the primary LACE mission. The purpose of the experiment is to provide on-orbit systems identification of the LACE spacecraft. The structural configuration of the LACE spacecraft is indicated in figure 1. Three deployable/retractable booms of maximum length 45.72 m (150 ft) are mounted on a rectangular parallelpiped bus of mass 1,200 kg. The zenith directed gravity gradient boom has a tip mass of 90.7 kg and includes a magnetic damper; the retroreflector boom and balance boom each have a tip mass of 15.9 kg. Attitude stabilization is accomplished by the gravity gradient torques and by a momentum wheel. The flight dynamics experiment hardware consists of 2 germanium corner cubes: one proposed to be on the bus and the other on the balance boom. The FIREPOND laser radar at the MIT Lincoln Laboratory will illuminate the cubes to measure the relative motion of the boom with respect to the bus. Absolute bus rotation rates will be measured by means of the on-board UltraViolet Plume Instrument (UVPI). Measurements will be made of vibration frequencies, damping ratios, and oscillation amplitudes.

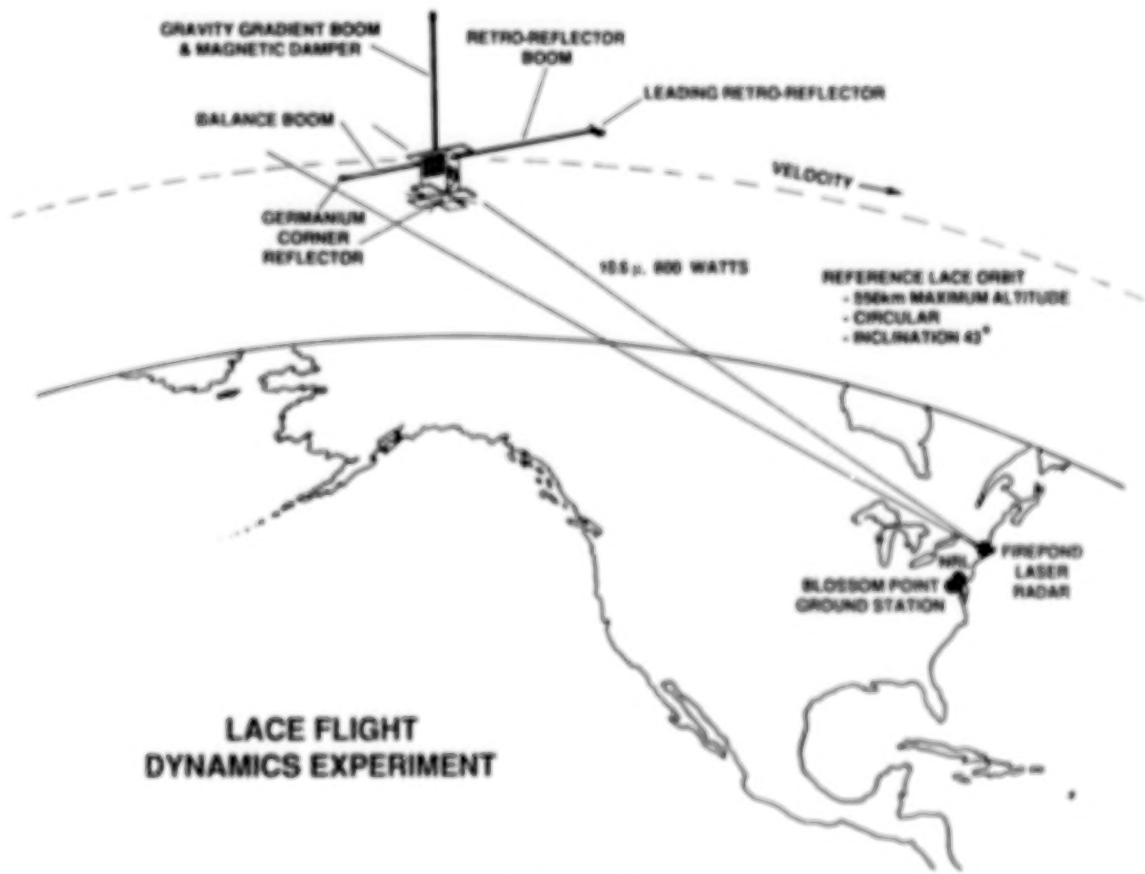


Figure 1

ISSUES ADDRESSED BY THE DYNAMICS EXPERIMENT

Structural modelling, environmental interactions, and boom deployment dynamics are areas where the LACE flight dynamics experiment can provide useful data. At the present time estimates of the vibration frequencies are based on static ground tests of the boom structure. The flexural rigidity value obtained thereby ranges from $1.26 * 10^4$ N-m^2 ($4.4 * 10^6$ lb-in^2) to $1.6 * 10^4$ N-m^2 ($5.5 * 10^6$ lb-in^2), giving an uncertainty in the vibration frequencies of about 20%. Further uncertainties in the vibration frequencies, as well as in the gravity gradient libration frequencies, are generated by twisting from differential day/night heating. The amount of vibration damping is not well known. For example, in the SAFE experiment of 1984* a flexible, deployable "wing" of polymer film was attached to a boom similar to the LACE booms. Damping rates were observed to be nonlinear (reference 1) with most of the damping induced by the attached wing. In the case of LACE, with no boom attachments, the experiment will measure the damping intrinsic to the boom structures.

Furthermore, the flight dynamics experiment will provide a mechanism for evaluating the influence of magnetic torques, gravity-gradient torques, and atmospheric drag on the LACE structure. Also, vibrations generated by boom deployments and retractions such as were observed in the SAFE experiment will be measurable by means of this experiment. (Fig. 2.)

*Lockheed Missiles & Space Company, "Solar Array Flight Experiment: Final Report," LMSC-F087173, National Aeronautics and Space Administration, Marshall Space Flight Center, Alabama, April 1986.

ISSUES ADDRESSED BY THE DYNAMICS EXPERIMENT

Accuracy of mathematical models and computer simulations

- Structural Models

  Damping rates of vibration oscillations: estimates .2 % to .5%

  Oscillation frequencies: uncertainties of 20%

  Thermoelastic changes: day/night changes in frequency
  twisting from differential heating

- Environmental interactions: atmospheric drag
  gravity gradient torques
  magnetic damping

- Oscillations generated by boom deployments/retractions

Figure 2

EXPERIMENTAL HARDWARE

With this experiment, two germanium corner cubes are proposed to be mounted on the spacecraft: one on the bottom of the spacecraft bus, the other at the tip of the balance boom. The corner cubes will serve as targets for the FIREPOND 10.6 micron laser radar at the MIT Lincoln Laboratory. It is anticipated that this experimental setup will provide resolutions of 2 mm/sec relative motion between the bus and the boom tip, and thereby readily resolve the lowest mode of 0.019 Hz. A typical relative motion is expected to be 18 mm/sec, based upon a NASTRAN simulation with an assumed 60 cm amplitude of vibration at the tip of the retro-boom. The FIREPOND laser radar has a 4 millisecond square wave pulse at a frequency of 62.5 Hz and pulse energy of 3.2 joules. It has tracked reflections from similar corner cubes on the LAGEOS spacecraft at ranges of 6000 km to resolve satellite spin motion (reference 2).

The Ultra-Violet Plume Instrument (UVPI), primarily installed for other experiments, will be used to measure the absolute bus rotation rate. It has the capability of resolving angular velocities of $5 * 10^{-5}$ radians/sec ($3 * 10^{-3}$ deg/sec). A typical angular rate is 0.2 deg/sec, based upon the NASTRAN simulation. The resolution capability is therefore almost 2 orders of magnitude better than what is needed. (Fig. 3.)

- **Two corner reflectors: one on bus and one at tip of balance boom**
  - **Targets for FIREPOND 10 microns laser radar (far infrared)**
  - **Germanium composition gives high acceptance angle**
  - **Will measure relative motion between boom tip and bus**
  - **FIREPOND has 2 mm/sec velocity resolution capability**
  - **Lowest vibration mode of spacecraft: 18mm/sec (assume 2 ft vibration amplitude at retro boom tip)**
  - **Factor of 10 better than needed for resolution**
- **Ultra-violet Plume Instrument (UVPI): bus rotation rate**
  - **Resolution capability of $5 * 10^{-5}$ radians/sec ($3 * 10^{-3}$ deg/sec)**
  - **Lowest vibration mode : 0.2 deg/sec**
  - **Factor of 60 better than needed for resolution**

Figure 3

LACE DEPLOYABLE/RETRACTABLE BOOM STRUCTURE

The LACE spacecraft incorporates three deployable/retractable booms, of maximum length 45.72 m (150 ft) and diameter 0.254 m (10 in). Figure 4 shows the basic design. The longerons are of fiberglass composition, are continuous, and are coiled when stowed in the canister. The diagonals and battens are attached to the longerons via the corner fitting assemblies. Basic characteristics of the booms, from static ground tests, are as follows:

weight of motor, cannister and gears:	16.8 kg (37.1 lb)
weight of booms:	13.3 kg (29.5 lb)
bending stiffness, EI:	$1.26 * 10^4$ to $1.58 * 10^4$ N-m^2 (4.4 to $5.5 * 10^6$ lb-in^2)
torsional stiffness, GJ:	631 N-m^2 ($2.2 * 10^5$ lb-in^2)
bending strength:	47.45 N-m (420 in-lb)
torsional strength:	13.6 N-m (120 in-lb)
stiffness of longerons:	$2.3 * 10^4$ N/m^2 ($8 * 10^6$ lb/in^2)
boom deployment/retraction rates (depend upon bus voltage)	6 to 9 cm/sec
deployment/retraction	7.6 cm/turn

BASIC DESIGN

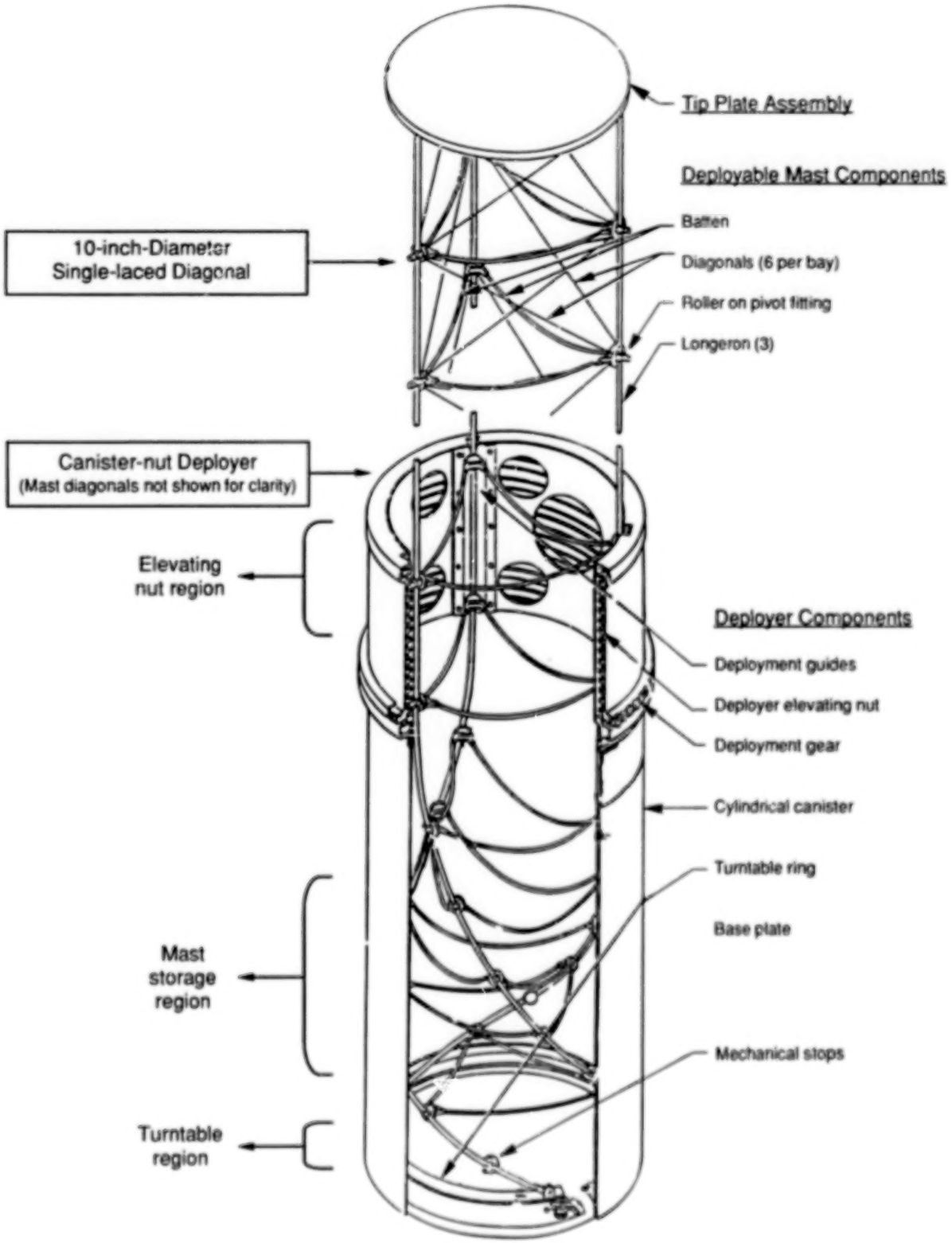


Figure 4

COORDINATE SYSTEM OF LACE ANALYSIS

Figure 5 shows the spacecraft oriented coordinate system used for the structural analysis and environmental modelling of the LACE experiment. The yaw or "z" axis is directed toward the zenith, with the pitch or "x" axis directed toward the negative orbit normal, and the roll or "y" axis is perpendicular to the other two to form a right-handed coordinate system. With LACE in a circular orbit, the roll axis is along the velocity vector.

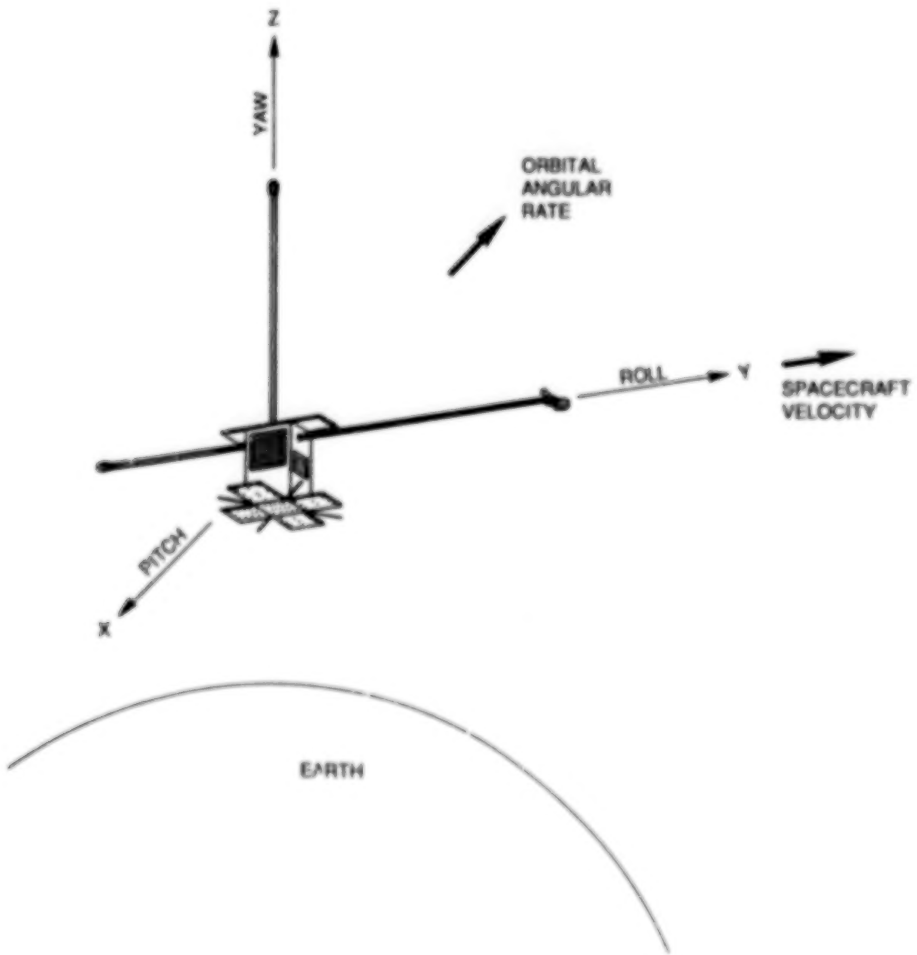


Figure 5

NASTRAN FINITE-ELEMENT ANALYSIS OF LACE SYSTEM

A NASTRAN finite-element analysis has been performed on the LACE system in its nominal operational configuration. This configuration has the gravity gradient boom at 45.72m (150 ft), the retro-boom at 45.72 m (150 ft), and the balance boom at 22.86 m (75 ft). The lowest four modes are shown in figures 6 and 7 with the frequencies and mode shapes from two different perspectives. The spacecraft coordinate system is as shown in figure 5. The first 7 modes are as follows:

mode #	frequency in Hz	mode type
1	.0194	transverse
2	.0473	"
3	.0536	"
4	.1104	"
5	.1808	"
6	.2019	"
7	.2304	torsion

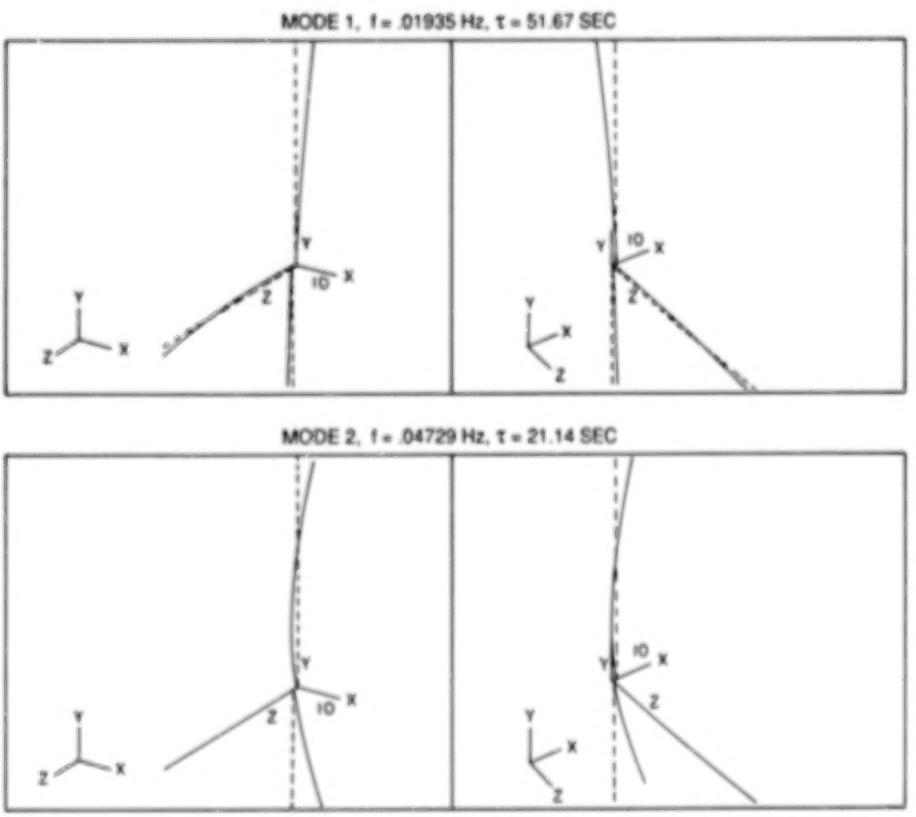


Figure 6

FINITE-ELEMENT MODELLING: LACE BUS MASS PROPERTIES

The finite-element modes were computed using the following weights, inertias and products of inertia about the LACE bus mass center; the boom masts and tip masses are not included. (Fig. 7.)

Weight	1177.68 kg	(2596.33 lb)
I_{xx}	1448.67 kg-m^2	(1068.48 slug-ft^2)
I_{yy}	1426.43 "	(1052.10 ")
I_{zz}	1026.16 "	(756.86 ")
I_{xy}	3.61 "	(2.66 ")
I_{xz}	19.985 "	(14.740 ")
I_{yz}	14.86 "	(10.959 ")

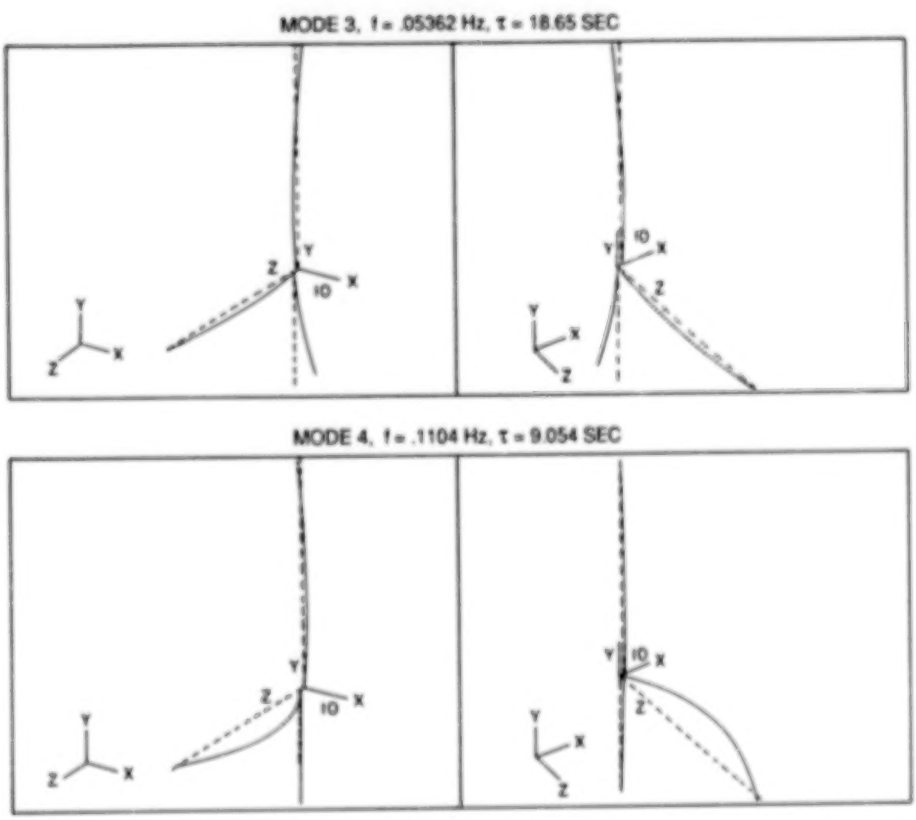


Figure 7

FLEXIBLE SYSTEM DYNAMICS IN THE SPACE ENVIRONMENT

The flexibility of the LACE spacecraft complicates the dynamical interaction of the system with the space environment even though the system modal frequencies, with the lowest mode of .019 Hz, are widely separated from the gravity gradient pitch libration frequency of $2.3 * 10^{-4}$ Hz. One complication, for example, is that elastic deformations from environmental stresses can generate 2nd order changes in the system inertial properties and thereby modify the biases in roll, pitch and yaw that apply to rigid-body spacecraft. Another complication is mode coupling generated by thermoelastic deformations. The environmental stresses include components that are time dependent functions of orbital motion and spacecraft orientation, as well as components that are more steady-state such as atmospheric drag.

The estimation of the magnitude of these effects is part of the LACE flight dynamics experiment. The study is proceeding by means of the DISCOS and TREETOPS simulation programs (reference 3**), using system vibration modal data obtained from a NASTRAN finite-element program. A 3 -D model of the boom structure has been developed with NASTRAN, to estimate the thermoelastic distortions generated by solar heating. (Fig. 8.)

**TREETOPS is a simulation program written by R.P. Singh and R. J. Vandervoort of Dynacs Engineering Co., Inc., Clearwater, Florida, under contract to Marshall Space Flight Center, Huntsville, Alabama.

Systems Dynamics in the Space Environment

- Structural deformations, vibrations, biases

  Gravity-gradient torques: LACE pitch freq ~ $2.3 * 10^{-4}$ Hz

  Atmospheric drag: changes with orbital decay

  Magnetic torques on damper at end of gravity-gradient boom

- Thermoelastic deformations from differential solar heating

  Mode coupling, effects on gravity gradient libration dynamics

NASTRAN modelling
DISCOS and TREETOPS simulations

Need to estimate magnitude of effects

Figure 8

EXPERIMENT DESIGN OVERVIEW

The experiment includes the modelling of the LACE system with NASTRAN and the multi-body simulation programs DISCOS and TREETOPS, together with environmental models of the atmospheric drag (reference 4), magnetic damping, and solar heating. An analysis of the on-orbit measurements requires a good estimate of system outputs through numerical simulation. Feedback between the measurements and predicted values enables upgrades of structural parameter estimations and environmental assumptions to improve the computer modelling. (Fig. 9.)

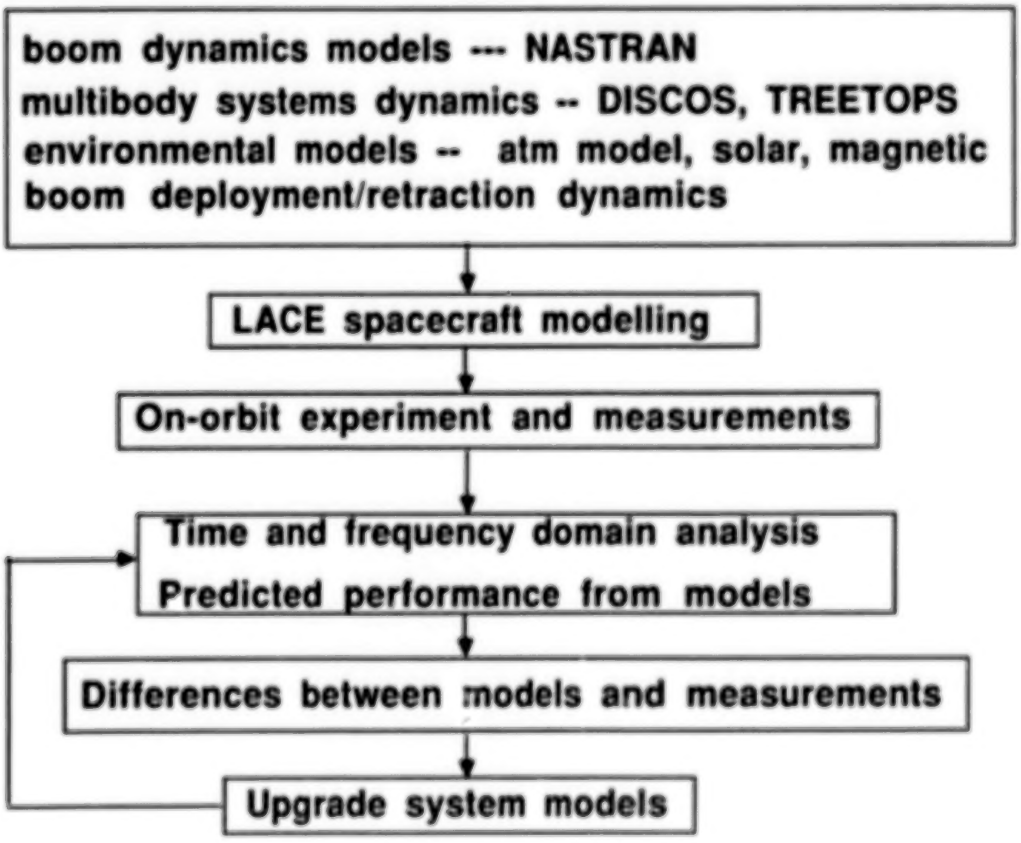


Figure 9

SCHEDULE FOR LACE FLIGHT DYNAMICS EXPERIMENT

Figure 10 shows the schedule for the experiment. Hardware procurement and integration on the LACE spacecraft is proceeding simultaneously with the LACE systems simulation. An analysis of expected sensor information requires inputs from simulation results. The projected launch of the LACE spacecraft is Fall, 1989. It is expected that valuable information will become available early in the LACE mission to allow an initial study of the dynamical behavior of the spacecraft. During the later phases of the 3 year projected lifetime, it is anticipated that the scheduling of boom deployments and retractions, together with a lower orbit and increased atmospheric drag, will allow for a thorough and complete analysis.

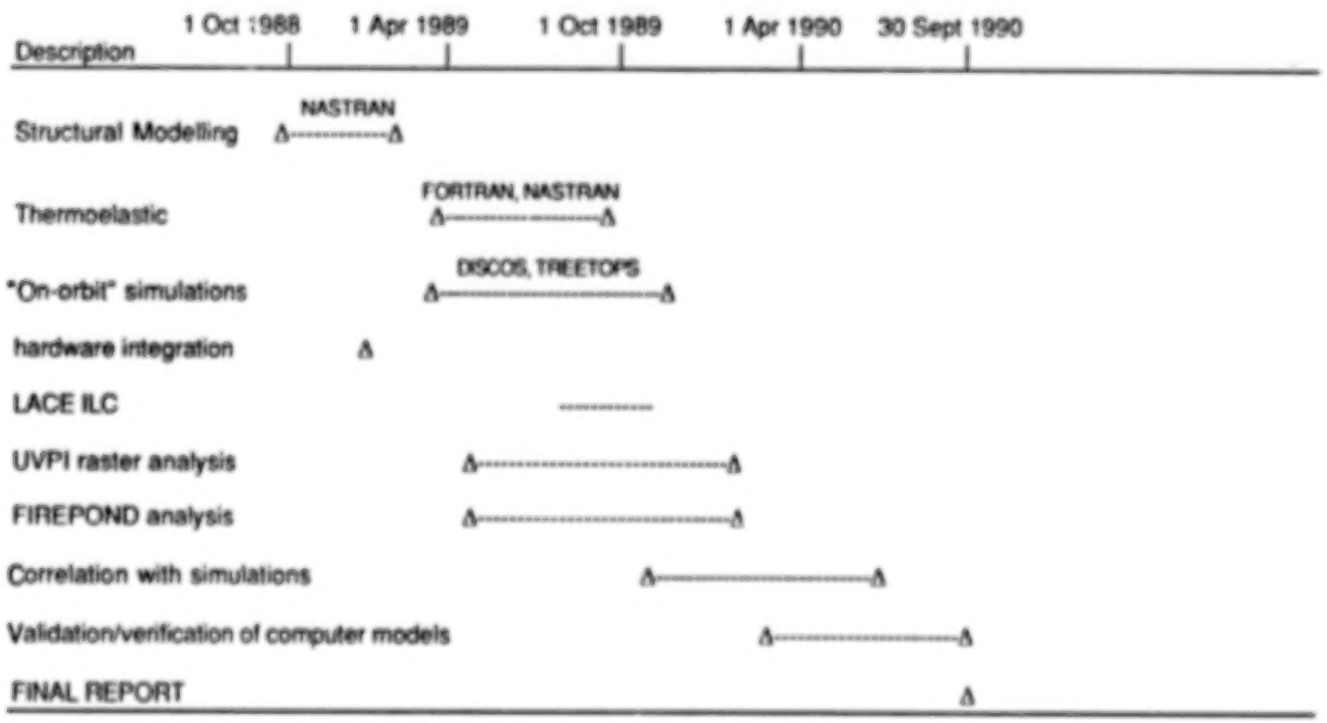


Figure 10

ACKNOWLEDGEMENTS

The author would like to thank J. Schaub and W. Adkins of the Spacecraft Engineering Department, NRL, for their assistance and cooperation in implementing the last-minute engineering modifications to LACE required by this experiment. D. Penn and D. Horan of the LACE spacecraft team have also been very helpful. He would also like to thank R. McClelland, an NRL contractor, for his assistance in design of the engineering modifications, and R. J. Dornsife of the US Army Corps of Engineers for assistance in the NASTRAN analysis. The author's supervisor, M. Brown, has been very supportive during the many phases of the development of this experiment. The experimental design was worked out by a committee composed of W. Keith Belvin of NASA, Langley, R. Sasiela of MIT Lincoln Laboratory, W.G. Stevenson and J. I. Perkins of Science Applications International Corporation, and Dr. G.K. Man of JPL. Useful discussions on the application of the FIREPOND lasar radar have been held with L. Sullivan and R.E. Knowlden of MIT Lincoln Laboratory.

REFERENCES

1. Leighton E. Young & Homer C. Pack, Jr.,"Solar Array Flight Experiment/Dynamic Augmentation Experiment," NASA Technical Paper 2690, National Aeronautics and Space Administration, Marshall Space Flight Center, Alabama, February 1987.

2. Steven C. Cohen and David E. Smith, "LAGEOS Scientific Results: Introduction," *Journal of Geophysical Research,* Vol. 90, No. B11, pages 9217-9220, September 30, 1985.

3. Bodley, C.S., Devers, A.D., Park, A.C., Frisch, H.P., "A Digital Computer Program for the Dynamic Interaction Simulation of Controls and Structure (DISCOS)," NASA Technical Paper # 1219, National Aeronautics and Space Administration, Goddard Space Flight Center, Greenbelt, Maryland, May, 1978.

4. Jacchia, L. G., "New Static Models of the Thermosphere and Exosphere with Empirical Temperature Profiles," SAO Special Report # 313, Smithsonian Institution, Astrophysical Observatory, Cambridge, Massachusetts, May, 1970.
   Jacchia, L.G., "Static Diffusion Models of the Upper Atmosphere with Empirical Temperature Profiles, " Smithsonian Contr. Astrophys., Vol. 8, No. 9, pp 215-257, 1965.

SPACE TRUSS ZERO GRAVITY DYNAMICS

Captain Andy Swanson
Air Force Wright Aeronautical Laboratories
Wright-Patterson AFB, Ohio

3rd NASA/DOD Control/Structures Interaction (CSI)
Technology Conference

29 Jan - 2 Feb 1989
San Diego Princess
San Diego California

OVERVIEW

The Structural Dynamics Branch of the Air Force Flight Dynamics Laboratory in cooperation with the Reduced Gravity Office of the NASA Lyndon B. Johnson Space Center (JSC) plans to perform zero-gravity dynamic tests of a 12-meter truss structure. This presentation describes the program and presents all results obtained to date.

I. HISTORICAL BACKGROUND

II. PROGRAM OBJECTIVES

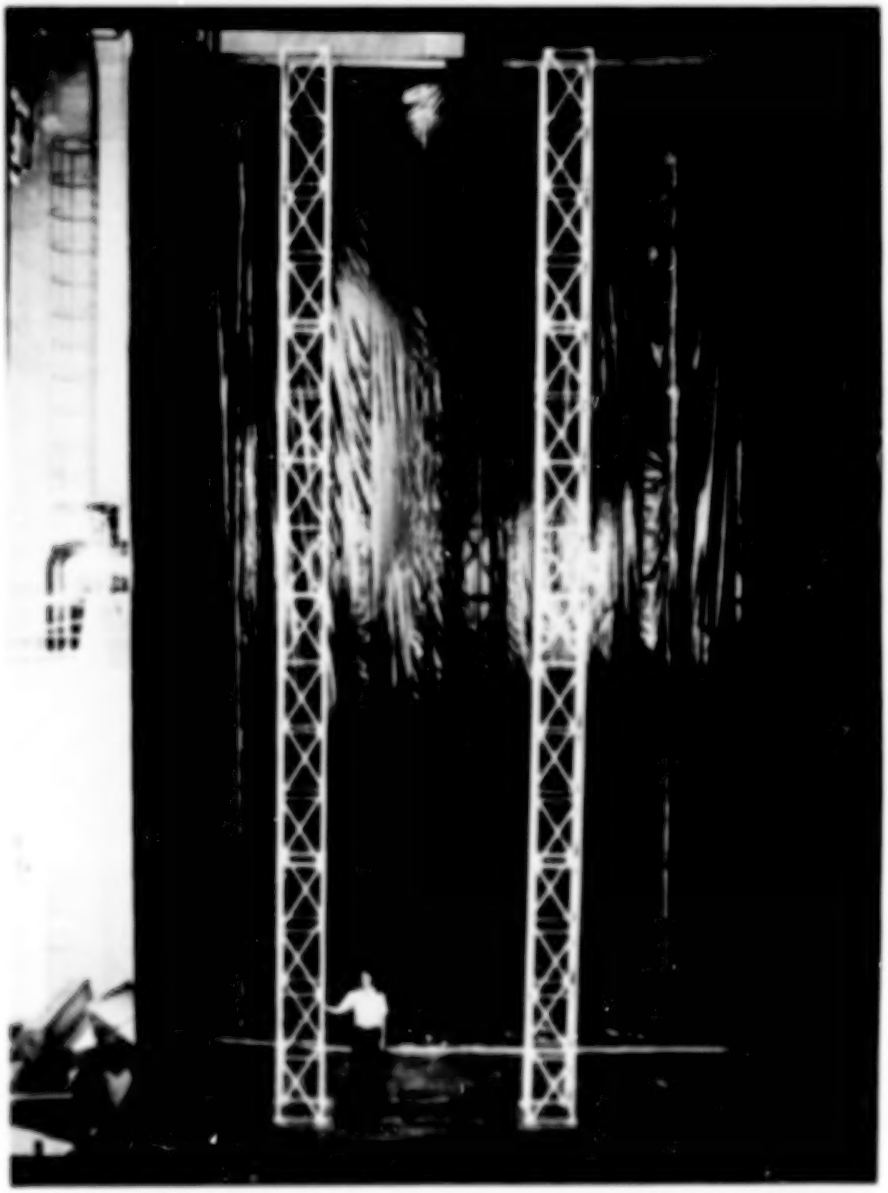
III. THE JSC FACILITY

IV. TEST SPECIFICS

V. CONCLUSIONS

BACKGROUND

The Flight Dynamics Laboratory's inhouse Large Space Structures Technology Program (LSSTP) is currently investigating methods for ground test and analysis of large space structures to predict on-orbit dynamic behavior. Two 12-meter truss structures were fabricated for analysis and modal characterization studies. These trusses are being tested in a cantilevered (see figure below) and a simulated free-free condition. Questions to be answered include how much damping a suspension device puts into the structure and the effect this has on the truss mode shapes and modal frequencies.



OBJECTIVES

A reduced gravity flight test will be performed to determine the 12-meter truss zero-g dynamic behavior for validation of space structure ground test and analysis methods. A primary aim of the test is to determine the effects ground suspension systems have on these structures. A secondary objective is to evaluate the reduced gravity aircraft facility for the testing of other large space structures.

- **DETERMINE EFFECTS OF SUSPENSION SYSTEMS ON LARGE SPACE STRUCTURE DYNAMICS**

- **EVALUATE REDUCED GRAVITY INSTRUMENTATION AND TEST ENVIRONMENT ON THE NASA AIRCRAFT**

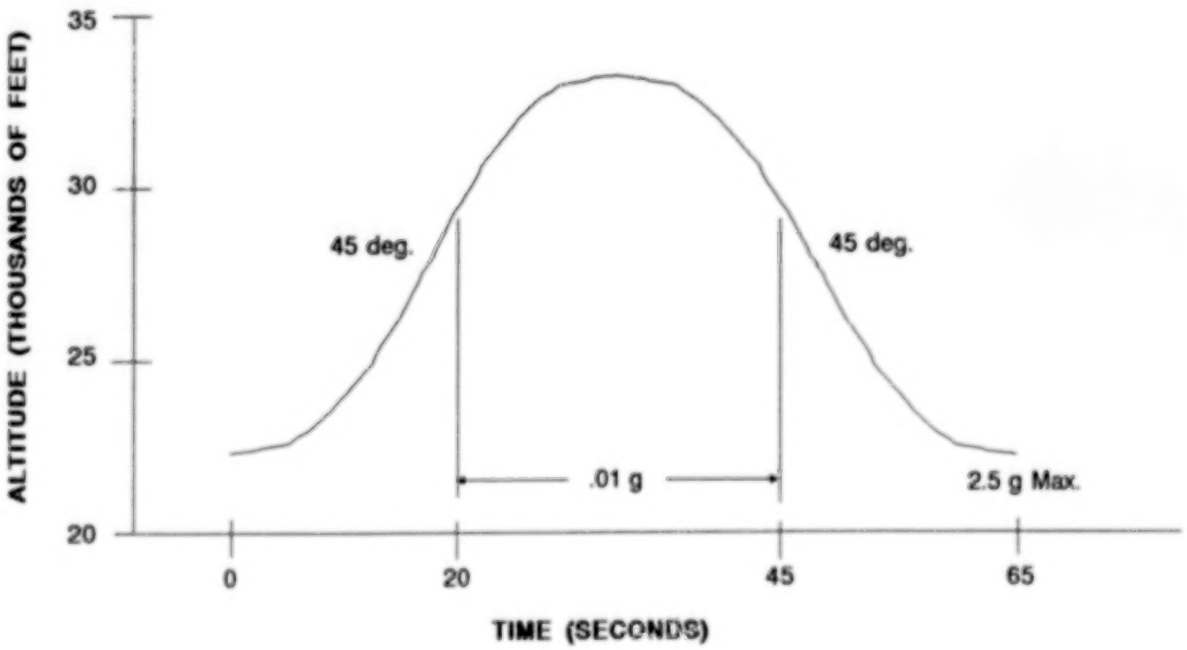
REDUCED GRAVITY FACILITY

The Reduced Gravity Office (RGO) of the Lyndon B. Johnson Space Center currently operates a modified KC-135A turbojet transport (see figure below) to provide a reduced gravity environment for research projects. The aircraft offers a sixty by six by ten foot test section, ample room for the truss and support equipment. Also available are 110V power, an attachment grid for securing test equipment, and audiovisual and test engineer support.



ZERO-g FLIGHT PROFILE

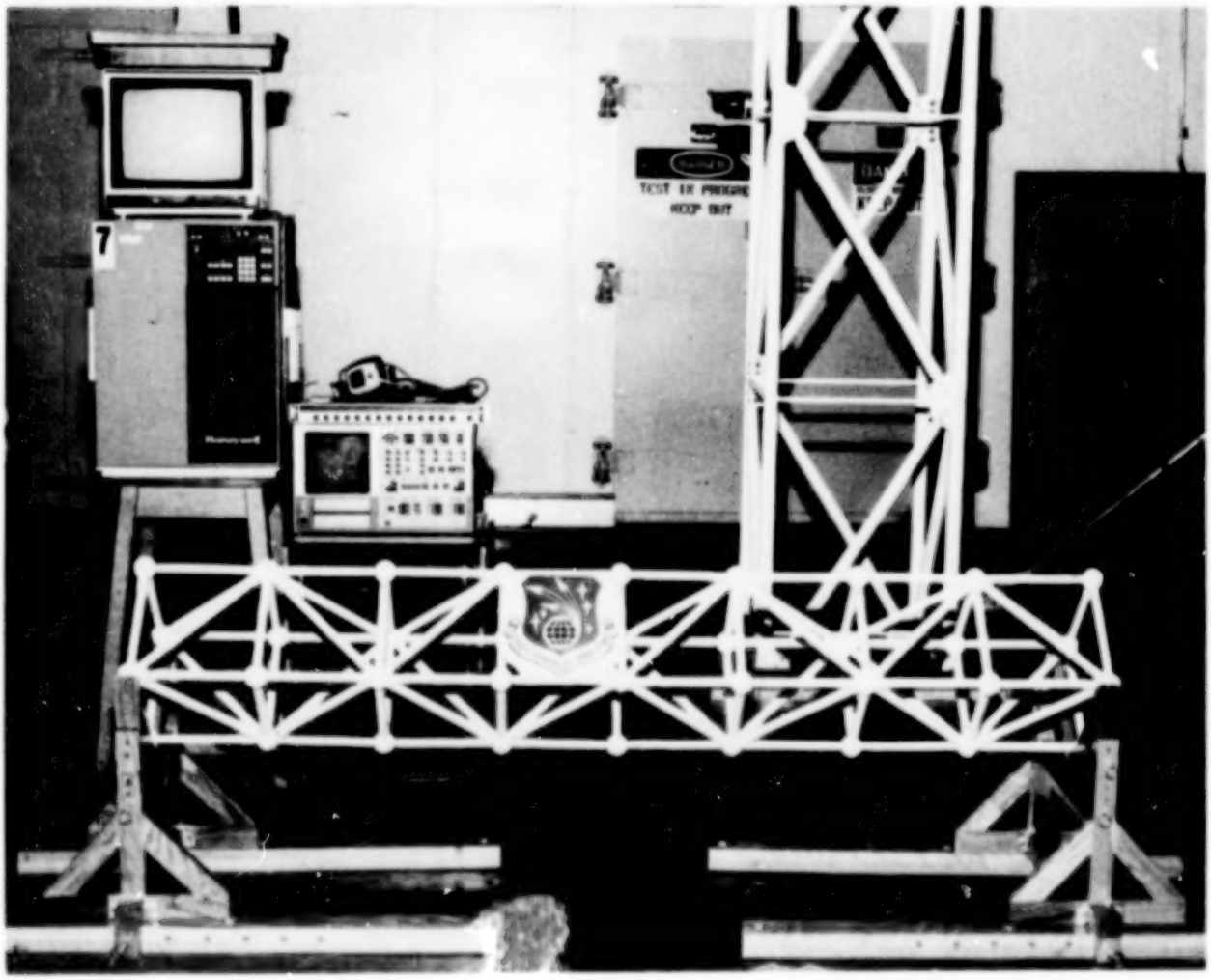
Zero-gravity (in reality, micro-gravity) will be achieved through parabolic flight profiles flown by the modified KC-135A. The RGO aircraft will provide up to forty 25 second intervals of zero gravity per flight by flying repetitive parabolic arcs as illustrated below.



PARABOLIC FLIGHT TRAJECTORY

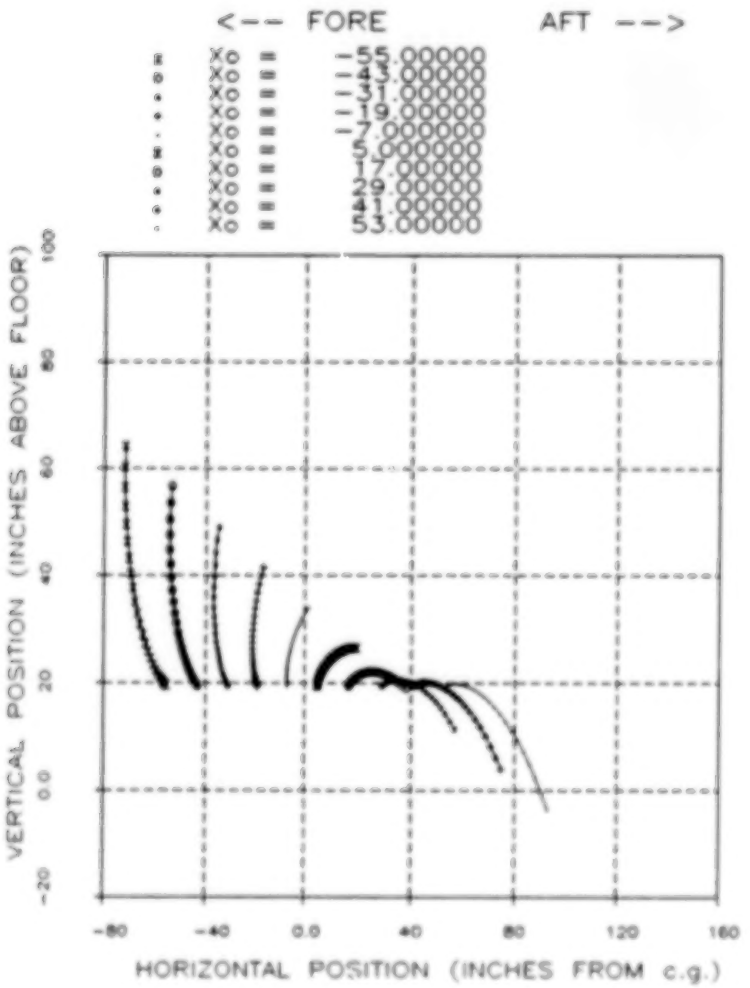
2-METER TRUSS

Preceding the tests of the 12-meter structure will be a series of ground tests and two flights with a two-meter truss. Because of the aircraft's mass distribution, it will be impossible to collocate its center of gravity with that of the truss. This will cause the truss to translate about the test section. The truss, shown below, will be released at different locations and its motion will be recorded with accelerometers and videotape. This first test will also measure the aircraft's deviations from the planned flight path. During the period of zero-g, the aircraft will be rotating at a constant rate of three degrees per second. If the truss is released during this period, its rotation will track that of the test section. Deviations from the nominal rotation rate will be important for the 12-meter truss and will be evaluated during the precursor flights.



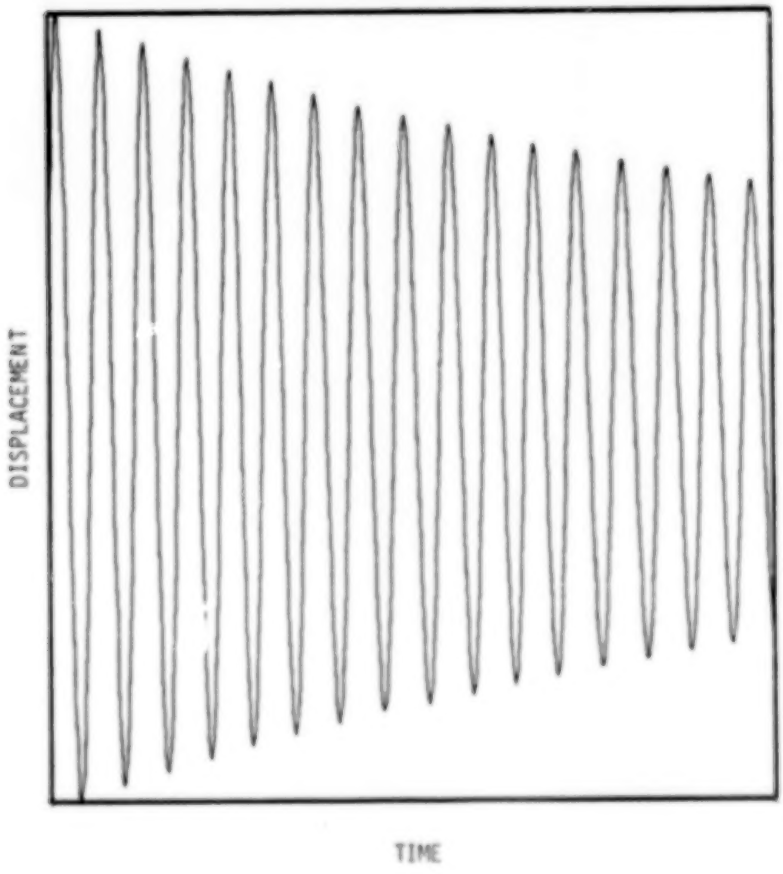
CENTER OF GRAVITY MOTION

The figure below shows the trajectory the center of gravity will take when released at different distances from the aircraft cg. In each case, the cg initially moves upward and eventually moves toward the rear of the aircraft. Total elapsed time is twenty-five seconds. Characterization of this motion is important so that the truss may be positioned to produce the least amount of travel and the longest test time. The advantage of placing the truss center of gravity close to the aircraft's center of gravity is clear.



MOTION ANALYSIS SYSTEM

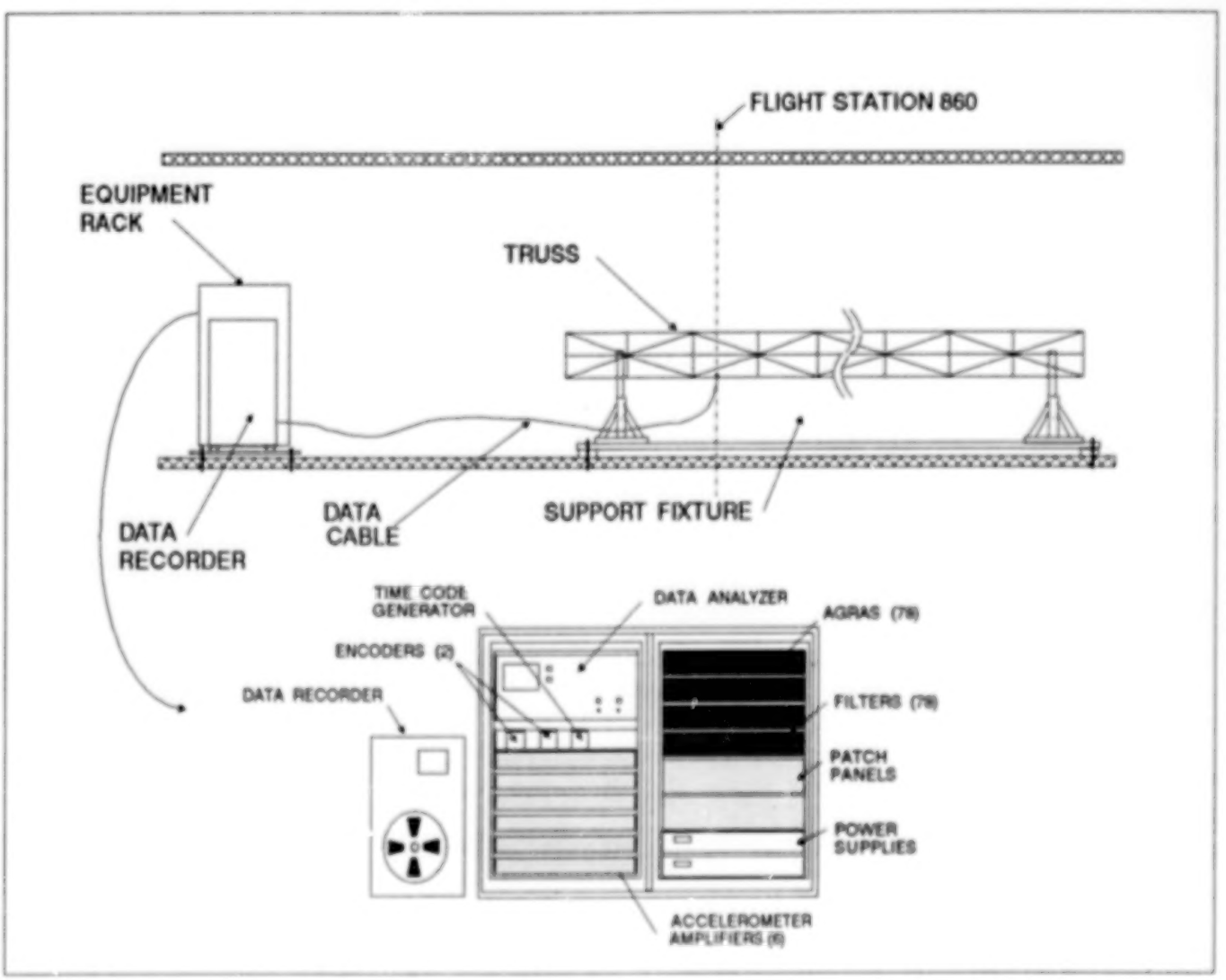
A set of light emitting diodes or pieces of retro-reflective tape will be fastened to the 2-meter truss and their translations recorded on videotape. The Motion Analysis System to be used operates on the motion of the centroids of the light sources (or reflectors) to calculate displacement, velocity, and acceleration. The figure below is from a bench test of a light emitting diode attached to an oscillating cantilevered beam. The Motion Analysis System will quantify the 2-meter truss rigid-body motion to verify the analytical predictions and to measure flight path deviations.



DATA ACQUISITION

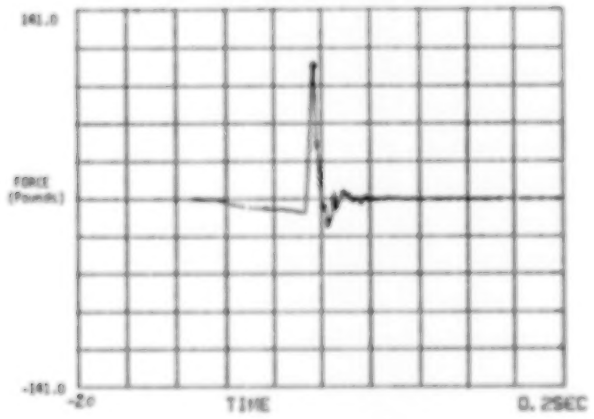
The 12-meter truss will be instrumented with 72 Structcel accelerometers. The accelerometers will be attached on every other bay, two positioned orthogonally at each corner. This arrangement is used to parallel the ground test setup to ease the comparison of results. The accelerometer signals will be amplified, filtered, multiplexed, and recorded on FM tape. A schematic of the test setup is shown below. During the test, data lines will be monitored real time on an FFT* analyzer and may be replayed during flight to verify that the system is operating properly.

*fast Fourier transform (FFT).



TRUSS EXCITATION

To provide excitation to the truss for modal parameter identification, impact devices have been fabricated from twenty pound-force solenoids. The devices may be oriented to produce both truss bending and torsion. An impact device and impulse function are shown below.





DIFFICULTIES AND SOLUTIONS

The difficulties particular to the reduced gravity test facility are listed in the figure below. The offset of the truss and aircraft centers of gravity causes the truss to drift. This effect can be minimized by proper initial location of the truss cg. The short (25 second maximum) test time adversely effects the low frequency resolution, especially important for lightly-damped structures. The effect can be minimized through analysis technique. The release of the structure without disturbance may also be difficult. Adding to the problem is the inherent aircraft noise and vibration. Analysis of release techniques will be investigated and the vibration environment will be measured. The aircraft vibration is likely to be well out of the bandwidth of the structure and may be eliminated with filtering and isolation. Finally, the roller-coaster environment may provide discomfort to the test crew. Backup crew and test experience appear to be the best solutions.

TEST DIFFICULTIES

- TEST ARTICLE MOTION
- SHORT TEST TIME
- TEST ARTICLE RELEASE
- DISCOMFORT
- AMBIENT AIRCRAFT NOISE/VIBRATION

SUMMARY

The Lyndon B. Johnson Space Center Reduced Gravity aircraft provides a low-cost, innovative means of validating large space structure ground test and analysis techniques. While the facility has its inherent difficulties, their effects may be eliminated or minimized through data analysis and test technique and equipment, training, and prudent selection of test article position.

UNITED STATES AIR FORCE ACADEMY GET-AWAY-SPECIAL FLEXIBLE BEAM EXPERIMENT

Captain Keith W. Bubb,
Major Steven E. Lamberson,
and Captain Thomas A. Lash

United States Air Force Academy
Colorado Springs, Colorado

NASA/DOD Control Structures Interaction Conference
1 February 1989

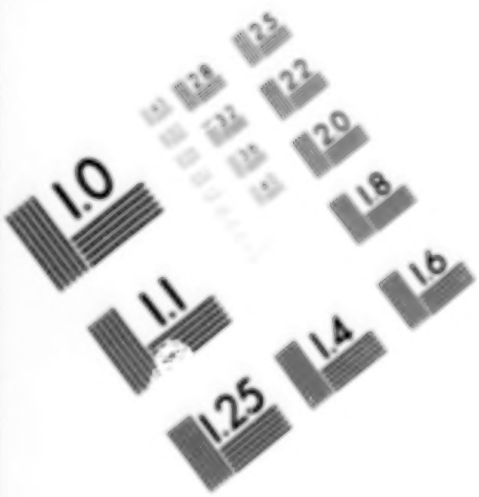
OBJECTIVES

The Department of Astronautics at the United States Air Force Academy is currently planning to fly an experiment in a NASA Get-Away-Special (GAS) canister. The experiment has been named the Flex Beam experiment and is being conducted jointly between the Department of Astronautics and Department of Engineering Mechanics. The experiment will allow the Departments to achieve several goals, both scientific and academic.

The primary technical objective of the Flex Beam experiment is to measure the damping of a thin beam in the vacuum and "zero G" environment of space. By measuring the damping in space, we hope to determine the amount of damping the beam normally experiences due to the gravitational forces present on Earth. This will allow us to validate models which predict the dynamics of thin beams in the space environment.

The experiment will also allow the Academy to develop and improve its ability to perform experiments within the confines of a NASA GAS canister. Several experiments, of limited technical difficulty, have been flown by the Academy. More complex experiments are currently planned and we hope to learn techniques with each Space Shuttle flight. Finally, we try to maintain some level of student involvement in our projects. This helps to motivate the cadets to strive for more challenging goals than pure coursework can offer.

- **Measure damping of thin beam in vacuum**
- **Validate models**
- **Develop GAS experiment capabilities**
- **Student involvement**

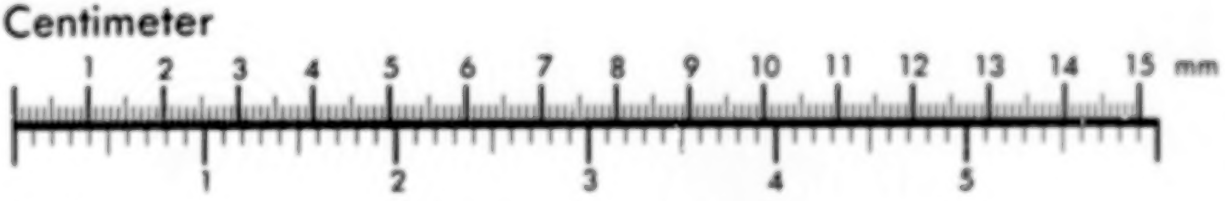


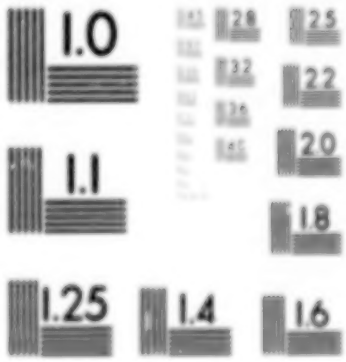


Association for Information and Image Management

1100 Wayne Avenue, Suite 1100
Silver Spring, Maryland 20910
301/587-8202











MANUFACTURED TO AIIM STANDARDS
BY APPLIED IMAGE, INC.

GAS CANISTER IMPLEMENTATION

We plan to physically implement the flex beam experiment in the GAS canister by using two thin stainless steel beams. One will be used as a control test condition to verify integrity of the data acquisition system. This beam will be put in a cantilever configuration, as the beam's natural frequency should not change in the absence of gravity. The second beam, which is the one of interest, will be put in a pinned-free configuration.

We will be measuring the motion of the beams with strain gauges placed along the beams at the points of maximum expected moment. Strain gauges will also be placed on the shim stock used to create the pinned end so the pendulum mode of the pinned-free beam can be measured.

The beams will be placed within the vacuum of space while the experiment electronics, data recorder, and batteries will be placed within a sealed container and maintained at approximately 1 atmosphere.

- **2 thin stainless steel beams - 2" x 24" x 0.025"**
- **Strain gauges at points of expected maximum moment**
- **Beams in vacuum of space**
- **Controller, recorder, batteries in sealed containers (1 atm)**

BEAM NATURAL FREQUENCIES

This chart shows the expected results of our experiment. We are planning to fly two stainless steel beams, one in a cantilever orientation and one as a pinned-free orientation. We will not be using a physical pin because of friction, but instead are using thin pieces of shim stock material bonded to the stainless steel beam. The frequency of the cantilever beam should not change based on the absence of gravity. We do, however, expect the frequencies of the pinned-free beam to change as shown on the figure.

Support Condition	Mode	Freq at 1 G	Freq in Space
Cantilever	**1 Bend**	**5.226 Hz**	**5.226 Hz**
	2 Bend	**32.75 Hz**	**32.75 Hz**
Pinned Free	**Pendulum**	**0.903 Hz**	**0.1 Hz**
	1 Bend	**22.92 Hz**	**22.92 Hz**
	2 Bend	**74.26 Hz**	**74.26 Hz**

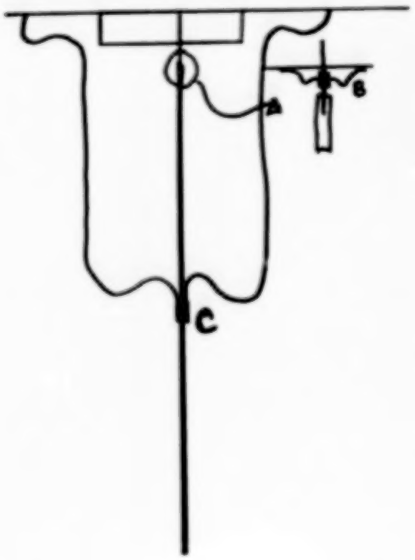
Note: An actual pin is not used due to friction. A thin shim is used instead.

BEAM STRUCTURES

The cantilever and pinned-free beam structures are shown in this chart. Also shown are the strain gauge locations envisioned using the placement method discussed earlier. Strain gauge locations are designated as A, B, or C and will be referred to later in this presentation.



Cantilever



Pinned-Free

ACTUATORS

The purpose of the actuators is to begin the vibration of the beams. Due to space and hardware limitations, we are planning on a maximum deflection of 1 inch. Regardless of the maximum deflection, we are interested in accurately knowing the deflection and being able to consistently repeat the deflection.

Another prime criteria for the actuators, as with all of our hardware, is low power consumption. Part of the problem with our first flight of this experiment was the lack of power once the experiment began operation. Cold soak of the batteries has been determined as the cause of failure with the dampers in the first flight.

- **Begin vibration of beams**
- **Known deflection - maximum of 1"**
- **Repeatable**
- **Low power consumption**

ACTUATOR POSSIBILITIES

Three types of actuators are currently under consideration. The first type we have experimented with is an electromagnet, which was used to pull the beams to start the vibration. This method adequately pulls the beams but we have so far experienced major problems with residual magnetism. This residual significantly affects the motion of the thin beams.

A mechanical striker was used on the first flight of our experiment, but we are not sure that we can implement one which will provide a known, repeatable deflection within the space and budget constraints we have. Another problem with a striker, assuming it operates in an "impulse" input fashion, is synchronization. The pinned-free beam must be deflected at the free end and part way up the beam simultaneously if we wish to achieve a symmetrical input (which we do). Again, our concern is the ability to develop high precision strikers in our budget.

The final option we will investigate is a push-pull rod concept. This would act much as a linear solenoid but must provide the ability to quickly retract the rods to let the vibration begin. This method also has synchronization concerns as well as the potential problem of limited maximum beam displacement.

- **Electromagnets**
  - **Meet objectives**
  - **Residual magnetism problems**
- **Mechanical striker**
  - **Simple to implement**
  - **Synchronization difficulty**
- **"Push-pull" rods**
  - **Space qualified solenoids - cost**
  - **Maximum displacement limited**

DAMPERS

The dampers are used to hold the free end of each beam fixed during all non-experiment times. In addition, they will be used to stop any remaining vibration in the beams between experiment samples.

Like the actuators, low power consumption is a requirement for the dampers. We are searching for on/off dampers which will move when power is applied and hold their position once power is removed. Thus far, the linear solenoids we have tested will not hold their position unless power is continuously applied. This was the cause of failure in our last flight and we are not willing to accept this problem again.

In our search for dampers, we may once again arrive at a "home grown" solution by designing our own mechanisms rather than purchasing something off the shelf. Our other concerns to date have been the cost of vacuum rated solenoids and the limited linear displacement available on the solenoids we have found.

- **Hold free end of beam during non-experiment times**
- **Stop vibrations between experiment samples**
- **Space qualified solenoids**
  - **Cost**
  - **Maximum displacement of 1"**

SEQUENCE OF OPERATIONS

For those not familiar with GAS operations, a brief statement may help. Once NASA has closed the relays, everything else in the experiment must be self contained. This means that the sequence of operations must be programmed to begin once the main power relay is closed.

For our experiment, we will repeat the test 20 times. We have a 45 minute time limit for data recording because of the data recorder we are using. Therefore, we want to allow about 2 minutes of vibration data for each sample, with a total of 20 samples. The remaining 5 minutes will allow 15 seconds for the dampers to close, stop the vibrations, and use the actuators to start the vibrations again.

At the end of this sequence the dampers will remain closed, the recorder will shut down, and NASA will open the main power relay to the canister.

- **NASA relay closed - activate experiment**
- **Start Recorder**
- **Open dampers to release free ends of beams**
- **Activate vibration actuators**
- **Wait 1 minute**
- **Close dampers to stop remaining vibration**
- **Repeat vibration tests for 40 minutes**
- **Stop Recorder**
- **NASA relay opened (experiment shutdown)**

DATA REDUCTION

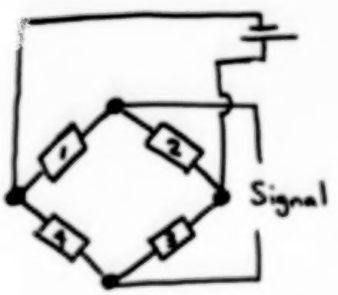
This chart shows the strain gauge locations planned. By designing the strain gauge circuit in a simplified wheatstone bridge arrangement, we are able to achieve compensation for thermal, axial, and torsional distortions which might otherwise appear in the data. Each strain gauge location planned will actually consist of this bridge arrangement. We will record time histories of the strain at each gauge location by means of an analog data recorder. The expected resolution of the data is 1 microstrain.

Strain Gauge Locations



Compensation Achieved

Thermal
Axial
Torsion



Simplified Wheatstone Bridge

Time histories will be obtained at each strain location
Expected Resolution: 1

RESOLUTION

This chart indicates the peak moment, peak strain, and percent of resolution available for strain location. The information is broken out by beam type, strain location, and vibration mode.

Cantilever Beam

Mode	Location	Peak Moment	Peak Strain*
1 Bend	A	5.713 in-lb	76.2
2 Bend	A	1.07 in-lb	14.3

Pinned-Free Beam

Mode	Location	Peak Moment	Peak Strain*
Pendulum	B	0.013 in-lb	207.9
1 Bend	B	0.051 in-lb	817
1 Bend	C	18.54 in-lb	247.5

* Values are in microstrains

VACUUM OPERATIONS

The requirements we face for operating part of our GAS canister experiment in a vacuum are indicated here. Most of these are expected kinds of requirements, but all of them are new for our department because of the limited experience we have with hardware in space. Much of our time is being spent searching our suppliers for the equipment. Another block of time is being spent and will be spent learning just what these requirements translate to in terms of actual hardware. These difficulties are the price we pay to become experienced in space operations and we expect this Flex Beam experiment to teach us a lot about GAS canister experiment design as well.

- **Space Qualified Parts**
  - **Electrical Connectors**
  - **Solenoids and Acuators**
- **Maintain Pressure for Electronics**
  - **Sequencer / Controller**
  - **Analog Tape Recorder**
  - **Power Supply**
- **Difficulties**
  - **Source for solenoids and actuators**
  - **Material selection: gaskets, glue**

PRE-FLIGHT TESTING

All good scientific experiments involve large amounts of testing, some with actual hardware, some with simulation. We plan to perform extensive hardware testing prior to turning our experiment over to NASA for flight. We want to insure our hardware is reliable, our expected results are reasonable, and our reason for space flight is valid.

The tests are aimed at determining the amount of atmospheric damping present at various atmospheric pressures. To accomplish this, we will test the system at a constant temperature with various atmospheric pressures. Testing will also be done to determine any temperature dependent damping the stainless steel beams may possess. Testing at cold temperatures will also provide important reliability information about our experiment hardware.

Test Description	**Objective**
Ground Test - 1 Atmosphere	**System Checkout - Benchmark**
Ground Test -	
Reduced pressures to near vacuum (constant Temp)	**Pendulum mode - Damping vs Air Pressure**
Reduced temperatures to -35 C (constant pressure)	**Damping vs Temperature**

SCHEDULE MILESTONES

The schedule for this experiment is shown below. If the actuator and damper mechanisms are determined by March 1989, hardware assembly should be complete by May or June 1989. This is only possible if we locate readily available off the shelf equipment. Hermetic electrical connectors currently look like the problem area in terms of cost and availability.

The schedule allows for testing throughout the summer with data reduction following. Once we are convinced of the validity of our test data and rationale for flight, we will inform NASA that we are ready for launch. From that time on, it becomes a waiting game.

June 1989	**Hardware Assembly Complete**
September 1989	**Pre-Flight Testing Complete**
October 1989	**Test Analysis Complete**
?????	**Shuttle Flight**
??? + 2 months	**Flight Data Analysis Complete**
??? + 3 months	**Report Complete and Available**

FOLLOW-ON RESEARCH

The Departments of Engineering Mechanics and Astronautics are currently working together on a six-foot hanging beam experiment. Some of the experiment goals deal with validating predicted modes of vibration and examining the effects of actuator placement on the beam's dynamics. These will both be accomplished using simple open loop configurations.

The goals also include closing the loop on the actuators and validating the closed loop performance of the vibrating beam with the pendulum mode involved (since the beam is under the gravitational attraction of Earth). The experimenters would then like to project what closed loop performance might be achieved when the pendulum mode is not present, as in space.

Finally, we hope to eventually develop a GAS canister implementation of this experiment with actuators operating in closed loop to try and verify the earlier projections.

Six - foot Hanging Beam Experiment

- **Open Loop**
  - **Validate Predicted Modes (including Pendulum)**
  - **Examine Effects of Actuator Placement onDynamics**
- **Closed Loop**
  - **Validate Closed Loop Performance with Pendulum Mode**
  - **Project Closed Loop Performance without Pendulum Mode**
- **Develop GAS canister implementation of experiment**

CSI TECHNOLOGY VALIDATION ON AN LSS GROUND EXPERIMENT FACILITY

S. J. Wang
D. B. Eldred
Jet Propulsion Laboratory
California Institute of Technology
Pasadena, California

The Third NASA/DOD CSI Conference
January 30 - February 2, 1989
San Diego, California

Flexible Spacecraft Control Dynamics
Simulator Development

For the last 10 years, JPL has been actively engaged in the development of new technologies for the identification and control of large flexible space structural systems. The objectives have been developing both new concepts, theories, and hardware, as well as to extend state-of-the-art methodologies to a breadboard level of maturity for in flight applications. To accomplish this, technology validation through experimental demonstration on a real physical structure becomes necessary.

Recognizing this need, JPL, under the joint sponsorship of the Air Force Astronautics Laboratory (AFAL) and NASA Office of Aeronautics and Space Technology (NASA/OAST), has developed a large ground structure test bed called: Flexible Spacecraft Control Dynamics Simulator.

The experiment structure, which is best described as resembling a large space antenna, was designed to possess generic LSS properties, particularly multiple, densely packed, lightly damped vibration modes. Multiple sensors and actuators are distributed throughout the structure, and a microcomputer workstation and a data acquisition system, together with an advanced programming environment (implemented in Ada), facilitate control experiments on the Simulator system.

- **OBJECTIVE**
  - DEMONSTRATE AND EVALUATE NEW, EVOLVING AND CRITICAL CONTROL METHODOLOGIES ON A REALISTIC LARGE FLEXIBLE STRUCTURE WITH PRACTICAL HARDWARE AND COMPUTATIONAL RESTRICTIONS
- **EXPERIMENT STRUCTURE**
  - RESEMBLES A LARGE ANTENNA
  - 40 MODES BELOW 5 Hz
  - 30 SENSORS AND 14 ACTUATORS
  - MICROCOMPUTER WORKSTATION CONTROL AND COMPUTERIZED DATA ACQUISITION SYSTEM
  - ADVANCED PROGRAMMING ENVIRONMENT
- **TARGET METHODOLOGIES FOR EVALUATION**
  - ADAPTIVE AND RECONFIGURABLE CONTROL
  - ROBUST AND DISTRIBUTED CONTROL
  - SYSTEM PARAMETER IDENTIFICATION
  - SHAPE DETERMINATION AND CONTROL
  - ADVANCED OPTICAL SENSING TECHNOLOGY

Experiment Structure

Figure 1 shows a schematic overview of the experiment structure. The main components of the structure consist of 12 ribs, the central hub, the flexible boom, and the feed mass. The overall diameter of the structure is 18.5 feet. Each of the steel ribs is supported at two locations by zero-stiffness "levitators" in order to prevent excessive sag due to gravity. A levitator consists of a counterweight hanging over a low friction pulley. This suspension design provides a nearly constant supporting force throughout a large range of motion. The ribs are each rigidly attached to the central hub which consists of three concentric rings constructed from tubular steel. The inner ring is rigidly mounted to the backup structure via a bipod arrangement. The center ring is attached to the inner ring via two flexure bearings, and it rotates about an axis which lies in the horizontal plane. The outer ring, which contains the rib mounting pads, is attached to the center ring via two more flexures.

The three rings together comprise a gimbal mounting arrangement. A flexible boom hangs downward, and a 10 pound weight hangs from its lowest point, simulating the feed and flexible feed boom of a large flexible antenna.

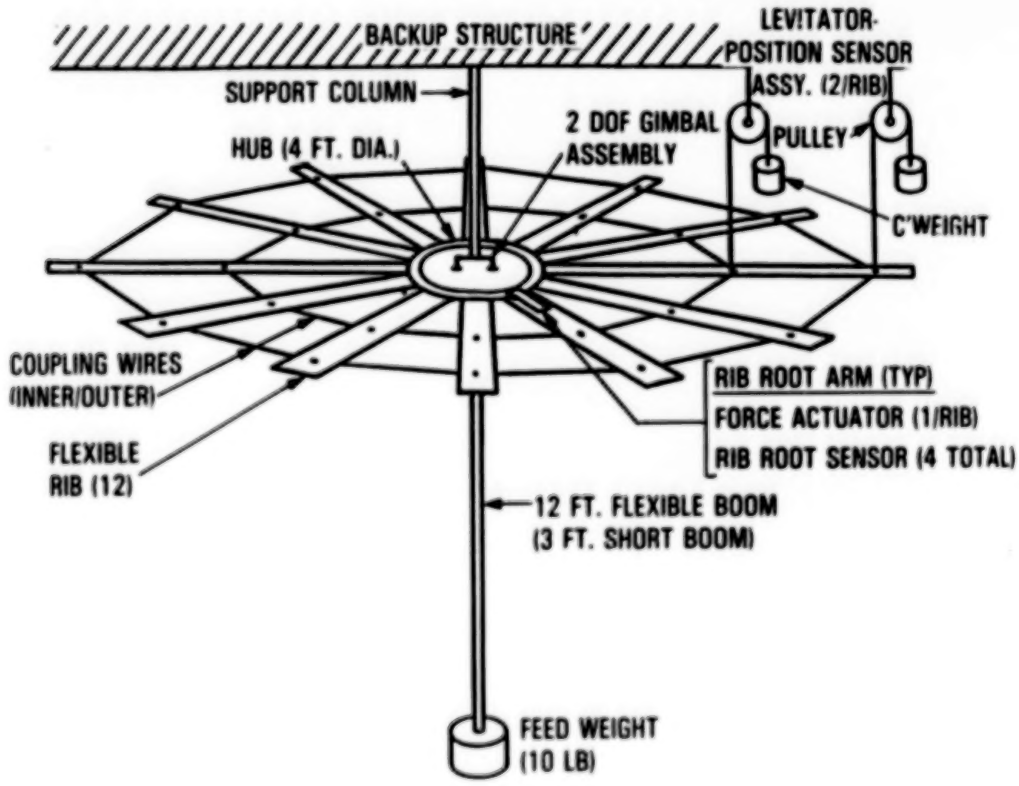


Figure 1.

Figure 2 shows a photograph of the experiment structure and supporting hardware. The 12 ribs and the gimbal-hub are painted white for visibility. The rib-to-rib coupling is provided by the two rings of pretensioned steel wires which can be identified by the tapes attached to them. Above the experiment structure is a backup structure which provides precision mounting for the levitators and for the hub gimbal bearings, and hence, for the entire experiment structure. The supporting structure is constructed of truss members and tension cables, and its lowest vibration frequency is 15 Hz; this high stiffness is sufficient to prevent interaction with the experiment structure.

The cables extending upward from the top of the backup structure allow the entire structure to be raised to the 20-foot level to allow for sharing of the laboratory with other programs.

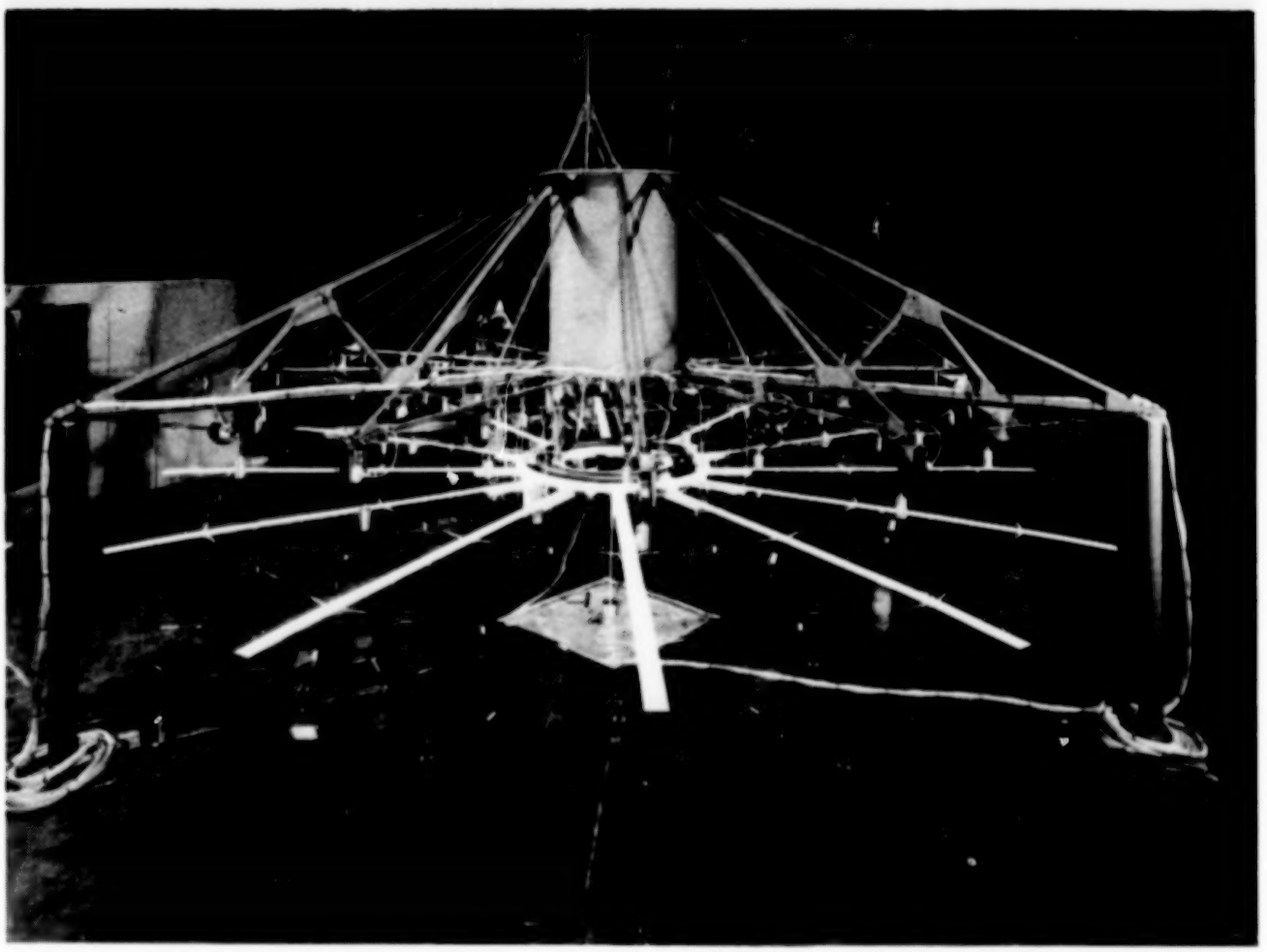


Figure 2.

Transducer Locations

Sensing instrumentation includes 24 levitator sensors, 4 rib-root sensors, and 2 hub-angle sensors, whose locations are shown in Figure 3. The levitator sensors consist of optical incremental encoders which are integrated with the levitator pulleys and measure pulley rotation. The rib root sensors employ LVDT's (linear variable differential transformer) to measure rib displacement at locations near their attachments to the hub, relative to brackets attached rigidly to the hub. The hub angle sensors are RVDT's (rotory variable differential transformer) which are mounted coaxial with the hub gimbal bearings and thus measure hub rotation about its two gimbal axes.

Actuation includes 12 rib-root actuators and 2 hub torquers. The rib-root actuators consist of linear voice-coil devices which react between the ribs and the rib-root sensor brackets. They are mounted close to the rib-root sensors to provide essentially collocated sensing and actuatuation. The hub torquers are non-contacting linear motors which react between the hub and the backup structure, thereby applying torques to the hub. These actuators use a flat air-core armature coil which passes between the poles of a larger permanent magnet.

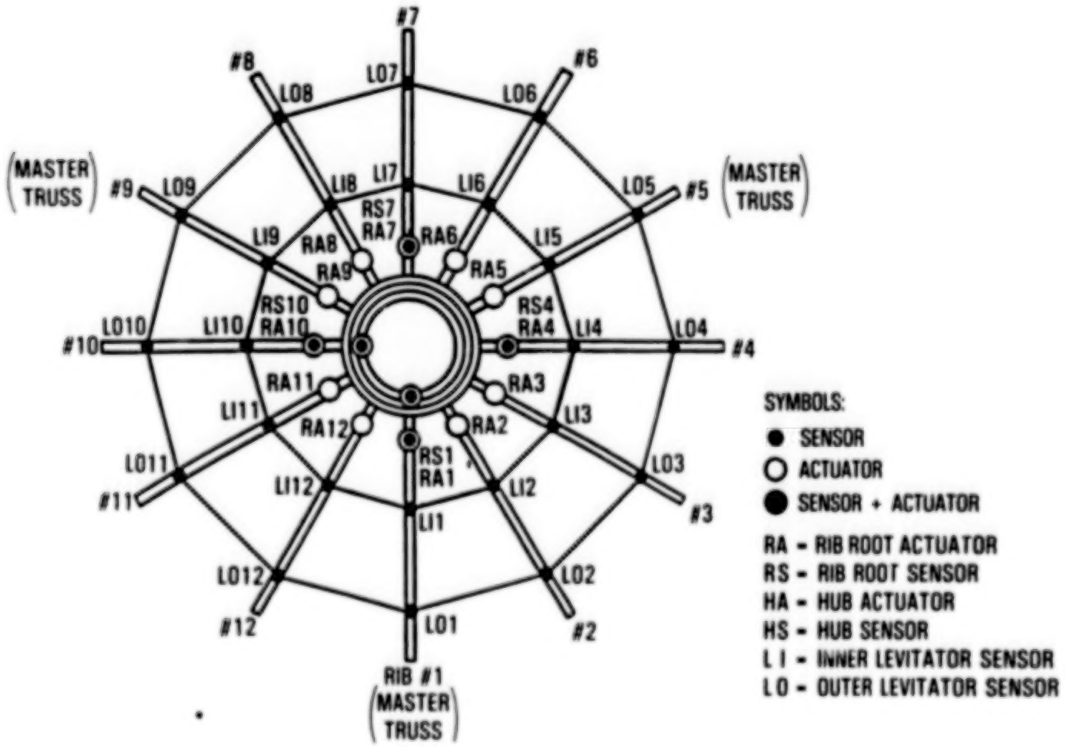


Figure 3.

Normal Modes

The following tables show the vibration modes of the experiment structure with higher modes (above 10 Hz) truncated from the lists. The modes are divided into two groups: the boom-dish modes and the dish modes. The former are the anti-symmetric modes about the central hub, and the later are the symmetrical ones. The distinguishing property of the antisymmetric modes is that these modes include rotation of the gimballed hub, whereas the hub remains stationary for all the symmetric modes. Table I shows the boom-dish modes when the short boom, 3 feet in length, is used, whereas Table II shows those corresponding to the long boom which is 12 feet long. As designed, the modes are densely packed with the lowest modal frequencies of 0.91 Hz and 0.112 Hz depending on what boom is attached to the system. There are 39 modes below 5 Hz in the system with the short boom, and 41 with the long boom arrangement. Dish modes are shown in Table III.

I. BOOM-DISH MODES
(SHORT BOOM CONFIG)

FREQUENCY (HZ)	PIVOT AXIS
0.091	4-10
0.091	1-7
0.616	4-10
0.628	1-7
1.685	4-10
1.687	1-7
2.577	4-10
2.682	1-7
4.858	4-10
4.897	1-7
9.822	4-10
9.892	1-7

II. BOOM-DISH MODES
(LONG BOOM CONFIG)

FREQUENCY(HZ)	PIVOT AXIS
0.112	4-10
0.113	1-7
0.332	4-10
0.332	1-7
0.758	4-10
0.774	1-7
2.264	4-10
2.354	1-7
4.724	4-10
4.726	1-7
4.926	4-10
4.967	1-7

III. DISH MODES (40)

FREQUENCY(HZ)	WAVE NUMBER	FREQUENCY(HZ)	WAVE NUMBER
0.210	0	4.656	0
0.253	2	4.658	2
0.253	2	4.658	2
0.298	3	4.660	3
0.298	3	4.660	3
0.322	4	4.661	4
0.322	4	4.661	4
0.344	5	4.662	5
0.344	5	4.662	5
0.351	6	4.663	6
1.517	0	9.474	0
1.533	2	9.474	2
1.533	2	9.474	2
1.550	3	9.474	3
1.550	3	9.474	3
1.566	4	9.474	4
1.566	4	9.474	4
1.578	5	9.475	5
1.578	5	9.475	5
1.583	6	9.475	6

Tables 1 – 3.

Model Characteristics

Figure 4 shows the plots of the first 12 lowest frequency mode shapes for this system with the short boom which is most commonly used in the experiments. The first (0.09 Hz) and the eighth (0.616 Hz) modes are boom-dish modes and the remainder are dish modes. Due to the symmetry of the structure, many of the modes come in degenerate pairs in that they have virtually identical frequencies and their mode shapes differ only by a phase angle. For higher frequency dish modes, these mode shapes become very close to linear combinations of contilevered rib modes, reflecting the reduced role that its coupling wires play in forming the mode shapes for higher frequency.

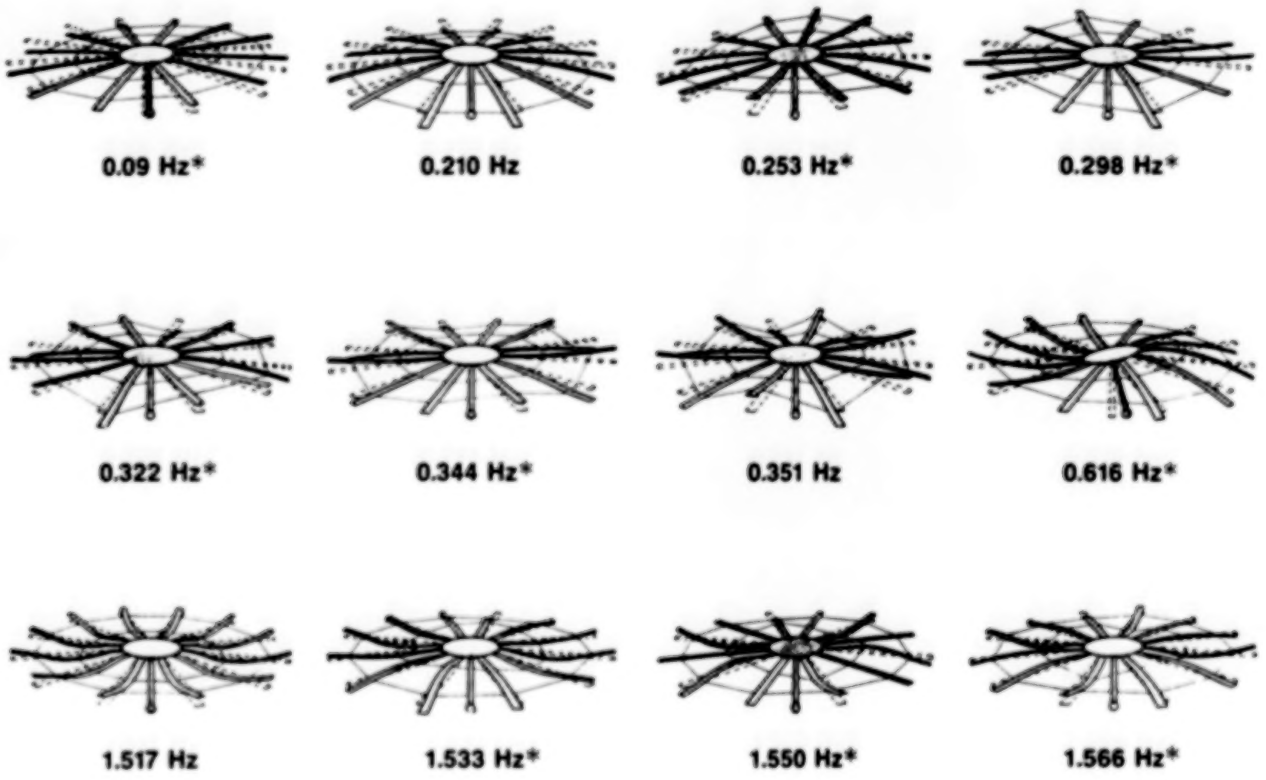


Figure 4.

Adaptive Transient/Deflection Regulation Experiment
(C. Ih, A. Ahmed, D. Bayard, S. Wang)

The objective of adaptive control technology research at JPL is to develop a subsystem adaptive control capability for future space mission applications. The overall approach involves a multilevel adaptation methodology in which a learning and decision making system is employed for high-level controller tuning and a servo level controller is used for adaptation to local properties such as drifting parameters, model uncertainties, and environmental disturbances. The purpose of these experiments is to validate the adaptive control technology on a physical flexible structure system and to demonstrate the controller's effectiveness and performance subject to large model parameter uncertainties, unmodeled dynamics, measurement noise, and dynamic disturbances.

The results of two phases of experiments are discussed here. The Phase I experiments employed two hub sensors and two hub actuators. The Phase II experiments used 6 sensors and 6 actuators consisting of 2 hub sensor and actuator pairs and 4 rib-root sensor and actuator pairs. (Fig. 5.)

OBJECTIVE

TO VALIDATE ADAPTIVE CONTROL TECHNOLOGY FOR UNCERTAINTY MANAGEMENT OF FLEXIBLE SPACE STRUCTURAL SYSTEMS

TO DEMONSTRATE THE EFFECTIVENESS OF ADAPTIVE CONTROL TECHNIQUES FOR TRANSIENT/DEFLECTION REGULATION ON A PHYSICAL PLANT

EXPERIMENT DESIGN

- **SENSORS:**
  - 2-AXIS HUB ANGLE SENSORS FOR CONTROL
  - 24 LEVITATION DISPLACEMENT SENSORS FOR MONITORING
- **ACTUATORS:**
  - 2-AXIS HUB TORQUERS
- **PLANT:**
  - INFINITE DIMENSIONAL AND LIGHT DAMPING
- **REF. MODEL:**
  - 2 MODES, HIGH DAMPING, AND LARGE PARAMETER UNCERTAINTIES (50-100%)
- **TRANSIENT REGULATION EXPERIMENT:**
  - REFERENCE MODEL AT QUIESCENT STATE
  - STRUCTURE EXCITATION USING HUB TORQUERS
  - ADAPTIVE CONTROLLER TO FORCE PLANT TO TRACK MODEL FOR VIBRATION SUPRESSION
- **DEFLECTION REGULATION EXPERIMENT:**
  - MANUALLY DEFLECT STRUCTURE
  - MODEL INITIALIZED TO APPROXIMATE STRUCTURE DEFLECTION
  - CONTROLLER TO FORCE PLANT OUTPUT TO TRACK MODEL OUTPUT
- **SAMPLING RATE:** 20 Hz

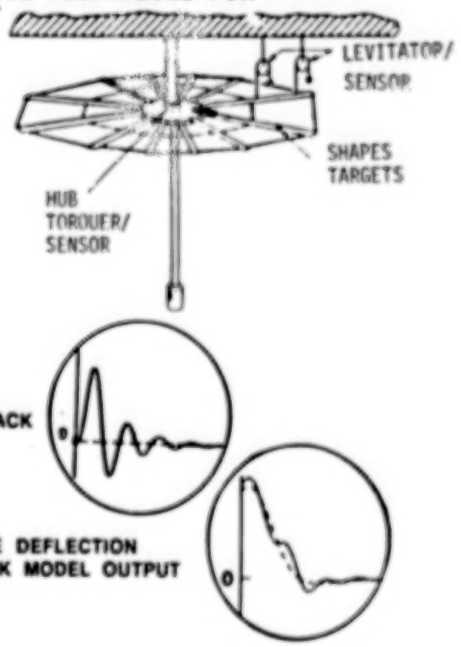
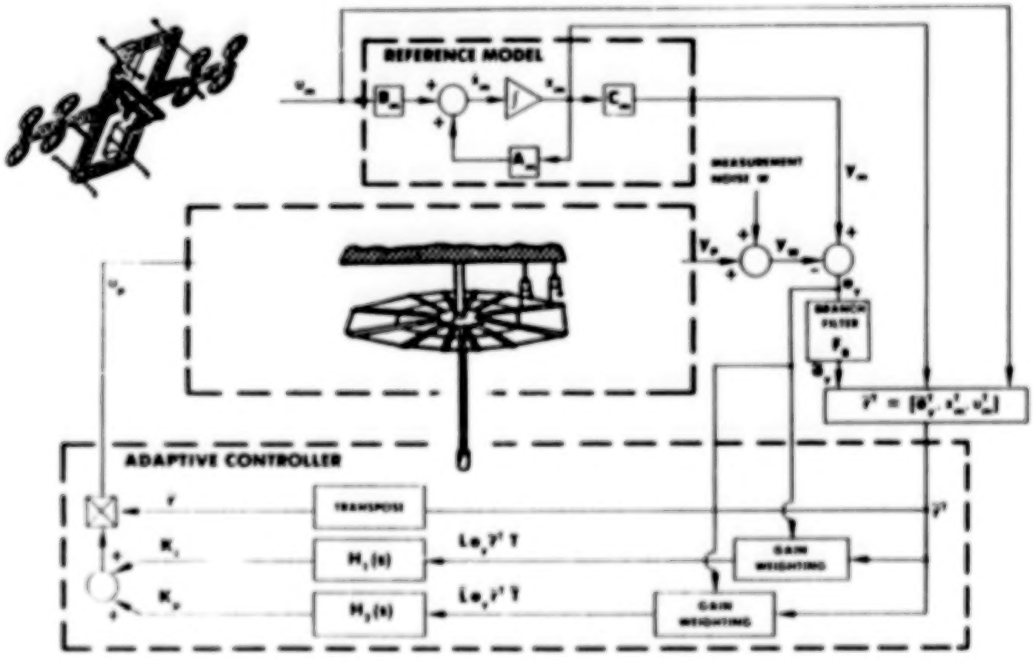


Figure 5.

Adaptive Control System

Figure 6 highlights the model reference adaptive control system concept implemented for the experiments. The system consists of a reference model, the plant, and the adaptive controller. The model is selected based on the knowledge of the plant and the desired performance of the system, and in general, is a low order and high damping system. The model is driven by u_m and its output is y_m. The output error e_y is formulated by comparing the model output with the noise corrupted plant output. The error signal is split into two paths: one fed to the branch filter and the other to the controller directly. Inside the controller, these signals along with the model inputs and states are pre- and post- multiplied by weighting matrices and then they are fed through SPR (strictly positive real) adaptive "filters" where the leakage terms are introduced for gain "retardation." Two sets of adaptive gains are generated: the integral gain K_I and the proportional gain K_P. The control signal u_p is generated by multiplying the gains by the filtered long vector $\bar{r}$.



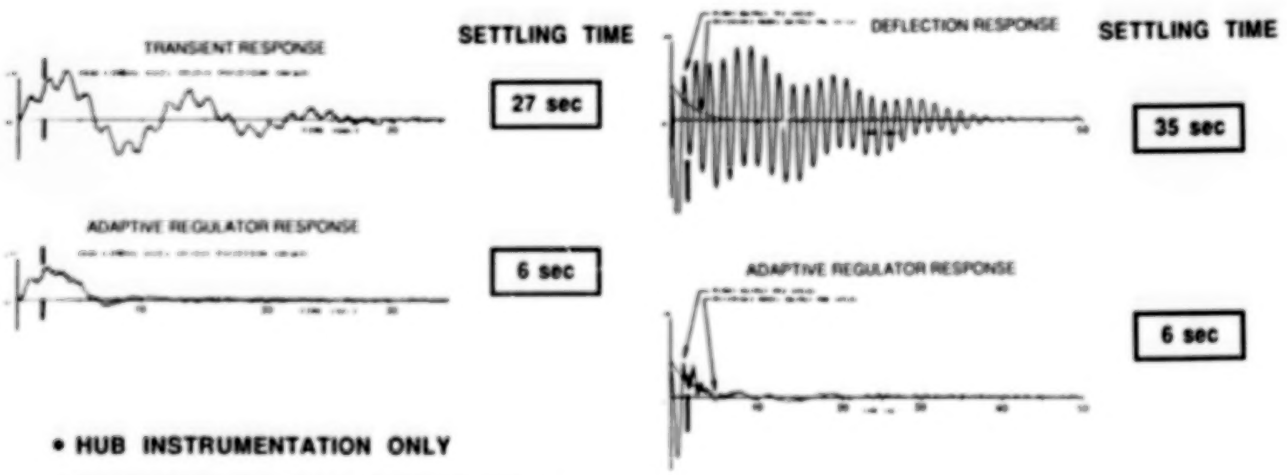
- **INNER-LOOP CONTROLLER TO STABILIZE RIGID BODY DYNAMICS**
- **INPUT GAIN WEIGHTING (L, $\bar{L}$) TO SPATIALLY DISTRIBUTE CONTROL EFFORT FOR REALIZING MULTI-OBJECTIVE DESIGN TRADES**
- **BRANCH FILTER/SPR ADAPTATION (F_B, H_1 (S), H_2 (S)) TO COMPENSATE FOR DESTABILIZING EFFECT OF MEASUREMENT NOISE**

Figure 6.

BEST COPY AVAILABLE

Adaptive Control Experiment I --
Transient/Deflection Regulation with Hub Sensing/Actuation

The left two plots show the results of the transient regulation experiment. The experiment structure was excited for 2 seconds. The free response shows at least two hub modes were excited: the 0.091 Hz and the 0.616 Hz. The results show a 4.5 to 1 improvement was achieved by the adaptive controller even with 50% - 100% uncertainty of the system parameters was assumed for the controller design. The other two plots show the results of the deflection regulation experiment. The data show that the plant followed the model very well with the transient damped out quickly. A 5.8 to 1 settling time reduction was observed. The controller is robust with high stability margin. (Fig. 7.)



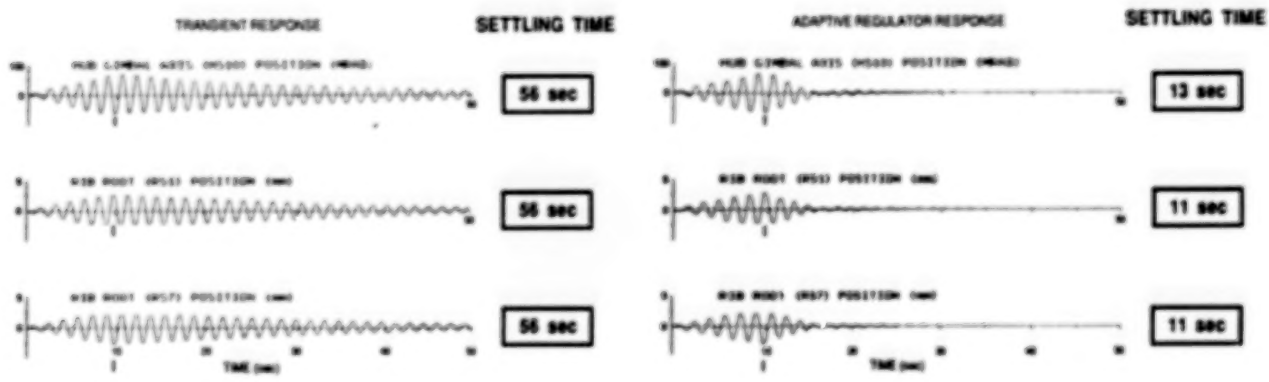
- HUB INSTRUMENTATION ONLY
- ESTIMATED HUB RATE SUBSTITUTED FOR RATE MEASUREMENT
- PLANT OUTPUT FOLLOWED SET POINT REFERENCE MODEL OUTPUT
- ACHIEVED HIGH RATE OF CONVERGENCE WITH LARGE KNOWLEDGE UNCERTAINTIES IN DESIGN

- PLANT OUTPUT TRACKED HIGHLY DAMPED REFERENCE MODEL OUTPUT AND CONVERGED RAPIDLY
- ACHIEVED 580% IMPROVEMENT OVER OPEN-LOOP SETTLING TIME

Figure 7.

Adaptive Control Experiment II --
Transient Regulation with Hub and Rib Sensing/Actuation

This experiment demonstrated the adaptive controller's performance for 6 inputs and 6 outputs (2 hub sensor/actuator pairs and 4 rib-root sensor/actuator pairs), again with high model uncertainties and truncation of unmodelled dynamics. The controller controls both boom-dish modes and dish modes. Because the sensor output is position and not rate, rates were estimated using a 24-state Kalman filter; this along with the computing hardware limitations has severely impacted on the performance of the controller. Even with these constraints, high performance has been achieved by the adaptive controller. (Fig. 8.)



- 6 INPUTS (2 HUB TORQUERS AND 4 RIB-ROOT ACTUATORS) AND 6 OUTPUTS (2 HUB ANGLE SENSORS AND 4 RIB-ROOT DISPLACEMENT SENSORS)
- ESTIMATED HUB AND RIB-ROOT RATES
- ACHIEVED HIGH PERFORMANCE WITH LARGE KNOWLEDGE UNCERTAINTIES IN DESIGN

Figure 8.

BEST COPY AVAILABLE

Vibration Damping and Robust Control
of Flexible Space Structure
Using μ-Synthesis Techniques
(G. Balas, C. Chu, J. Doyle)

This research employs μ-based control design methods for the analysis and synthesis of controllers for lightly damped flexible structures. The Flexible Spacecraft Control Dynamics Simulator provides a test bed for validation of this methodology and for exploration of critical robust control design issues.

The results discussed here (Experiment I) deal primarily with the design of a high performance vibration attenuation controller for the simulator using only the hub actuators and sensors and employing a design model with the first two global flexible modes. For robust control design, the effects of higher frequency modes of the structure were accounted for by the inclusion of high frequency unmodeled dynamics attenuation.

The μ-framework allows for the incorporation of structured and unstructured uncertainties of the plant model into the controller design. The focus of the research efforts is on robust control for flexible structures with both unstructured and structured uncertainties due to unmodeled dynamics, actuator and sensor dynamics and uncertainties in damping, frequencies and mode shapes. In the future experiment (II), the abundance of actuators and sensors on the experiment structure will make it possible to address one of the most challenging problems in larger flexible structures, non-collocated control. (Fig. 9.)

Objectives

- Experimental validation of μ-synthesis techniques for robust control of large flexible space structures on a ground experiment.
- Conduct technology experiments to quantify performance:
  - Experiment I: Employ Hub sensors/actuators to control Boom-Dish modes.
  - Experiment II: Employ Hub& Rib sensors/actuators to control Boom-Dish & Dish modes (Non-collocation of control and measurement devices).
- Design includes structured and unstructured uncertainties to cover unmodeled dynamics, sensor and actuator dynamics, and uncertainties in damping, frequencies, and mode shapes.

Figure 9.

Robust Control Design Methodology

The general framework to be used in this study is illustrated in the diagram "GENERAL FRAMEWORK" of Figure 10. Any linear interconnection of inputs, outputs, commands, perturbations, and controller can be rearranged to match this diagram. For the purpose of analysis, the controller may be thought of as just another system component and the diagram reduces to that in the diagram "ANALYSIS." The analysis problem involves determining whether the error e remains in a desired set of values for given norm-bounded sets of input v and perturbation Δ. The interconnection structure G can be partitioned so that the input-output map from v to e can be expressed as the linear fractional transformation $F_u(G,\Delta)$.

Similarly, for the purpose of synthesis, the Δ can be normalized properly so that the normalizing factor can be absorbed into P. This reduces the synthesis problem as that in the diagram "SYNTHESIS." Here, the synthesis problem involves finding a stabilizing controller K such that the performance requirements are satisfied under uncertainties. The interconnection structure P can be partitioned so that the input-output map from v' to e' can also be expressed as the linear fractional transformation $F_l(P,K)$. (Fig. 10.)

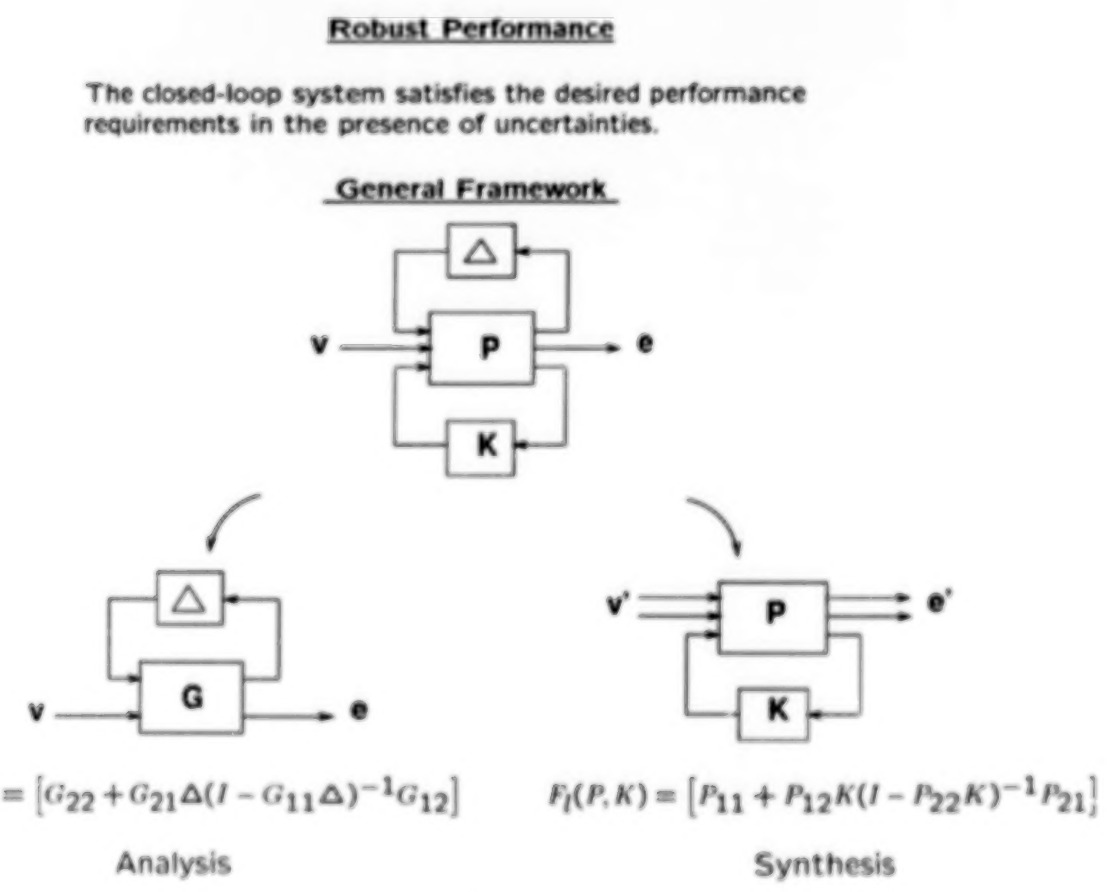


Figure 10.

Structured Singular Value Analysis
H_∞ Optimization and μ-Synthesis

The μ-synthesis methodology emerges as a practical approach in designing control systems with robust performance. This technique essentially integrates two powerful theories for synthesis and analysis into a systematic design technique that involves using the H_∞ optimization method for synthesis and the structured singular value (μ) for analysis. This technique is to find a stabilizing controller K and scaling matrix D such that the quantity

$$\| DF_l(P,K)D^{-1} \|_\infty$$

is minimized. One approach to solve this problem is to alternately minimize the above expression for either K or D while holding the other constant. For fixed D, it becomes an H_∞ optimal control problem and can be solved using the well-known state-space method. On the other hand, for fixed K, the problem can be minimized at each frequency as a convex optimization in $ln(D)$. The numerical results obtained for D can be fitted with an invertible, stable, minimum-phase, real-rational transfer function. This process is carried out iteratively until a satisfactory controller is constructed. (Fig.11.)

A frequency domain method for analyzing the robustness properties of the feedback system.

$$\mu(M) = \frac{1}{\min_{\Delta} \{\bar{\sigma}(\Delta) | det(I + M\Delta) = 0\}}$$

H_∞ Optimization

Find a stabilizing controller K such that

$$\|F_l(P,K)\|_\infty$$

is minimized.

μ – Synthesis

A synthesis technique to design closed-loop control system with robust performance. The technique is developed by combining H_∞ optimization method for controller synthesis with nominal performance and the structured singular value (μ) method for robust stability.

$$\min_{D} \min_{K} \|DF_l(P,K)D^{-1}\|_\infty$$

Iterate on D and K to obtain the solution.

Figure 11.

Controller Design

The block diagram shows the problem formulation used to design controller K. It is required to scale all the output errors to 1, so that when μ is less than 1, robust performance is achieved for the plant and uncertainty description defined by the interconnection structure P.

The PLANT is a 2-input/2-output model consisting of 2 decoupled two-mode SISO subsystems. An uncertainty weighting "W_{unc}," associated with the unmodeled dynamics is included between the actuators and sensors as an additive uncertainty with weighting function of 3.5(s + 1)/(s + 50). Output uncertainty associated with the sensors is formulated as multiplicative uncertainty on the sensor outputs which is treated as a constant 16% uncertainty across the entire frequency spectrum to account for possible coefficient errors associated with the plant model.

In the controller design for K, the actuator magnitude was limited to 1.11 Nm. The actual limitation on the actuator force is ±2Nm. The discrepancy is due to the model having too high of a damping value for the second mode. This leads to a difference of approximately a factor of 2 between theoretical and experimental actuator force levels. Sensor noises, on the order of ±1 mrad, are also included in the problem formulation.

The performance specification of the closed-loop transfer function between input disturbance and output sensors is defined. The performance weight consists of a constant weighting of 2.2. This requires the peak value of the magnitude in the closed-loop transfer function between the disturbance and sensors be reduced by 2.2. A straight H_∞ control design will not be able to take advantage of the knowledge of this structure, whereas controllers formulated using μ-synthesis can, via D scalings. (Fig. 12.)

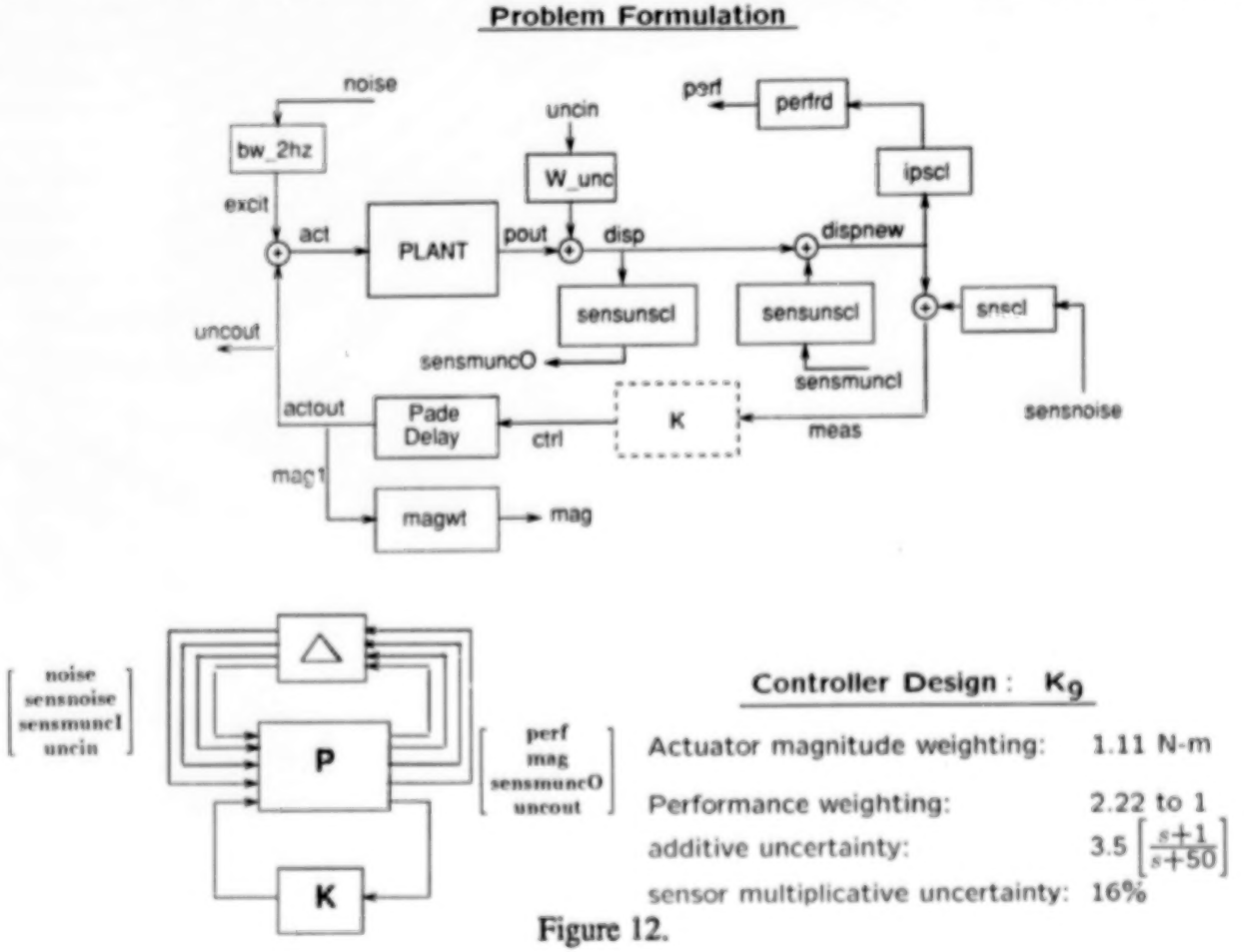


Figure 12.

Summary of Experiment Results

The unreduced controller has 16 states. Since the 2 axes are decoupled, the controller can be implemented with two independent channels where each channel is an 8th order system. To ease the computational burden, each of the 8th order systems was reduced to a 5th order system using balanced minimal realization methods. Theoretical analysis shows that the reduced order controller should have little effect on performance and robustness as compared with the full order controller.

Figure 13 shows the open-loop and closed-loop responses. The structure was first excited with 8 pulses of 0.8 second each. The force amplitude of each pulse was ± 1 Nm. The settling time was the time required for the response to drop to smaller than 2 milliradians. The closed-loop system is robust and stable. Its settling time is 4 times shorter than that of the open-loop response.

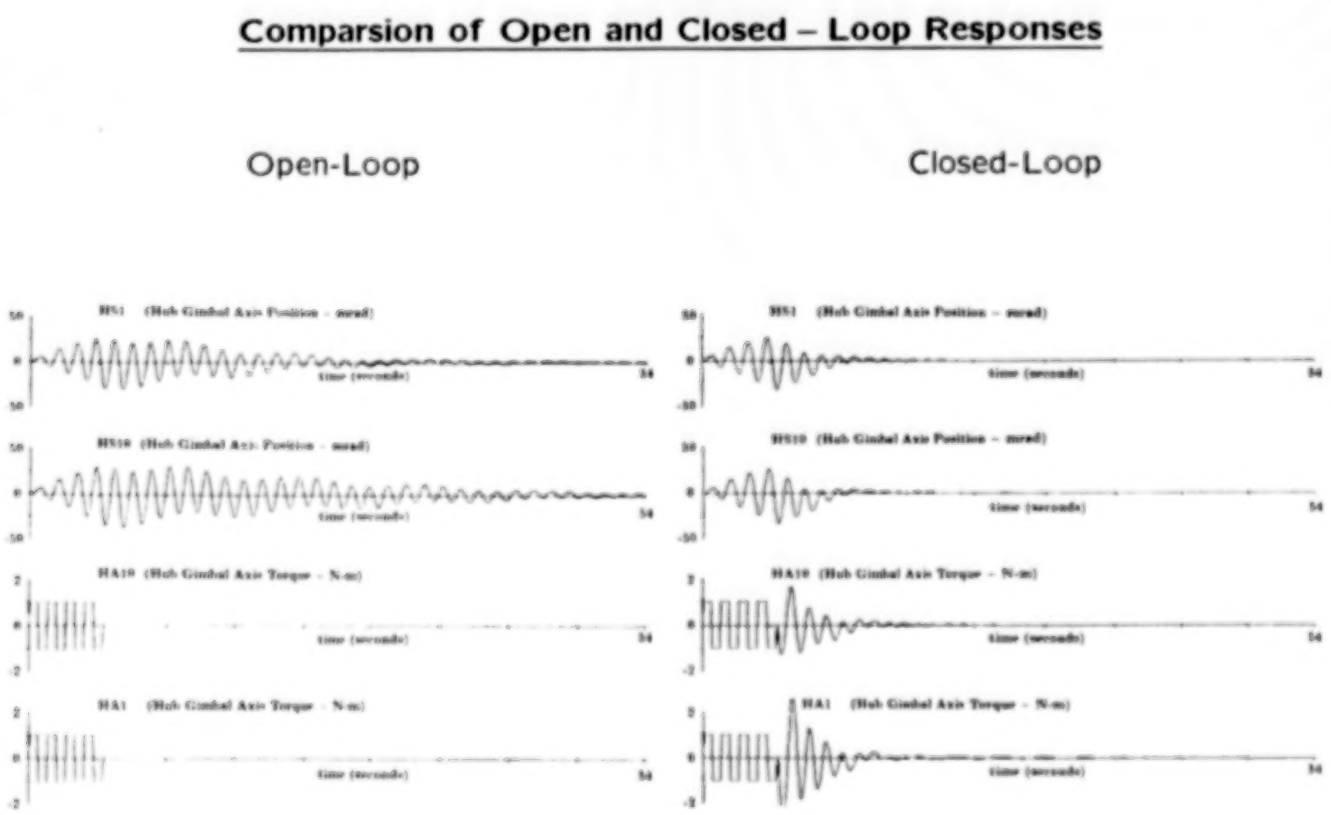


Figure 13.

BEST COPY AVAILABLE

Conclusions -- μ-Synthesis Experiment

Using the μ-framework, we were able to synthesize control designs which performed well on the experimental system. This control design achieves high vibration attenuation at the natural frequencies of the experiment structure. The performance of the experiment is limited by the actuator torque available. Increased actuator torque would certainly increase the performance capability of the stucture.

Future experiment work is planned. This work will include increasing the number of actuators and sensors used, and addressing the issues of non-collocated sensors and actuators. Additional sensors and actuators will allow more modes of the system to be damped and will potentially increase vibration attenuation across the frequency spectrum of the structure. Robustness issues will also be addressed. The control designs will be tested to determine their robustness to various types of uncertainties associated with the plant, actuators, and sensors. (Fig.14.)

- A robust control design using μ-synthesis was achieved which exhibited good performance on the experimental facility.
- Performance is severely compromised by the force limits in hub actuators.
- μ-synthesis provides an attractive design technique for vibration attenuation and robust control.
- Future work includes using additional sensors and actuators on the ribs to control a wide range of structural modes.

Figure 14.

System Identification Experiment
(Y. Yam, D. Bayard, F. Hadaegh, E. Mettler)

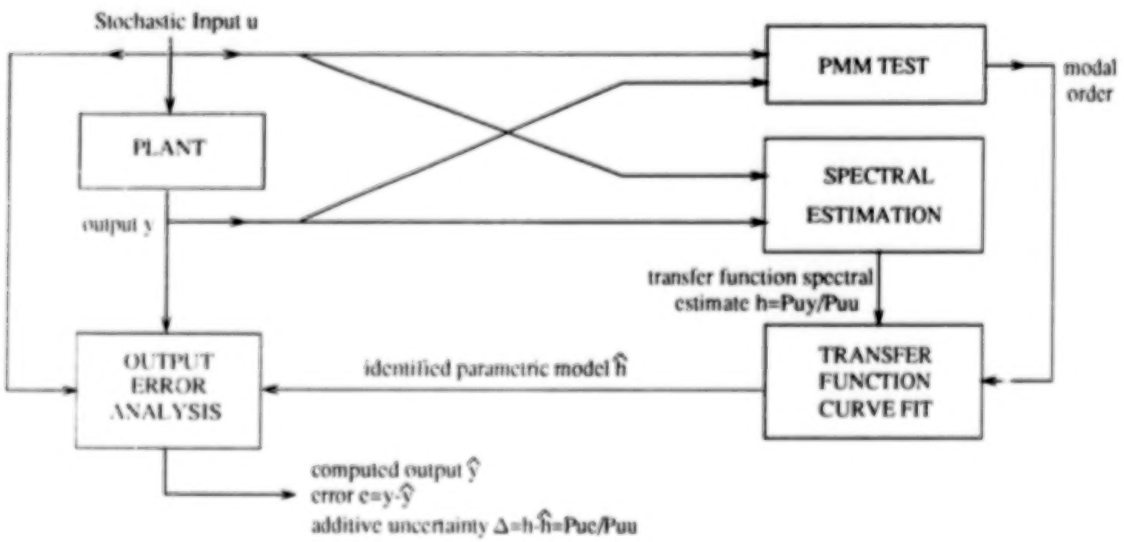
The analysis, design, and on-orbit tuning of robust controllers requires more information about the plant than simply a nominal estimate of the plant transfer function. Information is also required to characterize the uncertainty in the nominal estimate. A frequency domain identification methodology for large space structure has been developed by JPL which makes use of a simple but useful characterization of the model uncertainty based on the output error. This is a characterization of the "additive uncertainty" in the plant model, which has found considerable use in many robust control analysis and sysnthesis techniques. Experimental demonstration of the methodology via the experiment structure test bed is focused to support the objectives including: 1) to experimentally verify the performance of the system ID methodology; 2) to estimate system quantities useful for robust control analysis and redesign; 3) to demonstrate the automated operations of system identification in on-orbit scenarios; and 4) to obtain via actual dynamics a verified model of the testbed structure which will be available for analysis and controller design. (Fig. 15.)

- **OBJECTIVES**
  - **EXPERIMENTAL VERIFICATION OF THE SYSTEM ID METHODOLOGY**
  - **ESTIMATION OF SYSTEM QUANTITIES FOR ROBUST CONTROL ANALYSIS AND REDESIGN**
  - **DEMONSTRATION OF ON-ORBIT AUTOMATED SYSTEM ID SCENARIOS**
  - **DETERMINATION VIA ACTUAL DYNAMICS OF A "VERIFIED" MODEL FOR ANALYSIS/CONTROLLER DESIGN**
- **PHASE I EXPERIMENT CHARACTERISTICS**
  - **SIMO OPERATIONS**
  - **WIDEBAND, NARROWBAND, SINE-DWELL EXPERIMENTS**
  - **INSTRUMENTATION: HUB TORQUERS, HUB ANGULAR SENSORS, LEVITATOR SENSORS**
  - **BOOM-DISH MODAL EXCITATION: FREQUENCY < 10 Hz**

Figure 15.

Figure 16 (shown below) summarizes the Phase I experimental verification of the identification methodology. The experiments utilized single input and multiple (usually 5) outputs. Several investigations utilizing wideband, narrowband, and sine-dwell excitations were performed. Areas of investigation included reduced order model identification, residual mode excitation and analysis, system nonlinearity, and noise anomaly. Experiments were conducted about the 1-7 and 4-10 hub axes of the test bed structure using the corresponding hub torquers for actuation. The set of sensors utilized included the hub angular sensors and some levitator sensors for characterization of the system dynamics. The sampling frequency was 20 Hz, hence only modes with frequency under 10 Hz, were under investigation. Note that the dish modes, with their symmetric mode shapes about the hub, are not controllable and observable from the hub. Thus, the phase I identification experiments investigate only the boom-dish modes via actuation at the hub. Since these modes constitute a small subset of all system modes and have larger frequency separation, they provide a good first test of the performance of the ID methodology. As experience and confidence in experimentation and algorithm performance grows, the dish modes will be tackled in phase II identification experiments.

- **ON-LINE DIGITAL FILTER/OPTIMAL INPUT DESIGN**
- **MODAL ORDER DETERMINATION USING PRODUCT MOMENT MATRIX (PMM)**
- **PLANT TRANSFER FUNCTION ESTIMATED BY CROSS-CORRELATION h=Puy/Puu**
- **PARAMETRIC MODEL CURVE FIT BASED ON h AND PMM MODAL ORDER TEST RESULTS**
- **OUTPUT ERROR/ADDITIVE UNCERTAINTY DETERMINATION FOR ROBUSTNESS ANALYSIS**



AUTOMATED FREQUENCY DOMAIN SYSTEM IDENTIFICATION METHODOLOGY

Figure 16.

BEST COPY AVAILABLE

Experiment Results -- The 4-10 Axis

Results of a wideband excitation experiment are shown in figures 17A to H. The experiment was performed on the 4-10 hub axis of the experiment structure utilizing the hub torquer and sensor for instrumentation. The sampling frequency was 20 Hz. The experiment run time was 1638.4 sec. Figure A shows the white noise excitation u uniformly distributed between the range ± 1.5 Nm. The output response y is shown in figure B. Figure C shows the PMM test determinant values as a function of the assumed model order. This test yielded a model order of 3 for the system. Figure D presents the transfer function spectral estimate h. Transfer function curve fitting on h was performed assuming a model order of 3, giving rise to the identified parametric model of Figure E. Both gain and phase values of h are utilized in the curve fitting. The identified frequencies and damping coefficients are 0.114 Hz, 0.637 Hz, and 2.57 Hz, and 0.4, 0.0364, and 0.00604, respectively. Figure F shows the computed output y of the identified parametric model subjected to the same excitation. Figure G shows the output error e, which has a maximum of 2.6 mrad as compared to 10 mrad for $\hat{y}$. Finally, the additive uncertainty spectral estimate Δ is shown in Figure H. It indicates the identification of the modal dynamics to within 10% to 30%. There are two modes, apparent in figure D, that were not fitted. Figure H shows that the error resulting from omitting those modes is even smaller than the fitting error of the identified modes. The curve fitting algorithm has properly determined their omission and produced a reduced-order plant model which minimizes the additive uncertainty.

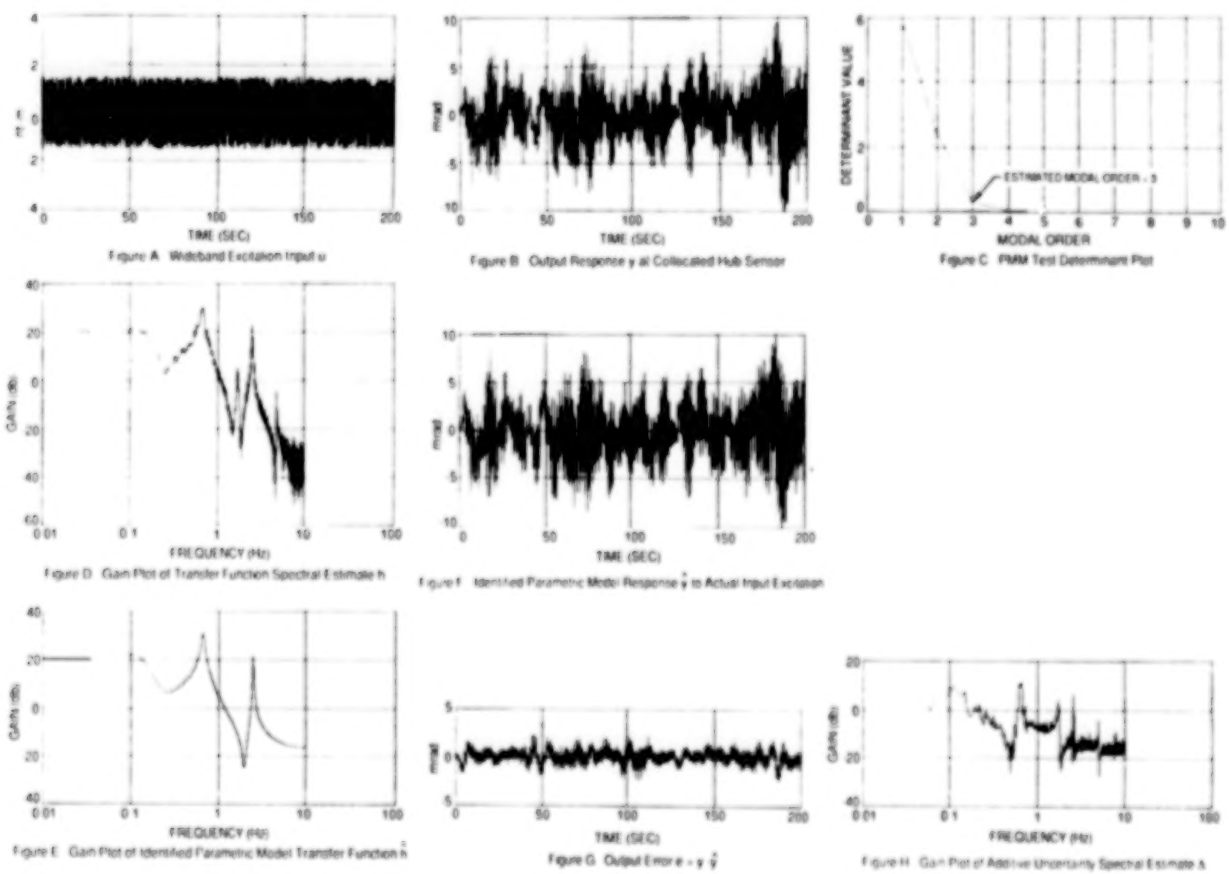


Figure 17.

Comparative Analysis and Summary

The table on the right tabulates the modal frequency values of the 1st, 2nd, and 4th modes for the two axes as determined from finite element modelling method and experiment results. The two sets of results agree exceptionally well for the 4th mode and reasonably well for the others. In general, the experimental results confirm that the 4-10 axis have slightly smaller frequency values than the 1-7 axis which was predicted analytically by the finite element model.

The high damping coefficients for mode 1 estimated by the experiment were caused by a hardware problem in the experiment facility at the time this experiment was performed which caused high damping levels. This problem was later corrected. High damping also reduces the accuaracy of the predicted modal frequencies. This may help to explain the relatively larger modal frequency. This may also explain the relatively larger frequency separation of this mode between the values predicted by the finite element model and determined from this experiment. (Fig. 18.)

(A) THE 1-7 AXIS

MODE #	FEM		EXPERIMENT	
	FREQ (Hz)	DAMPING COEF.	FREQ (Hz)	DAMPING COEF.
1	0.091	--	0.126	0.32
2	0.628	--	0.666	0.0564
4	2.682	--	2.68	0.00746

(B) THE 4-10 AXIS

MODE #	FEM		EXPERIMENT	
	FREQ (Hz)	DAMPING COEF.	FREQ (Hz)	DAMPING COEF.
1	0.091	--	0.114	0.4
2	0.616	--	0.637	0.0364
4	2.577	--	2.57	0.00604

SUMMARY

- **CURVE FITTING ALGORITHM PRODUCED A GOOD REDUCED-ORDER PLANT MODEL**
- **IDENTIFIED MODEL AND ADDITIVE UNCERTAINTY PROVIDE CRUCIAL INFORMATION FOR ROBUST CONTROL DESIGN**
- **AUTOMATED SYSTEM IDENTIFICATION METHODOLOGY VERIFIED**

Figure 18.

Summary and Conclusions

This paper has described the test bed developed at JPL for experimental evaluation of new technologies for the control of large flexible space structures. The experiment consists of a flexible spacecraft dynamic simulator, sensors, actuators, a microcomputer, and an advanced programming environment. The test bed has been operational for over a year, and thus far nine experiments have been completed or are currently in progress. Several of these experiments were reported at the 1987 CSI Conference, and several recent ones are documented in this paper, including high-order adaptive control, non-parametric system identification, and mu-synthesis robust control. An aggressive program of experiments is planned for the forseeable future. (Fig. 19.)

- **PROGRAM OBJECTIVE**
  - **DEMONSTRATE AND VALIDATE CRITICAL CONTROL METHODOLOGIES ON A PHYSICAL STRUCTURE**
- **EXPERIMENTS COMPLETED TO DATE OR IN PROGRESS**
  - **UNIFIED MODELING AND CONTROL DESIGN**
  - **MODEL REFERENCE ADAPTIVE CONTROL (TWO INPUT/TWO OUTPUT)**
  - **STATIC SHAPE DETERMINATION**
  - **SHAPE DETERMINATION VIA COMPUTER VISION**
  - **SENSOR VALIDATION (SHAPES)**
  - **FREQUENCY DOMAIN SYSTEM IDENTIFICATION**
  - **HIGH-ORDER ADAPTIVE CONTROL (SIX INPUT/SIX OUTPUT)**
  - **MU-SYNTHESIS ROBUST CONTROL (I – DONE, II – PLANNED)**
  - **MODAL SURVEY (IN PROGRESS)**
- **SEVERAL GI EXPERIMENTS PLANNED FOR FY'89 AND FY'90**

Figure 19.

STRAIN AND DYNAMIC MEASUREMENTS USING FIBER OPTIC SENSORS EMBEDDED INTO GRAPHITE/EPOXY TUBES

D. W. DeHart, T. Doederlein, and J. Koury
Air Force Astronautics Laboratory
Edwards AFB, CA

R. S. Rogowski, J. S. Heyman, and M. S. Holben, Jr.
NASA Langley Research Center
Hampton, VA

1. INTRODUCTION:

Smart is defined by The American Heritage Dictionary as, "Of, relating to, or being a device that imitates human intelligence."[1] The concept of smart structures meets this definition.

Several planned United States Air Force (USAF) and National Aeronautics and Space Administration (NASA) space systems such as Space Based Radar (SBR), Space Based Laser (SBL), and Space Station, pose serious vibration and control issues. See figure 1. Their low system mass combined with their large size, extreme precision pointing/shape control and rapid retargeting requirements will result in an unprecedented degree of interaction between the system controller and the modes of vibration of the structure. The resulting structural vibrations and/or those caused by foreign objects impacting the space structure could seriously degrade system performance, making it virtually impossible for passive structural systems to perform their missions. There resides a need for creating an active vibration control system which will sense these natural and spurious vibrations, evaluate them and then dampen them out. This active vibration control system must be impervious to the space environment and electromagnetic interference, have very low weight, and in essence become part of the structure itself. The concept of smart structures also meets these criteria. Smart structures is defined as the embedment of sensors, actuators, and possibly microprocessors in the material which forms the structure, particularly advanced composites. These sensors, actuators, and microprocessors will work interactively to sense, evaluate, and dampen those vibrations which pose a threat to large flexible space systems (LSS). The sensors will also be capable of sensing any degradation to the structure. (Fig. 1.)

CORPORATE FED ARRAY / PHASED ARRAY TYPICAL SPACECRAFT CONFIGURATION

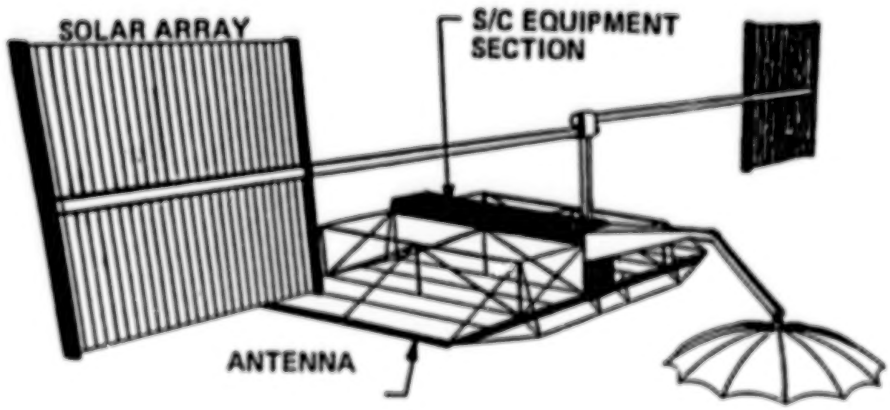


Figure 1

In conjunction with this problem, the Air Force Astronautics Laboratory (AFAL) and NASA Langley Research Center (NASA LaRC) have initiated a program to design, fabricate, and experimentally test composite struts and panels with embedded sensors, actuators, and microprocessors that can be used for dynamic sensing and controlling vibrations and motions in space structures. The sensors will also be able to monitor the health of space structures. This program is divided into four tasks. Task one is acquiring equipment necessary for embedding sensors and actuators into composite material. Baseline structures of aluminum and composite materials will be fabricated (coupons, flat panels, struts) to demonstrate concept feasibility. The baseline structures will be tested for stiffness, strength, and vibration for comparison with data from the structures that have embedded components. Task two will include the processing science studies required to process the composite components. Task three will include the fabrication of the selected composite struts with embedded components. Both sub-scale and full-scale struts will be fabricated. Task four will include non-destructive evaluation, mechanical testing, and vibration damping testing of the Task three components with the embedded control system for overall concept performance, endurance, reliability and response.[2] See figure 2.

SMART SPACE STRUCTURES PROJECT (IN-HOUSE)

I. Task one encompasses acquiring equipment necessary for embedding sensors and actuators into composite materials. Baseline structures of aluminum and composite material will be fabricated.

II. Task two will run parallel to Task I and will encompass studies of fabrication and processing technologies.

III. Task three will encompass the fabrication of subscale and fullscale composite structures with embedded sensors and actuators.

IV. Task four will encompass experimentation on the fabricated components. Such experiments will include non-destructive evaluation, mechanical testing, and vibration testing within a ground dynamic test facility.

Figure 2

The AFAL has been working in the area of dynamics and control of LSS for the past five years. They have had numerous programs, both contractual and in-house, to develop sensors and actuators for controlling LSS. Presently the AFAL is developing a large scale laboratory, called Advanced Space Structures Technology Research Experiments (ASTREX), which will have the capacity of performing large angle rapid retargeting maneuvers and vibration analysis on LSS. Also they have been fabricating advanced composite materials for the last four years. However, most of the composite components that were fabricated were rocket components such as: nozzles, payload shrouds, exit cones, and nose cones. For the last two years though, the AFAL has been fabricating composite space components such as trusses, tubes, beams and flat panels. Research on fiber optic sensors at NASA LaRC dates back to 1979. Recently an optical phase locked loop (OPLL) system has been developed that uses fiber optics for sensing. See figure 3. Static and dynamic strain measurements have been demonstrated using this device.[3]

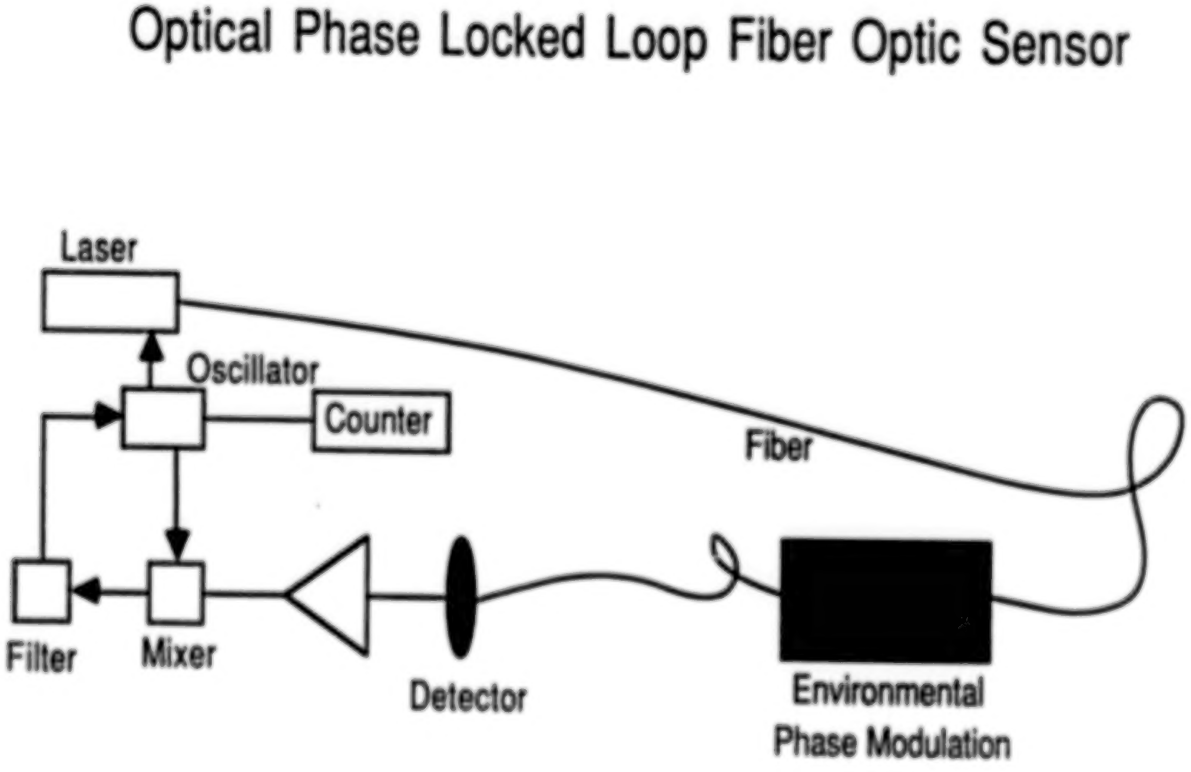


Figure 3

2. FABRICATION OF EXPERIMENTAL STRUTS

The first goal of the program is to demonstrate the feasibility of smart structures. A simple composite tube structure with a circular cross section was fabricated with a fiber-optic sensor embedded into it. The tube was chosen because it is a key structural element in most space truss systems. Optical fibers were chosen as the sensing element because of the demonstrated capability of the OPLL developed at NASA LaRC. To date, a total of three tubes fabricated at the AFAL have been tested at NASA LaRC. The results of two of these tubes are presented in this paper. All three tubes were fabricated in a similar manner, by filament winding on an En-Tec computer filament winding machine. The first two tubes were wound as one single tube on the same steel mandrel and then cut into two. The composite material used was graphite epoxy prepreg roving from Fiberite composed of medium strength G-40 graphite fibers from Union Carbide and 5245 epoxy resin. The single tube prior to cutting was approximately five and one half feet in length, with an inside diameter of one and one half inches. The single tube consisted of one layer of 90 degree fiber; two layers of +/- 45 degree fiber; and one layer of 90 degree fiber, with the fiber optics embedded under the final 90 degree layer. A schematic diagram of the tube lay-up is shown in figure 4. The fiber optics, made by the Newport Corporation, are F-MSD multimode fiber. The core has a diameter of 49 μm with a combined core and cladding diameter of 125 μm. They are coated with an acrylic jacket. The fiber optics were layed in longitudinally up to the center of the tube with both ends of the fiber coming out of the same end of the tube to prevent spurious vibrations of the fiber optics during the testing of the composite tube.

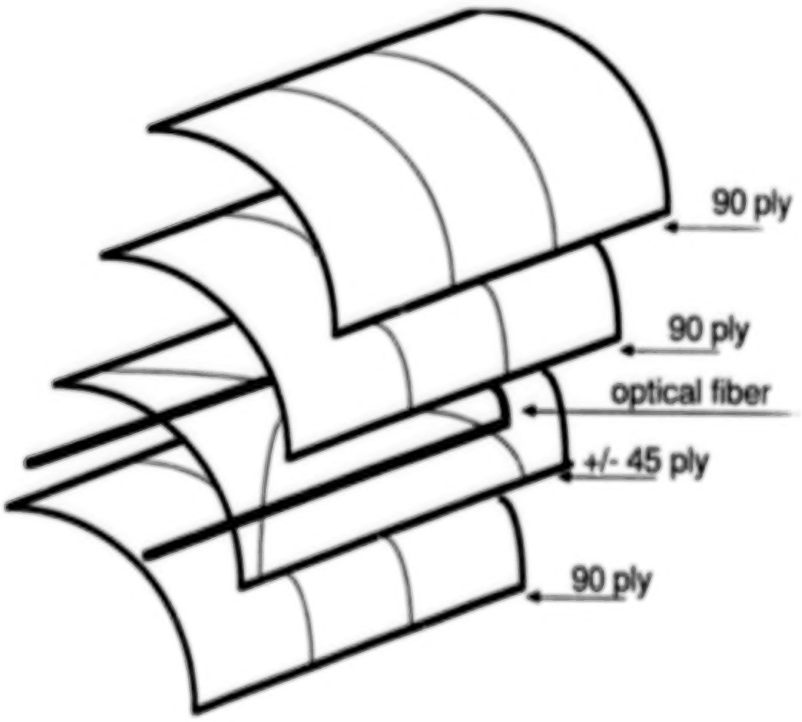


Figure 4

They were located every 90 degrees throughout the tube with a total of four sets of fiber optics embedded in the tube. After winding, the single tube was then bagged using standard bagging techniques. Special care was given in bagging the optical fibers since they are very delicate and fragile and due to the long leads coming out of the end of the tube. Prior to autoclaving, the optical fibers were coated with a high temperature silicone (RTV) coating. This coating prevents the flexible acrylic jacket from melting during the curing process which would then leave only the very brittle bare core and cladding and also acts as a stress relief where the optical fibers come out of the end of the composite tubes. The single tube was then placed in a Baron-Blackslee autoclave and cured at 350 degrees F and 85 psia for four hours. Upon cooling, the tube was removed from the mandrel and cut in two, giving special care to the optical fibers. Both tubes were then packaged and delivered to NASA LaRC for strain and vibration testing. The third filament-wound tube was fabricated very similar to the first two tubes. The only differences were in the material, size, and the angle of the composite plies. The composite material used was graphite/epoxy prepreg roving from Fiberite composed of medium strength IM-6 graphite fibers from Hercules and 934 epoxy resin. The first tubes had a fundamental frequency of approximately 33 hertz when cantelivered. The third tube was designed to have a significantly lower fundamental frequency. A tube with a length of 68 inches and a ply orientation of 90-(+/-)60-90-90 has a fundamental frequency of 10 hertz. The fiber optics were embedded in between the 60 and the second 90 degree layer. In this tube only two sets of fiber optics were embedded at 180 degrees to one another. Also, the fiber optics did not come out of the end of the tube as in the first two tubes. The fiber optics came out of the circumference of the tube at a distance of four inches from the end of the tube. This change allowed clamping of the tube at the end without crimping the optical fibers. See figure 5.

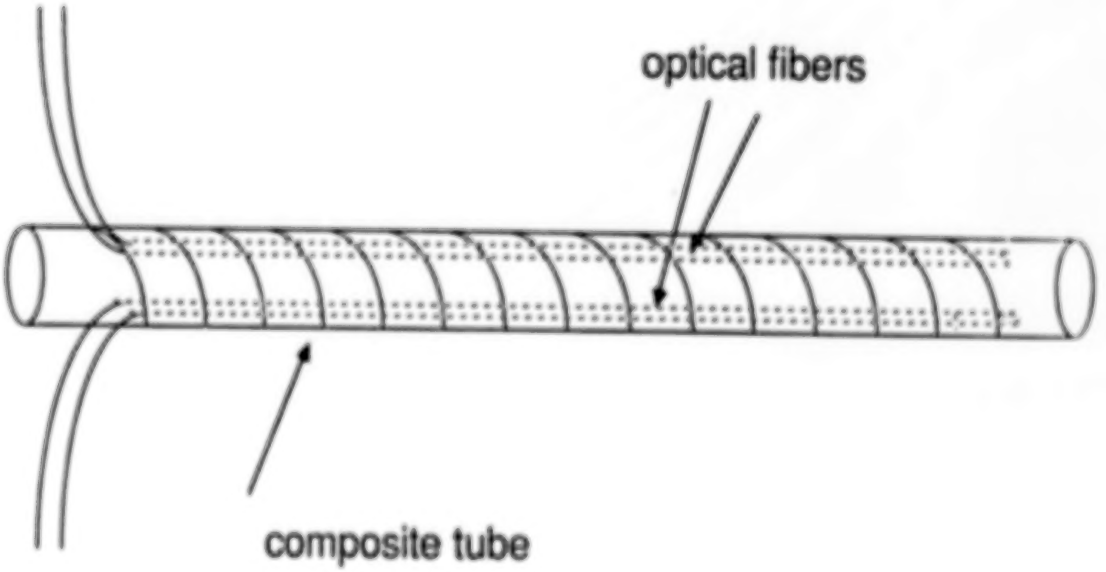


Figure 5

3. STRAIN AND VIBRATION MEASUREMENTS

The vibration and strain experiments were conducted at NASA Langley Research Center using a modulated diode laser and an optical phase locked loop (OPLL) system which is described in reference [3]. The optical fibers exiting the tube were fusion spliced to the fibers of the optical system. One end of the graphite/epoxy tube was clamped over a round piece of metal, which was inserted into the tube. For the first two tubes, this caused a problem with crimping of the optical fibers as they exited from the tube. For the first few readings, the data taken acted in a reverse fashion than as predicted. For the third tube, this problem was solved by having the fiber optics exit from the circumference of the tube, not from the end. The whole assembly was then clamped to an optical table to hold the end of the tube firmly in a cantilevered position. Four resistance strain gauges were attached longitudinally to the tube for comparison with the fiber optic sensors. The tube was statically stressed by hanging weights on a weight pan and attaching it to the free end. Data were taken while the weights were loaded and unloaded. When this force is applied to the tube, a strain is induced in the composite which in turn induces a strain into the optical fiber that produces a change in the modulation frequency of the OPLL. The optical fibers can measure both tension and compressive strain. This stain is governed by the equation change in frequency divided by the frequency is equal to the negative of the change in length divided by the length ($\frac{\Delta f}{f} = -\frac{\Delta L}{L}$). Strain on the surface of the tube was monitored with the strain gauges. The results of these experiments are shown in figures 6 and 7, which graphically indicate the correlation between the strain gauge measurements and the changes in modulation frequency. The data indicate very good correlation between the strain gauge readings and the fiber optic strain measurements. These runs were repeated with excellent reproducibility.

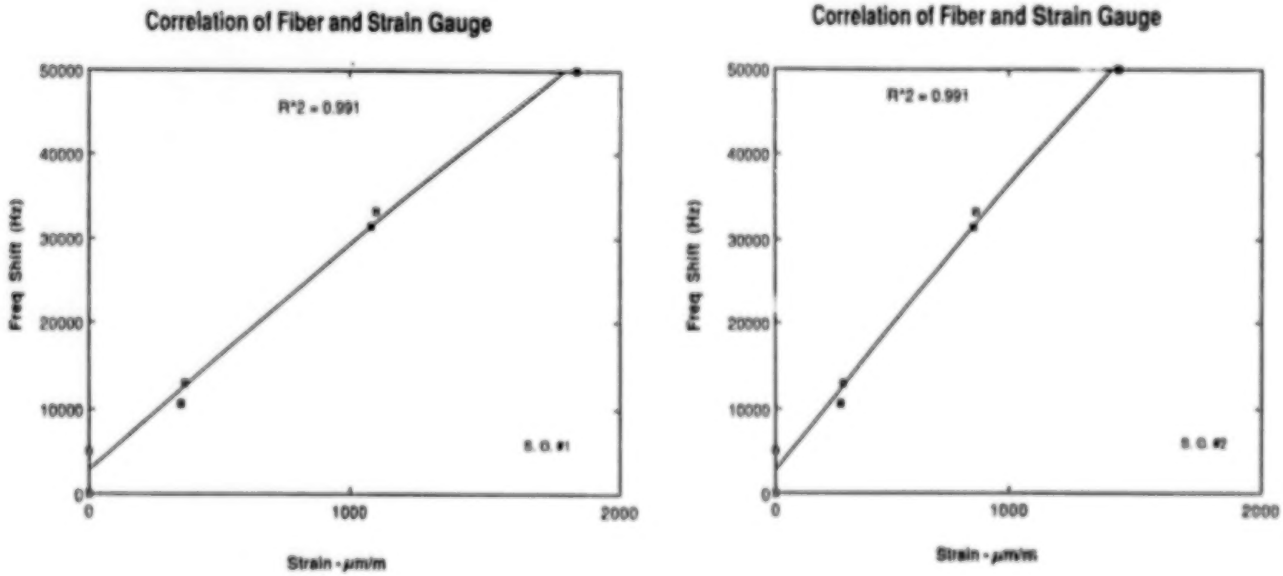
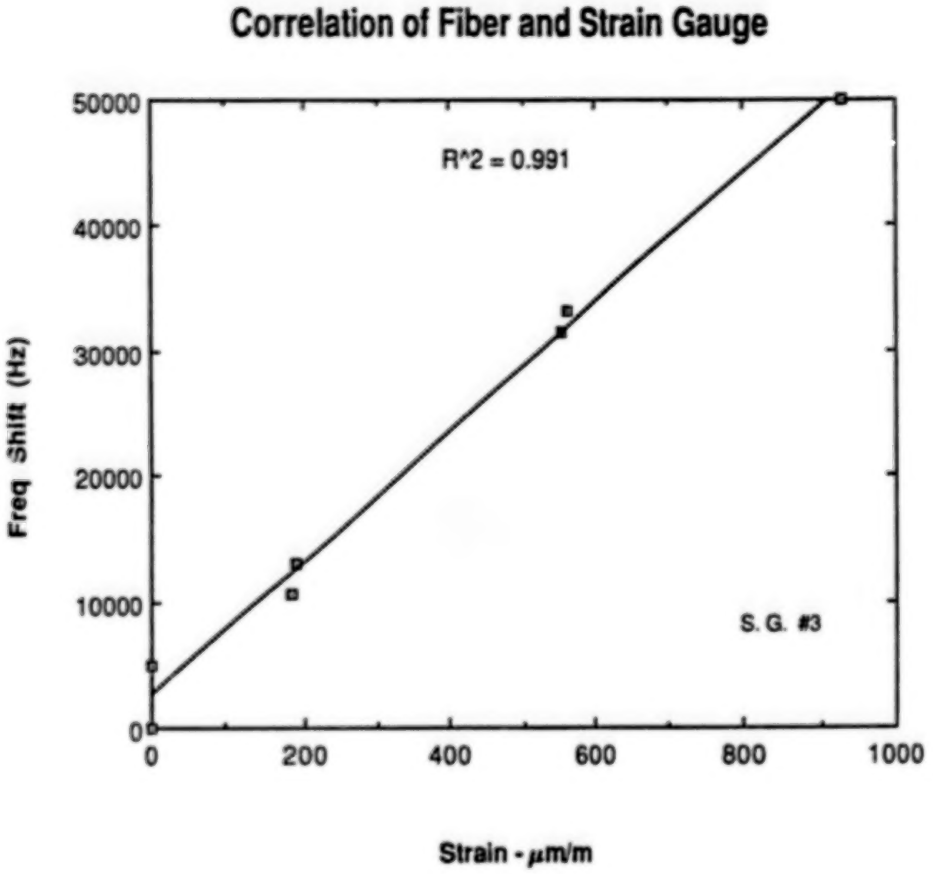


Figure 6


Correlation of Fiber and Strain Gauge
R^2 = 0.991
S. G. #3
Freq Shift (Hz)
Strain - μm/m
0
10000
20000
30000
40000
50000
0
200
400
600
800
1000

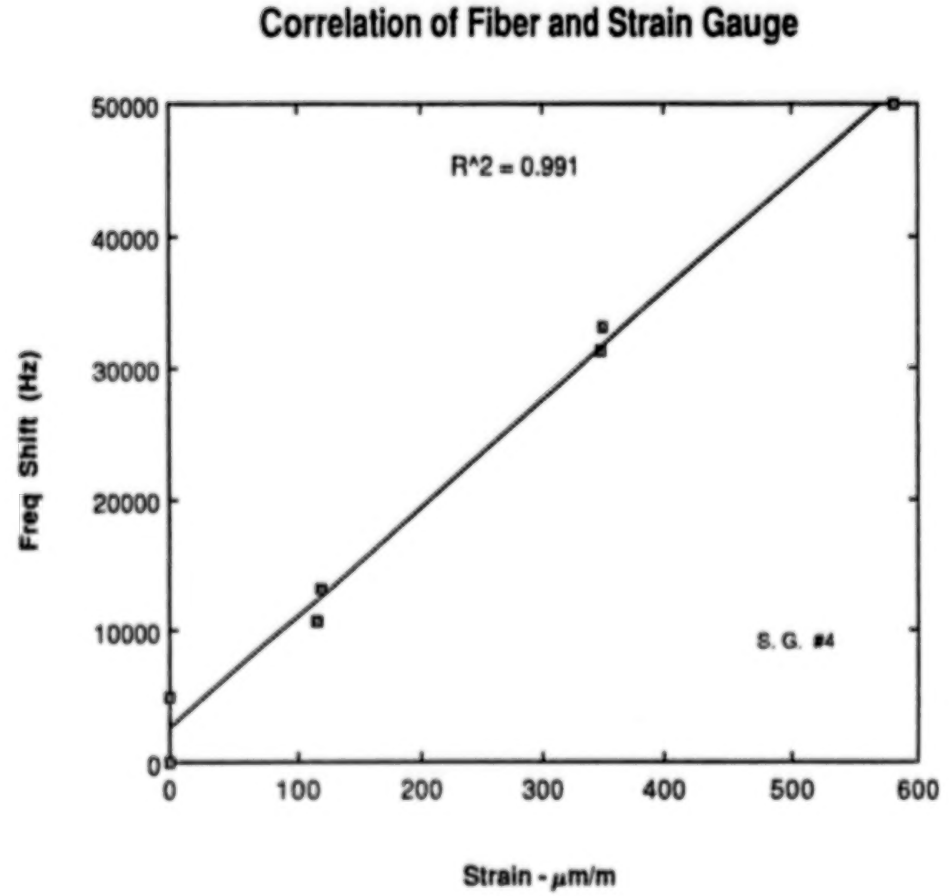

Correlation of Fiber and Strain Gauge
R^2 = 0.991
S. G. #4
Freq Shift (Hz)
Strain - μm/m
0
10000
20000
30000
40000
50000
0
100
200
300
400
500
600

Figure 7

Strain measurements were also made while the tube was vibrating. The end of the tube was impacted and the vibration response was analyzed. Figure 8 compares the results obtained by simultaneously monitoring a strain gauge and the fiber optic signal for the third tube. The time domain and frequency domain data agree very well, showing a fundamental vibration frequency of 10.4 Hz, which is very close to the design vibration frequency of 10 Hz. As you can see from the data, the fiber optics can detect the vibration response significantly better than the strain gauges.

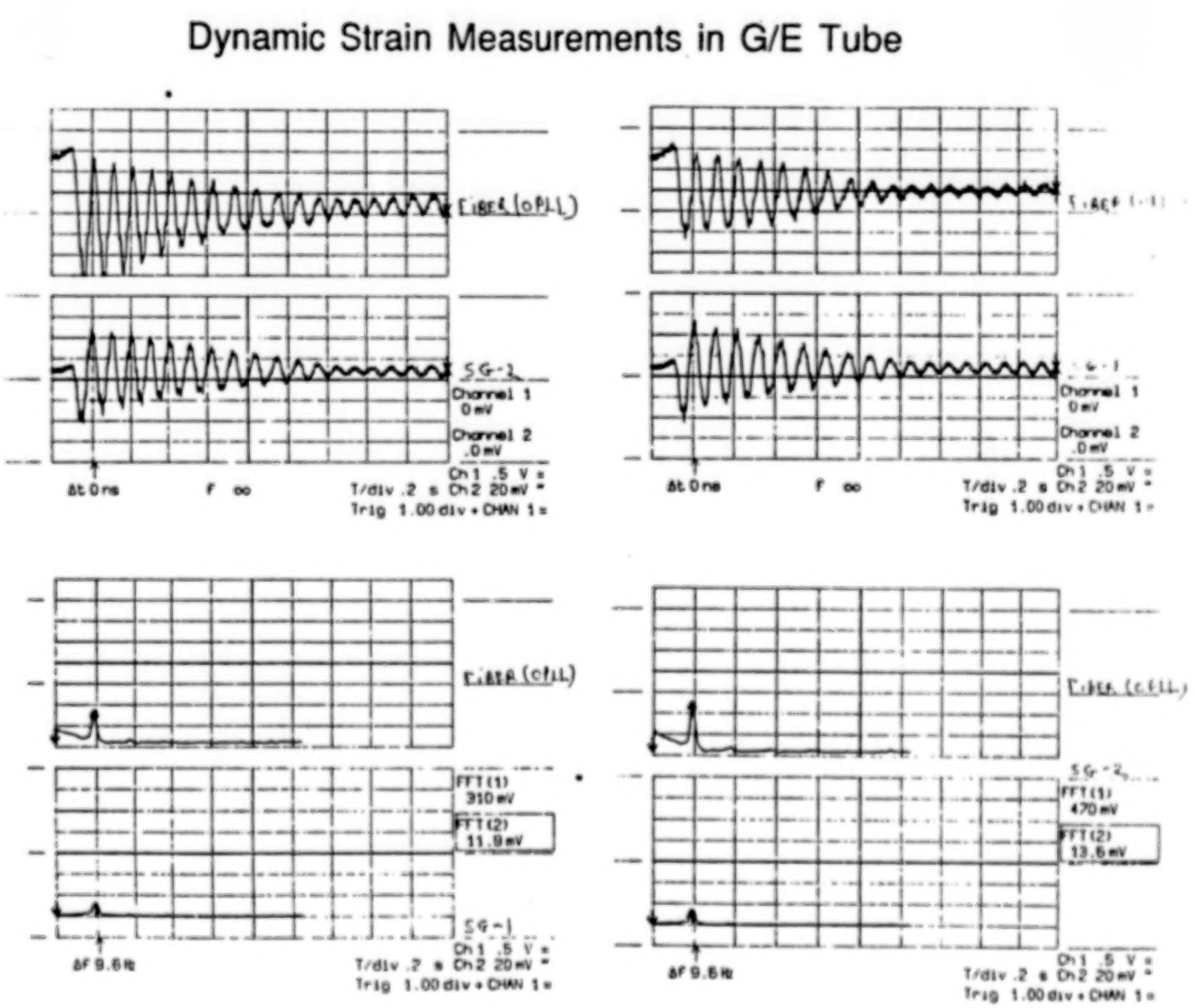


Figure 8

BEST COPY AVAILABLE

4. SUMMARY

Graphite / epoxy tubes were fabricated with embedded optical fibers to evaluate the feasibility of monitoring strains with a fiber optic technique. Resistance strain gauges were attached to the tubes to measure strain at four locations along the tube for comparison with the fiber optic sensors. Both static and dynamic strain measurements were made with excellent agreement between the embedded fiber optic strain sensor and the strain gauges. Strain measurements of 10^{-7} can be detected with the OPLL system using optical fiber. Because of their light weight, compatibility with composites, immunity to electromagnetic interference, and based on the static and dynamic results obtained, fiber optic sensors embedded in composites may be useful as the sensing component of smart structures.

REFERENCES

[1] The American Heritage Dictionary, Houghton Mifflin Co, Boston, MA 1982.

[2] Capt Ted Doederlein, Lt Douglas DeHart, Mr. Joe Sciabica, Smart Space Structures Project Directive, Air Force Astronautics Laboratory, Jan 1988.

[3] R. S. Rogowski, J. S. Heyman, M. S. Holben, Jr. and P. Sullivan, "A method for monitoring strain in large structures: Optical and radio frequency devices", Rev. Prog. Quant. NDE, vol 7a, p559 (Plenum Press, 1988).

INITIAL OPERATIONAL CAPABILITY OF THE ASTREX LARGE SPACE STRUCTURES TEST BED

1Lt G. A. Norris, USAF
Air Force Astronautics Laboratory
Edwards AFB, CA

Future DOD, NASA, and SDI space systems will be larger than any spacecraft flown before. The economics of placing these large space systems (LSS) into orbit dictates that they be as low in mass as possible. The combination of very large size and relatively low mass produces systems which possess little structural rigidity. This flexibility causes severe technical problems when combined with the precise shape and pointing requirements associated with many future LSS missions. Development of new control technologies which can solve these problems and enable future LSS missions is under way, but a test bed is needed for demonstration and evaluation of the emerging control hardware (sensors and actuators) and methodologies. In particular, the need exists for a facility which enables both large angle slewing and subsequent pointing/shape control of a variety of flexible bodies. The Air Force Astronautics Laboratory (AFAL) has conceived the Advanced Space Structures Technology Research Experiments (ASTREX) facility to fill this need.

Large Space System Dynamics & Control ...

The Problem:

* **Unprecedented Size and Low Structural Mass Density**
* **Very Precise Pointing and Shape Control Requirements**
* **Significant Onboard and Mission Induced Disturbances**

  - **Unprecedented Degree of Control-Structure Interaction**
  - **High Modal Density Complicates Control**
  - **No Prior Experience in Modeling/Control of Such Systems**
  - **Large Physical Size Makes Ground Testing Difficult**

Solution:

* **Combination of Passive and Active Vibration Damping**
* **Ground Facility to Test and Validate Emerging Space Structures Technology**

The range of technologies being developed in response to the LSS dynamics and control problem is broad. Included in this class of innovative technologies are many which must be demonstrated in ground test facilities. This class includes new actuators for slewing, vibration isolation, vibration suppression and shape control; structural sensors, including those embedded in composite structural elements during fabrication; structural solutions such as damping treatments, innovative materials, and advanced configurations; methodology advancements including new control and identification algorithms; and finally advances in ground test methods themselves, including scaling methodologies, micro-gravity simulation methods, etc.

NEW TECHNOLOGIES MUST BE DEMONSTRATED IN GROUND TEST FACILITIES

- Control Algorithms
- Slew Actuators
- Vibration Suppression Actuators
- Shape Control Actuators
- Structural Sensors
- Vibration Isolators
- Damping Treatments
- Structural Materials
- Structural Configurations
- Analytical Models
- Identification Algorithms
- Scaling Methodology
- Micro-gravity Simulation Methods

Given these testing needs, essential features of a new LSS ground test facility emerge. To ensure that test articles be fabricable with materials of reasonable cost, and to maximize the possibility of using materials which could actually fly, the facility should be large enough to accommodate test articles on the order of 1/3 to 1/2 scale. To ensure that experiments in the facility can address the breadth of LSS dynamics and control issues, the facility should not be "hard wired" to any specific test article or mission. This will allow for growth potential as well. Particular test articles should also be designed to incorporate modularity, so that they can readily accommodate substitution of innovative substructural elements (advanced materials, advanced structural designs, embedded sensors and actuators, etc). Finally, the facility should be accessible to as many users as possible. This serves two purposes. It provides a general test bed for the majority of LSS researchers who otherwise have no access to a realistic large-scale experimental facility, and also provides a means for comparatively evaluating the wide variety of hardware and methodologic solutions to the LSS dynamics and control problem.

DESIRABLE FEATURES FOR A NEW LSS GROUND TEST FACILITY

- **Size Large Enough to Accommodate 1/3 to 1/2 Scale Test Articles**
- **Do Not "Hard Wire" it to Any Specific Test Article or Mission**
- **Design Facility With Growth Potential**
- **Design For Test Article Modularity**
- **Make Facility Accessible to as Many Users as Possible**

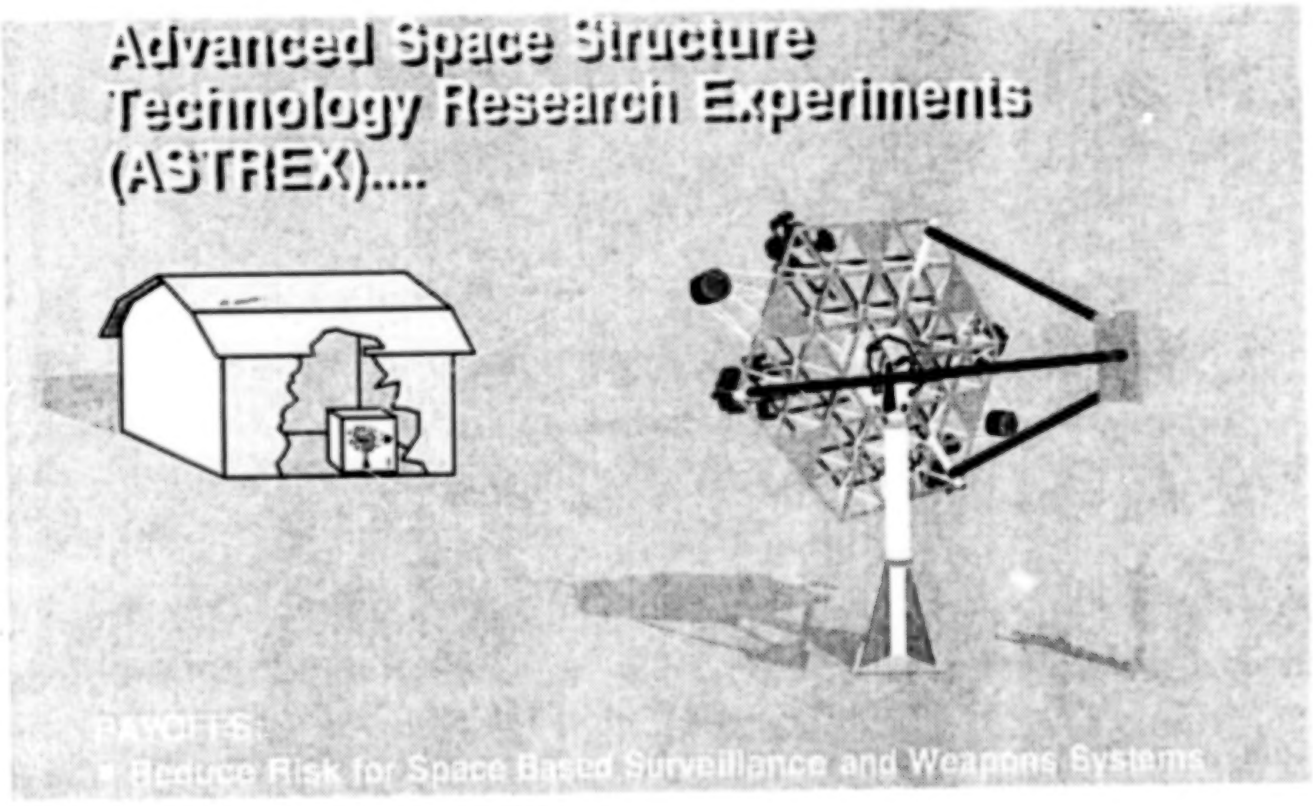
ASTREX has been designed to incorporate all of the essential LSS ground test facility needs identified. The components which comprise this design include the following

1. A temperature-controlled, 40'x40'x40' facility with an overhead crane;
2. A spherical air bearing for frictionless, 3-axis rotational test article motion;
3. A real time control and data acquisition computer;
4. A dynamically scaled model of a Space Based Laser (SBL) 3-mirror beam expander as the initial experimental article;
5. A complement of sensors and actuators for system identification, pointing and shape control, and active vibration suppression.

ASTREX Hardware - Summary ...

Facility	:	**40 ft X 40 ft X 40 ft Laboratory** **Overhead Crane** **Temperature Control**
Air Bearing	:	**Spherical (3-Axis) Air Bearing, 19 inch Ball** **Cable Follower, Two Gimbal - 3 Axis Mechanical Arrangement** **Rigid Body Attitude Sensing - 1 arc sec Accuracy**
Computer	:	**Real Time Control and Data Acquisition Computer** **32 Inputs, 32 Outputs, 1000 Hz Sampling Rate** **10 - 15 MFLOP Multi Processor / Array Processor System**
Structure	:	**3 Mirror Beam Expander** **1/3 - 1/2 Dynamically Scaled Structure** **Modular, Graphite Epoxy Construction**
Sensors/ Actuators	:	**Throttleable Cold Gas Thrusters** **Proof Mass Actuators, Reaction Wheels** **Provision for Control Moment Gyros (CMGs)** **Accelerometers** **Embedded Sensors and Actuators** **Optical Line of Sight Sensor**

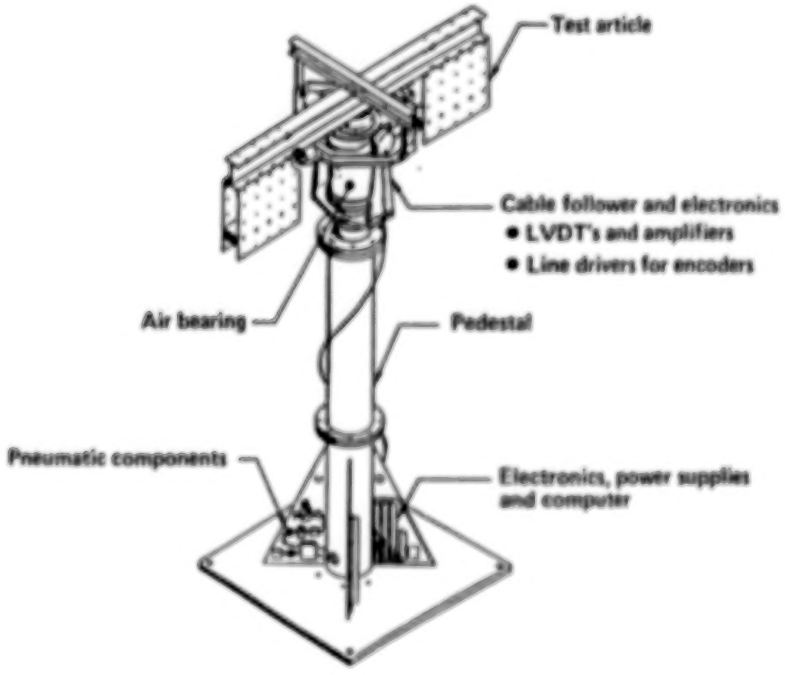
The facility will be housed in a large enclosure which is located inside an even larger hangar bay. The enclosure is air-tight to enable still-air conditions during experiments, and insulated so that temperatures will remain constant during experiments. The enclosure allows an unobstructed volume of 40'x40'x40', and includes an overhead crane capable of lifting up to 10,000 lbs. The seismic stability of the hangar floor has been tested, and the ASTREX site was found to be seismically quieter than many currently operational vibration test facilities.



BEST COPY AVAILABLE

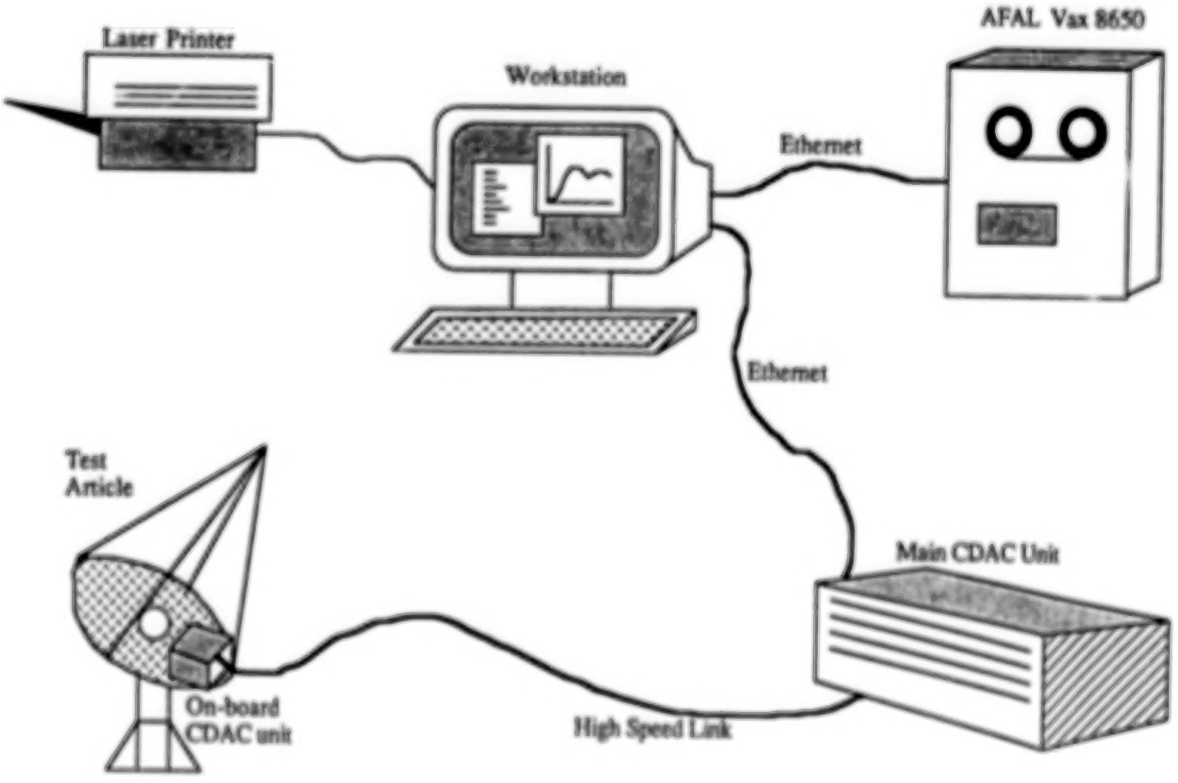
Experimental articles will be supported by a 19-inch spherical air bearing being developed by Boeing Aerospace. The air bearing is capable of supporting loads weighing up to 14,500 lbs. The air bearing system includes a sophisticated double gimbal, 3-axis cable follower which ensures that the multitude of supply lines to the experimental article will not induce measurable torque disturbances during slewing. The system will also provide rigid body attitude measurements of 1 arc second accuracy.

ASTREX Hardware - Pedestal



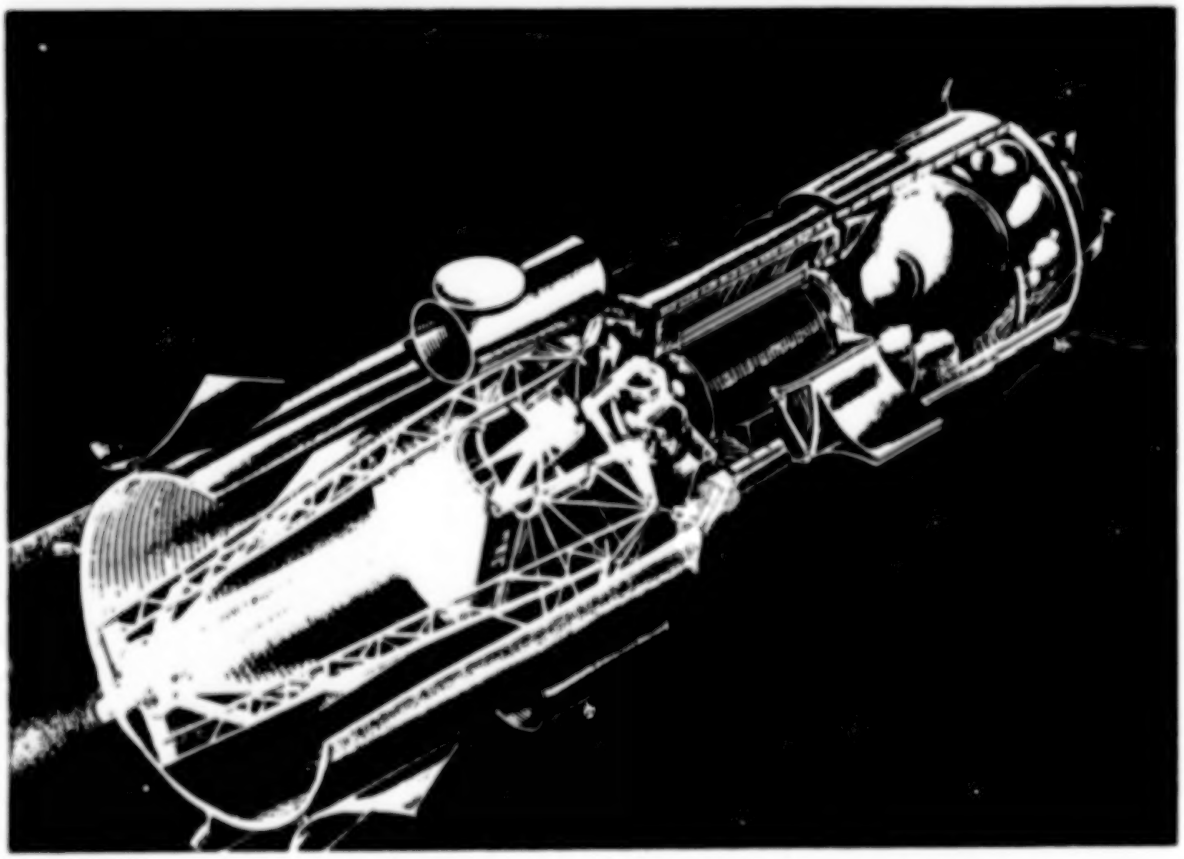
ASTREX will include a powerful real-time control and data acquisition computer (CDAC). The CDAC system will include the following components: a main computational unit for real time control processing; a remote unit, consisting primarily of A/D (analog to digital) and D/A (digital to analog) converters, to be located on the structure; and a workstation, which will run the control design and analysis software and provide the user interface for the CDAC system. The main CDAC unit will use multiple parallel processors to be capable of sustained calculation rates of 11 MFLOP (million floating point operations per second) under both linear and non-linear computational loads. The CDAC system will accommodate up to 32 input and 32 output channels, and will operate at sampling rates selectable by the user. The control design and analysis software running on the workstation will be highly integrated with the CDAC hardware, and will provide an extremely facile user interface, enabling time-efficient use of the CDAC by many different researchers and making high-speed computational performance possible without microcoding.

ASTREX Control/Data Acq. Computer (CDAC)



Initial success of the ASTREX facility depends largely upon design of an appropriate first experimental article. The experimental article must exhibit mission relevance, research relevance, technology relevance, and modularity. Mission relevance means that the structure should be closely representative of one or more Air Force or SDI future space missions. Research relevance means that the structure should exhibit many of the research challenges associated with the broad class of large space structures (for example, control/structures interaction, closely-spaced vibrational frequencies, etc.). Technology relevance means that the structure should be constructed with materials and hardware designs which are representative of those actually likely to be used on future missions (for example, graphite/epoxy construction, open truss construction, etc.) Finally, modularity means that the structure should be designed and constructed so that substructural elements can be removed and replaced with alternative components, such as "smart structural" elements. The attributes of modularity, mission relevance, research relevance and technology relevance have all been woven into the design of the initial ASTREX test article.

ASTREX Facility

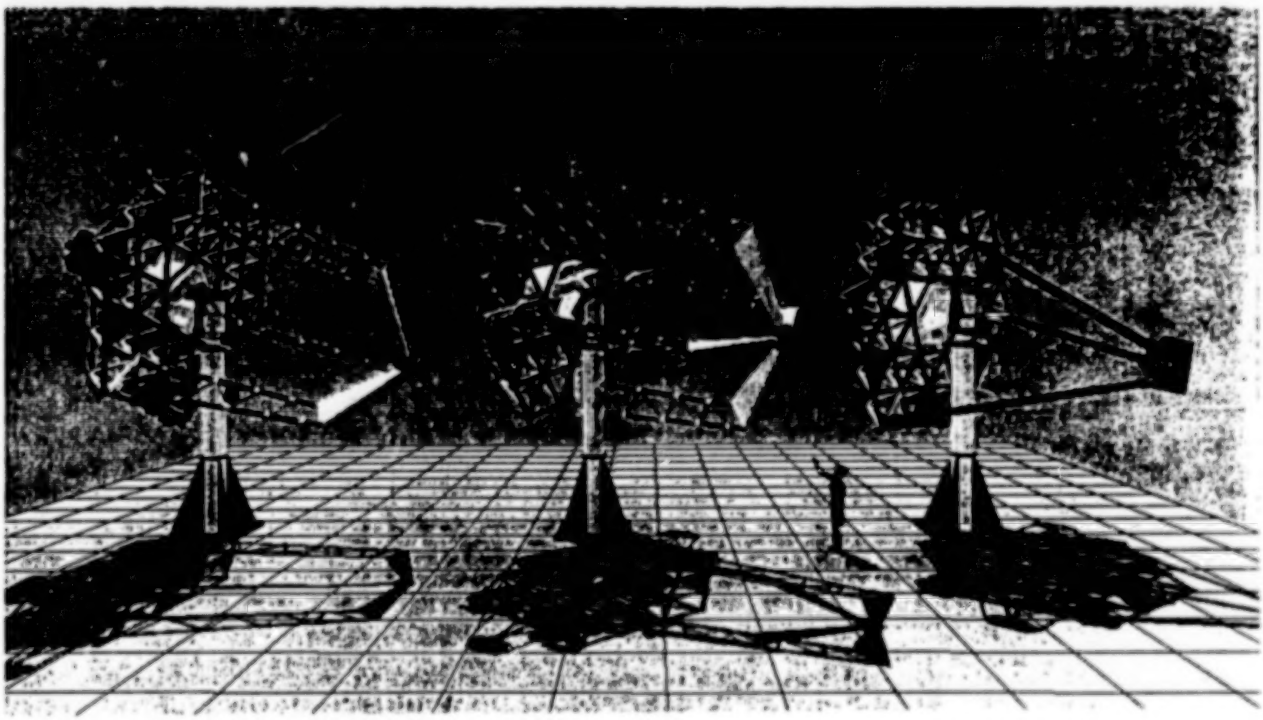


The ASTREX 3-mirror beam expander experimental article includes the following design details. The primary support structure is a tetrahedras space truss design, with graphite/epoxy (Gr/Ep) composite tubes and aluminum joints. The tripod metering truss is also of Gr/Ep construction with aluminum joints. A structural steel mass with aluminum struts will represent the inertial properties of the tertiary mirror. Steel masses will be used as well to represent all other non-structural masses, such as the primary mirror elements, optics control hardware, etc.

INITIAL ASTREX EXPERIMENTAL ARTICLE: 3-MIRROR SBL BEAM EXPANDER

- **Primary Support - tetrahedral space truss**
- **Truss struts - Gr/Ep composite tubes, aluminum joints**
- **Tripod metering truss - Gr/Ep composite tube, aluminum joints**
- **Tertiary mirror simulator - steel, with aluminum struts**
- **Non-structural masses - steel**

Modularity is a key feature of the ASTREX experimental article; this is incorporated in the following ways. First, two different secondary support trusses have been designed for the structure: a tubular tripod and a planar truss quadrapod. Either can be mounted onto the primary support structure. Also, the planar truss elements are removable, and can be exchanged with alternative elements (such as passively or actively damped elements, or struts constructed of innovative materials.) The primary support structural members are also removable/replaceable. Sensors and actuators will all be relocatable, with a multitude of mounting provisions located throughout the structure.



BEST COPY AVAILABLE

An initial complement of sensors and actuators for system identification and shape/pointing/vibration control will be selected from among the following:

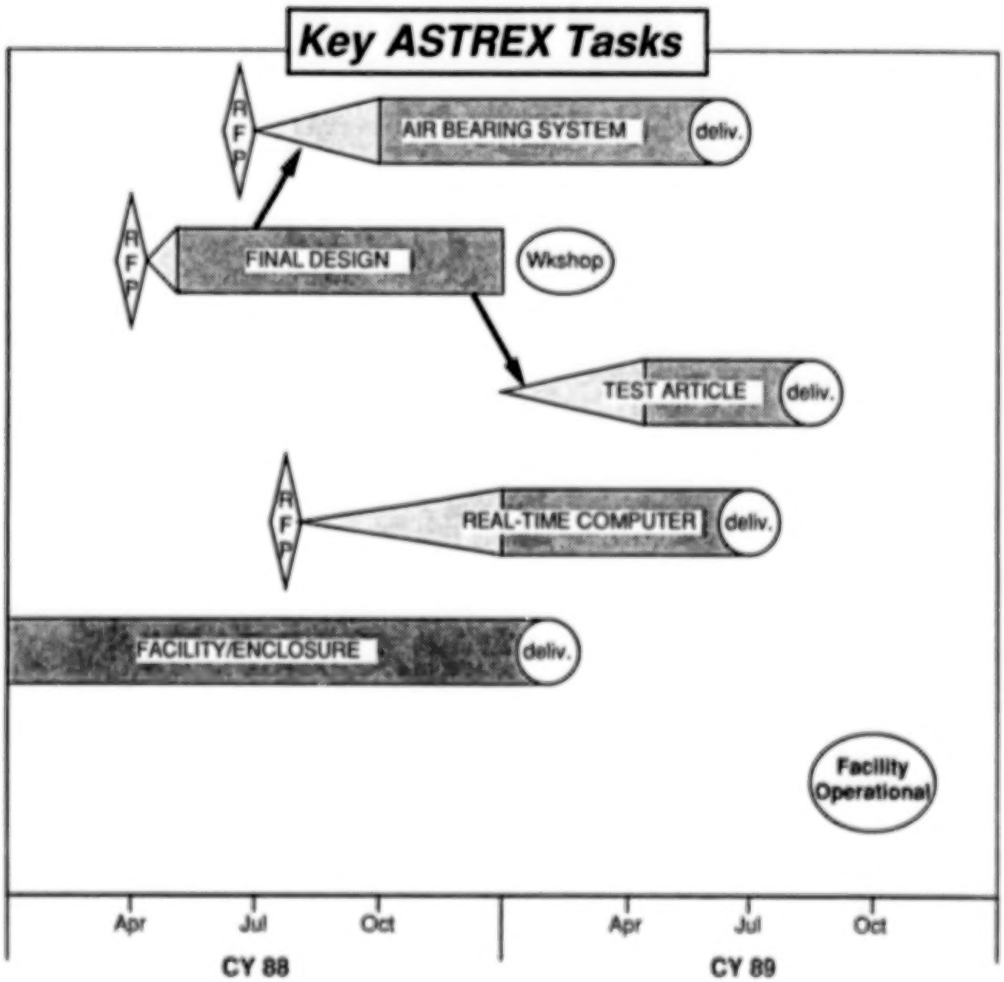
1) Throttleable Cold Gas Thrusters
2) Proof Mass Actuators
3) Reaction Wheels
4) Control Moment Gyros (CMGs)
5) Accelerometers
6) Embedded Sensors and Actuators
7) Optical Line of Sight Sensor

The sensors and actuators used in ASTREX will of course continue to change and evolve over time, and will not be restricted to those indicated on the above list.

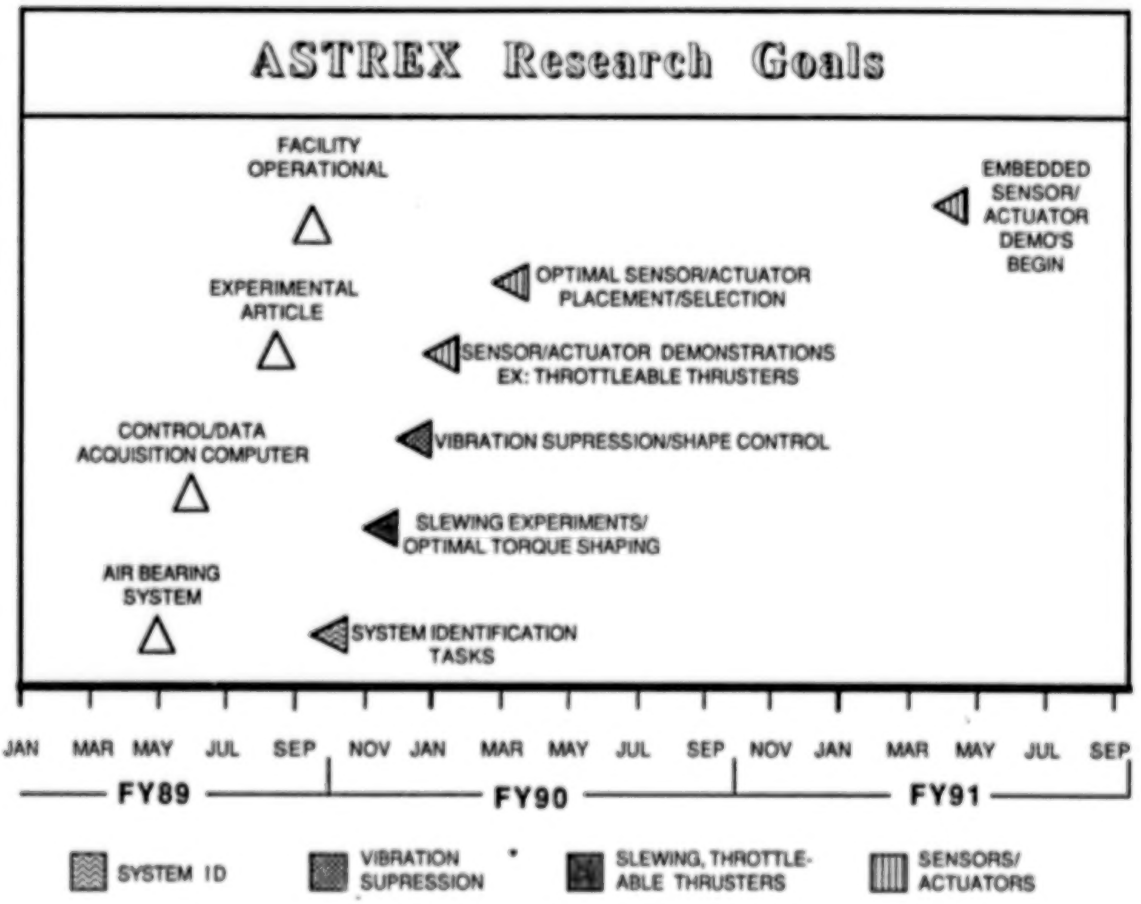
SENSORS AND ACTUATORS FOR ASTREX

- **Throttleable Cold Gas Thrusters**
- **Proof Mass Actuators**
- **Reaction Wheels**
- **Control Moment Gyros (CMGs)**
- **Accelerometers**
- **Embedded Sensors and Actuators**
- **Optical Line of Sight Sensor**

All key elements of the ASTREX facility are currently in procurement, except for the environmentally controlled enclosure, of which construction is now complete. The Air Bearing System will be delivered under a contract currently in progress, with final installation and check-out scheduled for 31 May 89. The Control and Data Acquisition Computer (CDAC) will also be delivered under a contract currently in progress, with final installation and check-out scheduled for 31 June 89. The beam expander structure was designed by Boeing Aerospace; component procurement and experimental article fabrication is being managed "in-house" by AFAL personnel, with final assembly scheduled for fall of '89.

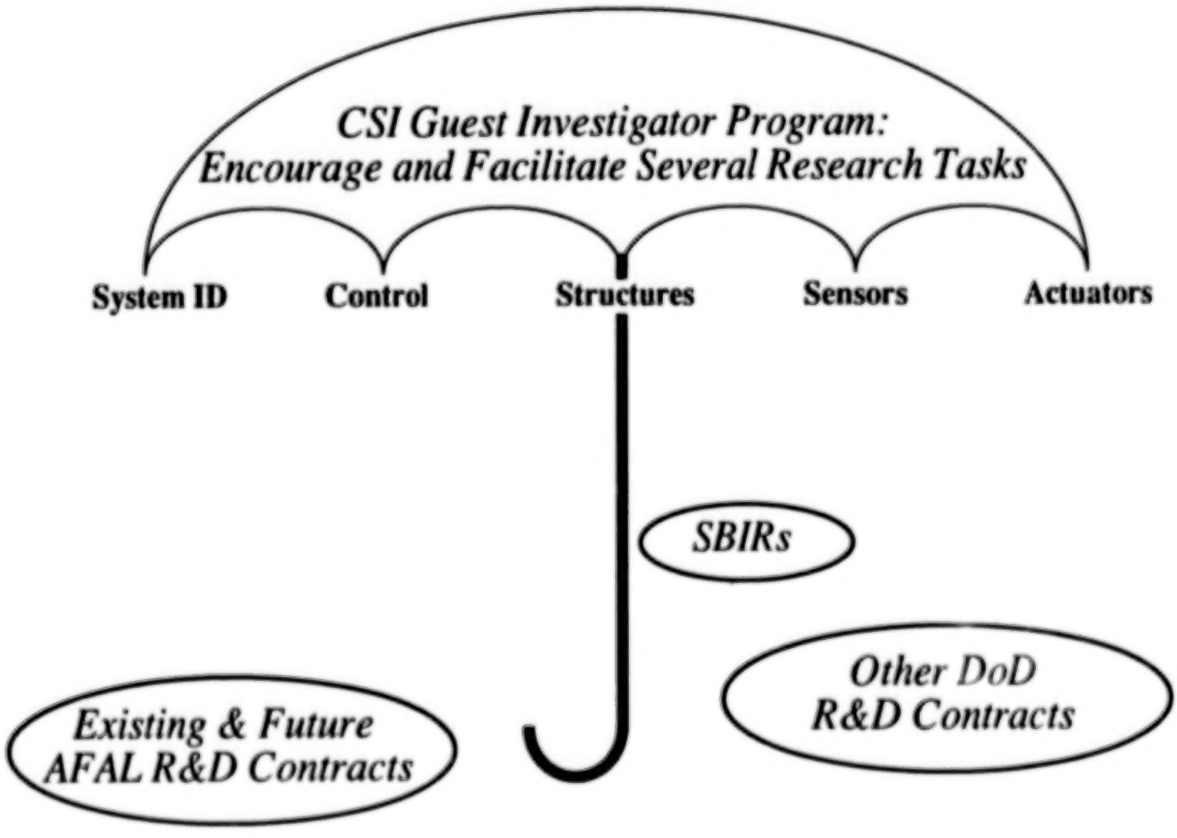


ASTREX will be the site of a variety of LSS experiments over the next several years. Currently, AFAL plans call for initial research to focus on system identification, which will generate progressively more refined models of the experimental article structure. Depending upon the initial slew actuators which are selected, initial control experiments may focus on thrust profile shaping for optimal slewing maneuvers. In conjunction with slewing, experiments will be a demonstration of multiple approaches to vibration suppression and shape control. In summer '91, ASTREX will provide the test bed for demonstration of the embedded sensor and actuator (ESA) members, or "smart structures," being developed under a contract at AFAL. Prior to these demonstrations, AFAL plans to demonstrate the smart structures which are developed under its own in-house development effort.



Several contractural vehicles will be available to researchers proposing to conduct research in the ASTREX facility. AFAL plans to collaborate with NASA on a joint guest investigator (GI) program for research in Controls/Structures Interaction (CSI) technologies. The CSI GI program will serve as a means to encourage and facilitate several concurrent 1-2 year research tasks in ASTREX (as well as in other NASA facilities). The initial emphasis of the research in ASTREX will be on experimental demonstration, comparison, and evaluation of existing state of the art control methodologies and hardware, as opposed to contract developing new theory. In addition to participation as a task under the CSI GI program, other potential users of ASTREX would include researchers with existing or future AFAL contracts (such as ESA) which called for experimental demonstration in a test bed. Likewise, researchers with contracts funded by other DOD agencies and NASA might use ASTREX for experimental demonstration. Finally, SBIR contracts might involve experiments in ASTREX. The key point to emphasize is the intended flexibility and open nature of the facility, which AFAL hopes will attract participation of many of the leading researchers in LSS control from Industry, Universities, and Government.

CONTRACTURAL VEHICLES FOR CONDUCTING RESEARCH IN ASTREX



A workshop was held on 16 February 89 at AFAL to inform researchers from Industry, Universities, and Government about the initial operational capability of ASTREX. The major objectives of the workshop were to fully inform participants about the following:

1) The final design and configuration for the facility's air bearing system (now in procurement); (This information will be especially useful for researchers with an interest in fabricating their own space structure test articles for experimentation in ASTREX in the future).
2) The completed final designs for the facility's first two test articles (space structure models); (This information will be relevant to all researchers interested in conducting research in ASTREX using one or both of the facility's initial test articles).
3) The operational capabilities of the facility's experiment control computer (in procurement); (Important information for researchers planning to develop and implement system identification and/or real-time control algorithms on the ASTREX computer).
4) AFAL's goals and projected research schedule for ASTREX.

ASTREX WORKSHOP (16 FEB 89) AT AFAL

PROVIDED DETAILS CONCERNING:

- **FINAL DESIGN & CONFIGURATION OF AIR BEARING SYSTEM**
- **FINAL DESIGN & CONFIGURATION OF INITIAL TEST ARTICLES**
- **OPERATIONAL CAPABILITIES OF CONTROL/DATA ACQ. COMPUTER**
- **GOALS, PROJECTED RESEARCH FOR ASTREX**

IN-HOUSE EXPERIMENTS IN LARGE SPACE STRUCTURES AT THE AIR FORCE WRIGHT AERONAUTICAL LABORATORIES FLIGHT DYNAMICS LABORATORY

Robert W. Gordon
AFWAL/FDSGC
Wright Patterson AFB, Ohio

Umit Ozguner and Steven Yurkovich
The Ohio State University
Columbus, Ohio

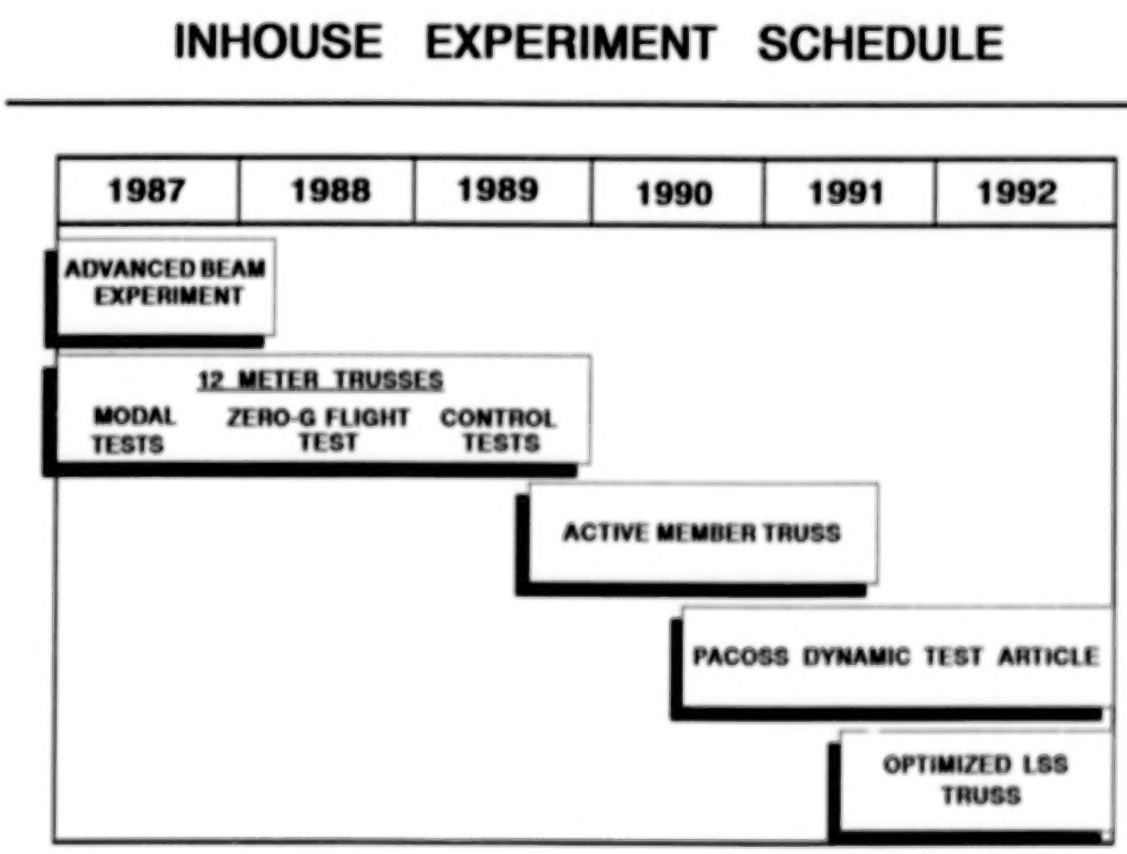
Third NASA/DOD CSI Technology Conference
January 30 - February 2, 1989

Introduction

The Structures Division of the Air Force Wright Aeronautical Laboratories Flight Dynamics Laboratory is conducting an inhouse exploratory development program in the dynamics and control of large space structures (LSS). The effort, entitled "Large Space Structures Technology Program," was initiated in 1985 to investigate several technical areas important to the development of future LSS. These areas include ground suspension and test methods, passive and active vibration control approaches, and sensors and actuators for vibration control. The program is being performed in the Structural Dynamics Branch. Support for active control development is provided by the Ohio State University, under contract.

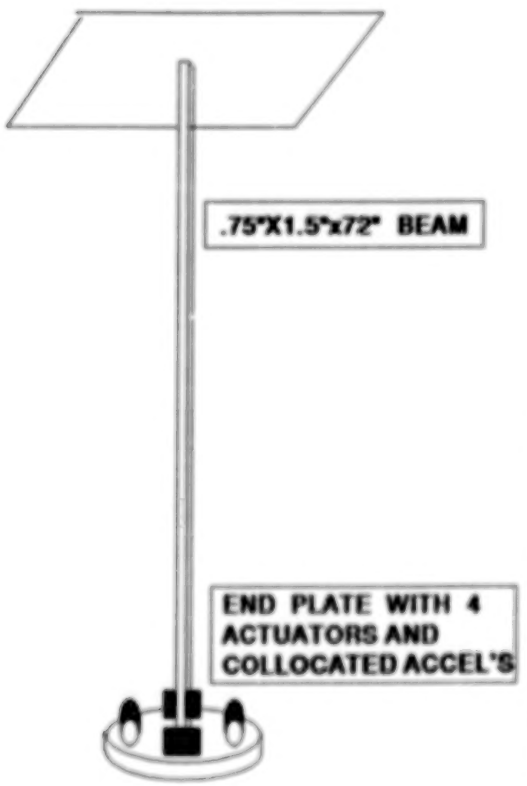
Program Plan

The overall objective of the Large Space Structures Technology Program is to establish a capability in the Structures Division for dynamic analysis and testing of large, flexible space structures with passive and active vibration control. The program approach is to conduct a series of experiments addressing the areas of ground testing, passive and active vibration control, and sensors and actuators. The figure depicts the schedule for these experiments. The first experiment, the Advanced Beam Experiment, evaluated the performance of active vibration control approaches on a bending-torsion cantilever beam equipped with two pairs of linear momentum exchange actuators. The 12 Meter Trusses provide a test bed for several experiments in modal testing and active control of large, low frequency truss structures with significant passive damping. The Active Member Truss Experiment will address the effectiveness of active members in providing low frequency vibration control in truss structures. In mid-1990, the PACOSS Dynamic Test Article (DTA) will be set up as a test facility for the evaluation of system identification and active control approaches for structures with significant passive damping. The DTA was developed on the Passive and Active Control of Space Structures (PACOSS) contract. The final experiment in the program is the Optimized LSS Truss which will be a modular truss test bed for evaluating optimized structures with passive and active control.



Advanced Beam Experiment

The Advanced Beam is a bending-torsion beam active vibration control experiment. The objective is to experimentally evaluate the performance of linear momentum exchange actuators and popular control approaches on a simple structure with multiple, low frequency modes. The experiment incorporates a vertically oriented slender aluminum beam, cantilevered at the top from a stiff frame. Control forces are provided by two pairs of actuators mounted on an aluminum disk at the beam free end. The aluminum disk serves to reduce the fundamental torsion mode frequency while providing an actuator mounting surface. A piezoelectric accelerometer is collocated with each actuator as a sensor. The actuators are modified versions of the VCOSS II design now in use at the NASA Marshall Space Flight Center's facility.



OBJECTIVE

DEMONSTRATE ACTIVE VIBRATION CONTROL ON A SIMPLE STRUCTURE WITH:

- NONGROUNDED SENSORS AND ACTUATORS
- MULTIPLE, LOW FREQUENCY MODES

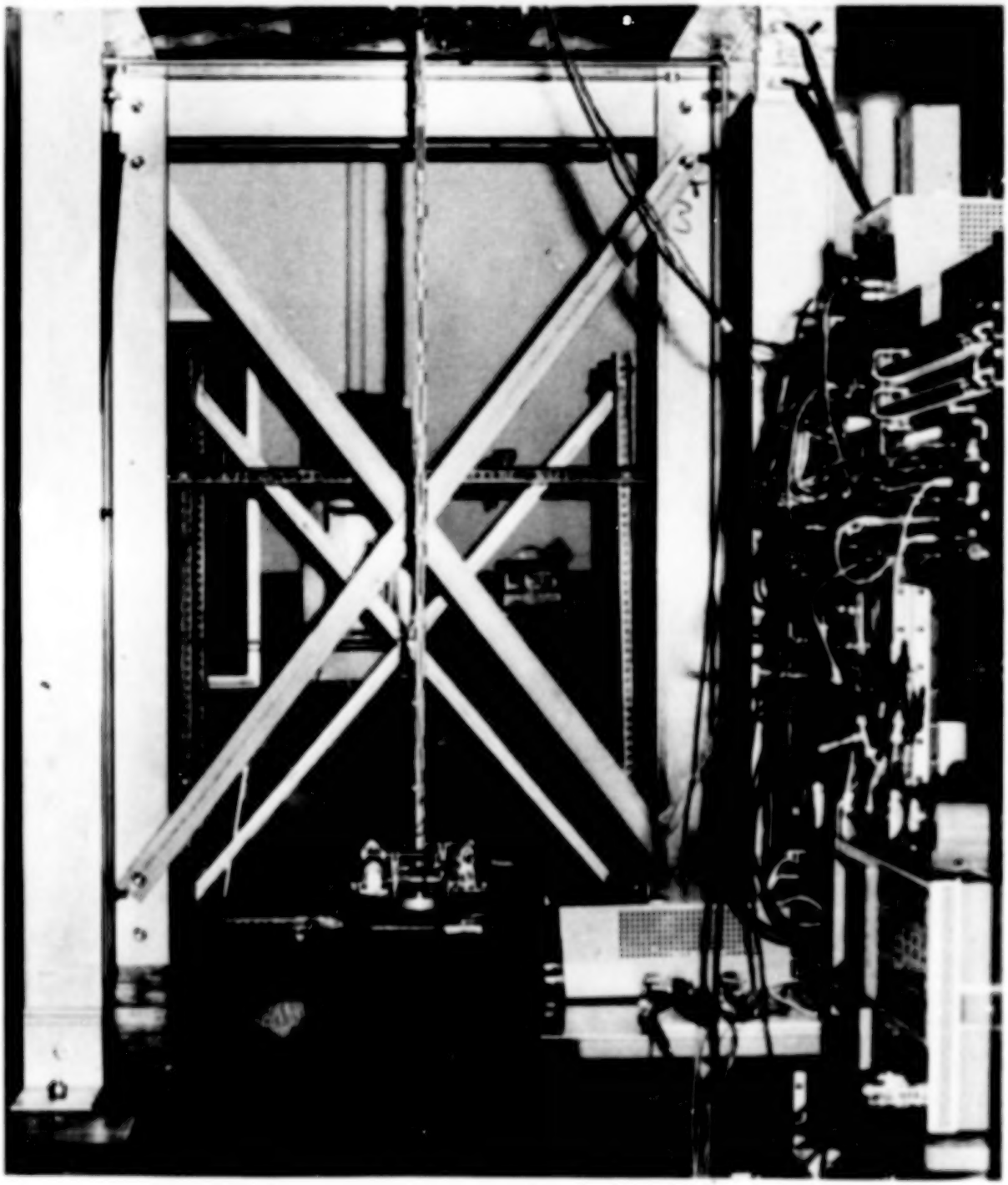
APPROACH

TEST A SLENDER CANTILEVER BEAM WITH END MASS

CONTROL BENDING AND TORSION MODES

Advanced Beam Experiment Hardware

The Advanced Beam hardware is shown in the figure. The support frame for the beam is mounted to a seismic table located in the vibration test facility at the Flight Dynamics Laboratory. The two pairs of linear momentum exchange actuators can be seen mounted on the disk at the free end of the beam. Each pair of actuators can be commanded in phase to control one bending plane while either pair can be commanded out of phase to control torsion. The beam has fundamental bending frequencies of approximately 1.3 Hz and 1.6 Hz in the two bending planes and a fundamental torsion frequency of about 13 Hz.



Ohio State University Work on the Advanced Beam Experiment

The Ohio State University provided considerable effort in support of the Advanced Beam Experiment. The effort included both analytical and experimental development of hardware and control system design and testing. They developed and verified an analytical model of the actuator as well as analog compensator circuitry to provide acceptable actuator dynamic response. They also developed a mathmatical model of the total system and corrected it with open loop test results. Several control approaches were developed for the beam, as listed in the figure. Controller performance was evaluated analytically and three controllers were tested; HAC/LAC, Maximum Entropy Optimal Projection (MEOP), and decentralized LQG with frequency shaping.

- **DEVELOPED ANALYTICAL AND EXPERIMENTAL ACTUATOR MODELS**
- **DESIGNED ACTUATOR COMPENSATOR**
- **DEVELOPED BEAM ANALYTICAL MODEL**
- **DESIGNED AND PERFORMED SIMULATION OF SEVERAL CONTROLLERS**
  - **HAC/LAC**
  - **LQG/LTR**
  - **MEOP**
  - **VARIABLE STRUCTURE CONTROL**
  - **PARAMETER ROBUST LQG**
  - **DECENTRALIZED LQG**
- **TESTED THREE CONTROLLERS ON THE BEAM**
  - **HAC/LAC**
  - **MEOP**
  - **DECENTRALIZED LQG / FREQUENCY SHAPING**

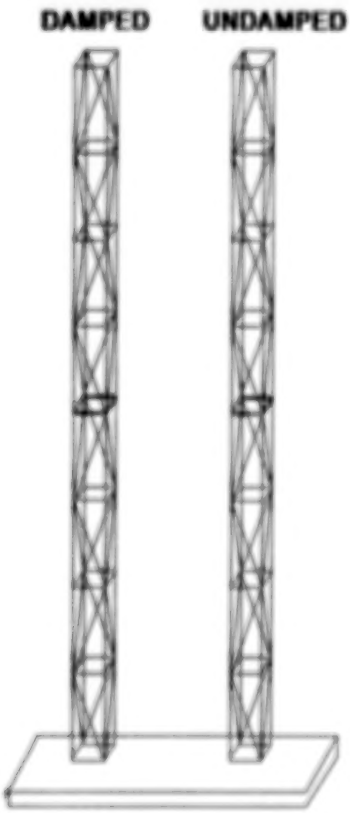
Advanced Beam Experiment Conclusions

Active control performance testing on the Advanced Beam Experiment was completed in April 1988. Several conclusions can be drawn from the completed work. A well characterized dynamic system was achieved. Initial analytical models agreed well with open-loop test and were improved based on the test data. Compensation circuitry designed to "tame" actuator dynamics worked reasonably well in practice, although a better actuator design might have eliminated the need for compensation altogether. Active modal damping in excess of 10% was achieved in the fundamental bending modes of the beam. Although higher damping might be expected, 10% is reasonable given the limited actuator output available. The actuators were the single biggest limiting factor in active control performance. The momentum exchange design is inherently limited in low frequency force output. The actuators were rated at over 4 pounds force output, but could only develop rated output above approximately 10 Hz. The actuators were capable of only 0.1 pounds force at the lowest beam frequency of 1.3 Hz. In addition, the actuators were relatively massive compared to the beam alone. This significant mass tended to limit modal displacement at the beam free end, and therefore control authority in other than the fundamental bending modes was severely limited. Finally, actuator dynamics increased open-loop damping in the fundamental bending modes. This is not necessarily bad, but it tended to mask the increase in modal damping achieveable though active control.

- **A WELL CHARACTERIZED SYSTEM WAS ACHIEVED**
- **ACTUATOR COMPENSATION WORKED REASONABLY WELL**
- **ACTIVE MODAL DAMPING OF OVER 10% WAS ACHIEVED**
- **ACTUATORS LIMITED ACTIVE CONTROL PERFORMANCE**
  - **LIMITED LOW FREQUENCY FORCE OUTPUT**
  - **POOR AUTHORITY IN HIGHER MODES**
  - **ACTUATORS INCREASED OPEN-LOOP DAMPING**

12 Meter Truss Modal Tests

The 12 Meter Truss Experiment is investigating ground test methods and active control approaches for large, lov frequency structures. The trusses are 12 meter long truss beams; one with relatively high modal damping, the other with light damping. A series of modal tests is being conducted on the trusses to evaluate modal parameter test and suspension methods for lightly and heavily damped truss structures. Both trusses have been tested in a vertical orientation, cantilevered to the floor. Modes in the 0 to 50 Hz frequency range are being identified and compared with finite element model predictions. The undamped truss will then be tested in a horizontal orientation, suspended on soft springs, to simulate the zero gravity space environment. Data from both test configurations are being used to improve the model of the undamped truss for subsequent active control analysis and testing. After completion of ground testing, the undamped truss will be tested in the NASA Johnson Space Center's zero-gravity test aircraft to obtain true zero-g modal parameters.



OBJECTIVES

EXPERIMENTALLY DETERMINE THE MODAL PARAMETERS OF LIGHTLY AND HEAVILY DAMPED TRUSS STRUCTURES

USE MULTIPLE BOUNDARY CONDITION TEST RESULTS TO IMPROVE ANALYTICAL MODELS

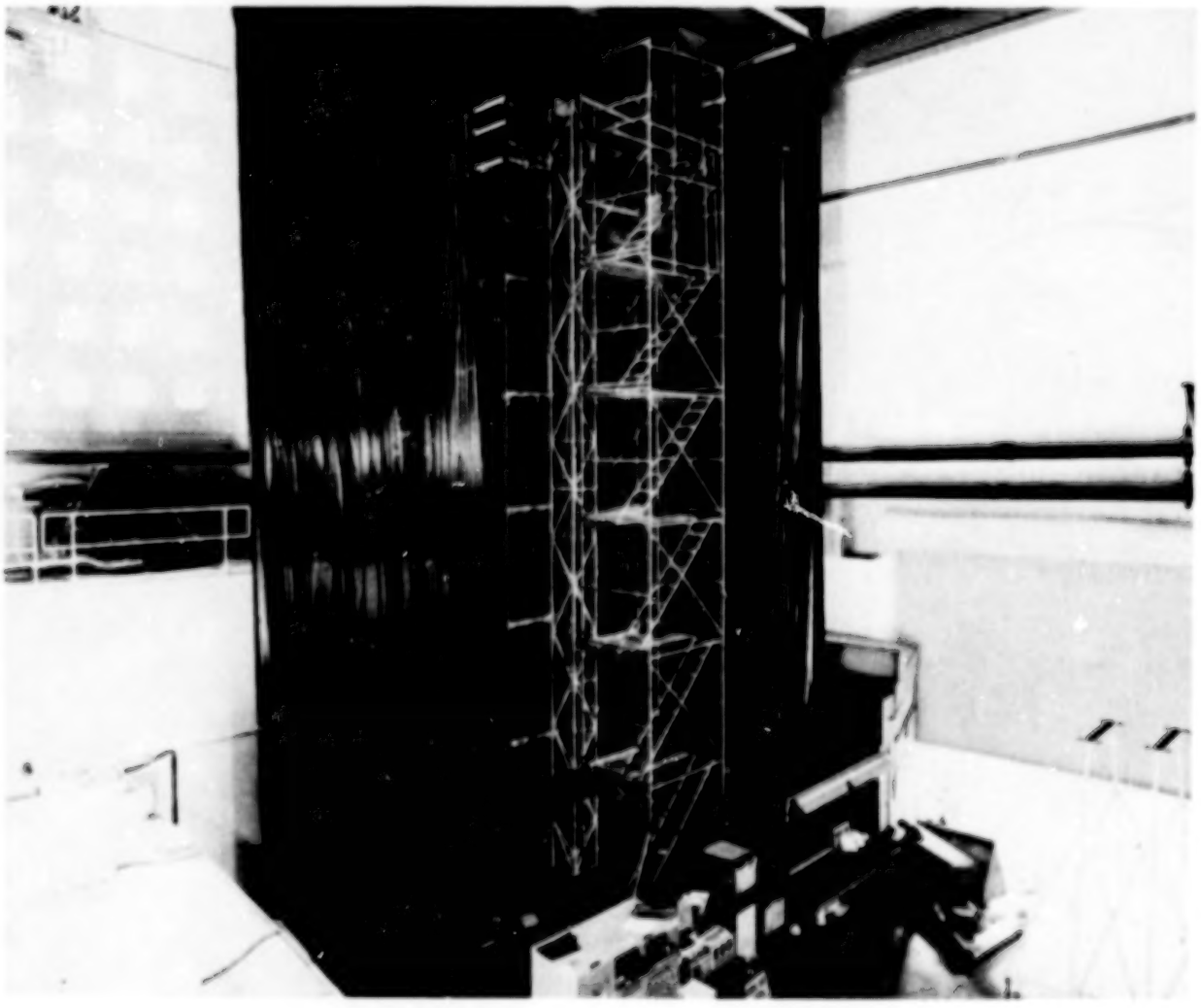
APPROACH

TEST TWO, 12 M LONG TRUSS BEAMS, ONE UNDAMPED AND ONE WITH VISCOELASTIC DAMPERS

TEST THE TRUSSES IN VERTICAL CANTILEVER AND HORIZONTAL FREE-FREE CONDITIONS

12 Meter Truss Vertical Cantilever Test Configuration

The undamped 12 meter truss is shown in the figure in the vertical cantilever test configuration. The truss can be seen near the center of the figure with access scaffolding mounted close to it on three sides. The undamped truss consists of a welded aluminum tube frame with bolt-in diagonal members of Lexan plastic. Lexan has a relatively low loss factor which results in modal damping values of less than .5% of critical damping for the lower order modes of the truss. Low damping coupled with fundamental bending frequencies of approximately 2 Hz provides a structure with dynamic characteristics representative of future large space structures. The damped truss has a welded aluminum frame identical to the undamped truss, but has aluminum diagonal members with viscoelastic dampers instead of the Lexan tubing. The diagonal members are arranged in the truss to maximize their modal strain energy content in the lower order modes and therefore maximize damping.



Undamped 12 Meter Truss Modal Test Results

Modal testing of the undamped 12 meter truss in the vertical cantilever configuration has been completed. Measured frequencies and modal damping values for the lowest 6 modes are listed in the figure along with predicted frequencies from a finite element model. The bending modes occur in pairs with nearly coincident frequencies, as predicted by the model. However, the model overestimates the fundamental bending frequencies by more than 10%. In contrast, the model underestimates the first torsion frequency by 11%. These discrepancies are partially due to the boundary conditions at the truss base which are modelled as clamped but actually provide some flexibility. Additional error is likely due to the lack of detail in the modelling of the truss joints. Results from the upcoming horizontal, free-free test of the truss will help separate these boundary condition effects from other model parameters. Measured modal damping values are in the range of .1% to .5% of critical damping, as desired.

	FREQUENCY (HZ)			DAMPING (%)
MODE	TEST	PREDICTED	ERROR (%)	TEST
1ST X BENDING	2.26	2.48	+9.5	.19
1ST Y BENDING	2.25	2.50	+10.9	.18
1ST TORSION	7.10	6.34	-10.8	.33
2ND X BENDING	10.72	10.90	+1.7	.18
2ND Y BENDING	10.72	11.00	+2.6	.21
2ND TORSION	21.27	19.04	-10.5	.27

Damped 12 Meter Truss Modal Test Results

Modal testing of the damped 12 meter truss in the vertical cantilever configuration is nearly completed. Measured frequencies and modal damping values for the lowest five truss modes are tabulated in the figure. Predicted frequencies and damping values are included in the figure for comparison. The Modal Strain Energy method was used to predict modal damping from finite element models incorporating 2 Hz and 10 Hz viscoelastic properties. The analysis is thus valid for modes which occur close in frequency to the VEM frequency used. The agreement between predicted and measured frequency for the bending modes is reasonably good. The predictions for all modes except 1st X bending are from a preliminary model based on 72 deg. F viscoelastic properties while the 1st X data are from an improved model which incorporated data for the exact test temperature. The damping estimate for the 1st X bending mode is in error by a factor of two while the the higher modes show even larger errors. These errors in predicted damping are most likely due to the unmodelled flexibility at the truss base. The 1st torsion mode, which is predicted to have almost 50% damping, has not yet been identified.

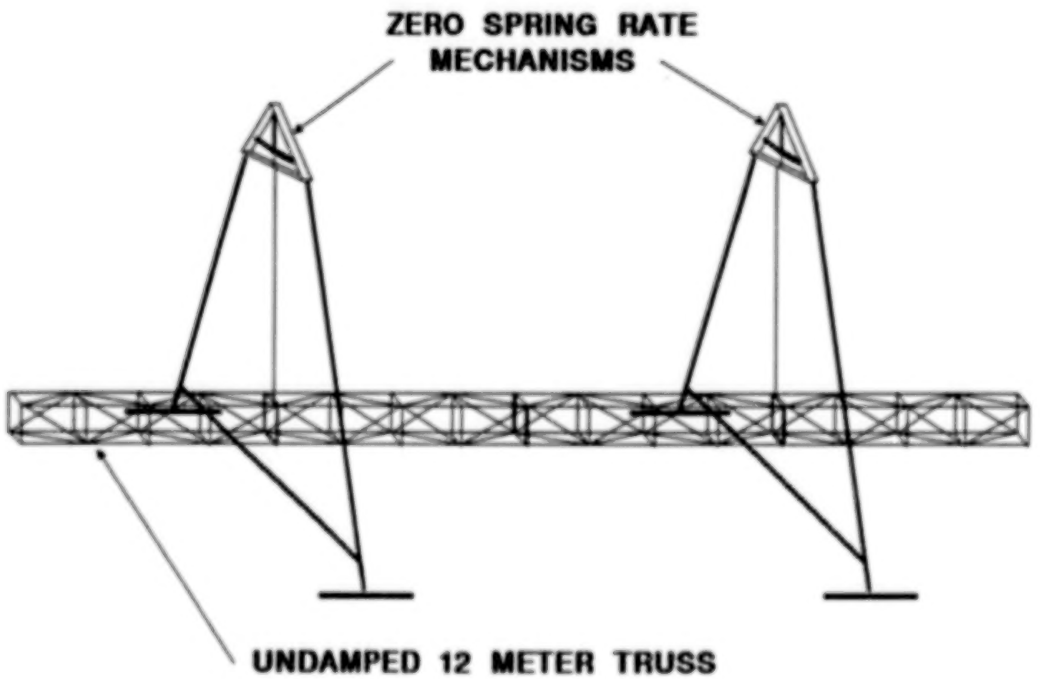
	FREQUENCY (HZ)			DAMPING (%)	
MODE	TEST	PREDICTED	VEM	TEST	PREDICTED
1ST X BENDING	1.87	1.88 *	2	4.3	8.6 *
1ST Y BENDING	1.91	2.03	2	4.1	16.4
1ST TORSION	**	4.35	2	**	42.7
1ST TORSION	**	6.40	10	**	47.0
2ND X BENDING	10.6	10.18	10	6.6	25.8
2ND Y BENDING	11.2	10.29	10	7.4	27.2

* CORRECTED MODEL RESULTS

** MODES NOT YET IDENTIFIED DUE TO HIGH DAMPING

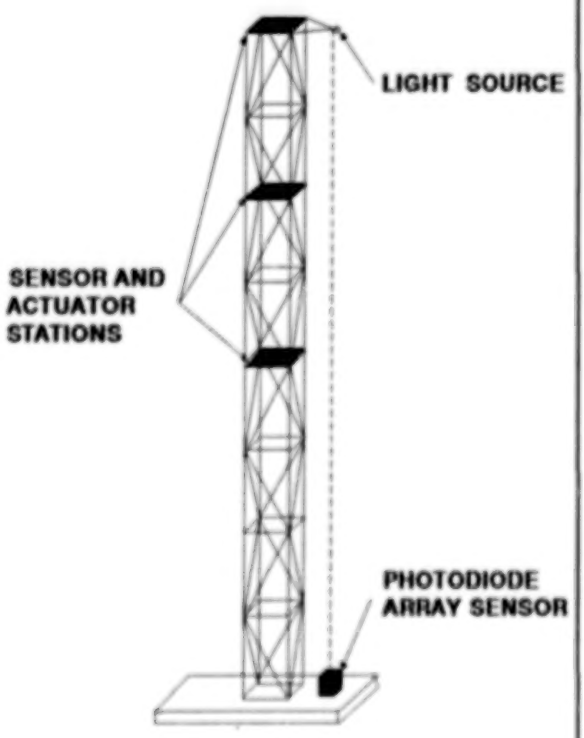
Undamped 12 Meter Truss - Horizontal Free-Free Test

A modal test of the undamped 12 meter truss will be performed in a horizontal configuration suspended from zero spring rate mechanisms (ZSRM's) to simulate the zero gravity conditions in space. The test configuration is illustrated in the figure. The truss will be suspended on flexible cables from two ZSRM's as shown. The ZSRM's act as very soft springs which uncouple the truss vibration response from suspension dynamics in the vertical direction. The ZSRM design being used was developed at NASA and has been adapted from a device currently in use at Martin Marietta Corporation. The suspension cables provide nearly free motion in the horizontal plane. Modal data measured from this test will be used in combination with the zero-g flight test data to evaluate the performance of the ZSRM's and to improve the undamped truss finite element model.



12 Meter Truss Active Vibration Control

Active vibration control testing will be performed on the undamped 12 meter truss following completion of all modal tests. The objective of this testing is to evaluate the performance of several leading control approaches on a large, low frequency truss beam with significant passive damping. The undamped truss will be fitted with sensors and actuators and mounted in the vertical cantilever configuration. Damped diagonal members from the damped truss will be selectively substituted for the Lexan diagonals in the undamped truss to provide a structure with adjustable passive damping. Several leading control approaches will be applied to the truss and their performance with different levels of passive damping will be measured. Control design and implementation will be provided by the Ohio State University. A photodiode optical sensor will be used to monitor truss tip displacement as a measure of controller performance. Active control approaches will be implemented on a new real-time control computer system at the Flight Dynamics Laboratory.



OBJECTIVES

ASSESS CONTROLLER PERFORMANCE ON A LARGE TRUSS BEAM

MEASURE THE EFFECT OF PASSIVE DAMPING ON CONTROLLER PERFORMANCE

EVALUATE NEW CONTROL COMPUTER ARCHITECTURE

APPROACH

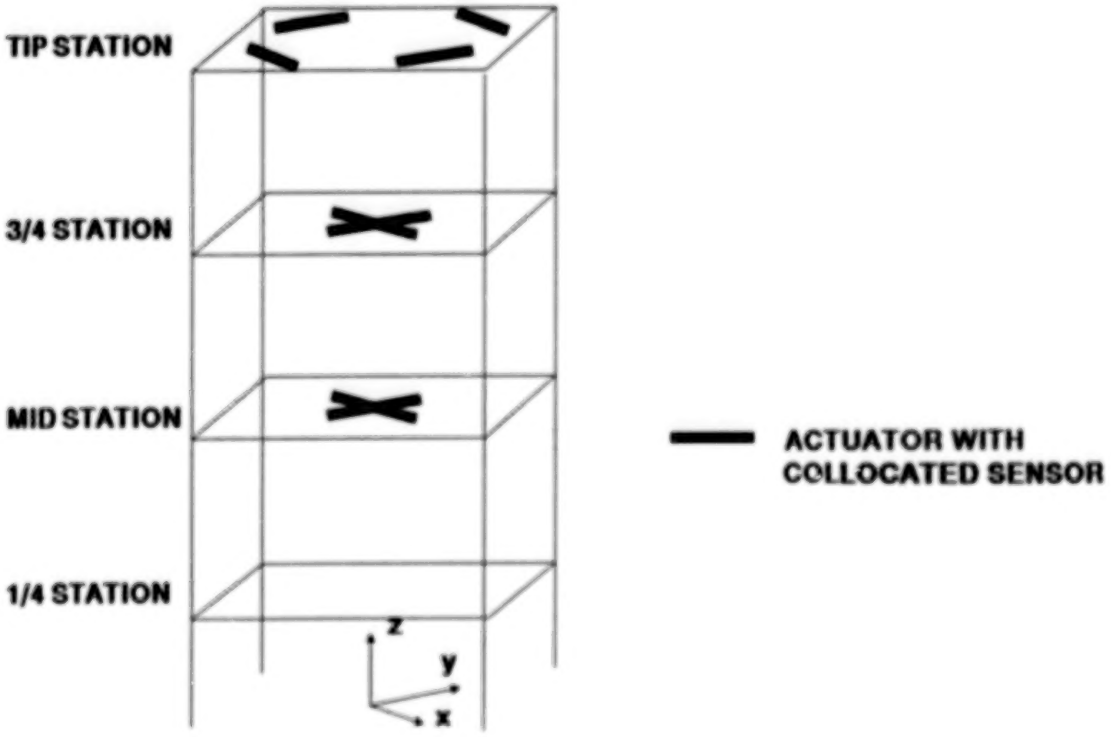
MOUNT SENSORS AND ACTUATORS ON THE UNDAMPED TRUSS

TAILOR MODAL DAMPING BY ADDING DAMPER MEMBERS

TEST CONTROLLERS AT SEVERAL LEVELS OF PASSIVE DAMPING

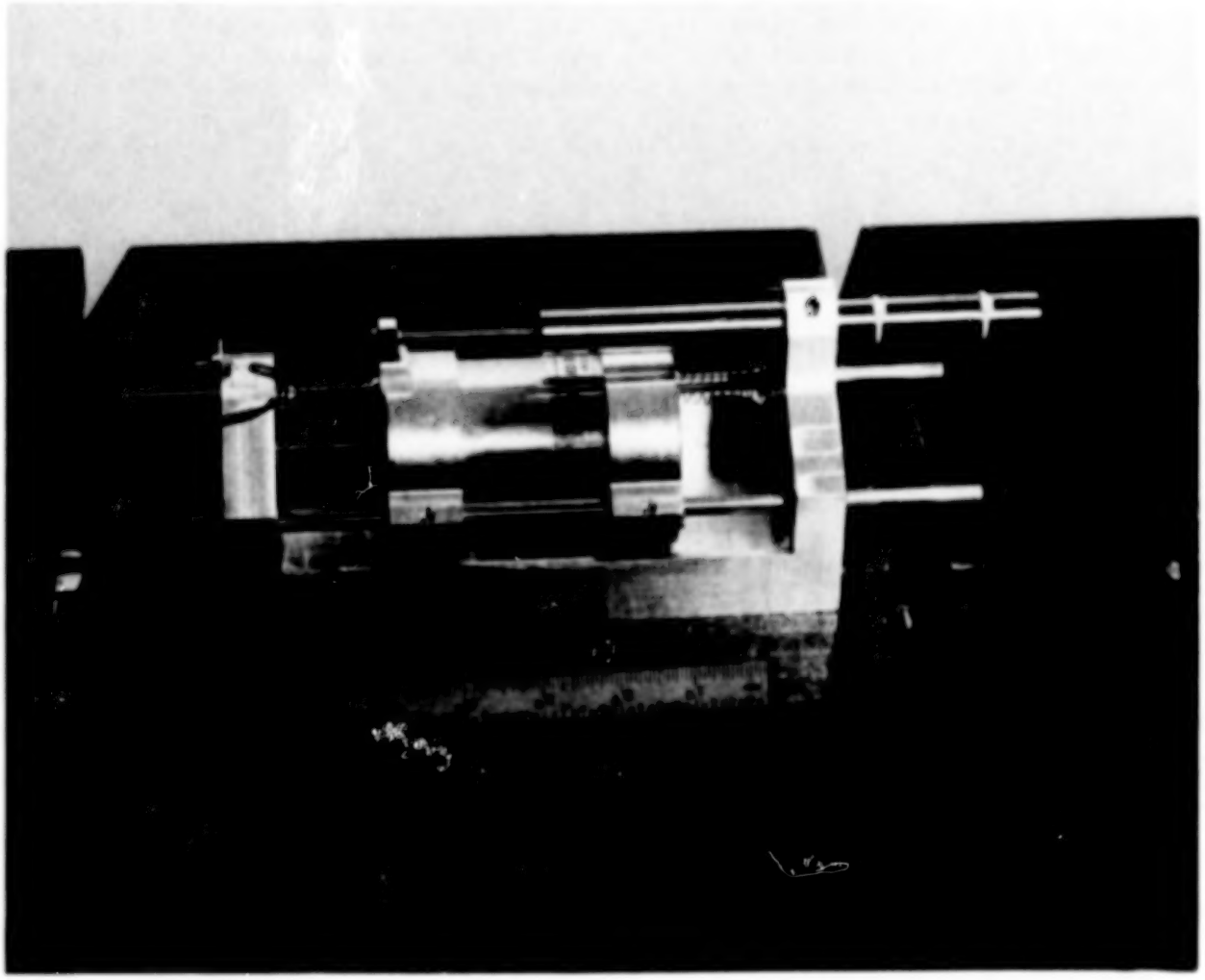
12 Meter Truss Sensor and Actuator Locations

Eight collocated pairs of sensors and actuators will be fitted to the undamped 12 meter truss to provide active vibration control forces. Linear momentum exchange type actuators will be used. Structural velocity signals will be obtained by integrating the output of linear accelerometers collocated with each actuator. The locations of the eight sensor/actuator pairs is shown in the figure. Two pairs of actuators will be positioned at the truss tip, with one pair parallel to each bending plane. Each pair can be commanded in-phase to control bending response while either pair can be commanded out-of-phase to provide a moment to control torsion response. Single pairs of actuators oriented parallel to the bending planes will be positioned at the truss 3/4 and mid-station locations. These actuators will provide bending mode control only.



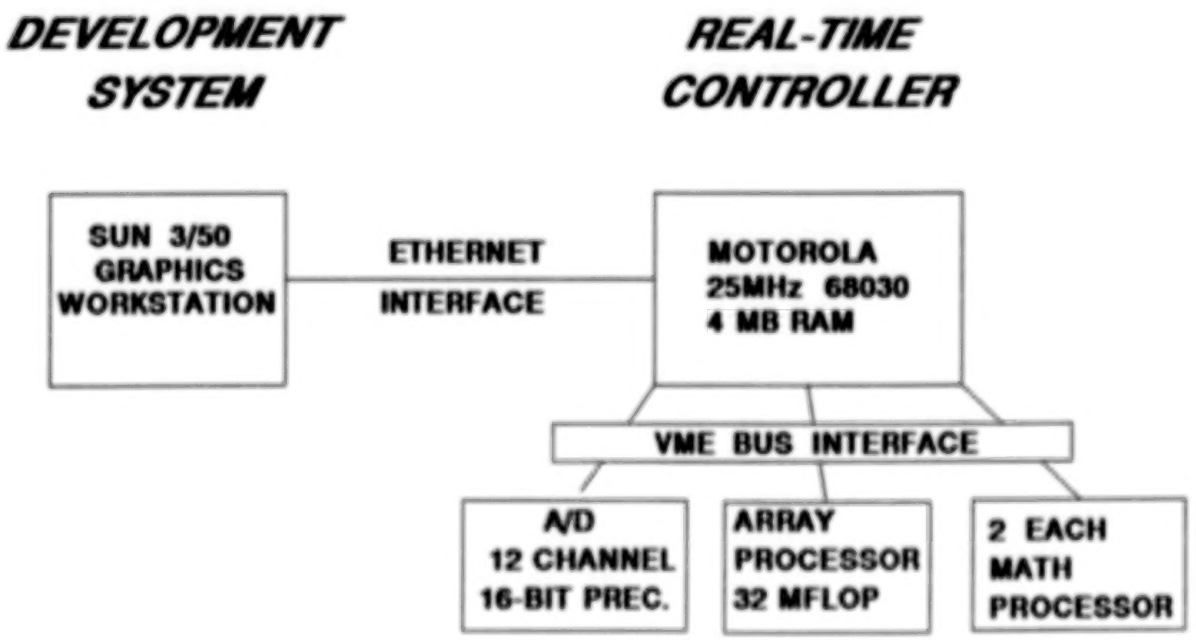
12 Meter Truss Actuator

Linear momentum exchange actuators will be used to provide control forces on the 12 meter truss. The actuator design is shown in the figure. This design is a modified version of the actuator developed at Martin Marietta Denver Aerospace on the Passive and Active Control of Space Structures (PACOSS) program. The actuator is a linear DC motor with the permanent magnet field mounted on lov friction shafts and the armature fixed to a support housing. The PACOSS design has been modified to provide dual support shafts for the moving mass instead of the original single shaft. This eliminates the hole though the proof mass required for the single shaft and restores the 40% loss in output due to the hole in the permanent magnet. Proof mass centering is provide by mechanical springs. A linear velocity transducer (LVT) is used to measure relative velocity between the proof mass and the structure. The relative velocity is fed back through the actuator with an adjustable gain to provide damping in the actuator resonance. The actuator is capable of 1 pound force output in the frequency range of 2 Hz to 100 Hz.



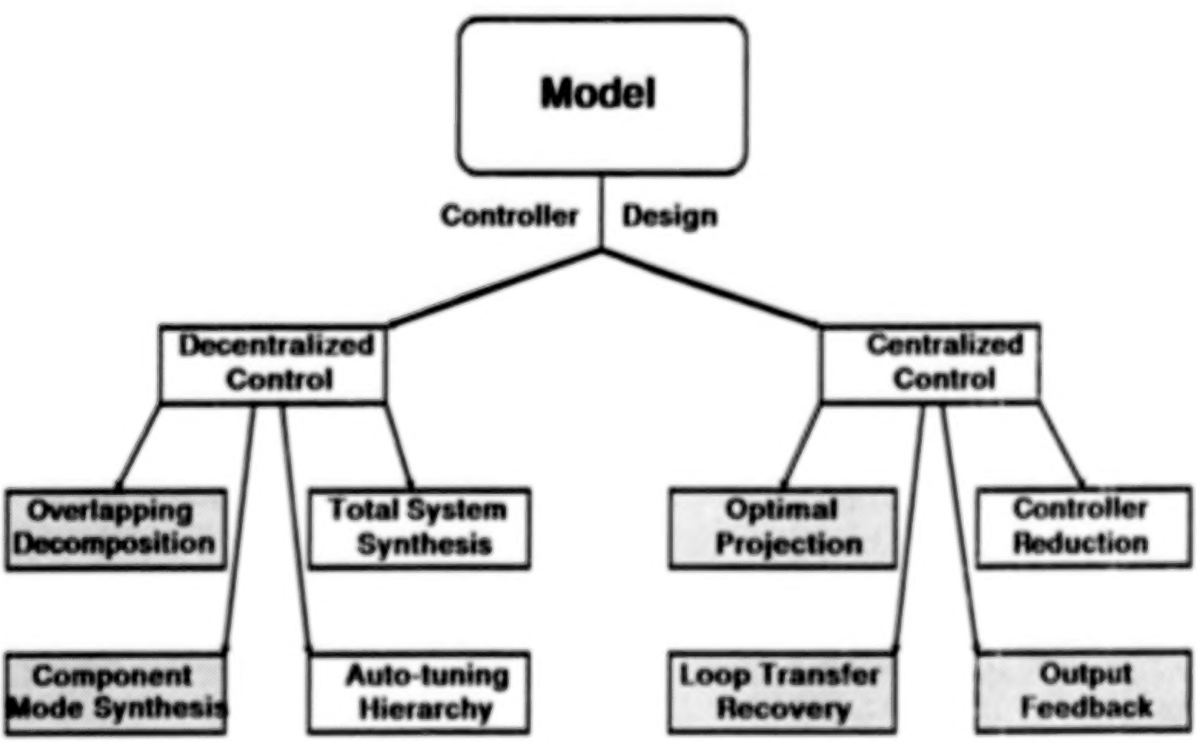
Real-Time Control Computer

A new digital computer system will be used to implement the active control approaches on the 12 meter truss and other future experiments at the Flight Dynamics Laboratory. The new system is based on the architecture that will be used to conduct Space Shuttle based control experiments. This architecture is based on the fact that the computer which executes the real-time control will not be directly accessible to the experimenter. It will be accessed only through data links and intermediate computers from a remote console on the ground. This is in contrast to the typical laboratory where a high speed development computer is fitted with data acquisition interfaces and real-time support modifications to its operating system. Such laboratory systems do not provide the necessary environment to develop experience for future flight experiments. The new system consists of two basic components; a development system and a real-time controller. The development system is a graphics workstation which is used for software design and simulation, system supervision and data analysis. The real-time controller is a fast, "black box" computer which executes the control and captures response data. The controller can be accessed only through a data interface from the development system. The controller has the same CPU as the development system so that software compiled on the development system will execute directly. A block diagram of the new system with some of the details of the real-time controller is shown in the figure.



Active Control Design for the 12 Meter Truss Experiment

Several active vibration control approaches are being pursued for the 12 Meter Truss Experiment. This work is being performed by Umit Ozguner and Steven Yurkovich of the Ohio State University under contract. The control approaches can be categorized as either centralized or decentralized types. In the centralized catagory, the design approaches being studied are Loop Transfer Recovery (LTR), Maximum Entropy / Optimal Projection and static output feedback. The decentralized approaches are Overlapping Decomposition, Total System Synthesis and Component Modal Synthesis. Also of interest in the future is the Auto-tuning Hierarchy control design. The figure portrays the several control design approaches being investigated. The control approaches shown in shaded blocks in the figure have been studied extensively in simulation runs on a preliminary finite element model of the control configured truss. The designs are implemented on a 28th order model made up of the 8 actuator modes and the lovest 4 bending and 2 torsion modes of the truss.



12 Meter Truss Active Controller Performance Predictions

Closed loop simulations have been performed on several of the active control approaches being pursued for the 12 Meter Truss Experiment. The approaches include the centralized techniques of LQG,* LTR, MEOP and static output feedback and the decentralized techniques of Overlapping Decomposition and Component Modal Synthesis. Closed loop damping estimates based on these control approaches are tabulated in the figure for the lowest 6 modes of the truss. The estimated open loop modal damping values are listed for comparison. The results for LQG, LTR and static output feedback are listed as a single column in the table since the results of these three approaches were nearly identical. Several observations can be made from the data. First, and most importantly, every control approach resulted in a significant increase in modal damping over open loop for every mode except 2nd torsion. Generally speaking, all the controllers did a better job of adding damping in the 2 first bending modes than in the higher modes and the decentralized approaches were better at adding damping to all six modes of interest than the centralized approaches were. These simulations will be compared to test data when the experimental hardware becomes operational in April or May 1989.

*Linear Quadratic Gaussian (LQG).

	OPEN-LOOP	LQG, LTR, OUTPUT FEEDBACK	MEOP	OVERLAPPING DECOMP	COMPONENT SYNTHESIS
1ST X BENDING	.80	9.36	4.49	8.02	7.24
1ST Y BENDING	.95	9.35	4.64	7.91	7.15
1ST TORSION	.15	0.96	0.95	6.46	6.54
2ND X BENDING	.16	1.45	1.38	3.19	2.97
2ND Y BENDING	.18	1.43	1.37	3.10	2.93
2ND TORSION	.11	0.17	0.17	1.01	1.02

Summary

In summary, the Flight Dynamics Laboratory is committed to an inhouse, experimental investigation of several technical areas critical to the dynamic performance of future Air Force large space structures. The Advanced Beam Experiment has been sucessfully completed and provided much experience in the implementation of active control approaches on real hardvare. A series of experiments is under way in evaluating ground test methods on the 12 meter trusses with significant passive damping. Ground simulated zero-g response data from the undamped truss will be compared directly with true zero-g flight test data. The performance of several leading active control approaches will be measured and compared on one of the trusses in the presence of significant passive damping. In the future, the PACOSS Dynamic Test Article will be set up as a test bed for the evaluation of system identification and control techniques on a complex, representative structure with high modal density and significant passive damping.

- **ADVANCED BEAM PROVIDED VALUABLE EXPERIENCE**
  - **LINEAR ACTUATOR DYNAMICS**
  - **CONTROLLER PERFORMANCE IN HARDWARE**
- **12 METER TRUSS MODAL TESTING IN PROGRESS**
  - **DATA FROM MULTIPLE BOUNDARY CONDITIONS**
  - **HIGH DAMPING IN TORSION MODES OF DAMPED TRUSS**
  - **ZERO-G FLIGHT TEST DATA TO COMPARE WITH GROUND TEST**
- **12 METER TRUSS ACTIVE CONTROL EXPERIMENT IN PREPARATION**
  - **8 ACTUATOR/SENSOR PAIRS**
  - **TEST SEVERAL ACTIVE CONTROL APPROACHES**
  - **EVALUATE CONTROLLER PERFORMANCE IN THE PRESENCE OF PASSIVE DAMPING**

NASA

Report Documentation Page

1. Report No.	2. Government Accession No.	3. Recipient's Catalog No.
NASA CP-3041		

4. Title and Subtitle	5. Report Date
NASA/DOD Controls-Structures Interaction Technology 1989	August 1989
	6. Performing Organization Code

7. Author(s)	8. Performing Organization Report No.
Jerry R. Newsom, Compiler	L-16602
	10. Work Unit No. 585-01-41-03

9. Performing Organization Name and Address	11. Contract or Grant No.
NASA Langley Research Center Hampton, VA 23665-5225	
	13. Type of Report and Period Covered: Conference Publication

12. Sponsoring Agency Name and Address	14. Sponsoring Agency Code
National Aeronautics and Space Administration Washington, DC 20546-0001	

15. Supplementary Notes

16. Abstract

This publication is a compilation of the papers presented at the Third NASA/DOD Controls-Structures Interaction (CSI) Technology Conference held in San Diego, California, January 29 - February 2, 1989. The conference, which was jointly sponsored by the NASA Office of Aeronautics and Space Technology and the Department of Defense, was organized by the NASA Langley Research Center. The purpose of this conference was to report to industry, academia, and government agencies on the current status of controls-structures interaction technology. The agenda covered ground testing, integrated design, analysis, flight experiments, and concepts.

17. Key Words (Suggested by Author(s))	18. Distribution Statement
Controls Structures Controls-structures interaction Large space systems Flexible structures	Unclassified - Unlimited Subject Category 18

19. Security Classif. (of this report)	20. Security Classif. (of this page)	21. No. of pages	22. Price
Unclassified	Unclassified	558	A24

NASA FORM 1626 OCT 86

For sale by the National Technical Information Service, Springfield, Virginia 22161-2171

NASA-Langley, 1989

National Aeronautics and
Space Administration
Code NTT-4

Washington, D.C.
20546-0001

Official Business
Penalty for Private Use, $300

NASA

National Aeronautics and
Space Administration

Washington, D.C.
20546

SPECIAL FOURTH CLASS MAIL
BOOK

Postage and Fees Paid
National Aeronautics and
Space Administration
NASA-451

Official Business
Penalty for Private Use $300

L: 001 CP-3041 0707243002370D
GOVERNMENT PRINTING OFFICE
LIBRARY PROGRAMS SERVICE/DLIA
ACQUISITIONS SECTION
WASHINGTON DC 20401

NASA

POSTMASTER: If Undeliverable (Section 158
Postal Manual) Do Not Return